HELLENIC REPUBLIC
National and Kapodistrian University of Athens
EST. 1837

School of Health Sciences

Department of Pharmacy

Section of Pharmaceutical Chemistry

Structure-based drug discovery research on the MmpL3 transporter of Mycobacterium tuberculosis and the M2 proton channel of Influenza A virus

PhD Dissertation

Marianna Stampolaki

Athens

2023

Supervisor:

Antonios Kolocouris, Professor, *Faculty of Pharmacy, Section of Pharmaceutical Chemistry, National and Kapodistrian University of Athens*

Seven member examination committee:

Antonios Kolocouris, Professor, *Faculty of Pharmacy, Section of Pharmaceutical Chemistry, National and Kapodistrian University of Athens*

Ioannis Papanastasiou, Associate Professor, *Faculty of Pharmacy, Section of Pharmaceutical Chemistry, National and Kapodistrian University of Athens*

Nikolaos Lougiakis, Associate Professor, *Faculty of Pharmacy, Section of Pharmaceutical Chemistry, National and Kapodistrian University of Athens*

Emmanouel Mikros, Professor, Director, *Faculty of Pharmacy, Section of Pharmaceutical Chemistry, National and Kapodistrian University of Athens*

Thomas Mavromoustakos, Professor, *Faculty of Chemistry, Section of Organic Chemistry, National and Kapodistrian University of Athens*

Loren Andreas, Professor, Group Leader, *Department of NMR-based Structural Biology, Max Planck Institute for Multidisciplinary Sciences*

Christian Griesinger, Professor, Director, *Department of NMR-based Structural Biology, Max Planck Institute for Multidisciplinary Sciences*

Abstract

SQ109 is a tuberculosis drug candidate that has high potency against *Mycobacterium tuberculosis* and is thought to function at least in part by blocking cell wall biosynthesis by inhibiting the MmpL3 transporter. It also has activity against bacteria and protozoan parasites that lack MmpL3, where it can act as an uncoupler, targeting lipid membranes and Ca^{2+} homeostasis. Here, we showed using molecular dynamics (MD) simulations that the binding profile of nine SQ109 analogs was consistent with the X-ray structure of MmpL3 – SQ109 complex. We showed that rotation of SQ109 around carbon–carbon bond in the monoprotonated ethylenediamine unit favors two *gauche* conformations as minima in water and lipophilic solvent using density functional theory (DFT) calculations as well as inside the transporter's binding area using MD simulations. Our results from MD simulations suggested that sizeable C-2 adamantyl adducts of SQ109 can fill a lipophilic region between Tyr257, Tyr646, Phe260 and Phe649 in MmpL3. This was confirmed quantitatively by our calculations of the relative binding free energies using the thermodynamic integration coupled with MD simulations method with a mean assigned error of 0.74 kcal mol^{-1} compared to the experimental values. We synthesized 18 analogs of SQ109 and tested them against *M. smegmatis*, *M. tuberculosis*, *M. abscessus*, *Bacillus subtilis*, and *Escherichia coli*, as well as against the protozoan parasites *Trypanosoma brucei*, *T. cruzi*, *Leishmania donovani*, *L. mexicana*, and *Plasmodium falciparum*. Activity against the mycobacteria was generally less than with SQ109 and was reduced by increasing the size of the alkyl adduct. Two analogs were ∼4−8-fold more active than SQ109 against *M. abscessus*, including a highly drug resistant strain harboring an A309P mutation in MmpL3. There was also better activity than found with SQ109 with other bacteria and protozoa. Of particular interest, we found that the adamantyl C-2 ethyl, butyl, phenyl, and benzyl analogs had 4−10× increased activity against *P. falciparum* asexual blood stages, together with low toxicity to a human HepG2 cell line, making them of interest as new antimalarial drug leads. We also used surface plasmon resonance (SPR) to investigate the binding of inhibitors to MmpL3 and differential scanning calorimetry to investigate binding to lipid membranes. There was no correlation between MmpL3 binding and *M. tuberculosis* or *M. smegmatis* cell activity, suggesting that MmpL3 is not a major target in mycobacteria. However, some of the more active species decreased lipid phase transition temperatures, indicating increased accumulation in membranes, which is expected to lead to enhanced uncoupler activity.

The tetrameric influenza A M2 proton channel is critical for viral replication. Proton conductance of the wild type (WT) protein, with serine at position 31, is inhibited by cage alkyl amines, like amantadine,

rimantadine and analogs, which bind in the channel pore. Conjugates of a cage alkyl amine with a methylene-linked aryl group have been shown to block the channel of the prevalent S31N strain with a different mechanism. Here, we investigate the binding and blocking of WT and S31N M2 (Udorn strain) by an expanded set of cage alkyl containing amines. Using a liposomal proton flux assay, we verified the channel-blocking activity of rimantadine (Rmt), its methyl analog AK59, and the tetramethyltetracyclodec-1-ylmethylamine (RL208), an isomer of amantadine for the conductance domain of WT M2 (M2CD; residues 18-60). The binding behavior of the ligands was explored using magic angle spinning NMR by recording 2D and 3D ^{1}H-^{15}N and ^{1}H-^{13}C-^{15}N spectra of M2CD reconstituted in DPhPC lipids. Ligand binding to WT M2 was detected via chemical shift perturbation (CSP). High kinetic energy barriers associated with entry into the M2CD pore were overcome by increased temperature or a pH shift protocol which proved to be more efficient. To assess the binding mode, MD simulations were performed. Cage alkyl amines Rmt and AK59 are known to block WT M2 with their ammonium group binding to water-lined sites at Gly34 or Ala30. By contrast, MD simulations show that the conjugates with an aryl group bind outward in S31N M2CD targeting Asn31. For S31N, the His37-His37 hydrogen bonding was not disrupted according to NMR, nor was the channel blocked in the liposomal proton flux assay. Our data suggest that there is a substantial structural barrier in the amphipathic helicix (AH)-bearing CD construct, which limits entry of RL208 and aryl conjugates.

Keywords: SQ109, MmpL3, MD simulations, alchemical relative binding free energy, MM-GBSA, binding affinity, organic synthesis, calorimetry, tuberculosis, malaria, leishmaniasis, adamantyl amine, cage alkyl amine, influenza A, S31N M2, WT M2, magic angle spinning, solid state NMR, liposomal proton flux assay.

ΠΕΡΙΛΗΨΗ

Το SQ109 είναι ένα υποψήφιο φάρμακο για τη φυματίωση που παρουσιάζει υψηλή δραστικότητα κατά του *Mycobacterium tuberculosis* και θεωρείται ότι λειτουργεί εν μέρει μέσω της παρεμπόδισης της βιοσύνθεσης του κυτταρικού τοιχώματος αναστέλλοντας τον μεταφορέα MmpL3. Επίσης παρουσιάζει δραστικότητα έναντι βακτηρίων και πρωτόζωων παρασίτων που στερούνται MmpL3, όπου μπορεί να δράσει ως αποζεύκτης, στοχεύοντας στις λιπιδικές μεμβράνες και την ομοιόσταση του Ca^{2+}. Σε αυτή την ερευνητική εργασία, δείξαμε χρησιμοποιώντας προσομοιώσεις μοριακής δυναμικής (MD) ότι το προφίλ πρόσδεσης εννέα αναλόγων του SQ109 ήταν συνεπές με τη X-ray κρυσταλλογραφική δομή του συμπλόκου MmpL3 - SQ109. Δείξαμε ότι η περιστροφή του SQ109 γύρω από τον δεσμό άνθρακα-άνθρακα στη μονοπρωτονιωμένη μονάδα αιθυλενοδιαμίνης ευνοεί δύο *gauche* διαμορφώσεις ως ενεργειακά ελάχιστα στο νερό ή στον λιπόφιλο διαλύτη χρησιμοποιώντας υπολογισμούς DFT καθώς και εντός της περιοχής πρόσδεσης του μεταφορέα χρησιμοποιώντας προσομοιώσεις μοριακής δυναμικής. Τα αποτελέσματά μας από τις προσομοιώσεις μοριακής δυναμικής υπέδειξαν ότι οι ευμεγέθεις C-2 αδαμαντυλικοί υποκαταστάτες του SQ109 μπορούν να γεμίσουν μια λιπόφιλη περιοχή μεταξύ των Tyr257, Tyr646, Phe260 και Phe649 στην πρωτεΐνη MmpL3. Αυτό επιβεβαιώθηκε ποσοτικά από τους υπολογισμούς των σχετικών ελεύθερων ενεργειών δέσμευσης με τη χρήση της μεθόδου θερμοδυναμικής ολοκλήρωσης σε συνδυασμό με προσομοιώσεις μοριακής δυναμικής (TI/MD) μ' ένα μέσο αποδιδόμενο σφάλμα 0,74 kcal mol^{-1} σε σύγκριση με τις πειραματικές τιμές. Συνθέσαμε 18 ανάλογα του SQ109 και δοκιμάσαμε τη δραστικότητά τους έναντι των *M. smegmatis*, *M. tuberculosis*, *M. abscessus*, *Bacillus subtilis* και *Escherichia coli*, καθώς και έναντι των πρωτοζωικών παρασίτων *Trypanosoma brucei*, *T. cruzi*, *Leishmania donovani*, *L. mexicana* και *Plasmodium falciparum*. Η δραστικότητα έναντι των μυκοβακτηριδίων ήταν γενικά μικρότερη από ό,τι με το SQ109 και μειώθηκε με την αύξηση του μεγέθους του αλκυλικού υποκαταστάτη. Δύο ανάλογα ήταν ~4-8 φορές πιο δραστικά από το SQ109 έναντι του *M. abscessus*, συμπεριλαμβανομένου ενός στελέχους με υψηλή αντοχή στα φάρμακα που έφερε μετάλλαξη A309P στη MmpL3 πρωτεΐνη. Υπήρξε επίσης καλύτερη δραστικότητα από αυτή που διαπιστώθηκε με το SQ109 σε άλλα βακτήρια και πρωτόζωα. Ιδιαίτερο ενδιαφέρον παρουσιάζει το γεγονός ότι τα ανάλογα του στη C-2 θέση του αδαμαντυλίου, αιθυλο, βουτυλο, φαινυλο και βενζυλο είχαν 4-10 φορές αυξημένη δραστικότητα έναντι των άφυλων σταδίων αίματος του *P. falciparum*, σε συνδυασμό με χαμηλή τοξικότητα σε ανθρώπινη κυτταρική σειρά HepG2, γεγονός που τα

καθιστά ενδιαφέροντα ως νέα φάρμακα οδηγούς για την καταπολέμηση της ελονοσίας. Χρησιμοποιήσαμε επίσης τη μέθοδο του επιφανειακού συντονισμού πλασμονίου (surface plasmon resonance – SPR) για να διερευνήσουμε την πρόσδεση των αναστολέων στον μεταφορέα MmpL3 και τη διαφορική θερμιδομετρία σάρωσης (differential scanning calorimetry – DSC) για να διερευνήσουμε την αλληλεπίδραση με λιπιδικές μεμβράνες. Δεν υπήρξε συσχέτιση μεταξύ της πρόσδεσης στον MmpL3 και της κυτταρικής δραστηριότητας στο *M. tuberculosis* ή *M. smegmatis*, γεγονός που υποδηλώνει ότι η MmpL3 πρωτεΐνη δεν αποτελεί σημαντικό στόχο στα μυκοβακτηρίδια. Ωστόσο, ορισμένα από τα πιο δραστικά ανάλογα μείωσαν τη θερμότητα μετάβασης της λιπιδικής φάσης, γεγονός που υποδηλώνει αυξημένη συσσώρευση στις μεμβράνες, η οποία αναμένεται να οδηγήσει σε αυξημένη δραστικότητα των αναλόγων ως αποσυζεύκτες.

Το τετραμερές κανάλι πρωτονίων της γρίπης Α M2 είναι κρίσιμο για την αντιγραφή του ιού. Η αγωγιμότητα πρωτονίων της πρωτεΐνης άγριου τύπου (WT), με σερίνη στη θέση 31, αναστέλλεται από αλκυλοαμίνες που περιέχουν αδαμαντάνιο ή άλλου τύπου κλωβό, όπως η αμανταδίνη, η ριμανταδίνη και τα ανάλογα τους, οι οποίες δεσμεύονται στον πόρο του καναλιού. Έχει αποδειχθεί ότι τα ανάλογα αυτών των παραγώγων που περιέχουν αρυλική ομάδα συνδεδεμένη με μεθυλένιο στην αμινομάδα εμποδίζουν το κανάλι του επικρατούντος στελέχους S31N με διαφορετικό μηχανισμό. Εδώ, διερευνούμε τη πρόσδεση και τον αποκλεισμό του WT και του S31N M2 καναλιού (στέλεχος Udorn) από ένα διευρυμένο σύνολο αλκυλικών αμινών που περιέχουν κλωβό. Χρησιμοποιώντας μια ανάλυση λιποσωμικής ροής πρωτονίων (liposomal proton flux assay), επαληθεύσαμε τη δραστικότητα αποκλεισμού της αγωγιμότητας του WT M2 διαύλου (M2CD - αμινοξέα 18-60) από τη ριμανταδίνη (Rmt), το μεθυλικό αναλόγο της, AK59, και ενός ισομερούς της αμανταδίνης - την τετραμεθυλοτετρακυκλοδεκ-1-υλομεθυλαμίνη, RL208. Η συμπεριφορά πρόσδεσης των προσδετών διερευνήθηκε με τη χρήση μαγικής γωνίας περιστροφής πυρηνικού μαγνητικού συντονισμού (magic angle spinning NMR) καταγράφοντας 2D και 3D φάσματα ^{1}H-^{15}N και ^{1}H-^{13}C-^{15}N του M2CD διαύλου που έχει ανασυσταθεί σε DPhPC λιπίδια. Η πρόσδεση του προσδέτη στο WT M2 δίαυλο ανιχνεύθηκε μέσω διαταραχής της χημικής μετατόπισης (chemical shift perturbation - CSP). Οι φραγμοί υψηλής κινητικής ενέργειας που σχετίζονται με την είσοδο στον πόρο M2CD ξεπεράστηκαν με αύξηση της θερμοκρασίας ή με τη χρήση πρωτοκόλλου αλλαγής του pH, το οποίο αποδείχθηκε πιο αποτελεσματικό. Για την αξιολόγηση του τρόπου πρόσδεσης πραγματοποιήθηκαν προσομοιώσεις μοριακής δυναμικής. Τα ανάλογα Rmt και AK59 είναι γνωστό ότι παρεμποδίζουν το WT M2 δίαυλο με την ομάδα αμμωνίου να δεσμεύει την περιοχή κοντά στη Gly34 ή Ala30 που περιβάλλονται από νερό. Αντίθετα, οι προσομοιώσεις μοριακής δυναμικής δείχνουν ότι τα

παράγωγα με την αρυλική ομάδα προσδένονται με κατεύθυνση προς τα έξω στον δίαυλο S31N M2CD στοχεύοντας την Asn31. Όσον αφορά τον δίαυλο S31N, ο δεσμός υδρογόνου His37-His37 δεν διαταράχθηκε σύμφωνα με το NMR, ούτε τα μόρια παρεμπόδισαν τον δίαυλο στην ανάλυση λιποσωμικής ροής πρωτονίων. Τα δεδομένα μας υποδηλώνουν ότι υπάρχει ένα ουσιαστικό δομικό εμπόδιο στην δομή της M2CD η οποία φέρει τις αμφιπαθικές έλικες (AH), γεγονός το οποίο περιορίζει την είσοδο του αναλόγου RL208 και των αρυλικών προσδετών.

Λέξεις-κλειδιά: SQ109, MmpL3, προσομοιώσεις μοριακής δυναμικής, αλχημική σχετική ελεύθερη ενέργεια πρόσδεσης, MM-GBSA, συγγένεια πρόσδεσης, οργανική σύνθεση, θερμιδομετρία, φυματίωση, ελονοσία, λεϊσμανίαση, αδαμαντυλοαμίνη, αλκυλοαμίνη κλωβού, ιός γρίπης A, S31N M2, WT M2, μαγική γωνία περιστροφής, NMR στερεάς κατάστασης, ανάλυση λιποσωμικής ροής πρωτονίων.

Acknowledgments

This PhD dissertation is a result of a combining work that was conducted in the research lab of "Computational Drug Design and Synthesis" of Professor Antonios Kolocouris at NKUA and the department of NMR-based structural biology at MPI Göttingen under the supervision of Dr. Loren Andreas.

I want to express my warm gratitude to my supervisor Professor **Antonios Kolocouris**, for his supervision, guidance and important advice and valuable help throughout the whole PhD and former studies. I thank wholeheartedly the group leader Dr **Loren Andreas** for his guidance, excellent collaboration, and all the knowledge I gained from him throughout my stay at the Max Planck Institute.

I thank my colleagues and the whole community both in NKUA and MPINAT for their considerable help and knowledge transfer on computational chemistry, organic synthesis, drug design, and biophysical methods and for creating a warm, friendly, and enjoyable working environment.

I also thank all the collaborators for their valuable contribution to the projects, which without this research would not be possible. Namely the collaborators and their affiliation:

Costas Demetzos, **Nikolaos Naziris**, **Maria Chountoulesi**, Department of Pharmaceutical Technology, NKUA for the DSC experiments.

Eric Oldfield, **Satish R. Malwal**, and coworkers, University of Illinois, USA, for testing against M. smegmatis, B. subtilis, and E. coli.

Santiago Vázquez, **Andreea L. Turcu**, and coworkers, Universitat de Barcelona, for the HRMS experiments, microsomal stability, and solubility studies.

Joo Hwan No, and coworkers, Institut Pasteur Korea, for testing against T. brucei, T. cruzi, and L. donovani.

Helen I. Zgurskaya, and coworkers, Stephenson Life Sciences Research Center, USA, for binding assays.

Gustavo Benaim, and coworkers, Instituto de Estudios Avanzados, Caracas, Venezuela, for testing against L. mexicana.

Michael Cynamon, **Carolyn Shoen**, and coworkers, Veterans Affairs Medical Center, Syracuse, USA, for testing against MtbErdman and MtbH37Rv.

Lyn-Marie Birkholtz, and coworkers, University of Pretoria, South Africa, for testing against P. falciparum parasites and HepG2 assays.

Laurent Kremer, and coworkers, Institut de Recherche en Infectiologie de Montpellier, France

Thomas Dick, and coworkers, Hackensack Meridian Health Center for Discovery and Innovation, New Jersey, USA, for testing against against Mtb HN878.

Lastly, I express my biggest gratitude to my family for their continuous support and strength that accompanied me through all my academic years.

Table of Contents

List of Figures

List of Schemes

List of Tables

Abbreviations

AH – Amphipathic Helices
Amt – Amantadine
CCCP – Carbonyl cyanide m-chlorophenylhydrazone
CD – Conductance Domain
COM – Center Of Mass
Cryo-EM – Cryogenic Electron Microscopy
CSP – Chemical Shift Perturbation
DEAD – Diethyl azodicarboxylate
DFT – Density Functional Theory
DMPC – 1,2-dimyristoyl-sn-glycero-3-phosphocholine
DPhPC – 1,2-diphytanoyl-sn-glycero-3-phosphocholine
DSPG – 1,2-distearoyl-sn-glycero-3-phosphoglycerol
DSC – Differential Scanning Calorimetry
EP – Electrophysiology
GAFF – Generalized Amber Force Field
GF – Front Gate
GB – Back Gate
GT – Top Gate
HA – Hemagglutinin
HFIP – Hexafluoroisopropanol
HOSA – Hydroxylamine-O-sulfonic acid
HRMS – High-resolution Mass Spectrometry
M1 – Matrix protein 1
M2 – Matrix protein 2
MAS – Magic Angle Spinning
MD – Molecular Dynamics
MM-GBSA – Molecular Mechanics-Generalized Born Surface Area
MmpL3 – Mycobacterium membrane protein Large 3
Mtb – Mycobacterium tuberculosis
NA – Neuraminidase
NMR – Nuclear Magnetic Resonance
OPM – Orientations of Proteins in Membranes
PBS – Phosphate-buffered saline
PCM – Polarizable Continuum Model
PD – Periplasmic Domain
PME – Particle Mesh Ewald
PMF – Proton Motive Force
POPE – 1,2-dimyristoyl-sn-glycero-3-phosphoethanolamine
POPC – 1-palmitoyl-2-oleoyl-sn-glycero-3-phosphocholine
Rmt – Rimantadine
RMSD – Root Mean Square Deviation
RND – Resistance Nodulation cell Division
RNP – Ribonucleoprotein
SID - Simulation Interaction Diagram
SPR – Surface Plasmon Resonance
SsNMR – Solid state NMR
TB – Tuberculosis
THF – Tetrahydrofuran
TMM – Trehalose Monomycolate
TM – Transmembrane
TI – Thermodynamic Integration
TPPM – Two Pulse Phase Modulation
WT – Wild Type

1 Introduction

Infectious diseases have been a burden to humanity since premodern times. The continental colonization brought with it war and consequently slavery and poverty, in other words, a favorable ground for the spread of infectious diseases (tuberculosis, polio, smallpox, diphtheria, malaria, etc.) with devastating consequences on human life. The advances in the development of countermeasures (vaccines, drugs, therapeutics, and health care) through the historical progression of human societies have dramatically lowered the high mortality rates linked to infectious diseases. However, despite those advances, a considerable burden still lingers in low-income countries, where sanitation and access to proper health care are scarce. [1] The recent example of COVID-19 made the danger of emerging and re-emerging infections more realistic and alarming, pointing to a new era of infectious diseases that might be a worldwide threat. [2–4] The risk of pathogen emergence or re-emergence and spread will increase due to the urgent problem of climate change in the forthcoming decades. Notably, climate change could modify the worldwide distribution of pathogens, enabling diseases to expand their reach into previously uncharted territories. [5,6]

Despite the vast developments in vaccine technology and the fact that vaccines are still the prime tool to control and eliminate the spread of an infectious disease, the recent pandemic has underscored the importance of the health system having alongside in their toolbox highly effective drug agents. Hence, it is evident that one of the outcomes arising from the COVID-19 pandemic is the global imperative for scientists and researchers to maintain a steadfast focus on drug research of highly potent therapeutics against infectious diseases, given the unpredictable evolution of pathogens in nature. [7,8]

This work focuses on two well-known infectious diseases, tuberculosis and flu, caused by Mycobacterium tuberculosis and Influenza A virus, respectively. It explores the drug design of novel inhibitors by utilizing methods and tools from medicinal and computational chemistry, structural biology, and biophysics as a holistic approach that can shed a broader light on the mechanism of action and the structural features of potent analogs. One aim of this research besides the design and the production of these analogs is to show how the combination of different scientific fields of research can facilitate drug development. In the next sections of the introduction, the reader can delve into a detailed representation of this study's two subjects, which include the protein target of the drug leads, the progress made up to date and related findings, and an overview of our drug discovery research.

1.1 Mycobacterium tuberculosis and MmpL3 transporter

In 2020 an estimated 1.9 million people died from tuberculosis (TB), according to the World Health Organization, [9] which is the leading cause of death among carriers of HIV. [10,11] The usual treatment consists of a combination of antibiotics (isoniazid, rifampicin, pyrazinamide, ethambutol) prescribed for six months, and can cure most people if the patients' care is under optimal conditions. From a global perspective, the cure rates are less than optimal. The reason is the reduced patient compliance to the long-term chemotherapy accompanied by side effects such as drug toxicity, and the fact that some *Mycobacterium tuberculosis* (*Mtb*) strains have acquired genetic mutations that render them resistant to most antibiotics. [12,13] Therefore, there is a need for new, potent antitubercular drugs that, in combination, create shorter, safer and simpler regimens against fully drug susceptible and drug-resistant TB strains. [10,11,14,15]

Numerous clinical trials of drug-resistant TB were completed in the last decade, providing promising new agents from various drug classes (aminoglycosides, thioamides, nitroimidazoles, fluoroquinolones, diarylquinoline, macrolides, oxazolidinones, ethylenediamines, etc.) [13,15,16] that could improve cure rates and shorten the therapy duration. Most of the antitubercular drugs or lead compounds under development target mycobacterial cell wall biosynthesis. The mycobacterial cell wall (Figure 1) is a complex structure that provides membrane stability and a barrier against the host environment and antibiotics; thus, it contributes to the intrinsic resistance of the organism. As a result, the cell wall is vital for the mycobacteria, and blocking its assembly would lead to inhibition of mycobacteria's growth. [17,18] In this part of mycobacterial research, we focus on a second generation ethylenediamine that was developed after the drug ethambutol, SQ109 (N-Geranyl-N′-(2-adamantyl)ethane-1,2-diamine) [19] which is in phase IIb/III of clinical trials and shows high potency against resistant *Mtb*. [20,21] One mechanism of SQ109's anti-TB activity has been proposed to be the inhibition of the mycobacterial membrane protein Large 3 (MmpL3) transporter of trehalose monomycolate (TMM). [20–25]

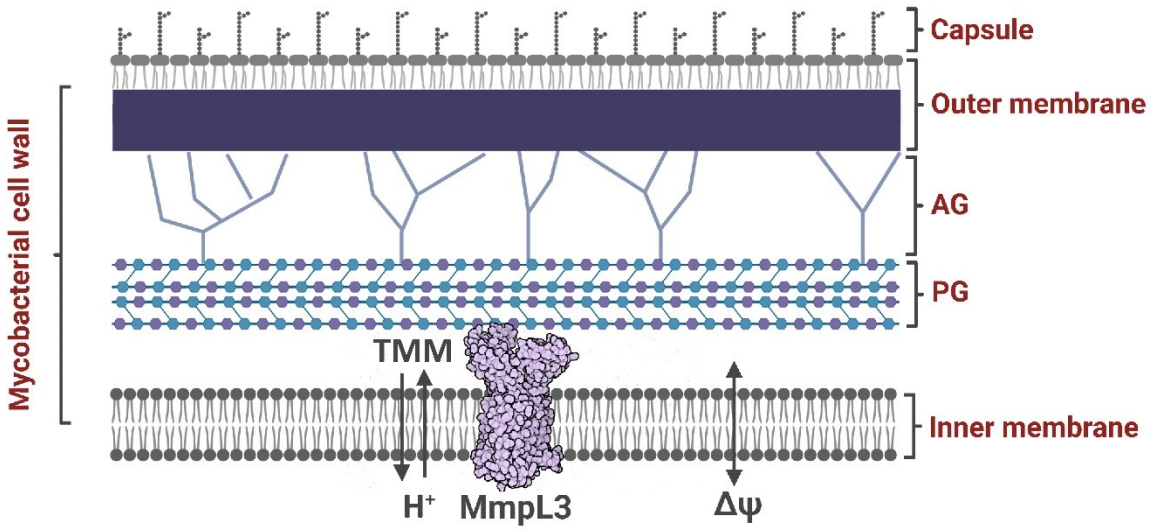

Figure 1 Schematical representation of the mycobacterial cell wall and its components: a capsule that mainly consists of polysaccharides and proteins; an impermeable asymmetrical outer membrane; arabinogalactan (AG); peptidoglycan (PG); a phospholipid inner membrane where MmpL3 transporter is located. The double arrow presents the membrane potential (Δψ). The two antiparallel arrows present the antiport mechanism of MmpL3 in which the protons flow to the cytoplasm to energize the TMM translocation to the periplasm by MmpL3.

MmpL3 is an inner membrane protein of 944 amino acids (101 kDa) and belongs to the RND protein superfamily (Resistance Nodulation cell Division proteins) (Figure 2). It consists of (a) one periplasmic domain composed of two subdomains, PD1 and PD2 (Figures 2A), that merge in such way to create a central cavity, and three openings or gates which could allow specific molecules to enter or exit, (b) a transmembrane domain comprised of 12 helixes, and (c) one big unstructured cytoplasmic domain whose its function is being speculated. [22,26] MmpL3, as a part of the cell envelope, is essential for the translocation of mycolic acids in the form of trehalose monomycolate (TMM) from their production site in the cytoplasm to the periplasmic space, where mycolic acids can then be used in assembly of the *Mtb* outer membrane. It has been shown that MmpL3 function is inhibited by molecules that alter the transmembrane potential (Δψ) or transmembrane electrochemical proton gradient (ΔpH) or both components of proton motive force (PMF). MmpL3 is a proton motive force (PMF)-dependent transporter that functions via an antiport mechanism, coupled with the movement of substrates toward the periplasm, protons flow into the cytoplasm to energize this translocation process. [25] Two pairs of hydrophilic amino acids Asp-Tyr (Asp256-Tyr646 and Asp645-Tyr257), which link the two helices by forming hydrogen bonds with their side chains,

allow the proton translocation (Figure 2B, C). These Asp-Tyr pairs are a conserved feature of the MmpL family of transporters. [22,27,28] In 2019, the X-ray structures (PDB ID 6AJG) [22] of MmpL3 in complex with SQ109 and other inhibitors of *Mtb* and in complex with one molecule of 1,2-dimyristoyl-sn-glycero-3-phosphoethanolamine (POPE) (PDB ID 6OR2) [26] became available providing a platform for structure-based drug design. Afterwards, structures of the apo-protein [29,30] or in complex with ligands [31,30] became available using cryogenic electron microscopy (cryo-EM) or X-ray crystallography. A very recent computational research work [32] on apo and SQ109 bound MmpL3 structures [22,26] proposes a theoretical translocation mechanism of MmpL3. They suggest a linked movement of TM and periplasmic domain (PD) by protonation of key residues inside the TM (Figure 3). Taking a closer look, water passes through the TM pore and protonates polar residues such as Asp257, Asp645, Tyr256, and Tyr646 which move away from each other by charge repulsion. That leads to a conformational change of TM7 and TM8 which subsequently closes the entry gate of TMM that is located in the PD between TM7 and TM8. This closing induces the formation of a bigger central cavity volume that accommodates the TMM substrate deeper between PD1–PD2 (Figure 3). It is assumed that the TMM substrate binds to PD while water protonates Asp257 and TM domain opening occurs. The release of TMM takes place when the channel pumps water out and thus the polar residues deprotonate resulting in closing of the TM domain and opening again of PD. Consequently, SQ109 must inhibit TMM binding allosterically by blocking the proton transport pathway. SQ109 interacts with the key residues and disrupts Asp645⋯Tyr257 and Asp256⋯Tyr646 H-bonding. Thus, it prevents the channel from closing and locks the TM domain in an open conformation. That way it doesn't allow the TMM translocation through the PD channel.

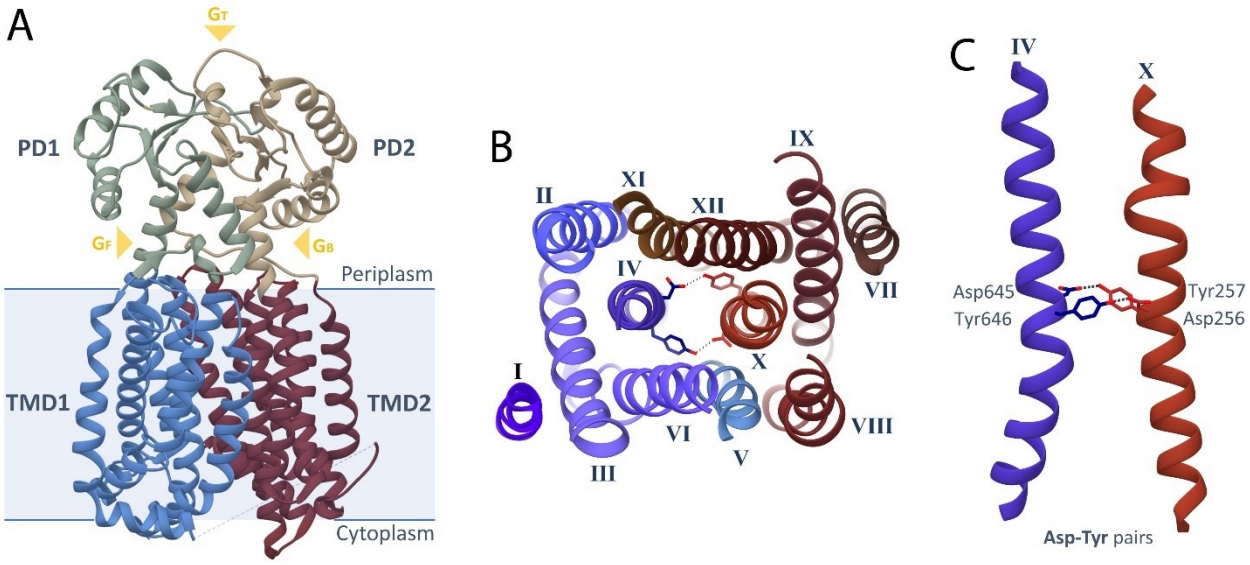

Figure 2 Crystal structure of MmpL3; PDB ID (6AJF) [22] (A) Different domains of MmpL3 structure; N-/C-terminal periplasmic subdomain (PD1/PD2); top gate (GT), front gate (GF), back gate (GB); N-/C-terminal transmembrane domain (TMD1/TMD2); the cytoplasmic domain is missing in the crystal structure. (B) Arrangement of the 12 transmembrane helices, and (C) the two conservative Asp-Tyr pairs that connect through hydrogen bond the two core transmembrane core helices IV and X.

Previous research has suggested similarly that SQ109 inhibitors can function by directly blocking the transporter's pore [22,24], but also indirectly [33,34] by acting as an uncoupler while preventing the movement of protons, *ie.* PMF downhill the electrochemical potential across the membrane (Figure 1). The latter can be accomplished by the membrane's structure perturbation [33–36] which may lead to an increase in the membrane lipid disorder/fluidity and, arguably, uncoupler activity. However, it has been concluded using *in vitro* MmpL3 binding and uncoupler assays that MmpL3 inhibitors activity on PMF and ΔpH is not a consequence of the suppression of MmpL3 activity but rather of secondary effects of these compounds. [24]

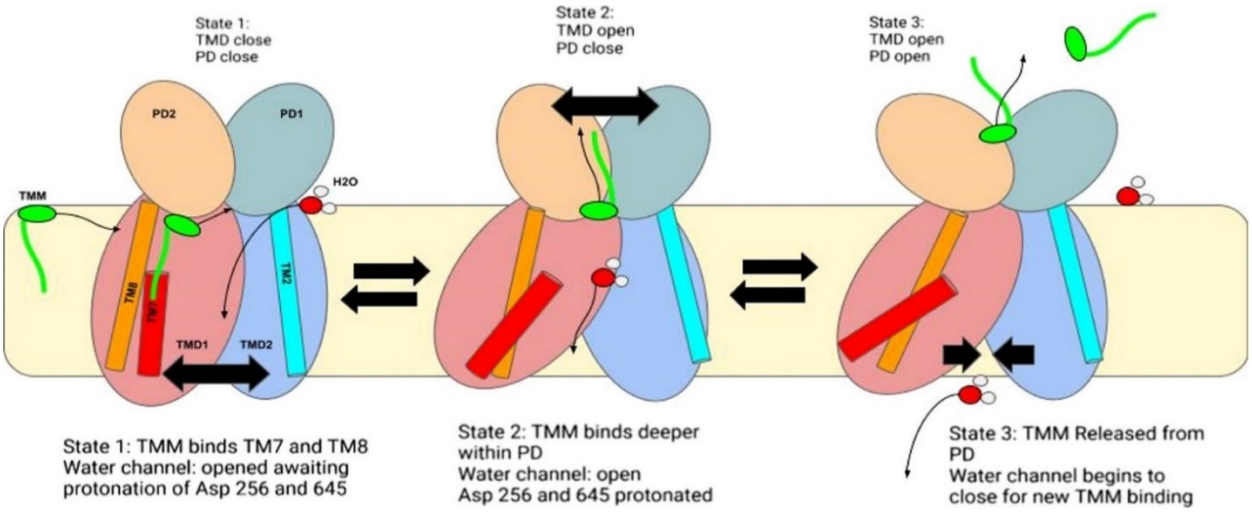

Figure 3 Proposed mechanism of the MmpL3 antiporter. Water enters the channel, while the TMM substrate (green) binds to the TMM binding site between TM8 (red) and TM7 (orange) (state 1). Water fills the central channel and causes protonation of polar residues within the channel, leading to repulsion of TMD2 from TMD1. This conformational change induced the closing of the TMM entry channel, which led the TMM substrate to translocate deeper between PD1–PD2 (state 2). As water begins to empty out of the water channel, polar residues holding the channel open will return to their normal interactions causing the closing of the channel and opening of the PD, allowing for TMM exit and re-entry (state 3). [32]

SQ109 also has a growth inhibitory activity against other bacteria (eg. *Helicobacter pylori* [37,38]), fungi (eg. *Candida albicans* [34]), malaria parasites (e.g., Plasmodium falciparum [39]), and the trypanosomatid parasite *Trypanosoma cruzi*, [40] all of which lack the MmpL3 gene or at least close homologs. In these organisms, there must be other targets/mechanisms of action. SQ109 analogs might thus be of interest as anti-infective leads against a range of organisms. There is, therefore, interest in the synthesis and testing of SQ109 analogs because these might have enhanced activity against not only mycobacteria but also other bacteria as well as protozoa, yeasts, and fungi.

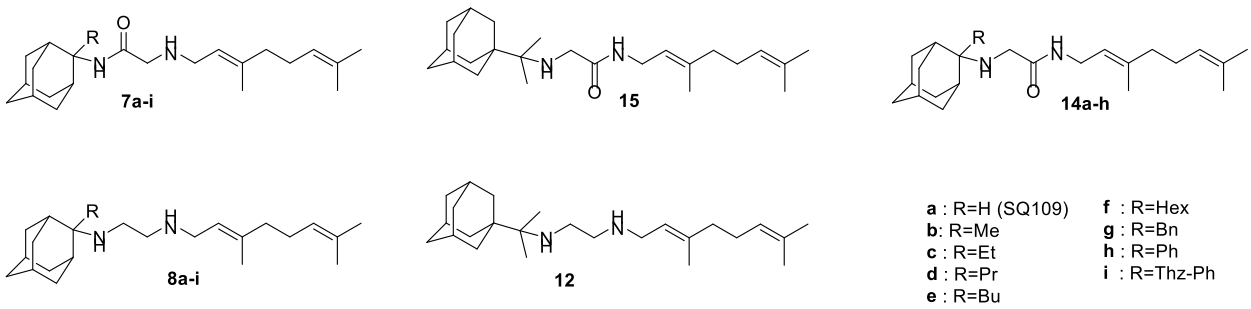

Scheme 1 Structure of SQ109 analogs that were synthesized and tested against Mycobecterium tuberculosis and other pathogens.

Molecular docking calculations and MD simulations suggested the installation of alkyl, aryl, or heteroaryl groups at C2-adamantyl position of SQ109. We synthesized and tested a series of new analogs of SQ109 against the following mycobacteria: *M. smegmatis*, *M. tuberculosis* HN878, *M. tuberculosis* Erdman (MtErdman), *M. tuberculosis* H37Rv (MtH37Rv), and *M. abscessus*. In addition, we tested these analogs against *Bacillus subtilis*; *Escherichia coli*; *Plasmodium falciparum* asexual blood stages; human hepatocyte carcinoma cells; *Trypanosoma brucei* bloodstream forms; *T. cruzi* epimastigotes, amastigotes, and their U20S host cells; *L. donovani* promastigote; and *L. mexicana* promastigotes. We also explored the interaction of SQ109 and its analogs against MmpL3 using surface plasmon resonance (SPR) [24], binding free energy calculations with the Molecular Mechanics-Generalized Born Surface Area (MM-GBSA) method, or alchemical free energy perturbation calculations using Thermodynamic Integration coupled with MD simulations (TI/MD) [41–44], in addition to using differential scanning calorimetry (DSC) [45,46] to explore the interactions of a subset of compounds with lipid bilayer membranes.

1.2 Influenza A virus and M2 proton channel

Influenza A virus still places a heavy burden on society, not only due to the five pandemics since 1889, but also due to seasonal H1N1, H3N2 strains.[47] Influenza can cause severe illness or even death, especially among high-risk groups. Therapeutics such as small molecule inhibitors are the first in line against virus infection, while before vaccines are accessible are the main tool available. Consequently, the development of new potent therapeutics against circulating influenza strains remains of critical importance.

The influenza A matrix 2 (M2) protein is a 97-residue single-pass homotetrameric membrane protein. It contains a short unstructured N-terminal, extracellular domain (residues 1-24) which is highly conserved and suggested to assist M2 incorporation into the virion, [48] a single transmembrane (TM) domain (residues 25-46), and a long C-terminal intracellular tail (residues 47-97) which interacts with the M1 protein. [49] Influenza M2 protein plays a key role during the early and late stages of the virus life cycle. The M2 protein forms a membrane-spanning acid-activated proton selective channel. [50,51] When the virus enters and infects a cell by endocytosis, the influenza M2 channel is activated in response to the lower pH of the endosome, [52] resulting in proton transport into the virus interior, which triggers the release of the viral RNA [53] and replication by the host cell. [54] In a later stage of virus replication, the M2 protein maintains the high pH of the trans-Golgi network and thus prevents premature conformational changes in hemagglutinin (HA) that occur at low pH to trigger membrane fusion. [55] M2 protein also affects plasma membrane deformation and membrane scission, through its amphipathic helix (AH), which begins at residue 47 and includes up to residues 60, 61, or 62 in reconstituted samples. The AH is needed for virus budding. [56–58] The TM together with the AH form the functional core of M2, which is called the M2 conductance domain (M2CD [59]) since it precisely reproduces the proton transport properties of full-length M2 (M2FL). [60] Four His37 residues, known to be the heart of the proton conducting channel, reside near the center of the TM helix and are the key to the proton transport mechanism. [61]

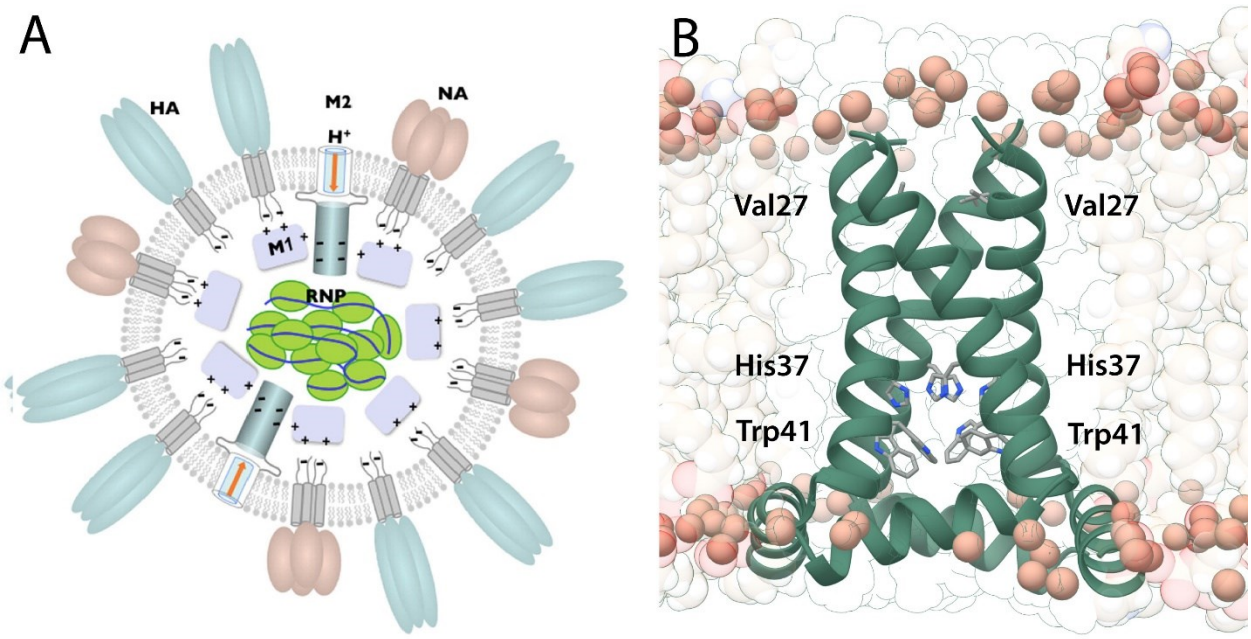

Figure 4 (A) Model of the viral particle; HA - hemagglutinin, NA - neuraminidase, M2 - matrix protein 2, M1 - matrix protein 1, RNP – ribonucleoprotein. [62] (B) $M2_{22-62}$ structure in lipid bilayer; PDB ID (2L0J) [63]. Three residue tetrads are depicted in TM domain; His37 is the proton-conducting residue of the channel; Trp41 is the channel-gating residue; Val27 corresponds to the secondary gate of proton entrance. Protein helices are shown in dark green colour, lipid heads in orange spheres and lipid tails are transparent.

Figure A is supplied from the article of Rafal M. Pielak, James J. Chou "Influenza M2 proton channels", license is acquired from Elsevier.

The channel activity is mediated by the His37xxxTrp41 sequence in the C-terminal half of the TM tetrameric helical bundle (Figure 4B), which is a characteristic motif for influenza proton channels. [64] It is the unique chemistry of this His37xxxW41 quartet that accounts for acid activation, proton selectivity [51] against other cations, and gating of the channel. In TM domain, His37 is the proton-conducting residue of the channel [65] and Trp41 is the channel-gating residue. [66] Neither His37 nor Trp41 are found mutated in circulating influenza strains. The conserved residue His37 located near the center of the channel has been identified as the pH sensor [61] that allows proton conduction and acidification of the virus interior through the channel at pH lower than 6.0 when the imidazole rings of the four His37 residues are protonated causing opening of channel by electrostatic repulsion and destabilization of helix-helix packing. [67,63] This is caused only when the virus particle reaches the low pH present in endosomes, leading ultimately to the unpacking of the influenza viral genome and pathogenesis.[53,63,67] Inside the pore, ordered waters form continuous hydrogen-bonding networks span the pore from the Val27 tetrad to His37 and transport

protons. [68] Under basic conditions the imidazole rings of the His37 residues are deprotonated at Nδ1 [63] and the Trp41 side chains, C-ward from His37, effectively block proton flow by forming hydrogen bonding interactions with imidazoles of His37. [52] Thus, Trp41 tetrad forms a pH-dependent gate that prevents proton flow through the pore and is known from mutation studies to function as the primary gate restricting proton conduction, [66,69] while Val27 tetrad corresponds to the secondary gate of proton entrance (Figure 4B).

The proton conduction of the wild type (WT) M2 protein, having a serine at position-31, can be blocked with amantadine (Amt) or rimantadine (Rmt) [70–74] and their analogs, as electrophysiology (EP) experiments have revealed. [72,75–80] Rmt and Amt are currently effective only for a minority of influenza strains. Amt-resistant mutations occur in the transmembrane domain such as L26F, and V27A, [81–83] while the majority of resistant strains (95%) have the S31N substitution (asparagine at position-31). Thus, Amt and Rmt drug usage has been abrogated. The S31N M2 variant maintains channel function nearly identical to the WT. Targeting of S31N M2 resistant strains is important since resistance to neuraminidase inhibitors is on the rise which may result in the need for new drugs. [84] Successful development of potent and strain-specific M2 inhibitors is a compelling strategy to control an influenza outbreak or pandemic due to a virus shift to WT M2. To this end, a second generation of amantadine-based drug molecules have been developed [85–89] that have been shown to block the S31N M2-mediated proton current by EP and inhibit influenza A virus. These include aryl or heteroaryl rings linked with amantadine through a methylene bridge and extensive structure-activity relationships investigations on activity and/or binding kinetics have been performed through modifications of the adamantyl group and the aryl head group. [87,89] Compound M2WJ332 (5-thiophenyl-3-(N-adamantyl)amimomethyl isoxazole) was a prototype S31N M2 blocker which blocked S31N M2 but did not block WT M2 by EP. [89]

Extensive high-resolution structural studies have been conducted on both WT and S31N M2, which were reconstituted in different detergent and lipid environments. These studies utilized solid-state NMR (ssNMR) in phospholipid bilayers, [63,73,90–95] as well as solution NMR in micelles [59,67,89,96] and X-ray crystallography using detergents. [67,74,97] We have performed ssNMR, [78,80,90,98–103] X-ray, [97,104,105] and MD simulation [80,106–109] studies on M2. These reports encompassed protein sequences of varying lengths, strains, WT or mutant M2 sequences, and measurements conducted both with and without bound adamantane-based drugs. As a result, a diverse range of structural observations have been reported.

One such observation is the formation of hydrogen bonds between His37 residues. Initially, such an interaction was proposed to take place for His-His$^+$ pairs based on nitrogen and proton chemical shifts. [61,63,110] Conduction was proposed to take place via protonation of one His-His$^+$ pair to form a +3 state for the His tetrad prior to deprotonation and reformation of the +2 state of the His tetrad. [61,63,110] Measurement of a J-coupling across the histidine residues provided further evidence for a hydrogen bond. [111] We also observed such a hydrogen bond interaction via a J-coupling, but at high pH for the neutral charge state of the channel (where His37 tetrad has +0 charge) [91,102,112,113] using M2CD. The CD construct (residues 18-60) assembles as a dimer-of-dimers in lipid bilayers, consistent with symmetry breaking via the hydrogen bond interaction at His37. [91,112,113]

Additionally, what has been clear is that adamantyl amines, e.g., Amt and Rmt, inhibit WT M2-mediated proton conductance by binding to the pore according to X-ray crystallography [97,104,105] and ssNMR with WT M2TM [73,114] or M2CD. [95,103] Furthermore, conjugates of amantadine with an aryl group also inhibit S31N M2-mediated proton conductance by occlusion of the pore with their ammonium groups binding to asparagine-31 side chains and the aryl group clustering with Val27 side chains as was shown using solution NMR spectroscopy, [86,89] ssNMR [115] and MD simulations. [86,89,108] In the ssNMR studies direct ^{13}C–^{2}H distance measurements of the binding of adamantane-based derivatives to WT M2TM and M2CD [95] or ^{15}N-^{13}C distance measurements of WT M2CD [103] and S31N M2 [115] consistently located drug molecules within the pore of M2.

Although both of these two classes of drugs occlude the M2 pore, only the adamantyl amines are “mechanism-based” inhibitors in the case of WT M2. That means that their ammonium groups bind to water-lined sites at Gly34 or Ala30 of WT M2 that are hypothesized to stabilize transient hydronium ions bound to His37. The hydronium ions that interact with His37 are formed in the proton-conduction mechanism according to X-ray crystallography [97,104,105] and multi-scale MD simulations [116] and lower the pKa of His37. [117] Note that this proposed mechanism is distinct from the proposal of charge stabilization through His-His hydrogen bonds. [61]

Drug binding is commonly inferred through NMR experiments using chemical shift perturbations (CSPs) for pore-lining residues. [78,80,95,101,115,118] These measurements are sensitive to both direct effects of binding, as well as indirect conformational changes in M2, which may vary depending on the M2 construct and the phospholipid bilayer being used which have also been shown to impact the binding energetics. For

example, bound Amt is detected in M2(21–61) reconstituted in 1,2-dimyristoyl-sn-glycero-3-phosphocholine (DMPC) bilayers. Yet when a virus-mimetic membrane containing 30% cholesterol was used, no ^{15}N or ^{13}C CSPs were observed for pore-lining residues, whereas M2(22-46) in the same membrane exhibited drug-induced chemical shift changes. [95] These observations showed that the energetics of drug binding interactions may considerably differ depending on the properties (e.g., lipid membrane, length of M2 construct) and conditions of the protein sample (e.g., pH, temperature). We recently observed slow kinetics of drug binding for M2CD (residues 18-60), which are modulated by the lipid composition and pH and can kinetically trap the sample in the pore-unbound state. [112] Such insights help to understand the lack of binding observed previously for M2CD (residues 21-61). [95]

In previous work [102,112] we observed disruption of the N-H--N hydrogen bond between imidazoles of His37 residues in adjacent TM helices upon Rmt binding to WT M2CD (residues 18-60) using MAS ssNMR. This was consistent for several bilayer preparations including 1,2-diphytanoyl-sn-glycero-3-phosphocholine (DPhPC), DPhPC with cholesterol, and in a virus-mimetic membrane. [102,112] This finding is consistent with a mechanism-based inhibition in which the drug binding perturbs the His37 structure. It may also be related to the mechanism-based inhibition proposed previously based on disruption of the structure of water. [97,116] This observation is significant since it has a straightforward association with the inhibition mechanism of the WT M2 proton conductance inside the pore by adamantyl amines.

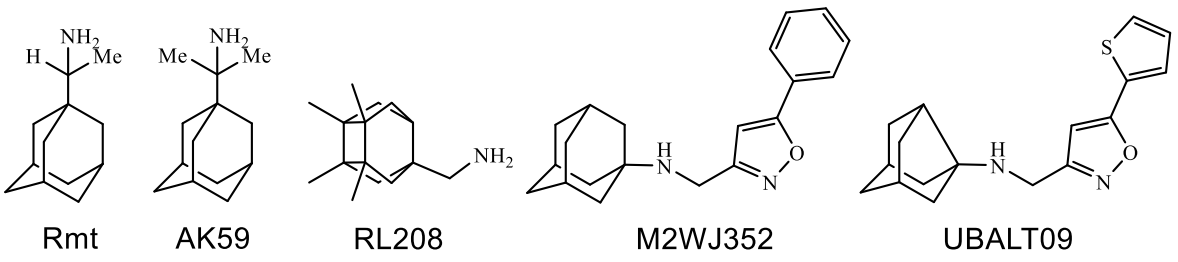

Scheme 2 Chemical structures of Rmt, AK59, RL208, M2WJ352, and UBALT09 tested against WT and S31N M2(18-60).

To expand on this mechanism-based inhibition hypothesis, based on our previous ssNMR findings in refs. [102,112], in this work we compared the binding of Rmt and four previously synthesized compounds using MAS ssNMR. We used in our experiments the cage alkyl amines Rmt, AK59, [109] RL208, [119] and the conjugates of a cage alkyl amine with an aryl group M2WJ352 [89,115] and UBALT09 shown in (Scheme 2).

AK59 has an added methyl group in comparison to Rmt, while RL208 (3,4,8,9-tetramethyltetracyclo[4.4.0.0^{3,9}.0^{4,8}]dec-1-yl)methylamine) bears a tetracyclic alkyl cage isomeric to adamantyl but compound RL208 is larger than Amt. The blocking efficiency of Rmt, [72,104] AK59, [109] and RL208 [120] have been assessed by EP against M2FL at 2 min of 100 µM drug exposure using the TEVC assay (Table S5). All cage alkyl amines Rmt, AK59, and RL208 block WT M2-mediated proton current but not S31N M2 by EP. We showed recently that RL208 produced CSPs when bound to L26F M2CD and V27A M2CD but not to WT M2CD in DPhPC bilayers at pH 7.8 at room temperature although it is a triple blocker of M2FL protein channels by EP. [120] Furthermore, we tested the conjugate M2WJ352 [89,115] a prototype selective S31N M2 blocker by EP. We also tested its analog UBALT09, a conjugate of 3-noradamantanamine with 5-(thiophen-2-yl)isoxazole, which is also a selective blocker of S31N M2 by EP. This previously measured blocking activity by EP against the M2FL is included in Table S5. We showed previously that conjugates of rimantadine with aryl groups did not block S31N M2 by EP compared to the amantadine-based conjugates. The rimantadine conjugates cannot fit inside the S31N M2TM because of the minimal increase of the length of the cage alkyl amine by one carbon. Thus, here we tested a minimal reduction of the size of amantadine using the 3-noradamantanamine in the conjugate. To further test the inhibitory activity of the selected compounds we used a liposomal proton flux assay and MD simulations were performed to assess the binding mode. All three methods utilized M2CD 18-60 construct.

2 Scope of research

This research centers on drug discovery applications in two important infectious diseases, tuberculosis and infection or flu from Influenza A. For each infection drug leads have been chosen for study, depending on their recent development progress and efficacy.

In the case of tuberculosis, we chose SQ109 ethylendiamine which is currently in phase IIb/III clinical trials. SQ109 is a promising lead as it is highly active against resistant *Mtb* [20,21] and it is also effective against other pathogens. The first step of this study is to design new SQ109 analogs through the application of computational methods. The analogs that result from the computational studies are synthesized following synthetic routes from previous work and new optimized methods [121–124]. Then, their activity is explored (a) against pathogens such as mycobacteria, bacteria, and protozoan parasites, and (b) against MmpL3 protein using the SPR method and TI/MD computational method. Considering that SQ109 can inhibit MmpL3 function indirectly by interacting with membranes, interactions of SQ109 analogs with lipid bilayer membranes are additionally explored using the DSC method.

In the case of Influenza A infection, we chose five adamantane and cage amine analogs that were synthesized in Prof. Kolocouris and Prof. Vazquez lab and were potent inhibitors of WT or S31N M2 protein by EP measurements [89,109,119,120]. In this project, the molecular basis of binding and blocking of those compounds to WT and S31N M2 is being investigated. The binding behavior is explored using magic angle spinning NMR by recording 2D and 3D ^{1}H-^{15}N and ^{1}H-^{13}C-^{15}N spectra of M2 (residues 18-60) reconstituted in lipids. MD simulations and a liposomal proton flux assay are performed complementarily to assess their binding mode and channel blocking, respectively.

In both projects, we aim to give a detailed insight into the structural features of the protein – drug complexes utilizing computational or biophysical methods. Besides providing potent inhibitors or future drug leads, the results of this study can improve the understanding of the corresponding inhibitors' mechanism of action, as well as how these membrane protein systems accommodate these inhibitors in certain environments. Hence, these findings can be helpful to future drug discovery studies.

3 Drug design, synthesis, and testing of analogs of the anti-tubercular drug SQ109 against bacteria and protozoa

3.1 Results

3.1.1 Improved synthesis of the antitubercular agent SQ109

The reported methods for the synthesis of SQ109 (**8a**), couple geranylamine (**4**) with 2-adamantanamine (**5a**) through an ethylenediamine linker and include condensation of one of these amines [19,38,121,122] with chloroacetyl chloride or bromoacetyl chloride, [38,121,122] following a condensation reaction with the second amine, and then reduction of the amide group of the two carbon linker with $LiAlH_4$ in refluxing tetrahydrofuran (THF) [38,121,122] or with Red-Al in THF under reflux [121] or room temperature [19]. Alternatively, condensation of 2-adamantanone with *N*-geranyl ethylenediamine (prepared from 1-geranyl bromide **2** and ethylenediamine) is followed by reductive amination with $NaBH_4$ in methanol. [38,122] This procedure is much more convenient and can be applied to the synthesis of SQ109 analogues having a second substituent, such as an alkyl group, at the 2-adamantyl position.

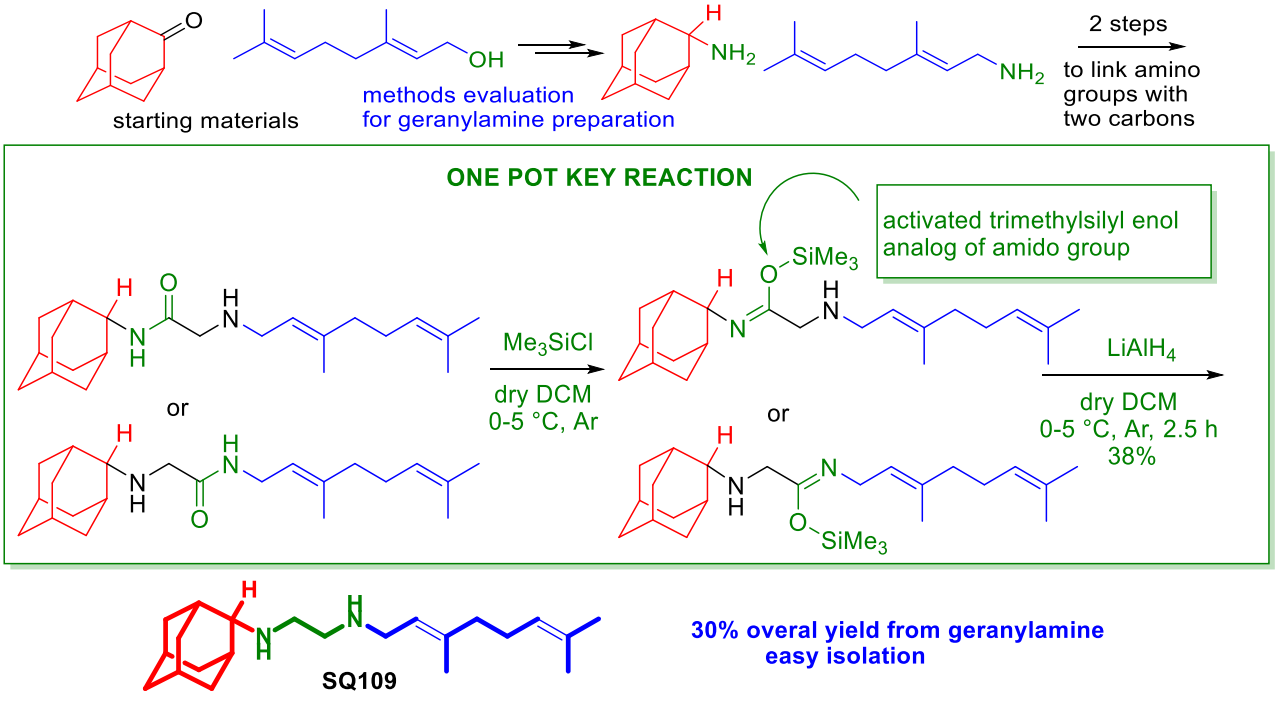

Scheme 3 Schematic representation of the key steps of the improved synthesis of SQ109 analog.

The preparation of geranylamine (**4**) has been reported using the low-cost precursor geraniol (**1**) and phthalimide, which were subjected to a Mitsunobu reaction to afford *N*-geranyl phthalimide (**3a**). [121,125] Geraniol (**1**) can also be converted quantitatively into geranyl bromide (**2**) [38,122] that can be reacted with potassium phthalimide using the Gabriel reaction [38,122,125,126] or with phthalimide under microwave conditions, [126] affording *N*-geranyl phthalimide (**3a**) (Schemes 4 and 5). The *N*-geranyl phthalimide (**3a**) is then treated with an aqueous solution of hydrazine 60% w/v to afford geranylamine (**4**) (without chromatographical purification according to the literature) in 37–49%, [121] 69 %, [125] or 62% [38,122] yield from geraniol (**1**) using the Mitsunobu or Gabriel reaction, respectively. In the original literature procedure, we found geranylamine (**4**) was synthesized by Gabriel reaction in 20% yield from geranyl chloride [127] and 77% from geranyl bromide. [38,122,125,126] Reduction of 1-geranyl azide (**3b**) with Lindlar catalyst has been reported as effective for the selective reduction of the azido group to an allylic azide. [128] Additionally, the Staudinger reaction of geraniol acetate, [129] using PPh_3 and NH_3 has been applied for the preparation of **4** in 59% yield.

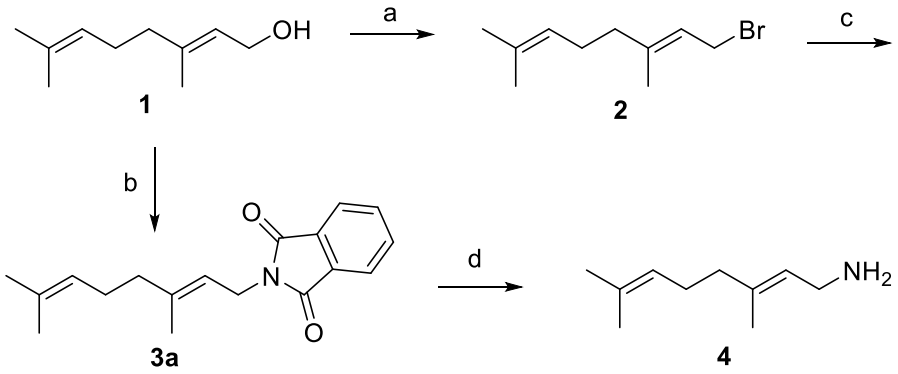

Scheme 4 Synthesis of geranylamine; Reagents and conditions: (a) PBr_3, dry Et_2O, -5 °C, 3h, (quant.); (b) Ph_3P, DIAD, pthalimide, anh THF, rt, 24h (81%); (c) Phthalimide, K_2CO_3, anh THF, reflux, 24h, (88%); (d) (1) N_2H_4 60%, EtOH, reflux, 6h; (81%).

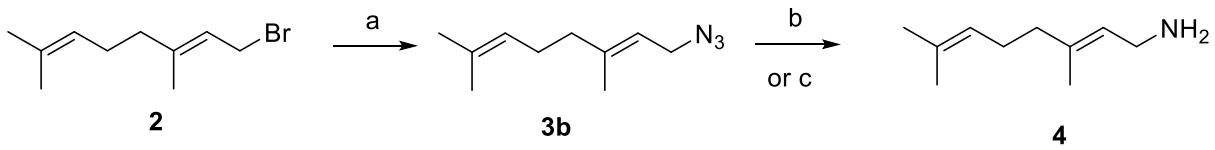

Scheme 5 Synthesis of geranylamine; Reagents and conditions: (a) NaN_3, EtOH, reflux, 5h (92%); (b) PPh_3, THF/H_2O, rt, 12h (34%); (c) $LiAlH_4$, anhydrous (anh.) Et_2O, rt, 24 h (24%).

We managed to synthesize SQ109 (**8a**) and analogs according to the first of the above-mentioned procedures for SQ109 (**8a**) preparation, [19,38,121,122] which also enables the preparation of analogs substituted at the 2-adamantyl position. We report herein our observations of inconsistencies and improvements regarding previously reported results.

We first describe our observations during the preparation of the commercially available but expensive geranylamine (**4**). We reacted geraniol (**1**) with phosphorus tribromide in dry diethyl ether at –5 °C and obtained 1-geranyl bromide (**2**) in 99.5% yield (Scheme 4), which was converted into *N*-geranyl phthalimide (**3a**) using both the Mitsunobu reaction at room temperature [121,125] or Gabriel reaction under reflux. [38,122,125,126] Hydrazinolysis of *N*-geranyl phthalimide (**3a**) [38,121,122,125] under refluxing conditions afforded geranylamine (**4**) in 81% yield. During workup use of aqueous hydrochloric acid should be avoided since the double bond at 6-position of geranylamine (**4**) reacts, as evidenced by the observation of a doublet at δ = 1.19 ppm in the 1H NMR spectrum, which is attributed to an isobutyl group, and the disappearance of the unsaturated CH proton resonance at ca. δ = 5 ppm leading to secondary amine contamination of the product.

We also tested the reaction of 1-geranyl bromide (**2**) with sodium azide in refluxing ethanol to afford 1-geranyl azide (**3b**) in 92% yield. We then examined the reduction of 1-geranyl azide (**3b**) by Staudinger reaction, [130,131] using PPh_3 in THF/H_2O (10:1) and isolated geranylamine (**4**) in 34% yield as a solid hydrochloride salt (Scheme 5). We were not able to improve the yield and did not isolate any other amine side product. However, we observed minor peaks in the ^{1}H NMR spectrum of geranylazide. It has been shown [132] that geranylazide is in equilibrium with linalyl azide in a ratio of ca. 80:20, as is shown in the spectrum of 1-geranyl azide (**3b**) (Appendix A). Perhaps, the equilibrium between geranylazide and linalyl azide of different stability (the last having a tertiary carbon azide bond) is the reason for the low yield of geranylamine (**4**) which is formed through the corresponding triphenyl(*N*-geranylimino)phosphorane. This may be the reason why the authors [132] improved the Staudinger reaction conditions using geranyl acetate and PPh_3/NH_3 to obtain geranylamine (**4**) in 59% yield. However, we did not apply these reaction conditions since we obtained geranylamine (**4**) in a better yield following a procedure using Mitsunobu or Gabriel conditions as described above.

Next, we examined the reduction of 1-geranyl azide (**3b**) with $LiAlH_4$ at room temperature and obtained geranylamine (**4**) as the free amine in 24% yield. It should be borne in mind that the Staudinger reaction has the disadvantage of the need to remove the phosphine oxide side product from the resulting reaction mixture.

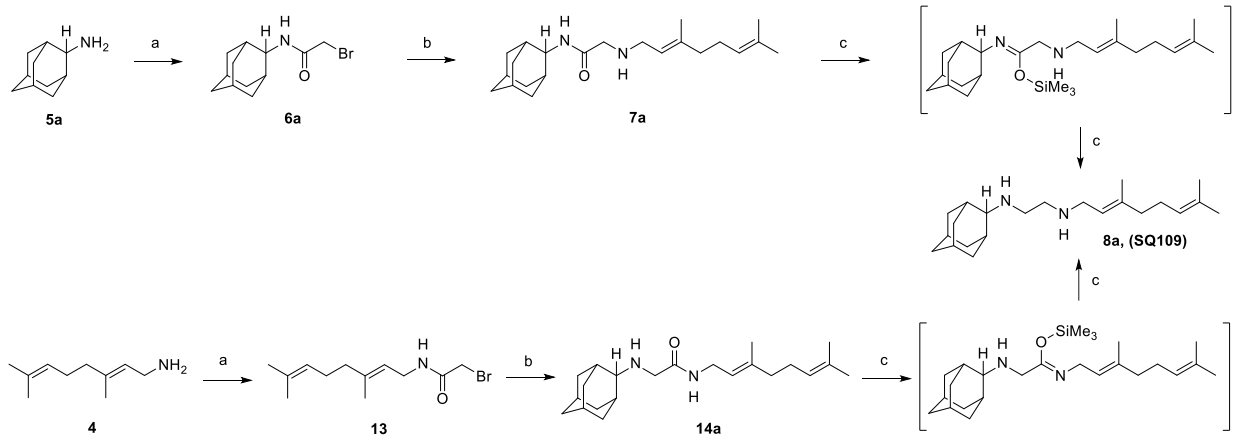

Scheme 6 Synthesis of SQ109. *Reagents and conditions*: (a) $ClCOCH_2Br$, K_2CO_3 (aqueous), DCM, rt, 24 h (**6a**: 83%, **13**: 91%); (b) **4** or **5a**, Et_3N, dry THF, rt, 48 h, (**7a**: 86%, **14a**: 72 %); (c) (i) Me_3SiCl, $LiAlH_4$, dry DCM, 0–5 °C, Ar, 2.5 h; (ii) NaOH 10%, 0 °C (31–38%).

We then proceeded to the connection of geranylamine (**4**) and commercially available 2-adamantanamine (**5a**, alternatively prepared by reduction of the oxime of 2-adamantanone [78] with $LiAlH_4$ through the two-methylene linker). We treated either 2-adamantanamine (**5a**) or geranylamine (**4**) with a mixture of 1-bromoacetylcloride and potassium carbonate at room temperature and produced the corresponding bromoacetamides **6a** or **13** in 83% or 91% yield, respectively (Scheme 6). Subsequently, adding solution of **6a** or **13** in dry THF to a solution of geranylamine (**4**) or 2-adamantanamine (**5a**) and triethylamine in dry THF at room temperature furnished **7a** or **14a**, which are aminoamide precursors of SQ109 (**8a**), in 86% or 72% yield, respectively.

We applied the literature conditions for the reduction of aminoamide **7a**, which involves the reaction with $LiAlH_4$ in refluxing dry THF under inert atmosphere for 16 h. [34,122,123] Although it was reported that this reduction yielded SQ109 (**8a**) in 50% yield after column chromatography, our two repeats afforded SQ109 (**8a**) in 8% and 14% yield after column chromatography. We also observed the formation of geranylamine (**4**) and a byproduct formed due to the partial reduction of the geranyl chain since the double bond close

to the reaction center becomes saturated. This is evidenced immediately by the disappearance of the corresponding unsaturated CH proton resonance at δ = 5.25 ppm (m) in the ^{1}H NMR spectrum. Additionally, an aqueous hydrochloride solution should not be used during the reaction workup since, as mentioned previously, we observed that the distant double bond from the reaction center becomes saturated. We also tested the reduction with $LiAlH_4$ in dry tetrahydrofuran or diethyl ether at room temperature, but we obtained again the same mixture of amines.

We then explored more selective reduction conditions of the amido group and examined the use of $Me_3SiCl/LiAlH_4$ [133]. This reagent can activate the amide carbonyl functionality through the formation of the trimethylsilyl enol intermediates (Scheme 6); the *in situ* generated imine being reduced efficiently with $LiAlH_4$ to the amino group under mild conditions. Thus, when we treated aminoamides **7a** or **14a** with a mixture of $LiAlH_4$ and distilled Me_3SiCl in dry dichloromethane (DCM) at 0–5 °C for 2.5 h under an inert atmosphere, we isolated SQ109 (**8a**) in 31–38% yield after column chromatography (Scheme 6). Increasing the reaction time or temperature to gentle reflux did not improve the yield of SQ109 (**8a**).

The yield for converting geraniol (**1**) into geranylamine **4** was 20% in ref. [122] and 37% in ref. [121] compared to 66% in our work. The overall yield for SQ109 (**8a**) starting from geraniol (**1**) in ref. [122] is 5% and in ref. [121] is 16% compared to our ca. 20% yield. The yield for SQ109 (**8a**) synthesis in ref. [19] was reported to be 24% from geranylamine (**4**), or the overall yield from geraniol (**1**) was ca. 5–8% (based on the yields for converting geraniol (**1**) into geranylamine (**4**) using the Gabriel [122] or Mitsunobu reaction [121].

The yield of a second reported procedure including the condensation of 2-adamantanone with *N*-geranyl-ethylenediamine (prepared from geranyl bromide **2** and ethylenediamine), followed by reductive amination with $NaBH_4$ in methanol, [38,122] is 18% from geranyl bromide (**2**), and the overall yield from geraniol (**1**) is 17%. However, as mentioned, this procedure is not general for SQ109 analogs with a second substituent at 2-adamantyl group position.

3.1.2 Study of SQ109 analogs binding to mycobacterium MmpL3 transporter using MD simulations and alchemical relative binding free energy calculations

3.1.2.1 Conformational analysis of monoprotonated ethylenediamine unit in SQ109

The ethylenediamine unit in SQ109 (**8a**) involves three dihedrals affecting the drug's orientation inside the MmpL3 pore through rotation around (2-Ad)$NHCH_2$–$CH_2NH_2^+$Ger, (2-Ad)$NHCH_2CH_2$–NH_2^+Ger and $C_{1,Ad}C_{2,Ad}$–$NHCH_2CH_2NH_2^+$Ger bonds (where $C_{1,Ad}$ or $C_{2,Ad}$ are adamantyl carbons at position-1, or -2 in 2-adamantyl group) described in Tables 1–3. Using the B3LYP functional with dispersion interactions correction (B3LYPD3) [134–137] and the 6-31G(d,p) basis set calculations we performed full geometry optimization and calculated the free energies of the conformational minima of SQ109 (**8a**), by manual rotation around these three dihedrals in a hydrophilic and a hydrophobic environment. Dispersion correction improves the calculation of the forces acting on the atoms in distances > 3 Å and the accuracy of relative conformational energies calculation which are shown in Table 1. The hydrophilic environment was simulated with an implicit water environment and a dielectric constant (ε) = 80 and the hydrophobic environment was simulated with an implicit chloroform environment and ε = 4.8 using the polarizable continuum model (PCM) [138] and taking advantage of a smooth switching function [139].

The rotation around the carbon–carbon bond, (2-Ad)$NHCH_2$–$CH_2NH_2^+$Ger, in SQ109 (**8a**), (Figure 5A) generated the *gauche*(-), *gauche*(+), *anti* and *eclipsed* conformations and changed the relative orientation of the (2-Ad)NH and NH_2^+Ger groups and the hydrogen bonding profile of the ethylenediamine unit inside the MmpL3 receptor. The gauche conformations have the lowest free energy following the anti conformation, which is substantially destabilized, while the eclipsed conformer corresponds to the rotation barrier and was not stable. Both gauche conformations are stabilized since a hydrogen bond is formed between protonated and unprotonated nitrogen atoms in the ethylenediamine unit.

The rotation around (2-Ad)CH_2CH_2–$NH_2^+CH_2$Ger dihedral favors the *anti* orientation (Table 2) since in the *gauche* conformation the steric energy increases due to repulsion between the geranyl and 2AdNH_2^+ groups. In these *gauche* conformations, the geranyl moiety of the SQ109 (**8a**) cannot adopt an extended structure that fits inside the narrow pore of the transporter.

Table 1 Calculations of conformational free energies by rotation of (2Ad)CH_2–$CH_2NH_2^+$Ger in SQ109 (**8a**) using the B3LYP-D3/6-31G(d,p) and PCM for water (ε=80) or chloroform (ε=4.8).

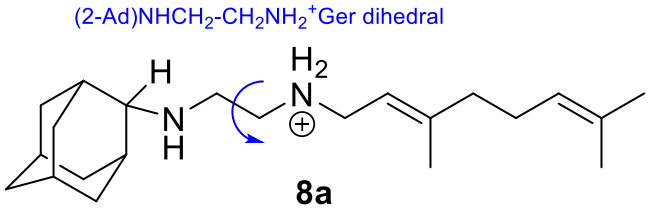

8a

Dielectric	Δ*G* (kcal mol^{-1}) for SQ109(**8a**)		
	conformer		
	gauche(-)	*gauche*(+)	*anti*
ε=80	2.95	0	10.23
ε=4.8	2.92	0	8.80

Table 2 Calculations of conformational energies by rotation of (2Ad)CH_2CH_2–NH_2^+Ger in SQ109 (**8a**) using the B3LYP-D3/6-31G(d,p) and PCM for water (ε=80) or chloroform (ε=4.8).

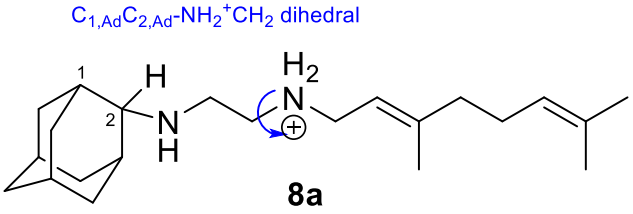

8a

Dielectric	Δ*G* (kcal mol^{-1}) for SQ109(**8a**)		
	conformer		
	gauche(-)	*gauche*(+)	*anti*
ε=80	2.77	2.78	0
ε=4.8	2.85	2.94	0

Table 3 Calculations of conformational energies by rotation around $C_{1,Ad}C_{2,Ad}$–$NHCH_2$ in SQ109 (**8a**) using the B3LYP-D3/6-31G(d,p) and PCM for water (ε=80) and chloroform (ε=4.8).

$C_{1,Ad}C_{2,Ad}$-$NH_2^+CH_2$ dihedral

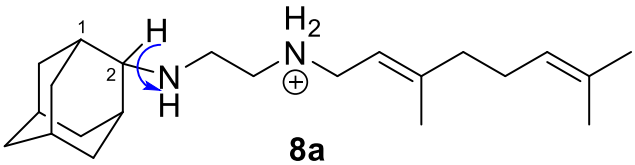

8a

Dielectric	ΔG (kcal mol^{-1}) for SQ109(**8a**)		
	conformer		
	gauche(-)	*gauche*(+)	*anti*
ε=80	3.69	8.24	0
ε=4.8	3.61	9.25	0

The rotation around the $C_{1,Ad}C_{2,Ad}$–$NHCH_2$ dihedral (where $C_{1,Ad}$ or $C_{2,Ad}$ are adamantyl carbons at position-1, or -2 in 2-adamantyl group) defines the position of the alkyl and the 2-adamantyl ammonium groups and the density functional theory (DFT) calculations results are shown in Table 3. The $C_{1,Ad}C_{2,Ad}$–$NHCH_2$ moiety cannot adopt the two *gauche* conformations (which place the nitrogen of the ammonium group at C2-adamantyl position and C_{n-1} at symmetrical positions) due to the severe steric repulsions of the axial $NHCH_2$ with the cyclohexane subunit group of the 2-adamantyl group (Figure 5B).

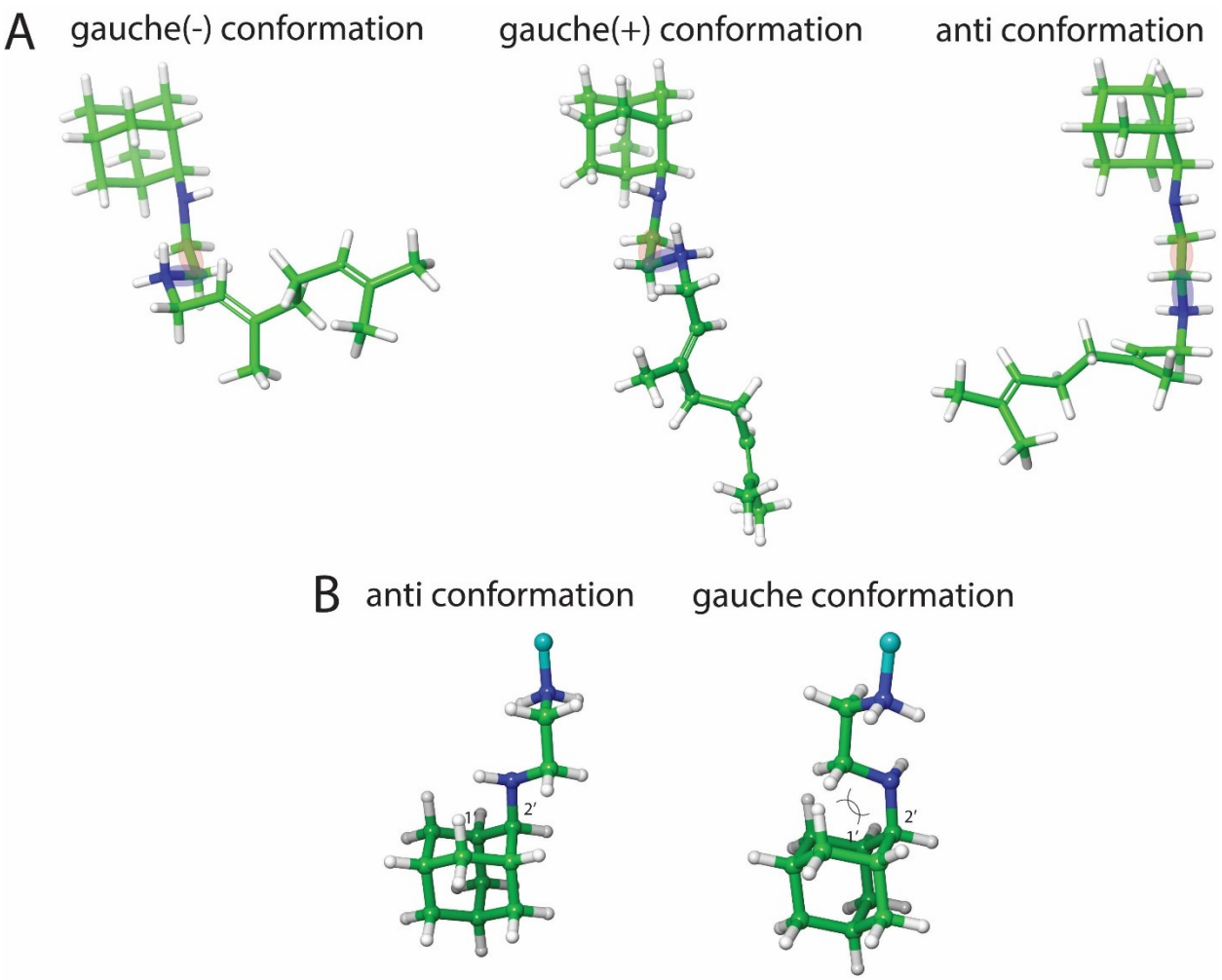

Figure 5 Important conformational features of SQ109 (**8a**). In (A) are shown the conformations *gauche*(-) or *gauche*(+) or *anti* by rotation around the ethylenediamine's unit carbon–carbon bond, (2Ad)CH_2–$CH_2NH_2^+CH_2$Ger (Table 1), which defines the relative orientation of 2-adamantyl and geranyl groups. The conformation around the (2Ad)CH_2CH_2–$NH_2^+CH_2$Ger dihedral was *anti*. In (B) are shown the conformations generated by rotation around the $C_{1,Ad}C_{2,Ad}$–$NHCH_2$ dihedral (Table 3) which defines the position of axial $NHCH_2$ as regards the cyclohexane subunit of 2-adamantyl group (geranyl group is shown with a light blue sphere); in the structure shown in the right-hand part the axial $NHCH_2$ brings CH_2 above the cyclohexane subunit of 2-adamantyl increasing steric repulsion (shown with two cross circular arc lines).

In summary, our DFT study showed that rotation of SQ109 around (2Ad)$NHCH_2$–$CH_2NH_2^+$Ger dihedral favors two *gauche* conformations as minima while other conformers were unpopulated in both dielectric media as well as inside the transporter's pore demonstrated by our MD simulations (see the next section).

Rotation around (2Ad)$NHCH_2CH_2$–NH_2^+Ger bond favors an *anti* orientation and rotation around (2Ad)–$NHCH_2CH_2NH_2^+$Ger bond showed that the position of $NHCH_2$ group above the cyclohexane subunit is prohibited.

3.1.2.2 MD Simulations of SQ109 analogs in complex with MmpL3

MmpL3 protein consists of 12 transmembrane (TM) α-helices and the transmembrane region also contains two extra α-helices attached to the cytoplasmic membrane surface. We used structure PDB ID 6AJG [22]of the protein that has M1-E749 residues after excluding the C-terminus. The transmembrane domain consists of the following α-helices and their residues: TM1: (14-33), TM2: 174-199, TM3: 208-224, TM4: 238-264, TM5: 271-301, TM6:306-338, TM7:396-415, TM8: 552-576, TM9: 583-601, TM10: 625-648, TM11: 660-690, TM12: 697-728.

The X-ray structure (PDB ID 6AJG) [22] showed that the complex is stabilized through numerous van der Waals interactions between the geranyl-ethylenediamine moiety of SQ109 (**8a**) and surrounding amino acids of MmpL3, including Ile249, Ile253, Ile297 in the upper part and Leu642, Tyr257, Tyr646, Leu686 in the bottom part of the pocket while the 2-adamantyl group lies close to Phe260 and Phe649. Ethylenediamine molecule has $pK_{a,1}$ = 10.71 and $pK_{a,2}$ = 7.56 [140] and at pH 7.4 the mono and diprotonated species will be equally populated. However, since the basic amino group close to adamantyl group is more hindered to protonation, we assumed that the monoprotonated species must be predominated inside the hydrated MmpL3 pore, although actual protonation states are not known and would probably require neutron diffraction structures. Strikingly, in the X-ray structure (PDB ID 6AJG) [22] the ethylenediamine unit adopts a high energy conformation by rotation around its carbon–carbon bond (2Ad)$NHCH_2$–$CH_2NH_2^+$Ger having *eclipsed* the C-N bonds. Protein−ligand coordinates obtained from crystallography or cryo-em experiments provide a static model corresponding to a snapshot. While is not uncommon to find ligand conformers in complex with a protein that differ significantly from the lowest energy conformation in solution, due to stabilizing interactions inside the receptor, it is appropriate to judge the stability of the ligand's conformation in the experimental structure using MD simulations, as previously suggested.[141–145]

We performed 100ns-MD simulations (two repeats – Figure S3) using the SQ109 (**8a**)-MmpL3 complex (PDB ID 6AJG) [22] embedded in a hydrated 1-palmitoyl-2-oleoyl-*sn*-glycero-3-phosphocholine (POPC) bilayer using the amber99sb force field (ff99sb) [134] and a 500ns-MD simulation (Figure S4) for testing the

stability of the protein complex in longer time scale. For each simulation, initial atom velocities were assigned randomly and independently. Structure of SQ109 (**8a**)-MmpL3 complex with PDB ID 6AJG [17] has ~ 2.6 Å resolution which is higher than other structures resolved in refs [30,31] while no other structure of MmpL3 in complex with an SQ109 (**8a**) analog has been resolved.

We observed a rotation of the carbon-carbon bond in the ethylenediamine unit that converts the *eclipsed* conformation of SQ109 in the MmpL3 X-ray structure (PDB ID 6AJG), [22] into the two possible *gauche* conformations, with no population of the *eclipsed* conformer over the whole trajectory. In each of the two *gauche* conformations, the monoprotonated ethylenediamine unit can form stabilizing hydrogen bond interactions with both Asp256 and Asp645, as compared to the *eclipsed* conformation which forms hydrogen bonds only with Asp645. Thus, in the *gauche* conformation the amine NH_2^+ group of the monoprotonated ethylenediamine unit forms direct ionic hydrogen bonds with both Asp256 and Asp645 while the unprotonated NH acts as a donor in one direct and one water-mediated hydrogen bond with Asp256 (Figure 6). We observed also that water molecules enter the pore forming hydrogen bonds between the monoprotonated ethylenediamine unit and side chains of Tyr257/Tyr646, Asp256/Asp645, Ser293, or carbonyl groups backbone peptide bonds. The geranyl-ethylenediamine chain is tightly enclosed in a narrow area of the transporter's pore with geranyl chain having the surrounding amino acids Tyr257, Ile297, Leu642, Tyr646 while at the bottom, wider part of the binding area, 2-adamantyl group has van der Waals contacts with Phe260 and Phe649.

3.1.2.3 Simulations of the complexes of MmpL3 with SQ109 analogs 8b-i, 12

Docking calculations results

The X-ray structure of the MmpL3−SQ109 (**1a**) complex (PDB ID 6AJG [22]) was used as the template structure for the docking calculations of SQ109(**8a**) and suggested ligands **8b-i, 12** with MmpL3 after excluding C-terminus, consisting of M1-E749 residues as previously described. The highest score docking pose of SQ109 (**8a**) inside the MmpL3 pore (ChemScore [146] scoring function) had a root-mean-square-deviations of heavy atoms ($RMSD_{ligand}$) 1.7 Å compared to the structure with PDB ID 6AJG [22]. This suggested that the calculated docking poses can accurately describe the binding orientation of SQ109 analogues. The docking poses of the monoprotonated ethylenediamine SQ109 analogues **8b-i**, **12** showed that the new adamantyl moieties can fit in the empty region at the bottom of the binding area where for example

the bigger alkyl adducts linked at C-2 adamantyl position can be accommodated. The docking calculations showed that the addition of alkyl, aryl, or heteroaryl adducts, e.g. Me, Et, nPr, nBu, Ph, Bn, Hex, 5-phenyl thiazol-2-yl (Ph-Thz) at the adamantyl C-2 of SQ109 (**8a**), in compounds **8b-i**, respectively, or replacement of the 2-adamantyl group by a 1-adamantyl-dimethylmethylene (C-1 dimethylmethylene) group in compound **12**, resulted in highest score docking poses having a *gauche*(-) or *gauche*(+) by rotation of (2Ad)CH_2–$CH_2NH_2^+CH_2$Ger that bind MmpL3 pore. The docking algorithm produced 30 docking solutions. We visually inspected and realized that the first 4-5 highest docking solutions corresponded to a similar conformation of the ligand inside the receptor.

For diprotonated mainly the *gauche*(-) or *gauche*(+) by rotation of (2Ad)CH_2–$CH_2NH_2^+CH_2$Ger were obtained as highest score docking poses, but also in two cases the *anti* and *eclipsed* conformations were also provided (see Table S2) since these later conformers can be stabilized inside the receptor with strong hydrogen bonding interactions despite their much lower stability in solution compared to the *gauche* conformation (see Table 1). It was not unusual that the highest docking pose for each ligand could be different since this reflected the high flexibility of the ligands and the random nature of the docking algorithm (genetic algorithm runs). For the MD simulations, we used the highest scoring docking pose as starting conformations. We also tested as starting structure a conformation for the ligands **8b-i**, **12** that resulted from superposition with the last snapshot from 100ns-MD simulation of MmpL3-SQ109 (**8a**) complex.

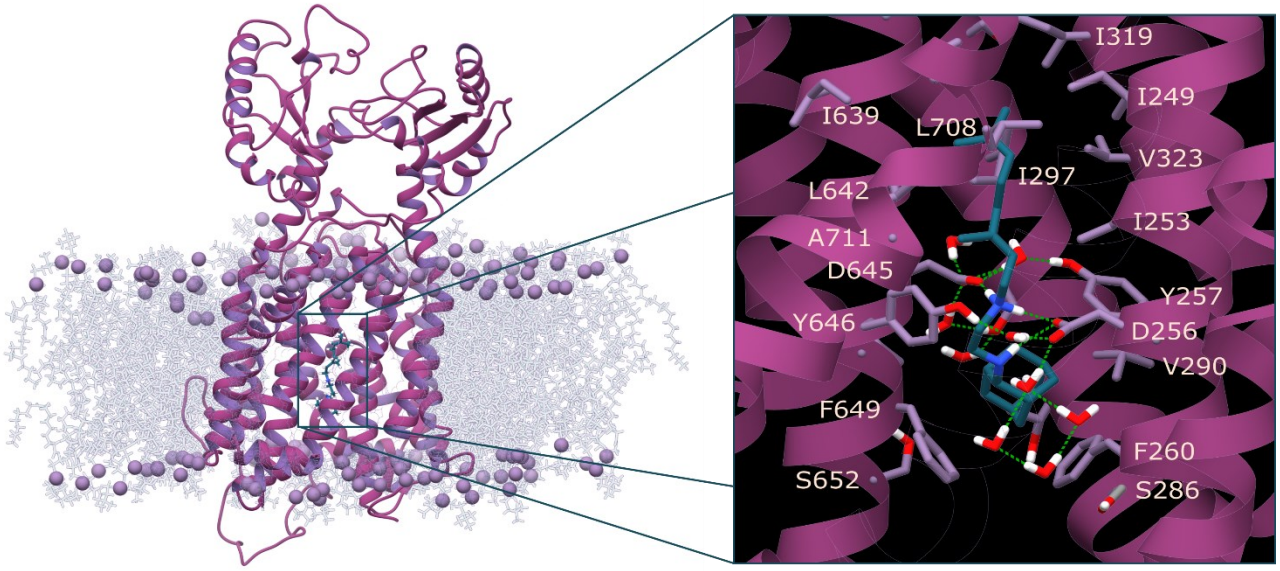

Figure 6 Structure of MmpL3 in complex with SQ109 (**8a**) after 100 ns MD simulations with ff99sb [147] (left) [42,43] and a close-up view of the binding site (right). SQ109 (**8a**) forms hydrogen bond interactions with two Asp-Tyr pairs: the Asp256-Tyr646 pair and the Asp645-Tyr257 pair. Color scheme for frames: Ligand=petrol sticks, receptor = purple ribbons, residues as light purple sticks. Hydrogen bonding interactions = green dashes. For the protein, the experimental structure of SQ109 (**8a**) in complex with MmpL3 (PDB ID 6AJG [17]) from *Ms*, was used as the starting structure for the MD simulations.

MD Simulations of SQ109 analogs in complex with MmpL3

To explore the dynamic behavior between the ligands **8a-i**, **12,** and MmpL3 we performed 100ns-MD simulations (two repeats – Figure S3) with starting structures the docking poses with the highest score. Thus, the docking poses were embedded in hydrated POPC bilayers of ~ 140 lipids and subjected to MD simulations using ff99sb.

For the sizeable alkyl substituents at C-2 adamantyl position, e.g., in analogs **8f**, **g**, **i**, 500 ns-MD simulations were also performed to test the stability of the protein complexes in a longer time scale (Figure S4). For each simulation, initial atom velocities were assigned randomly and independently. We observed from the 100 ns-MD simulations or the 500 ns-MD simulations that the RMSD values of the protein TM Cα carbons converged after 10–40 ns with RMSDprotein (Ca TM) ≤ 2.1 A, suggesting small changes compared to the X-ray structure (Figure 7, S1, Table 4). A different stabilization between the full protein and the TM region was observed reflected by the different RMSDprotein (Ca full protein) and RMSDprotein (Ca TM)

with values for the latter much smaller than the former. It is not unusual that the loops connecting the TM-helices are very flexible and increase the RMSD (Ca full protein). The ligands, which contained very flexible moieties such as the geranyl and ethylenediamine groups, shifted considerably from the starting docking pose, as revealed by the high values of RMSD ligand and in most cases the ligand binding conformation equilibrated in a stable position inside the transporter's pore after 70 ns (Figure 7, S1, Table 4). The last frame provides a good description of the ligand–protein interaction frequency plots. Figure 7 shows last frames and ligand–protein interaction frequency plots for SQ109 (**8a**) and selected alkyl and aryl groups attached at the adamantyl C-2 of **8a** (R = H) including analogs **8e** (R = nBu), **8h** (R = Ph), **8i** (R = Ph-Thz) while the last frames, ligand–protein interaction frequencies for the other analogs, as well as the RMSD plots from MD simulations can be found in Figure S1.

The MD simulations showed that the monoprotonated ethylenediamine unit of the ligands **8b-i**, **12** adopted a *gauche* conformation, which favored hydrogen bonding interactions with Asp256 and/or Asp645 of MmpL3 (Figure 7, S1). According to the MD simulations, the complexes between **8b-i**, **12**, and MmpL3 formed common van der Waals interactions with the protein's residues along the narrow area of the transporter pore. Compared to SQ109 (**8a**) the geranyl-ethylenediamine moiety was surrounded similarly by the amino acid residues Leu642, Tyr646, and Tyr257 while the 2-adamantyl group lay close to Phe260 and Phe649 at the bottom part of the binding area. However, the alkyl adducts increased the hydrophobic interactions at the bottom of the binding area with Phe260 and Phe649 and also increased the hydrophobic interactions with residues in the walls of the narrow area of the pore, e.g., Ile253 (see **8e**, **h**, **i** in Figure 7). Water molecules formed hydrogen bonds between the monoprotonated ethylenediamine unit and receptor's residues, as described previously for SQ109 (**8a**).

We explored the disposition of the important residues for binding of the ligands (Asp256, Asp645, Tyr257, Tyr646, Phe260, Phe649) along the MD simulation and checked for other frames that could better accommodate the ligands. The RMSD (Ca) of these important residues for binding were plotted (Figure S5). The RMSD (Ca) converged to values that range between 0.5 and 1.5 confirming not important disposition of these residues along the MD simulation. Thus, two repeats were performed for each of the MD simulations for **8b-i**, **12** while for sizeable substituents, e.g. in **8f, g, i** 500ns-MD (Figure S4) simulations were also performed for testing the stability of the protein complexes in a longer time scale. For each simulation, initial atom velocities were assigned randomly and independently. We performed the 100ns-

MD simulations using as starting structure a conformation for the ligands **8b-i** resulted from superposition with SQ109 (**8a**) but the results were similar.

While the monoprotonated form of SQ109 (**8a**) and analogs most likely predominated inside the hydrated MmpL3 pore, we also performed MD simulations for the diprotonated species (Figure S2). The MD simulations showed that the ligands in the diprotonated ethylenediamine form had similar coordinates inside the MmpL3 (Figure S2) compared to the monoprotonated form.

3.1.2.4 MM-GBSA binding free energy calculations

We applied the MM-GBSA method [148–150] using the OPLS2005 force field [151] for the calculation of binding free energies (ΔG_{eff}) of ligands **8a-i, 12** inside the MmpL3 pore, using ensembles from 20ns-MD simulations and calculated binding free energies without or with considering the membrane environment of the protein complex. For each simulation, initial atom velocities were assigned randomly and independently. Thus, we tested the membrane protein – ligand systems using an implicit membrane, i.e. a hydrophobic slab, [152–155] and explicitly considering water molecules inside the binding area. [156] The range of molecular weight of the ligands is 400-500 Da which corresponds to tripeptides [149] and their carbon skeleton is long enough to interact with many residues inside the receptor area. If a correct ranking of the binding affinities of **8b-i**, **12** for the MmpL3 pore could be accomplished with the MM-GBSA method this would be a significant reduction in computational resources, compared to the accurate binding free energy perturbation methods for **8b-i**, **12** - MmpL3 complexes in lipid bilayers containing ~ 10^5 atoms.

However, the calculated mean values of three repeats for the monoprotonated forms (Table 4) and diprotonated forms (Table S2) showed that the MM-GBSA method (applied with or without modifications to consider the membrane environment of the protein complex using a hydrophobic slab [152–155] and the explicit waters inside the binding area) [156] did not afford valuable results. The binding free energy values were dispersed and did not follow any trend (see Table 4, S2). Indeed, as a calculation method, MM-GBSA can show large deviations (e.g., 4 kcal mol^{-1}) in standard binding free energies compared to the experimental binding free energies. The method normally can provide useful results [157] for ranking of substituents [148] in the same series of ligands when the experimental binding affinities range is ~ 1000-fold or higher [149] which is not the case for **8b-i, 12** since their K_D values differ only by 4-fold (see chapter 3.1.5).

Compared to the monoprotonated species, we observed that the diprotonated ethylenediamine moieties in compounds **8a-i**, **12** form stronger hydrogen bonding interactions with the receptor area, compared to the monoprotonated forms. This agreed with the MM-GBSA binding free energy values for the monoprotonated forms compared to the diprotonated forms since in the latter case the values are significantly lower which is consistent with enhanced hydrogen bonding interactions between the ligands and the receptor's binding site (Table 4, S2). Because of the stronger hydrogen bonding interactions, the ligands have smaller flexibility as was shown by the lower $RMSD_{protein}$ (Ca TM) and lower $RMSD_{ligand}$ (Figure S1, S2, Table 4, S2).

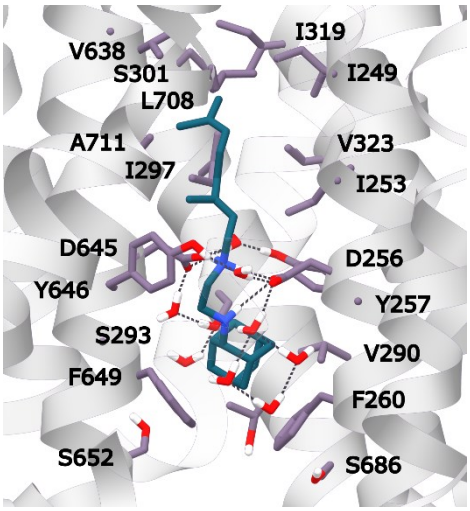

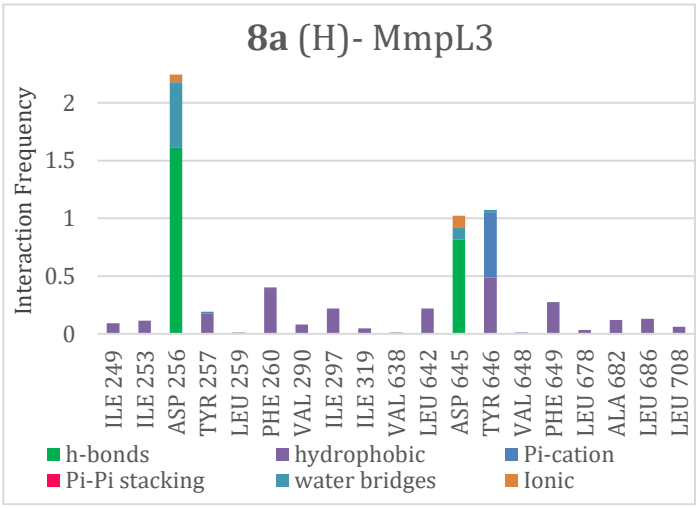

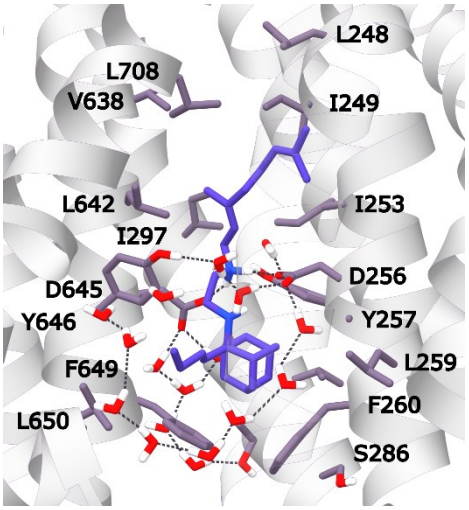

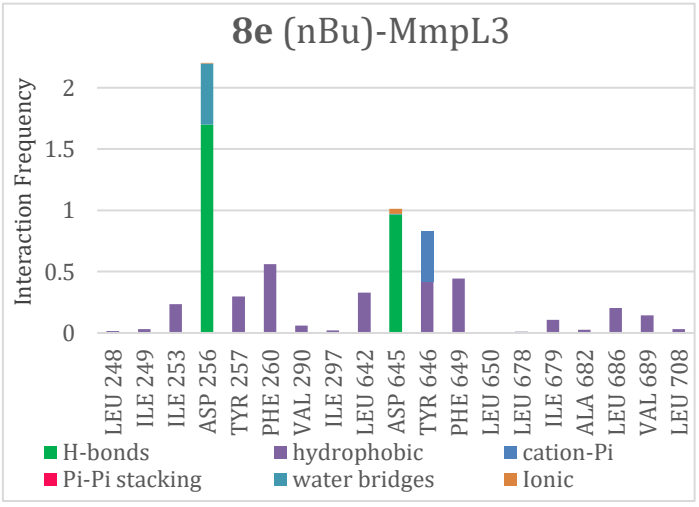

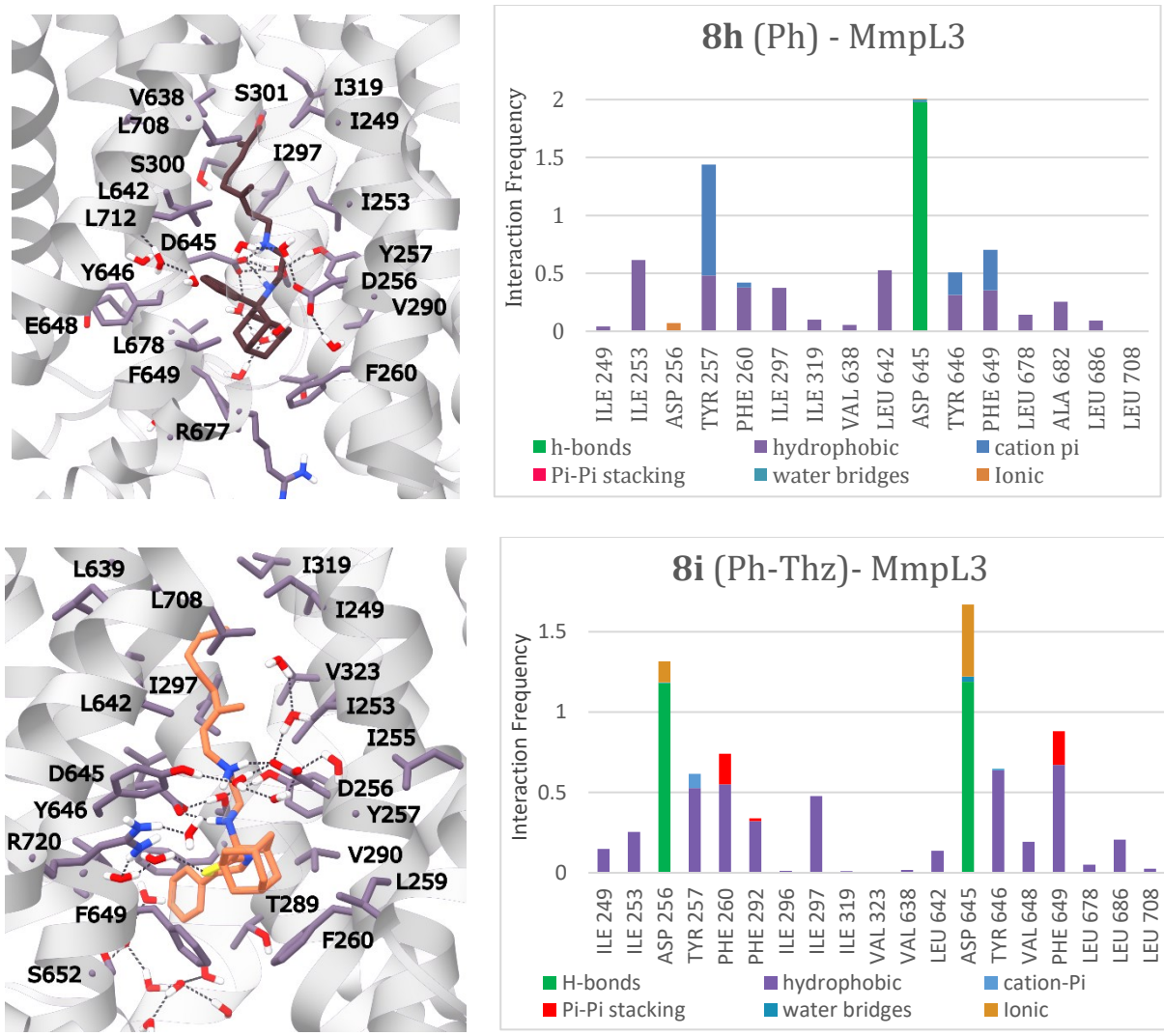

Figure 7 Last frames (left part) of the monoprotonated ethylenediamine form for SQ109 (**8a**), **8e**, **8h**, **8i** inside the MmpL3 transporter in a POPC lipid bilayer from 100ns-MD simulations with ff99sb [147]. The receptor-ligand interaction frequency histograms plotted for the whole trajectory are shown on the right (the alkyl group connected at the adamantyl C-2 is shown inside the parenthesis following the compound number). Color scheme for frames: Ligand=petrol or purple or brown or orange sticks, receptor = white ribbons, residues in light purple sticks, hydrogen bonding interactions=dark grey dashes. For the protein, the experimental structure of SQ109 (**8a**) in complex with MmpL3 (PDB ID 6AJG) was used as the reference structure for the MD simulations after excluding C-terminus which included M1-E749 residues.

Table 4 Ligand-MmpL3 binding free energies (ΔG_{eff}) calculated using MM-GBSA [148–150]method with OPLS2005 [151] force field for the calculations of the intermolecular interactions without or with using a hydrophobic slab [152–155] to model the membrane environment of the protein, $RMSD_{ligand}$ and $RMSD_{protein}$ (Ca TMD) mean values from 100ns-MD simulations for **8a-i**, **12**. The ligands have a monoprotonated ethylenediamine unit.

Cmp No	Structure	$RMSD_{ligand}$ [a] (Å)	$RMSD_{protein}$ (Ca) [b] (Å)	$RMSD_{protein}$ (Ca TMD) [c] (Å)	ΔG_{eff} [d] (kcal mol^{-1})
8a	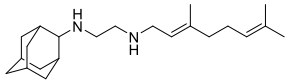	3.29 ± 0.21	3.50 ± 0.12	1.17 ± 0.09	-169.91 ± 7.37
8b	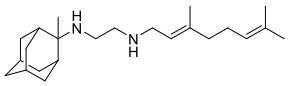	4.05 ± 0.28	4.28 ± 0.20	2.06 ± 0.07	-131.80 ± 7.81
8c	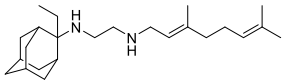	3.02 ± 0.32	3.92 ± 0.19	1.83 ± 0.09	-141.76 ± 9.72
8d	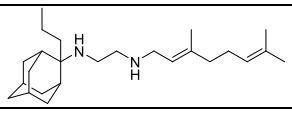	3.11 ± 0.21	3.57 ± 0.26	1.41 ± 0.08	-159.92 ± 7.44
8e	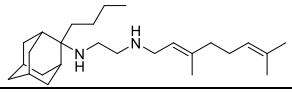	4.00 ± 0.20	3.73 ± 0.17	1.29 ± 0.07	-162.90 ± 8.18
8f	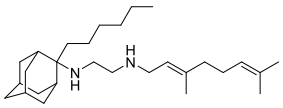	2.21 ± 0.21	3.61 ± 0.11	1.30 ± 0.05	-160.48 ± 8.81
8g	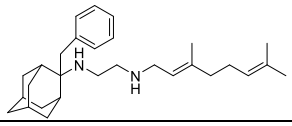	5.43 ± 0.28	3.33 ± 0.15	1.37 ± 0.06	-143.97 ± 7.68
8h	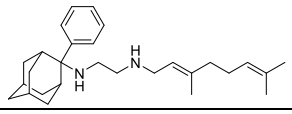	3.29 ± 0.18	2.71 ± 0.11	1.50 ± 0.07	-153.60 ± 7.61
8i	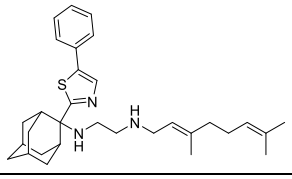	3.12 ± 0.17	3.08 ± 0.17	1.38 ± 0.07	-179.63 ± 8.75
12	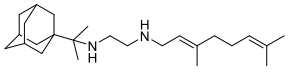	3.21 ± 0.21	4.15 ± 0.30	1.26 ± 0.06	-151.80 ± 8.74

The ligands have a monoprotonated ethylenediamine unit.

[a] Mean ± SD (Å); Ligand RMSD was calculated after superposition of each protein-ligand complex to that of the starting structure (snapshot 0) based on the C_α atoms of the protein, for the last 20 ns of the trajectories.

[b] Mean ± SD (Å); Protein RMSD was calculated for the C_α atoms of the whole protein, for the last 20 ns of the trajectories, using as starting structure snapshot 0 of the production MD simulation.

[c] Mean ± SD (Å); Protein RMSD was calculated for the C_α atoms of only the α-helices of the TMD, for the last 20 ns of the trajectories, using as starting structure snapshot 0 of the production MD simulation.

[d] Mean calculated effective binding free energy (kcal mol^{-1}) between ligand and MmpL3 receptor from three repeats. ΔG_{eff} was calculated from the last 20 ns of the trajectories using 40 ps intervals (i.e., 500 frames per trajectory) using a MM-GBSA model that considered the membrane as hydrophobic slab.

3.1.2.5 Structure-activity relationships of SQ109 analogs against MmpL3 using alchemical binding free energy calculations with TI/MD

We measured [158] (see chapter 3.1.5) the binding affinities of SQ109 (**8a**) and 9 active analogs **8b-i**, **12** against MtMmpL3 [24] using SPR with K_d values R=H (SQ109 (**8a**), 2060 μM); R=Me (**8b**, 248 μM); R=Et (**8b**, 190 μM); R=nPr (**8d**, 106 μM); R=nBu (**8e**, 108 μM); R=nHex (**8d**, 81 μM). It was observed that the Kd decreased showing tighter binding to MmpL3 as the R substituent at C-2 adamantyl (which is an H in SQ109) became larger and more hydrophobic. A similar effect was observed with phenyl (**8h**, 136 μM); benzyl (**8g**, 74 μM) (Table S1). The C-1 dimethylmethylene analog **12** had a K_d of 106 μM which is close to the isomeric **8d** (n-Pr) which had a K_d of 120 μM, and **8i** (Ph-Thz) with a K_d 91 μM.

The FEP/MD [159–161] or TI/MD [41,43,44] methods which are based on statistical mechanics can provide accurate results for relative binding free energies with an error 1 kcal mol^{-1} and have been applied in membrane protein-ligand complexes, e.g., GPCRs. [162–167] We applied the TI/MD method [162,167] combined with a thermodynamic cycle method to examine if the binding profile of the ethylenediamine analogs **8b-i**, **12** is the same with SQ109 (**8a**) in its complex with MmpL3 (PDB ID 6AJG [17]). This might be likely if there is an agreement between calculated and experimental relative binding free energies for alchemical transformations between pairs of compounds **8a-i**, **12**. We performed TI/MD calculations for alchemical transformations in selected pairs of SQ109 analogs that were not accompanied with large changes in ligand's alkyl. Thus, we calculated perturbations by one or two methylene groups in the C-2 alkyl adduct (Table 5).

Table 5 Free energy perturbation values computed with the MBAR [168] method from alchemical binding free energy simulations with TI/MD for pairs of ligands bound to Mmpl3.

Alchemical Transformation	$\Delta\Delta G_{b,exp}$ (kcal mol^{-1})	$\Delta\Delta G_{b,TI/MD}$ (kcal mol^{-1})	$\lvert\Delta\Delta G_{b,TI/MD} - \Delta\Delta G_{b,exp}\rvert$ (kcal mol^{-1})
8a (H) → **8b** (Me)	-1.30 ± 0.79	-0.49 ± 0.06	0.81
8b (Me) → **8c** (Et)	-0.16 ± 0.14	0.06 ± 0.08	0.23
8c (Et) → **8d** (n-Pr)	-0.36 ± 0.29	-0.87 ± 0.09	0.51
8d (n-Pr) → **8e** (n-Bu)	0.01 ± 0.30	0.20 ± 0.11	0.18
8e (n-Bu) → **8f** (n-Hex)	-0.18 ± 1.01	-1.42 ± 0.12	1.245
8h (Ph) → **8g** (Bn)	-0.38 ± 0.02	-1.83 ± 0.15	1.45

The end states in the alchemical calculations tested were similar to the structure in the corresponding complexes resulted from the converged 100ns-MD simulations. This was checked to certify that the 2ns-MD simulation in each λ-state was enough for the complexes to converge in an equilibrium structure. Two repeats of TI/MD calculations were performed for each alchemical transformation.

The effect in binding free energy by increasing the length of the alkyl chain by one methylene, which was examined with the alchemical perturbations **8a** (H) → **8b** (Me) or **8b** (Me) → **8c** (Et) or **8c** (Et) → **8d** (n-Pr) or **8d** (n-Pr) → **8e** (n-Bu), was to increase binding affinity (Table 5). As noted previously, in the 100 ns-MD simulations of MmpL3 - **8a-e** complexes the $RMSD_{protein}$ (Ca TMD) ≤ 2.1 Å (Table 4). Thus, the last snapshots of the MD simulations were suitable starting structures for the TI/MD simulations of these studied perturbations (Figure 7, S1).

The biggest change in experimental binding free energy was noted when H (SQ109) changed to Me (**8b**), $\Delta\Delta G_{b,exp}$ = - 1.30 kcal mol^{-1} ± 0.79 kcal mol^{-1}, and when Ph (**8h**) changed to Bn (**8g**), $\Delta\Delta G_{b,exp}$ = -0.38 ± 0.02 kcal mol^{-1} or Et (**8c**) changed to Pr (**8d**), $\Delta\Delta G_{b,exp}$ = - 0.36 kcal mol^{-1} ± 0.29 kcal mol^{-1}. The binding free energy changes for **8a** (H) → **8b** (Me) were $\Delta\Delta G_{b,exp}$ = - 1.30 kcal mol^{-1} ± 0.79 kcal mol^{-1}, $\Delta\Delta G_{b,TI/MD}$ = -0.49 ± 0.06 kcal mol^{-1}, for **8b** (Me) → **8c** (Et) were $\Delta\Delta G_{b,exp}$ = -0.16 ± 0.14 kcal mol^{-1}, $\Delta\Delta G_{b,TI/MD}$ = 0.06 ± 0.08 kcal mol^{-1}, for **8c** (Et) → **8d** (n-Pr) were $\Delta\Delta G_{b,exp}$ = -0.36 ± 0.29 kcal mol^{-1}, $\Delta\Delta G_{b,TI/MD}$ = -0.87 ± 0.09 kcal mol^{-1} and for **8d** (n-Pr) → **8e** (n-Bu) were $\Delta\Delta G_{b,exp}$ = 0.01 ± 0.30 kcal mol^{-1}, $\Delta\Delta G_{b,TI/MD}$ = 0.20 ± 0.11 kcal mol^{-1}.

We considered next the perturbation in the C-2 adamantyl alkyl by two methylenes in **8e** (n-Bu) → **8f** (n-Hex) and we studied the change by one methylene from phenyl to benzyl in C-2 substituent in **8h** (Ph) →

8g (Bn) where the perturbation in conformational space should be relatively important. The binding free energy changes were $\Delta\Delta G_{b,exp}$ = - 0.18 kcal mol^{-1} ± 0.01 kcal mol^{-1}, $\Delta\Delta G_{b,TI/MD}$ = -1.42 ± 0.15 kcal mol^{-1} and $\Delta\Delta G_{b,exp}$ = -0.38 ± 0.02 kcal mol^{-1}, $\Delta\Delta G_{b,TI/MD}$ = -1.83 ± 0.15 kcal mol^{-1}, respectively. We did not test larger perturbations that are not consistent with the method's principles. [41]

In general, the deviation from experimental values was smaller than 1 kcal mol^{-1} when the perturbation was one methylene, e.g., for **8a** (H) → **8b** (Me), **8b** (Me) → **8c** (Et), **8c** (Et) → **8d** (n-Pr), **8d** (n-Pr) → **8e** (n-Bu), see Table 5. When the perturbation in the conformational space was bigger, e.g., two methylene groups in **8e** (n-Bu) and **8f** (n-Hex) or from phenyl to benzyl in **8h** (Ph) and **8g** (Bn), the deviation was larger, 1.25 kcal mol^{-1} or 1.45 kcal mol^{-1} but was smaller than 1.5 kcal mol^{-1}. Overall, the mean assigned error (mue) was 0.739 kcal mol^{-1} which is consistent with the fact that **8a-h** bind similarly with SQ109 (**8a**) to MmpL3 in its experimental structure (PDB ID 6AJG [22]), and that alkyl or aryl substituents at the adamantyl C-2 of SQ109 can fill the lipophilic region between Tyr257, Tyr646, Phe260 and Phe649 in MmpL3 pore and increase the binding affinity.

3.1.3 Synthesis of SQ109 Analogs

As mentioned in chapter 3.1.2, based on the observation that the X-ray structure of SQ109 bound to MmpL3 [22] has the adamantyl group located close to four aromatic rings, we selected to synthesize a series of analogs with substituents at the adamantyl C-2 position that we reasoned might have enhanced hydrophobic interactions with the protein, as well as with membranes. For the synthesis of compounds **8b-i, 12** we used as starting material geranylamine (**4**), [121,125] which we prepared from geraniol (**1**) using the Mitsunobu reaction (phthalimide, PPh_3, DIAD), and amines **5a-i**, **9a,** which we synthesized as described previously [78,109,169] (Schemes 6 and 7). We carried out the preparation of the alcohol **5i** from the reaction of the 2-thiazolyl lithium reagents (generated from **16** [170] with n-BuLi) and 2-adamantanone. We prepared the bromoacetamide (Scheme 7) with Thz-Ph group **6i** as well as **10**, through a modified [169] Ritter reaction ($BrCH_2CN$, AcOH, H_2SO_4) from the corresponding tertiary alcohols **5i**, and **9b**. We prepared the bromoacetamide derivatives **6b-i** and aminoacetamides **7b-i, 11** or **14b-h**, **15** as previously described for SQ109 (**8a**). In aminoamides **14a-h**, **15** or **7a-i, 11**, compared to SQ109 (**8a**), it seemed possible that the bulkier substituents at the adamantyl C-2 carbon might hinder the reduction of the amide carbonyl, leading to a mixture of the desired ethylenediamines, accompanied by amine decomposition by-products, formed when $LiAlH_4$ in THF is used. [122,123,171] We thus synthesized the amide precursors **7a-i, 11** or **14a-h**,

15 using $LiAlH_4$ in combination with freshly distilled trimethylchlorosilane (Me_3SiCl) in THF with stirring for 2.5 h at 0-10 °C under an argon atmosphere, as described for SQ109 (**8a**). [124] We obtained the diamines **8a-i**, **12** which were purified by using column chromatography, and were then converted to crystalline monofumarate or difumarate salts for cell growth inhibition testing. Aminoacetamides were tested as crystalline monofumarate salts.

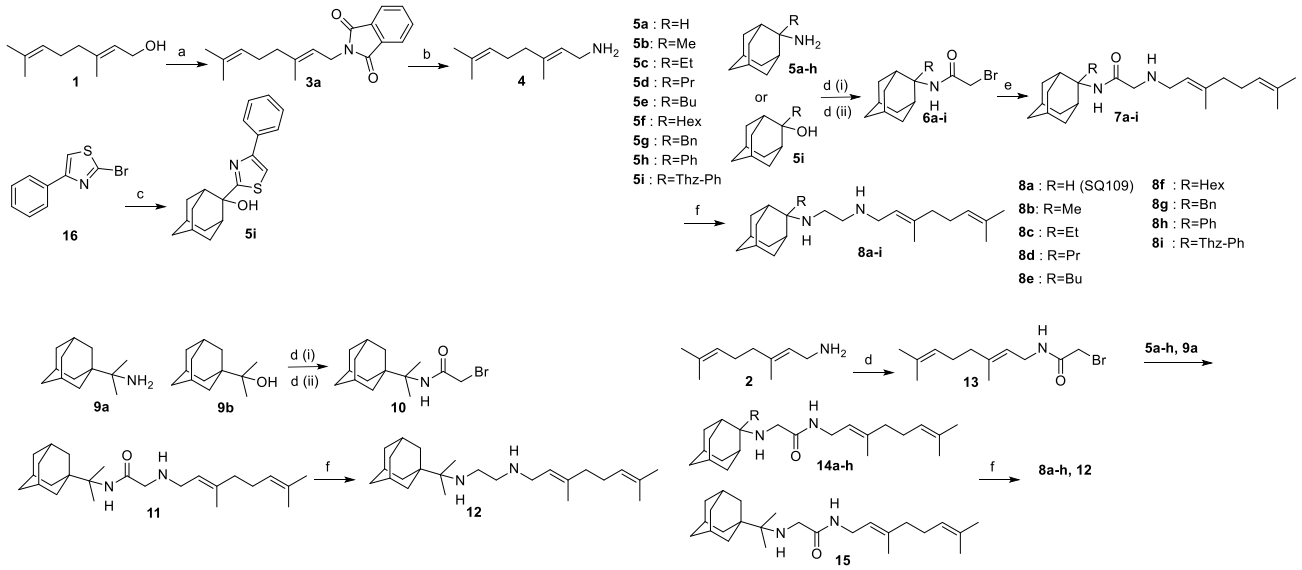

Scheme 7 Synthesis of SQ109 analogs. Reagents and conditions: (a) Phthalimide, PPh_3, DEAD, and THF, rt, 24h (81%); (b) $N_2H_4{\cdot}H_2O$, EtOH, reflux, 6h; (81%); (c) (i) n-BuLi, THF, -75 °C, 30 min; (ii) 2-adamantanone, THF, -75 °C, 1h; (iii) H_2O, 0 °C, (56%). (d_i) $ClCOCH_2Br$, K_2CO_3 (aq), CH_2Cl_2, rt, 24h (83-93%); (d_{ii}) $BrCH_2CN$, AcOH, H_2SO_4, rt, 1h (61%-quant.); (e) geranylamine (**4**), Et_3N, dry THF, rt, 48h (86-90%); (f) (i) Me_3SiCl, $LiAlH_4$, dry CH_2Cl_2, 0-5°C, Ar, 2.5 h; (ii) NaOH 10%, 0°C (20-40%).

3.1.4 Antibacterial and antiprotozoal activity of SQ109 analogs

We next investigated the activity of SQ109 (**8a**), its ethylenediamine analogs **8b–i** and **12**, and several aminoamide analogs, i.e., **7a**, **7c**, **7e**, **7g**, **7h**, **14a**, **14b**, **14d**, **11**, and **15** (Scheme 1), against several bacteria as well as protozoan parasites. We measured IC_{50} or MIC values (Table 6) against the following bacteria: *M. smegmatis*, *M. tuberculosis* HN878 (a virulent clinical strain), MtErdman, MtH37Rv, *M. abscessus*, *B. subtilis*, and *E. coli*. The protozoa were *T. brucei* bloodstream forms, *T. cruzi* Dm28c epimastigotes and intracellular amastigotes (together with results for the U2OS host cells), *L. donovani* promastigotes, *L.*

mexicana promastigotes, and *P. falciparum* asexual bloodstream forms (ABS). For the protozoa, we determined parasite IC_{50} and EC_{50} values, as well as CC_{50} values for host cells. Results are shown in Tables 7 and 8.

Table 6 Anti-bacterial activity of SQ109 analogs[a]

Comp. No	Chemical structure	*Ms* IC_{50} (μM)	*Mtb* HN878 IC_{50} (μM)	*Mtb* HN878 MIC (μM)	*Mtb* Erdman MIC (μM)	*Mtb* H37Rv MIC (μM)	*Ma*(S) MIC (μM)	*Ma*(R) MIC (μM)	*Bs* IC_{50} (μM)	*Ec* IC_{50} (μM)
8a	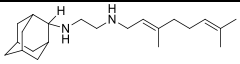	2.4 ± 0.3	0.27 ± 0.02	0.4	1.8	1.8	44	22	16	15
8b	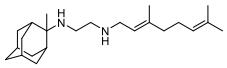	4.4 ± 0.5	0.86 ± 0.06	0.8	3.5	3.5	43	22	ND	25
8c	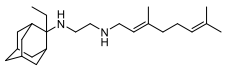	4.0	1.9 ± 0.06	1.6	6.8	6.8	22	10.7	4.3	18
8d	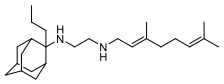	4.3 ± 0.8	2.6 ± 1	3	13	13	10	10	ND	7.6
8e	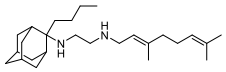	2.5	2.5 ± 0.2	3	9.7	12.9	6.2	6.2	0.54	7.8
8f	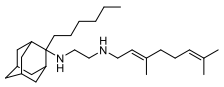	4.7	3.4 ± 0.6	3	12	12	12	12	1.0	9.2
8g	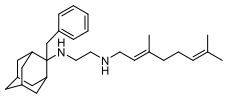	6.0	2.0 ± 0.5	1.6	6.1	6.1	5.8	5.8	0.59	1.3 x 10^2
8h	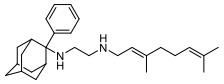	5.8	2.3 ± 0.2	1.6	13	13	12	6	ND	NI
12	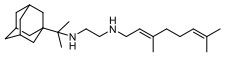	15 ± 2	3.4 ± 0.6	3	13	13	12.9	12.9	ND	8.9
8i	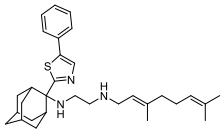	21	ND	ND	ND	ND	21.5	21.5	ND	ND
7a	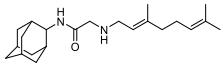	45 ± 6	>25	25	340	340	ND	ND	ND	2.3 x 10^2
7c	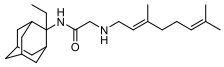	7.7	6.6 ± 0.2	6.25	16	16	ND	ND	1.9	NI
7e	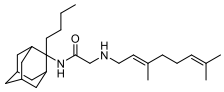	17	13 ± 0.3	12.5	15	15	ND	ND	2.8	NI

7g	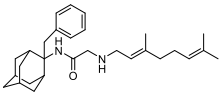	17	11 ± 1	12.5	29	29	ND	ND	2.3	NI
7h	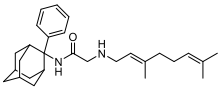	26	ND	ND	38	38	ND	ND	4.5	NI
11	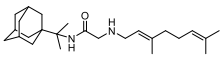	44 ± 4	13 ± 2	12.5	19	19	ND	ND	ND	NI
14a	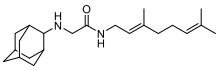	5 ± 0.8	3.7 ± 0.6	3	16	21	ND	ND	ND	695
14b	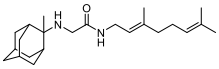	9	4.9 ± 0.1	6.25	20	30	ND	ND	ND	NI
14d	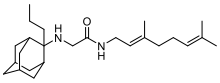	49 ± 5	>25	25	32	32	ND	ND	ND	NI
15	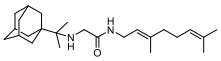	31 ± 3	17 ± 6	12.5	38	38	ND	ND	ND	NI

[a]Abbreviations used: *Ms*, *M. smegmatis*; *Mtb*, *M. tuberculosis*; *Ma*, *M. abscessus*; S, smooth variant; R, rough variant; *Bs*, *Bacillus subtilis*; *Ec*, *E. coli*. ND=not determined. NI = no inhibition.

Table 7 Activity of SQ109 analogs against Trypanosomatid parasites

Comp. No	Chemical structure	*T. brucei* IC_{50} µM	IC_{50} *(EPI)* µM	*T. cruzi* IC_{50} *(PAR)* µM	CC_{50} *(U20S)* µM	*L. donovani* IC_{50} µM	*L. mexicana* IC_{50} *(µM)*
8a	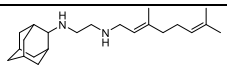	0.91 ± 0.03	6.8 ± 2	0.74 ± 0.04	4.1 ± 0.2	2.0 ± 0.1	0.73 ± 0.2
8b	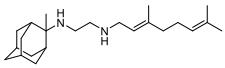	2.1 ± 0.02	3.5 ± 1	0.77 ± 0.2	2.8 ± 0.7	2.0 ± 1	0.43 ± 0.08
8c	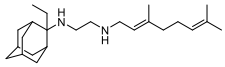	1.4 ± 0.2	8.0 ± 2	1.3 ± 0.06	2.5 ± 0.3	2.1 ± 0.4	ND
8d	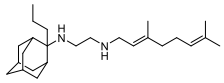	0.88 ± 0.2	2.1 ± 0.9	0.60 ± 0.5	1.6 ± 0.1	2.0 ± 0.2	1.9 ± 0.2
8e	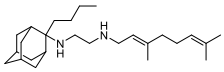	0.37 ± 0.02	2.5 ± 1	0.84 ± 0.5	1.7 ± 1	4.0 ± 0.4	ND
8f	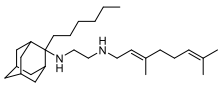	0.98 ± 0.09	8.2 ± 0.4	1.3 ± 0.07	4.1 ± 1	8.8 ± 0.4	ND
8g	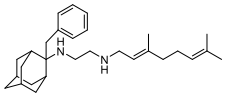	0.85 ± 0.09	6.6 ± 1	0.92 ± 0.06	2.0 ± 0.4	6.1 ± 0.06	ND
8h	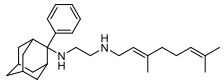	1.3 ± 0.3	7.3 ± 2	0.60 ± 0.04	3.5 ± 1	1.4 ± 1	ND

12	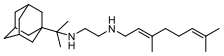	1.4 ± 0.03	2.4 ± 0.7	0.56 ± 0.9	1.4 ± 0.2	2.3 ± 0.1	4.7 ± 0.2
7a	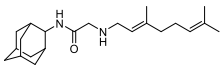	12 ± 1	>100	4.2 ± 0.4	14 ± 0.7	10 ± 0.5	2.2 ± 0.8
7c	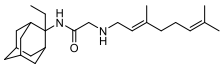	3.9 ± 0.3	14 ± 0.04	3.2 ± 0.2	7.5 ± 0.6	44 ± 11	ND
7e	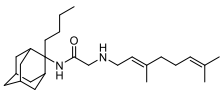	3.0 ± 0.2	48 ± 0.07	8.8 ± 1.3	15 ± 0.5	25 ± 14	ND
7g	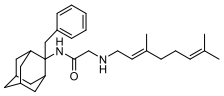	5.6 ± 1	17 ± 4	2.9 ± 0.3	7.0 ± 0.2	27 ± 0.8	ND
7h	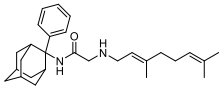	4.1 ± 0.6	18 ± 2	3.4 ± 0.2	7.0 ± 0.4	26 ± 28	ND
11	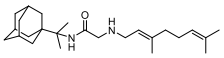	6.2 ± 0.2	16 ± 4	4.4 ± 0.3	6.9 ± 0.1	5.0 ± 0.6	5.2 ± 0.2
14a	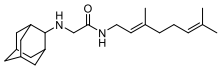	9.9 ± 0.7	28 ± 4	2.7 ± 0.2	9.5 ± 0.9	12 ± 0.9	2.0 ± 0.2
14b	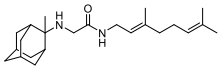	6.6 ± 0.03	18 ± 4	2.3 ± 0.2	7.2 ± 0.9	11 ± 0.9	2.4 ± 0.7
14d	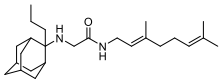	2.3 ± 0.1	14 ± 5	2.8 ± 0.3	9.1 ± 0.4	8.4 ± 2	0.73 ± 0.2
15	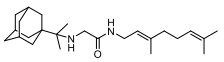	5.9 ± 0.1	15 ± 3	2.6 ± 0.1	7.1 ± 0.5	12 ± 8	5.0 ± 0.1

Table 8 Activity of SQ109 analogs against *Plasmodium falciparum* asexual blood stages

Comp. No	Chemical structure	PfABS IC_{50} (µM ± S.E.)	HepG2 % viability @ 20 µM
8a	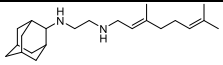	1.58 ± 0.2	97
8b	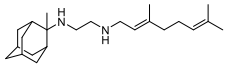	0.66 ± 0.18	100
8c	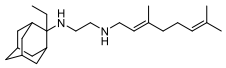	0.16 ± 0.07	43 (85% @ 2 µM)
8d	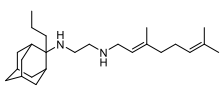	0.53 ± 0.22	100
8e	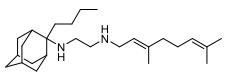	0.27 ± 0.04	50 (83% @ 2 µM)

8g	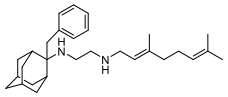	0.32 ± 0.03	100
8h	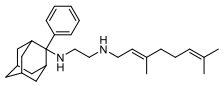	0.42 ± 0.09	100
7a	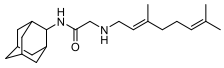	6.49 ± 0.33	100
11	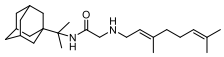	7.63 ± 1.13	100
12	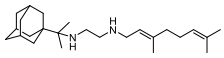	0.77 ± 0.1	100
14a	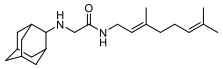	>10	99
14b	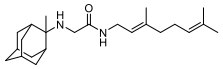	6.47 ± 0.65	94
14d	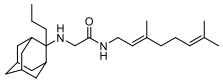	5.27 ± 0.41	100
15	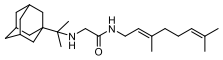	5.44 ± 0.32	76 (91% @ 2 μM)

We first screened the 19 SQ109 analogs (together with SQ109) against *M. smegmatis* (Table 6). The IC_{50} value for SQ109 (**8a**) against *M. smegmatis* was 2.4 μM, in good accord with previous work. [172] Addition of an *n*-butyl group at C-2 (**8e**) yielded essentially the same result (IC_{50} = 2.5 μM, Table 6), whereas shorter as well as bulkier substituents had less activity. For example, methyl (**8b**), ethyl (**8c**), *n*-propyl (**8d**), *n*-hexyl (**8f**), phenyl (**8h**), and benzyl (**8g**) group analogs had IC_{50} values in the ∼4−6 μM range. The larger substituted thiazole (**8i**) was even less active, with IC_{50} = 20 μM (Table 6). Likewise, the C-1 substituted analog **12**, containing a dimethylmethylene group, was less active, with an IC_{50} value of 15 μM. Thus, the most active compounds have a relatively small substituent at C-2 and have IC_{50} values in the ∼2−4 μM range. We then investigated the activity of SQ109 and the SQ109 analogs against MtHN878, a hypervirulent *M. tuberculosis* strain. Representative dose−response curves are shown in Figure 8A. MIC values are also shown in Table 6, and a correlation (R^2 = 0.96) between the log IC_{50} values from the dose−response curves and the log MIC values from visual inspection is shown in Figure 8B. MIC value determination using visual inspection rather than a plate reader is particularly important with *M. abscessus*, described below, because in the rough (R) form, cells are prone to clumping. As can be seen in Table 6, the presence of a methyl group at C-2 (**8b**) yielded an IC_{50} = 0.86 μM, which is ∼3-fold higher than the IC_{50} = 0.27 μM of SQ109. The larger alkyl adducts, e.g., ethyl (**8c**), *n*-propyl (**8d**), *n*-butyl (**8e**), *n*-hexyl

(**8f**), benzyl (**8g**), and phenyl (**8h**) analogs, showed comparable IC_{50} values in the ~2−3 μM range. In addition, we tested compounds against the *M. tuberculosis* Erdman and H37Rv strains, finding generally similar patterns of activity with the methyl adduct yielding an IC_{50} = 2 μM and other analogs with alkyl groups having IC_{50} values in the 4−8 μM range (Table 6). This activity was at least 2-fold lower than found with SQ109 (**8a**) (IC_{50} = 1 μM), and the aminoamides (**7a**, **7c**, **7e**, **7g**, **7h**, **14a**, **14b**, **14d**, **11**, and **15**) were generally less active than the more basic ethylenediamine analogs.

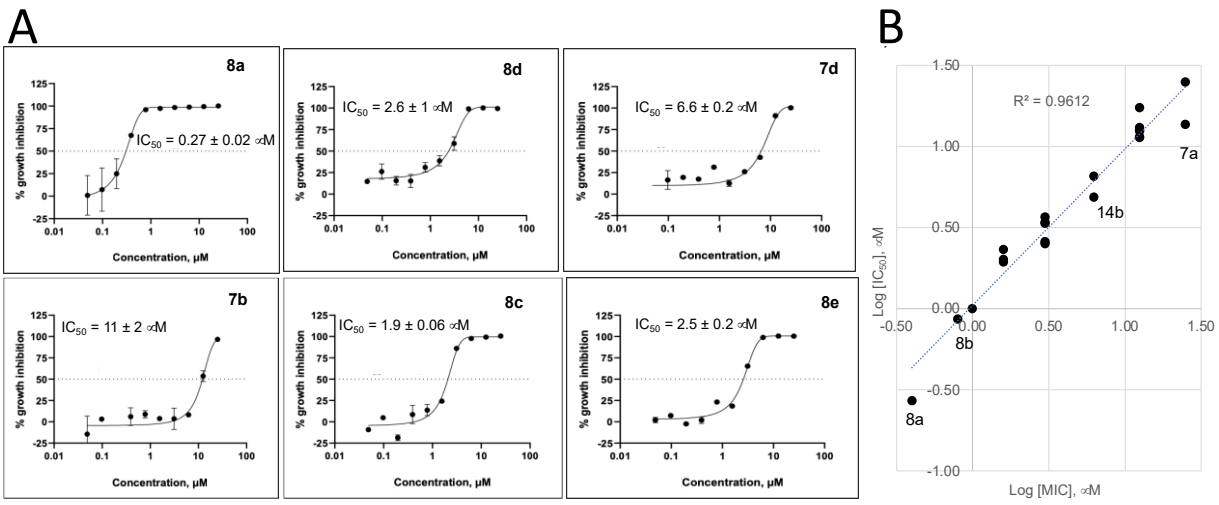

Figure 8 Dose-response curves for SQ109 and the SQ109 analogs against MtHN878 and correlation between log IC_{50} and log MIC values. (A) Representative dose response curves. (B) Correlation between log IC_{50} and log MIC values (R^2 = 0.9612).

In addition to investigating *M. tuberculosis*, we also investigated activity against *M. abscessus*, which is increasingly recognized [173] as an emerging opportunistic pathogen causing severe lung disease, particularly in cystic fibrosis patients. Because it is intrinsically resistant to most conventional antibiotics, there is an unmet need for effective treatments. [173] We determined the *in vitro* activity of SQ109 and a series of analogs against both smooth (S) and rough (R) variants of *M. abscessus*, which differ in their susceptibility profile to several antibiotics. As has been shown previously, [174] the MIC of SQ109 (**8a**) was much higher against *M. abscessus* (here, 22−44 μM) than against *M. tuberculosis* (~0.3−1 μM). However, the *n*-butyl analog **8e** as well as the benzyl analog **8g** had significantly improved activity against both the S and R variants (MICs of 5.8−6.2 μM), warranting future work on benzyl derivatives. The MIC values of all compounds against the R and S strains were either identical to or within a factor of 2× of each other. We

also investigated an *M. abscessus* strain harboring an A309P mutation located in the transmembrane domain in MmpL3 (strain PIPD1R1). Surprisingly, this mutant was not resistant to SQ109 or its analogs, having essentially the same MIC values as the wild-type strains.

We then questioned whether any of the compounds investigated had activity against other bacteria, ones that lack MmpL3. In the Gram-positive bacterium *B. subtilis*, SQ109 (**8a**) had an IC_{50} value of 16 μM (Table 6), and of interest, several of the SQ109 analogs had much better activity. For example, *n*-butyl (8e), *n*-hexyl (**8f**), and phenyl (**8h**) analogs had IC_{50} values in the 0.5−1.0 μM range (Table 6). We also observed that some tested aminoamides had activity in the 2−5 μM range. In the Gram-negative bacterium *E. coli*, the IC_{50} value for SQ109 (**8a**) was 15 μM, and the *n*-alkyl (propyl, butyl, hexyl) analogs had IC_{50} values in the ∼8−10 μM range, slightly better than found with SQ109 (**8a**). Because neither *B. subtilis* nor *E. coli* contain the MmpL3 protein, other targets must be involved, so the promising activity of some compounds is of interest for future work. There was either no inhibition or very low inhibition (IC_{50} values >70 μM) with the aminoamides tested (Table 6), suggesting that the ethylenediamine group might play a role in activity as an uncoupler as previously suggested for *Mtb* and protozoa.

Next, we investigated the activities of the SQ109 analogs against the following protozoa: *T. brucei*, *T. cruzi*, and two *Leishmania* species. In each case, the activity of SQ109 (**8a**) against these protozoa has been reported previously and has been proposed to arise from protonophore uncoupling, as well as effects on Ca^{2+} homeostasis. [40,175,176] Results for SQ109 (**8a**) and the analogs are shown in Table 7, and representative dose−response curves are shown in Figure S6. With *T. brucei* bloodstream forms, SQ109 (**8a**) had an IC_{50} value of 0.91 μM, and slightly better activity was found with the adamantyl C-2 *n*-propyl (**8d**), *n*-butyl (**8e**), *n*-hexyl (**8f**), and benzyl (**8g**) analogs (IC_{50} values of 0.88, 0.37, 0.98, and 0.85 μM, respectively), but activity is slightly less with phenyl (**8h**) and C-1 dimethylmethylene (**12**) analogs (IC_{50} values of 1.3 and 1.4 μM, respectively). Of interest, the aminoamides also had activity, although IC_{50} values were ∼5−10-fold larger (in the range of ∼2−12 μM) compared to the ethylenediamines (**8b−g**, **12**). With *T. cruzi*, we investigated both the epimastigote as well as (clinically relevant) amastigote forms and the activity against the host cell (U2OS). With epimastigotes, the IC_{50} of SQ109 was 6.8, μM, which is ∼3−4× larger than that found with the C-2 ethylene diamine analogs *n*-propyl (**8d**) and *n*-butyl (**8e**) and the C-1 dimethylmethylene analog (**12**). With aminoamide analogs, activity was again lower than with the ethylene diamine analogs. With the intracellular amastigote form, SQ109 (**8a**) had an IC_{50} value of 0.74 μM, and all of the ethylenediamine analogs had good activity, with the phenyl (**8h**) analog being comparable to (though not

clearly better) SQ109. The aminoamides were all less active, with IC_{50} values in the range of ∼2−9 μM. The same trends in activity were seen with the inhibition of host cell growth, with the ethylenediamines being more potent host cell growth inhibitors than the amides. With *L. donovani*, we tested SQ109 and 18 analogs (Table 7). The IC_{50} value for SQ109 was 2 μM, and the adamantyl C-2 methyl (**8b**), ethyl (**8c**), *n*-propyl (**8d**), *n*-butyl (**8e**), phenyl (**8h**), and dimethylmethylene (**12**) analogs had higher or similar activity (in the 1−4 μM range), whereas the *n*-hexyl (**8f**) analog was less active (IC_{50} = 8.8 μM), as was the benzyl (**8g**) analog (IC_{50} = 6.1 μM). As with *T. brucei* and *T. cruzi*, the aminoamides were in general less (or much less) active with IC_{50} values in the range of ∼5−44 μM. With *L. mexicana*, the IC_{50} value for SQ109 (**8a**) was 0.50 μM, and the adamantyl C-2 methyl (**8b**) had an IC_{50} = 0.43 μM, whereas *n*-propyl (**8d**) was ∼4-fold less active (IC_{50} = 1.94 μM). Several aminoamides had similar activity with **8d** and amide **14d** having IC_{50} = 0.73 μM (Table 7).

In addition to investigating the trypanosomatid parasites, we also investigated the asexual bloodstream form of the apicomplexan parasite *P. falciparum* (PfABS). As previously reported, [172] SQ109 (**8a**) has activity against the PfABS parasite and only modest toxicity against HepG2 (human hepatocellular carcinoma) cells. We thus evaluated SQ109 and 13 of its analogs, finding more potent (∼100−900 nM) PfABS activity with the adamantyl C-2 methyl (**8b**), ethyl (**8c**), *n*-propyl (**8d**), *n*-butyl (**8e**), phenyl (**8h**), and benzyl (**8g**) analogs, as well as with the C-1 dimethylmethylene analog (**12**), compared to SQ109 (IC_{50} = 1.6 μM, Table 8). The ethyl (**8c**) analog had ∼10-fold better activity than that obtained with SQ109 (160 nM versus 1.6 μM), whereas the phenyl (**8h**) and benzyl (**8g**) analogs had 4× and 5× increased potency, respectively. Using HepG2 cell line viability as a test of overt toxicity, we found that there was 43% cell viability at 20 μM with the ethyl analog but 100% viability with both phenyl and benzyl analogs, making them of potential interest as an antimalarial hit with low toxicity against mammalian cells.

3.1.5 MmpL3–Inhibitor Binding Interactions

We next used SPR to investigate the binding of SQ109 and several analogs to an expressed *M. tuberculosis* MmpL3 (MtMmpL3). [24] We focused on the measurement of the K_D values for SQ109 (**8a**) and the nine ethylenediamine analogs (**8b–i** and **12**) together with four aminoamides (**7a**, **14a**, **14b**, and **14d**). The experimental SPR results are shown in Figure S7. Data were fit using the two-state model, as described previously, [24] together with the 1:1 binding model.

The rate constants and the equilibrium dissociation constants K_D's for both models are shown in Tables 9 and 10. The two-state binding model that postulates a conformational change in the protein upon binding of an inhibitor gave improved statistical fits as seen from lower residual values. However, as can be seen in Table 9, there are essentially no differences between the K_D values obtained using either model.

What has been puzzling about the SPR result for SQ109 binding to *M. tuberculosis* MmpL3 (MtMmpL3) reported previously is that the K_D value for SQ109 (**8a**) was high (~1.5 mM), whereas the IC_{50} against *M. tuberculosis* itself (IC_{50} ≈ 0.4–1 μM, Table 6) is very low. The IC_{50} for *M. smegmatis* (Table 6) is higher (~2.4 μM) but again much lower than the K_D value measured against MtMmpL3 (Table 9). The K_D values for all 14 compounds tested are lower than the one found for SQ109 (**8a**) (Tables 9 and 10). What is of particular interest is that, compared to SQ109 (**8a**), there is a general decrease in the K_D value, meaning tighter binding to MmpL3, as the compounds become more hydrophobic. For example, using the K_D values from the two-state binding model that are shown in Table 10, with SQ109 (**8a**) and the adamantyl C-2 substituted species (see structure of R in Scheme 7), we found the following K_D values: R = H (**8a** or SQ109, 2060 μM); R = methyl (**8b**, 248 μM); R = ethyl (**8c**, 190 μM); R = *n*-propyl (**8d**, 106 μM); R = *n*-butyl (**8e**, 108 μM); R = *n*-hexyl (**8f**, 81 μM). That is, as the R substituent at C-2 (which is an H in SQ109) becomes larger and more hydrophobic, the K_D decreased. A similar effect was observed with phenyl (**8h**, 136 μM) and benzyl (**8g**, 74 μM) C-2 substituents (Table 10). The C-1 dimethylmethylene analog **12** had a K_D of 106 μM, which was close to the isomeric C-2 *n*-propyl **8d** that had a K_D of 120 μM. The thiazole **8i** was also a relatively good binder with K_D ~90 μM (Table 9).

Table 9 SPR results *for M. tuberculosis* MmpL3-ligand binding using a 1:1 binding model[a]

Comp. No	Chemical structure	k_{on} ($^1/_{M \times s}$)	k_{off} ($^1/_s$)	K_D, μM 1:1 model	Residuals χ^2 (RU)^2
8a	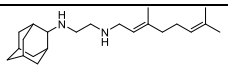	351.9	0.882	2510	58.7
8b	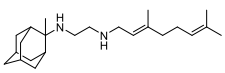	3658	0.6882	188	16
8c	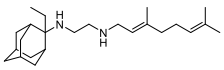	4710	0.8409	180	37.9
12	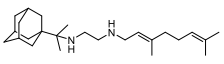	6276	0.6646	106	62.2

8d	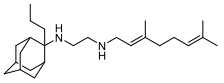	5926	0.5403	91	48.9
8e	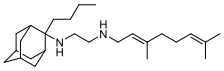	3998	0.3888	97	22.6
8f	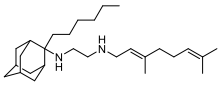	4441	0.2964	67	126
8g	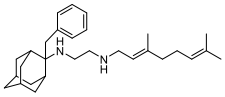	5789	0.3999	69	85.1
8h	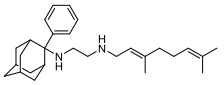	4060	0.465	115	110
8i	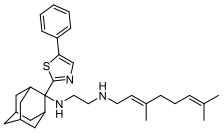	5627	0.4902	87	108
7a	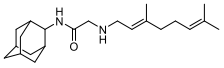	9.44E+02	0.236	250	19.4
14a	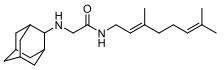	4537	1.27	280	10.7
14b	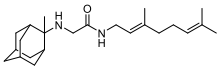	1762	0.7506	426	44.1
14d	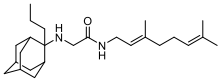	3.00E+03	0.754	252	24.2

[a]Data were fit globally using the 1:1 Langmuir binding model. Equilibrium dissociation constants (K_D's) were calculated from the ratio of the dissociation and association rate constants.

Table 10 SPR results *for M. tuberculosis* MmpL3-ligand binding using the two-state model[a]

Comp. No	Chemical structure	k_{a1} ($^1/_{M \times s}$)	k_{d1} ($^1/_s$)	k_{a2} ($^1/_s$)	k_{d2} ($^1/_s$)	K_D, µM 2-state	Residuals χ^2 (RU)^2
8a	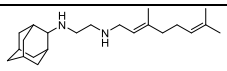	429.8	1.098	0.005315	0.02222	2060	34.5
8b	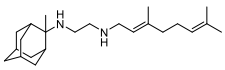	4958	1.613	0.01084	0.03486	248	9.52
8c	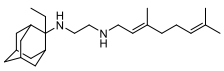	5473	1.284	0.006994	0.03012	190	7.57
12	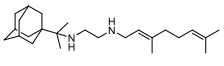	7245	1.05	0.007539	0.03558	120	15
8d	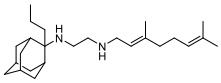	7325	0.9488	0.00968	0.04246	106	12.2

8e	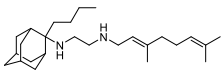	5151	0.7008	0.009897	0.03763	108	7.48
8f	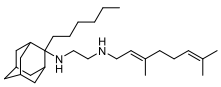	4642	0.4552	0.008637	0.03992	81	38.9
8g	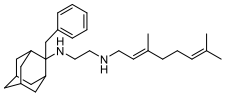	6462	0.5715	0.006528	0.03248	74	30.3
8h	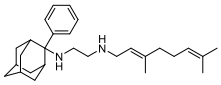	2.59E+04	4.085	0.00526	0.03247	136	29.5
8i	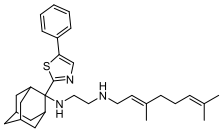	3946	0.434	0.006253	0.03057	91	31.1
7a	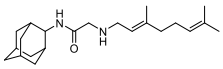	1.23E+04	4.816	0.01065	0.04928	321	4.38
14a	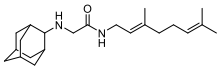	2345	2.023	0.009004	0.02642	644	4.18
14b	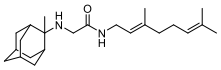	1917	1.363	0.009268	0.02741	531	12.6
14d	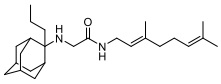	3277	1.04	0.005907	0.03103	267	9.59

[a]Data were fit globally using the two-state model. k_{a1}, k_{d1}, k_{a2}, and k_{d2} are microscopic rate constants. Equilibrium dissociation constants (K_D's) were calculated from the ratio of the dissociation and association rate constants.

As can be seen in Figure 9A, there is a significant correlation between the log K_D values for all 14 compounds (i.e., including the four amides) and log $D_{7.4}$, the computed oil−water partition coefficient at pH = 7.4, with a Pearson R coefficient = 0.73 and $p < 0.003$. That is, the strongest binding occurs with the most hydrophobic species. This is not unexpected; however, we find no correlation between cell growth inhibition and log K_D (Figure 9B) or between cell growth inhibition and log $D_{7.4}$ for all of the compounds tested (Figure 9C). Essentially the same results were obtained using either the 1:1 or two-state models for K_D.

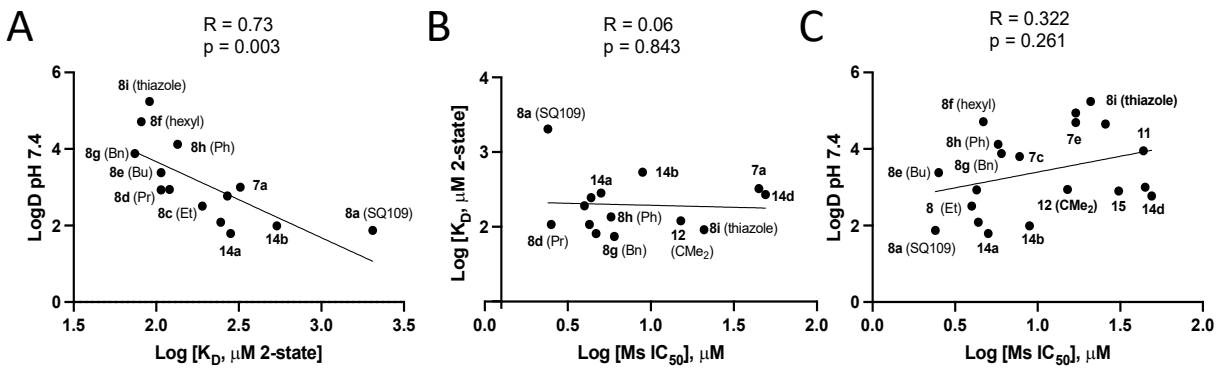

Figure 9 Graphs showing correlations between log K_D, Log $D_{7.4}$, and *M. smegmatis* cell growth inhibition. (A) Log K_D versus log$D_{7.4}$; R=0.73, p=0.003. (B) Log Ms IC_{50} and log K_D; R=0.06, p=0.843 (C) Log Ms IC_{50} and log$D_{7.4}$, for all compounds tested; R=0.322, p=0.261. Selected compound numbers are shown.

3.1.6 Membrane–Inhibitor Interactions

Another target for SQ109 (**8a**) in both bacteria and protozoa involves effects on the proton motive force and Ca^{2+} homeostasis – both of which involve cell membranes. In previous work, [36] we investigated the pH dependence of the activity of inhibitors, including SQ109 analogs, on *M. smegmatis* cell growth inhibition (IC_{50} values) and found that there were correlations between the IC_{50} values and uncoupling (ΔpH collapse), as well as with changes in the gel-to-liquid crystal phase transition temperature (T_m) in DSC experiments with lipid bilayer membranes, and with computed log D values. We showed [36] that cell growth inhibition activity increased from pH 5 to 7 to 9, and this correlated with increasing uncoupler activity, decreasing T_m values, and increasing log D values. That is, increased hydrophobicity results in more membrane binding leading to more fluidity and uncoupling activity, as well as providing a reservoir of inhibitor for binding to membrane protein targets. Such effects could be important in the protozoa.

We therefore next used DSC to investigate the effects of SQ109 (**8a**) and analogs **8b–h** and **12** on the gel-to-liquid crystal phase transition in 1,2-dimyristoyl-*sn*-glycero-3-phosphocholine (DMPC) bilayers (10 wt % inhibitor, pH 7.4) as well as with 1,2-distearoyl-*sn*-glycero-3-phosphoglycerol (DSPG) bilayers. The zwitterionic DMPC is a model for protozoal membranes that are primarily phosphatidylcholines and phosphatidylethanolamines, whereas DSPG is an anionic species and is a model for the mycobacterial inner membrane lipids. DSC scans of each compound during heating (Figure 10A, B, and Table 11) and

cooling (Figures S8 and S9 and Table S3) were then compared with measurements on DMPC or DSPG alone. The DSC scans of the main transition for the DMPC systems (Figure 10A) showed that compared to DMPC without any inhibitor, SQ109 (**8a**) and **12** decreased T_m by 3−4 °C, whereas **8b** (Me), **8c** (Et), **8d** (Pr), **8e** (Bu), **8f** (Hex), **8g** (Bn), and **8h** (Ph) decreased T_m by ca. 5.6, 6.6, 6, 7.8, 9.7, 6.9, and 8.8 °C, respectively (Table 11). The DSC scans for DSPG systems in Figure 10B showed that compared to DSPG alone, SQ109 (**8a**), **8b** (Me), **12**, and **8d** (Pr) decreased the T_m by 3−4 °C, whereas **8e** (Bu), **8f** (Hex), **8g** (Bn), and **8h** (Ph) decreased T_m by ∼5 °C (Table 11).

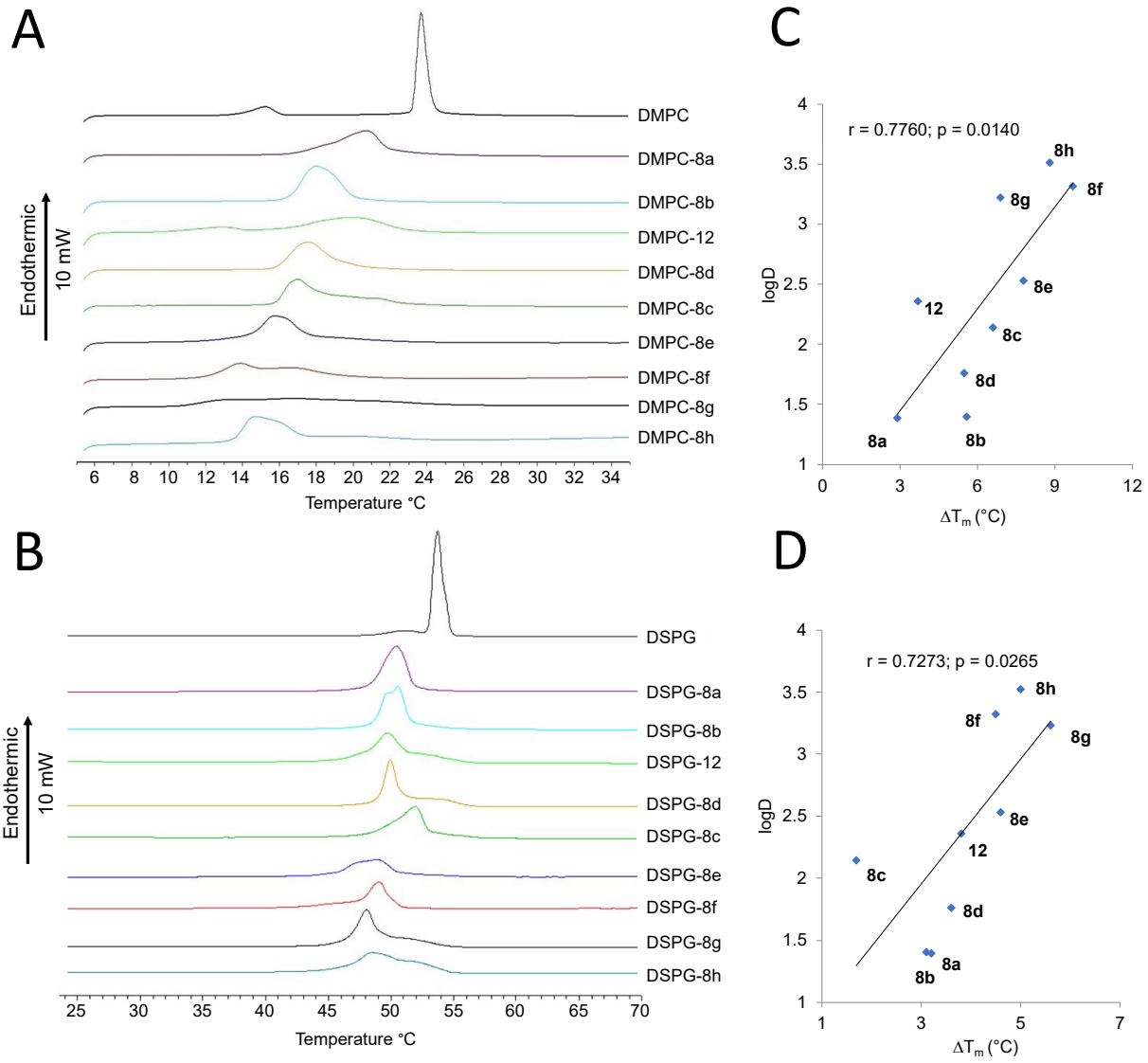

Figure 10 DSC results for DMPC and DSPG with and without SQ109 (**8a**) and 8 ethylenediamine analogs and correlations between ΔT_m and $logD_{7.4}$. (A) DSC heating scans for DMPC. (B) DSC heating scans for

DSPG. (C) Correlation between $logD_{7.4}$ and the decrease in T_m (ΔT_m) for DMPC. Pearson R coefficient = 0.776, p = 0.014. (D) as in (C) but for DSPG. Pearson R coefficient = 0.727, p = 0.026.

Table 11 DSC results (Heating) for the DMPC:SQ109 analog systems in DMPC hydrated with PBS (phosphate buffered saline, pH=7.4) and calculated $logD_{7.4}$ values at the same pH.[a]

Sample	T_m	$\Delta T_{1/2}$	ΔH	Sample	T_m	$\Delta T_{1/2}$	ΔH	$logD_{7.4}$
DMPC	23.5	0.59	30.3	DSPG	53.6	0.9	48.1	
DMPC:**8a** (H)	20.6	2.6	23.3	DSPG:**8a** (H)	50.4	2.1	54.0	1.39
DMPC:**8b** (Me)	17.9	2.2	25.6	DSPG:**8b** (Me)	50.5	2.0	53.2	1.40
DMPC:**12**	19.8	4.1	17.8	DSPG:**12**	49.8	2.4	55.8	2.36
DMPC:**8d** (Pr)	17.5	2.2	22.6	DSPG:**8d** (Pr)	50.0	1.1	48.1	2.14
DMPC:**8c** (Et)	16.9	2.0	24.0	DSPG:**8c** (Et)	51.9	2.5	49.9	1.76
DMPC:**8e** (Bu)	15.7	2.2	24.4	DSPG:**8e** (Bu)	49.0	3.6	38.5	2.53
DMPC:**8f** (Hex)	13.8	5.1	24.6	DSPG:**8f** (Hex)	49.1	1.7	36.6	3.32
DMPC:**8g** (Bn)	16.6	10	21.6	DSPG:**8g** (Bn)	48.0	1.7	55.5	3.23
DMPC: **8h** (Ph)	14.7	2.7	29.8	DSPG: **8h** (Ph)	48.6	5.3	55.4	3.52

[a]m: main transition; T_m (°C), temperature at which heat capacity (ΔC_P) at constant pressure is the maximum; $\Delta T_{1/2}$ (°C), half width at half peak height of the main transition; ΔH (kJ mol^{-1}), main transition enthalpy normalized per gram of the bilayer. Results were the same after two repeats.

These results indicated that SQ109 (**8a**) and the analogs incorporate into the phospholipid bilayers and fluidize the membranes, generating a structure that melts at a lower temperature, T_m, compared to the pure membrane, and this effect was more pronounced as the size of the inhibitor increases. Compared to the pure DMPC bilayer, SQ109 (**8a**), **8b** (Me), **8c** (Et), **8d** (Pr), **8e** (Bu), **8h** (Ph), and **12** broadened the main transition peak by $\Delta T_{1/2}$ = 0.7−2.4 °C (Table 11), whereas compounds **12**, **8f** (Hex), and **8g** (Bn) broadened the peak by $\Delta T_{1/2}$ = 3.5, 4.4, and 9.6 °C most likely as a result of the formation of inhomogeneous domains that melt over a broad temperature range. Similarly, compared to the pure DSPG bilayer, SQ109 (**8a**), **8b** (Me), **8c** (Et), **8d** (Pr), **8f** (Hex), **8g** (Bn), and **12** broadened the main transition peak by $\Delta T_{1/2}$ = 0.2−1.6 °C, whereas compounds **8e** (Bu) and **8h** (Ph) broadened the peak by 2.7 and 4.4 °C, respectively, again most likely as a result of the formation of inhomogeneous domains that melt over a broad temperature range.[45]

3.1.7 Microsomal Stability and Solubility

Finally, we investigated the microsomal stability of analog **8b** (Me) and analog **8h** (Ph) as well as of SQ109 (**8a**) in human, mice, and rat liver microsomes. In a previous work, Jia et al. [177,178] found that SQ109 was metabolized in rats, mice, and dogs with [14C-SQ109] half-life values of 5 h in mice [177] and >5 h in rats and dogs. [178] Using liver microsomes and cells expressing P450 enzymes, they concluded that SQ109 was rapidly metabolized to oxygenated species, and we recently reported their structures. [172] It was thus of interest to investigate using liver microsome assays whether SQ109 analogs were also metabolized. We found that, as expected, [177,178] SQ109 (**8a**) was rapidly metabolized (Table S2), whereas the methyl analog **8b** was ∼2−4× more stable (% remanent at 60 min) than SQ109 (**8a**). The phenyl analog **8h** had the same % remanent as SQ109 (**8a**) (at 60 min) in mice microsomes, although it was more rapidly metabolized in human and rat liver microsomes. The intrinsic clearance rates (CLint's) in mice microsomes were essentially the same as found with SQ109 for **8b** and **8h** but were about twice as large as found with SQ109 (**8a**) in the human and rat liver microsome assays (Table S4). Although all of these rates are high, it is of course well known that SQ109 (**8a**) is, nevertheless, effective against *M. tuberculosis* in humans where it accumulates in the lungs, and in addition, it has efficacy against both trypanosomatid as well as apicomplexan parasites in mice models of infection [179] where the lungs are not targeted. Clearly, it will be of interest to determine how, e.g., **8h** is metabolized and whether any metabolites have activity, and further work on this topic as well as on the synthesis of **8h** analogs is of interest. To determine the susceptibility of the phenyl group in **8h** to oxygenation, we used three computer programs: the GloryFame2 program, [180,181] the Xenosite program, [182] and the SmartCyp program. [183] Results are shown in Figure S10. Based on these results, it is apparent that, in general, the major sites targeted by P450 cytochromes are – as with SQ109 (**8a**) itself – at the ends of the molecule (the terminal methyl groups and the adamantyl group) and at C_{10}, but the phenyl group is also a potential target and may form a phenol (C_{19}, Figure S10A GloryFame2 result; Figure S10A, SmartCyp result) or a quinone (Figure S10B) moiety.

3.2 Discussion

3.2.1 Exploring the conformation and binding features of SQ109 and its analogs to MmpL3 protein

SQ109 (**8a**) [20] is an ethylenediamine-based inhibitor of MmpL3 undergoing clinical trials [174,184] that also has activity against a broad range of bacteria, protozoa, and even some yeasts/fungi. [162] Previous research suggested that SQ109 (**8a**) can block the MmpL3-mediated transport of trehalose monomycolates [20,21] by preventing the proton transportation by (a) binding directly to the transporter's pore [22,24] in *Mtb*, as supported by the X-ray structure of the MmpL3 from M. *smegmatis* in complex with SQ109 (**8a**) (PDB ID 6AJG [22]) or (b) indirectly [23,33,34,36,158] which in principle can be accomplished by membrane structure perturbation [33,34,141,156,157,162] leading to increased membrane lipid disorder/fluidity and, arguably, to uncoupler activity on the PMF. [20,33,185,186]

The sequence of MmpL3 is highly conserved across *Mycobacteria*. [23] Of the MmpL proteins encoded by mycobacterial genomes, MmpL3 and MmpL11 are the only MmpL genes conserved across *Mycobacteria*. [187] The importance of MmpL3 is illustrated by the fact that it is the only MmpL gene that cannot be successfully knocked out in *Mtb*. [28] That MtMmpL3 could rescue the viability of the *Ms* MmpL3 knockout mutant further indicates that these MmpL3 orthologs have highly conserved functions. [21] Therefore, *Ms* MmpL3 is a reasonable model for the *Mtb* counterpart since the two MmpL3 orthologs can substitute each other to function. [26]

Here, we investigated the binding profile of compounds **8b-i, 12** using MD simulations and alchemical relative binding free energy calculations based on the X-ray structure of the MmpL3-SQ109 (**8a**) complex from *Ms* (PDB ID 6AJG [22]). We performed MD simulations of the X-ray structure with PDB ID 6AJG [22] in POPC bilayers containing ~ 140 lipids and showed that the *eclipsed* conformer observed in the X-ray structure represents the transition state for rotation around $NHCH_2$-$CH_2NH_2^+$ dihedral compared to the preferred *gauche* conformations inside the MmpL3 shown in the docking calculations and MD simulations.

To fully understand the conformational properties of SQ109 (**8a**) we performed DFT calculations of the *gauche* and *anti* conformations generated by rotation around (2Ad)$NHCH_2$–$CH_2NH_2^+$Ger, (2Ad)$NHCH_2CH_2$–

$NH_2^+CH_2$Ger and $C_{1,Ad}C_{2,Ad}$–$NHCH_2CH_2NH_2^+$Ger bonds. Thus, we calculated the free energies of SQ109 (**8a**) conformation in an implicit water environment (ε=80) or in a lipophilic environment (chloroform, ε=4.8) using the B3LYP-D3/6-31G(d,p) [188] theory (Table 1-3, Figure 5) and identified two *gauche* conformations as minima by rotation around Ad$NHCH_2$–$CH_2NH_2^+$Ger dihedral. These *gauche* conformations are stabilized with a hydrogen bond between the protonated ammonium group and the unprotonated nitrogen; the next more stable is the *anti* conformation, being more than ~ 9 kcal mol^{-1} higher in energy and thus unpopulated (Table 1, Figure 5), while the eclipsed conformer observed in the X-ray structure represents the transition state by rotation around Ad$NHCH_2$-$CH_2NH_2^+$Ger bond. In both dielectric media and inside the transporter's pore, rotation around Ad$NHCH_2CH_2$–$NH_2^+CH_2$Ger bond favors the *anti* orientation (Table 2), in agreement with the extended geranyl chain structure that fits inside the narrow pore of MmpL3 transporter, since in the *gauche* conformation the steric energy increases due to repulsion between the geranyl and NH_2^+(2-Ad) groups. The DFT calculations for the $C_{1,Ad}C_{2,Ad}$–$NHCH_2CH_2NH_2^+$Ger bond rotation, which define the position of axial $NHCH_2$ as regards the cyclohexane subunit of adamantyl group, showed that the position of axial $NHCH_2$ brings CH_2 above the cyclohexane subunit is prohibited as increasing considerably the steric repulsion.

In addition, we performed MD simulations of the complexes between MmpL3 and **8b-i, 12** which showed that the ligands can form hydrogen bonding interactions with Asp256 and/or Asp645 of MmpL3 (Figure 7, S1) and have common van der Waals interactions with the protein's residues along the transporter's pore axis. In these complexes, the geranyl-ethylenediamine moiety was surrounded by the amino acid residues Leu642, Tyr646, Tyr257 while the 2-adamantyl group lied close to Phe260 and Phe649 at the bottom part of the binding area. We observed that increasing the length of the alkyl chain the hydrophobic interactions with Phe260 and Phe649 were increased as well as with residues in the pore, e.g., Ile253 (Figure 7, S1) which is consistent with the SPR binding affinities.

To further confirm that the new SQ109 analogs **8b-i, 12** bind to the Mmpl3 pore according to the experimental structure of SQ109 (**8a**) bound to MmpL3 (PDB ID 6AJG [22]), we compared the calculated binding free energy values with the MM-GBSA method [148–150] (without or with using an implicit membrane model [152–155] and considering also explicitly water molecules inside the binding area [156]) with the binding strength ranking from the experimental SPR results. The results showed that no valuable correlation was observed.

We performed alchemical relative binding free energy calculations using the accurate TI/MD method [43,44,162] which, along with FEP/MD method, [159] have been shown to perform with an error of 1 kcal mol^{-1}. For full accuracy, we included in the TI/MD calculations the whole protein-membrane system consisting of 10^5 atoms. We applied the TI/MD method in alchemical transformations including changes in alkyl adduct at C-2 adamantyl by one or two methylene groups (Table 5) and examined how the calculated relative binding free energies were compared with experimental values that we measured using SPR (Table S1). [158] For one methylene perturbations the deviation from experimental values was smaller than 1 kcal mol^{-1} and for two methylenes or for Ph to Bn perturbations the deviation was bigger, but smaller than 1.5 kcal mol^{-1}. We observed a mue = 0.74 kcal mol^{-1} that is consistent with the fact that alkyl or aryl substituents at the adamantyl C-2 of SQ109 (**8a**) can fill the empty lipophilic region close to Phe260 and Phe649.

3.2.2 Evaluating the activity of SQ109 analogs against bacteria and protozoa

We next investigated the activity of SQ109 (**8a**), and analogs **8b–i**, **12**, and several aminoamide analogs, against bacteria *M. smegmatis*, *M. tuberculosis* HN878 (a virulent clinical strain), MtErdman, MtH37Rv, *M. abscessus*, *B. subtilis*, *E. coli*, and protozoan parasites *T. brucei* bloodstream forms, *T. cruzi* Dm28c epimastigotes and intracellular amastigotes (together with results for the U2OS host cells), *L. donovani* promastigotes, *L. mexicana* promastigotes, and *P. falciparum* asexual bloodstreamforms (ABS) (Table 6, 7, 8).

The most active compounds against *M. smegmatis* have a relatively small substituent at C-2 and have IC_{50} values in the ∼2−4 μM range with *n*-butyl group analog **8e** having the closest activity to SQ109. For MtHN878, a hypervirulent *M. tuberculosis* strain the methyl group analog **8b** yielded an IC_{50} ∼3-fold higher than the SQ109, while the larger alkyl adducts showed comparable IC_{50} values in the ∼2−3 μM range. Activity against *M. tuberculosis* Erdman and H37Rv strains had generally similar patterns with the methyl adduct yielding an IC_{50} in the 2 μM range and other analogs with alkyl groups having IC_{50} values in the 4−8 μM range, which is at least 2-fold lower than found with SQ109 (**8a**) (IC_{50} = 1 μM).

When taken together, the results with *M. tuberculosis* cell growth inhibition indicate that it is difficult to improve upon the activity of SQ109 (**8a**) by adding substituents at the C-2 position. For example, the methyl (**8b**) and benzyl (**8g**) substituents at the adamantyl C-2 group had ∼2−4-fold less activity against

MtbHN878, MtErdman, and MtH37Rv (Table 6). However, there was promising activity against both the S and R variants of *M. abscessus* with the *n*-butyl analog **8e** and the benzyl analog **8g** standing out. Another surprising observation is that A309P mutant was not resistant to SQ109 or its analogs. This mutation is located in the transmembrane domain in MmpL3 and displays very high resistance to the piperidinol-containing molecule PIPD1, [189] the indole-2 carboxamide Cpd12, and the benzimidazole EJMCh-6. [171] This is a potentially important observation because resistance to other MmpL3 inhibitors can be very large (e.g., 32−64× for PIPD1 [189]). This lack of resistance may indicate that binding to MmpL3 is not the primary target of SQ109 (**8a**) and its analogs in *M. abscessus*. What is also of course of interest is the observation that some of the analogs do have better activity than SQ109 against bacteria that lack the putative MmpL3 target, e.g., *B. subtilis* and *E. coli*, as also found with the malaria parasite *P. falciparum*. A question then arises as to whether there is any correlation between MmpL3 binding and cell activity in the mycobacteria.

Comparing cell inhibition results of *M. tuberculosis* (Table 6) with binding to MtMmpL3 (Table 9, 10) we came to a puzzling observation that the K_D value for SQ109 (**8a**) was high (∼1.5 mM), whereas the IC_{50} against *M. tuberculosis* itself (IC_{50} ≈ 0.4−1 μM) is very low. In addition, the K_D values for all 14 compounds tested were lower than found with SQ109 (**8a**) meaning tighter binding to MmpL3, as the compounds become more hydrophobic, while their inhibition activity is lower than SQ109 and decreases as the compounds become bulkier. One possible reason for this is that although the more hydrophobic species **8b–i** and **12** do bind more strongly to MmpL3 compared to SQ109 (**8a**), there may be unfavorable steric interactions with the highly glycosylated mycobacterial cell wall with the larger substituents [190,191] or with any transporters that may facilitate cell entry. It is also of course possible that there may be other targets such as MenA and MenG, involved in menaquinone biosynthesis, which could contribute to the observed differences in activities. [123] The activity of other proteins may also be targeted, together with binding to lipid membranes, affecting uncoupling activity and the proton motive force, as well as affecting lipid membrane inhibitor concentrations (and thus activity). The importance of steric effects in influencing poor cell uptake in the mycobacteria seems likely because as can be seen in Table 6 and Figure 9, the bulky adamantyl C-2 phenylthiazoyl (**8i**) analog – while exhibiting stronger binding to MmpL3 than does SQ109 (**8a**) – had only very weak activity against *M. smegmatis* cell growth. With *M. tuberculosis* HN878, where full dose−response curves were obtained, there was a similar trend, with SQ109 (**8a**) being most active (IC_{50} = 0.4 μM) followed by the C-2 Me analog **8b** (IC_{50} = 0.8 μM), the ethyl analog **8c** (IC_{50} = 1.6 μM), and *n*-propyl (**8d**) and *n*-hexyl (**8f**) analogs both having IC_{50} = 3 μM. In *M. tuberculosis* HN878, the phenyl (**8h**) and benzyl (**8g**) analogs had the same activity, IC_{50} = 1.6 μM. Overall then, the SPR results do not support

the idea that MmpL3 is the major target for SQ109 (**8a**) or analog activity in the mycobacteria, meaning that other targets such as uncoupling activity or indeed other mechanisms of action are involved, consistent of course with the activity (for SQ109) seen against other bacteria as well as against yeasts, fungi, and protozoa.

3.2.3 Interaction of SQ109 and its analogs with membranes

We used DSC to investigate the effects of SQ109 (**8a**) and analogs **8b–h** and **12** on the gel-to-liquid crystal phase transition in zwitterionic DMPC bilayers (model for protozoal membranes) as well as in anionic DSPG bilayers (model for the mycobacterial inner membrane lipids), as it is known that another target for SQ109 (**8a**) in both bacteria and protozoa involves effects on the proton motive force and Ca^{2+} homeostasis which involve cell membranes. [36] The results from both membrane models showed that SQ109 (**8a**) and its analogs can incorporate into the phospholipid bilayers and fluidize the membranes, generating a structure that melts at a lower temperature, T_m, compared to the pure membrane. This effect was more significant as the size of the analogs was increasing. Additionally, compared to the pure DMPC or DSPG bilayer, SQ109 (**8a**) and its analogs caused a general broadening of the main transition peak which most likely is a result of forming inhomogeneous domains in the membrane bilayer. However, rather than simply a very large broadening of the gel-to-liquid crystal phase transition, as seen with the fluidizing effect of cholesterol, [192] in all cases, T_m shifted to lower temperatures. The DSC thermograms obtained on cooling (Figure S8 and S9 and Table S3) showed a similar decrease in *T*m as seen with DMPC on heating but a more complex hysteresis effect with DSPG.

What is perhaps surprising is that, in general, the effects on T_m seen with DPMC were clearly larger than those seen with DSPG. What might the reasons for this be? Interestingly, similar effects have been reported for the binding of another cationic antibiotic, the anthracycline pirarubicin [193] binding to DSPG and to distearoylphosphatidylcholine (DSPC), in which the acyl chain lengths are the same (C_{18}). In that work, [193] it was proposed (based on the results of DSC, Fourier transform infrared spectroscopy, and quantum chemical calculations) that the ammonium group of the antibiotic bound more tightly to the PO_2^- group in DSPG than to the PO_2^- group in DSPC as a result of charge repulsion with the choline Me_3N^+ group in DSPC and that this resulted in decreased drug incorporation into the lipid bilayer. These observations led us to the following model for SQ109-DMPC/DSPG interactions. First, incorporation of the SQ109 geranyl (C_{10}) chain into the lipid bilayer was expected to decrease T_m in the same way that

incorporation of a farnesyl (C_{15}) group in farnesol [194] decreased and broadened the DMPC main transition as a result of disrupted packing of the DMPC alkyl chains. A similar effect would be predicted for both DMPC as well as DSPG, but the effect would be larger with the shorter-chain species DMPC, which has a similar alkyl chain length to that of the geranyl chain in SQ109. The enthalpy of the phase transition was also of course much larger with the longer chain species DSPG (Table 11). However, there is a second interaction that may also be of importance: the electrostatic interaction between the PO_2^- group in the phospholipid and the protonated ethylenediamine group of SQ109 (**8a**) (or analog). The binding of cationic species (e.g., Ca^{2+}, UO_2^{2+}) to anionic lipids increases T_m, [195] and it is possible that SQ109 (**8a**) may help "cross-link" the anionic DSPG, thereby offsetting to some extent the fluidizing effect of the geranyl group in SQ109 (**8a**).

What is also of particular interest about the DSC results shown in Figure 10A, B is that there are good correlations between the change in T_m that correlates with the computed log $D_{7.4}$ of the inhibitor (Figure 10C, D) with a Pearson *R* coefficient = 0.776 and $p = 0.014$ for DMPC and a Pearson *R* coefficient = 0.727 and $p = 0.026$ for DSPG. For the cooling curves, there was again a correlation between ΔT_m and log D with DMPC ($r = 0.75$, $p = 0.021$), but there were more complex effects with DSPG (Figure S9). The stronger binding of the more hydrophobic analogs to lipid membranes would be expected to result in more cell activity either by increasing membrane fluidity/uncoupling activity or by providing higher membrane concentrations for a membrane protein target. However, the more hydrophobic analogs were not found to be more active against *M. tuberculosis* or *M. smegmatis*, but we did find an increased activity (a 4−8-fold decrease in MIC) in *M. abscessus*, as well as large increases in activity against *B. subtilis* and *E. coli* (Table 6) and *P. falciparum* (with the phenyl and benzyl analogs). The DSC results thus suggest that the larger analogs may simply not reach their target(s) in *M. tuberculosis* and *M. smegmatis*, e.g., because of unfavorable steric interactions with the mycolyl−arabinogalactan−peptidoglycan cell wall.

3.3 Methods and materials

3.3.1 General materials and synthesis

All solvents and chemicals were used as purchased without further purification except for Me_3SiCl that was distilled just before use. Dry ether and dry dichloromethane were prepared by leaving the solvents over CaH_2 for 24 h before use. Anhydrous THF was purchased in sealed bottles from Acros Organics. The

progress of all reactions was monitored on Merck precoated silica gel plates (with fluorescence indicator UV254) using diethyl ether/n-hexane, n-hexane/ethyl acetate, or chloroform/methanol as eluents. Column chromatography was performed with Acros Organics silica gel 60A 40−60 μm with the solvent mixtures described in the experiment section. Compounds' spots were visualized based on their absorbance at 254 nm. The structures of **8a–i** and **12** were identified using ^{1}H, ^{13}C, NMR and LC−MS. High-resolution mass spectrometry (HRMS) was carried out using a UHR-TOF maXis 4G instrument (Bruker Daltonics, Bremen, Germany). ^{1}H NMR spectra were recorded in $CDCl_3$ solutions for the amines and CD_3OD solutions for the fumarate salts of amines on Bruker NMR spectrometers: DRX 200, DRX 400, or DRX 600 at 200, 400, or 600 MHz, respectively. 13C NMR spectra were recorded at 50, 100, or 150 MHz, respectively. Carbon multiplicities were assigned using the DEPT experiment. Two-dimensional NMR HMQC and COSY spectra were used for the elucidation of the structures of intermediates and final products and NMR peak assignments. All final compounds were confirmed to have greater than 95% purity via HPLC−MS analysis. Besides the synthesis of SQ109 compounds, we describe [124] additionally an improved preparation of geranylamine (**4**). The raw materials for amines **5b**–**h** and **12** were the corresponding adamantanols obtained from the reaction of 2-amantanone with alkyl lithium reagents. The tertiary alcohols were then reacted with a mixture of sodium azide and trifluoroacetic acid in dichloromethane, and the produced tertiary alkyl azides were reduced with $LiAlH_4$ in ether at rt to afford the amines **5b**–**h** and **12**. [78,169] The 2-adamantylamine **5a** was prepared from reduction of 2-adamantanone oxime with $LiAlH_4$ in THF.

1-Bromo-3,7-dimethylocta-2,6-diene (1-geranyl bromide), **2**

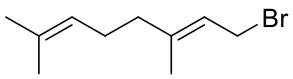

A mixture of geraniol (**1**, 500 mg, 3.24 mmol) and PBr_3 (351 mg, 1.30 mmol) in anhydrous diethyl ether was stirred at –5 ° for 3 h. The resulting solution was extracted with $NaHCO_3$ 5% w/v and brine. The organic extract was dried over Na_2SO_4 and evaporated *in vacuo* to give a yellow oil; yield 700 mg (99.5%). ^{1}H NMR ($CDCl_3$, 400 MHz) δ (ppm) 1.60 (s, 3H, 8-geranyl), 1.68 (s, 3H, 7-geranyl CH_3), 1.73 (s, 3H, 3-geranyl CH_3), 2.08 (m, 4H, 4,5-geranyl), 4.03 (d, J = 8.4 Hz, 2H, 1-geranyl), 5.07 (m, 1H, 6-geranyl), 5.53 (t, J = 8.5 Hz, 1H, 2-geranyl).

1-Phthalimido-3,7-dimethylocta-2,6-diene (1-geranyl phthalimide), **3a**

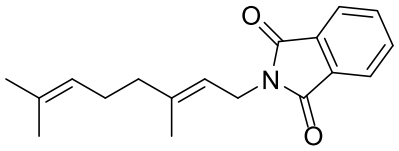

A solution of 1-geranyl bromide (**2**) (520 mg, 2.40 mmol), phthalimide (353 mg, 2.40 mmol), and K_2CO_3 (994 mg, 7.2 mmol) in anhydrous THF (10 mL) was heated to reflux overnight. The solvent was then evaporated *in vacuo*, water was added, and the mixture was extracted twice with diethyl ether. The combined organic extracts were dried over Na_2SO_4, filtered, and concentrated *in vacuo*. The crude product was purified by column chromatography using *n*-hexane/EtOAc (15:1) as eluent to afford geranyl phthalimide as a pale-yellow oil; yield 600 mg (88%).

1-Azido-3,7-dimethylocta-2,6-diene (1-geranylazide), **3b**

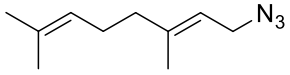

3b

A mixture of 1-geranyl bromide (**2**) (500 mg, 2.30 mmol) and NaN_3 (299 mg, 4.60 mmol) in ethanol (7 mL) was heated to reflux for 5 h, the mixture was concentrated under reduced pressure, and water (15 mL) was added. The resulting solution was extracted with DCM (2 × 20 mL) and the combined organic extracts were washed with brine, dried over Na_2SO_4, filtered, and evaporated *in vacuo* to afford a yellow oil; yield 380 mg (92%). ^{1}H NMR ($CDCl_3$, 400 MHz) δ (ppm) 1.61 (s, 3 H, 8-H), 1.69 (s, 3 H, 7-CH_3), 1.71 (s, 3 H, 3-CH_3), 2.10 (m, 4 H, 4-H, 5-H), 3.76 (t, *J* = 7.4 Hz, 2 H, 1- H), 5.09 (m, 1 H, 6-H), 5.33 (t, *J* = 7.5 Hz, 1 H, 2-H).

1-Amino-3,7-dimethylocta-2,6-diene (1-geranylamine), **4**

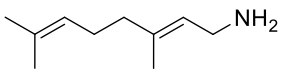

4

Procedure A

A solution of 1-geranyl phthalimide (**3a**) (600 mg, 2.12 mmol) and hydrazine monohydrate (0.160 mL, 3.18 mmol, 1.5 equiv) in absolute EtOH (10 mL) was heated to reflux for 6 h. The solvent was evaporated *in*

vacuo, 15% aq. NaOH was added, and the mixture extracted twice with DCM. The combined organic phases were washed with water, dried over Na_2SO_4, filtered, and concentrated *in vacuo*. After column chromatography 81% of geranylamine **4** was obtained.

Procedure B

A mixture of 1-geranylazide (**3b**) (240 mg, 1.34 mmol) and PPh_3 (386 mg, 1.47 mmol) in THF/water (10:1, 7 mL) was stirred at room temperature for 12 h. The solvent was evaporated under vacuum, and equal quantities of water (20 mL) and DCM (20 mL) were added for extraction. The organic solution was then washed with HCl 6% v/v, the aqueous extract was made alkaline with solid Na_2CO_3 and extracted with DCM. After solvent evaporation *in vacuo* the crude amine product was obtained (90 mg). Anhydrous diethyl ether (15 mL) was added, and the organic solution was treated with a saturated solution of ethanol with hydrogen chloride at 0 °C to afford the hydrochloride salt as a white precipitate. After overnight cooling at 5 °C and suction filtration, geranylamine (**4**) hydrochloride was obtained as a white solid (87 mg, 34% yield).

Procedure C

To a suspension of $LiAlH_4$ (152 mg, 4.0 mmol) in anhydrous diethyl ether (8 mL), a solution of1-geranylazide (480 mg, 2.68 mmol) in anhydrous diethyl ether (5 mL) was added dropwise at 0 °. The mixture was left stirring at room temperature overnight and was quenched with water (2 mL), 15% w/v NaOH (2 mL), and then water (6 mL) at 0 °. The resulting inorganic precipitate was filtered off and washed thoroughly with diethyl ether. The filtrate was extracted twice with HCl 6 % v/v, and the aqueous phase was made alkaline with solid Na_2CO_3 and extracted twice with DCM. The combined organic extracts were washed with water and dried over solid Na_2SO_4. After filtration, the solvent was evaporated *in vacuo* to afford geranylamine (**4**) as a pale yellow oil (98 mg, 24% yield). Hydrochloride salt: ^{1}H NMR ($CDCl_3$, 400 MHz) δ (ppm) 1.60 (s, 3H, 8-geranyl), 1.63 (s, 3H, 7-geranyl CH_3), 1.68 (s, 3H, 3-geranyl CH_3), 1.97–2.07 (m, 4H, 4,5-geranyl), 3.30 (d, J = 7.4 Hz, 2H, 1-geranyl), 5.07–5.11 (m, 1H, 6-geranyl), 5.26 (t, J = 7.5 Hz, 1H, 2-geranyl). ^{13}C NMR ($CDCl_3$, 150 MHz) δ (ppm) 16.5 (3-geranyl CH_3), 18.0 (7-geranyl CH_3), 26.0 (8-geranyl), 26.8 (5-geranyl), 39.7 (4-geranyl), 39.9 (1-geranyl), 124.4 (2-geranyl), 125.1 (6-geranyl), 131.9 (7-geranyl), 137.5 (3-geranyl).

2-Adamantanamine, **5a**

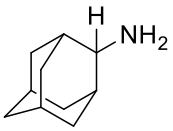

5a

A solution of 2-adamantanone (3.0 g, 20 mmol) in ethanol (35 mL) was heated at 70 ℃. To this solution an aqueous solution (20 mL) of $HCl{\cdot}H_2NOH$ (2.08 g, 30.0 mmol) with solid Na_2CO_3 (3.82 g, 36.0 mmol) was added portion-wise at 70 ℃. The mixture was stirred at the same temperature for 10 min, and the ethanol was evaporated under reduced pressure. The aqueous suspension was allowed to cool at room temperature, and the white solid of 2-adamantanone oxime was filtered off; yield 2.86 g (86%). ^{1}H NMR ($CDCl_3$, 400 MHz) δ (ppm) 1.81–1.99 (m, 14H, 1,3,4,5,6,7,8,9,10-adamantyl).

To a suspension of $LiAlH_4$ (1.97 g, 51.9 mmol) in anhydrous THF (35 mL) a solution of 2-adamantanone oxime (2.86 g, 17 mmol) in anhydrous THF (40 mL) was added dropwise at 0 ℃, and the suspension was then heated to reflux and left overnight under stirring. The mixture was allowed to return to room temperature, then cooled at 0 ℃, and then water (2 mL), NaOH 15% w/v (2 mL), and water (6 mL) were added. The resulting inorganic precipitate was filtered off and washed thoroughly with diethyl ether. The filtrate was extracted twice with HCl 6 % w/v, the aqueous phase was made alkaline with solid Na_2CO_3 and extracted with DCM. The combined organic extracts were washed with water and dried over Na_2SO_4. After filtration, the DCM was evaporated *in vacuo* to afford a pale oil of 2-adamantanamine (**5a**, 1.45 g, 56% yield). ^{1}H NMR ($CDCl_3$, 400 MHz) δ (ppm) 1.53 (d, *J* = 12 Hz, 2H, 4eq,9eq-adamantyl), 1.70–1.85 (m, 10H, 1,3,5,7,6,8,10-adamantyl), 1.99 (d, *J* = 12 Hz, 2H, 4ax,9ax-adamantyl), 2.22 (br s, 2H, NH_2), 3.02 (s, 1H, 2- adamantyl) ppm. ^{13}C NMR ($CDCl_3$, 50 MHz) δ (ppm) 27.1 (7-adamantyl), 28.0 (5-adamantyl), 31.1 (4,9-adamantyl), 35.1 (8,10-adamantyl), 38.0 (1,3-adamantyl), 38.3 (6-adamantyl), 55.9 (2-adamantyl).

N-(2-Adamantanyl)-2-bromoacetamide, **6a**

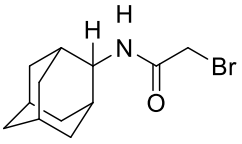

6a

Bromoacetyl chloride (801 mg, 5.09 mmol) in DCM (13 mL) was added dropwise at 0 °C to a vigorously stirred suspension of 2-adamantanamine (**5a**, 700 mg, 4.63 mmol) in DCM (23 mL) and K_2CO_3 (806 mg)

and water (8 mL). The mixture was stirred for 24 h, and then the aqueous phase was extracted twice with DCM. The combined organic extracts were evaporated *in vacuo*, and the crude product was dissolved in diethyl ether. The solution was washed sequentially with $NaHCO_3$ 10% w/v, water, HCl 3% v/v, water, and brine. The solvent was then evaporated *in vacuo*, and the product was filtered through silica gel using *n*-hexane/EtOAc (3:1) as eluent to afford a white solid (1.05g, 83% yield). ^{1}H NMR ($CDCl_3$, 400 MHz) δ (ppm) 1.67 (d, *J* = 12 Hz, 2H, 4eq,9eq-adamantane H), 1.75–1.93 (m, 10H, 1,3,5,7,6,8,10-adamantanyl), 2.04 (s, 2H, 4ax,9ax-adamantanyl), 3.91 (s, 2H, $COCH_2Br$), 4.02–4.04 (s, *J* = 8.4 Hz, 1H, 2-adamantyl).

N-(2-Adamantanyl)-2-[(3,7-dimethylocta-2,6-dien-1-yl)-amino]acetamide, **7a**

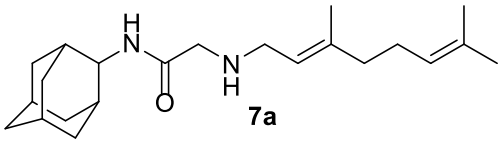

7a

Bromoacetamide **6a** (1.05 g, 3.86 mmol) in dry THF (20 mL) was added dropwise at 0 °C to a stirred solution of geranylamine **4** (590 mg, 3.86 mmol) and triethylamine (390 mg, 3.86 mmol) in dry THF (30 mL). The stirring continued for 48 h at room temperature. Then the aqueous phase was extracted twice with DCM, the combined organic extracts were evaporated in vacuo, and the crude product was purified through column chromatography using a) diethyl ether/*n*-hexane (1:1), b) $CHCl_3$/MeOH (9:1) as solvent systems. The acetamide **7a** was obtained as a pale-yellow oil; yield 1.14 g (86%). ^{1}H NMR ($CDCl_3$, 400 MHz) δ (ppm) 1.59 (s, 3H, 8-geranyl), 1.62 (s, 3H, 7-geranyl CH_3), 1.67 (s, 3H, 3-geranyl CH_3), 1.65–1.90 (m, 14H, 1,3,4,5,6,7,8,9,10-adamantanyl), 2.02–2.07 (m, 4H, 4,5-geranyl), 3.17 (s, 2H, $COCH_2NH$), 3.31 (d, *J* = 7.4 Hz, 2H, 1-geranyl), 3.18 (s, 1H, 2-adamantyl), 4.01 (s, 1H, NH-adamantyl), 5.05 (m, 1 H, 6-geranyl), 5.25 (t, *J* = 7.4 Hz, 1H, 2-geranyl), 7.04 (s, 1 H, N*H*-geranyl) ppm. Hydrochloride salt: ^{13}C NMR (CD_3OD, 100 MHz) δ (ppm) 17.9 (3-geranyl CH_3), 18.7 (8-geranyl), 26.7 (7-geranyl CH_3), 28.0 (5-C), 29.5 (5,7-adamantyl), 33.4 (4,9-adamantanyl), 34.1 (1,3-adamantyl), 39.1 (8,10-adamantyl), 39.4 (6-adamantyl), 41.7 (4-C), 55.7 (1-geranyl), 56.2 ($COCH_2NH$), 56.9 (2-adamantyl), 114.1 (2-geranyl), 125.3 (6-geranyl), 134.1 (7-geranyl), 151.9 (3-geranyl), 166.0 (C=O); HRMS (ESI-TOF (+)) *m/z* $[M + H]^+$ calculated for $[C_{22}H_{37}N_2O]^+$: 345.2906, found 345.2888; Purity of the product determined by HPLC-MS: 95.2%.

2-Bromo-N-(3,7-dimethylocta-2,6-dien-1-yl)acetamide, **13**

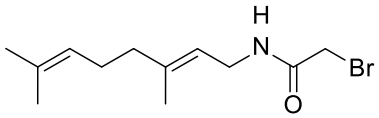

13

Bromoacetyl chloride (1.13 g, 7.18 mmol) in DCM (17 mL) was added dropwise at 0 °C to a vigorously stirred solution of geranylamine **4** (1 g, 6.53 mmol) in DCM (30 mL) and aqueous K_2CO_3 (1.14 g, 10 mL H_2O). The mixture was stirred for 24 h, and then the aqueous was extracted twice with DCM. The combined organic extracts were concentrated *in vacuo*, and the crude product was dissolved in diethyl ether. The solution was washed with $NaHCO_3$ 10% w/v, H_2O, HCl 3% v/v, H_2O, and brine. The solvent was then evaporated *in vacuo*, and the product was filtered through silica gel using *n*-hexane/EtOAc (3:1) as eluent to afford 1.64 g of bromoacetamide (**13**) as a yellow solid (91% yield). ^{1}H NMR ($CDCl_3$, 400 MHz) δ (ppm) 1.60 (s, 3H, 8-geranyl), 1.68 (s, 6H, 7-CH_3, 3-CH_3), 2.00–2.12 (m, 4H, 4,5-geranyl), 3.88 (s, 2H, $COCH_2Br$), 5.06 (t, *J* = 7.0 Hz, 1H, 6-geranyl), 5.19 (t, *J* = 7.0 Hz, 1H, 2-geranyl).

2-[(2-Adamantyl)amino]-N-(3,7-dimethylocta-2,6-dien-1-yl)acetamide, **14a**

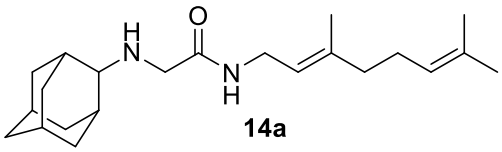

14a

Bromoacetamide **13** (960 mg, 3.50 mmol) in dry THF (20 mL) was added dropwise at 0 °C to a stirred solution of 2-adamantanamine (**5a**) (530 mg, 3.50 mmol) and triethylamine (354 mg, 3.50 mmol) in anhydrous THF (30 mL), and stirring was continued for 48 h at room temperature. The aqueous phase was extracted twice with DCM, the combined organic extracts were evaporated *in vacuo*, and the crude product was purified by column chromatography, eluting with a) diethyl ether/*n*-hexane (1:1), b) $CHCl_3$/MeOH (9:1). Acetamide **14a** was obtained as a yellow oil (870 mg, 72% yield). ^{1}H NMR ($CDCl_3$, 400 MHz) δ (ppm) 1.56–1.59 (m, 5 H, 8-geranyl, 4eq,9eq-adamantyl), 1.67 (s, 6 H, 7-geranyl CH_3, 3-geranyl CH_3), 1.67–1.71 (m, 4H, 1,3,6-adamantyl), 1.81–1.92 (m, 6H, 4ax,5,7,8ax,9ax,10ax-adamantyl), 1.98–2.10 (m, 4H, 4,5-geranyl), 2.77 (s, 1H, 2-adamantyl), 3.27 (s, 1H, NHCH_2CO), 3.43 (s, 1H, NHCH_2CO), 3.84–3.89 (m, 2H, 1-geranyl), 5.07 (m, 1H, 6-geranyl), 5.19 (m, 1H, 2-geranyl). ^{13}C NMR (CD_3OD, 100 MHz) δ (ppm) 17.2 (3-geranyl CH_3), 18.6 (8-geranyl), 26.7 (7-geranyl CH_3), 28.3 (5-geranyl), 28.9 (5-adamantyl), 29.2 (7-adamantyl), 31.6 (4,9-adamantyl), 32.1 (1,3-adamantyl), 38.7 (8,10-adamantyl), 38.8 (6-adamantyl), 39.3

(4-geranyl), 41.4 (1-geranyl), 48.0 ($NHCH_2CO$), 65.8 (2-adamantyl), 121.5 (2-geranyl), 125.8 (6-geranyl), 133.4 (7-geranyl), 141.9 (3-geranyl), 166.6 (C=O) ppm. HRMS (ESI-TOF (+)): *m/z* $[M + H]^+$ calculated for $[C_{22}H_{37}N_2O]^+$: 345.2906, found 345.2897; Purity of the product determined by HPLC-MS: 99.6%.

N-(2-Adamantanyl)-N'-(3,7-dimethylocta-2,6-dien-1-yl)-ethane-1,2-diamine (SQ109, **8a**)

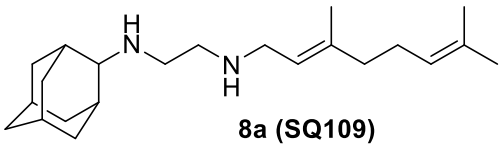

8a (SQ109)

Acetamide **7a** (870 mg, 2.52 mmol) in dry DCM (11 mL) was stirred at 0–5 °C for 15 min under an argon atmosphere. Freshly distilled trimethylsilyl chloride (328 µL, 3.02 mmol) was then added at the same temperature, and the mixture was stirred for another 15 min. A suspension of $LiAlH_4$ (134 mg, 3.53 mmol) in a small quantity of anhydrous THF was added between –10 °C and 0 °C, and the stirring was continued for 2.5 h at the same temperature. The mixture was then treated with NaOH 10%, the resulting inorganic precipitate was filtered off, the organic phase was separated, and the aqueous phase was extracted twice with DCM. The combined organic extracts were evaporated *in vacuo*, and the crude product was dissolved in DCM and washed with brine. After separation and evaporation of the solvent, the crude product was purified by column chromatography using either $CHCl_3$/MeOH (9:1) or $CHCl_3$/MeOH/NH_3 (88:10:2), eluents, to afford diamine **8a** as a pale-yellow oil; yield 260 mg (31%). Acetamide **14a** (290 mg, 0.84 mmol) in dry DCM (4 mL) was stirred at 0–5 °C for 15 min under an argon atmosphere. Freshly distilled trimethylsilyl chloride (110 µL, 1.01 mmol) was then added at the same temperature, and the mixture was stirred for a further 15 min. A suspension of $LiAlH_4$ (45 mg, 1.18 mmol) in a small quantity of THF was added at –10 °C to 0 °C and stirring was continued for 2.5 h at the same temperature. The mixture was then treated with 10% aqueous NaOH, the resulting inorganic precipitate was filtered off, the organic phase was separated, and the aqueous phase was extracted twice with DCM. The combined organic extracts were evaporated *in vacuo*, and the crude product was dissolved in DCM and washed with brine. After separation and evaporation of the solvent, the crude product was purified by column chromatography using either $CHCl_3$/MeOH (9:1) or $CHCl_3$/MeOH/NH_3 (88:10:2) as eluents to afford diamine **8a** as a pale-yellow oil (111 mg, 38% yield). ^{1}H NMR ($CDCl_3$, 400 MHz) δ (ppm) 1.47 (d, J = 12 Hz, 2H, 4eq,9eq-adamantane H), 1.59 (s, 3 H, 8-H), 1.64 (s, 3 H, 7-CH_3), 1.67 (s, 3 H, 3-CH_3), 1.70–1.85 (m, 10H,

1,3,5,6,7,8,10-adamantyl), 1.95 (d, *J* = 12 Hz, 2H, 4ax,9ax-adamantyl), 1.98–2.02 (m, 2H, 5-geranyl), 2.06–2.11 (m, 2H, 4-geranyl), 2.71 (s, 1H, 2-geranyl), 2.74 (s, 4H, NHC$\underline{H_2}$C$\underline{H_2}$NH), 3.25 (d, *J* = 7.0 Hz, 2H, 1-geranyl), 5.09 (m, 1H, 6-geranyl), 5.26 (m, 1H, 2-geranyl). ^{13}C NMR ($CDCl_3$, 100 MHz) δ (ppm) 16.5 (3-geranyl CH_3), 18.0 (8-geranyl), 26.0 (7-geranyl CH_3), 26.8 (5-geranyl), 27.9 (5-adamantyl), 28.1 (7-adamantyl), 31.7 (4,9-adamantyl), 32.5 (1,3-adamantyl), 37.9 (8,10-adamantyl), 38.3 (6-adamantyl), 40.2 (4-geranyl), 46.8 (1-geranyl), 47.4 (NHCH_2C$\underline{H_2}$NH-geranyl), 49.8 (NH$\underline{C}H_2CH_2$NH-geranyl), 62.3 (2-adamantyl), 121.9 (2-geranyl), 123.3 (6-geranyl), 131.9 (7-geranyl), 137.9 (3-geranyl). HRMS (ESI-TOF (+)) *m/z* $[M + H]^+$ calculated for $[C_{22}H_{39}N_2]^+$: 331.3108; found 331.3101; Purity of the product determined by HPLC-MS: 95.8%.

2-(4-Phenylthiazol-2-yl)adamantan-2-ol, **5i**

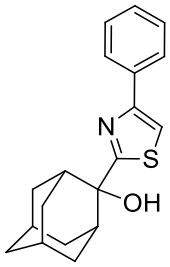

5i

N-butyllithium (3,0 mL,1.6 M solution in hexane, 4.86 mmol, 1.6 eq) was added to a stirred solution of the 2-bromo-4-phenylthiazole (**16**) (731 mg, 3.04 mmol, 1 eq) in anhydrous THF (5 mL), at -75 °C, under argon atmosphere. Then a solution of 2-adamantanone (457 mg, 3.04 mmol, 1 eq) in anhydrous THF (6 mL) was added into the reaction mixture, which was stirred at the same temperature for 1-3 h and then was allowed to reach room temperature. The reaction was quenched by adding water at 0 °C. Organic solvent was removed in vacuo, water was added to the mixture and was extracted with EtOAc. The combined organic extracts were washed with water, dried over Na_2SO_4 and concentrated in vacuo. The residue was purified by flash column chromatography to give a solid product.

5i: eluent of 10% EtOAc in *n*-hexane; yield 56%; ^{1}H NMR (400 MHz, $CDCl_3$) δ (ppm) 1.64 (d, 2H, 4eq,9eq-adamantyl), 1.68 (s, 2H, 6-adamantyl), 1.76 (m, 3H, 7,8eq,10eq-adamantyl), 1.84 (s, 1H, 5-adamantyl), 2.04 (d, 2H,8ax,10ax-adamantyl), 2.23 (s, 1H, OH), 2.35 (d, *J* = 12.5 Hz, 2H, 4ax,9ax-adamantyl), 2.42 (s, 2H, 1,3-adamantyl), 7.24 (t, *J* = 7.4 Hz, 1H,phenyl), 7.34 (d, *J* = 10.4 Hz, 2H, phenyl), 7.39 (s, 1H, 5-thiazolyl), 7.84(d, 2H, *J* = 10.4 Hz, phenyl); ^{13}C NMR (100 MHz, $CDCl_3$) δ (ppm) 27.27 (5,7-adamantyl), 33.10 (4,9-adamantyl), 34.83 (8,10-adamantyl), 37.78 (1,3-adamantyl), 37.97 (6-adamantyl), 77.36 (2-adamantyl),

112.87 (5-thiazolyl), 126.46 (phenyl), 128.11 (phenyl), 128.85 (phenyl), 134.81 (1-phenyl), 154.45 (4-thiazolyl), 177.30 (2-thiazolyl).

2-Bromo-N-(2-methyl-2-adamantanyl)acetamide, **6b**

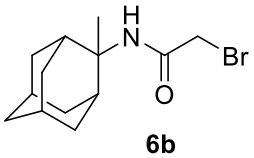

6b

Bromoacetylchloride (1.05 g, 6.66 mmol) in dichloromethane (17 mL) was added dropwise at 0°C to a vigorously stirred suspension of 2-methyl-adamantanamine (**5b**) (1 g, 6.06 mmol) in dichloromethane (30 mL) and K_2CO_3 (1.06 g) in water (10 mL). The mixture was stirred for 24 h and then the aqueous phase was extracted twice with dichloromethane. The combined organic extracts were evaporated in vacuo vacuum and the crude product was dissolved in ether. The solution was washed with $NaHCO_3$ 10% w/v, water, HCl 3% v/v, water and brine. The solvent was then evaporated in vacuo and the product was filtered through silica gel using n-hexane:EtOAc (3:1) as eluent to afford a white solid; yield 1.61 g (93%); ^{1}H-NMR ($CDCl_3$, 400 MHz) δ (ppm) 1.53 (s, 3H, CH_3), 1.63-1.68 (m, 4H, 4eq,8eq,9eq,10eq-adamantyl), 1.71 (m, 4H, 1,3,6-adamanty), 1.83 (s, 2H, 5,7-adamantyl), 1.94-2.00 (m, 4H, 4ax,9ax,8ax,10ax-adamantyl), 3.84 (s, 2H, COC$\underline{H_2}$Br), 2.17 (s, 1H, NH).

2-((3,7-Dimethylocta-2,6-dien-1-yl)amino)-N-(2-methyl-2-adamantanyl)acetamide, **7b**

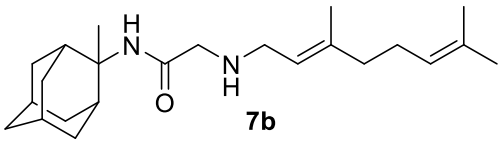

7b

Bromoacetamide **6b** (660 mg, 2.31 mmol) in dry THF (13 mL) was added dropwise at 0 °C to a stirred mixture of geranylamine **4** (353 mg**,** 2.31 mmol) and triethylamine (233 mg, 2.31 mmol) in dry THF (20 mL). The stirring continued for 48 h at room temperature. Then the aqueous phase was extracted twice with dichloromethane, the combined organic extracts were evaporated in vacuo and the crude product was purified through column chromatography using a. ether:n-hexane (1:1), b. $CHCl_3$:MeOH (9:1), as eluents. Acetamide **7b** was obtained as a pale yellow oil; yield 744 mg (90%); ^{1}H-NMR ($CDCl_3$, 400 MHz) δ (ppm) 1.51 (s, 3H, 2-adamantyl-CH_3), 1.59 (s, 3H, 8-geranyl), 1.64 (s, 3H, 7-geranyl CH_3), 1.67 (s, 3H, 3-

geranyl CH_3), 1.80 (s, 2H, 5,7-adamantyl), 1.96-2.05 (m, 6H, 4,5-H, 8ax,10ax-adamantyl), 2.18 (d, *J* = 12 Hz, 2H, 4ax,9ax-adamantyl) 3.17 (d, *J* = 7.4 Hz, 2H, 1-geranyl) 3.28-3.30 (m, 2H, COC$\underline{H_2}$NH), 5.07 (m, 1H, 6-geranyl), 5.23 (m, 1H, 2-geranyl); ^{13}C-NMR ($CDCl_3$, 100MHz) δ (ppm) 16.7 (3-geranyl CH_3), 18.1 (8-geranyl), 23.5 (2-adamantyl-CH_3), 26.0 (7- geranyl CH_3), 27.2 (5-geranyl), 27.2 (5-adamantyl), 27.8 (7-adamantyl), 33.6 (4,9-adamantyl), 35.7 (1,3-adamantyl), 38.9 (8,10-adamantyl), 39.9 (6-adamantyl), 40.1 (4-geranyl), 47.3 (1-geranyl), 58.5 (2-adamantyl), 59.7 (CO$\underline{C}H_2$NH), 123.1 (2-geranyl), 124.1 (6-geranyl), 132.2 (7-geranyl), 138.5 (3-geranyl), 168.9 (C=O); HRMS (ESI-TOF (+)) *m/z* $[M + H]^+$ calculated for $[C_{23}H_{39}N_2O]^+$ 359.3057, found 359.3062.

N-(3,7-dimethylocta-2,6-dien-1-yl)-N′-(2-methyl-2-adamantanyl)ethane-1,2-diamine, **8b**

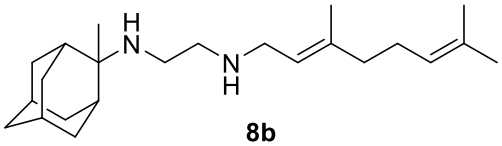

8b

Acetamide **7b** (790 mg, 2.21 mmol) in dry dichloromethane (10 mL) was stirred at 0-5 ℃ for 15 min under argon atmosphere. Recently distilled trimethylsilyl chloride (288 µL, 2.65 mmol) was then added at the same temperature and the mixture was stirred for another 15 min. A suspension of $LiAlH_4$ (117 mg, 3.09 mmol) in a small quantity of THF was added at -10-0℃ and the stirring continued for 2.5 h at the same temperature. The mixture was then treated with NaOH 10%, the resulting inorganic precipitate was filtered off, the organic phase was separated and the aqueous phase was extracted twice with dichloromethane. The combined organic extracts were evaporated in vacuo and the crude product was dissolved in dichloromethane and washed with brine. After the evaporation of the solvent, the crude product was purified through column chromatography using a. $CHCl_3$:MeOH (9:1), b. $CHCl_3$:MeOH:NH_3 (88:10:2), as system solvents to afford diamine **8b** as a pale yellow oil; yield 190 mg (25%); ^{1}H-NMR ($CDCl_3$, 400 MHz) δ (ppm) 1.21 (s, 3H, 2-adamantyl-CH_3), 1.51 (d, *J* = 12Hz, 2H, 4eq,9eq-adamantyl), 1.53 (s, 2H, 8eq,10eq-adamantyl), 1.59 (s, 3H, 8-geranyl), 1.63 (s, 3H, 7-geranyl CH_3), 1.67 (s, 3H, 3-geranyl CH_3), 1.80 (d, *J* = 12Hz, 2H, 5,7-adamantyl), 1.98-2.12 (m, 4H, 4,5-geranyl), 2.64 (t, *J* = 6Hz, 2H, NHC$\underline{H_2}$$CH_2$NH-geranyl), 2.74 (t, *J* = 6Hz, 2H, NHCH_2C$\underline{H_2}$NH-geranyl), 3.23 (d, *J* = 7.0 Hz, 2H, 1-geranyl), 5.09 (m, 1H, 6-geranyl), 5.25 (m, 1H, 2-geranyl); ^{13}C NMR ($CDCl_3$, 100MHz) δ (ppm) 16.6 (3-geranyl CH_3), 18.0 (8-geranyl), 23.2 (2-adamantyl CH_3), 26.0 (7-adamanytyl CH_3), 26.9 (5-geranyl), 27.5 (5-adamantyl), 28.4 (7-adamantyl), 32.9

(4,9-adamantyl), 34.5 (1,3-adamantyl), 36.3 (8,10-adamantyl), 39.3 (6-adamantyl), 40.0 (4-geranyl), 40.2 (1-geranyl), 47.4 ($NH\underline{C}H_2CH_2NH$-geranyl), 50.1 ($NHCH_2\underline{C}H_2NH$-geranyl), 56.3 (2-adamantyl), 123.3 (2-geranyl), 124.5 (6-geranyl), 131.8 (7-geranyl), 138.0 (3-geranyl); HRMS (ESI-TOF (+)) *m/z* $[M + H]^+$ calculated for $[C_{23}H_{41}N_2]^+$ 345.3264, found 345.3269; Purity of the product determined by HPLC-MS: 96.4%.

N-(3,7-dimethylocta-2,6-dien-1-yl)-2-((2-methyl-2-adamantanyl)amino)acetamide, **14b**

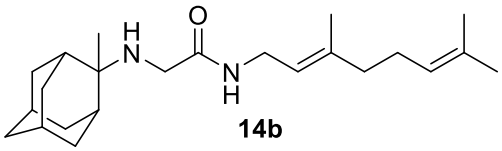

14b

Bromoacetamide **13** (664 mg, 2.42 mmol) in dry THF (14 mL) was added dropwise at 0 °C to a stirred solution of 2-methyl-2-adamantanamine (**5b**) (400 mg**,** 2.42 mmol) and triethylamine (244 mg, 2.42 mmol) in dry THF (24 mL). The stirring continued for 48 h at room temperature. Then the aqueous phase was extracted twice with dichloromethane, the combined organic extracts were evaporated in vacuo and the crude product was purified through column chromatography using a. ether:n-hexane (1:1), b. $CHCl_3$:MeOH (9:1), as eluents. Acetamide **14b** was obtained as a yellow oil; yield 520 mg (60%); ^{1}H-NMR ($CDCl_3$, 400 MHz) δ (ppm) 1.14 (s, 3H, 2-adamantyl CH_3), 1.55 (d, *J* = 12Hz, 2H, 4eq,9eq-adamantyl), 1.59 (s, 3H, 8-geranyl), 1.67 (s, 6H, 3,7-geranyl CH_3), 1.91-1.94 (m, 2H, 4ax,9ax-adamantyl), 1.99-2.08 (m, 4H, 4,5-geranyl), 3.20 (s, 2H, $NHC\underline{H_2}CO$), 3.86 (t, *J* = 6 Hz, 2H, 1-geranyl), 5.08 (m, 1H, 6-geranyl), 5.19 (m, 1H, 2-geranyl). Hydrochloride salt; ^{13}C-NMR (CD_3OD, 100MHz,) δ(ppm) 17.2 (3-geranyl CH_3), 18.6 (8-geranyl), 21.4 (2-adamanyl CH_3), 26.7 (7-geranyl CH_3), 28.3 (5-geranyl), 28.4 (5-adamantyl), 29.1 (7-adamantyl), 33.4 (4,9-adamantyl), 35.4 (8,10-adamantyl), 36.1 (1,3-adamantyl), 39.6 (6-adamantyl), 39.9 (4-geranyl), 41.4 (1-C), 43.3 ($NH\underline{C}H_2CO$), 67.3 (2-adamantyl), 121.3 (2-geranyl), 125.8 (6-geranyl), 133.5 (7-geranyl), 142.1 (3-geranyl), 167.1 (C=O); HRMS (ESI-TOF (+)) *m/z* $[M + H]^+$ calculated for $[C_{23}H_{39}N_2O]^+$ 359.3057, found 359.3057; Purity of the product determined by HPLC-MS: 98.0%.

N-(2-(adamantan-1-yl)propan-2-yl)-2-bromoacetamide, **10**

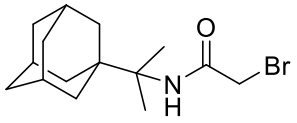

10

Bromoacetylchloride (476 mg, 3.02 mmol) in dichloromethane (8 mL) was added dropwise at 0 °C to a vigorously stirred suspension of 2-(1-adamantanyl)propan-2-amine (**9a**) (530 mg, 2.75 mmol) in dichloromethane (15 mL) and K_2CO_3 (479 mg) in water (5 mL). The mixture was stirred for 24 h and then the organic phase was separated and the aqueous was extracted twice with dichloromethane. The combined organic extracts were evaporated in vacuo and the crude product was dissolved in ether. The solution was washed with $NaHCO_3$ 10% w/v, water, HCl 3% v/v, water and brine. The solvent was then evaporated in vacuo and the product was filtered through silica gel using n-hexane:EtOAc (3:1) as eluent to afford a yellow solid; yield 680 mg (78%); ^{1}H-NMR ($CDCl_3$, 400MHz) δ (ppm) 1.35 (s, 6H, $C(CH_3)_2$), 1.61-1.73 (m, 12H, 2,4,6,8,9,10-adamantyl), 2.04 (s, 3H, 3,5,7-adamantyl), 3.85 (s, 2H, $COCH_2Br$).

N-(2-(adamantan-1-yl)propan-2-yl)-2-((3,7-dimethylocta-2,6-dien-1-yl)amino)acetamide, **11**

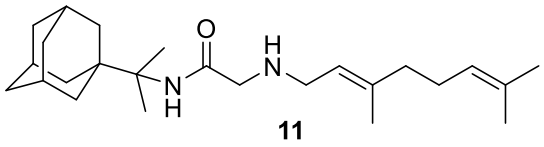

11

Bromoacetamide **10** (680 mg, 2.16 mmol) in dry THF (15 mL) was added dropwise at 0 °C to a stirred solution of geranylamine **4** (330 mg**,** 2.16 mmol) and triethylamine (218 mg, 2.16 mmol) in dry THF (20 mL). The stirring continued for 48 h at room temperature. Then the aqueous phase was extracted twice with dichloromethane, the combined organic extracts were evaporated in vacuo and the crude product was purified through column chromatography using a. ether:n-hexane (1:1), b. $CHCl_3$:MeOH (9:1), as eluents. Acetamide **11** was obtained as a yellow oil; yield 750 mg (90%); ^{1}H-NMR ($CDCl_3$, 400 MHz) δ (ppm) 1.34 (s, 6H, 1-adamantyl $C(CH_3)_2$), 1.59-1.71 (m, 21H, 2,4,6,8,9,10-adamantyl, 8-geranyl, 3,7-geranyl CH_3), 2.01-2.09 (m, 7H, 3,5,7-adamantyl, 4,5-geranyl), 3.15 (d, J = 7.4 Hz, 2H, 1-geranyl), 3.23-3.26 (m, 2H, $COCH_2NH$), 5.07 (m, 1H, 6-geranyl), 5.22 (m, 1H, 2-geranyl); ^{13}C-NMR ($CDCl_3$, 100MHz) δ(ppm) 16.7 (3-geranyl CH_3), 18.0 (8-geranyl), 21.4 (1-adamanyl $C(CH_3)_2$), 21.9 (1-adamantyl $C(CH_3)_2$), 26.0 (7-geranyl CH_3),

26.8 (5-geranyl), 28.9 (3,5,7-adamantyl C), 36.5 (4,6,10-adamantyl), 37.4 (2,8,9-adamantanyl), 39.5 (1-adamantanyl), 39.8 (4-geranyl), 40.0 (1-geranyl), 47.3 ($CO\underline{C}H_2NH$), 59.01 (1-adamanyl $\underline{C}(CH_3)_2$), 119.8 (2-geranyl), 124.2 (6-geranyl), 132.1 (7-geranyl), 140.4 (3-geranyl), 169.1 (C=O); HRMS (ESI-TOF (+)) *m/z* [M + H]$^+$ calculated for $[C_{25}H_{43}N_2O]^+$ 387.337, found 387.337; Purity of the product determined by HPLC-MS: 99.2%.

N-(3,7-dimethylocta-2,6-dien-1-yl)-N´-(2-(adamantan-1-yl)propan-2-yl)ethane-1,2-diamine, **12**

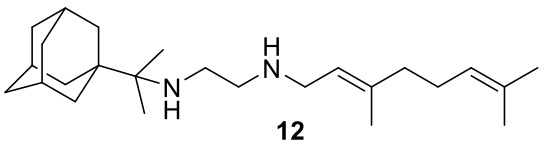

12

Acetamide **11** (280 mg, 0.72 mmol) in dry dichloromethane (4 mL) was stirred at 0-5 ℃ for 15 min under argon atmosphere of Ar. Recently distilled trimethylsilyl chloride (94 µL, 0.87 mmol) was then added at the same temperature and the mixture was stirred for another 15 min. A suspension of $LiAlH_4$ (38.3 mg, 1.01 mmol) in a small quantity of THF was added at -10-0℃ and the stirring continued for 2.5 h at the same temperature. The mixture was treated with NaOH 10%, the resulting inorganic precipitate was filtered off, the organic phase was separated and the aqueous phase was extracted twice with dichloromethane. The combined organic extracts were evaporated in vacuo and the crude product was dissolved in dichloromethane and washed with brine. After the evaporation of the solvent, the crude product was purified through column chromatography using a. $CHCl_3$:MeOH (9:1), b. $CHCl_3$:MeOH:NH_3 (88:10:2), as system solvents, to afford diamine **12** as a yellow oil; yield 70mg (26%); ^{1}H-NMR ($CDCl_3$, 400 MHz) δ (ppm) 0.96 (s, 6H, 1-adamantyl $C(CH_3)_2$), 1.60-1.67 (m, 21H, 2,4,6,8,9,10-adamantane H, 8-geranyl, 3,7-geranyl CH_3), 2.01-2.09 (m, 7H, 3,5,7-adamantyl, 4,5-geranyl), 2.70 (s, 4H, $NHC\underline{H_2}C\underline{H_2}NH$), 3.23 (d, J = 7.0 Hz, 2H, 1-geranyl), 5.09 (m, 1H, 6-geranyl), 5.26 (m, 1H, 2-geranyl); ^{13}C NMR ($CDCl_3$, 100MHz) δ(ppm) 16.6 (3-geranyl CH_3), 18.0 (8-geranyl), 20.7 (1-adamantyl $C(\underline{C}H_3)_2$), 26.0 (7-geranyl CH_3), 26.9 (5-geranyl), 29.2 (3,7,5-adamantyl), 36.5 (4,6,10-adamantyl), 37.6 (2,8,9-adamantyl), 39.2 (1-adamantyl), 40.0 (4-geranyl), 41.9 (1-geranyl), 47.2 ($NH\underline{C}H_2CH_2NH$-geranyl), 50.2 ($NHCH_2\underline{C}H_2NH$-geranyl), 57.2 (1-adamantyl $\underline{C}(CH_3)_2$), 123.0 (2-geranyl), 124.5 (6-geranyl), 131.9 (7-geranyl), 138.3 (3-geranyl); HRMS (ESI-TOF (+)) *m/z* [M + H]$^+$ calculated for $[C_{25}H_{45}N_2]^+$ 373.3577, found 373.357; Purity of the product determined by HPLC-MS: 96.6%.

2-((2-(Adamantan-1-yl)propan-2-yl)amino)-N-(3,7-dimethylocta-2,6-dien-1-yl)acetamide, **15**

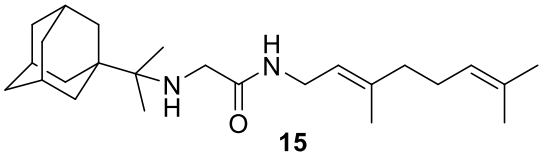

15

Bromoacetamide **13** (200 mg, 0.73 mmol) in dry THF (6 mL) was added dropwise at 0 °C to a stirred solution of 2-(1-adamantanyl)propan-2-amine (**9**) (141 mg**,** 0.73 mmol) and triethylamine (74 mg, 0.73 mmol) in dry THF (8 mL). The stirring continued for 48 h at room temperature. Then the aqueous phase was extracted twice with dichloromethane, the combined organic extracts were evaporated in vacuo and the crude product was purified through column chromatography using a. ether:n-hexane (1:1), b. $CHCl_3$:MeOH (9:1), as eluents. Acetamide **15** was obtained as a yellow oil; yield 125 mg (44%); ^{1}H-NMR ($CDCl_3$, 400 MHz) δ (ppm) 0.92 (s, 6H, 1-adamantyl C(CH_3)$_2$), 1.59-1.73 (m, 21H, 2,4,6,8,9,10-adamantyl, 8-geranyl, 3,7-geranyl CH_3), 2.01-2.10 (m, 7H, 3,5,7-adamantyl, 4,5-geranyl), 3.28 (s, 2H, NHC$\underline{H_2}$CO), 3.85 (t, J = 6.2 Hz, 2H, 1-geranyl), 5.08 (m, 1H, 6-geranyl), 5.21 (m, 1H, 2-geranyl); ^{13}C-NMR ($CDCl_3$, 100MHz) δ(ppm) 16.7 (3-geranyl CH_3), 18.0 (8-geranyl), 20.3 (1-adamantyl C($\underline{C}H_3$)$_2$), 26.0 (7-geranyl CH_3), 26.9 (5-geranyl), 29.0 (3,5,7-adamantyl), 36.5 (4,6,10-adamantyl), 37.4 (2,8,9-adamantyl), 37.9 (1-adamantyl), 39.0 (4-geranyl), 39.8 (1-geranyl), 46.1 (NH$\underline{C}H_2$CO), 120.3 (2-geranyl), 124.2 (6-geranyl), 132.0 (7-geranyl), 140.2 (3-geranyl), 169.2 (C=O); HRMS (ESI-TOF (+)) *m/z* $[M + H]^+$ calculated for $[C_{25}H_{43}N_2O]^+$ 387.337, found 387.3369; Purity of the product determined by HPLC-MS: 95.8%.

2-Bromo-N-(2-ethyl-2-adamantanyl)acetamide, **6c**

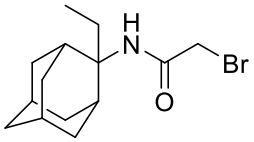

6c

Bromoacetylchloride (464 mg, 2.95 mmol) in dichloromethane (9 mL) was added dropwise at 0 °C to a vigorously stirred suspension of 2-ethyl-2-adamantanamine (**5c**) (480 mg, 2.68 mmol) in dichloromethane (15 mL) and K_2CO_3 (467 mg) in water (5 mL). The mixture was stirred for 24 h and then the aqueous was extracted twice with dichloromethane. The combined organic extracts were evaporated in vacuo and the crude product was dissolved in ether. The solution was washed with $NaHCO_3$ 10% w/v, water, HCl 3% v/v,

water and brine. The solvent was then evaporated in vacuo and the product was filtered through silica gel using n-hexane:EtOAc (3:1) as eluent to afford a white solid; yield 680 mg (84%); ^{1}H-NMR ($CDCl_3$, 400 MHz) δ (ppm) 0.77 (t, J = 7Hz, 3H, 2-adamanyl $CH_2C\underline{H}_3$), 1.59-1.67 (m, 4H, 4eq,8eq,9eq,10eq-adamantyl), 1.71 (s, 2H, 1,3-adamantyl), 1.84 (s, 2H, 6-adamantyl), 1.92-1.95 (m, 4H, 5,7,8ax,10ax-adamantyl), 2.06 (q, 2H, 2-adamanyl $C\underline{H}_2CH_3$), 2.24 (s, 2H, 4ax,9ax-adamantyl), 3.84 (s, 2H, $COC\underline{H}_2Br$).

2-((3,7-Dimethylocta-2,6-dien-1-yl)amino)-N-(2-ethyladamantan-2-yl)acetamide, **7c**

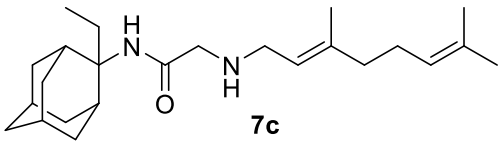

7c

Bromoacetamide **6c** (680 mg, 2.26 mmol) in dry THF (15 mL) was added dropwise at 0 °C to a stirred solution of geranylamine **4** (346 mg, 2.26 mmol) and triethylamine (228 mg, 2.26 mmol) in dry THF (20 mL). The stirring continued for 48 h at room temperature. Then the aqueous phase was extracted twice with dichloromethane, the combined organic extracts were evaporated in vacuo and the crude product was purified through column chromatography using a. ether:n-hexane (1:1), b. $CHCl_3$:MeOH (9:1), as eluents. Acetamide **7c** was obtained as a pale yellow oil; yield 710 mg (84%); ^{1}H-NMR ($CDCl_3$, 400 MHz) δ (ppm) 0.75 (t, J = 7Hz, 3H, 2-adamantyl $CH_2C\underline{H}_3$), 1.60 (s, 3H, 8-geranyl), 1.63 (s, 3H, 7-geranyl CH_3), 1.68 (s, 3H, 3-geranyl CH_3), 1.60-1.70 (m, 6H, 1,3,4eq,8eq,9eq,10eq-adamantyl), 1.81 (s, 2H, 6-adamantyl), 1.93-2.11 (m, 10H, 5,7,8ax,10ax-adamantyl, 2-adamanyl $C\underline{H}_2CH_3$, 4,5-geranyl), 2.25 (s, 2H, 4ax,9ax-adamantyl), 3.19 (s, 2H, $COC\underline{H}_2NH$), 3.23 (d, J = 7.4 Hz, 2H, 1-geranyl), 5.07 (t, J = 7.4 Hz, 1H, 6-geranyl), 5.20 (t, J = 7.4 Hz, 1H, 2-geranyl); ^{13}C-NMR ($CDCl_3$, 100MHz) δ (ppm) 7.43 (2-adamantyl $CH_2\underline{C}H_3$), 16.6 (3-geranyl CH_3), 18.0 (8-geranyl C), 25.0 (2-adamantyl $\underline{C}H_2CH_3$), 26.0 (7-geranyl CH_3), 26.8 (5-geranyl C), 27.6 (5,7-adamantyl), 33.2 (4,9-adamantyl), 33.1 (1,3-adamantyl), 33.7 (8,10-adamantyl), 39.0 (6-adamantyl), 40.0 (4-geranyl), 47.7 (1-geranyl), 52.7 ($CO\underline{C}H_2NH$), 60.4 (2-adamantyl), 122.2 (2-geranyl), 123.6 (6-geranyl), 132.1 (7-geranyl), 139.3 (3-geranyl), 170.3 (C=O); HRMS (ESI-TOF (+)) m/z $[M + H]^+$ calculated for $[C_{24}H_{41}N_2O]^+$ 373.3213, found 373.3213; Purity of the product determined by HPLC-MS: 99.2%.

N-(3,7-dimethylocta-2,6-dien-1-yl)-N'-(2-ethyladamantan-2-yl)ethane-1,2-diamine, **8c**

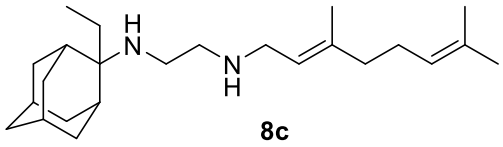

8c

Acetamide **7c** (420 mg, 1.13 mmol) in dry dichloromethane (5 mL) was stirred at 0-5 ℃ for 15 min under argon atmosphere. Recently distilled trimethylsilyl chloride (147 µL, 1.35 mmol) was then added at the same temperature and the mixture was stirred for another 15 min. A suspension of $LiAlH_4$ (60 mg, 1.58 mmol) in a small quantity of THF was added at -10-0℃ and the stirring continued for 2.5 h at the same temperature. The mixture was then treated with NaOH 10%, the resulting inorganic precipitate was filtered off, the organic phase was separated and the aqueous phase was extracted twice with dichloromethane. The combined organic extracts were evaporated in vacuo and the crude product was dissolved in dichloromethane and washed with brine. After evaporation of the solvent, the crude product was purified through column chromatography using a gradient of $CHCl_3$:MeOH (20:1, 18:1), as system solvents, to afford diamine **8c** as a pale yellow oil; yield 150 mg (37%); ^{1}H-NMR ($CDCl_3$, 400 MHz) δ (ppm) 0.75 (t, *J* = 7Hz, 3H, 2-adamantyl $CH_2C\underline{H}_3$), 1.48 (d, *J* = 12Hz, 2H, 4eq,9eq-adamantyl), 1.59 (s, 3H, 8-geranyl), 1.63 (s, 3H, 7-geranyl CH_3), 1.67 (s, 3H, 3-geranyl CH_3), 1.59-1.67 (m, 4H, 1,3,8eq,10eq-adamantyl), 1.80 (s, 2H, 6-adamantyl), 1.90 (d, *J* = 12 Hz, 2H, 5,7-adamantyl), 1.99-2.18 (m, 10H, 4ax,8ax,9ax,10ax-adamantyl, 2-adamantyl $C\underline{H}_2CH_3$, 4,5-H), 2.54 (t, *J* = 6Hz, 2H, $NHC\underline{H}_2CH_2$NH-geranyl), 2.74 (t, *J* = 6 Hz, 2H, $NHCH_2C\underline{H}_2$NH-geranyl), 3.26 (d, *J* = 7.0 Hz, 2H, 1-geranyl), 5.08 (t, *J* = 7 Hz, 1H, 6-geranyl), 5.26 (t, *J* = 7 Hz, 1H, 2-geranyl); ^{13}C NMR ($CDCl_3$, 100MHz) δ (ppm) 6.6 (2-adamantyl $CH_2\underline{C}H_3$), 16.6 (3-geranyl CH_3), 18.1 (8-geranyl), 24.0 (2-adamantyl $\underline{C}H_2CH_3$), 26.0 (7-geranyl CH_3), 26.8 (5-geranyl), 28.1 (5,7-adamantyl), 32.9 (4,9-adamantyl), 33.9 (1,3,8,10-adamantyl), 39.4 (6-adamantyl), 40.0 (1,4-geranyl), 47.2 ($NH\underline{C}H_2CH_2$NH-geranyl), 49.9 ($NHCH_2\underline{C}H_2$NH-geranyl), 57.7 (2-adamantyl), 122.7 (2-geranyl), 124.4 (6-geranyl), 131.9 (7-geranyl), 138.5 (3-geranyl); HRMS (ESI-TOF (+)) *m/z* $[M + H]^+$ calculated for $[C_{24}H_{43}N_2]^+$ 359.3421, found 359.342; Purity of the product determined by HPLC-MS: 95.9%.

2-Bromo-N-(2-propyl-2-adamantanyl)acetamide, **6d**

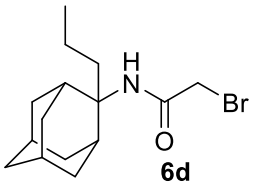

6d

Bromoacetylchloride (548 mg, 3.48 mmol) in dichloromethane (9 mL) was added dropwise at 0 °C to a vigorously stirred suspension of 2-propyl-2-adamantanamine (**5d**) (610 mg, 3.16 mmol) in dichloromethane (18 mL) and K_2CO_3 (550 mg) in water (10 mL). The mixture was stirred for 24 h and then the aqueous was extracted twice with dichloromethane. The combined organic extracts were evaporated in vacuo and the crude product was dissolved in ether. The solution was washed with $NaHCO_3$ 10% w/v, H_2O, HCl 3% v/v, H_2O and brine. The solvent was then evaporated in vacuo and the product was filtered through silica gel using n-hexane:EtOAc (3:1) as eluent to afford a white solid; yield 850 mg (85%); ^{1}H-NMR ($CDCl_3$, 400 MHz) δ (ppm) 0.92 (t, J = 7.4 Hz, 3H, 2-adamantyl $CH_2CH_2C\underline{H_3}$), 1.15-1.25 (m, 2H, 2-adamantyl $CH_2C\underline{H_2}CH_3$), 1.62-1.71 (m, 8H, 1,3,4eq,8eq,9eq,10eq-adamantyl, 2-adamantyl $C\underline{H_2}CH_2CH_3$), 1.92 (s, 2H, 6-adamantyl), 1.95-2.02 (m, 6H, 4ax,5,7,8ax,9ax,10ax-adamantyl), 2.24 (s, 1H, NH) 3.84 (s, 2H, $COC\underline{H_2}Br$).

2-((3,7-Dimethylocta-2,6-dien-1-yl)amino)-N-(2-propyladamantan-2-yl)acetamide, **7d**

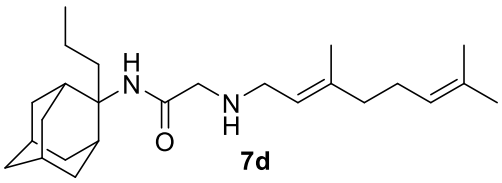

7d

Bromoacetamide **6d** (850 mg, 2.70 mmol) in dry THF (15 mL) was added dropwise at 0 °C to a stirred solution of geranylamine **4** (413 mg, 2.70 mmol) and triethylamine (273 mg, 2.70 mmol) in dry THF (25 mL). The stirring continued for 48 h at room temperature. Then the aqueous phase was extracted twice with dichloromethane, the combined organic extracts were evaporated in vacuo and the crude product was purified through column chromatography using a. ether:n-hexane (1:1), b. $CHCl_3$:MeOH (9:1), as eluents. Acetamide **7d** was obtained as a pale yellow oil; yield 750 mg (72%); ^{1}H-NMR ($CDCl_3$, 400 MHz) δ (ppm) 0.89 (t, J = 7.4 Hz, 3H, 2-adamantyl $CH_2CH_2C\underline{H_3}$), 1.12-1.25 (m, 2H, 2-adamantyl $CH_2C\underline{H_2}CH_3$), 1.58-

1.71 (m, 21H, 1,3,4eq,8eq,9eq,10eq-adamantyl, 8-geranyl, 3,7-geranyl CH_3, 2-adamantyl $C\underline{H}_2CH_2CH_3$), 1.81 (s, 2H, 6-adamantyl), 1.96-2.05 (m, 8H, 5,7,8ax,10ax-adamantyl, 4,5-geranyl), 2.24 (d, *J* = 12 Hz, 2H, 4ax,9ax-adamantyl) 3.19 (d, *J* = 7.4 Hz, 2H, 1-geranyl) 3.30-3.31 (m, 2H, $COC\underline{H}_2NH$), 5.07 (m, 1H, 6-geranyl), 5.24 (m, 1H, 2-geranyl); ^{13}C-NMR ($CDCl_3$, 100MHz) δ (ppm) 14.9 (2-adamantyl $CH_2CH_2\underline{C}H_3$), 15.0 (2-adamantyl $CH_2\underline{C}H_2CH_3$), 16.4 (3-geranyl CH_3), 18.0 (8-geranyl), 26.0 (7-geranyl CH_3), 26.8 (5-geranyl), 27.6 (5,7-adamantyl), 33.3 (4,9-adamantyl), 33.5 (8,10-adamantyl), 33.7 (1,3-adamantyl), 33.9 (2-adamantyl $\underline{C}H_2CH_2CH_3$), 35.4 (6-adamantyl), 39.0 (4-geranyl), 40.0 (1-geranyl), 47.5 ($CO\underline{C}H_2NH$), 52.0 (2-adamantyl), 119.7 (2-geranyl), 124.2 (6-geranyl), 132.1 (7-geranyl), 140.1 (3-geranyl), 168.7 (C=O); HRMS (ESI-TOF (+)) *m/z* $[M + H]^+$ calculated for $[C_{25}H_{43}N_2O]^+$ 387.337, found 387.337.

N-(3,7-dimethylocta-2,6-dien-1-yl)-N´-(2-propyladamantan-2-yl)ethane-1,2-diamine, **8d**

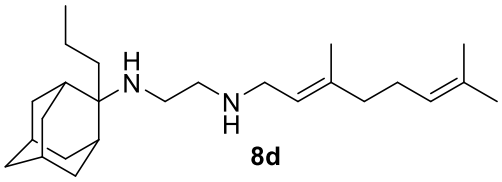

8d

Acetamide **7d** (1.22 g, 3.16 mmol) in dry dichloromethane (14 mL) was stirred at 0-5 ℃ for 15 min under argon atmosphere. Recently distilled trimethylsilyl chloride (412 µL, 3.79 mmol) was then added at the same temperature and the mixture was stirred for another 15 min. A suspension of $LiAlH_4$ (168 mg, 4.42 mmol) in a small quantity of THF was added at -10-0℃ and the stirring continued for 2.5 h at the same temperature. The mixture was then treated with NaOH 10%, the resulting inorganic precipitate was filtered off, the organic phase was separated and the aqueous phase was extracted twice with dichloromethane. The combined organic extracts were evaporated in vacuo and the crude product was dissolved in dichloromethane and washed with brine. After the evaporation of the solvent, the mixture was purified through column chromatography using a. $CHCl_3$:MeOH (9:1), b. $CHCl_3$:MeOH:NH_3 (88:10:2), as system solvents to afford diamine **8d** as a pale yellow oil; yield 390 mg (33%); ^{1}H-NMR ($CDCl_3$, 400 MHz) δ (ppm) 0.90 (t, *J* = 7.4 Hz, 3H, 2-adamantyl $CH_2CH_2C\underline{H}_3$), 1.15-1.25 (m, 2H, 2-adamantyl $CH_2C\underline{H}_2CH_3$), 1.45 (d, *J* = 12 Hz, 2H, 4eq,9eq-adamantyl), 1.55-1.72 (m, 17H, 1,3,6,8eq,10eq-adamantyl, 8-geranyl, 3,7-geranyl CH_3, 2-adamantyl $C\underline{H}_2CH_2CH_3$), 1.79 (d, *J* = 12 Hz, 2H, 5,7-adamantyl), 1.92 (d, *J* = 11.4 Hz, 2H, 8ax,10ax-adamantyl), 1.90-2.02 (m, 2H, 5-geranyl), 2.06-2.11 (m, 2H, 4-geranyl), 2.15 (d, *J* = 12.5 Hz, 4ax,9ax-adamantyl), 2.52 (t, *J* = 6Hz, 2H, $NHC\underline{H}_2CH_2NH$-geranyl), 2.69 (t, *J* = 6 Hz, 2H, $NHCH_2C\underline{H}_2NH$-

geranyl), 3.23 (d, *J* = 7.0 Hz, 2H, 1-geranyl), 5.08 (t, *J* = 7 Hz, 1H, 6-geranyl), 5.25 (t, *J* = 7 Hz, 1H, 2-geranyl); ^{13}C NMR ($CDCl_3$, 100MHz) *δ* (ppm) 15.2 (2-adamantyl $CH_2CH_2\underline{C}H_3$), 15.3 (2-adamantyl $CH_2\underline{C}H_2CH_3$), 16.6 (3-geranyl CH_3), 18.0 (8-geranyl), 26.0 (7-geranyl CH_3), 26.9 (5-geranyl C), 28.1 (5-adamantyl), 28.3 (7-adamantyl), 33.0 (4,9-adamantyl), 34.0 (8,10-adamantyl), 34.4 (1,3-adamantyl), 34.6 (2-adamantyl $\underline{C}H_2CH_2CH_3$), 39.5 (6-adamantyl), 39.7 (4-geranyl), 40.0 (1-geranyl), 47.5 ($NH\underline{C}H_2CH_2NH$-geranyl), 50.5 ($NHCH_2\underline{C}H_2NH$-geranyl), 57.5 (2-adamantyl), 123.3 (2-geranyl), 124.5 (6-geranyl), 131.8 (7-geranyl), 137.9 (3-geranyl); HRMS (ESI-TOF (+)) *m/z* $[M + H]^+$ calculated for $[C_{25}H_{45}N_2]^+$ 373.3577, found 373.3575; Purity of the product determined by HPLC-MS: 100.0%.

N-(3,7-dimethylocta-2,6-dien-1-yl)-2-((2-propyladamantan-2-yl)amino)acetamide, **14d**

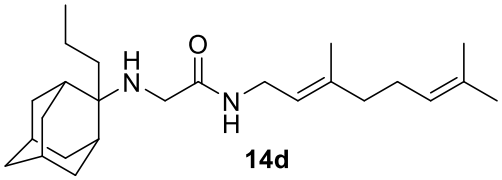

14d

Acetamide **13** (184 mg, 0.67 mmol) in dry THF (6 mL) was added dropwise at 0 °C to a stirred solution of 2-propyl-2-adamantanamine (**5d**) (130 mg**,** 0.67 mmol) and triethylamine (68 mg, 0.67 mmol) in dry THF (8 mL). The stirring continued for 48 h at room temperature. Then the aqueous phase was extracted twice with dichloromethane, the combined organic extracts were evaporated in vacuo and the crude product was purified through column chromatography using a. ether:n-hexane (1:1), b. $CHCl_3$:MeOH (9:1), as eluents. Acetamide **14d** was obtained as a pale yellow oil; yield 90 mg (35%); ^{1}H-NMR ($CDCl_3$, 400 MHz) *δ* (ppm) 0.90 (t, *J* = 7.4 Hz, 3H, 2-adamantyl $CH_2CH_2C\underline{H_3}$), 1.14-1.20 (m, 2H, 2-adamantyl $CH_2C\underline{H_2}CH_3$), 1.51-1.68 (m, 21H, 1,3,4,6,8eq,9,10eq-adamantyl, 8-geranyl, 3,7-geranyl CH_3, 2-adamantyl $C\underline{H_2}CH_2CH_3$), 1.83 (s, 2H, 5,7-adamantyl), 1.90-1.93 (m, 2H, 4ax,9ax-adamantyl), 2.01-2.09 (m, 4H, 4,5-geranyl), 3.12 (s, 2H, $NHC\underline{H_2}CO$), 3.87 (t, *J* = 6 Hz, 2H, 1-geranyl), 5.08 (t, *J* = 7 Hz, 1H, 6-geranyl), 5.20 (t, *J* = 7 Hz, 1H, 2-geranyl); ^{13}C-NMR ($CDCl_3$, 100MHz) *δ* (ppm) 15.0 (2-adamantyl $CH_2CH_2\underline{C}H_3$), 15.5 (2-adamantyl $CH_2\underline{C}H_2CH_3$), 16.6 (3-geranyl CH_3), 18.0 (8-geranyl), 26.0 (7-geranyl CH_3), 26.8 (5-geranyl), 28.0 (5,7-adamantyl), 33.2 (4,9-adamantyl), 33.8 (8,10-adamantyl), 34.4 (1,3-adamantyl), 35.2 (2-adamantyl $\underline{C}H_2CH_2CH_3$), 37.2 (6-adamantyl), 39.3 (4-geranyl), 39.8 (1-geranyl), 44.2 ($NH\underline{C}H_2CO$), 120.4 (2-geranyl), 124.2 (6-geranyl), 132.1 (7-geranyl), 140.1 (3-geranyl), 168.8 (C=O); HRMS (ESI-TOF (+)) *m/z* $[M + H]^+$ calculated for $[C_{25}H_{43}N_2O]^+$ 387.337, found 387.3369; Purity of the product determined by HPLC-MS: 98.3%.

2-Bromo-N-(2-butyl-2-adamantanyl)acetamide, **6e**

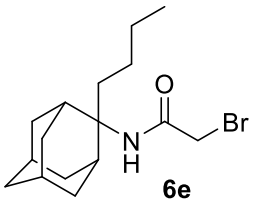

6e

Bromoacetylchloride (117 mg, 0.74 mmol) in dichloromethane (2 mL) was added dropwise at 0 °C to a vigorously stirred suspension of 2-butyl-2-adamantanamine (**5e**) (140 mg, 0.67 mmol) in dichloromethane (4 mL) and K_2CO_3 (117 mg) in water (1 mL). The mixture was stirred for 24 h and then the aqueous phase was extracted twice with dichloromethane. The combined organic extracts were evaporated in vacuo and the crude product was dissolved in ether. The solution was washed with $NaHCO_3$ 10% w/v, water, HCl 3% v/v, water, and brine. The solvent was then evaporated in vacuo and the product was filtered through silica gel using n-hexane:EtOAc (3:1) as eluent to afford a yellow solid; yield 190 mg (85%).

2-((3,7-Dimethylocta-2,6-dien-1-yl)amino)-N-(2-butyladamantan-2-yl)acetamide, **7e**

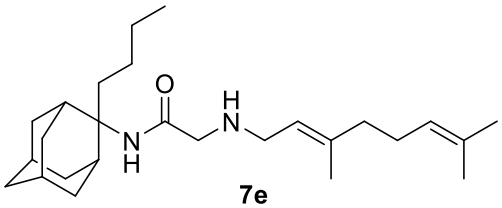

7e

Bromoacetamide **6e** (190 mg, 0.58 mmol) in dry THF (4 mL) was added dropwise at 0 °C to a stirred solution of geranylamine **4** (89 mg, 0.58 mmol) and triethylamine (58 mg, 0.58 mmol) in dry THF (5 mL). The stirring continued for 72 h at room temperature. Then the aqueous phase was extracted twice with dichloromethane, the combined organic extracts were evaporated in vacuo and the crude product was purified through column chromatography using a. ether:n-hexane (1:1), b. $CHCl_3$:MeOH (9:1), as eluents. Acetamide **7e** was obtained as a pale yellow oil; yield 160 mg (69%); ^{1}H-NMR ($CDCl_3$, 400 MHz) δ (ppm) 0.73-0.77 (m, 3H, 2-adamantyl $(CH_2)_3C\underline{H}_3$), 1.08-1.34 (m, 4H, 2-adamantyl $CH_2(C\underline{H}_2)_2CH_3$), 1.60 (s, 3H, 8-geranyl), 1.63 (s, 3H, 7-geranyl CH_3), 1.68 (s, 3H, 3-geranyl CH_3), 1.59-1.71 (m, 6H, 1,3,4eq,8eq,9eq,10eq-adamantyl), 1.82 (s, 2H, 6-adamantyl), 1.89-2.08 (m, 10H, 5,7,8ax,10ax-adamantyl, 2-adamantyl $C\underline{H}_2(CH_2)_2CH_3$, 4,5-geranyl), 2.24 (d, J = 12.5 Hz, 2H, 4ax,9ax-adamantyl), 3.20 (d, J = 7.4 Hz, 2H, 1-geranyl),

3.30 (s, 2H, COC<u>H</u>$_2$NH), 5.07 (t, *J* = 7.4 Hz, 1H, 6-geranyl), 5.24 (t, *J* = 7.4 Hz, 1H, 2-geranyl). Fumarate salt; ^{13}C-NMR (MeOD, 100MHz,) *δ* (ppm) 14.5 (2-adamantyl $(CH_2)_3\underline{C}H_3$), 15.6 (3-geranyl CH_3), 16.8 (8-geranyl), 18.0 (7-geranyl CH_3), 23.5 (4,9-adamantyl), 25.4 (5-geranyl), 26.0 (2-adamantyl $(CH_2)_2\underline{C}H_2CH_3$), 26.8 (2-adamantyl $CH_2\underline{C}H_2CH_2CH_3$), 27.6 (5,7-adamantyl), 32.7 (2-adamantyl $\underline{C}H_2(CH_2)_2CH_3$), 33.3 (8,10-adamantyl), 33.7 (1,3-adamantyl), 39.0 (6-adamantyl), 40.0 (4-geranyl), 47.3 (1-geranyl), 60.8 (CO$\underline{C}$H$_2$NH), 66.2 (2-adamantyl), 119.8 (2-geranyl), 124.1 (6-geranyl), 132.2 (3,7-geranyl), 168.7 (C=O); HRMS (ESI-TOF (+)) *m/z* $[M + H]^+$ calculated for $[C_{26}H_{45}N_2O]^+$ 401.3526, found 401.3527; Purity of the product determined by HPLC-MS: 98.6%.

N-(3,7-dimethylocta-2,6-dien-1-yl)-N′-(2-butyladamantan-2-yl)ethane-1,2-diamine, **8e**

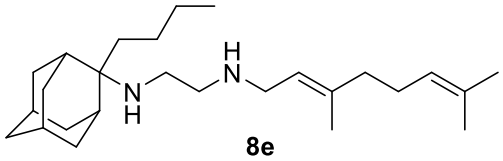

8e

Acetamide **7e** (160 mg, 0.40 mmol) in dry dichloromethane (2 mL) was stirred at 0-5 ℃ for 15 min under argon atmosphere. Recently distilled trimethylsilyl chloride (52 µL, 0.48 mmol) was then added at the same temperature and the mixture was stirred for another 15 min. A suspension of $LiAlH_4$ (21 mg, 0.56 mmol) in a small quantity of THF was added at -10-0℃ and the stirring continued for 2.5 h at the same temperature. The mixture was then treated with NaOH 10%, the resulting inorganic precipitate was filtered off, the organic phase was separated and the aqueous phase was extracted twice with dichloromethane. The combined organic extracts were evaporated in vacuo and the crude product was dissolved in dichloromethane and washed with brine. After the evaporation of the solvent, the crude product was purified through column chromatography using ether:n-hexane (1:1) and a gradient of $CHCl_3$:MeOH (25:1, 20:1), as system solvents to afford diamine **8e** as a pale yellow oil; yield 20 mg (13%). Fumarate salt; ^{1}H-NMR (MeOD, 400 MHz) *δ* (ppm) 0.91 (t, *J* = 7Hz, 3H, 2-adamantyl $(CH_2)_3C\underline{H}_3$), 1.12-1.33 (m, 4H, 2-adamantyl $CH_2(C\underline{H}_2)_2CH_3$), 1.49 (d, *J* = 12Hz, 2H, 4eq,9eq-adamantyl), 1.59 (s, 3H, 8-geranyl), 1.64 (s, 3H, 7-geranyl CH_3), 1.67 (s, 3H, 3-geranyl CH_3), 1.59-1.69 (m, 8H, 1,3,6,8eq,10eq-adamantyl, 2-adamantyl-$C\underline{H}_2(CH_2)_2CH_3$), 1.81 (s, 2H, 5,7-adamantyl), 1.92 (d, *J* = 12Hz, 2H, 8ax,10ax-adamantyl), 1.99-2.11 (m, 4H, 4,5-geranyl), 2.16 (d, *J* =12Hz, 2H, 4ax,9ax-adamantyl), 2.59 (t, *J* = 6Hz, 2H, NHC$\underline{H}_2$CH$_2$NH-geranyl), 2.79 (t, *J* = 6 Hz, 2H, $NHCH_2C\underline{H}_2$NH-geranyl), 3.29 (d, *J* = 7.0 Hz, 2H, 1-geranyl), 5.08 (t, *J* = 7 Hz,

1H, 6-geranyl), 5.26 (t, *J* = 7 Hz, 1H, 2-geranyl); ^{13}C NMR (MeOD, 100MHz) δ (ppm) 15.4 (2-adamantyl $(CH_2)_3\underline{C}H_3$), 17.5 (3-geranyl CH_3), 18.7 (8-geranyl), 19.7 (7-geranyl CH_3), 23.4 (5-geranyl), 25.2 (4-adamantyl), 25.7 (9-adamantyl), 26.7 (2-adamantyl $(CH_2)_2\underline{C}H_2CH_3$), 28.1 (2-adamantyl $CH_2\underline{C}H_2CH_2CH_3$), 29.8 (5,7-adamantyl), 33.1 (2-adamantyl $\underline{C}H_2(CH_2)_2CH_3$), 34.1 (8-adamantyl), 35.4 (10-adamantyl), 35.7 (1,3-adamantyl), 38.9 (6-adamantyl), 40.8 (4-geranyl), 41.6 (1-geranyl), 47.3 ($NH\underline{C}H_2CH_2NH$-geranyl), 48.2 ($NHCH_2\underline{C}H_2NH$-geranyl), 62.1 (2-adamantyl), 117.2 (2-geranyl), 125.6 (6-geranyl), 136.7 (3,7-geranyl); HRMS (ESI-TOF (+)) *m/z* $[M + H]^+$ calculated for $[C_{26}H_{47}N_2]^+$ 387.3734, found 387.3737; Purity of the product determined by HPLC-MS: 98.2%.

2-Bromo-N-(2-hexyl-2-adamantanyl)acetamide, **6f**

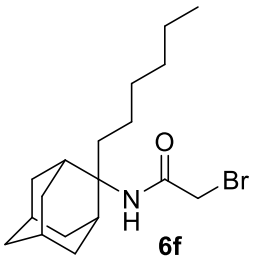

6f

Bromoacetonitrile (609 mg, 5.08 mmol) was added to a stirring solution of 2-hexyl-2-adamantanol (600 mg, 2.54 mmol) in AcOH (1 mL) at room temperature. The resulting solution was cooled to 0 ℃ and concentrated H_2SO_4 (1 mL) was added whilst the temperature was maintained below 10 ℃. The mixture was stirred for 1 h and then was poured onto ice and made alkaline with solid Na_2CO_3. The aqueous phase was extracted twice with EtOAc and the combined organic extracts were washed with water. The solvent was evaporated in vacuo and bromoacetamide **6f** was obtained as an orange solid; yield 869 mg (96%); ^{1}H-NMR ($CDCl_3$, 400 MHz) δ (ppm) 0.87 (t, *J* = 7Hz, 3H, 2-adamantyl $(CH_2)_5C\underline{H}_3$), 1.12-1.33 (m, 8H, 2-adamantyl $CH_2(C\underline{H}_2)_4CH_3$), 1.58-1.72 (m, 6H, 1,3,4eq,8eq,9eq,10eq-adamantyl), 1.84 (s, 2H, 6-adamantyl), 1.91-2.04 (m, 6H, 5,7,8ax,10ax-adamantyl H, 2-adamantyl $C\underline{H}_2(CH_2)_4CH_3$), 2.24 (s, 2H, 4ax,9ax-adamantyl), 3.84 (s, 2H, $COC\underline{H}_2Br$).

2-((3,7-Dimethylocta-2,6-dien-1-yl)amino)-N-(2-hexyladamantan-2-yl)acetamide, **7f**

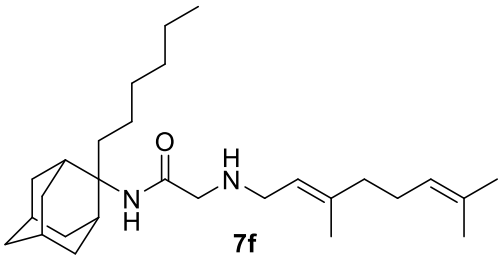

7f

Bromoacetamide **6f** (70 mg, 0.20 mmol) in dry THF (1.5 mL) was added dropwise at 0 °C to a stirred solution of geranylamine **4** (31 mg, 0.20 mmol) and triethylamine (20 mg, 0.20 mmol) in dry THF (2 mL). The stirring continued for 72 h at room temperature. Then the aqueous phase was extracted twice with dichloromethane, the combined organic extracts were evaporated in vacuo and the crude product was purified through column chromatography using a. ether:n-hexane (1:1), b. $CHCl_3$:MeOH (9:1), as eluents. Acetamide **7f** was obtained as a yellow oil; yield 50 mg (60%); ^{1}H-NMR ($CDCl_3$, 400 MHz) δ (ppm) 0.88 (t, J = 7Hz, 3H, 2-adamantyl $(CH_2)_5C\underline{H}_3$), 1.11-1.33 (m, 8H, 2-adamantyl $CH_2(C\underline{H}_2)_4CH_3$), 1.51-1.68 (m, 19H, 1,3,4eq,6,8eq,9eq,10eq-adamantyl, 3-geranyl CH_3, 7-geranyl CH_3, 8-H, 2-adamantyl $C\underline{H}_2(CH_2)_4CH_3$), 1.82-1.83 (m, 2H, 5,7-adamantyl), 1.91 (d, J = 8.5 Hz, 2H, 8ax,10ax-adamantyl), 2.01-2.10 (m, 6H, 4ax,9ax-adamantyl, 4,5-geranyl), 3.11 (s, 2H, $COC\underline{H}_2NH$), 3.88 (t, J = 4 Hz, 2H, 1-geranyl), 5.08 (t, J = 7.4 Hz, 1H, 6-geranyl), 5.21 (t, J = 7.4 Hz, 1H, 2-geranyl); ^{13}C-NMR ($CDCl_3$, 100MHz) δ (ppm) 15.6 (2-adamantyl $(CH_2)_5\underline{C}H_3$), 16.6 (3-geranyl CH_3), 18.0 (8-geranyl), 22.2 (2-adamantyl $(CH_2)_4\underline{C}H_2CH_3$), 23.0 (2-adamantyl $(CH_2)_3\underline{C}H_2CH_2CH_3$), 26.0 (7-geranyl CH_3), 26.8 (5-geranyl), 28.0 (5,7-adamantyl), 30.3 (2-adamantyl $CH_2)_2\underline{C}H_2(CH_2)_2CH_3$), 32.4 (2-adamantyl $CH_2\underline{C}H_2(CH_2)_3CH_3$), 32.7 (2-adamantyl $\underline{C}H_2(CH_2)_4CH_3$), 33.3 (4,9-adamantyl), 33.9 (8,10-adamantyl), 34.4 (1,3-adamantyl), 37.2 (6-adamantyl), 39.3 (4-geranyl), 39.8 (1-geranyl), 58.0 ($CO\underline{C}H_2NH$), 66.2 (2-adamantyl), 120.5 (2-geranyl), 124.2 (6-geranyl), 132.1 (7-geranyl), 140.1 (3-geranyl), 172.8 (C=O).

N-(3,7-dimethylocta-2,6-dien-1-yl)-N´-(2-hexyladamantan-2-yl)ethane-1,2-diamine, **8f**

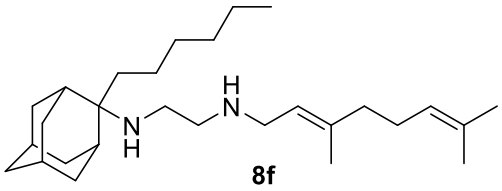

8f

Acetamide **7f** (50 mg, 0.12 mmol) in dry dichloromethane (1 mL) was stirred at 0-5 ℃ for 15 min under argon atmosphere. Recently distilled trimethylsilyl chloride (15 µL, 0.14 mmol) was then added at the same temperature and the mixture was stirred for another 15 min. A suspension of $LiAlH_4$ (7 mg, 0.17 mmol) in a small quantity of THF was added at -10-0 ℃ and the stirring continued for 2.5 h at the same temperature. The mixture was then treated with NaOH 10%, the resulting inorganic precipitate was filtered off, the organic phase was separated and the aqueous phase was extracted twice with dichloromethane. The combined organic extracts were evaporated in vacuo and the crude was dissolved in dichloromethane and washed with brine. After the evaporation of the solvent, the crude product was purified through column chromatography using ether:n-hexane (1:1) and $CHCl_3$:MeOH (30:1), as system solvents to afford diamine **8f** as a yellow oil; yield 20 mg (40%); ^{1}H-NMR ($CDCl_3$, 400 MHz) δ (ppm) 0.87 (t, *J* = 7Hz, 3H, 2-adamantyl $(CH_2)_5C\underline{H}_3$), 1.18-1.27 (m, 8H, 2-adamantyl $CH_2(C\underline{H}_2)_4CH_3$), 1.49 (d, *J* = 12Hz, 2H, 4eq,9eq-adamantyl), 1.59 (s, 3H, 8-geranyl), 1.64 (s, 3H, 7-geranyl CH_3), 1.66 (s, 3H, 3-geranyl CH_3), 1.59-1.69 (m, 8H, 1,3,6,8eq,10eq-adamantyl, 2-adamantyl $C\underline{H}_2(CH_2)_4CH_3$), 1.81 (s, 2H, 5,7-adamantyl), 1.91 (d, *J* = 8.5 Hz, 2H, 8ax,10ax-adamantyl), 1.99-2.10 (m, 4H, 4,5-geranyl), 2.16 (d, *J* = 8.5 Hz, 2H, 4ax,9ax-adamantyl), 2.58 (t, *J* = 6Hz, 2H, $NHC\underline{H}_2CH_2NH$-geranyl), 2.78 (t, *J* = 6 Hz, 2H, $NHCH_2C\underline{H}_2NH$-geranyl), 3.29 (d, *J* = 7.0 Hz, 2H, 1-geranyl), 5.07 (t, *J* = 7 Hz, 1H, 6-geranyl), 5.25 (t, *J* = 7 Hz, 1H, 2-geranyl); ^{13}C NMR ($CDCl_3$, 100MHz) δ (ppm) 14.4 (2-adamantyl $(CH_2)_5\underline{C}H_3$), 16.7 (3-geranyl CH_3), 18.0 (8-geranyl), 22.0 (2-adamantyl $(CH_2)_4\underline{C}H_2CH_3$), 23.1 (2-adamantyl $(CH_2)_3\underline{C}H_2CH_2CH_3$), 26.0 (7-geranyl CH_3), 26.8 (5-geranyl), 27.9 (5,7-adamantyl), 30.4 (2-adamantyl $CH_2)_2\underline{C}H_2(CH_2)_2CH_3$, 32.0 (2-adamantyl $CH_2\underline{C}H_2(CH_2)_3CH_3$), 32.3 (2-adamantyl $\underline{C}H_2(CH_2)_4CH_3$), 32.9 (4,9-adamantyl), 33.9 (8,10-adamantyl), 34.2 (1,3-adamantyl), 39.1 (6-adamantyl), 39.3 (4-geranyl), 40.0 (1-geranyl), 46.9 ($NH\underline{C}H_2CH_2NH$-geranyl), 49.2 ($NHCH_2\underline{C}H_2NH$-geranyl), 66.2 (2-adamantyl), 121.9 (2-geranyl), 124.3 (6-geranyl), 131.9 (7-geranyl), 139.2 (3-geranyl); HRMS (ESI-TOF (+)) *m/z* $[M + H]^+$ calculated for $[C_{28}H_{51}N_2]^+$ 415.4047, found 415.404; Purity of the product determined by HPLC-MS: 100.0%.

2-Bromo-N-(2-benzyl-2-adamantanyl)acetamide, **6g**

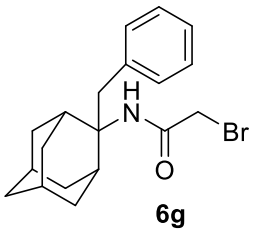

6g

Bromoacetylchloride (288 mg, 1.83 mmol) in dichloromethane (5 mL) was added dropwise at 0 °C to a vigorously stirred suspension of 2-benzyl-2-adamantanamine (**5g**) (400 mg, 1.66 mmol) in dichloromethane (10 mL) and K_2CO_3 (289 mg) in water (3 mL). The mixture was stirred for 24 h and then the aqueous was extracted twice with dichloromethane. The combined organic extracts were evaporated in vacuo and the crude product was dissolved in ether. The solution was washed with $NaHCO_3$ 10% w/v, water, HCl 3% v/v, water and brine. The solvent was then evaporated in vacuo and the product was filtered through silica gel using n-hexane:EtOAc (3:1) as eluent to afford a white solid; yield 530 mg (88%); ^{1}H-NMR ($CDCl_3$, 400 MHz) δ (ppm) 1.55 (s, 2H, 4eq,9eq-adamantyl), 1.64 (d, J = 12Hz, 2H, 8eq,10eq-adamantyl), 1.76-1.97 (m, 6H, 1,3,5,6,7-adamantyl), 2.23-2.27 (m, 4H, 4ax,8ax,9ax10ax-adamantyl), 3.36 (s, 2H, COC<u>H</u>$_2$Br), 3.80 (s, 2H, benzyl), 5.77 (s, 1H, NH), 7.09-7.11 (m, 2H, phenyl), 7.20-7.29 (m, 3H, phenyl).

2-((3,7-Dimethylocta-2,6-dien-1-yl)amino)-N-(2-benzyladamantan-2-yl)acetamide, **7g**

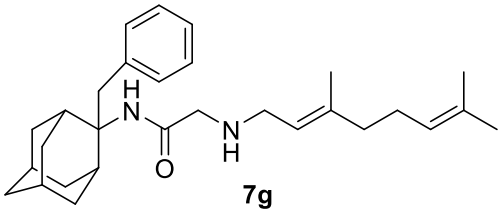

7g

Bromoacetamide **6g** (530 mg, 1.46 mmol) in dry THF (8 mL) was added dropwise at 0 °C to a stirred solution of geranylamine **4** (223 mg, 1.46 mmol) and triethylamine (147 mg, 1.46 mmol) in dry THF (12.5 mL). The stirring continued for 48 h at room temperature. Then the aqueous phase was extracted twice with dichloromethane, the combined organic extracts were evaporated in vacuo and the crude product was purified through column chromatography using a. ether:n-hexane (1:1), b. $CHCl_3$:MeOH (9:1), as eluents. Acetamide **7g** was obtained as a pale yellow oil; yield 560 mg (88%); ^{1}H-NMR ($CDCl_3$, 400 MHz) δ

(ppm) 1.57 (s, 3H, 8-geranyl), 1.59 (s, 3H, 7-geranyl CH_3), 1.67 (s, H, 3-geranyl CH_3), 1.57-1.84 (m, 9H, 1,3,4eq,5,6eq,7,8eq,9eq,10eq-adamantyl), 1.90 (s, 1H, 6ax-adamantyl), 1.98-2.08 (m, 4H, 4,5-geranyl), 2.24-2.30 (m, 4H, 4ax,8ax,9ax,10ax-adamantyl), 3.14 (d, *J* = 7.4 Hz, 2H, 1-geranyl), 3.25 (s, 2H, $COC\underline{H_2}NH$), 3.38 (s, 2H, benzyl), 5.07 (t, *J* = 7.4 Hz, 1H, 6-geranyl), 5.26 (t, *J* = 7.4 Hz, 1H, 2-geranyl), 7.06-7.14 (m, 2H, phenyl), 7.16-7.19 (m, 1H, phenyl), 7.22-7.25 (m, 2H, phenyl); ^{13}C-NMR ($CDCl_3$, 100MHz) δ (ppm) 16.8 (3-geranyl CH_3), 18.0 (8-geranyl), 26.0 (7-geranyl CH_3), 26.7 (5-geranyl), 27.3 (5-adamantyl), 27.8 (7-adamantyl), 33.5 (4,8,9,10-adamantyl), 33.6 (1,3-adamantyl), 38.1 (benzyl), 38.9 (6-adamantyl), 39.9 (4-geranyl), 47.1 (1-geranyl), 56.7 ($CO\underline{C}H_2NH$), 62.0 (2-adamantyl), 123.9 (6-geranyl), 126.5 (phenyl), 128.3 (phenyl), 130.6 (phenyl), 138.5 (quaternary-phenyl), 163.6 (C=O); HRMS (ESI-TOF (+)) *m/z* $[M + H]^+$ calculated for $[C_{29}H_{43}N_2O]^+$ 435.337, found 435.3371; Purity of the product determined by HPLC-MS: 97.8%.

N-(3,7-dimethylocta-2,6-dien-1-yl)-N´-(2-benzyladamantan-2-yl)ethane-1,2-diamine, **8g**

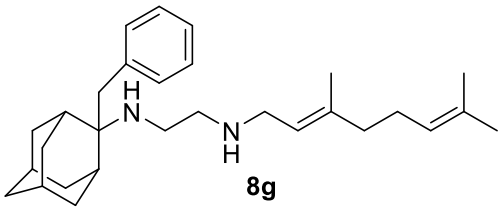

8g

Acetamide **7g** (560 mg, 1.29 mmol) in dry dichloromethane (5 mL) was stirred at 0-5 ℃ for 15 min under argon atmosphere. Recently distilled trimethylsilyl chloride (168 µL, 1.55 mmol) was then added at the same temperature and the mixture was stirred for another 15 min. A suspension of $LiAlH_4$ (69 mg, 1.81 mmol) in a small quantity of THF was added at -10-0℃ and the stirring continued for 2.5 h at the same temperature. The mixture was then treated with NaOH 10%, the resulting inorganic precipitate was filtered off, the organic phase was separated and the aqueous phase was extracted twice with dichloromethane. The combined organic extracts were evaporated in vacuo and the crude product was dissolved in dichloromethane and washed with brine. After the evaporation of the solvent, the crude product was purified through column chromatography using ether:n-hexane (1:1) and $CHCl_3$:MeOH (9:1), as system solvents to afford diamine **8f** as a pale yellow oil; yield 141 mg (26%); ^{1}H-NMR ($CDCl_3$, 400 MHz) δ (ppm) 1.45 (d, *J* = 12Hz, 2H, 4eq,9eq-adamantyl), 1.59 (s, 3H, 8-geranyl), 1.63 (s, 3H, 7-geranyl CH_3), 1.67 (s, 3H, 3-geranyl CH_3), 1.59-1.75 (m, 6H, 1,3,5,7,8eq,10eq-adamantyl), 1.81 (s, 1H, 6eq-adamantyl), 1.95

(s, 1H, 6ax-adamantyl), 1.99-2.10 (m, 4H, 4,5-geranyl), 2.18-2.23 (m, 4H, 4ax,8ax,9ax,10ax-adamantyl), 2.75 (t, *J* = 6Hz, 2H, NHC<u>H</u>$_2$CH$_2$NH-geranyl), 2.84 (t, *J* = 6 Hz, 2H, NHCH$_2$C<u>H</u>$_2$NH-geranyl), 2.99 (s, 2H, benzyl), 3.32 (d, *J* = 7 Hz, 2H, 1-geranyl), 5.07 (t, *J* = 7 Hz, 1H, 6-geranyl), 5.26 (t, *J* = 7 Hz, 1H, 2-geranyl), 7.16-7.30 (m, 5H, phenyl); ^{13}C NMR ($CDCl_3$, 100MHz) δ (ppm) 16.8 (3-geranyl CH_3), 18.0 (8-geranyl), 26.0 (7-geranyl CH_3), 26.8 (5-geranyl), 27.8 (5-adamantyl), 28.3 (7-adamantyl), 33.1 (4,9-adamantyl), 34.0 (8,10-adamantyl), 34.4 (1,3-adamantyl), 37.3 (benzyl), 38.8 (NH<u>C</u>H$_2$CH$_2$NH-geranyl), 39.3 (6-adamantyl), 39.9 (4-geranyl), 46.9 (1-geranyl), 49.3 (NHCH$_2$<u>C</u>H$_2$NH-geranyl), 59.0 (2-adamantyl), 124.2 (6-geranyl), 126.4 (phenyl), 128.5 (phenyl), 130.5 (phenyl), 132.0 (7-geranyl), 138.7 (quaternary-phenyl); HRMS (ESI-TOF (+)) *m/z* [M + H]$^+$ calculated for [$C_{29}H_{45}N_2$]$^+$ 421.3577, found 421.3571; Purity of the product determined by HPLC-MS: 98.6%.

2-Bromo-N-(2-phenyl-2-adamantanyl)acetamide, **6h**

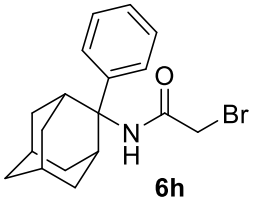

6h

Bromoacetylchloride (610 mg, 3.87 mmol) in dichloromethane (10 mL) was added dropwise at 0 ℃ to a vigorously stirred suspension of 2-phenyl-2-adamantanamine (**5h**) (800 mg, 3.52 mmol) in dichloromethane (18 mL) and K_2CO_3 (612 mg) in water (6 mL). The mixture was stirred for 24 h and then the aqueous phase was extracted twice with dichloromethane. The combined organic extracts were evaporated in vacuo and the crude product was dissolved in ether. The solution was washed with $NaHCO_3$ 10% w/v, water, HCl 3% v/v, water and brine. The solvent was then evaporated in vacuo and the product was filtered through silica gel using n-hexane:EtOAc (3:1) as eluent to afford a white solid; yield 1.17 g (96%); ^{1}H-NMR ($CDCl_3$, 400 MHz) δ (ppm) 1.68-1.86 (m, 9H, 1,3,4eq,5,6eq,7,8eq,9eq,10eq-adamantyl), 1.95 (s, 1H, 6ax-adamantyl), 2.14 (d, *J* = 13.6Hz, 2H, 8ax,10ax-adamantyl), 3.10 (s, 2H, 4ax,9ax-adamantyl), 3.66 (s, 2H, COC<u>H</u>$_2$Br), 7.23-7.25 (m, 1H, phenyl), 7.32-7.36 (m, 2H, phenyl), 7.56-7.58 (m, 2H, phenyl).

2-((3,7-Dimethylocta-2,6-dien-1-yl)amino)-N-(2-phenyladamantan-2-yl)acetamide, **7h**

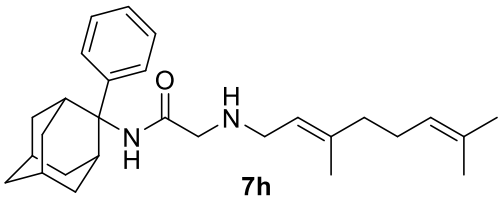

7h

Bromoacetamide **6h** (1.17 g, 3.36 mmol) in dry THF (20 mL) was added dropwise at 0 °C to a stirred solution of geranylamine **4** (514 mg, 3.36 mmol) and triethylamine (340 mg, 3.36 mmol) in dry THF (30 mL). The stirring continued for 48 h at room temperature. Then the aqueous phase was extracted twice with dichloromethane, the combined organic extracts were evaporated in vacuo and the crude product was purified through column chromatography using a. ether:n-hexane (1:1), b. $CHCl_3$:MeOH (9:1), as eluents. Acetamide **7h** was obtained as a yellow oil; yield 920 mg (35%); ^{1}H-NMR ($CDCl_3$, 400 MHz) δ (ppm) 1.54 (s, 3H, 8-geranyl), 1.60 (s, 3H, 7-geranyl CH_3), 1.68 (s, 3H, 3-geranyl CH_3), 1.68-2.18 (m, 18H, 1,3,4,5,6,7,8,9,10-adamantyl, 4,5-geranyl), 3.07 (d, *J* = 7.4 Hz, 2H, 1-geranyl), 3.13 (s, 2H, COC$\underline{H_2}$NH), 5.07 (t, *J* = 7.4 Hz, 1H, 6-geranyl), 5.14 (t, *J* = 7.4 Hz, 1H, 2-geranyl), 7.17-7.33 (m, 3H, phenyl), 7.58-7.59 (m, 2H, phenyl); ^{13}C-NMR ($CDCl_3$, 100MHz) δ (ppm) 16.6 (3-geranyl CH_3), 18.0 (8-geranyl), 26.0 (7-geranyl CH_3), 26.8 (5-geranyl), 27.0 (5-adamantyl), 27.8 (7-adamantyl), 32.8 (4,9-adamantyl), 33.7 (1,3,8,10-adamantyl), 38.2 (6-adamantyl), 39.9 (4-geranyl), 47.4 (1-geranyl), 52.6 (CO$\underline{C}H_2$NH), 61.0 (2-adamantyl), 122.1 (2-geranyl), 124.3 (6-geranyl), 126.7 (phenyl), 128.3 (phenyl), 132.0 (7-geranyl), 139.3 (quaternary-phenyl), 143.5 (3-geranyl), 169.8 (C=O); HRMS (ESI-TOF (+)) *m/z* $[M + H]^+$ calculated for $[C_{28}H_{41}N_2O]^+$ 421.3213, found 421.3214; Purity of the product determined by HPLC-MS: 97.8%.

N-(3,7-dimethylocta-2,6-dien-1-yl)-N′-(2-phenyl-adamantan-2-yl)ethane-1,2-diamine, **8h**

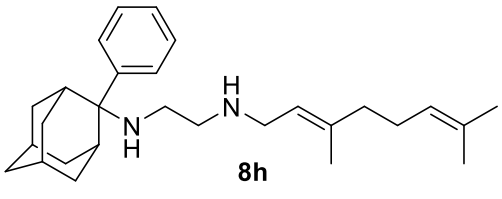

8h

Acetamide **7h** (800 mg, 1.90 mmol) in dry dichloromethane (10 mL) was stirred at 0-5 °C for 15 min under argon atmosphere. Recently distilled trimethylsilyl chloride (247 µL, 2.28 mmol) was then added at the

same temperature and the mixture was stirred for another 15 min. A suspension of $LiAlH_4$ (101 mg, 2.66 mmol) in a small quantity of THF was added at -10-0℃ and the stirring continued for 2.5 h at the same temperature. The mixture was then treated with NaOH 10%, the resulting inorganic precipitate was filtered off, the organic phase was separated, and the aqueous phase was extracted twice with dichloromethane. The combined organic extracts were evaporated in vacuo and the crude product was dissolved in dichloromethane and washed with brine. After the evaporation of the solvent, the crude product was purified through column chromatography using ether:n-hexane (1:1) and $CHCl_3$:MeOH (9:1), as system solvents to afford the diamine **8h** as a pale yellow oil; yield 290 mg (36%); ^{1}H-NMR ($CDCl_3$, 400 MHz) δ (ppm) 1.56 (s, 3H, 8-geranyl), 1.59 (s, 3H, 7-geranyl CH_3), 1.67 (s, 3H, 3-geranyl CH_3), 1.67-1.75 (m, 9H, 1,3,4eq,5,6eq,7,8eq,9eq,10eq-adamantyl), 1.89 (s, 1H, 6ax-adamantyl), 1.98-2.09 (m, 4H, 4,5-geranyl), 2.40 (d, *J* = 12.3Hz, 2H, 8ax,10ax-adamantyl), 2.23 (t, *J* = 6Hz, 2H, NHC$\underline{H_2}$$CH_2$NH-geranyl), 2.48-2.51 (m, 4H, 4ax,9ax-adamantyl, $NHCH_2C\underline{H_2}$NH-geranyl), 3.05 (d, *J* = 7.0 Hz, 2H, 1-geranyl), 5.07 (t, *J* = 7 Hz, 1H, 6-geranyl), 5.15 (t, *J* = 7 Hz, 1H, 2-geranyl), 7.16-7.20 (m, 1H, phenyl), 7.30-7.37 (m, 4H, phenyl); ^{13}C NMR ($CDCl_3$, 400MHz) δ (ppm) 16.6 (3-geranyl CH_3), 18.0 (8-geranyl), 26.0 (7-geranyl CH_3), 26.8 (5-geranyl C), 27.4 (5-adamantyl), 28.4 (7-adamantyl), 33.0 (4,9-adamantyl), 33.2 (1,3-adamantyl), 34.4 (8,10-adamantyl), 38.5 (6-adamantyl), 39.9 (4-geranyl), 46.7 (1-geranyl), 49.4 (NH$\underline{C}$$H_2CH_2$NH-geranyl), 61.3 ($NHCH_2\underline{C}H_2$NH-geranyl), 66.2 (2-adamantyl), 122.2 (2-geranyl), 124.4 (6-geranyl), 126.2 (phenyl), 126.6 (phenyl), 128.4 (phenyl), 131.9 (7-geranyl), 138.8 (quaternary-phenyl), 145.0 (3-geranyl); HRMS (ESI-TOF (+)) *m/z* $[M + H]^+$ calculated for $[C_{28}H_{43}N_2]^+$ 407.3421, found 407.3414; Purity of the product determined by HPLC-MS: 97.0%.

2-Bromo-N-(2-(5-phenylthiazol-2-yl)adamantan-2-yl)acetamide, **6i**

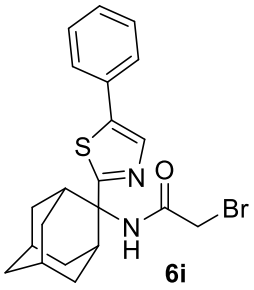

6i

Bromoacetonitrile (230 mg, 1.92 mmol) was added to a stirring solution of 2-(5-phenylthiazol-2-yl)adamantan-2-ol (**5i**) (300 mg, 0.96 mmol) in AcOH (1 mL) at room temperature. The resulting solution was cooled to 0 ℃ and concentrated H_2SO_4 (1 mL) was added whilst the temperature was maintained

below 10 ℃. The mixture was stirred for 1 h and then was poured onto ice and made alkaline with solid Na_2CO_3. The aqueous phase was extracted twice with EtOAc and the combined organic extracts were washed with water. The solvent was evaporated in vacuo and bromoacetamide **6i** was obtained as a pale yellow solid; yield 414 mg (100%); ^{1}H-NMR ($CDCl_3$, 400 MHz) δ (ppm) 1.78-1.86 (m, 7H, 4eq,5,6eq,7,8eq,9eq,10eq-adamantyl), 1.96 (s, 1H, 6ax-adamantyl), 2.10-2.17 (m, 4H, 4ax,8ax,9ax,10ax-adamantyl), 3.14 (s, 2H, 1,3-adamantyl), 3.76 (s, 2H, COC$\underline{H}_2$Br), 6.60 (s, 1H, NH), 7.29-7.32 (m, 1H, phenyl), 7.39-7.43 (m, 2H, phenyl), 7.46 (s, 1H, 4-thiazolyl), 7.90 (d, *J* = 6.8 Hz, 2H, phenyl).

2-((3,7-Dimethylocta-2,6-dien-1-yl)amino)-N-(2-(5-phenylthiazol-2-yl)adamantan-2-yl)acetamide, **7i**

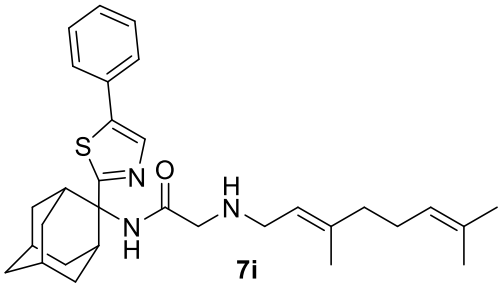

7i

Bromoacetamide **6i** (414 mg, 0.96 mmol) in dry THF (6 mL) was added dropwise at 0 ℃ to a stirred solution of geranylamine **4** (147 mg, 0.96 mmol) and triethylamine (97 mg, 0.96 mmol) in dry THF (8.5 mL). The stirring continued for 48 h at room temperature. Then the aqueous phase was extracted twice with dichloromethane, the combined organic extracts were evaporated in vacuo and the crude product was purified through column chromatography using a. ether:n-hexane (1:1), b. $CHCl_3$:MeOH (9:1), as eluents. Acetamide **7i** was obtained as a pale yellow oil; yield 400 mg (83%); ^{1}H-NMR ($CDCl_3$, 400 MHz) δ (ppm) 1.55 (s, 3H, 8-geranyl), 1.59 (s, 3H, 7-geranyl CH_3), 1.67 (s, 3H, 3-geranyl CH_3), 1.54-1.83 (m, 7H, 4eq,5,6eq,7,8eq,9eq,10eq-adamantyl), 1.86-1.99 (s, 3H, 6ax,8ax,10ax-adamantyl), 2.02-2.17 (m, 6H, 4ax,9ax-adamantyl, 4,5-geranyl), 3.12 (s, 2H, COC$\underline{H}_2$NH), 3.14 (s, 1H, 1,3-adamantyl), 3.16 (m, 2H, 1-geranyl), 5.05 (m, 1H, 6-geranyl), 5.16 (m, 1H, 2-geranyl), 7.27-7.31 (m, 1H, phenyl), 7.36-7.42 (m, 3H, phenyl, thiazoly) 7.85-7.90 (m, 2H, phenyl); ^{13}C-NMR ($CDCl_3$, 100MHz) δ (ppm) 16.6 (3-geranyl CH_3), 18.0 (8-geranyl), 26.0 (7-geranyl CH_3), 26.8 (5-geranyl), 27.3 (5-adamantyl), 27.4 (7-adamantyl), 33.6 (4,9-adamantyl), 33.9 (8,10-adamantyl), 35.0 (1,3-adamantyl), 38.2 (6-adamantyl), 39.9 (4-geranyl), 47.4 (1-geranyl), 52.5 (CO$\underline{C}H_2$NH), 59.0 (2-adamantyl), 113.1 (phenyl), 124.2 (2-geranyl), 126.6 (phenyl), 128.0 (thiazolyl), 128.9 (phenyl), 132.0 (6-geranyl), 135.3 (7-geranyl), 153.7 (3-geranyl), 168.9 (C=O), 170.2

(quaternary-C thiazolyl), 174.6 (quaternary-C thiazolyl); HRMS (ESI-TOF (+)) *m/z* $[M + H]^+$ calculated for $[C_{31}H_{42}N_3OS]^+$ 504.3043, found 504.3054.

N-(3,7-dimethylocta-2,6-dien-1-yl)-N′-(2-(5-phenylthiazol-2-yl)adamantan-2-yl)ethane-1,2-diamine, **8i**

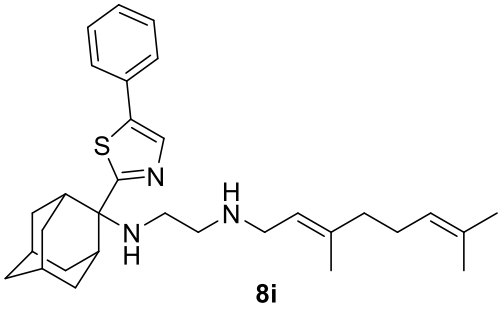

8i

Acetamide **7f** (400 mg, 0.79 mmol) in dry dichloromethane (4 mL) was stirred at 0-5 ℃ for 15 min under argon atmosphere. Recently distilled trimethylsilyl chloride (103 µL, 0.95 mmol) was then added at the same temperature and the mixture was stirred for another 15 min. A suspension of $LiAlH_4$ (42 mg, 1.11 mmol) in a small quantity of THF was added at -10-0 ℃ and the stirring continued for 2.5 h at the same temperature. The mixture was then treated with NaOH 10%, the resulting inorganic precipitate was filtered off, the organic phase was separated, and the aqueous phase was extracted twice with dichloromethane. The combined organic extracts were evaporated in vacuo and the crude was dissolved in dichloromethane and washed with brine. After the evaporation of the solvent, the crude product was purified through column chromatography using ether:n-hexane (1:1) and $CHCl_3$:MeOH:NH3 (88:10:2), as system solvents to afford diamine **8i** as a pale yellow oil; yield 120 mg (31%); ^{1}H-NMR ($CDCl_3$, 400 MHz) δ (ppm) 1.54 (s, 3H, 8-geranyl), 1.57 (s, 3H, 7-geranyl CH_3), 1.65 (s, 3H, 3-geranyl CH_3), 1.67-1.79 (m, 7H, 4eq,5,6eq,7,8eq,9eq,10eq-adamantyl), 1.92 (s, 1H, 6ax-adamantyl), 1.99-2.06 (m, 6H, 8ax,10ax-adamantyl, 4,5-geranyl), 2.35-2.38 (d, *J* = 13.8 Hz, 2H, 4ax,9ax-adamantyl), 2.47 (s, 2H, 1,3-adamantyl), 2.61 (t, *J* = 5.5Hz, 2H, NHC$\underline{H_2}$$CH_2$NH-geranyl), 2.70 (t, *J* = 5.5Hz, 2H, NHCH_2C$\underline{H_2}$NH-geranyl), 3.29 (d, *J* = 7.6 Hz, 2H, 1-geranyl), 5.02 (t, *J* = 7.6 Hz, 1H, 6-geranyl), 5.24 (t, *J* = 7.6 Hz, 1H, 2-geranyl), 7.28-7.33 (m, 1H, phenyl), 7.38-7.42 (m, 3H, phenyl, thiazolyl), 7.89 (d, *J* = 6.2 Hz, 2H, phenyl); ^{13}C NMR ($CDCl_3$, 400MHz) δ (ppm) 16.7 (3-geranyl CH_3), 18.0 (8-geranyl), 26.0 (7-geranyl CH_3), 26.6 (5-geranyl), 27.6 (5-adamantyl), 27.8 (7-adamantyl), 33.0 (4,9-adamantyl), 34.6 (8,10-adamantyl), 35.7 (1,3-adamantyl), 38.5 (6-adamantyl), 39.9 (4-geranyl), 45.1 (1-geranyl), 47.3 (NH$\underline{C}$$H_2$$CH_2$NH-geranyl), 64.0 (NH$CH_2$$\underline{C}$$H_2$NH-geranyl),

66.2 (2-adamantyl), 112.5 (phenyl), 124.0 (2-geranyl), 126.6 (phenyl), 128.2 (thiazolyl), 129.0 (phenyl), 132.2 (6-C), 135.1 (7-C), 154.0 (3-C), 178.1 (quaternary-C thiazolyl); HRMS (ESI-TOF (+)) *m/z* $[M + H]^+$ calculated for $[C_{31}H_{44}N_3S]^+$ 490.3250, found 490.3253. Purity of the product determined by HPLC-MS: 99.3%.

3.3.2 Docking, MD simulations and binding free energy calculations

DFT calculations

For the DFT calculations, the B3LYP functional in combination with D3 Grimme's correction for dispersion was used. [188] All structures were fully optimized at B3LYP-D3/6-31G(d,p) [134–136] level using the GAUSSIAN 03 [196] package; frequency calculations were also performed to locate minima.

Ligands preparation

The 2D structures of the compounds SQ109(**8a**), **8b-i, 12** were sketched with Marvin Program (Marvin version 21.17.0, ChemAxon, https://www.chemaxon.com), model-built with Schrödinger 2017-1 platform (Schrödinger Release 2021-1**:** Protein Preparation Wizard; Epik, Schrödinger, LLC, New York, NY, 2021; Impact, Schrödinger, LLC, New York, NY; Prime, Schrödinger, LLC, New York, NY, 2021) and the compounds' 3D structures in their monoprotonated form were energy minimized using the conjugate gradient method, the MMFF94 [197] force field and a distance-dependent dielectric constant of 4.0 until a convergence threshold of 2.4 10^{-5} kcal mol^{-1} $Å^{-1}$ was reached. The ionization state of the compounds at pH 7.5 were checked using the Epik program [198] implemented in Schrödinger suite (Prime Version 3.2, Schrödinger, LLC, New York, NY, 2015). The most likely state for the ethylenediamine unit is the mono-protonated but we also performed all the calculations for the deprotonated state as well.

Molecular Docking Calculations

The X-ray structure of the MmpL3−SQ109 complex (PDB ID 6AJG [22]) was used as the template structure for the docking calculations of ligands SQ109(**8a**), **8b-i, 12** with MmpL3. The part of the protein sequence that extends to the periplasmic area and includes amino acids Phe750-His929, was deleted as this part is very distant from the binding site. Additionally, the 34 amino acid sequence K355-G388 that was missing from the X-ray structure (PDB ID 6AJG [22]) was added using the Prime module of Maestro (Schrödinger Release 2021-1**:** Protein Preparation Wizard; Epik, Schrödinger, LLC, New York, NY, 2021; Impact,

Schrödinger, LLC, New York, NY; Prime, Schrödinger, LLC, New York, NY, 2021). In the next step, the MmpL3−SQ109 complex was optimized using the Protein Preparation Wizard implementation in Schrödinger suite (Schrödinger Release 2021-1**:** Protein Preparation Wizard; Epik, Schrödinger, LLC, New York, NY, 2021; Impact, Schrödinger, LLC, New York, NY; Prime, Schrödinger, LLC, New York, NY, 2021). [199] In this process, the bond orders and disulfide bonds were assigned, and missing hydrogen atoms were added. The N- and C-termini of the protein model were capped by acetyl and N-methyl-amino groups, respectively. All hydrogens of each protein complex were minimized with the OPLS2005 force field [200,201] by means of Maestro/Macromodel 9.6 [202] using a distance-dependent dielectric constant of 4.0. The molecular mechanics minimizations were performed with the conjugate gradient method and a threshold value of 2.4 10^{-5} kcal mol^{-1} $Å^{-1}$ as the convergence criterion. Each protein was subjected to an all atom minimization using the OPLS2005 [200,201] force field with heavy atom root mean square deviation (RMSD) value constrained to 0.30 Å until the RMS of conjugate-gradient reached values < 0.05 kcal·mol^{-1}·$Å^{-1}$. Then SQ109 (**8a**), utilized as a reference ligand, and the apo protein MmpL3, utilized as template protein, were saved separately or the docking calculations of the tested compounds SQ109 (**8a**), **8b-i, 12** to MmpL3 using GOLD software [203] (GOLD Suite, Version 5.2; Cambridge Crystallographic Data Centre: Cambridge, U.K., 2015. GOLD Suite, version 5.2; Cambridge Crystallogr. Data Cent. Cambridge, U.K., 2015) and ChemScore [146] as the scoring function. Each compound was docked in the binding site of SQ109 (**8a**) in an area of 10 Å around the experimental coordinates of SQ109 and 30 genetic algorithm runs were applied for each docking calculation. The "allow early termination" option, which terminates ligand conformational sampling if the top three solutions have an RMSD difference less than 1.5 Å was inactivated, and the "Generate Diverse Solutions" option, which sets the smallest inter-cluster RMSD to 1.5 Å, was activated. All other parameters were used with their default values. We performed the docking calculations also for the SQ109 analogs **8a-i, 12** in the diprotonated form of ethylenediamine unit. The visualization of produced docking poses was performed using the program Chimera, [204] and the top-scoring docking poses were used as starting structures for the complexes for MD simulations to investigate the binding profile of the SQ109 (**8a**) and analogs **8b-i, 12** inside the MmpL3 pore.

MD simulations

Each protein-ligand complex from docking calculations was inserted in a pre-equilibrated hydrated 1-palmitoyl-2-oleoyl-*sn*-glycero-3-phosphocholine (POPC) membrane bilayer according to Orientations of Proteins in Membranes (OPM) database. [205] The orthorhombic periodic box boundaries were set 10x10x18 Å away from the protein, consisting of ca. 140 lipids and 22,000 TIP3P water molecules, [206] using the

System Builder utility of Desmond v4.9 (Schrödinger Release 2021-1**:** Desmond Molecular Dynamics System, D. E. Shaw Research, New York, NY, 2021. Maestro-Desmond Interoperability Tools, Schrödinger, New York, NY, 2021). Sodium and chloride ions were added randomly in the water phase to neutralize the systems and reach the experimental salt concentration of 0.150 M NaCl. The total number of atoms of the complex was approximately 100,000 and the simulation box dimensions was (86 x 83 x 141 $Å^3$). We used the Desmond Viparr tool to assign amber99sb [134] force field parameters for the calculations of the protein and lipids and intermolecular interactions, and Generalized Amber Force Field (GAFF) [207] for assigning parameters to ligands. Ligand atomic charges were computed according to the RESP procedure [188,208] using the Gaussian03 program [196] and the antechamber module of Amber18. [209]

The MD simulation of each protein-ligand complex inside the lipid bilayer was performed using the default protocol provided with Desmond v4.9 program. Thus, the MD simulations protocol consists of a series of MD simulations designed to relax the system, while not deviating substantially from the initial coordinates. During the first stage, a simulation was run for 200 ps at a temperature of 10 K in the NVT ensemble (constant volume), with solute-heavy atoms restrained by a force constant of 50 kcal mol^{-1} $Å^{-2}$. The temperature was raised to 310 K during a 200 ps MD simulation in the NPT ensemble (constant pressure), with the same force constant applied to the solute atoms. The temperature of 310 K was used in MD simulations to ensure that the membrane state is above the main phase transition temperature of 296 K for POPC bilayers. [210] The heating was then followed by equilibration simulations. First, two 1 ns stages of NPT equilibration were performed. In the first 1 ns stage, the heavy atoms of the system were restrained by applying a force constant of 10 kcal mol^{-1} $Å^{-2}$, and in the second 1 ns stage, the heavy atoms of the protein-ligand complex were restrained by applying a force constant of 2 kcal mol^{-1} $Å^{-2}$ to equilibrate water and lipid molecules. In the production phase, the relaxed systems were simulated without restraints under NPT ensemble conditions for at least 100 ns or 500 ns.

Particle Mesh Ewald (PME) [211,212] was employed to calculate long-range electrostatic interactions with a grid spacing of 0.8 Å. The SHAKE method was used to constrain heavy atom-hydrogen bonds at ideal lengths and angles.[213] Van der Waals and short-range electrostatic interactions were smoothly truncated at 10 Å. The Nosé-Hoover thermostat [214] was utilized to maintain a constant temperature in all simulations, and the Martyna-Tobias-Klein method [215] was used to control the pressure. The equations of motion were integrated using the multistep reversible reference system propagator algorithms (RESPA) integrator [216] with an inner time step of 2 fs for bonded interactions and non-bonded interactions within

a cutoff of 10 Å. An outer time step of 6.0 fs was used for non-bonded interactions beyond the cutoff. Replicas of the system were saved every 10 ps. Within the 100ns-MD simulation time, the total energy (not shown) and RMSD (root mean square deviation) of the protein backbone C_α atoms reached a plateau, and the systems were considered equilibrated and suitable for statistical analysis (see Table 4, S2). The protein RMSD calculated for the C_α atoms of the α-helices, for the last 50 ns was < 2.0 Å (see blue curves in Figure S1). Two MD simulation repeats (Figure S3) were performed for each system using the same starting structure and by applying in the MD simulations randomized velocities. We also used the same protocol and performed the MD simulations for the SQ109 analogs **8a-i, 12** in their doubly protonated form of ethylenediamine unit (Figure S2). All the MD simulations with Desmond or Amber software were run on GTX 1060 GPUs in lab workstations or the ARIS Supercomputer.

The visualization of the trajectories was performed using the graphical user interface (GUI) of Maestro and the protein-ligand interaction analysis was done with the Simulation Interaction Diagram (SID) tool, available with Desmond v4.9 program. For hydrogen bonding interactions, a 2.5 Å distance between donor and acceptor heavy atoms, and an angle ≥120^o between donor-hydrogen-acceptor atoms and ≥ 90^o between hydrogen-acceptor-bonded atoms were applied. Non-specific hydrophobic contacts were identified when the side chain of a hydrophobic residue fell within 3.6 Å from a ligand's aromatic or aliphatic carbon, while π-π interactions were characterized by stacking of two aromatic groups face-to-face or face-to-edge. Water-mediated hydrogen bonding interactions were characterized by a 2.7 Å distance between donor and acceptor atoms, as well as an angle ≥ 110^o between them.

MM-GBSA calculations

For these calculations, structural ensembles were extracted in intervals of 40 ps from three 20 ns MD simulation repeats for each complex running with randomized velocities. Prior to the calculations all water molecules, ions, and lipids were removed, except 20 waters in the vicinity of the ligand, [217] and the structures were positioned such that the geometric center of each complex is located at the coordinate origin. The MD trajectories were processed with the Python library MDAnalysis [218] in order to extract the 20 water molecules closest to any atom in the ligand for each of the 501 frames. During the MM-GBSA calculations, the explicit water molecules were considered as being part of the protein. Binding free energies of compounds in complex with MmpL3 were estimated using the 1-trajectory MM-GBSA approach. [148–150] The binding free energy for each complex was calculated using Eqs. (1)-(6)

$$\Delta G_{bind} = \langle G_{complex} - G_{protein} - G_{ligand} \rangle_{complex} \quad (1)$$

$$G_i = V_{MM} - T\langle S_{MM} \rangle + \Delta G_{solv} \quad (2)$$

$$V_{MM} = V_{bonded} + V_{coul} + V_{LJ} \quad (3)$$

$$\Delta G_{solv} = \Delta G_P + \Delta G_{NP} \quad (4)$$

The binding free energy for each complex can be calculated according to Eq. (5)

$$\Delta G_{bind} = \langle \Delta E_{coul} + \Delta E_{LJ} \rangle - T\langle \Delta S_{MM} \rangle + \Delta\Delta G_{solv} \quad (5)$$

and after neglecting entropy eq. (5) is converted to eq. (6)

$$\Delta G_{eff} = \langle \Delta E_{coul} + \Delta E_{LJ} \rangle + \Delta\Delta G_{solv} \quad (6)$$

In Eqs. (1)-(4) G_i is the free energy of system *i*, that being the ligand, the protein, or the complex; V_{MM} is the potential energy in vacuum as defined by the molecular mechanics (MM) model, which is composed of the bonded potential energy terms (V_{bonded}) and nonbonded Coulombic (V_{coul}) and Lennard-Jones (V_{LJ}) terms; S_{MM} is the entropy; ΔG_{solv} is the free energy of solvation for transferring the ligand from water in the binding area calculated using the PBSA model, composed by a polar (ΔG_P) and nonpolar (ΔG_{NP}) term; *T* is the temperature and angle brackets represent an ensemble average. Molecular mechanics energies for Lennard-Jones (V_{LJ}) and Coulombic electrostatic (Coul) V_{coul} were calculated with OPLS2005 [219] force field; in these calculations $\Delta V_{bonded} = 0$ as the single trajectory method was adopted and $\Delta V_{MM} = \Delta V_{LJ}$ and ΔV_{coul}. The polar part of the solvation free energy was determined by calculations using the Generalized-Born model. [220] The nonpolar term was considered proportional to the solvent accessible surface area (SASA), $\Delta G_{NP} = \gamma \cdot \text{SASA}$, where $\gamma = 0.0227$ kJ mol^{-1} Å^{-2}. Because the SQ109 analogues tested are very similar, entropy term was neglected and ΔG_{bind} is termed as effective binding energy, ΔG_{eff} which is calculated according to eq. (6). [221] We applied a dielectric constant $\varepsilon_{solute} = 1$ to the binding area and to account for the lipophilic environment of the protein an heterogeneous dielectric implicit membrane model was used along the bilayer z-axis. [152–155] The post-processing thermal_mmgbsa.py script of the Schrodinger Suite was used which takes snapshots from the MD simulations trajectory and calculated ΔG_{eff} according to Eq. (6).

Alchemical TI/MD binding free energies calculated with MBAR method

Method's principles

The TI/MD method has been described. [41] Free energy is a state function, and thus the free energy difference between states is independent of the path that connects them. To compare two ligands 0 and 1 binding to a receptor the calculation of $\Delta A_1(b)$ and $\Delta A_0(b)$, respectively, is needed and then the difference $\Delta\Delta A_{0\to1}$ (b) or $\Delta\Delta A_{0,1}$ (b). The calculation of $\Delta A_1(b)$ and $\Delta A_0(b)$ is demanded because it includes large changes between the two states. Thus, the calculation of the relative binding free energies for two ligands bound to MmpL3 (for the 6 pairs of ligands shown in Table 5, respectively) can be performed instead using the MBAR method [168] and applying a thermodynamic cycle [42–44] (Figure 5), ie. using the Δ*G* values obtained for the transformations of the ligands in the bound (b) ($\Delta G_{0,1}$(b) and the solvent (s) (water) state, respectively, $\Delta G_{0,1}$(b) and $\Delta G_{0,1}$(s), according to Eq. (7)

$$\Delta\Delta A_{b,0\to1}\ or\ \Delta\Delta A_{b,0,1} = \Delta A_1(b) - \Delta A_0(b) = \Delta A_{0,1}(b) - \Delta A_{0,1}(s) \qquad (7)$$

Using this method, we can calculate the difference between $\Delta A_{0,1}(b)\ and\ \Delta A_{0,1}(s)$ which corresponds to the unphysical alchemical transformation 0 1 in the bounds state and in the water known as alchemical transformation which may be chosen to include small change or perturbation of ligand structure (eg. from H to CH_3 at 2-position of adamantyl group) to lower the error for the free energy perturbation calculation $\Delta A_{0,1}(b)\ or\ \Delta A_{0,1}(s)$.

Because the phase space overlap between two states 0, 1 of interest can be near zero, doing free energy calculations for the two states alone will often have very large errors. Free energy is a state function, we can construct a thermodynamic path that takes us through a set of states that improves phase space overlap between states that can be unphysical. By this, we mean that our intermediate states do not have to be observable experimentally. To put this mathematically, we can improve our results by constructing high phase space overlap intermediates and calculating our free energy difference $\Delta\Delta A_{0\to1}$ by the sum of the binding free energy differences between the intermediate states.

Briefly, a thermodynamic parameter λ that smoothly connects states 0 and 1 through a λ-dependent potential $U(r^N; \lambda)$, such that $U(r^N; 0) = U_0(r^N)$ and $U(r^N; 1) = U_1(r^N)$. The transformation is broken down into a series of *M* steps corresponding to a set of λ values $\lambda_1, \lambda_2, ..., \lambda_M$ ranging from 0 to 1, such that there is

sufficient phase space overlap between neighboring intermediate λ states. TI computes the free energy change of transformation 0 → 1 by integrating the Boltzmann averaged d$U(\lambda)$/dλ as is described in Eq. (8)

$$\Delta A_{0\to1} = \int_0^1 d\lambda \left\langle \frac{dU(r^N;\lambda)}{d\lambda} \right\rangle_\lambda$$

$$= \Delta A_{0\to1} \approx \sum_{k=1}^{M} w_k \langle \frac{dU(r^N;\lambda)}{d\lambda} \rangle_{\lambda_k} \qquad (8)$$

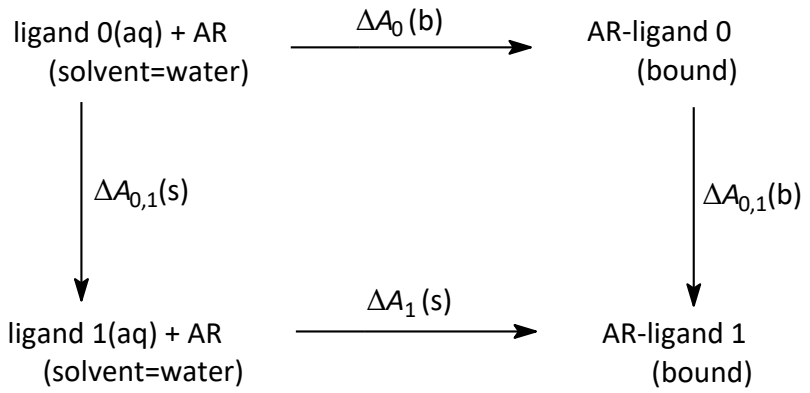

Scheme 8 Thermodynamic cycle used for the calculation of relative binding free energies.

where the second sum indicates numerical integration over M quadrature points (λ_k, for k = 1, ..., M) with associated weights w_k. A linear extrapolation between states can be applied for the construction of $U_1(r^N; \lambda)$ while with Amber18 softcore potentials [44,160,222] the LJ and Coulomb term potentials are described according to Eq. (9)

$$U(r^N;\lambda) = U_0^{SC}(r^N;\lambda) + \lambda \Delta U^{SC}(r^N;\lambda)$$

$$= U_0^{SC}(r^N;\lambda) + \lambda \left(U_1^{SC}(r^N;1-\lambda) - U_0^{SC}(r^N;\lambda) \right) \qquad (9)$$

MBAR [168] calculated the free energy difference between neighboring intermediate states using Eq. (10)

$$\Delta A_{\lambda\to\lambda+1} = -ln\ ln\ \frac{\langle wexp(-\beta U_{\lambda+1})\rangle_\lambda}{\langle wexp(-\beta U_{\lambda+1})\rangle_{\lambda+1}} \qquad (10)$$

where w is a function of $A(\lambda)$ and $A(\lambda + 1)$. The equation is solved iteratively to give the free energy change of neighboring states $\Delta A(\lambda \rightarrow \lambda + 1)$, which via combination yield the overall free energy change. MBAR method has been shown to minimize the variance in the calculated free energies, by making more efficient use of the simulation data. [168,223–225]

TI/MD simulations protocol

For the TI/MD calculations, the relaxed complexes of compounds **8a-h** with MmpL3 from the 100ns-MD simulations in a POPC lipid bilayer with the ff99sb [147] were used as starting structures for the alchemical calculations. The setup procedure was the same as previously reported for the MD simulations with Amber18 program. [209] TI/MD calculations were also performed for the ligands in solution. The bond constraint SHAKE [213] algorithm is disabled for TI mutations in AMBER GPU-TI module pmemdGTI, [226] and therefore a time step of 1 fs was used for all MD simulations.

Initial geometries were minimized using 20,000 steps of steepest descent minimization at λ= 0.5. These minimized geometries were then used for simulations at all λ values. Eleven λ values were used, equally spaced between 0.0 to 1.0. Each simulation was heated to 310 K over 500 ps using the Langevin thermostat, [227,228] with a collision frequency set to 2 ps^{-1}. The Berendsen barostat [229] was used to adjust the density over 500 ps at constant pressure (NPT), with a target pressure of 1 bar and a 2 ps coupling time. Then, 500 ps of constant volume equilibration (NVT) was followed by 2 ns NVT production simulations. Energies were recorded every 1 ps, and coordinates were saved every 10 ps. Production simulations recalculated the potential energy at each λ value every 1 ps for later analysis with MBAR. [168]

For each calculation, the 1-step protocol was performed, i.e., disappearing one ligand and appearing the other ligand simultaneously, and the electrostatic and van der Waals interactions are scaled simultaneously using softcore potentials from real atoms that are transformed into dummy atoms. [44] We carried out the calculations using the 1-step protocol which changes charges and van der Waals interactions in a single simulation by activating both Lennard-Jones and Coulomb softcore potentials simultaneously, reducing the computational cost. [230] The 1-step protocol offers a less computational expensive and more accurate approach to free energy estimates according to recent studies. [222]

The final states 0 and 1 of the alchemical calculations 0 → 1 or 1 → 0, ie. the structures of ligand 0-AR and 1-AR complexes, as resulted from the alchemical transformations, were compared with these complexes' structure resulted from converged 100ns-MD simulations. This was performed to certify that the 2 ns MD simulation for each λ-state during the alchemical calculations was enough for the complexes 0-AR and 1-AR to converge to the same structure with 100ns-MD simulations. Two repeats were performed for the TI/MD calculation for each alchemical transformation.

In summary, we performed for the ~ 100,000 atoms protein complexes studied here for the single protonation state 100ns-MD simulations in 2 repeats x 9 ligands (18 MD simulations) and for the double protonation state 80ns-MD simulations in 9 ligands (9 MD simulations). Additionally, we performed for 4 representative ligands 500 ns-MD simulations (4.52 μs MD simulation time). We performed the simulations using Desmond program, which performed much faster than Amber or Gromacs programs, using an amber force field (ff99sb) that can fairly describe the protein conformation.

We tested the MM-GBSA calculations using ensembles from 20 ns-MD simulations with ff99sb for 10 ligands in 3 repeats x 2 protonation states (60 MD simulations). For the monoprotonated form of the ligands, we tested an environment without or with an implicit model for membrane (2 environments). The simulation time for these simulations was 2.4 μs. We calculated the MM-GBSA interaction energies with the free available OPLS2005 force field with Desmond software.

We used the last snapshot of the converged MD simulations and performed TI/MD simulations to calculate the relative binding free energies using alchemical perturbations and the amber software and ff14sb. Thus, we performed 2 repeats x 6 ligands x 10-λ values (120 2ns-MD simulations). The total simulation time for the simulations performed here was 7.16 μs.

3.3.3 Differential scanning calorimetry

Samples for DSC were prepared by mixing the tested ligands SQ109 (**8a**) and analogs **8b–h** and **12** with DMPC or DSPG membranes at 10% w/w concentration. This was achieved by mixing a solution of the ligand's fumarate salt in methanol and a solution of DMPC lipid in chloroform or a solution of DSPC in chloroform/methanol (5:1) and subsequently evaporating the solvent. The films that were formed were utilized for DSC analysis by weighting approximately 3 mg of each film in a 40 μL aluminum crucible, adding

3 μL of PBS (pH = 7.4) as a hydration medium, sealing the crucible, vortexing, and allowing it to anneal for a 15 min period to achieve sample equilibration. The DSC thermogram of each sample was obtained by utilizing a DSC822e Mettler-Toledo calorimeter (Schwerzenbach, Switzerland) calibrated with pure indium (*T*m = 156.6 °C). An empty sealed crucible was used as reference. Each analysis included equilibration at 5 °C for 10 min followed by two heating−cooling cycles in the range between 5 and 35 °C with a 5 °C/min scanning rate for DMPC samples or between 10 and 70 °C with a 2.5 °C/min scanning rate for DSPG samples. The obtained calorimetric data (characteristic transition temperatures *T*onset and *T*, transition enthalpy Δ*H*, and width at half peak height of the *C*p profiles $\Delta T_{1/2}$) were analyzed with the Mettler-Toledo STARe software. The transition enthalpy is expressed as joules per total sample mass and as kilojoules per mole of DMPC and is presented as the absolute value in endothermic and exothermic processes (Table 11). Log D values in Table 11 were calculated with the ChemAxon software.

3.3.4 Cell growth inhibition assays

Cell growth inhibition assays were performed as previously reported [123,231,232] and are described in Appendix A including representative dose−response curves of SQ109 analogs against the protozoan parasites (Figure S6).

3.3.5 Surface plasmon resonance

The MtMmpL3 protein was purified from *M. smegmatis* DmmpL3/pMVGH1-mmpL3tb cells [233] following the previously reported protocol. [24] For the amino coupling of MmpL3tb, CM5 chip surfaces were activated with 0.05 M *N*-hydroxysuccinimide and 0.2 M *N*-ethyl-*N*-(3-diethylaminopropyl)carbodiimide (BIAcore). Purified MmpL3tb was injected over surfaces immediately after activation. The immobilized density of the protein (ligand) was 17,654 response units (RU). For kinetic modeling, we considered only the simplest models that would be compatible with one or two distinct events during both inhibitor binding and dissociation. These four models are (i) simple 1:1 binding model; (ii) heterogeneous ligand (HL), in which different protein populations' on-chip surfaces have different kinetic properties; (iii) two-state reaction or ligand-induced conformational change, wherein conformational change occurs on the same time scale as ligand binding; and (iv) bivalent analyte, where multiple analytes bind independently at nonidentical sites.[24,234]

The best global fit for compound binding to MmpL3 was obtained using the two-state reaction model. Schematic representations and equations relevant to this model are given below:

$$A+B \leftrightarrow A{\cdot}B \leftrightarrow [A{\cdot}B^{*}] \qquad (1)$$

$$\partial(A{\cdot}B)/\partial t = k_{a1}[A][B] - (k_{d1}[A{\cdot}B] - k_{d2}[A{\cdot}B^{*}]) \qquad (2)$$

$$\partial(A{\cdot}B^{*})/\partial t = k_{a2}[A{\cdot}B^{*}] - k_{d2}[A{\cdot}B^{*}] \qquad (3)$$

$$R_t = [A{\cdot}B] + [A{\cdot}B^{*}] \qquad (4)$$

The equilibrium dissociation constant for this model is:

$$K_D = k_{d1}k_{d2}/k_{a1}k_{a2}, \qquad (5)$$

where [*A*] is the concentration of analyte; [*B*] is the ligand binding capacity; [*A·B*] and [*A·B**] are intermediate and final complexes, respectively; K_{d1}, k_{d2}, k_{a1}, and k_{a2} are microscopic rate constants; and R_t is the total SPR response, which is directly proportional to [*A·B*] + [*A·B**].

4 Binding and blocking of influenza A WT and S31N M2 conductance domain by cage alkyl amine containing inhibitors

4.1 Results

4.1.1 MAS NMR Spectroscopy

4.1.1.1 Drug binding to M2CD tetramer at elevated temperatures

We recorded proton-detected (H)NH MAS ssNMR spectra of the M2(18-60) (M2CD) construct reconstituted in perdeuterated DPhPC membranes. [235] The lipid to tetramer molar ratio was 25:1 which favors sensitivity due to a high concentration of tetrameric M2CD. [236–238] The site-specific resolution allows tracking of Gly34 and His37 side chain resonances that are strongly affected by drug binding to the pore. Thus, the binding was tracked primarily by measuring changes in the chemical shifts (CSPs) of ^{15}N and ^{1}H nuclei in Gly34 or His37. A solution of 300 µM of drug was equilibrated with M2CD embedded in DPhPC lipid at 4°C. When lack of binding occurred, the sample was held at elevated temperature, at 55 °C for 2-5 hours in the case of WT M2 and for up to >10 h at 70°C in the case S31N M2, which helps to overcome the high energy barrier to drug entry. [112] Table S6 summarizes the CSPs observed in the spectra, categorized into small and large shifts (SS and LS). It is important to note that no CSPs are observed after incubation at an elevated temperature without the presence of a drug indicating that the protein structure is stable at these temperatures.

WT M2CD. As shown in Figure 11C-E, we did not observe significant CSPs of WT M2CD protein resonances in the presence of the tested compounds Rmt, AK59, and RL208 at 4 °C. For Rmt, CSPs were smaller than 0.5 ppm for ^{13}C and ^{15}N and smaller than 0.2 ppm for ^{1}H nuclei. These changes occur due to non-specific effects, rather than pore binding since entry to the pore is exceedingly slow under these conditions. [90,112]

After incubation at a higher temperature of 55 °C, large shifts were induced by Rmt for WT M2CD. These CSPs have values of ca. 2 ppm in the ^{15}N resonance of Gly34 and > 4 ppm in the His37-Nε2 side chain and ca. 5 ppm in the ^{1}H resonance of His37-Nε2 side chain (Table S6, Figure 11F), suggesting, as previously reported, significant restructuring of the protein, [90,102,239,112] during pore-binding. [95] One clear structural change that occurs upon pore binding by Rmt is the disruption of the imidazole-imidazole hydrogen bonding between His37 residues in adjacent TM helices indicated by the absence of the proton resonance

at 14.3 and 11.7 ppm [102] (Figure 11F). This is also evident for AK59 – M2CD complex but the remaining intensity of His37-Nε2 side chain peaks at 14.3 and 11.7 ppm or of Gly34 in the (H)NH spectrum after 5 hours at 55 °C (Figure 11G) suggested the presence of two populations, the bound and unbound form of M2CD. From measuring the intensity of the His37-Nε2 side chain peaks, ca. 20% of the population corresponds to the unbound protein, based on the ~80% disruption of the hydrogen bonding (~20% of remaining intensity of His37-Nε2 peaks). The CSPs of AK59 binding were similar in magnitude to Rmt binding. Specifically, the CSPs in the ^{15}N resonance of Gly34 and ^{15}N and ^{1}H resonances of His37-Nε2 were > 4 ppm. We observed no binding for RL208 at the elevated temperature (Figure 11H).

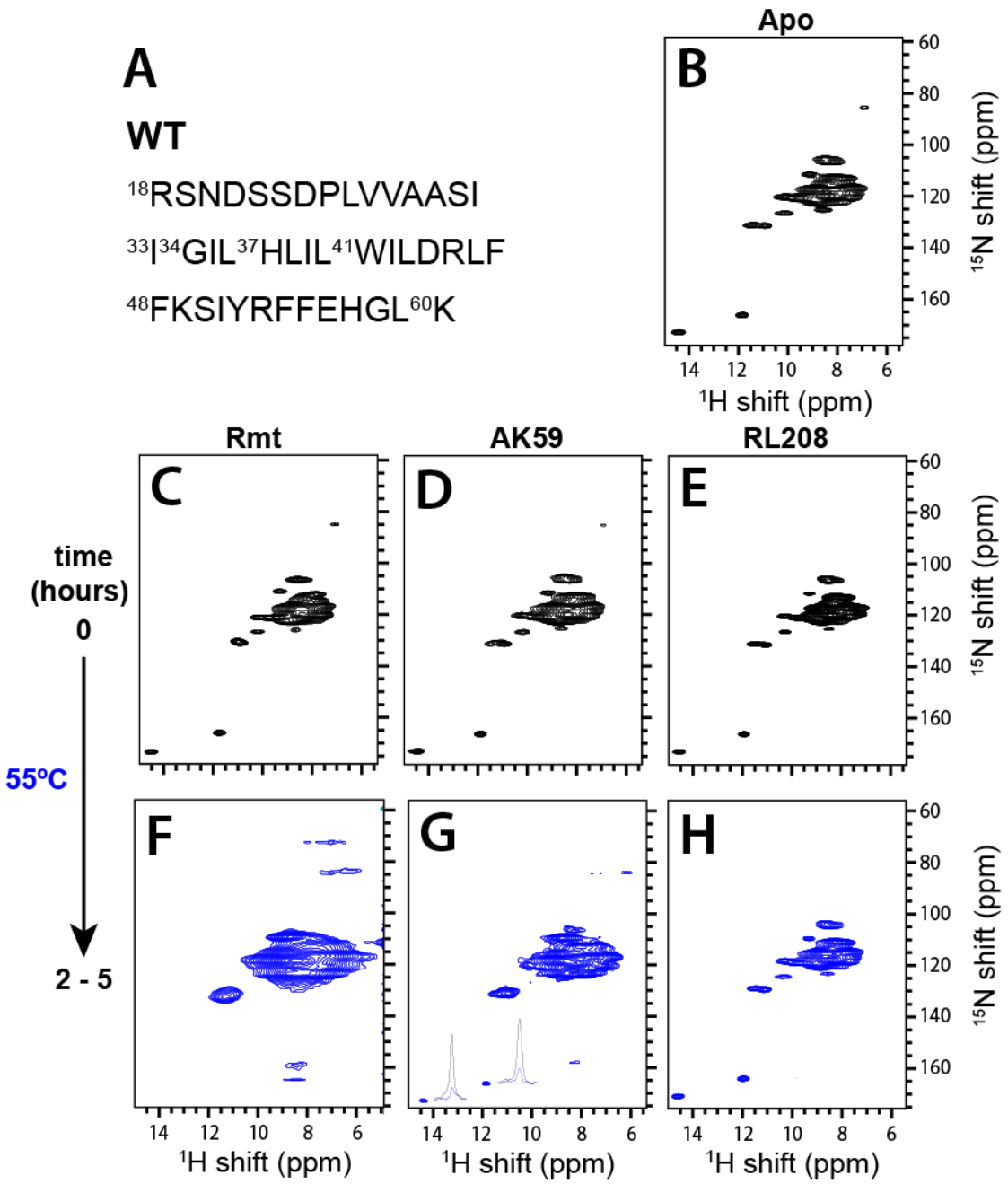

Figure 11 Monitoring the ^{1}H and ^{15}N CSPs in WT M2CD spectra in the presence of small molecules. (A) shows the amino acid sequence of M2CD; (B) shows the (H)NH spectrum of WT M2CD (without ligand); (C)-(E) show the (H)NH spectra of WT M2CD with Rmt or AK59 or RL208, respectively, incubated at 4 °C; (F)-(H) show the (H)NH spectra of WT M2CD with Rmt or AK59 or RL208, respectively, after 2-5 hours of incubation at 55 °C, and the His37 side chain peak intensities for selected spectra. The samples were reconstituted in DPhPC bilayers at pH 7.8 using a lipid:tetramer molar ratio of 25:1, and incubated with 300 µM drug.

S31N M2CD. In the (H)NH spectra of S31N M2CD, none of the tested compounds showed any significant effect on the imidazole-imidazole hydrogen bond between His37 residues or other residues in S31N M2 (Figure 12) which was unexpected for M2WJ352 and UBALT09 that block the S31N M2 channel in EP experiments (Table S5).

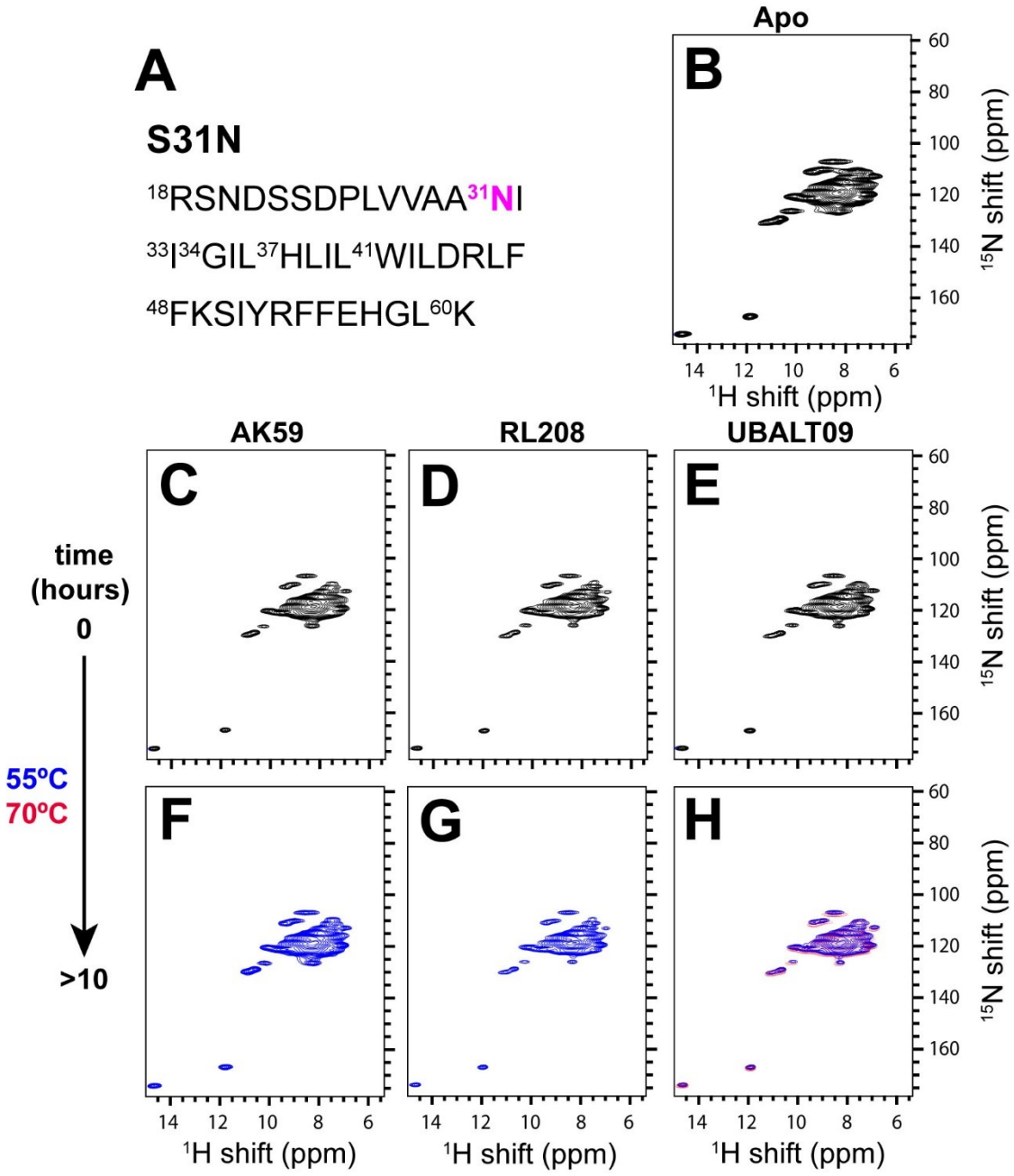

Figure 12 Monitoring the ^{1}H and ^{15}N CSPs from S31N M2CD spectra in the presence of small molecules. (A) shows the amino acid sequence of the construct; (B) shows the (H)NH spectrum of S31N M2CD

(without ligand); (C)-(E) show (H)NH spectra of M2CD with AK59 or RL208 or UBALT09, incubated at 4 °C, respectively. (F)-(H) show the (H)NH spectra of S31N M2CD with AK59 or RL208 or UBALT09, after >10 hours of incubation at 55 °C (70 °C for UBALT09 in red), respectively. The samples were reconstituted in DPhPC bilayers at pH 7.8 using a lipid:tetramer molar ratio of 25:1, and incubated with 300 µM drug.

4.1.1.2 Drug binding to M2CD tetramer at high pH after relaxation of the protein at low pH

Based on the measures pKas [61,91,117,240] at the acidic pH 3.5 the imidazoles of the four His37 become protonated, and M2 adopts an open conformation at the C-terminal end in which His37-His37 hydrogen bonding is disrupted. A more open conformation is consistent with crystallography data [68,74] and with a large change in the measured TM helical tilt in WT M2CD. [241] Following this data, we adopted a protocol, previously applied to M2TM, [242] by first shifting the M2CD protein sample to pH 3.5 and incubated overnight in the presence of the drug at 4 °C, and then shifted the pH back to 7.8 for NMR-based analysis of CSPs, still in the presence of drug. The spectrum was then measured at pH 7.8.

Spectral changes induced by low pH are reversible in the absence of drug. Figure S13A,B or S14A,B show the relevant spectra for the apo WT or S31N M2CD, respectively. At the starting protein sample at pH 7.8 the (H)NH spectra showed the His37-Nε2 proton resonances at 14.3 and 11.7 ppm, which are characteristic of the imidazole-imidazole hydrogen bonded state. [102,112] After overnight incubation at pH 3.5, we observed the expected His37-His37 hydrogen bonding disruption for both WT and S31N M2 M2CD (Figure S13B, S14B). After incubating the protein at pH 7.8 again, the peaks characteristic of the imidazole-imidazole hydrogen bond returned in the spectra of apo WT or S31N M2CD (Figure S13C, S14C). [70]

WT M2CD. Figure 13, 14 show spectra of a more complete drug binding event at pH 7.8 of WT M2CD with Rmt, [102,112] and AK59 at 300 µM concentration. As shown in Figure 13A, 14A we observed the clear disruption of the His37-His37 hydrogen bond in the presence of Rmt or its analog AK59. For the latter only 0.5% of the population was left unbound, based on the His37 peaks. Other distinct CSPs that revealed binding are those of well-separated peaks, for example Gly34, Lys49, Ser50, Ile51, and Trp41 side chains. The rest of the residues in the (H)NH spectrum were not resolved, which is not surprising since the protein was not deuterated. To obtain spectra with increased resolution, we recorded 3D (H)CANH spectra that turned out to be very similar for Rmt and AK59, showing large CSPs along the whole transmembrane helix, as well as the characteristic disappearance of signals from the amphipathic helix. The ^{15}N-^{13}Cα projection

of the (H)CANH spectra for Rmt and AK59 samples are shown in Figure 13B and 14B, respectively. Compound RL208 at 300 µM did not disrupt the His37-His37 hydrogen bond (Figure S13C), the amide region in the 2D (H)NH spectrum showed a small broadening and the ^{15}N-^{13}Cα spectrum was unchanged from the spectrum of the apo-protein [101] (Figure S13C, upper part). When we increased the drug concentration to 6 mM, RL208 still did not disrupt His37-His37 hydrogen bonding although it produced broadening in the main peak region of (H)NH spectrum and CSPs of 0.5 ppm and 1.5 ppm in ^{1}H and ^{15}N resonances, respectively, of one of the Trp41-NE1 side chain peaks (Figure S15). There were also minor CSPs in the well-separated peaks from Gly34, Lys49, Ser50, Ile51. In the 3D (H)CANH spectrum the CSPs from the better resolved peaks did not exceed 0.5 ppm in both ^{15}N and ^{13}C resonances (Figure S15).

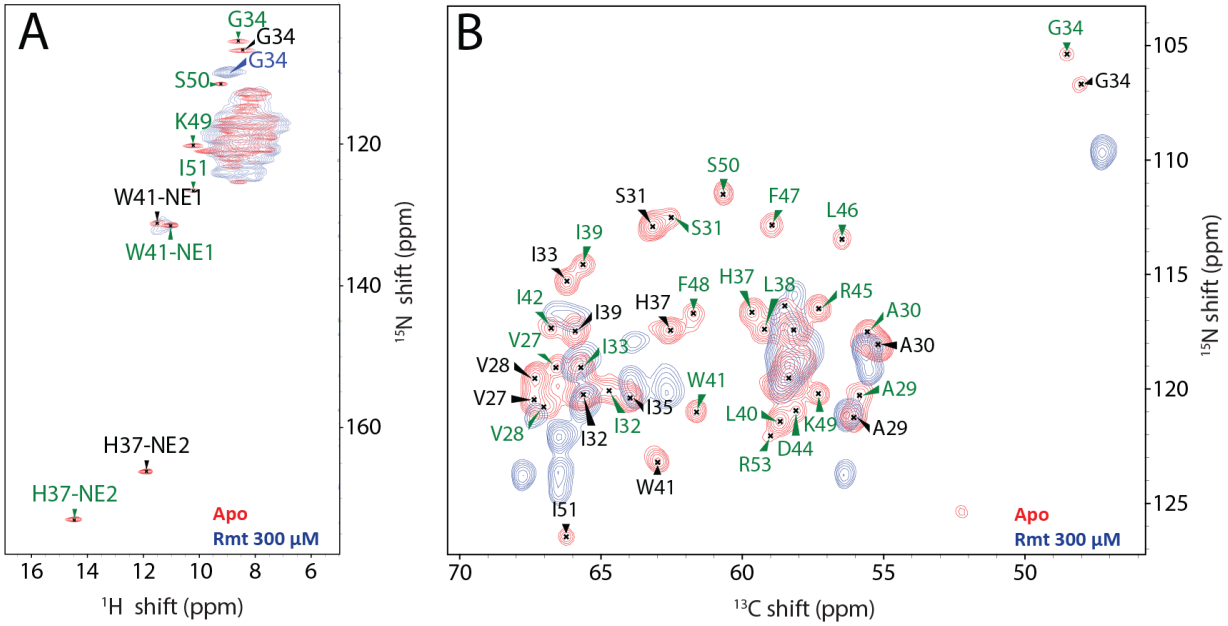

Figure 13 Monitoring the ^{1}H, ^{15}N, and ^{13}C CSPs in WT M2CD resonances in the presence of 300 µM of Rmt. [102,112] (A) (H)NH spectrum of WT M2 with (blue) and without Rmt (red). (B) ^{15}N-^{13}Cα projection of the (H)CANH spectrum of WT M2 with (blue) and without Rmt (red). The samples were reconstituted in DPhPC bilayers at pH 7.8 using a lipid:tetramer molar ratio of 25:1. Both spectra were recorded at pH 7.8 after incubating the system at acidic pH 3.5 in the presence of the drug and switching back to alkaline pH.

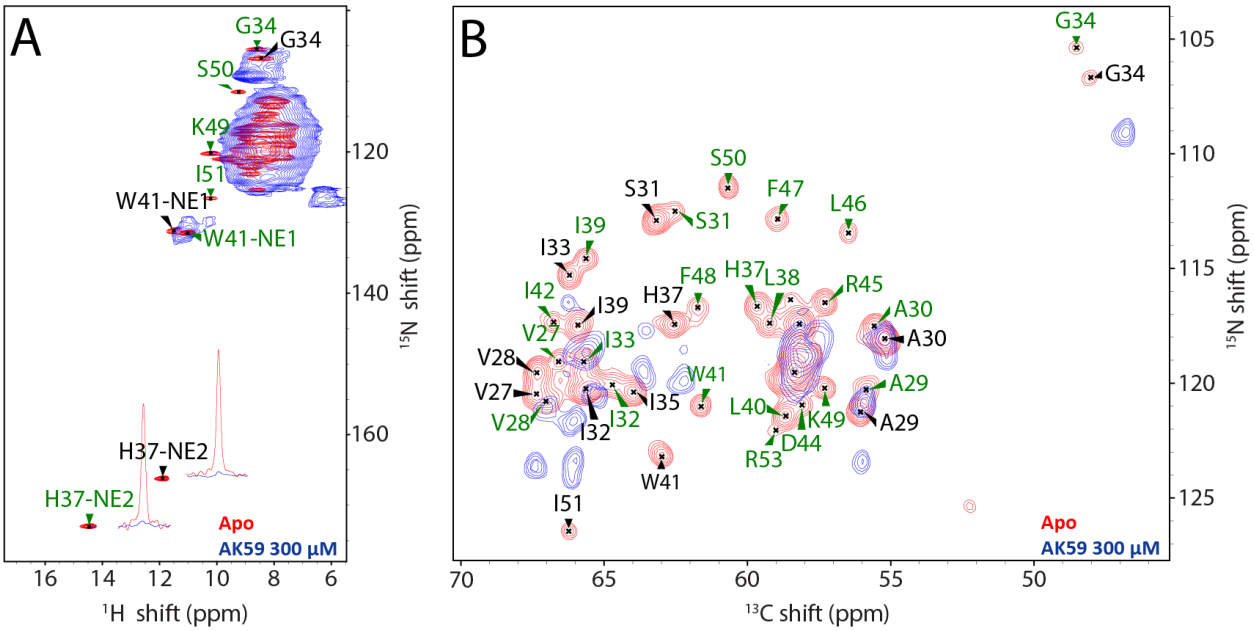

Figure 14 Monitoring the ^{1}H, ^{15}N, and ^{13}C CSPs in WT M2CD resonances in the presence of 300 µM of AK59. (A) (H)NH spectrum of WT M2 with (blue) and without AK59 (red) and His37 side chain peak intensities. (B) ^{15}N-$^{13}C\alpha$ projection of the (H)CANH spectrum of WT M2 with (blue) and without AK59 (red). The samples were reconstituted in DPhPC bilayers at pH 7.8 using a lipid:tetramer molar ratio of 25:1. Both spectra were recorded at pH 7.8 after incubating the system at acidic pH 3.5 in the presence of the drug and switching back to alkaline pH.

In the case of UBALT09, which is not a blocker of WT M2 channel by EP (Table S5), using a drug concentration of 300 µM we did not observe His37-His37 hydrogen bonding disruption (Figure 15). Interestingly, the (H)NH spectrum showed doubling of the His37-Nε peaks and a broadening of the main peak region (Figure 15A, upper part) as well as chemical shift perturbation of 0.5 ppm and 1.5 ppm in ^{1}H and ^{15}N resonances, respectively, of one of Trp41-Nε side chains. However, in the (H)CANH spectra no doubling of peaks or other significant CSPs are evident. We incubated the sample in a higher drug concentration of 6 mM. The results are shown in Figure 15 where in the (H)NH spectrum we observed ~30% of the His37-Nε2 side chain peak intensity remaining, as well as a CSP in the ^{15}N resonance of Trp41 side chain, and a general broadening of the amide region of the (H)NH spectrum. Additionally, in the (H)CANH spectrum we observed large CSPs but also peaks which revealed two populations, which we assign to the apo-form and drug-bound M2 (Figure 15).

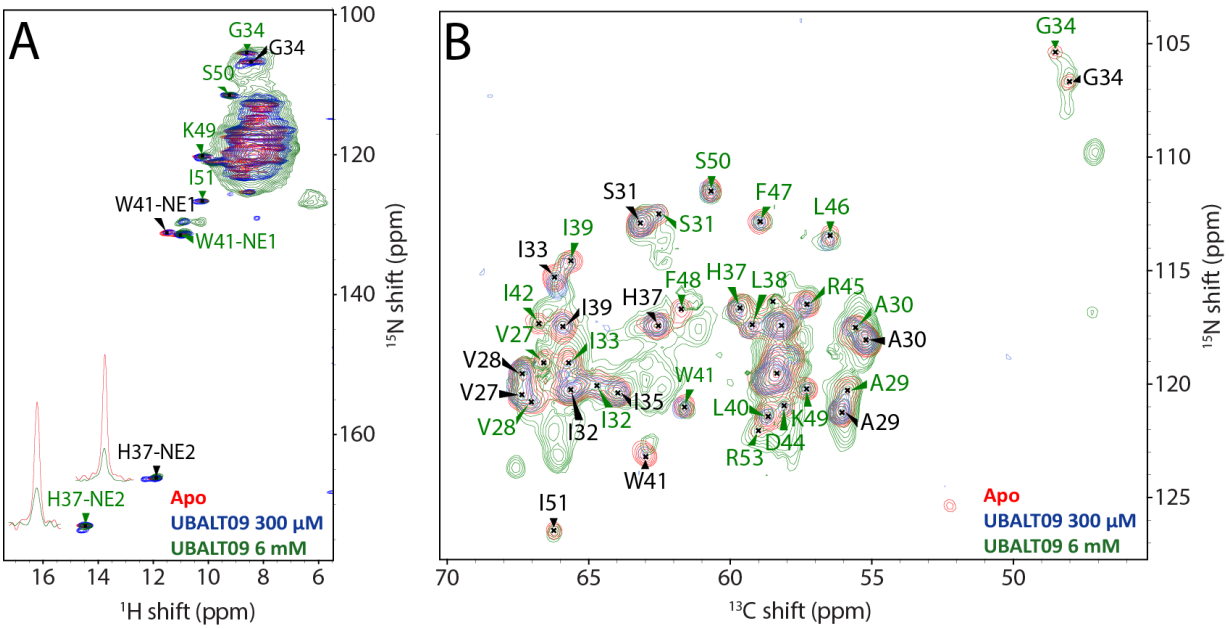

Figure 15 Monitoring the ^{1}H, ^{15}N, and ^{13}C CSPs in WT M2CD resonances in the presence of 300 µM or 6 mM UBALT09. (A) (H)NH spectrum of WT M2 with UBALT09 at 300 µM (blue), or 6 mM (green) and without UBALT09 (red) and His37 side chain peak intensities. (B) ^{15}N-$^{13}C\alpha$ projection of the (H)CANH spectrum of WT M2 with UBALT09 at 300 µM (blue), or 6mM (green) and without UBALT09 (red). The samples were reconstituted in DPhPC bilayers at pH 7.8 using a lipid:tetramer molar ratio of 25:1. Both spectra were recorded at pH 7.8 after incubating the system at acidic pH 3.5 in the presence of the drug and switching back to alkaline pH.

S31N M2CD. No NMR-based evidence of drug binding was found for S31N M2CD with Rmt, AK59, or RL208. However, M2WJ352 and UBALT09 were efficient blockers in the EP assay (Table S5). In the samples of all drugs, we observed the His37-Nε2 proton resonances at 14.3 and 11.7 ppm and we did not observe CSPs in the 2D or 3D MAS ssNMR spectra (Figure S14C), i.e., the spectra from all the tested drugs were almost identical to the spectrum of the apo S31N M2. When we increased the drug concentration to 6 mM for M2WJ352 and UBALT09 His37-His37 hydrogen bonding was again maintained but some small CSPs were observed. In particular, at Gly34 the CSPs in ^{15}N or ^{13}C resonances in both 2D and 3D spectra were not larger than 0.5 ppm (Figure S17, S18).

4.1.2 MD Simulations

4.1.2.1 Docking calculations

Compared to the GOLD program with the scoring function Gold Score [203], the Glide program with the scoring function Glide XP [243] produced a higher proportion of docking poses of the compounds having the ammonium group oriented inward inside the WT M2CD [244] and of M2WJ352 and UBALT09 with the ammonium group oriented outward inside the S31N M2CD [60] in agreement with the experimental results [60,97] (Figure 16, 17). The combination of Glide with the induced fit [245] method produced the best fit. The M2CD complexes were embedded in lipid buffers and subjected to MD simulations.

4.1.2.2 MD simulations

We carried out 250ns-MD simulations of WT or S31N M2CD with or without drugs inside the M2 pore. We simulated the Rmt enantiomers (R-Rim, S-Rim), AK59, RL208, M2WJ352, and UBALT09 in complex with WT or S31N M2CD embedded in POPC bilayers using the CHARMM36m force field. [244,246]

WT M2CD. We generated docking poses of the adamantyl amine drugs, RL208, or M2WJ352, and UBALT09 inside WT M2CD having their ammonium group oriented toward the C-terminus (inward) as suggested from experiments and MD simulations of complexes between Amt or Rmt or other inhibitors and M2 using different WT or S31N constructs. [97,104,114] Our MD simulations of adamantyl amines (R-Rim, S-Rim, AK59) and RL208 showed that the cage alkyl amines form ~ 3 hydrogen bonds with waters between the ligand and His37 (Figure 16, see measures in Table 12, 13). Compared to the apo WT M2CD, where a free flow of waters from the Val27 secondary gate to Trp41 was observed (Figure 18), in these complexes no waters passed from the Val27 gate. In contrast, in the complexes with M2WJ352 and UBALT09, waters were able to pass the Val27 secondary gate (Figure 16).

S31N M2CD. Experimental data have shown that in contrast to WT M2, Amt and other adamantyl amine analogs are oppositely oriented in the S31N M2(22-46) mutant pore with the ammonium group facing the N-terminus (outward) and the adamantyl group inward (Figure 17). [80] We started from docking poses with ammonium group oriented inward and performed 250 ns MD simulations of S31N M2CD complexes with R/S-Rmt, AK59, RL208, UBALT09, and M2WJ352. The simulations showed that Rmt, AK59 and RL208 finally were oriented outward forming hydrogen bonds with Asn31 (Figure 17, see measures in Table 12, 13),

but allowed water passage through the M2 pore. [80,247,248] The 250 ns MD simulations of the S31N M2CD complexes with M2WJ352 or UBALT09, led to a conformation of M2CD in which the ammonium group forms hydrogen bonds with the Asn31 amide side chains and waters, and the aryl group is outward between the Val27 side chains blocking water passage (measures are shown in Table 12, 13).[30]

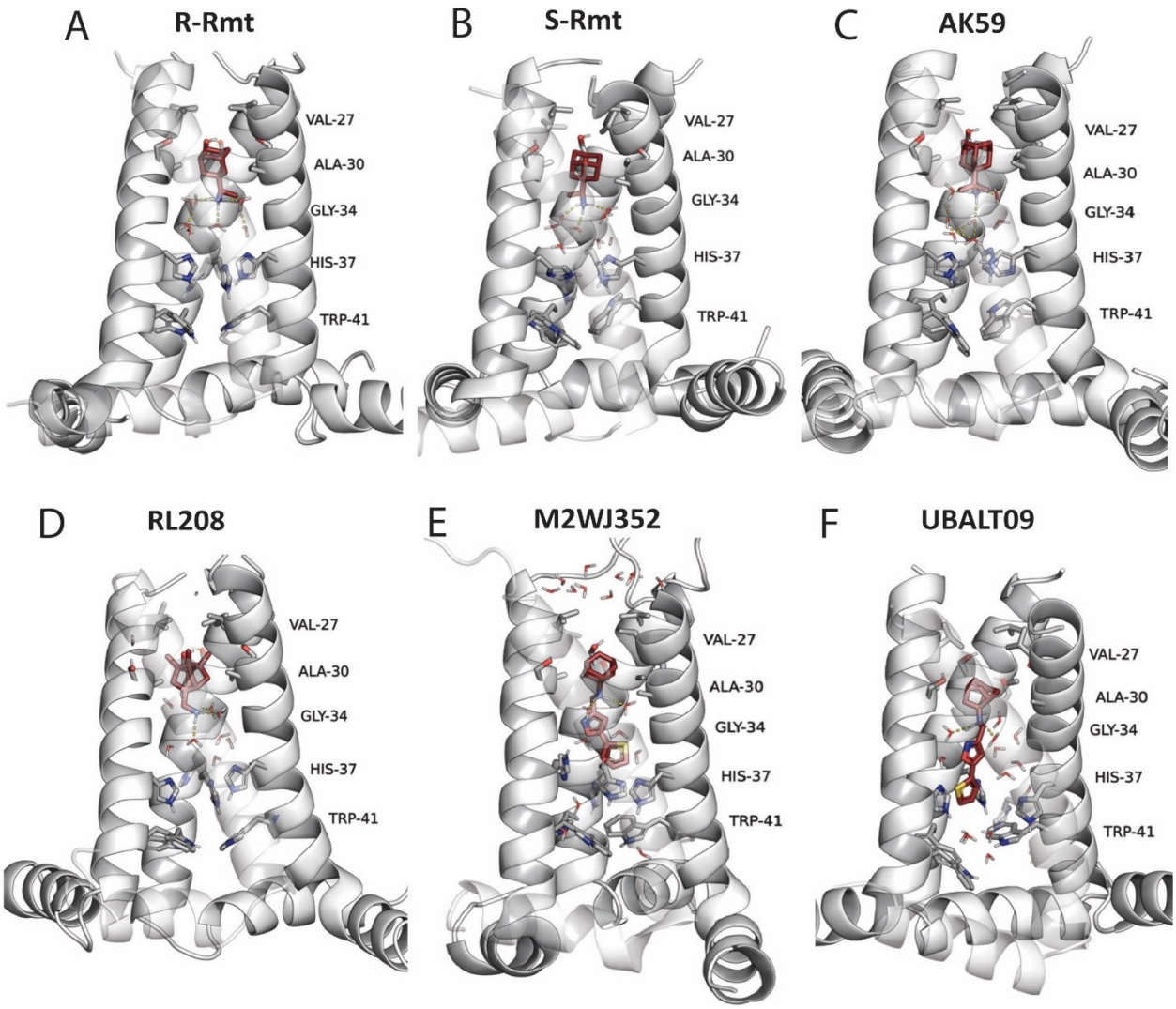

Figure 16 Representative structures from 250ns-MD simulations of WT M2CD – drug complexes embedded in POPC bilayers using the CHARMM36m force field. [244,246] (A) R-Rim, (B) S-Rim, (C) AK59, (D) RL208, (E) M2WJ352, (F) UBALT09. The M2 channel is shown with a white cartoon representation, each ligand is shown with a stick representation and colored red and protein residues in grey color. Water

molecules are shown in stick representation with the oxygen atom in red and hydrogen atoms displayed in white color.

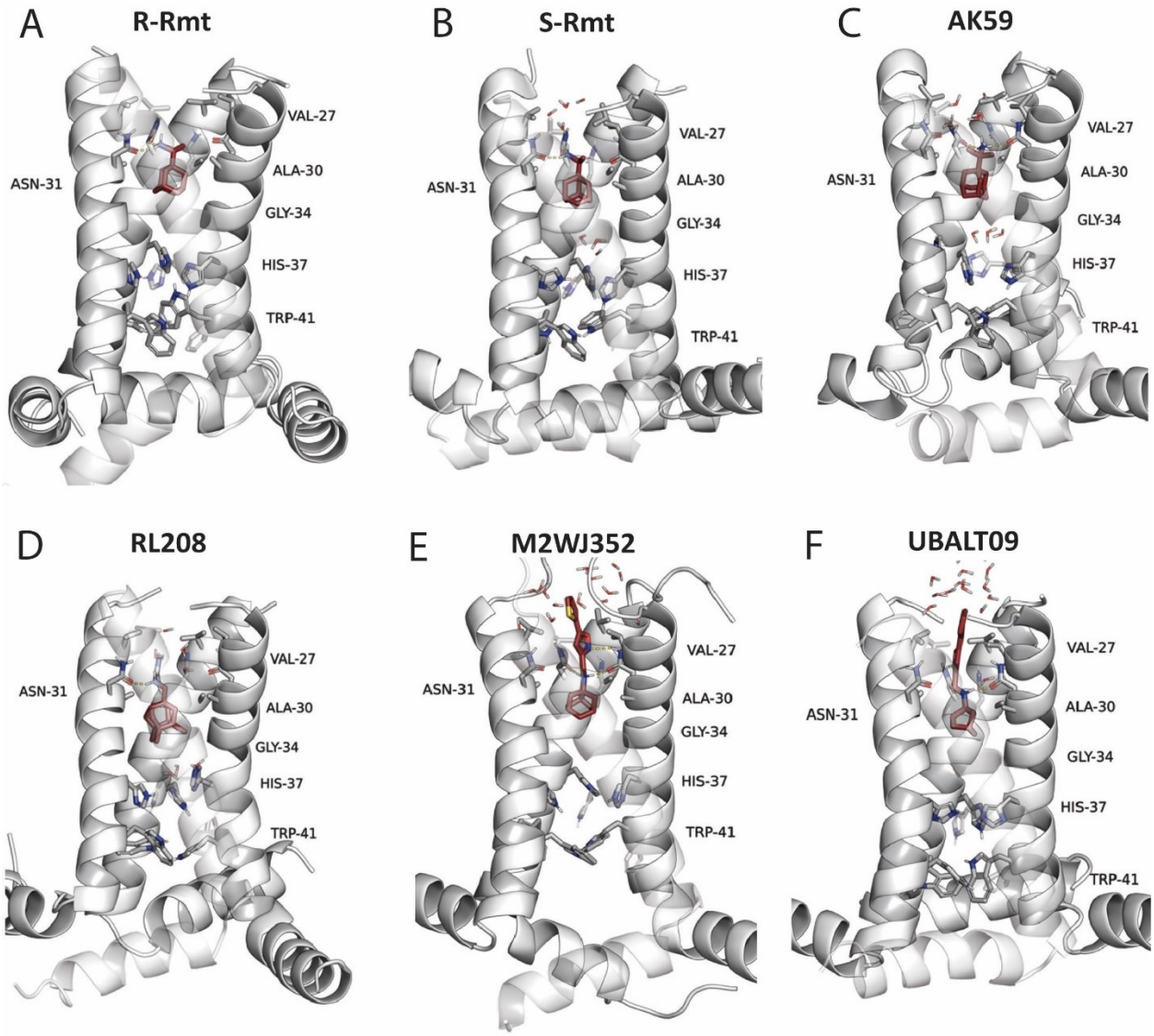

Figure 17 Representative structures from 250ns-MD simulations of S31N M2 M2CD – drug complexes embedded in POPC bilayers using the CHARMM36m force field. [244,246] (A) R-Rim, (B) S-Rim, (C) AK59, (D) RL208, (E) M2WJ352, (F) UBALT09. The M2 channel is presented with the cartoon representation in white color, each ligand is colored deep red in stick representation as well as the protein residues in grey color. Water molecules are shown in stick representation with the oxygen atom in red and hydrogen atoms displayed in white color.

4.1.2.3 Measures in the MD simulations

We carried out MD simulations in the complexes of WT or S31N M2CD correspondingly with Rmt enantiomers (R-Rim, S-Rim), AK59, RL208, M2WJ352, and UBALT09 at pH 7.8, with M2CD adopting the closed conformation at the C-terminal side of the membrane [97] (His37-tetrad charge 0). The M2CD (H37 Nε) tetramer was embedded in 13 Å lipid buffer. These bilayers include ca. 130 – 140 lipids surrounding M2CD. We applied the CHARMM36m force field for the simulations. [244,246]

We investigated:

A) The blockage/passage of bulk waters from the Val27 gate in the WT and S31N M2CD pore in the apo-protein and in complex with an inhibitor and the orientation of the ligand inside the M2CD pore.
B) The stability of the M2–ligand complexes and the location of the blockers inside the M2CD pore. The location of the pore blockers depends on the conformation of M2CD and their interactions with the M2TM.
C) The H–bonds between the four His37 in the apo-protein WT M2CD and between ligand and waters, Ala30 or Asn31 (in S31N M2CD complexes).

A. Water blockage/passage and orientation of the ligands in the WT or S31N M2CD channels

By analyzing the M2CD trajectories of 250 ns with the CHARMM36m force field without ligand within the M2TM pore, we confirmed the free flow of waters from the Val27 tetrad to Trp41 tetrad (Figure 18A). The 250 ns MD simulations of the WT M2CD in complex with R-Rim, S-Rim, AK59 or RL208 showed the blockage of waters from the Val27 secondary gate and the ligand (Figure 18B). In contrast M2WJ352 or UBALT09 which can best fit with their ammonium group inward do not block the passage of waters from the M2CD pore. The 250 ns MD simulations with the CHARMM36m force field of the S31N M2CD-M2WJ352 or S31N M2CD-UBALT09 complexes showed that no waters passed between the Val27 secondary gate and the ligand. Experimental data have shown that in contrast to WT M2, Amt and analogs are oppositely oriented in the S31N mutant pore with the ammonium group facing outward and the adamantyl group inward. [80] In the latter orientation the ammonium group forms tight hydrogen bonds with Asn31 side chains and backbone carbonyls while the adamantyl group is placed in the broad area

defined by Gly34 without having stabilizing van der Waals contacts. [80] These structural changes resulted in the weakening of the binding interactions and water passing through consequently. We observed in the MD simulations that the S31N M2CD channel is not blocked by R–Rim, S–Rim, AK59, and RL208 (Figure 17) abolishing these drugs from the market.

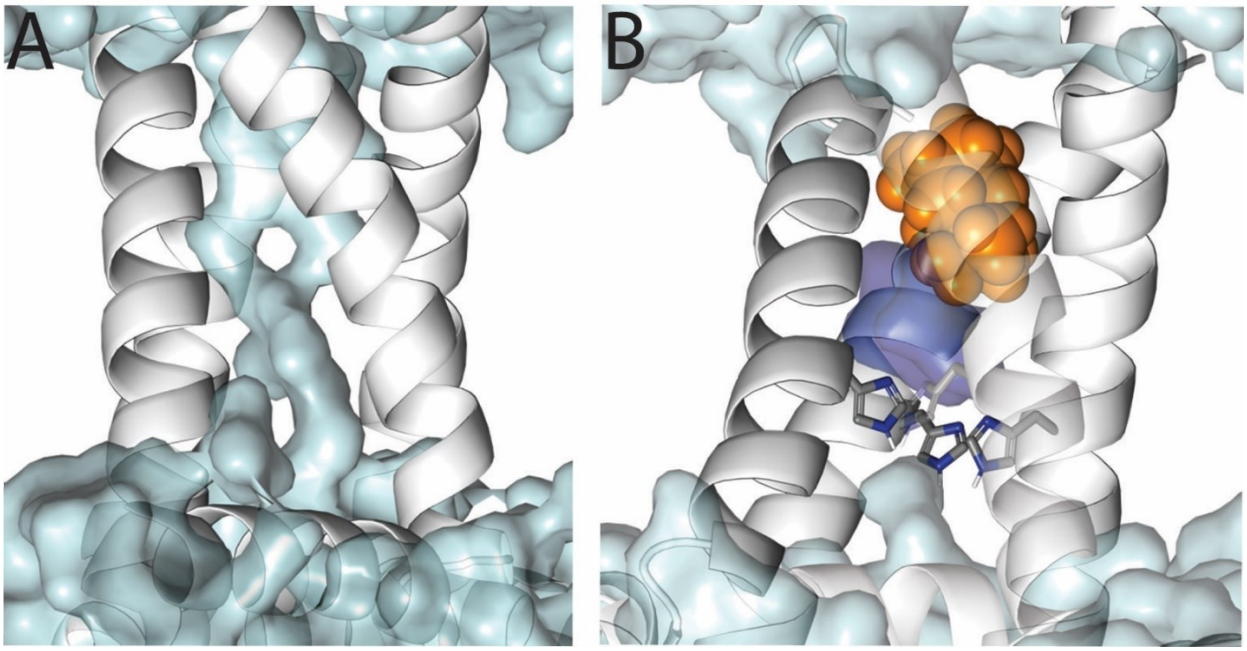

Figure 18 Water density inside the pore is shown in WT M2CD (PDB ID 2L0J) in 13 Å lipid buffer. (A) WT M2CD apo protein, there is free flow of water molecules within the TM pore. (B) WT M2CD in complex with a ligand shows the blockage of the water flow within the TM pore and the trapped water molecules between ligand and His37. Ligand atoms are shown in Van der Waals spheres colored orange, the trapped water molecules are shown in blue color in surface representation, and with cyan color the rest of water molecules in surface representation as well. The WT M2CD is shown with cartoon representation in white color and the His37 of the TM domain with stick representation in deep gray color.

B. Stability of the M2CD–ligand complexes and location of the molecules

The RMSD(Ca) and RMSD(ligand) are shown in Figure S19; as is shown the systems reached equilibration inside the 250 ns-MD simulations.

We measured distances between the ligand and some of the TM residues. Table 12 shows the distance between the COM of the Val27, Ala30, and Gly34 tetrad and the COM of the cage alkyl of each ligand in the 250 ns MD simulations. The MD simulations of Rim enantiomers in complex with M2CD suggested that both enantiomers adopt the same position inside the M2 channel pore. This agrees with the thermodynamic and kinetic data showing that the enantiomers have the same binding free energy, channel blockage efficiency, and k_{on} and k_{off} rate constants measured with EP, and *in vitro* antiviral potencies against M2 protein. [88,109]

Table 12 Distance between the COM of the ligand's cage alkyl and the COM of the four Val27, Ala30, Gly34, or N+ from 250 ns MD simulation with CHARMM36m [244,246] force field.

Molecule	Type	COM cage alkyl – COM Val27	COM cage alkyl – COM Ala30	COM cage alkyl – COM Gly34	COM His37 - N+ ligand
R–Rim	WT	4.87 ± 0.27	0.56 ± 0.22	5.11 ± 0.30	7.20 ± 0.32
S–Rim	WT	4.85 ± 0.28	0.58 ± 0.23	5.12 ± 0.31	7.18 ± 0.32
AK59	WT	5.16 ± 0.24	0.38 ± 0.16	4.80 ± 0.26	7.08 ± 0.26
RL208	WT	4.67 ± 0.41	0.87 ± 0.37	5.52 ± 0.46	6.98 ± 0.49
M2WJ352	WT	4.29 ± 0.36	1.07 ± 0.36	5.53 ± 0.41	-
UBALT09	WT	4.37 ± 0.41	0.971 ± 0.39	5.32 ± 0.44	-
R–Rim	S31N	5.90 ± 0.39	0.53 ± 0.29	4.40 ± 0.39	-
S–Rim	S31N	5.86 ± 0.50	0.59 ± 0.34	4.33 ± 0.51	-
AK59	S31N	6.01 ± 0.42	0.68 ± 0.30	3.90 ± 0.45	-
RL208	S31N	6.74 ± 0.53	1.32 ± 0.52	3.43 ± 0.56	-
M2WJ352	S31N	6.76 ± 0.26	1.20 ± 0.25	3.59 ± 0.27	-
UBALT09	S31N	6.47 ± 0.29	0.98 ± 0.28	3.84 ± 0.31	-

Table 13 H–bonds analysis from the 250 ns simulations of protein–ligand complexes in WT/S31N M2CD in CHARMM36m [244,246] force field.

Molecule	Type	Ligand - waters H-bonds	Ligand - A30 H-bonds	Ligand - N31 H-bonds
R–Rim	WT	2.98 ± 0.33	0.00 ± 0.05	-
S–Rim	WT	3.00 ± 0.24	0.00 ± 0.00	-
AK59	WT	2.99 ± 0.13	0.00 ± 0.00	-
RL208	WT	2.97 ± 0.42	0.00 ± 0.00	-
M2WJ352	WT	2.09 ± 0.35	0.02 ± 0.03	-
UBALT09	WT	2.12 ± 0.44	0.00 ± 0.00	-
R–Rim	S31N	1.02 ± 0.43	-	1.93 ± 0.28
S–Rim	S31N	1.08 ± 0.52	-	1.90 ± 0.34
AK59	S31N	1.07 ± 0.43	-	1.93 ± 0.29
RL208	S31N	1.38 ± 0.65	-	1.54 ± 0.52
M2WJ352	S31N	0.41 ± 0.57	-	2.59 ± 0.70
UBALT09	S31N	0.84 ± 0.68	-	2.21 ± 0.75

4.1.3 Liposomal proton flux assay

We used a proteoliposomal functional assay published before [249] to examine the activity of the tested drugs to block WT and S31N M2CD and compare with EP and MAS NMR results. With this in-house assay, we could use the same WT and S31N M2 constructs containing residues 18 to 60, as used in the MAS NMR experiments. [11,45] The mechanism of this method is based on a proton gradient that is initiated via the addition of hydrochloride to a suspension of liposomes that contain M2CD. Whether M2 protein conducts protons inside the liposomes is monitored by recording the pH of the external solution after the addition of 1M HCl solution under continuous fast stirring. A gradual increase in the pH of the liposome exterior is an indication of the M2CD-mediated proton conduction. The assay is terminated by the addition of a proton uncoupler, carbonyl cyanide m-chlorophenylhydrazone (CCCP), and a rapid recovery of the pH is observed.

Drug inhibition of M2CD activity was qualitatively detected by a decrease or nearly complete disappearance of pH recovery after the initial hydrochloride solution addition. The drugs were added to the prepared proteoliposome samples in 50 μM final concentration and the system was allowed to equilibrate for one hour before the first hydrochloride addition. The results are depicted in Figure 19A-D for the two protein variants. In the case of WT M2CD, the results are categorized as strong (Figure 19A), mediocre or non-blockers (Figure 19B).

Inhibition by a drug results in a very slow recovery of the pH after the addition of 1M HCl. Thus, Amt, Rmt, and AK59 effectively block the WT M2CD proton channel as is shown by the minor increase of pH (ΔpH ~0.016) after the pH equilibration of the external solution around pH 6.3 (Figure 19A, S20). As a control, we added the same volume (50 μL) of the solution (water) used for drug solubilization. The control shows a higher pH increase (ΔpH 0.07) than the drug tests (ΔpH 0.016) validating the assay. Following the same measurements, M2WJ352 and UBALT09 showed no effective inhibition as the recovery of pH in both cases was almost the same as in the case of the sample with no drug (Figure 19B). RL208 showed a partial blocking of the proton conductance (Figure 19B).

The same procedure was followed for investigating drug inhibition of S31N M2CD. Slower conductance was observed for the S31N channel compared to the WT channel, revealing possibly a tighter tetrameric bundle. Hence, S31N M2CD proton conductance was also measured for a longer time interval by 1 min. In all cases, none of the drugs inhibited proton transport to the interior of the proteoliposomes (Figure 19 C,D).

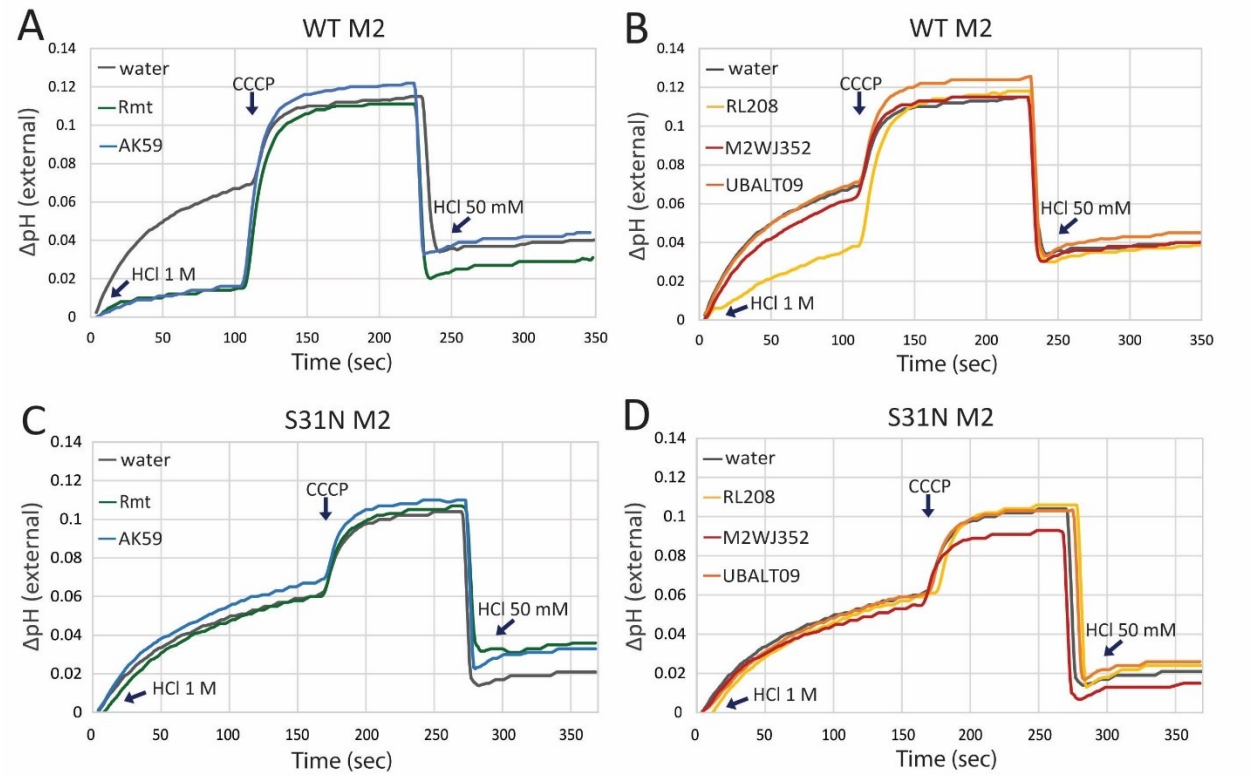

Figure 19 Liposomal proton flux assay applied to WT and S31N M2CD in the presence of five drugs (Rmt, AK59, RL208, M2WJ352, UBALT09). The 5-point moving average method was used to smoothen the data points of the curves. Time zero corresponds to the pH equilibration of the external solution at pH ~ 6.3 after the addition of 1 M HCl. M2CD activation and proton translocation into the liposome interior is shown as an increase of pH. Addition of the proton uncoupler CCCP terminates the experiment. The buffering capacity of the system is evaluated by adding 50 mM HCl. (A), (B) Proton conduction of WT M2CD is strongly inhibited by 50 µM of Rmt and its analog AK59 and partially blocked by RL208. The bulkier ligands M2WJ352 and UBALT09 did not show blocking of the proton channel in 50 µM final concentration. (C), (D) Proton conduction of S31N M2CD is not inhibited by any of the drugs tested. The time interval for measuring the proton conduction is extended in this case by 1 min.

4.2 Discussion

4.2.1 Suggested drug binding and blocking mechanisms of M2 pore

The tetrameric M2 channel was proposed to transport protons through the breaking and reforming of bonds between His37 residues in adjacent monomers. [61] Indeed, these interactions have been observed using M2CD at pH 7.8 [102,112] and M2FL at pH 6.2. [98] Additionally, MAS ssNMR suggested the presence of hydrogen bonding interactions between His37 and waters using M2(22-46) [250] or M2CD [98] or M2FL. [61,63,110] The M2-mediated proton transport is blocked by adamantyl amines and other conjugates by binding to the pore of M2. [73,114,116] Mechanistically, drug binding and blocking have been proposed to occur a) by drugs occluding the M2 pore and thus preventing the proton transport, [73,74] b) by acting as hydronium mimic that interacts with water layers inside the pore that stabilize transient hydronium ions formed during the proton conduction, [97,116] c) by disrupting the imidazole-imidazole hydrogen bond between His37 side chains. [102,112] It is also possible that multiple mechanistic aspects are needed to explain how amantadine (Amt), [70] rimantadine (Rmt), [72,104] and adamantyl amine analogs, [78,80,109,251,252] or other cage amine analogs, [76,108,253–255] inhibited the proton transportation of the WT or amantadine-resistant mutants of M2FL in oocytes. [87,105,108]

Structurally, it was shown that adamantyl amine inhibitors of M2(22-46) bind inside the WT M2 pore. [73,114] Their lipophilic part is accommodated from the side chains of the Val27 tetrad while their ammonium group is oriented towards the C-terminus. A network of stable waters, comprising two layers, connects the ammonium group of adamantyl amines and His37 residues. In the X-ray structures, the ammonium group of Amt, Rmt forms hydrogen bonds with the Ala30 water layer, while a more elongated spiranic adamantyl amine displaces the Ala30 water layer and forms hydrogen bonds with waters in the Gly34 layer. [97,104] To interpret the mechanism of blockage observed in EP [87,108] and liposomal proton flux assay [249] these adamantyl amines were considered as mechanism-based inhibitors. [97,104,116] Here it refers to the fact that their ammonium groups bind to water-lined sites of WT M2 which stabilize transient hydronium ions bound to His37 during proton conduction. This was proposed based on X-ray structures of truncated constructs [73,114] and multi-scale MD simulations [116] using a QM-based potential. Meanwhile, for longer constructs that include the amphipathic helix (M2CD or M2FL), structural and mechanistic evidence based on crystallography has remained less developed.

In this work, we explore further the potential mechanism of inhibition, using WT or S31N M2CD (residues 18-60) as our protein model. Although M2CD is a truncated protein, it was shown that its proton conductance is very similar to that observed for the M2FL reconstituted into liposomes. It is evident that the use of only one method is not enough to fully explore drug binding and blocking mechanisms of M2 due to limitations that can emerge from the use of different constructs (e.g. M2TM, M2CD, or M2FL), sample preparation (e.g. lipids, or lipid:drug:tetramer ratios), or experimental setup. For example, it was shown using MAS ssNMR that while Amt fully binds to WT M2TM (residues 22-46) and partially binds to M2CD (residues 21-61) in DMPC, it does not bind to M2CD in a virus-mimetic membrane, but after increasing the protein length to residues 21-97 Amt binding is rescued. [95,239] Every method we used in this work gives access to exploring different aspects of binding/blocking mechanisms. For example, using ssNMR we were able to explore what occurs to the important His37-His37 H-bond after drug-binding and confirmed that when binding takes place the bond gets disrupted. Using MD simulations, we were able to explore two blocking mechanisms; one involves stabilizing interactions between the drug and water molecules while the drug also interacts with important residues for protein function, and the other involves blocking by occluding the pore and not allowing water passage. We were able to see the drugs block the channel with one or both mechanisms. Liposomal proton flux assay, on the other hand, allowed us to use the same M2 construct and directly explore the outcome of such interactions, inhibition or not of proton conductance.

4.2.2 Monitoring drug binding to WT M2CD using MAS ssNMR

We previously showed that MAS ssNMR can detect the hydrogen bond between His37 side chains. [102,112] The His H-bonding was proposed before by Cross and coworkers [61] as a mechanism to tune the His37 pKa's. Rmt bound to WT M2CD disrupts this interaction. Whether the disruption is due to the drug inducing conformational changes of the protein or perturbation of water layers that interact with the histidines has not yet been clarified by ssNMR. In order to monitor this interaction, we recorded spectra of WT or S31N M2CD with and without the drug. When we tested the binding of cage alkyl amines Rmt, AK59, RL208 to WT M2CD at a low temperature of 4 °C, we did not observe significant CSPs of protein resonances; only small CSPs (<0.5 ppm) were observed in the ^{1}H and ^{15}N resonances of His37 side chain in the (H)NH spectrum. These CSPs suggested non-specific interactions between the protein and the compound. The small CSPs at 4 °C can be due to the ligand concentration inside the lipid bilayer [73] since it has been reported that adamantyl amines have slow entrance rates inside the WT M2(22-46) pore by EP

studies. [104,109] In addition, MAS ssNMR data of WT M2CD revealed slow entrance of Rmt [112] or are consistent with slow binding of Amt. [40]

Consequently, we increased the temperature of the samples to 55 °C (or 70 °C for S31N) to overcome high kinetic energy barriers for drug entry into the M2CD pore. Those were observed also previously in MAS ssNMR [102,112] where we estimated a high activation energy of ca. 122 ± 16 kJ mol^{-1} for pore binding by following binding kinetics using the ^{15}N His37 and Gly34 chemical shift changes at different temperatures. [112] The incubation at 55 °C resulted, for Rmt or AK59, in large CSPs in both ^{1}H and ^{15}N resonances (Figure 12F, G). These large CSPs suggested significant structural rearrangements of the protein, [90,95,102,239] upon pore-binding as previously reported for Amt in DMPC bilayers [95,239] and Rmt in DPhPC bilayers. [102,112] The His37-Nε2 proton resonances at 14.3 and 11.7 ppm, which are characteristic of the imidazole-imidazole hydrogen bonding, were not detected upon Rmt binding and were reduced by 80% in the case of AK59 suggesting that the protein is about 80% in the bound state. This is a striking example of how subtle differences in ligand's structure close to the amine group affect binding strength since AK59 differs from Rmt only by one methyl group attached in the methine linker (CHMe) between amine and adamantyl group. In contrast to Rmt and AK59, incubation at 55°C was not sufficient for detecting binding of RL208 to WT M2CD. According to the efficacy of RL208 in EP (Table S5), liposomal proton flux assay (Figure 19), and MD simulations, we expected to see the same evidence of a clear disruption of His37 imidazole-imidazole hydrogen bonding. However, we observed the same spectrum with apo WT M2 with His37 residues hydrogen bonded.

Therefore, we applied a pH-shift based protocol, as an alternative to high temperature, in order to access states with positive charge at His37 residues and thereby loosen the protein-protein interactions that may prevent fast drug binding. A similar procedure was previously applied to follow changes in ^{1}H spectra during the binding of a fluorinated adamantyl amine drug in M2(22-46) (M2TM) in DMPC liposomes. [242] M2CD at pH 3.5 adopts a C-open conformation, which may facilitate binding from the C-terminal side of the channel. Alternatively, the channel dynamics may be impacted by the loss of the stabilizing intermolecular hydrogen bond between histidine residues, allowing the drug to enter from either side. [102,112]

Although we used a protocol that enabled complete binding for Rmt and AK59 to WT M2CD, when we tested the binding of RL208 to WT M2CD we observed that it did not disrupt His37-His37 hydrogen

bonding at 300 μM and did not produce significant CSPs throughout the protein as we observed with the other WT blockers. The CSPs that were produced were very small and mainly in the amide region of (H)NH spectrum. We also tested RL208 at a higher concentration of 6 mM but still the His37-His37 hydrogen bond was not disrupted. However, it produced broadening in the amide region of the (H)NH spectrum and one distinct CSP, that of Trp41-NE1 side chain resonance (0.5 ppm in ^{1}H and 1 ppm in ^{15}N resonance). We have noted the sensitivity of this peak to changes in the lipid bilayer composition. [112] All those changes resemble what has been reported for Rmt as non-specific binding. [102,112] It is then possible that RL208 having a tetracyclic cage isomeric to adamantane and being bulkier than Amt or Rmt can less easily enter the WT M2CD channel. The results presented here show that a small increase in the size of the drug can affect its entrance and binding to M2CD. Another interesting point is that RL208 causes partial blocking of proton transport in the liposomal assay. As regards the discrepancy between the liposomal assay and ssNMR, showing partial vs no binding of RL208, respectively, we cannot rule out effects of slow drug binding kinetics due to different membrane composition. [112] The liposomal assay samples have a much higher lipid to protein ratio (400:1 by mass compared to 1:1 by mass used in ssNMR) and use an *E.Coli* lipid extract rather than single component lipids.

In the case of the bulkier molecules, M2WJ352 and UBALT09, which are not blockers of WT M2 channel according to EP or the liposomal proton flux assay, we observed consistently, that the NMR spectrum of the protein is unperturbed after the addition of the compound at 300 μM concentration (Figure 15, Figure S13). However, in the (H)NH spectrum of UBALT09 we observed doubling of the His37 side chain peaks, a small broadening of the amide region (Figure 15), as well as small CSPs ≤ 1.5 ppm in one of Trp41 side chains. To confirm that partial drug binding might have occurred, we tested a higher drug concentration of 6 mM. As a result, a significant peak broadening was observed in the (H)NH spectrum (Figure 15), similar to previous examples of WT M2CD drug binding (see for example Figure 13,14). ^{1}H and ^{15}N CSPs close to 1 ppm in the Trp41 side chain region were also present at a higher concentration, but in this case we observe ~ 70% loss of the His37-Nε2 side chain peak intensity. In the (H)CANH spectrum, the bound and unbound M2 form are evident at the higher drug concentration since we observed peaks of the apo M2 as well as large CSPs indicative of drug binding. We cannot rule out that other non-specific binding also occurred since a 20-fold higher drug concentration was used. Complementary to the NMR data, the MD simulations in Figure 6 show that, in contrast to Rmt, AK59, or RL208, the molecules UBALT09 or its similar analog M2WJ352 do not fit well between Val27 and His37 to block the WT M2 pore and allow waters to pass the Val27 secondary gate (see measures in Table 12, 13). In ref. [108] we showed also using MD

simulations and binding free energy calculations that analogs of M2WJ352 can bind, weakly to WT M2TM in the inward orientation, without blocking the channel (as evidenced by EP) (see Table S5). Consistently, we did not observe inhibition of the proton transport in the liposomal proton flux assay. Consequently, we can derive from these results that UBALT09 binds weakly to WT M2 but may or may not block the channel.

4.2.3 Blocking and Inhibition of S31N M2CD

The Amt - aryl conjugate molecules such as M2WJ352 and UBALT09 were developed to block S31N M2 after the pandemic S31N strains became prevalent since the adamantyl amines and cage alkyl amine analogs were ineffective. Indeed, Rmt, AK59, and RL208 did not block S31N M2 by EP (Table S5) or S31N M2CD in the liposomal proton flux assay (Figure 19). Additionally, we observed that all three drugs flipped from their initial docking poses (ammonium group oriented inward) by 180 degrees outward after being subjected to MD simulations. (Figure 18). In this orientation, the ammonium group forms tight hydrogen bonds with Asn31 side chains and backbone carbonyls while the adamantyl group is placed in a broad area defined by Gly34, as previously suggested by MAS ssNMR experiments and MD simulations. [80,247,248] In this orientation the drug does not appear to interact with the water molecules between Gly34 or Ala30 and His37 and thus would not be expected to alter the stabilization of hydronium ions. In addition, there are no stabilizing van der Waals contacts, and thus water molecules can pass through the channel.

Generally, the Amt - aryl conjugates selectively inhibit S31N M2 proton conductance [87–89,256] by occluding the M2 pore with their ammonium groups binding to Asn31 side chains and aryl group clustering with Val27 side chains. These results were evident using solution NMR spectroscopy applied in S31N M2(19-49), [86,89] ssNMR with S31N M2(22-46) [115] and MD simulations with S31N M2(19-49) or S31N M2(22-46). [86,89,108] Solution NMR studies of the S31N M2CD – M2WJ332 complex showed that Asn31 amide side chains can be oriented toward the space between TM helices.[257] Studies of apo S31N M2CD at pH 7 also showed that the Asn31 side chains are oriented in the interhelical space in an X–ray structure. [258] However, two conformations were observed in a later X–ray structure, one conformation with Asn31 side chains pointing between TM helices (open state) and a second conformation with the Asn31 side chains facing the pore (shut state). [259] Our 250 ns MD simulations of the complex between M2WJ352 or UBALT09 and S31N M2CD, using a starting structure with Asn31 side chains oriented to the interhelical space, led to a conformation of M2CD with a reorientation of Asn31 amide side chains toward the S31N M2 pore. The

ammonium group forms three hydrogen bonds with the Asn31 amide side chains and waters, and the aryl group is trapped between the Val27 side chains at the N-terminus, blocking water passage (Figure 18, see measures in Table 12, 13).

Interestingly, we observed that while M2WJ352 and UBALT09 were efficient blockers of S31N M2 by EP (Table S5), also confirmed by our MD simulation results, they did not block S31N M2CD in the liposomal proton flux assay. Similarly, there were no signs of binding in our NMR data. Neither of the drugs at 300 µM induced significant CSPs using the elevated temperature or pH-shift protocol, and the presence of His37 peaks indicated an intact H-bond interaction (Figure S14C). Of note, second generation adamantane-based drugs, e.g., M2WJ352 while tested with the small construct S31N M2TM, have not been tested against S31N M2CD using MAS ssNMR. We also tested the molecules at a higher drug concentration of 6 mM but the CSPs in ^{15}N or ^{13}C resonances in both 2D and 3D spectra were not more than 0.5 ppm which can again be attributed to non-specific effects due to higher partitioning of the drug to the membrane [95,260] as well as binding to the periphery of the protein [59,103] (Figure S17, S18). On the other hand, small CSPs (< 0.5 ppm) and broadening of peak linewidths have been previously observed in the drug bound form of S31N in ssNMR experiments, for example binding of M2WJ352 to S31N (residues 19-49) in different lipid membranes and a drug-tetramer molar ratio of 10:1, which should correspond to an estimated drug concentration of 1.2 mM.[115]

Thus, we can consider the possibility that the binding of M2WJ352 and UBALT09 to S31N M2CD can occur in a higher drug concentration, but the drugs do not perturb the His37 environment, as was also shown with MD simulations (Figure 18). Additionally, the same solution and solid-state NMR data of S31N M2 (19-49) – M2WJ352 complex, mentioned before, in DPC micelles [86,89] and DMPC or a virus mimetic m[115], showed that Asn31 has the largest ^{15}N, ^{13}C CSPs when the drug is bound to the M2 pore followed by His37 and Gly34, same way as Amt [73,95] or Rmt [114] to WT M2TM. In our MAS ssNMR experiments with S31N M2CD, we didn't observe significant CSPs on Asn31 with both drugs tested. It is worth noting that in previous studies on S31N M2 and inhibitors, S31N(19-49) or (22-46) structures are being used in which the amphipathic helices are missing. [86,89,115] It seems that AHs could generate a structural barrier for those drugs to enter the S31N M2CD pore i.e., induce conformational changes in M2 structure that hinder drug binding.

4.3 Methods and materials

4.3.1 Magic angle spinning solid state NMR spectroscopy

The M2 conductance domain (M2CD; residues 18 to 60) of influenza A was obtained and purified following methods described previously. [59,90,103,261] Briefly, the M2 amino acid sequence from the A/Udorn/1972 H3N2 strain, designated as wild type (WT), was utilized, incorporating C19S and C50S mutations. The S31N variant was generated from the WT sequence by introducing the corresponding mutation. ^{15}N and ^{13}C labeled M2 was expressed using U-^{13}C-glucose, and ^{15}N-ammonium chloride as the sole carbon and nitrogen sources, respectively. Escherichia coli was used to express the protein in inclusion bodies, which were then resuspended in 6 M guanidinium and subsequently purified using a nickel column. Cyanogen bromide was used to cleave the His-9 and TrpLE tags. Protein was then subjected to C4 HPLC column purification following a gradient elution using a mixture of 3:2 isopropanol:acetonitrile. The HPLC fractions were dialyzed against water and then lyophilized. The resulting lyophilized protein was resuspended in NMR buffer (40 mM sodium phosphate, 30 mM glutamate, 3 mM sodium azide, pH 7.8) containing octyl glucoside detergent and reconstituted in deuterated DPhPC lipids (FB Reagents) with a lipid:tetramer molar ratio of 25:1 by mol or 1:1 by mass. Finally, the samples were packed in a 1.3 mm rotor at room temperature using a benchtop centrifuge and had an estimated tetramer concentration of 12 mM. For the drug binding experiments a solution of 300 µM or 6 mM of drug was equilibrated with the membrane pellet from one rotor (2 to 3 µL) in a volume of 200 µL. This is sufficient total drug, since the estimated drug:tetramer molar ratio is 2.5:1 or 50:1 during incubation. The final concentration in the membrane pellet depends on the partitioning between the aqueous phase and the pellet. For the experiments where we changed temperature, the packing of the rotor with the sample was done at ambient temperature (~21 °C). After the first measurement, the rotor was kept for 2-5 h (unless otherwise indicated) in a 55° C water bath. Samples were stored at 4 °C and the temperature during NMR measurements was ~55 °C. For the drug binding measurements by changing the pH, the drugs were added by pushing the membrane pellet out of the rotor into a 300 µM (unless otherwise indicated) drug solution in citrate buffer of the desired pH (40 mM disodium phosphate, 22 mM citric acid, 3 mM sodium azide). Following overnight incubation at 4 °C, the pellet was moved to the same buffer, but at pH 7.8 for measurement.

All spectra were acquired on an 800 MHz Bruker Avance III spectrometer using a Bruker 1.3 mm HCN probe. The spinning frequency was 55 kHz and the gas flow was set to 900 liters per hour, the temperature

of cooling gas was set to 243 K, which results in an estimated sample temperature of 25 °C based on the chemical shift of water. The proton spectrum was referenced by setting the chemical shift of water to 4.7 ppm. 2D (H)NH spectra, were processed with a cosine squared function using 8 ms in the proton dimension, and 10 or 26 ms in the nitrogen dimension. Proton and ^{15}N hard pulse powers were 100 kHz and 80 kHz respectively. For ^{1}H to ^{15}N and ^{15}N to ^{1}H CP, the contact time was 800 µs and 550 µs, respectively, with a 20% linear ramp on ^{1}H and constant irradiation of ^{15}N at 38.5 kHz. 3D (H)CANH spectra were processed with a cosine squared function using 10 ms in the proton dimension, 15 ms in the nitrogen dimension, and 9 ms in the carbon dimension. Proton, ^{15}N and ^{13}C hard pulse powers were 100 kHz, 80 kHz, and 80 kHz, respectively. We set the H−Cα CP contact time to 600 µs with a 20% linear ramp on ^{1}H centered at about 95 kHz and 41.2 kHz on ^{13}C, a Cα-N CP with a contact time of 10 ms using 43.0 kHz and 19.6 kHz on ^{15}N and ^{13}C, respectively, and a 30% tangential ramp on the ^{15}N channel. The N−H CP had a contact time of 400 µs, a 20% linear ramp on ^{1}H centered at about 93 kHz and 38.5 kHz on ^{15}N. All spectra were acquired with frequency swept TPPM [262] ^{1}H decoupling at 12 kHz during indirect acquisition times and WALTZ-16 [263] decoupling at 10 kHz on both ^{13}C and ^{15}N channels. For water suppression, the MISSISSIPPI [264] method was used at 13 kHz. Spectra were processed in Topspin 3.5 (Bruker) and analyzed in Sparky. [265]

4.3.2 Computational biochemistry

Molecular docking calculations

Protein and ligands preparation for the docking calculations are included in the Supporting Information. The WT M2(22-62) structure with PDB ID 2L0J [63] from ssNMR in phospholipid bilayers was used to prepare the M2(18-60) tetrameric structure. Mutant S31N M2(18-60) protein complexes were obtained by manually mutating serine 31 to asparagine in PDB ID 2L0J [63] protein.M2(18-60) was superimposed to complex WT M2(22-46) - Amt, with PDB ID 2KQT, [73] to introduce ligand coordinates. Protein WT M2(18-60) and ligand Amt and its coordinates were used as reference coordinates for the docking calculations. Amt, R-Rim, S-Rim, AK59, RL208, and M2WJ352, UBALT09, were docked to the WT M2(18-60) protein, with GOLD 5.2 software (GOLD Suite, version 5.2; Cambridge Crystallogr. Data Cent. Cambridge, U.K., 2015) and the Gold Score. [266] For the docking calculations of the compounds, the waters clathrate between the ligands and His37 tetrad was maintained as part of the protein structure in agreement with the X-ray structures. [97] All the protein atoms within 10 Å of the reference ligand were used for binding site definition. For the docking calculations, 30 genetic algorithm runs were applied (instead of 10 runs as the

default choice), and the "allow early termination" option (which is also not the default choice) was chosen while all other options were kept as default. The resulting docking poses were visually inspected using the UCSF Chimera package. [267] Docking calculations in M2 constructs were also performed with Glide (Glide Schrödinger LLC, New York, NY, 2012. Glide, version 5.7. Glide Schrödinger LLC, New York, NY, 2011) using the scoring function Glide XP, [243] an empirical function that approximates ligand binding free energies, as well as the induced-fit method. As a measure of docking calculation accuracy, the experimentally determined coordinates of Amt in PDB ID 2KQT [73] were compared with the docking results. The root-mean-square deviation (RMSD) of the docked Amt compared to the X-ray position, with either GOLD 5.2 or Glide, was < 0.1 Å, which suggested that docking calculations would be accurate also for the other docked ligands. The generated complexes of M2(18-60) were used as starting structures for MD simulations.

MD simulations

The complexes between R-Rim, S-Rim, AK59, RL208, and M2WJ352, UBALT09 and M2CD from docking calculations were aligned with the membrane using the Orientations of Proteins in Membranes (OPM) Server. [205] The insertion of the OPM – protein complexes into the bilayer was performed with the Desmond System Builder utility of Maestro (Schrödinger Release 2021-2: Desmond Molecular Dynamics System, D. E. Shaw Research, New York, NY, 2021. Maestro-Desmond Interoperability Tools, Schrödinger, New York, NY, 2021-2). Protein–ligand complexes were inserted in pre-equilibrated hydrated bilayers of POPC lipids expanding from the furthermost vertex of the protein to the simulation box edge 13 Å in the *x,y*-plane and 17 Å in *z*-axis. The simulation box dimensions were (75 x 75 x 100 $Å^3$) and periodic boundary conditions were applied. For the M2CD systems, the system contained 130 – 140 lipids per tetramer. Sodium and chloride ions were randomly added in the aqueous phase to neutralize the system based on a Monte-Carlo approach, as implemented in Desmond. The NaCl concentration was chosen to be the physiological 150 mM. The CHARMM36m force field [244,246,268,269] was used for protein, lipid, and ions and the intermolecular interactions, and TIP3P for waters [206]. Ligands were parameterized with SwissParam [270] for the MD simulations. In the SwissParam force field, the dihedral angle terms, harmonic part of the bonds, angle and improper terms, and charges were taken from the MMFF94 [197] force field and van der Waals parameters from the closest atom type in the CHARMM22 [271] force field. For the MD simulations with the CHARMM36m force field, the CHARMM36 implementation of TIP3P waters was used. To assign CHARMM parameters, the Schrödinger viparr utility (Schrödinger Release 2021-2: Desmond Molecular Dynamics System, D. E. Shaw Research, New York, NY, 2021. Maestro-Desmond Interoperability Tools,

Schrödinger, New York, NY, 2021) was used. All simulations were performed with the Desmond MD simulation algorithm[272] (Schrödinger Release 2021-2: Desmond Molecular Dynamics System, D.E. Shaw Research, New York, NY, 2021. Maestro-Desmond Interoperability Tools, Schrödinger, New York, NY, 2021). The particle mesh Ewald method was used for the calculation of long-range electrostatic interactions [273] with a grid spacing of 0.8 Å. The Shake [213] method was used to keep all bonds with hydrogen rigid, at ideal lengths and angles. The Nose – Hoover thermostat [214] was utilized, and the Martyna – Tobias − Klein method [215] was used for pressure control. The equations of motion were integrated using the multistep RESPA integrator [216] with an inner time step of 2.0 fs for bonded interactions and nonbonded interactions within the cutoff. An outer time step of 6.0 fs was used for nonbonded interactions beyond the cutoff. Periodic boundary conditions were applied. For all MD simulations, the same relaxation protocol was used and run in a CPU. In short, two rounds of steepest descent minimization were performed: one with a maximum of 2000 steps and a harmonic restraint of 50 kcal mol^{-1} $Å^{-2}$ on all heavy solute atoms and a second of 10000 steps without restraints until convergence to 1.0 kcal mol^{-1} $Å^{-1}$. Next, a series of MD simulations were performed to smoothly relax the system; 200 ps starting at 10 K with gradual heating until 310 K in the NVT ensemble with solute heavy atoms restrained with a force constant of 50 kcal mol^{-1} $Å^{-2}$. A temperature of 310 K was used to ensure that the membrane state was above the melting temperature for POPC lipids [210]. The heating was followed by equilibration runs. First, a 1 ns simulation under NPT conditions was conducted, with solute heavy atoms restrained with a force constant of 10 kcal mol^{-1} $Å^{-2}$ to equilibrate solvents and lipids. This was followed by two 1 ns MD simulations with the NPT ensemble. Briefly, harmonic constraints were gradually decreased from 10.0 to 2.0 kcal mol^{-1} $Å^{-2}$ on solute heavy atoms while 2.0 kcal mol^{-1} $Å^{-2}$ constraints were retained on all other solute atoms. Next, the harmonic constraints were removed except for a 2.0 kcal mol^{-1} $Å^{-2}$ set on protein C_α atoms. Finally, a 5 ns unrestrained MD simulation in NPT conditions was performed before the production phase. This equilibration protocol was followed by 250 ns unrestrained MD simulations in the NPT ensemble with CHARMM36m force field. Within this simulation time, the RMSD of the protein backbone C_α atoms of the TM domain (RMSD(Cα)) reached a plateau and the system was considered equilibrated and suitable for statistical analysis. The coordinates of the systems were saved every 100 ps. MD simulations were performed in workstations with GPUs using the GPU implementation algorithm of the MD simulation code provided by Desmond software, (Schrödinger Release 2021-1: Desmond Molecular Dynamics System, D. E. Shaw Research, New York, NY, 2021. Maestro-Desmond Interoperability Tools, Schrödinger, New York, NY, 2021). In total, MD simulations for 12 different systems were performed (6 ligands x 2 proteins).

4.3.3 Liposomal proton flux assay

This assay was performed as described previously. [249] Briefly, M2CD proton channels were reconstituted in a glass tube into liposomes by mixing 25 µg of protein, 750 µL of *Escherichia coli* polar lipid extract (Avanti Polar Lipids) in chloroform (~10 mg of lipids), 5 µL of 0.04 mM valinomycin solution in ethanol and 350 µL of methanol for homogenized mixing that provided a solution. The solvents were evaporated under continuous nitrogen gas and a thin film was obtained. The films were redissolved in 750 µL of chloroform and dried down again under a nitrogen stream in order to form high quality transparent lipid films and were left overnight in the lyophilizer to remove any solvent trace. The dried films were then resuspended in strongly buffered internal liposome buffer (26 mM potassium citrate, 17 mM citric acid, 28 mM sodium citrate, 25 mM K_2HPO_4, 25 mM Na_2HPO_4, 6 mM NaN_3; pH 7.7) to form liposomes which were then extruded 11 times through 0.2 M polycarbonate membrane to get a homogenized size distribution. Buffer was exchanged on a PD-10 column (GE Health Sciences) such that the external liposome buffer was a weak buffer (4% v/v IVB, 117 mM KCl, 117 mM NaCl, 6 mM NaN_3, pH 7.7). Every tested sample contained 2.25 mL of liposome mixture which consists of 5 mg/mL lipids, 0.6 µM M2 tetramer, and 0.1 µM valinomycin as a potassium ionophore that transports potassium ions in the opposite direction of protons. The initial decrease of external pH was initiated by the addition of 3.75 µL of 1M HCl under continuous fast stirring. The experiment was terminated by the addition of 3 µL of the proton uncoupler carbonyl cyanide m-chlorophenylhydrazone (CCCP). The buffering capacity of the final mixture was evaluated by the addition of 7.5 µL of 50 mM HCl. M2 drug inhibition was investigated by adding 2.25 µL of 5 mM stocks in water (or ethanol in the case of M2WJ352) for 50 µM concentration in the final tested samples. The drugs were added 1 hour before the first HCl addition. Addition of 2.25 µL of water or ethanol was tested as separate experiment controls and no change in M2 proton conduction was observed.

5 Conclusions

5.1 SQ109 analogs as potent inhibitors of MmpL3 transporter

In this work, we report an improved synthesis of analogs of the antitubercular drug candidate SQ109 (**8a**), an ethylenediamine-based inhibitor of MmpL3 currently undergoing clinical trials that also has activity against a broad range of bacteria, protozoa, and even some yeasts/fungi. We synthesized a series of 18 SQ109 (**8a**) analogs containing adamantane C-2 alkyl, aryl, or heteroaryl adamantyl groups (Me, Et, Pr, Bu, Ph, Bn, Hex, and 4-phenylthiazol-2-yl), with ethylenediamine or aminoamide linkers between the adamantyl and geranyl groups, in addition to an adamantyl C-1 dimethylmethylene analog. We report inconsistencies and improvements for more efficient preparation of important intermediates such as geranylamine **4** and the reduction of aminoamides leading to SQ109 and its analogs.

The MD simulations data that we produced based on the X-ray structure of the SQ109 (**8a**) and MmpL3 complex (PDB ID 6AJG) showed that our designed SQ109 analogs **8b-i, 12** bind to the same binding area with SQ109 (**8a**). Compared to SQ109 (**8a**), in the analogs with larger alkyl or aryl adducts in the adamantane ring, the geranyl-ethylenediamine moiety was similarly surrounded by the amino acid residues Leu642, Tyr646, Tyr257. However, the larger adducts at 2-adamantyl carbon can fit close to Phe260 and Phe649 increasing the hydrophobic interactions at the bottom of the binding area.

We tested SQ109 (**8a**) and the analogs against five bacteria: *M. smegmatis*, *M. tuberculosis* (three strains), *M. abscessus* (two strains), *B. subtilis*, and *E. coli*, as well as against five protozoa: *T. brucei*, *T. cruzi* (epimastigotes and amastigotes), *L. donovani*, *L. mexicana*, and *P. falciparum* (asexual blood stages). There was good activity of ethylenediamine analogs containing small substituents against the mycobacteria, although activity was generally less than with the SQ109 parent molecule. The interesting exception was in *M. abscessus* where we found two SQ109 analogs, the butyl (**8e**) and benzyl (**8g**) species, in which activity was ∼4−8-fold higher than found with SQ109 (**8a**). Moreover, activity was the same against a highly drug resistant M*. abscessus* strain harboring an A309P mutation located in the transmembrane domain in MmpL3, indicating that MmpL3 is not a major target in this species.

We then used SPR to investigate the binding of SQ109, nine ethylenediamine analogs, and four amide analogs to a mycobacterial MmpL3 protein target, finding that tighter MmpL3 binding correlated with

increasing ligand hydrophobicity with $R = 0.73$ and $p < 0.003$ for the log K_D/log $D_{7.4}$ correlation. However, there were no significant correlations between cell growth inhibition and either log D or log K_D. The low activity of the more potent MmpL3 binders against MmpL3-containing bacteria suggests that MmpL3 inhibitors with large C-2 substituents may not be able to penetrate the cell wall.

Using DSC, we found that these inhibitors caused larger decreases in *T*m than found with SQ109 (**8a**), indicating efficient accumulation in lipid membranes, and there were clear correlations between ΔT_m and log $D_{7.4}$ for both DMPC ($R = 0.776$, $p = 0.014$) as well as for DSPG ($R = 0.727$, $p = 0.026$). Taken together, the SPR and DSC results are consistent with the idea that the larger, more potent MmpL3 inhibitors are less effective than SQ109 (**8a**) in penetrating the arabinogalactan−peptidoglycan cell wall in mycobacteria. In contrast, in *B. subtilis* and *E. coli*, several analogs were more potent than SQ109 (**8a**). In these organisms, MmpL3 is absent as is the mycolyl−arabinogalactan−peptidoglycan cell wall, although the mechanism of action of SQ109 (**8a**) itself in these bacteria remains to be reported. On the other hand, in the trypanosomatid parasites, SQ109 (**8a**) is reported to act as a protonophore uncoupler that also affects Ca^{2+} homeostasis. In these organisms, there is again no cell wall, and many of the analogs are active against the parasites. With the malaria parasite *P. falciparum*, there are likewise no cell wall and no MmpL3 and SQ109, and analog activity could similarly be dependent on their protonophore properties. We found that several analogs had 4−10× increased activity over SQ109 as well as low toxicity against the HepG2 human cell line, making them of interest as a new antimalarial drug hit and warranting further development of these bulkier analogs as antimalarial drug leads.

5.2 Binding and blocking of M2 protein inhibitors to M2CD pore

In this work, we use a set of methods to further explore our previous ssNMR findings and investigate how different biophysical methods, used regularly, can inform on the binding and blockage of WT or S31N M2 by cage alkyl amine containing inhibitors. We applied MAS ssNMR complemented with MD simulations to assess the potential blocking mechanism for both WT and S31N M2, while liposomal proton flux assay was performed along with the previous EP measurements to test the ability of the compounds to inhibit the M2-mediated proton conductance. We developed two protocols for the MAS ssNMR sample conditions that could overcome high kinetic energy barriers associated with drug entry into the M2CD pore.

We showed that low pH can be used to more reliably allow equilibration with drugs, presumably by opening of the tetramer at the C-terminal side of the membrane upon imidazole protonation, with NMR data subsequently recorded at alkaline pH in the closed M2 conformation. We found that a small increase in drug size can dramatically affect the kinetics of binding to M2CD pore, in contrast to M2TM, emphasizing the conformational constraints posed by the AHs. Disruption of the imidazole-imidazole hydrogen bonding was a clear indicator for drugs that block WT M2-mediated conductance. On the other hand, lack of disruption was observed for S31N M2CD for drugs reported to be active. This does not appear to be an effect caused by concentrated samples, as the more dilute conditions of the liposome assay showed no evidence of blocking. It will be important to compare these results with testing of full length M2 in the future and using NMR methods that include isotopically labeled drugs.

6 APPENDIX A

Table S1 Binding affinities from SPR against MtMmpL3 and biological activities against *Ms* and *Mtb* HN878 using the two-states model taken from ref. [158]

Comp. No	Chemical Structure	K_d (µM)	IC_{50} (µM) *Ms*	IC_{50} (µM) [158] *Mtb* HN878
8a	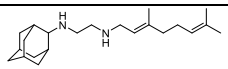	2060 ± 34.5	2.4	0.4
8b	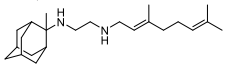	248 ± 9.52	4.4	0.8
8c	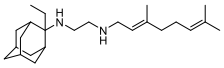	190 ± 7.57	4.0	1.6
12	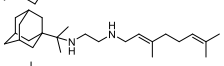	120 ± 15	15	3
8d	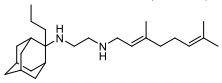	106 ± 12.2	4.3	3
8e	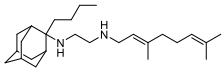	108 ± 12.2	2.5	3
8f	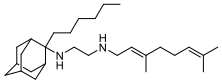	81 ± 38.9	4.7	3
8g	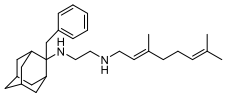	74 ± 30.3	6.0	1.6
8h	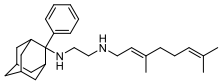	136 ± 29.5	5.8	1.6
8i	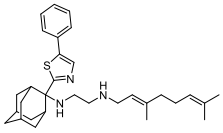	91 ± 31.1	21	ND [a]

[a] ND, not determined; [b] The Kd values are determined by global fitting of sensorgrams collected at different concentrations of an analyte to the same set of parameters. Residuals are the measure of goodness of the fit.

Table S2 Ligand-MmpL3 binding free energies (ΔG_{eff}) calculated using MM-GBSA [150,274] method with OPLS2005 [275] force field for the calculations of the intermolecular interactions without or with using a hydrophobic slab [154,155] to model the membrane environment of the protein. $RMSD_{lig}$ mean values and $RMSD_{prot}$ mean values for the whole protein or only transmembrane helices from 80ns-MD simulations for 8a-h, 12. The ligands have a diprotonated ethylenediamine unit.

Cmp No	**$RMSD_{lig}$** [a] (Å)	**$RMSD_{prot}$** [b] (Å)	**ΔG_{eff}** [c] (kcal mol^{-1})	**ΔG_{eff}** [d] (kcal mol^{-1})	Conformation of the ethylenediamine unit of the ligand in the starting conformation [e]	Conformation of the ethylenediamine unit of the ligand in the last snapshot in the MD simulation
8a	1.72 ± 0.12	2.96 ± 0.12	-192.19 ± 8.27	-78.74 ± 4.61	g(-)	g(-),g(+),g(+)
8b	1.18 ± 0.11	3.40 ± 0.35	-174.66 ± 6.46	-73.06 ± 3.95	g(-)	g(-),g(-),g(-)
8c	2.12 ± 0.19	3.11 ± 0.10	-170.74 ± 8.57	-68.30 ± 5.54	g(+)	g(+)g(-),g(+),g(+)
8d	1.93 ± 0.14	2.75 ± 0.13	-185.80 ± 7.25	-93.05 ± 4.62	anti	g(+),g(+),g(+)
8e	2.09 ± 0.09	2.60 ± 0.10	-195.04 ± 8.55	-84.65 ± 4.73	anti	g(-),g(-),g(-)
8f	2.15 ± 0.25	4.13 ± 0.20	-190.04 ± 9.02	-80.18 ± 5.69	eclipsed	g(+),g(+),g(+)
8g	2.13 ± 0.10	2.70 ± 0.13	-190.79 ± 11.7	-85.88 ± 7.03	g(+)	g(+),g(-),g(-)
8h	2.21 ± 0.12	3.84 ± 0.20	-173.45 ± 7.48	-81.60 ± 4.55	g(+)	g(+),g(-),g(-)
12	1.37 ± 0.15	3.31 ± 0.12	-184.31 ± 7.83	-80.43 ± 7.21	g(-)	g(-),g(-),g(+)

[a] Mean±SD (Å); Ligand RMSD is calculated after superposition of each protein-ligand complex to that of the starting structure (snapshot 0) based on the C_α atoms of the protein, for the last 20 ns of the trajectories.

[b] Mean±SD (Å); Protein RMSD is calculated for the C_α atoms of the α-helices, for the last 20 ns of the trajectories, using as starting structure snapshot 0 of the production MD simulation.

[c] Mean calculated effective binding free energy (kcal mol^{-1}) between ligand and MmpL3 receptor from three repeats. ΔG_{eff} is calculated from the last 20 ns of the trajectories using 40 ps intervals (i.e. 500 frames per trajectory) using a MM-GBSA model that is taking into account the membrane as hydrophobic slab. [153–155]

[d] Mean calculated effective binding free energy (kcal mol^{-1}) between ligand and MmpL3 receptor from three repeats. ΔG_{eff} is calculated from the last 20 ns of the trajectories using 40 ps intervals (i.e. 500 frames per trajectory) without taking into account the membrane. Using the last frame of the MD simulation trajectory, two additional 20 ns MD simulations were performed and structural ensembles were similarly selected.

[e] Highest scored docking pose.

100ns MD simulations plots of the single protonated SQ109 analogs in complex with MmpL3

Figure S1. Molecular dynamics results for complexes of monoprotonated SQ109 analogs with MmpL3. In panels (A) for **8a-i**, **12** are shown the chemical structures of the ligands and the RMSD plots for the Ca carbons (blue) for the full protein (upper RMSD plots) and the ligand heavy atoms (orange) or (B) only the RMSD plots for the Ca carbons (blue) of transmembrane helices and the ligand heavy atoms (orange). (C) Last frames of monoprotonated SQ109 analogs **8b** (Me), **12**, **8d** (Pr), **8f** (Hex), **8g** (Bn), **8c** (Et) inside the MmpL3 pore from 100ns-MD simulations with amberff99sb; [276,277]. **(D)** Receptor-ligand interaction frequency histograms; (C), (D) for SQ109 or **8a** (H), **8e** (Bu), **8h** (Ph), **8i** (Thz-Ph) are shown in the main manuscript. Color scheme for frames: Ligand=petrol or purple or orange or green or blue sticks, receptor = white ribbons, residues in light purple sticks, hydrogen bonding interactions=dark grey dashes. For the protein, the experimental structure of SQ109 in complex with MmpL3 (PDB ID 6AJG [22]) was used. The protein structure (excluding C-terminus) consists of M1-E749 residues. The transmembrane domain consists of the following helices and their residues: TM1: 14-33, TM2: 174-199, TM3: 208-224, TM4: 238-264, TM5: 271-301, TM6:306-338, TM7:396-415, TM8: 552-576, TM9: 583-601, TM10: 625-648, TM11: 660-690, TM12: 697-728.

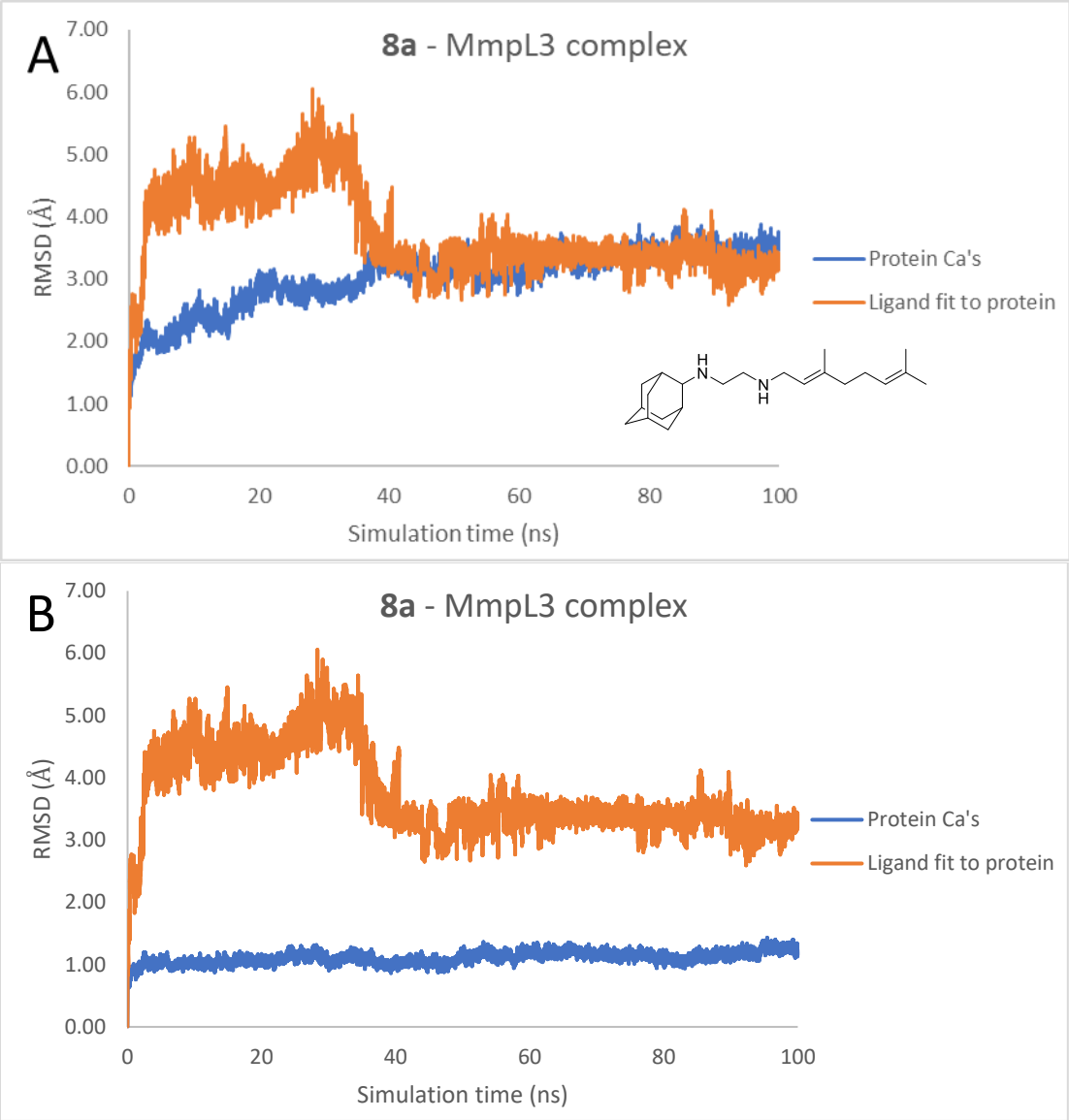

Figure S1 MD simulation results for MmpL3 with SQ109 (**8a**).

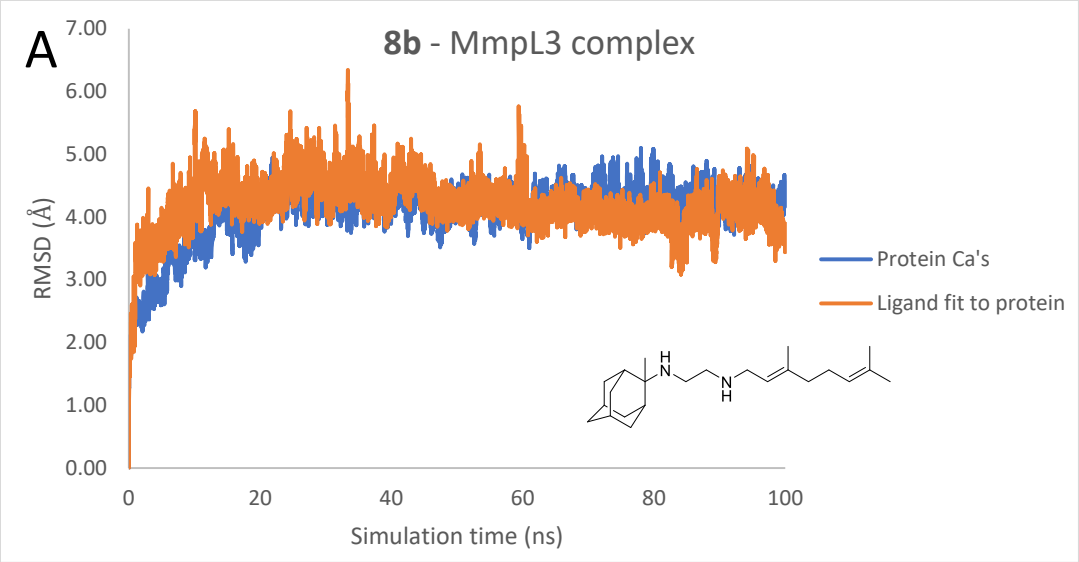

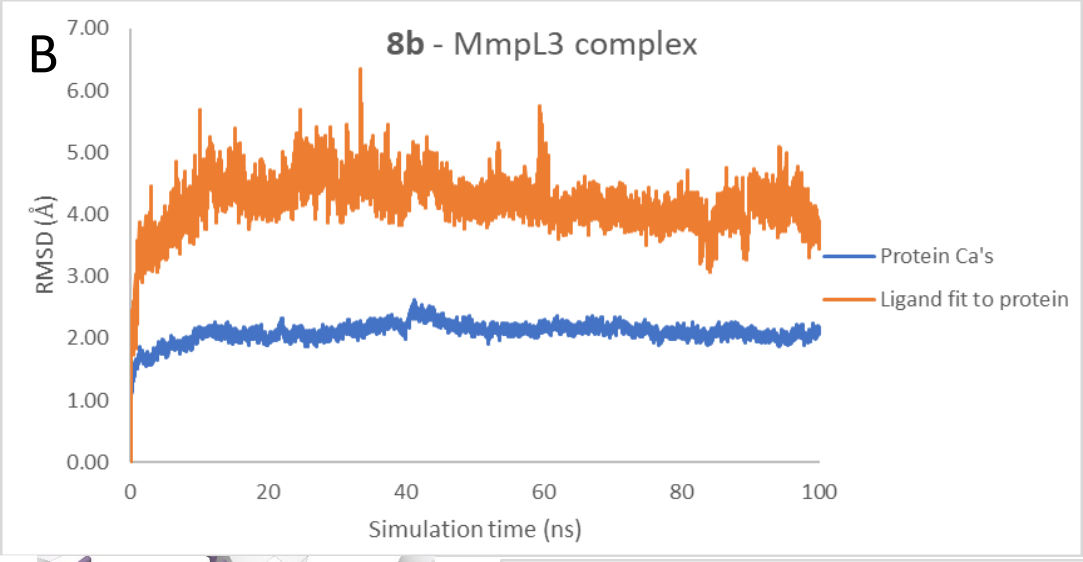

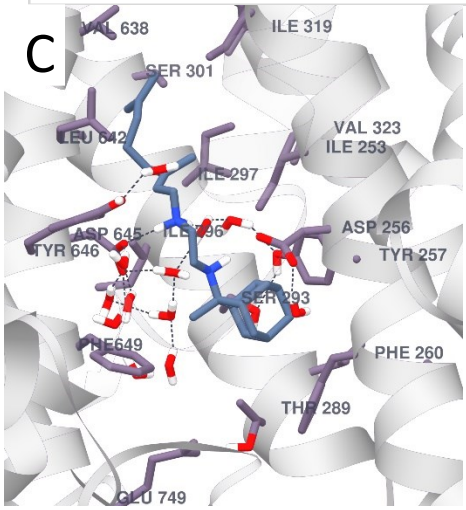

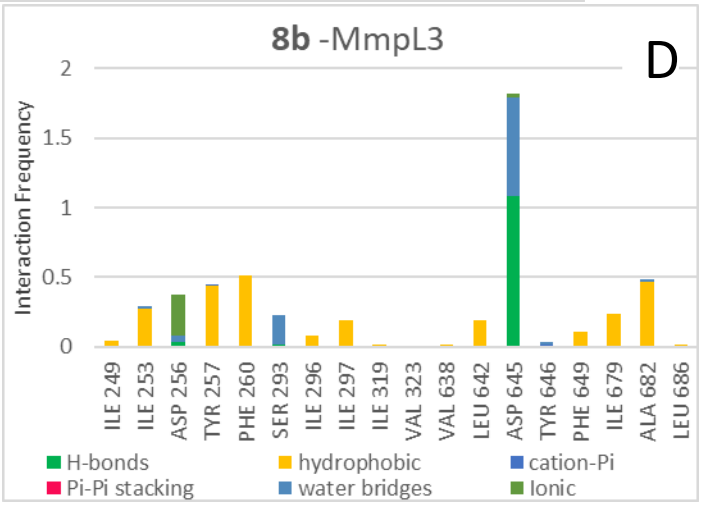

Figure S1 (contd.). MD simulation results for MmpL3 with **8b**.

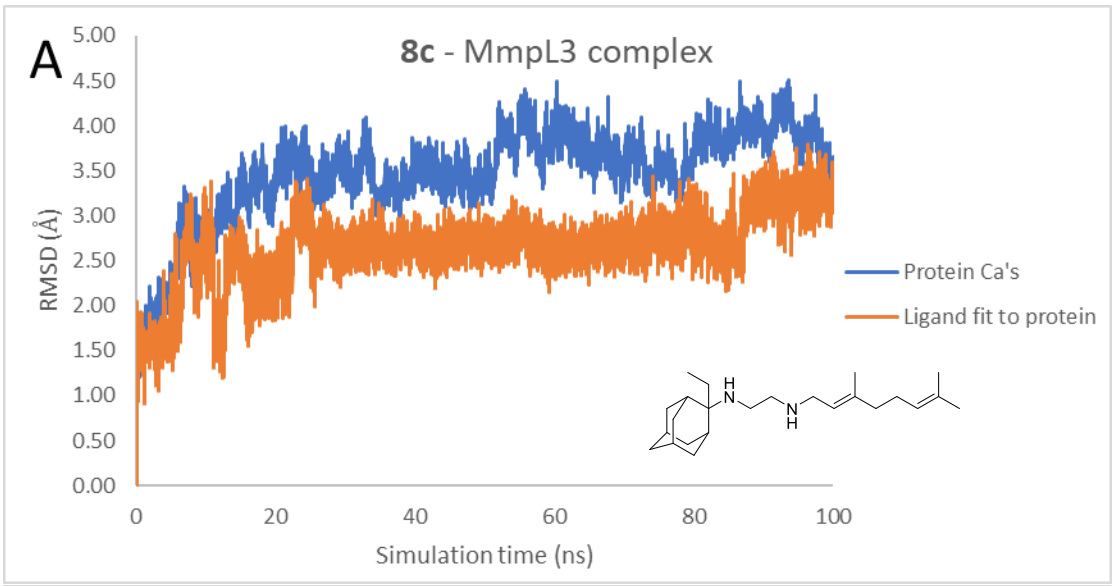

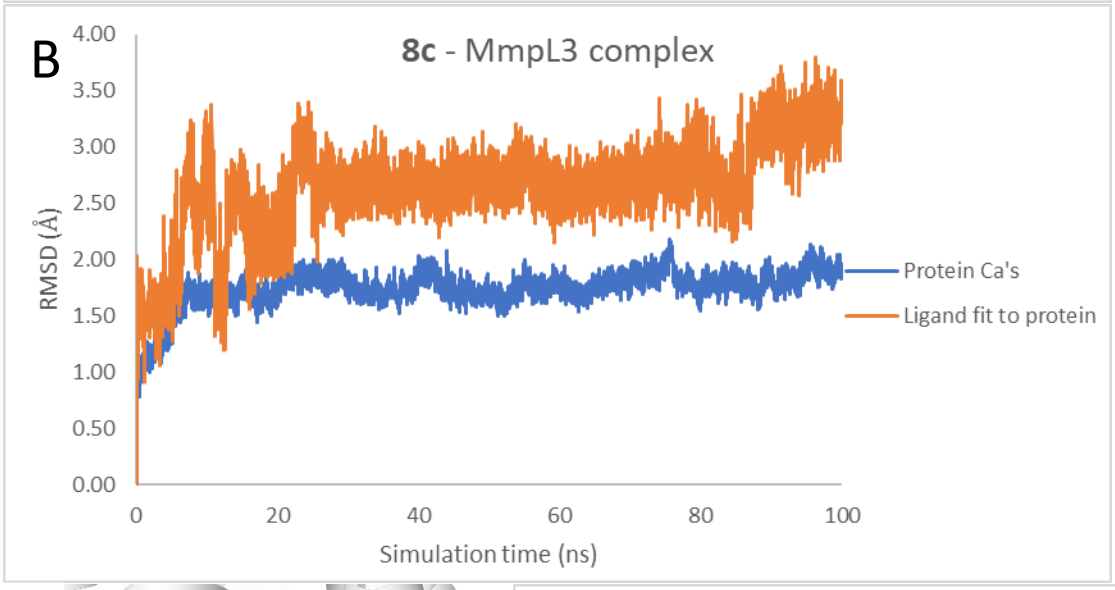

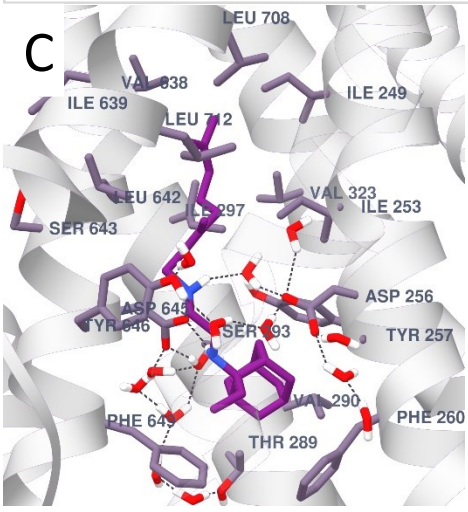

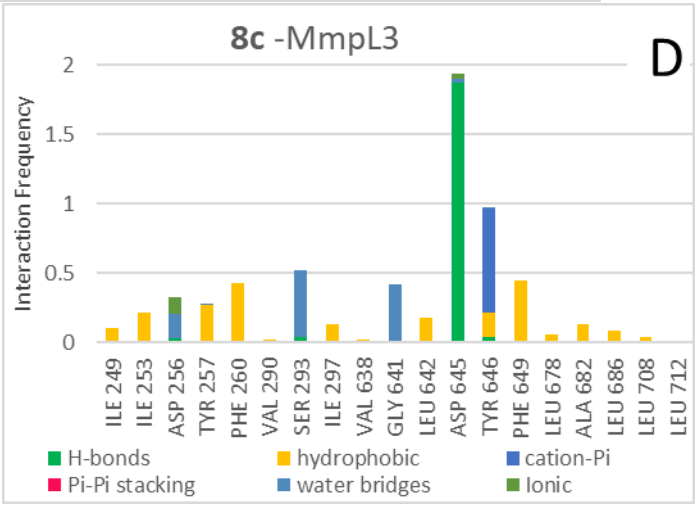

Figure S1 (contd.). MD simulation results for MmpL3 with **8c**.

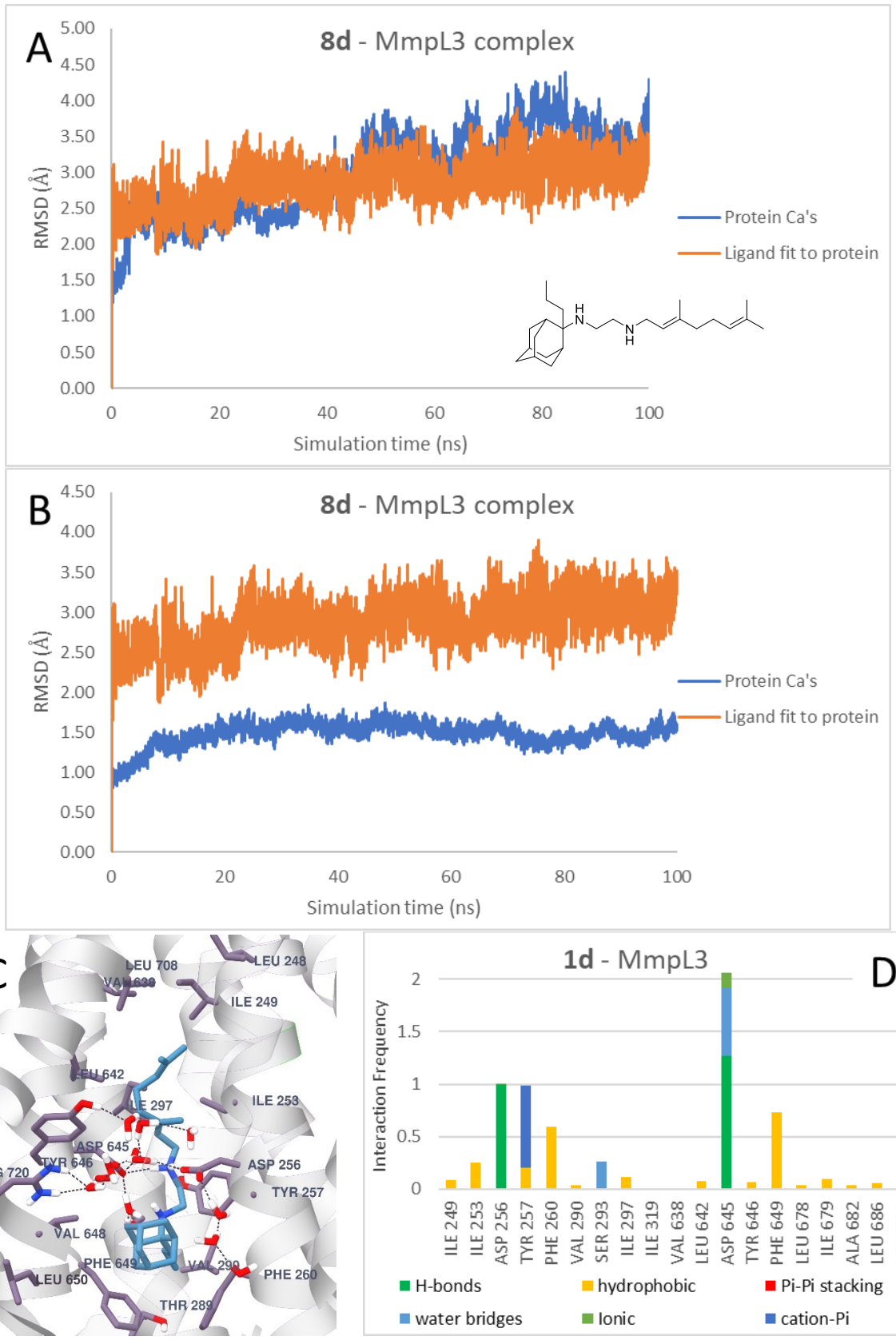

Figure S1 (contd.). MD simulation results for MmpL3 with **8d**.

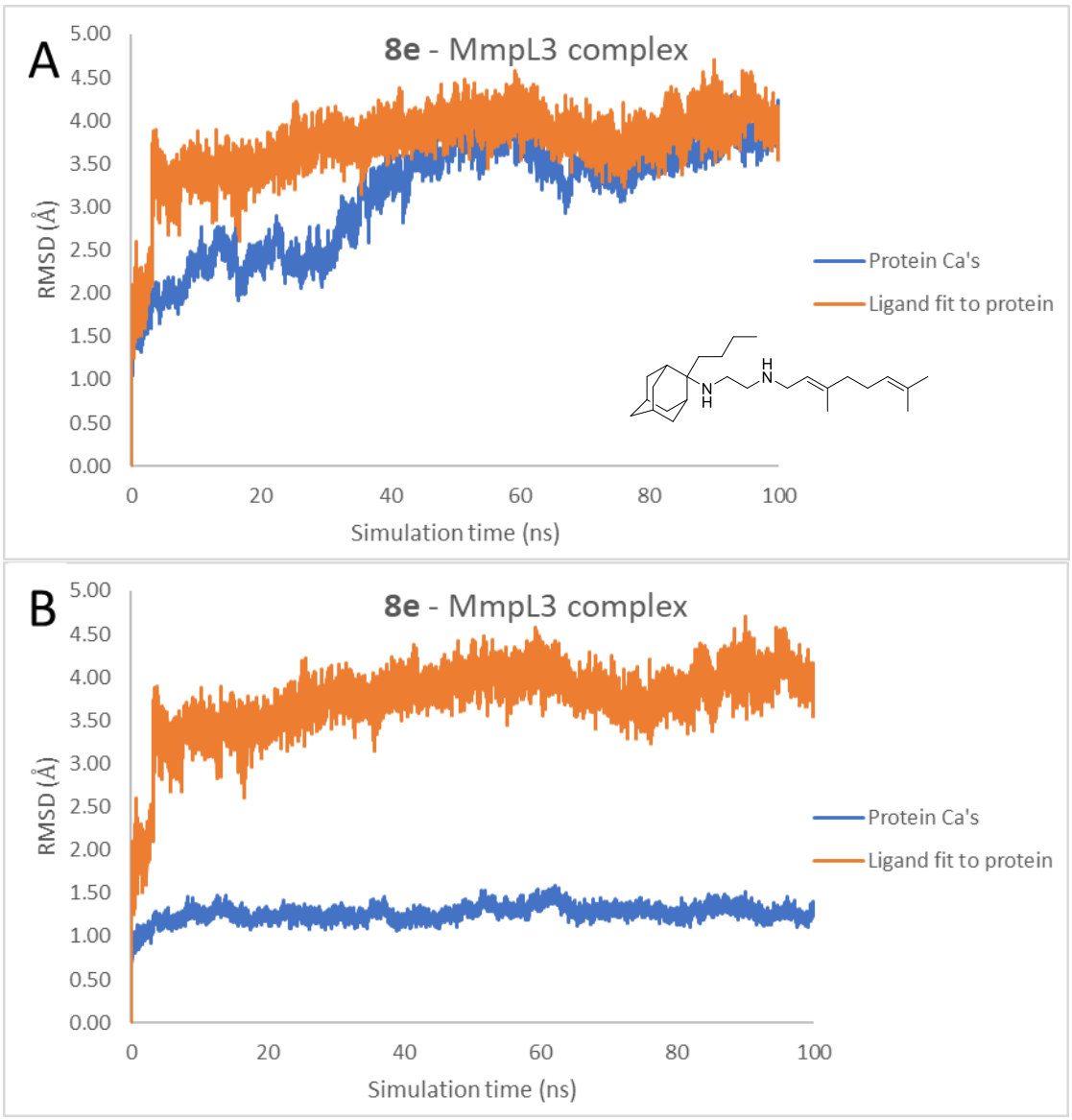

Figure S1 (contd.). MD simulation results for MmpL3 with **8e**.

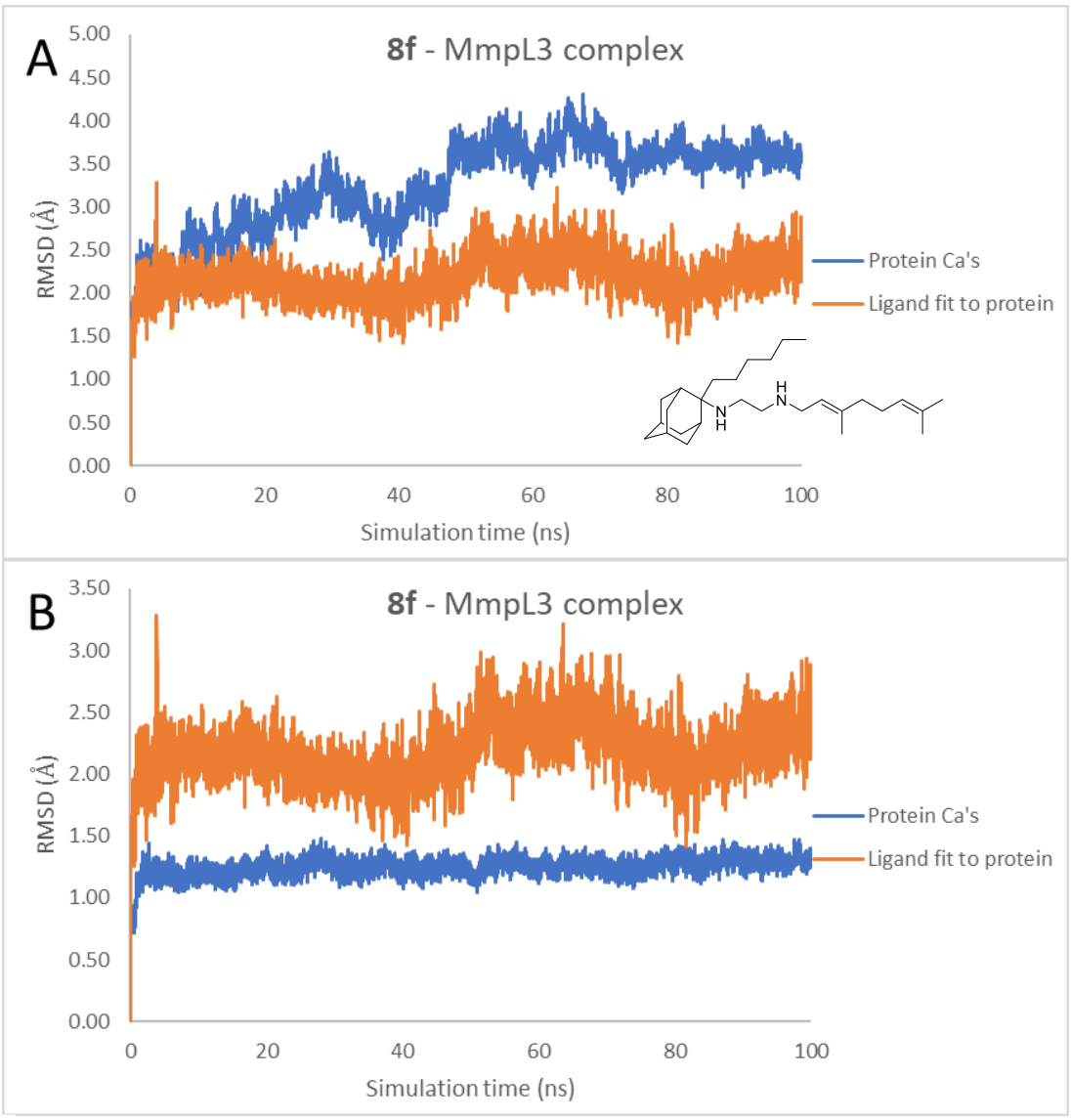

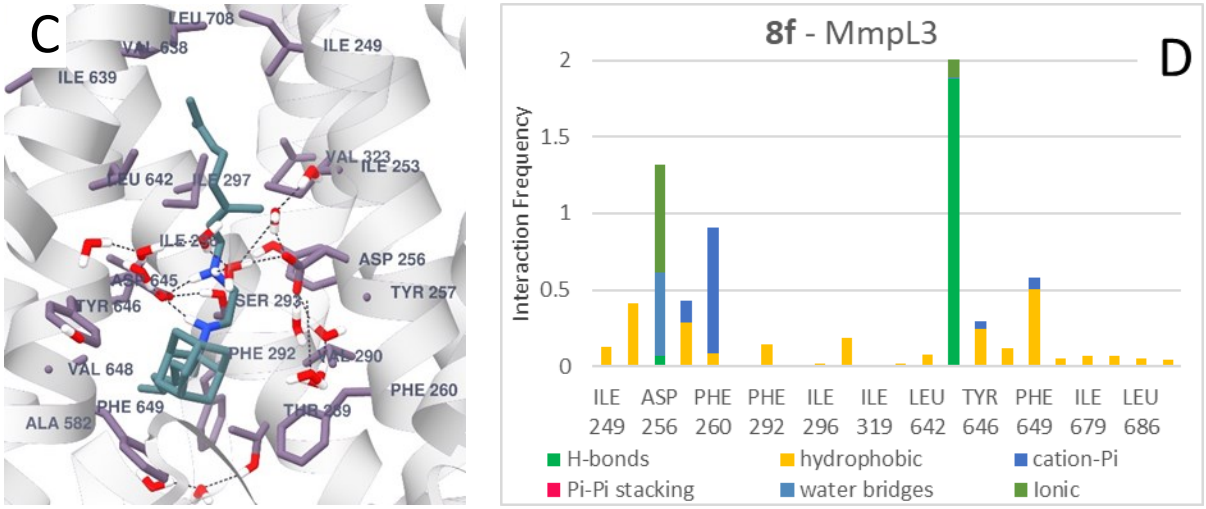

Figure S1 (contd.). MD simulation results for MmpL3 with **8f**.

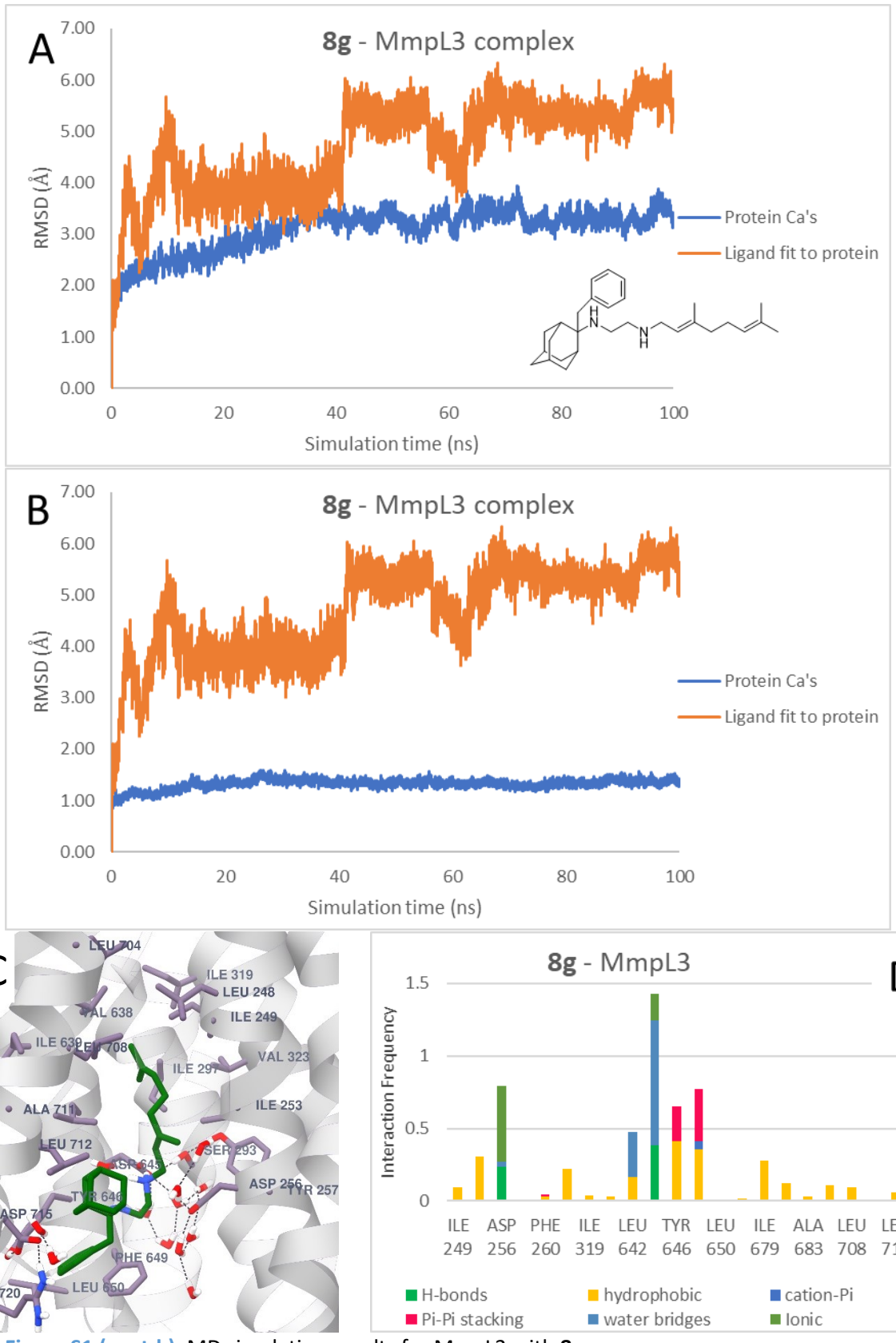

Figure S1 (contd.). MD simulation results for MmpL3 with **8g**.

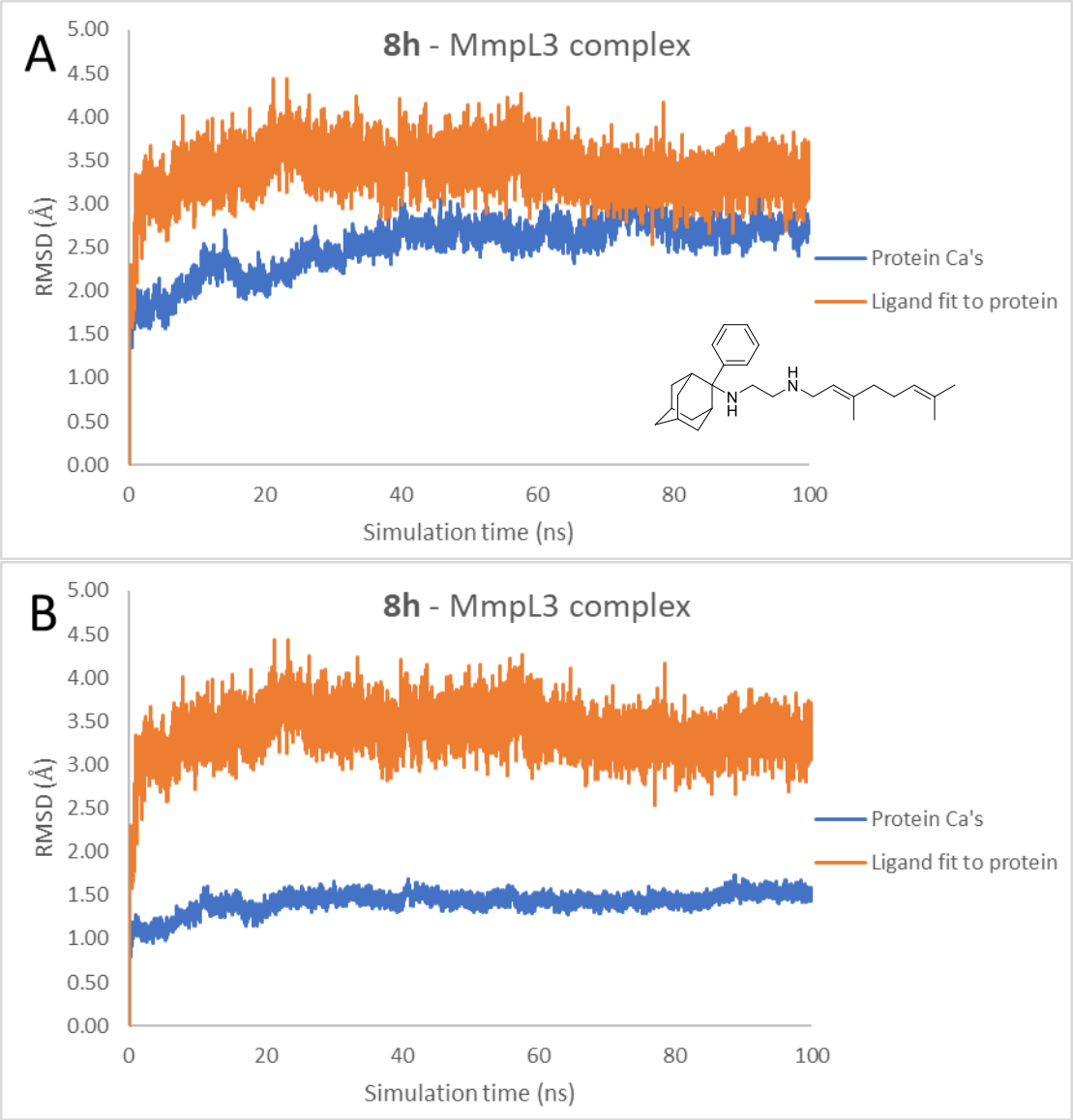

Figure S1 (contd.). MD simulation results for MmpL3 with **8h**.

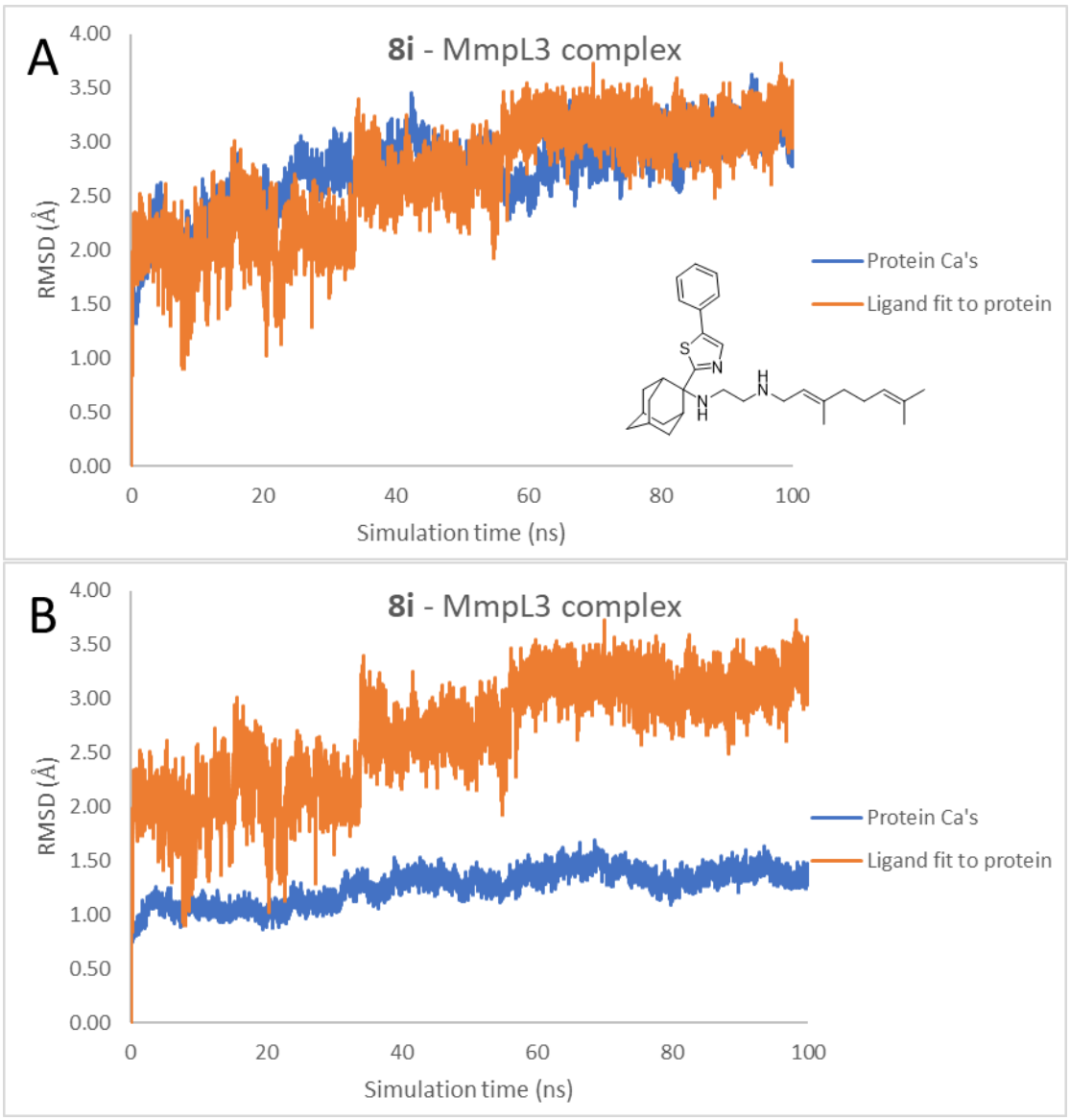

Figure S1 (contd.). MD simulation results for MmpL3 with **8i**.

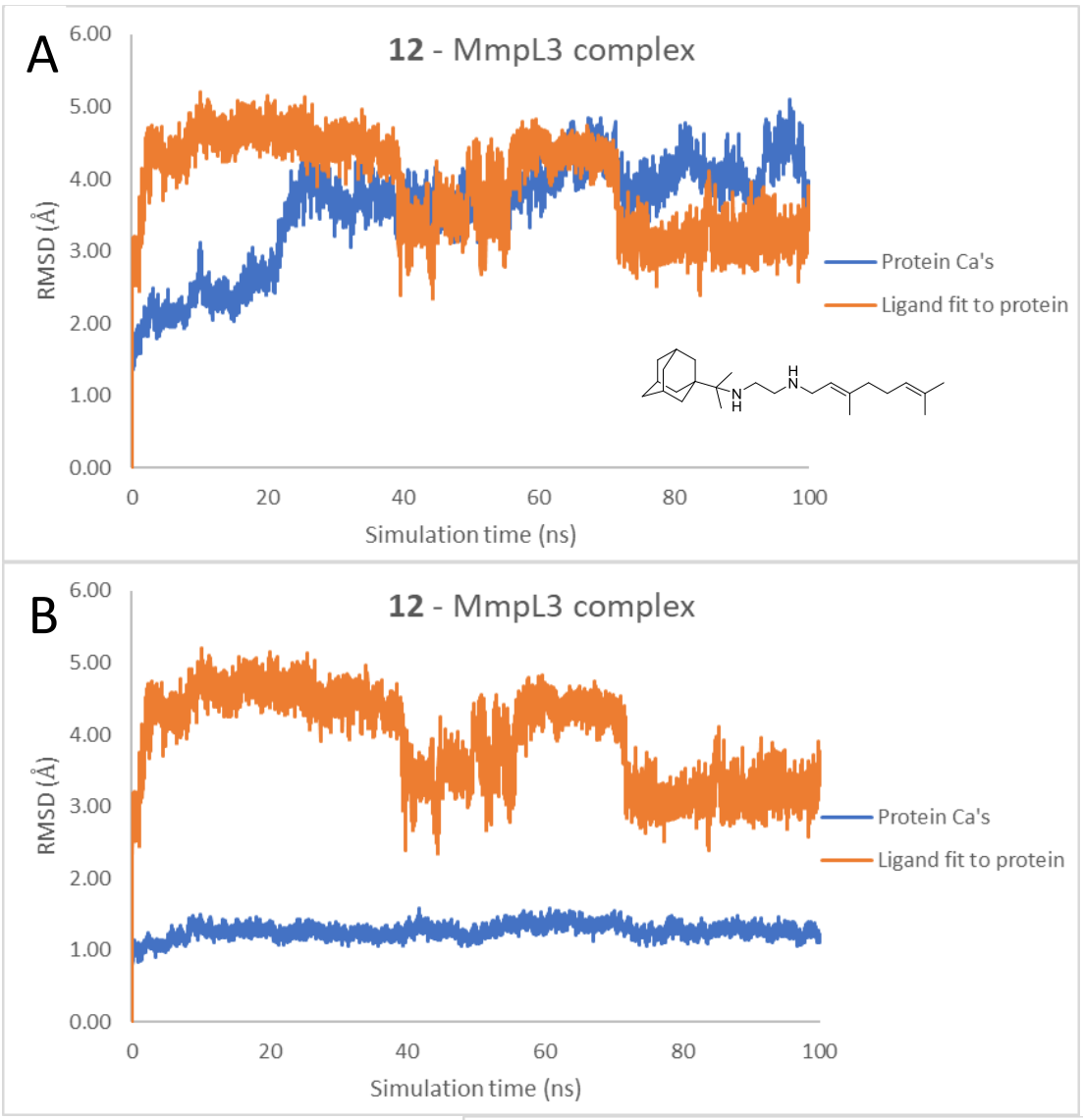

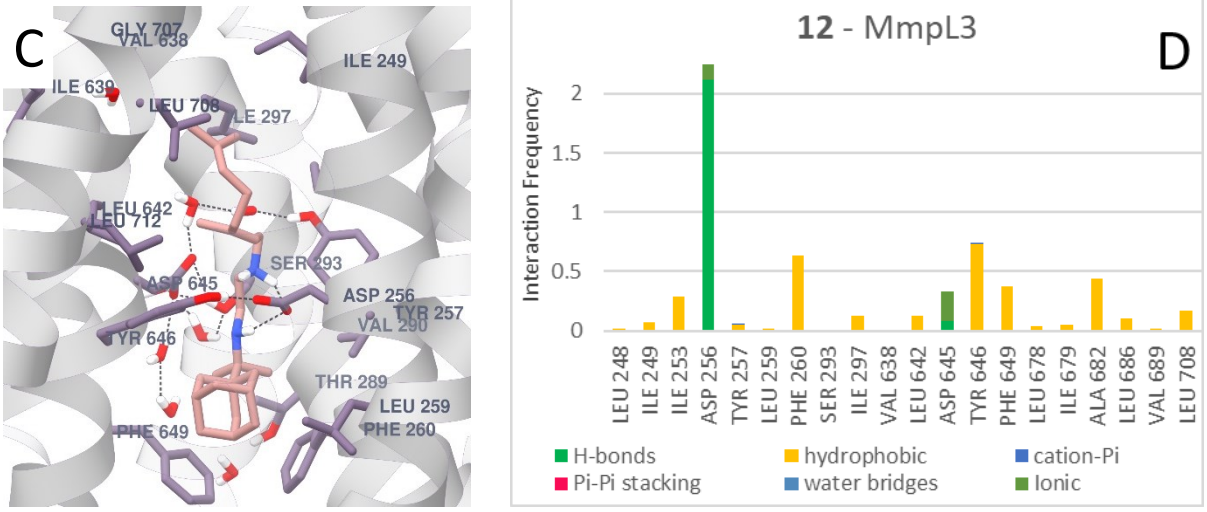

Figure S1 (contd.). MD simulation results for MmpL3 with **12**.

80 ns MD simulations plots of the doubly protonated SQ109 analogs in complex with MmpL3

Figure S2. In panels (A) for **8a-h** are shown the chemical structures of the ligands and the receptor-ligand interaction frequency histograms recorded from the 80 ns MD simulation trajectories of SQ109 analogues (doubly protonated ethylenediamine form) in complex with MmpL3. Hydrogen bonding interaction bar are depicted in green, Van der Waals in yellow, cation-pi in blue, pi-pi stacking in pink, water bridges in light blue and ionic in light green. (B) The RMSD plots for the Ca carbons (blue) of the full protein and the ligand heavy atoms (orange). For the protein, the experimental structure of SQ109 in complex with MmpL3 (PDB ID 6AJG) was used. The protein structure (excluding C-terminus) consists of M1-E749 residues. The transmembrane domain consists of the following helices and their residues: TM1: 14-33, TM2: 174-199, TM3: 208-224, TM4: 238-264, TM5: 271-301, TM6:306-338, TM7:396-415, TM8: 552-576, TM9: 583-601, TM10: 625-648, TM11: 660-690, TM12: 697-728.

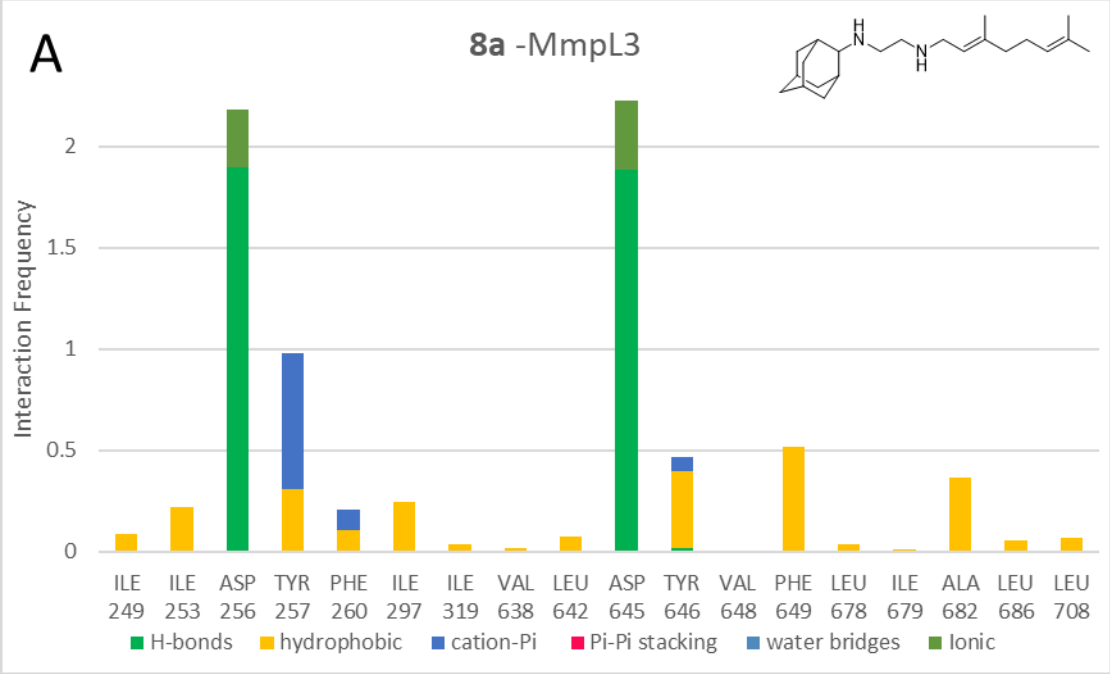

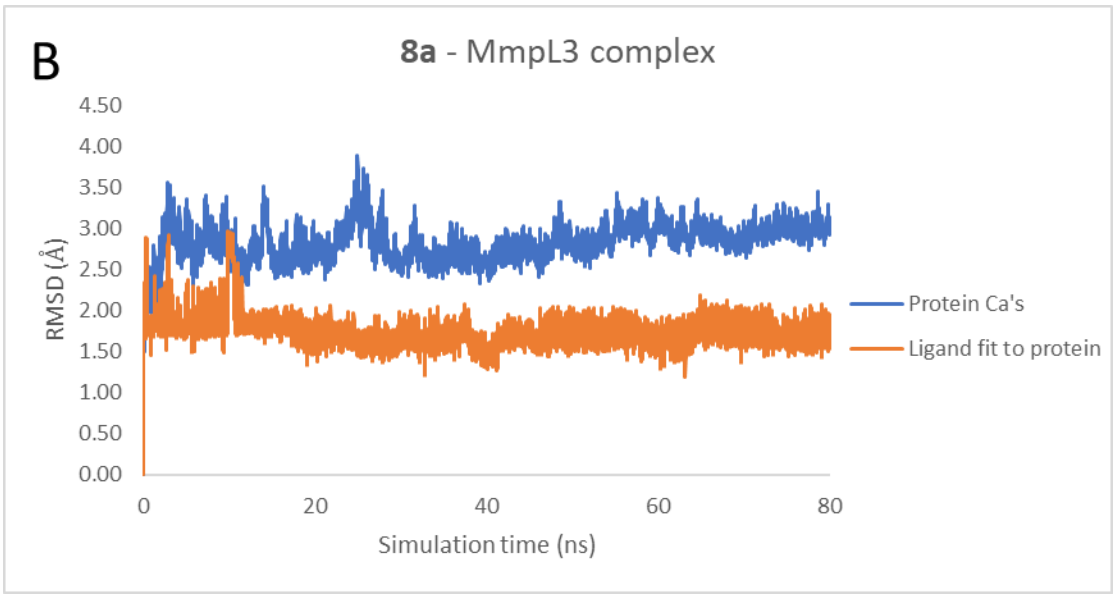

Figure S2 MD simulation results for MmpL3 with **8a**.

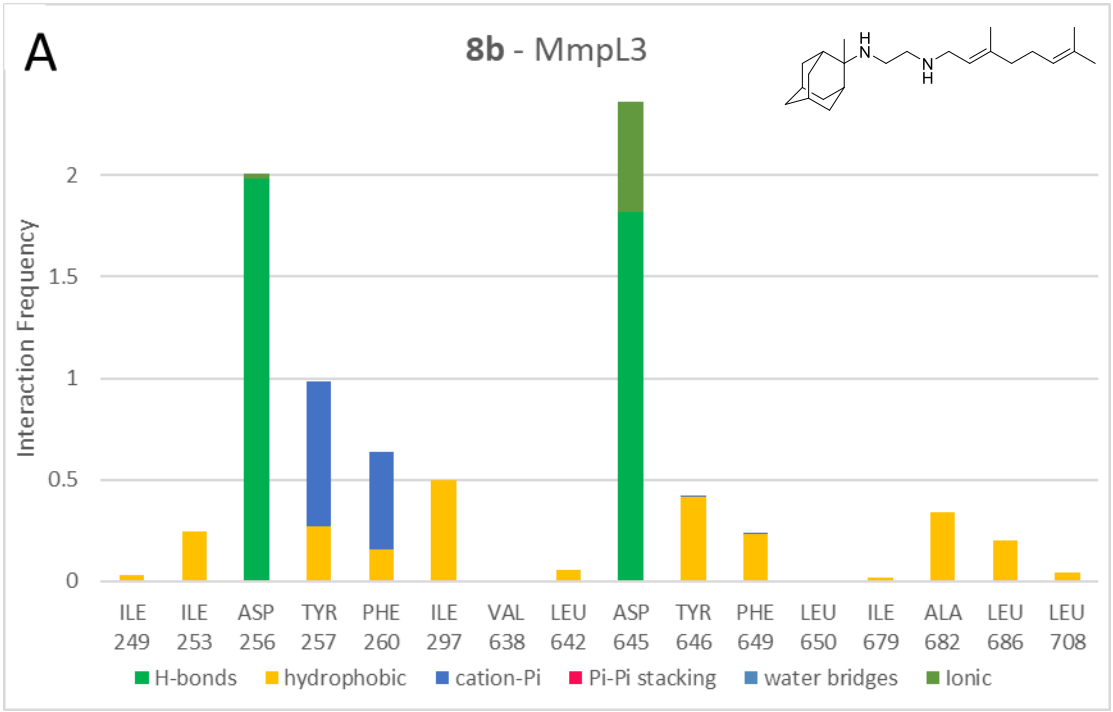

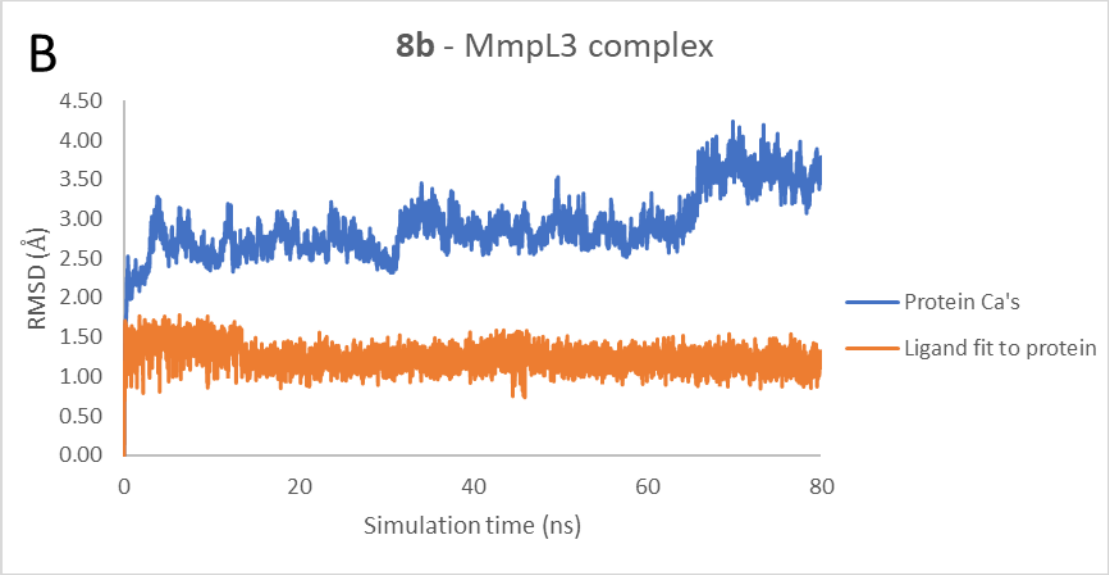

Figure S2 (contd.). MD simulation results for MmpL3 with **8b**.

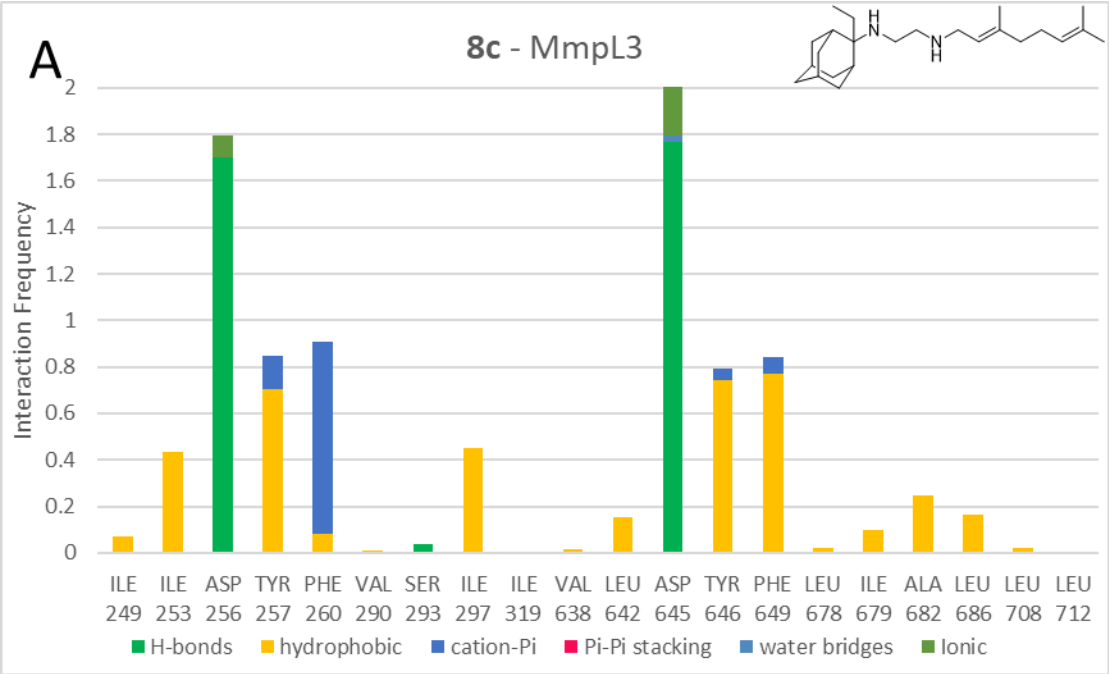

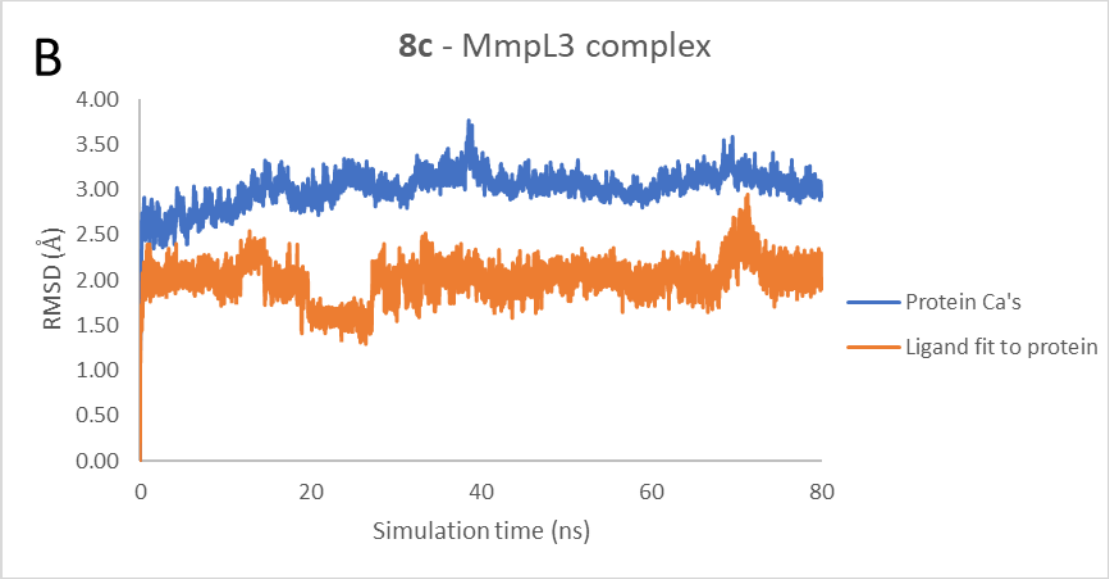

Figure S2 (contd.). MD simulation results for MmpL3 with **8c**.

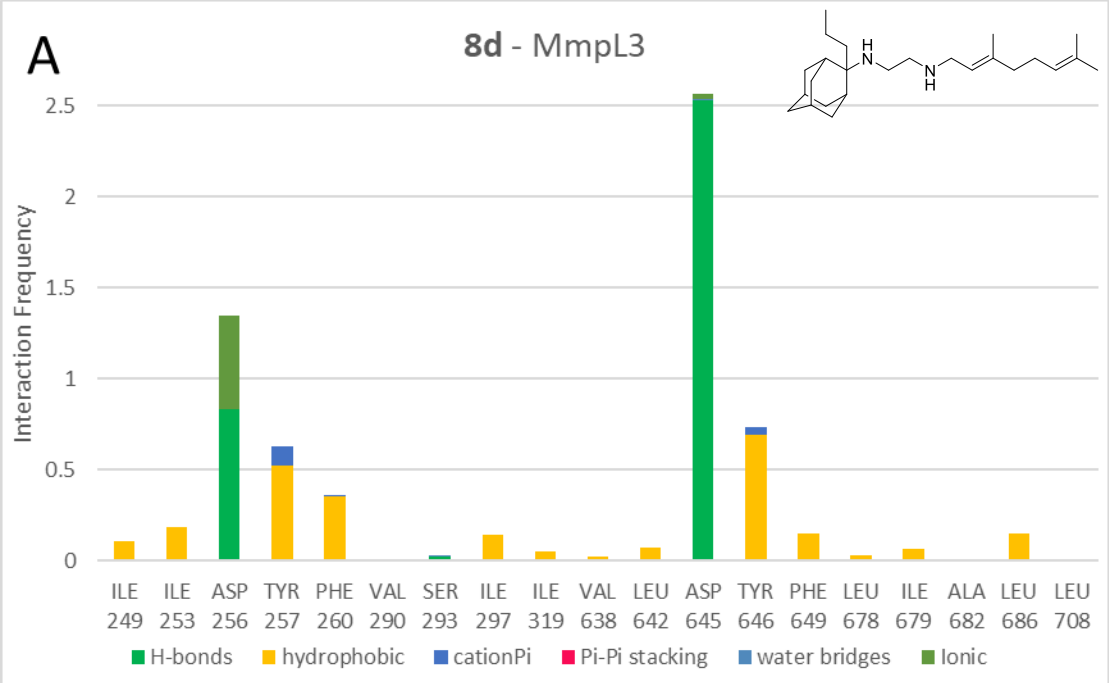

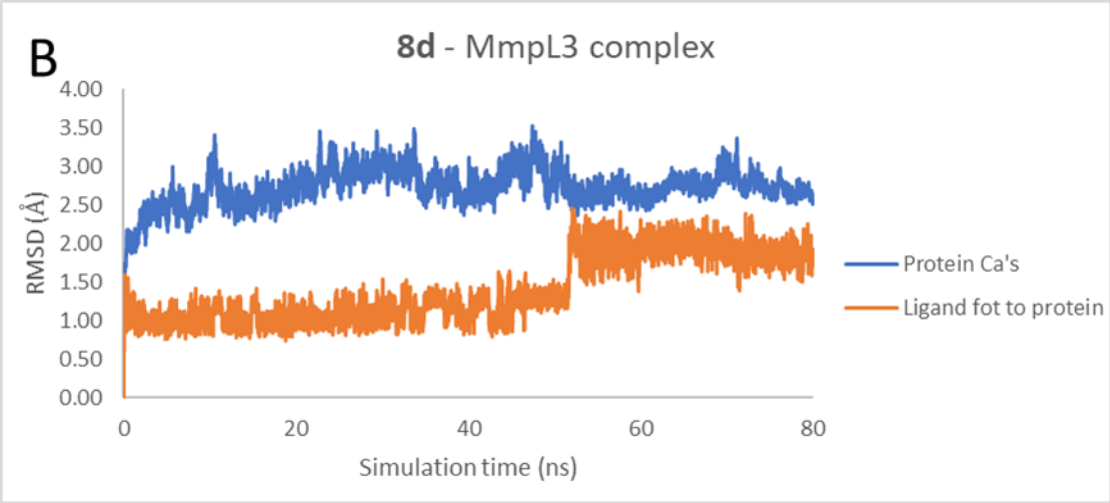

Figure S2 (contd.). MD simulation results for MmpL3 with **8d**.

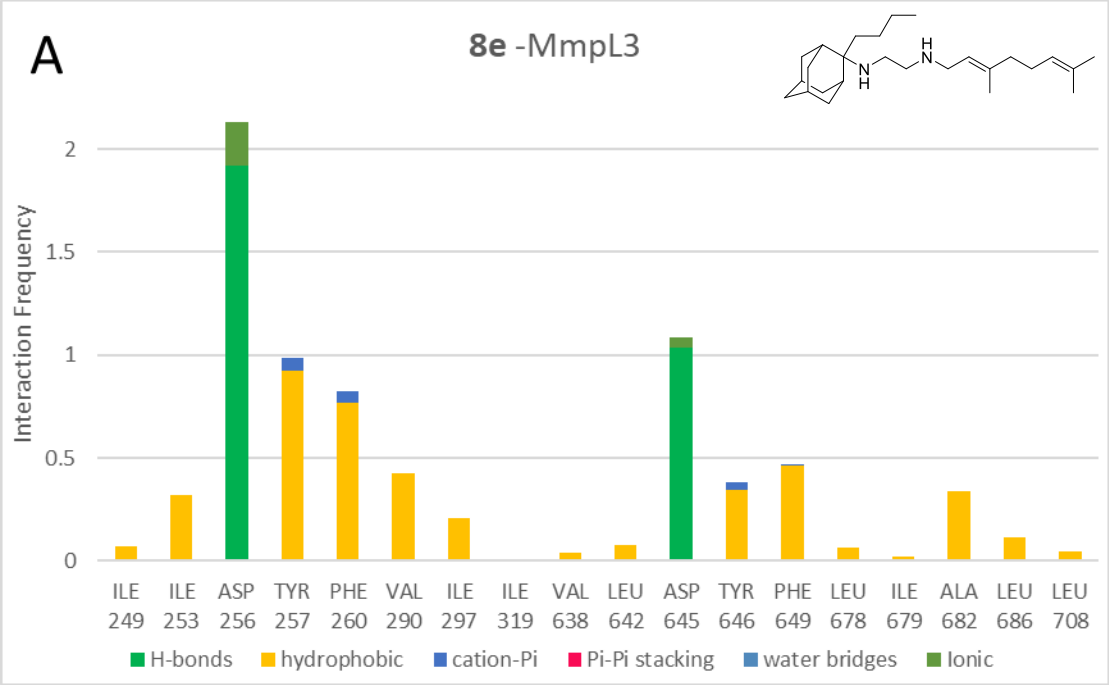

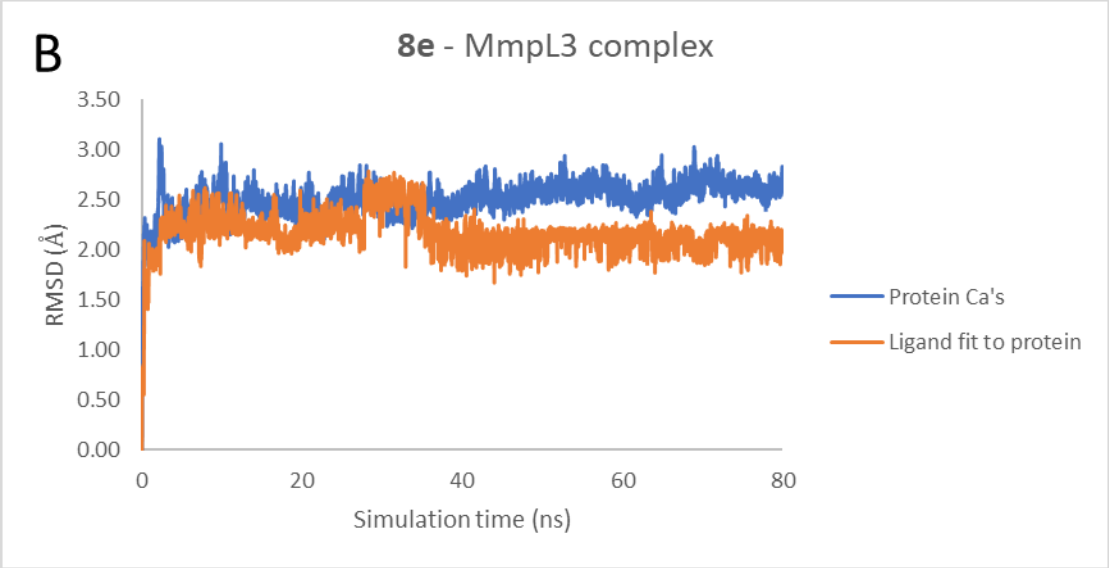

Figure S2 (contd.). MD simulation results for MmpL3 with **8e**.

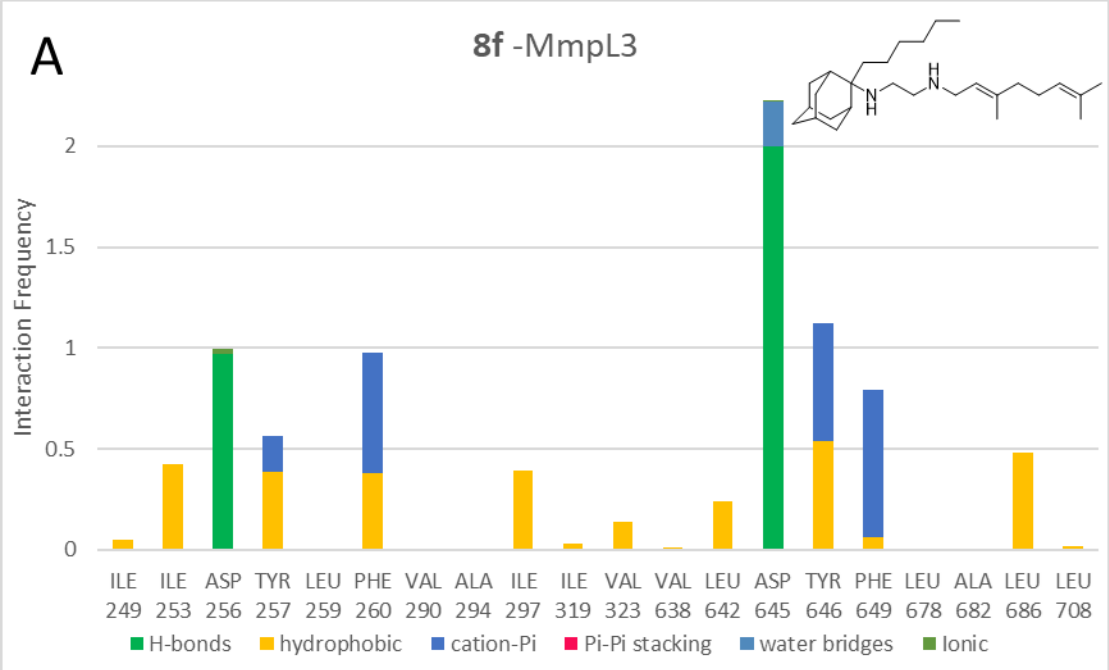

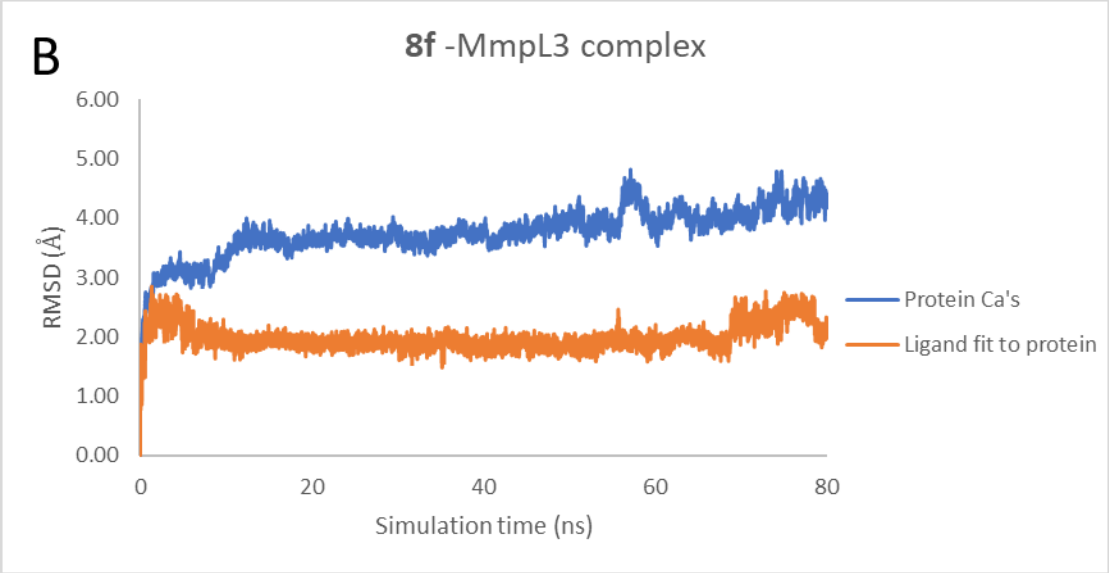

Figure S2 (contd.). MD simulation results for MmpL3 with **8f**.

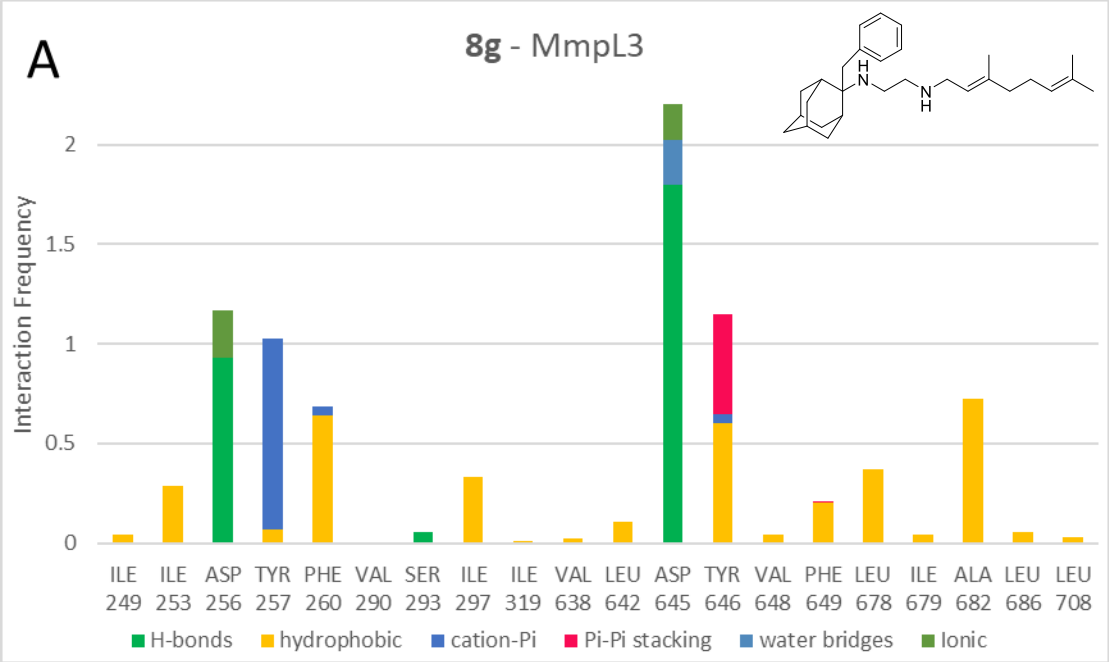

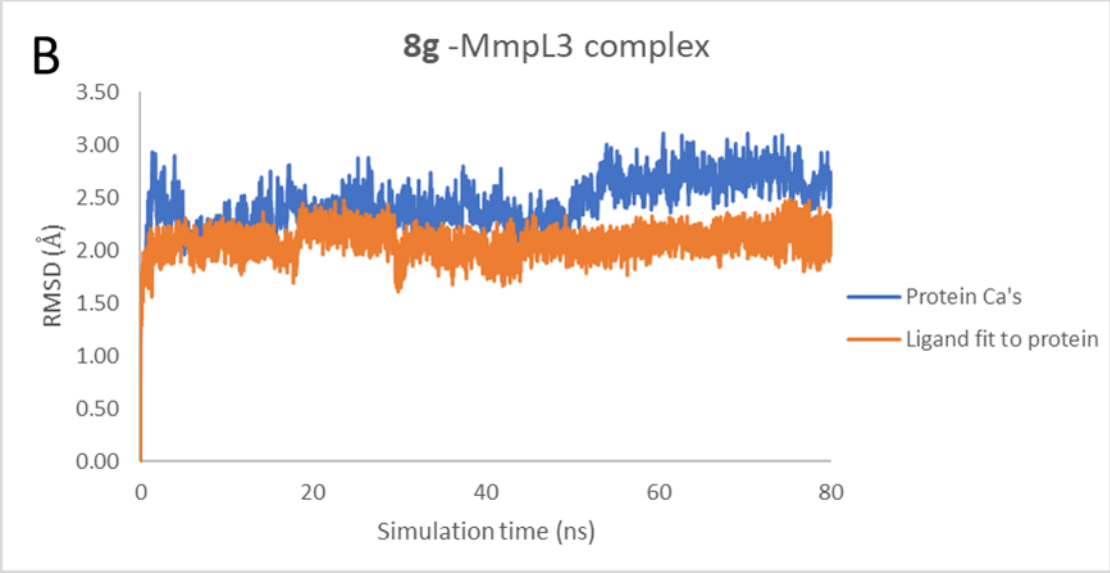

Figure S2 (contd.). MD simulation results for MmpL3 with **8g**.

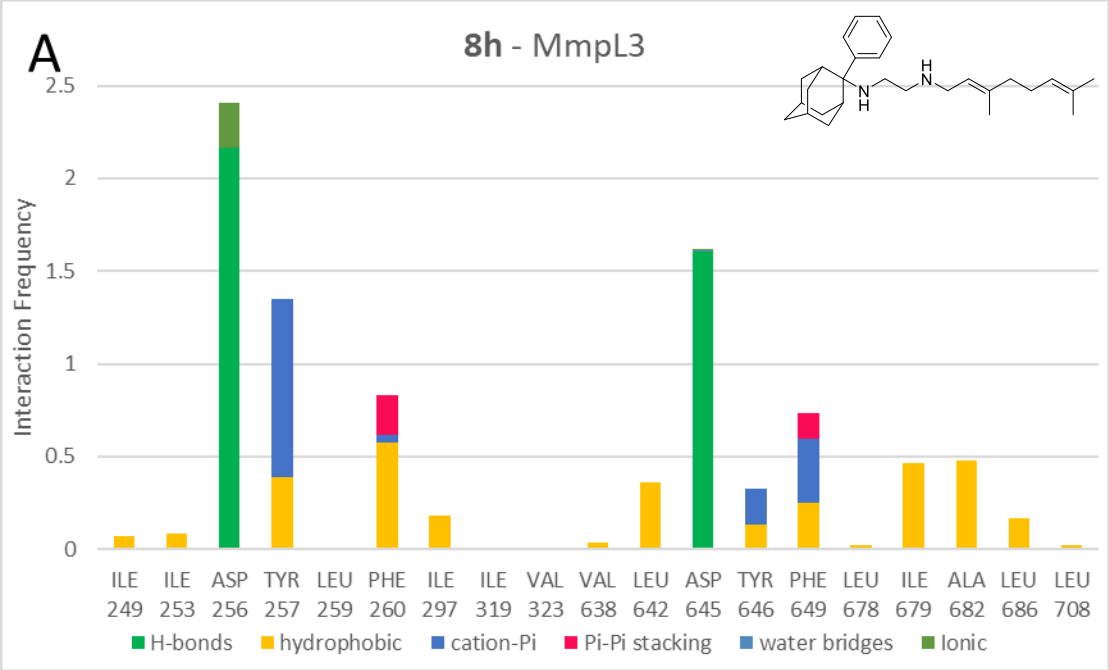

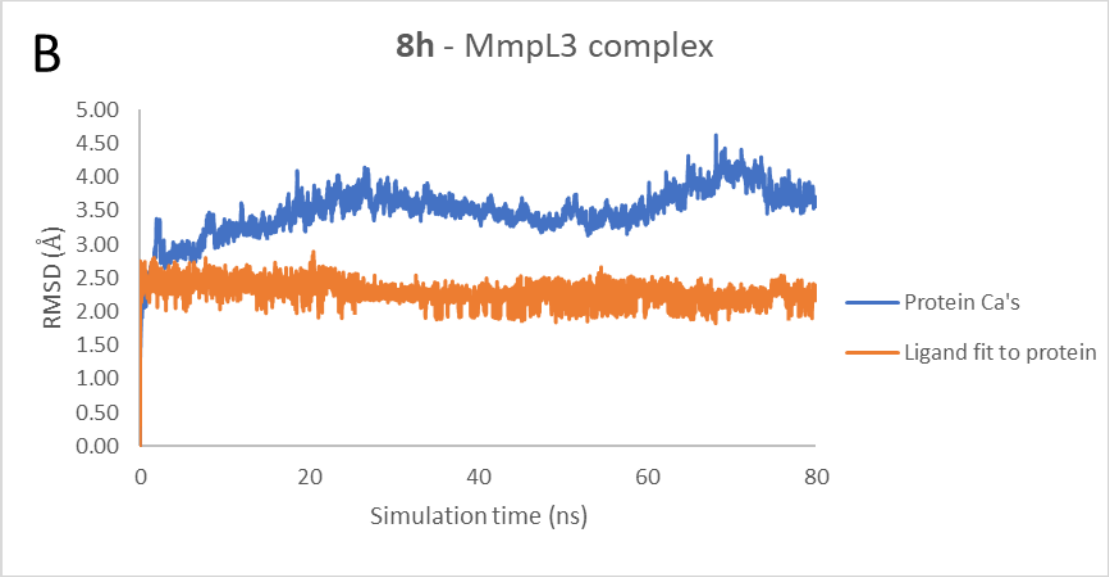

Figure S2 (contd.). MD simulation results for MmpL3 with **8h**.

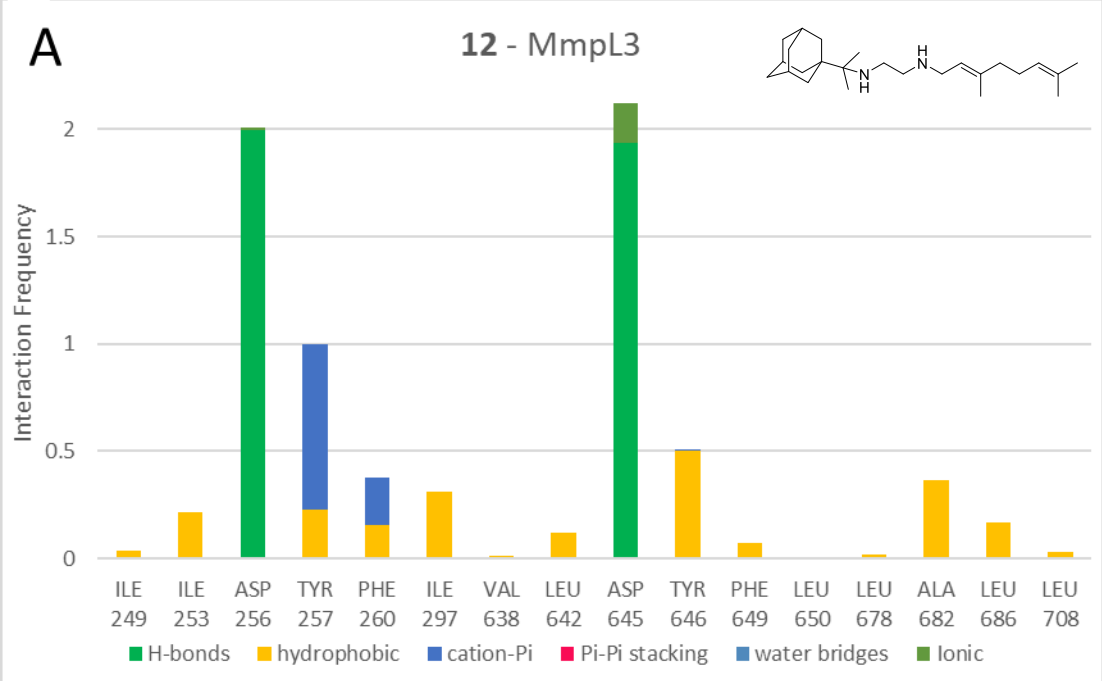

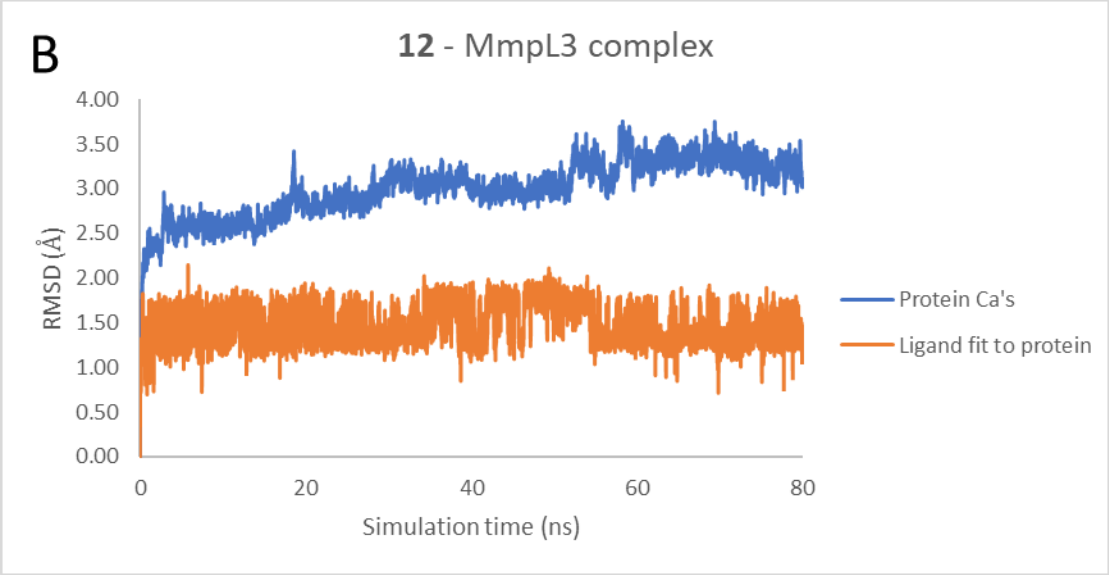

Figure S2 (contd.). MD simulation results for MmpL3 with **12**.

100ns MD simulations plots of two replicas of the single protonated SQ109 analogs in complex with MmpL3

Figure S3. Molecular dynamics results of two replicas for complexes of monoprotonated SQ109 analogs with MmpL3. In panels (A) for **8a-i**, **12** are shown the chemical structures of the ligands and the receptor-ligand interaction frequency histograms as an average of two replicas: hydrogen bonding interaction bar are depicted in green, Van der Waals in yellow, cation-pi in blue, pi-pi stacking in red, water bridges in light blue and ionic in light green, (B) the RMSD plots for the Ca carbons (blue) of transmembrane helices and the ligand heavy atoms (orange) separately for the two replicas and as an average. For the protein, the experimental structure of SQ109 in complex with MmpL3 (PDB ID 6AJG) was used as the starting structure for the MD simulations after excluding C-terminus, consisting of M1-E749 residues. The transmembrane region included the following helices and their residues: TM1 (14-33), TM2 (174-199), TM3 (208-224), TM4 (238-264), TM5 (271-301), TM6 (306-338), TM7 (396-415), TM8 (552-576), TM9 (583-601), TM10 (625-648), TM11 (660-690), TM12 (697-728).

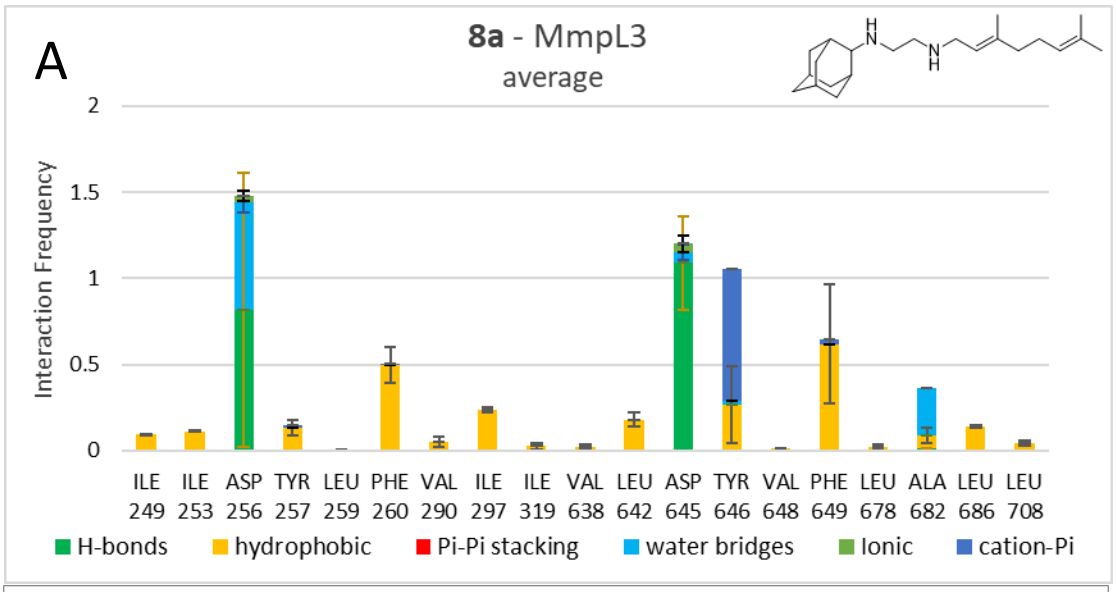
A
8a - MmpL3
average
Interaction Frequency
2
1.5
1
0.5
0
ILE 249
ILE 253
ASP 256
TYR 257
LEU 259
PHE 260
VAL 290
ILE 297
ILE 319
VAL 638
LEU 642
ASP 645
TYR 646
VAL 648
PHE 649
LEU 678
ALA 682
LEU 686
LEU 708
H-bonds
hydrophobic
Pi-Pi stacking
water bridges
Ionic
cation-Pi

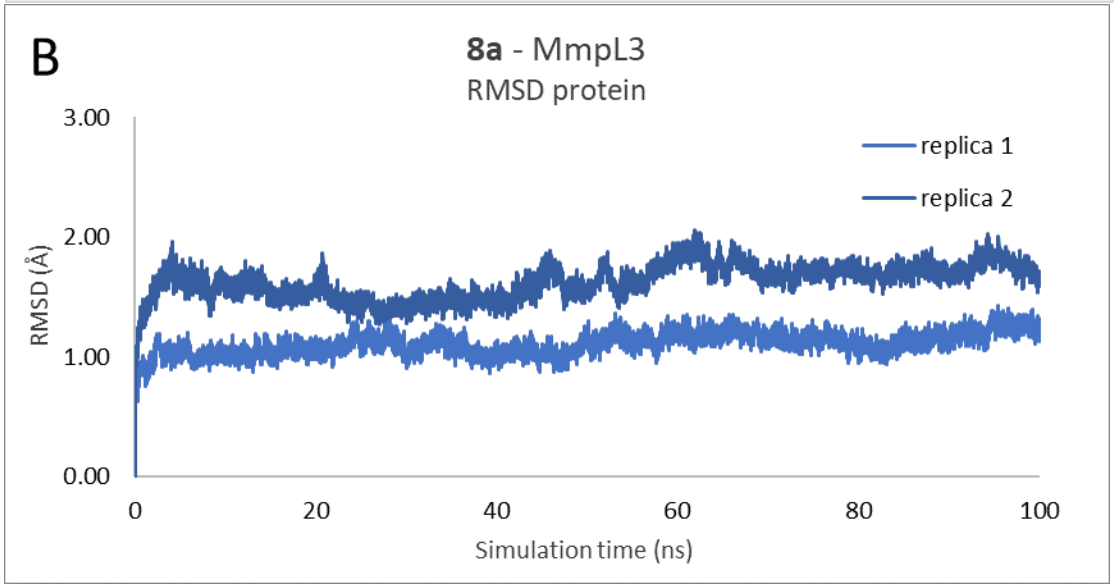
B
8a - MmpL3
RMSD protein
RMSD (Å)
3.00
2.00
1.00
0.00
0
20
40
60
80
100
Simulation time (ns)
replica 1
replica 2

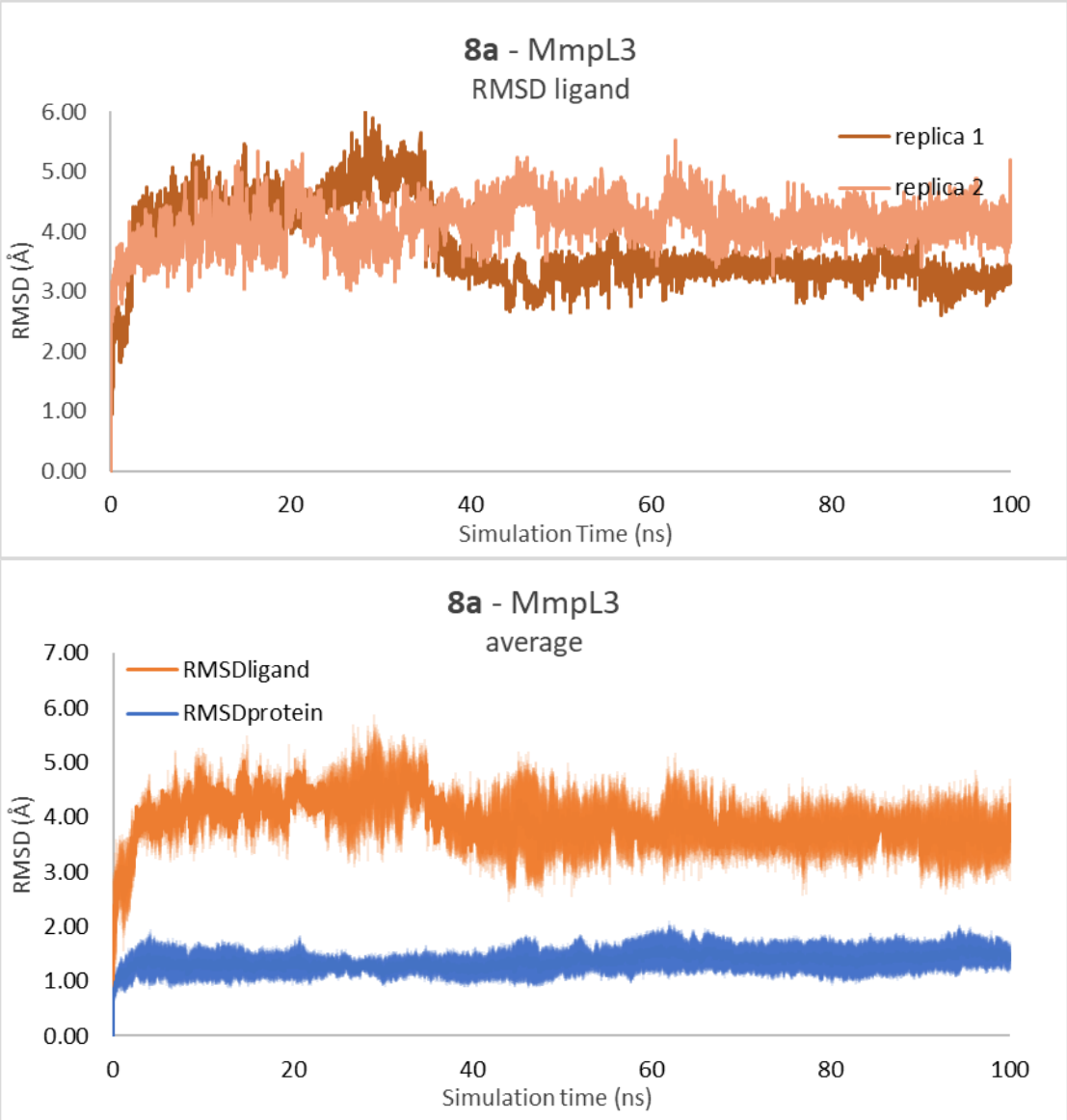

Figure S3 MD simulation results of two replicas for MmpL3 with **8a**.

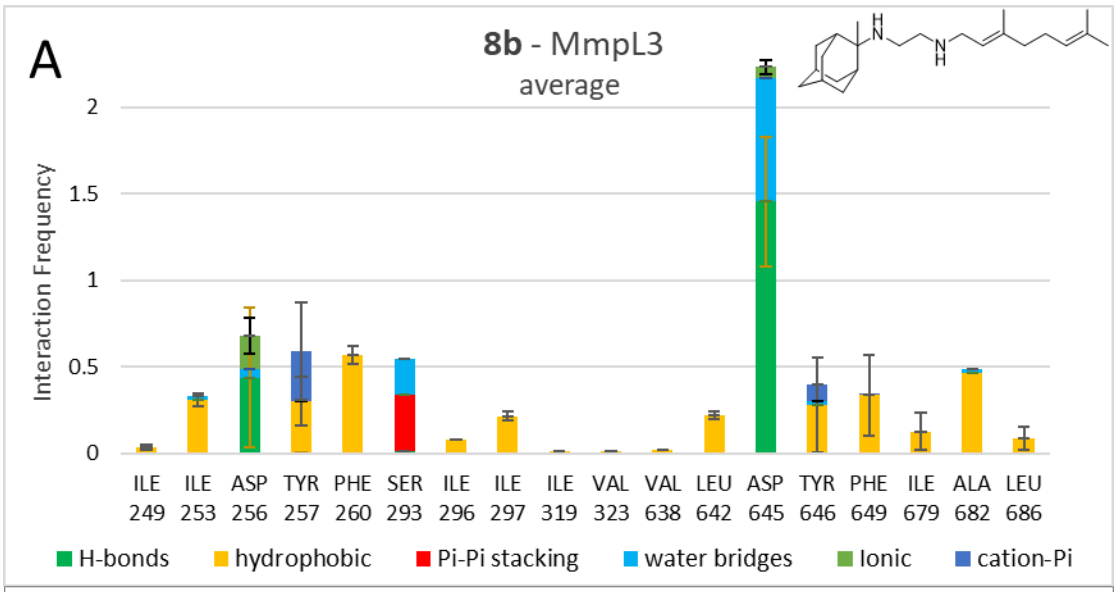
A
8b - MmpL3
average
Interaction Frequency
2
1.5
1
0.5
0
ILE 249
ILE 253
ASP 256
TYR 257
PHE 260
SER 293
ILE 296
ILE 297
ILE 319
VAL 323
VAL 638
LEU 642
ASP 645
TYR 646
PHE 649
ILE 679
ALA 682
LEU 686
H-bonds
hydrophobic
Pi-Pi stacking
water bridges
Ionic
cation-Pi

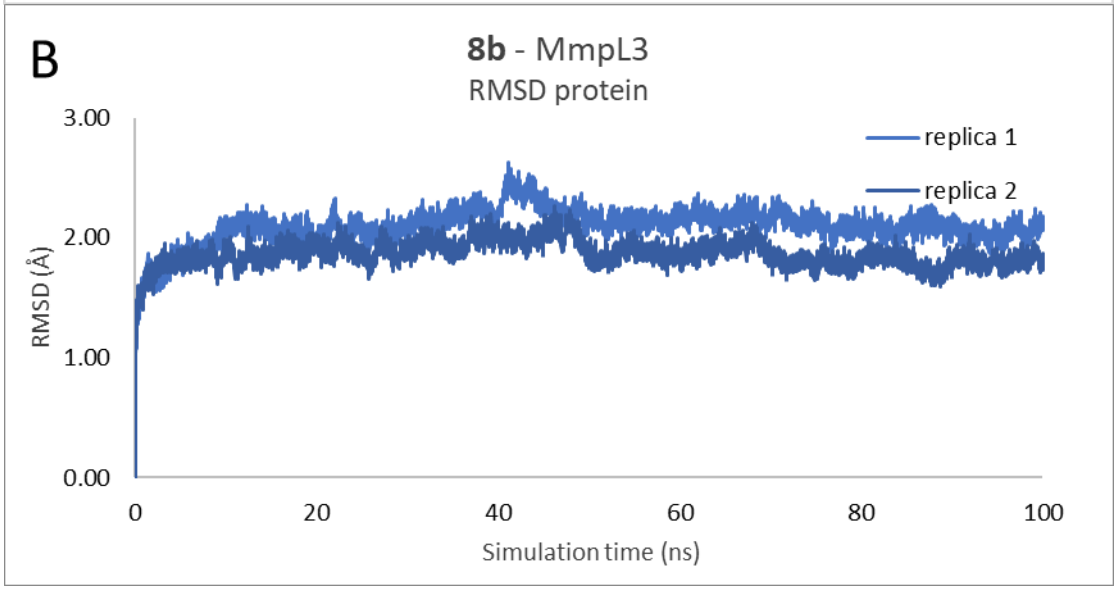
B
8b - MmpL3
RMSD protein
RMSD (Å)
3.00
2.00
1.00
0.00
0
20
40
60
80
100
Simulation time (ns)
replica 1
replica 2

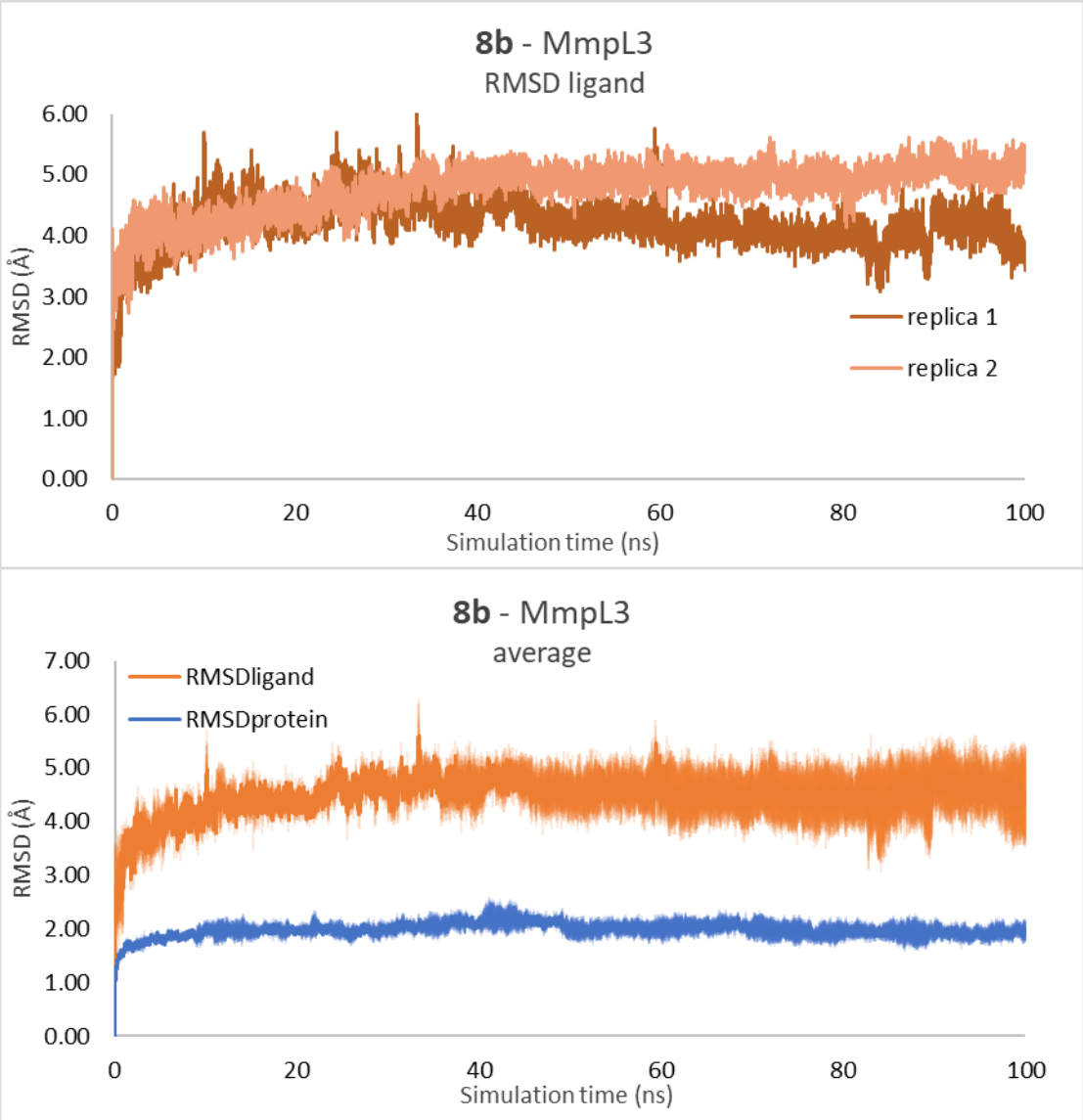

Figure S3 (contd.). MD simulation results of two replicas for MmpL3 with **8b**.

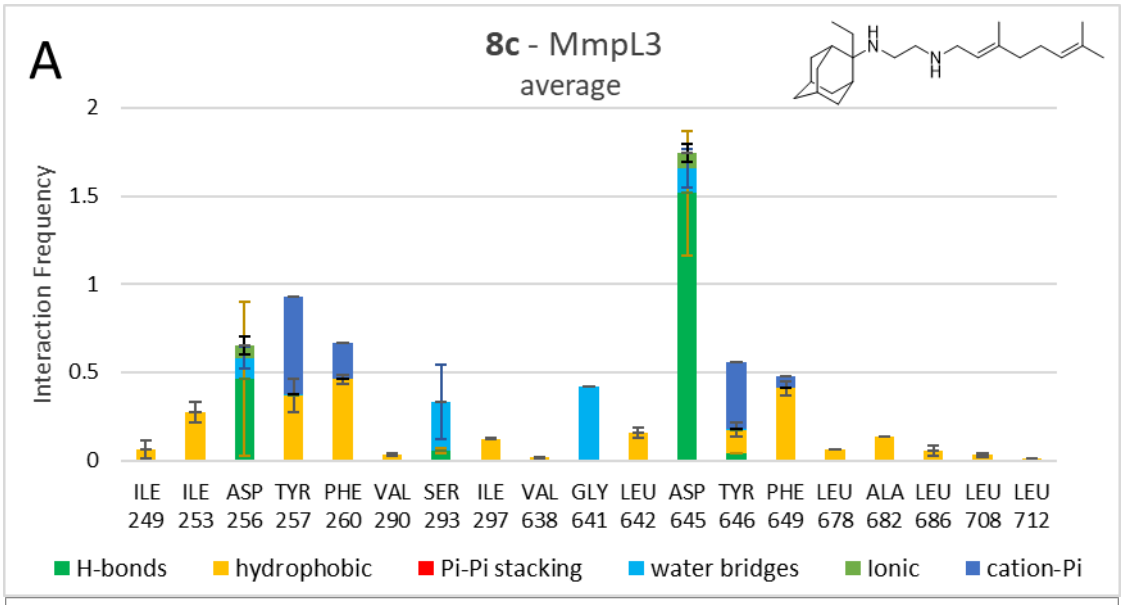
A
8c - MmpL3
average
Interaction Frequency
2
1.5
1
0.5
0
ILE 249
ILE 253
ASP 256
TYR 257
PHE 260
VAL 290
SER 293
ILE 297
VAL 638
GLY 641
LEU 642
ASP 645
TYR 646
PHE 649
LEU 678
ALA 682
LEU 686
LEU 708
LEU 712
H-bonds
hydrophobic
Pi-Pi stacking
water bridges
Ionic
cation-Pi

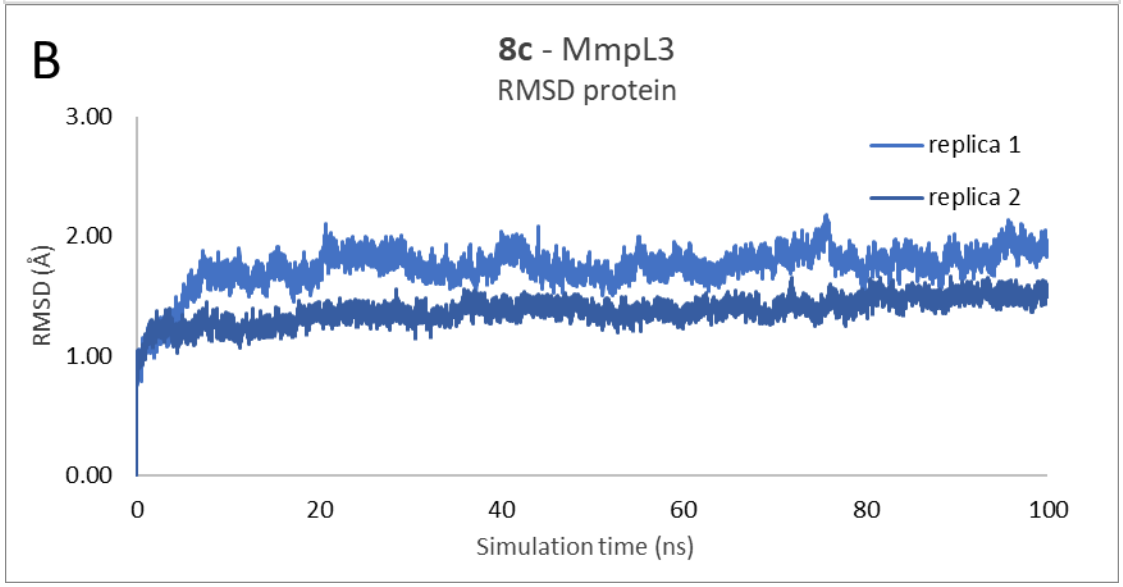
B
8c - MmpL3
RMSD protein
RMSD (Å)
3.00
2.00
1.00
0.00
0
20
40
60
80
100
Simulation time (ns)
replica 1
replica 2

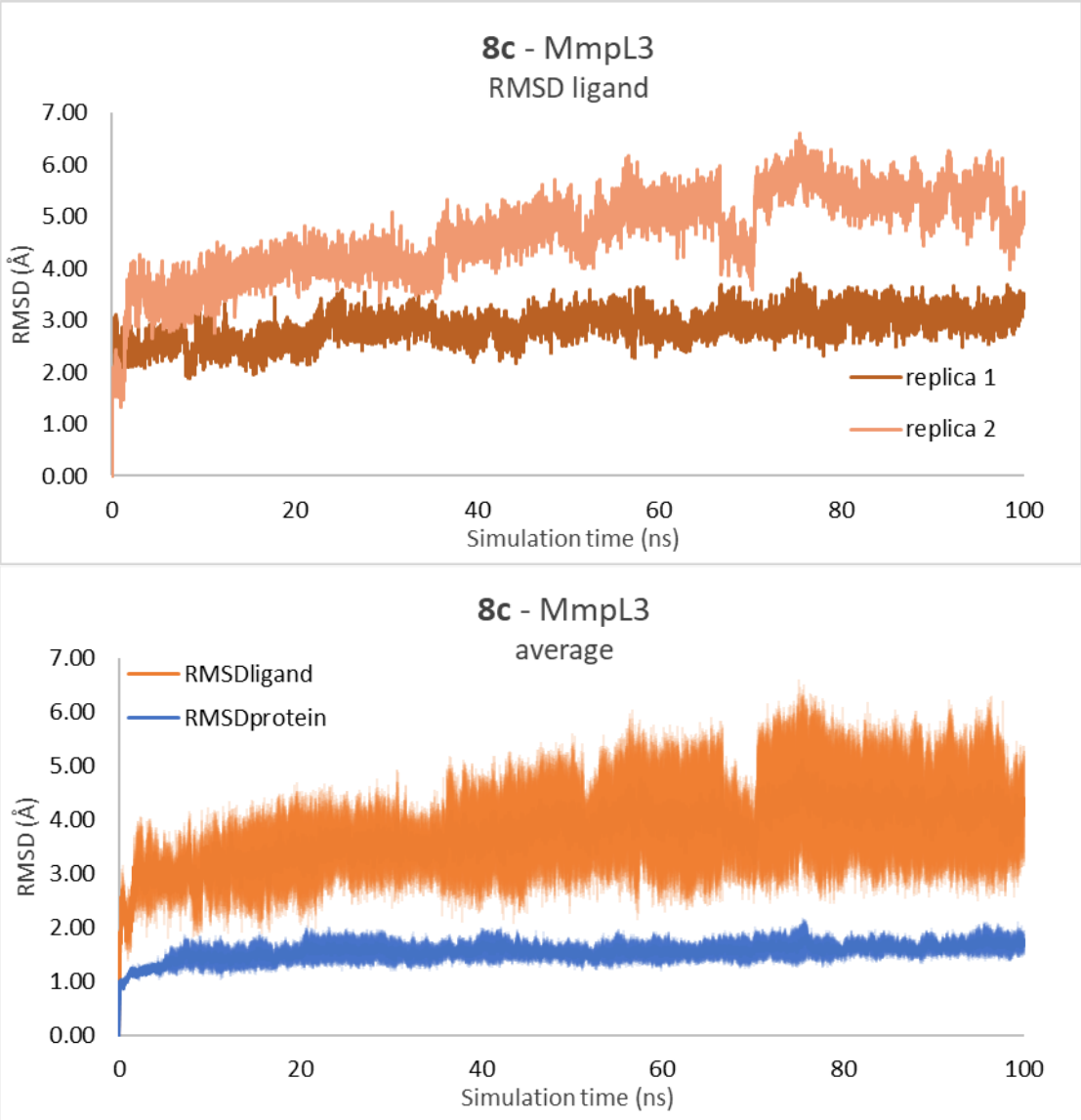

Figure S3 (contd.). MD simulation results of two replicas for MmpL3 with **8c**.

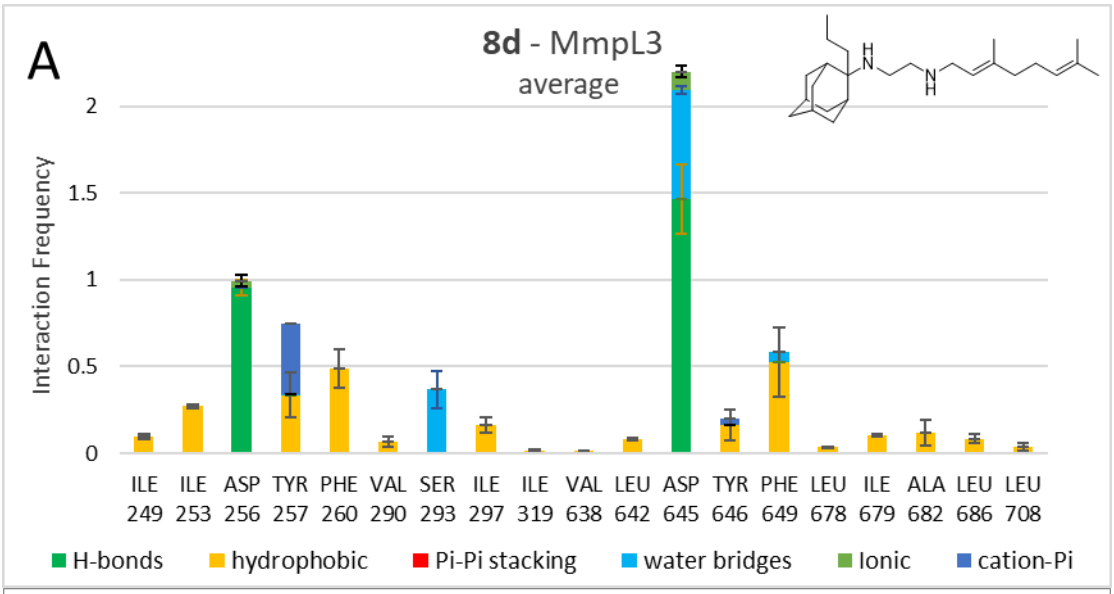
A
8d - MmpL3
average
Interaction Frequency
2
1.5
1
0.5
0
ILE 249
ILE 253
ASP 256
TYR 257
PHE 260
VAL 290
SER 293
ILE 297
ILE 319
VAL 638
LEU 642
ASP 645
TYR 646
PHE 649
LEU 678
ILE 679
ALA 682
LEU 686
LEU 708
H-bonds
hydrophobic
Pi-Pi stacking
water bridges
Ionic
cation-Pi

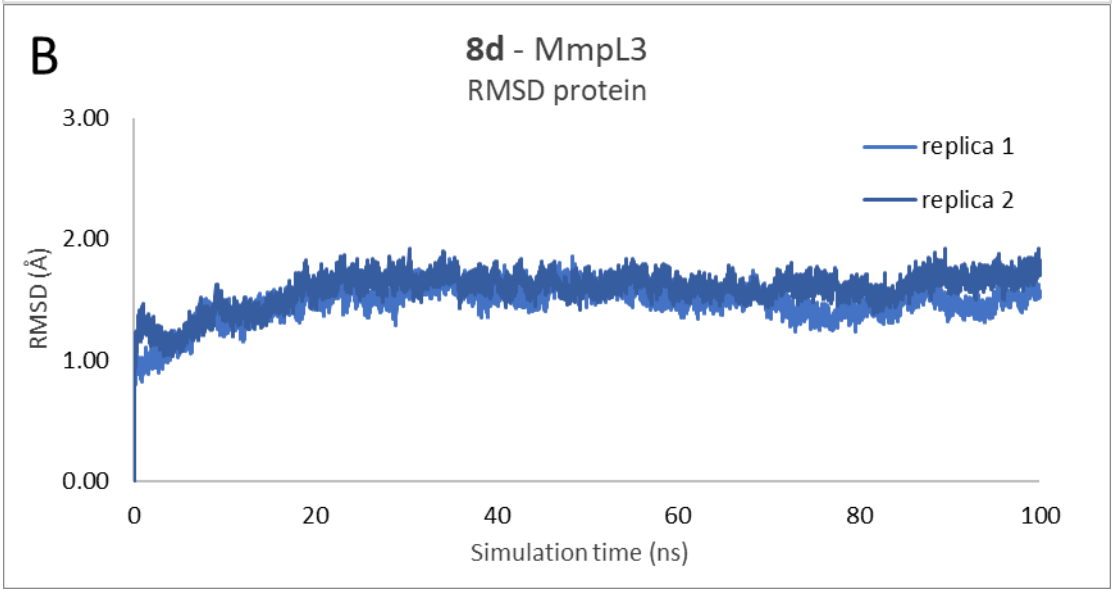
B
8d - MmpL3
RMSD protein
RMSD (Å)
3.00
2.00
1.00
0.00
0
20
40
60
80
100
Simulation time (ns)
replica 1
replica 2

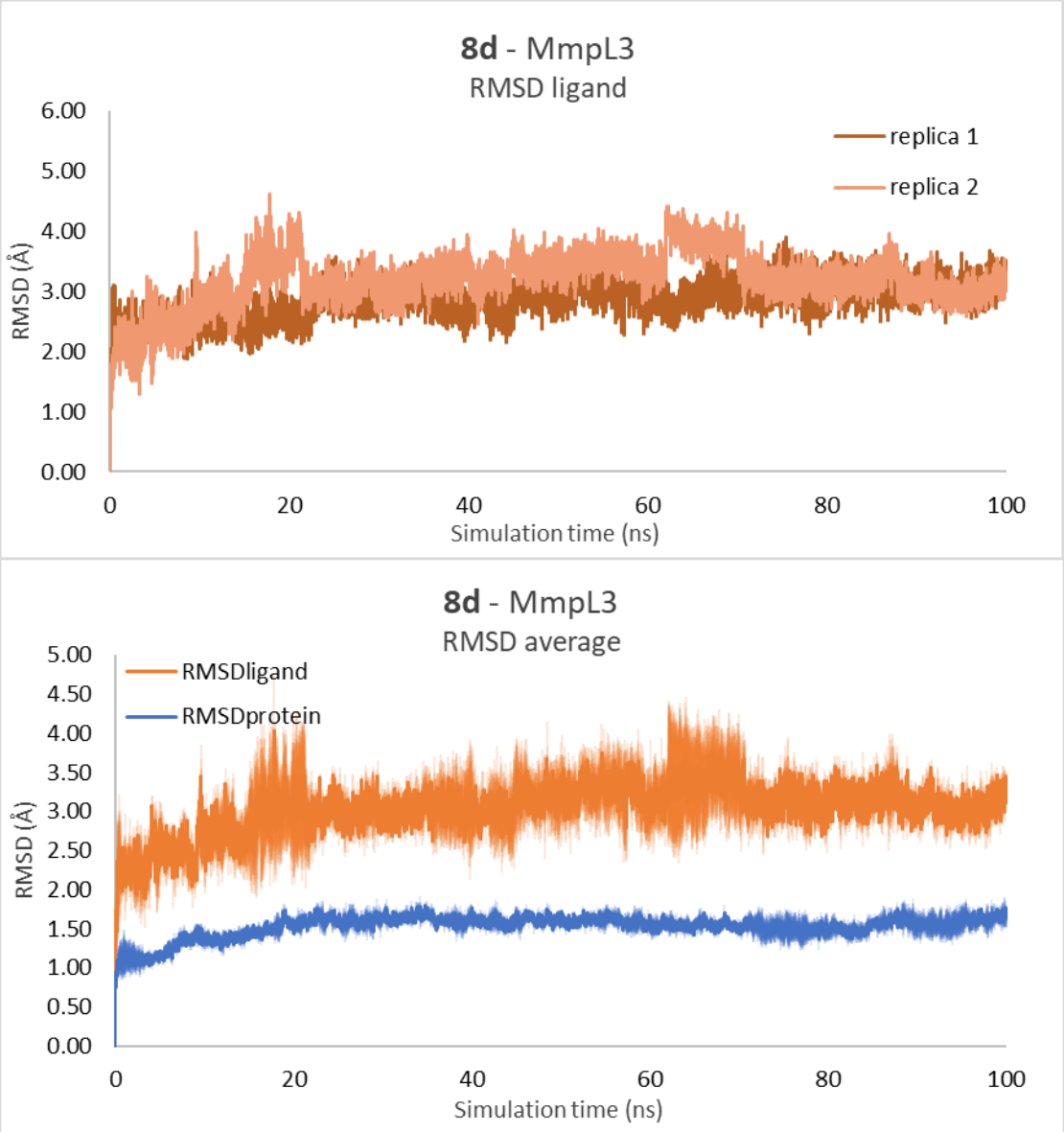

Figure S3 (contd.). MD simulation results of two replicas for MmpL3 with **8d**.

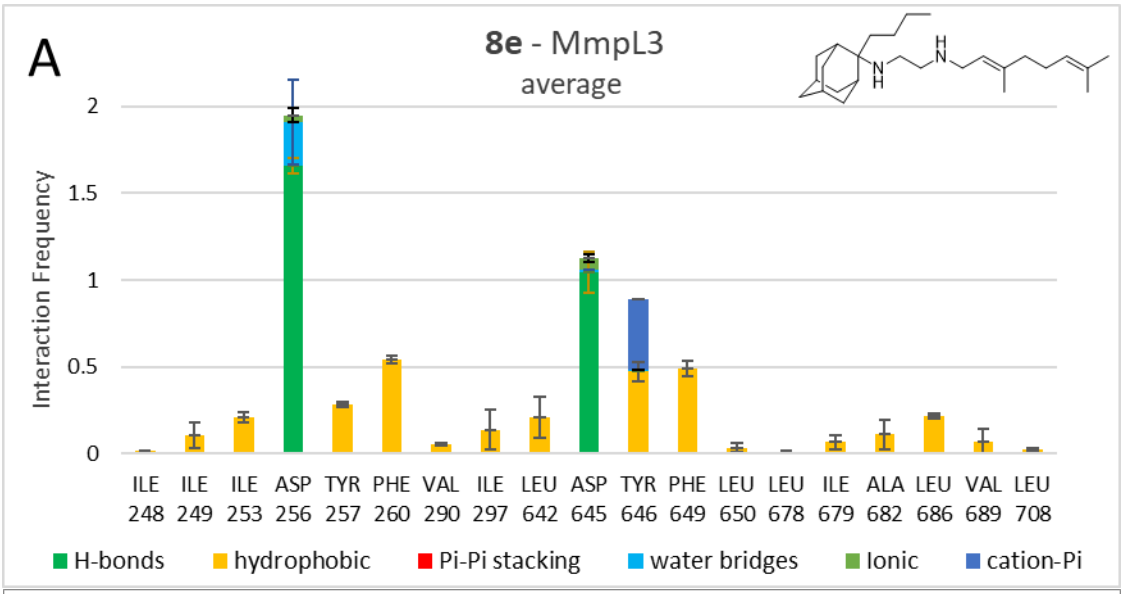
A
8e - MmpL3
average
Interaction Frequency
2
1.5
1
0.5
0
ILE 248
ILE 249
ILE 253
ASP 256
TYR 257
PHE 260
VAL 290
ILE 297
LEU 642
ASP 645
TYR 646
PHE 649
LEU 650
LEU 678
ILE 679
ALA 682
LEU 686
VAL 689
LEU 708
H-bonds
hydrophobic
Pi-Pi stacking
water bridges
Ionic
cation-Pi

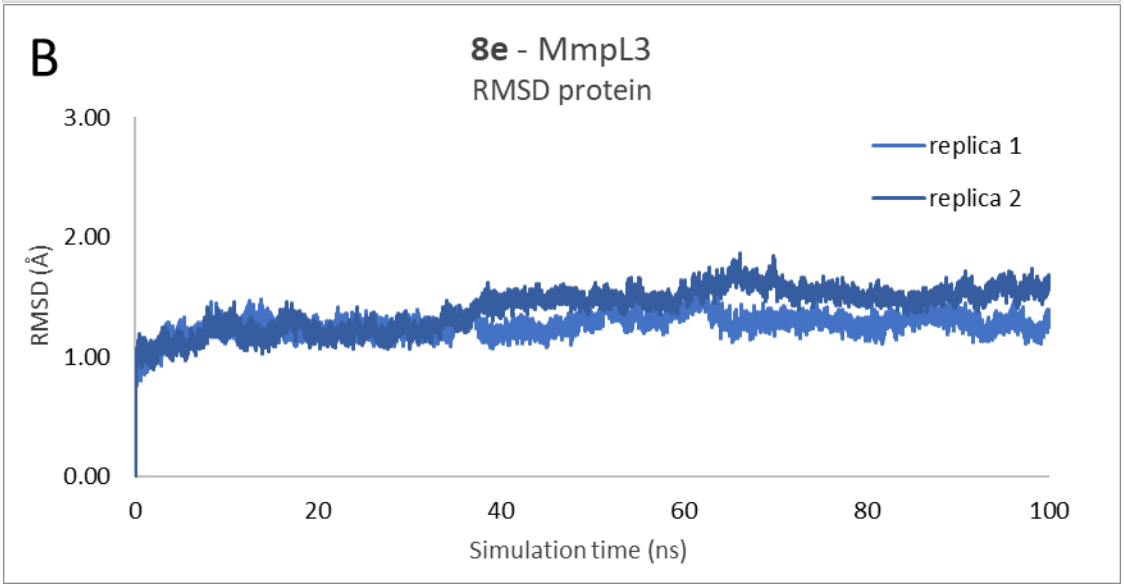
B
8e - MmpL3
RMSD protein
RMSD (Å)
3.00
2.00
1.00
0.00
0
20
40
60
80
100
Simulation time (ns)
replica 1
replica 2

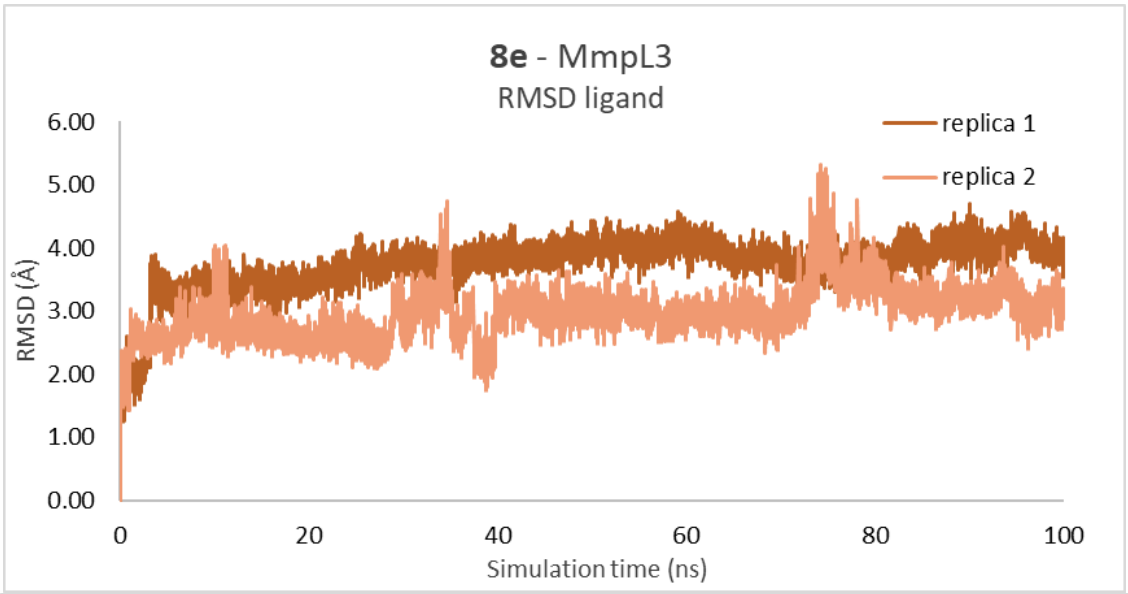

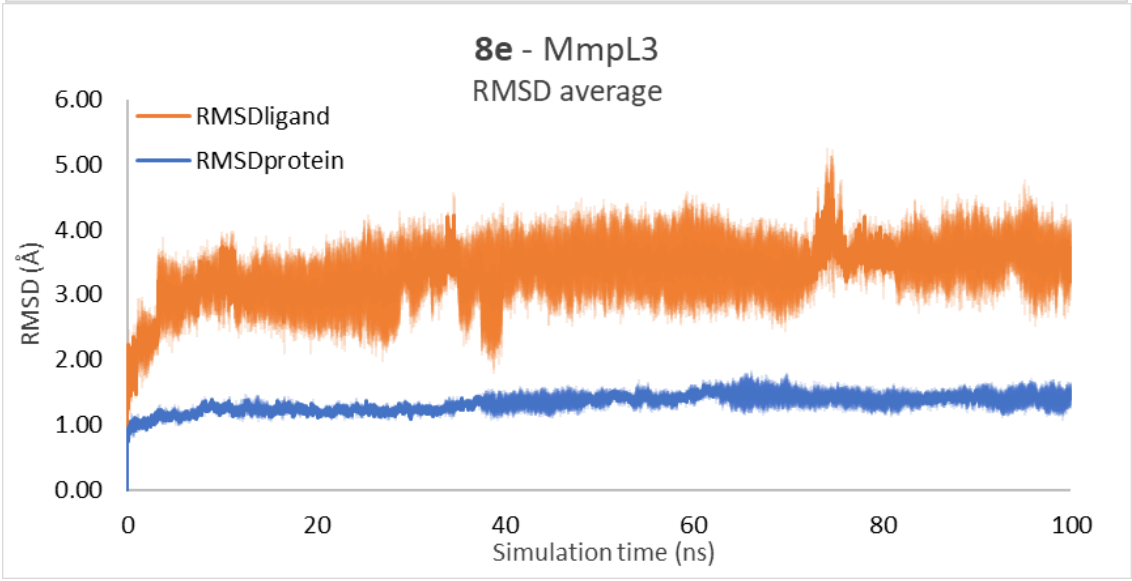

Figure S3 (contd.). MD simulation results of two replicas for MmpL3 with **8e**.

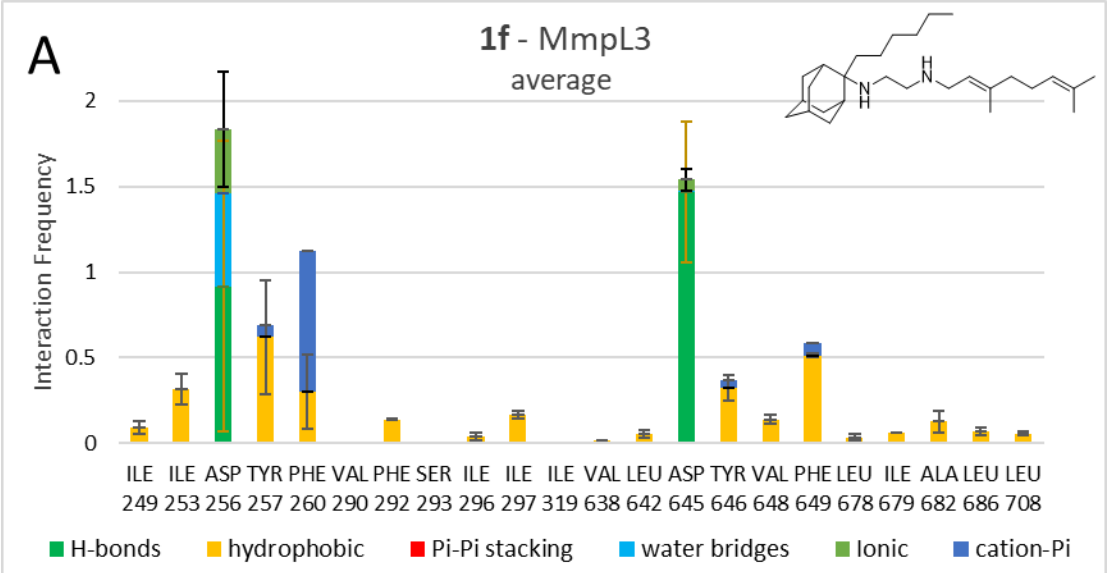
A
1f - MmpL3
average
Interaction Frequency
2
1.5
1
0.5
0
ILE 249
ILE 253
ASP 256
TYR 257
PHE 260
VAL 290
PHE 292
SER 293
ILE 296
ILE 297
ILE 319
VAL 638
LEU 642
ASP 645
TYR 646
VAL 648
PHE 649
LEU 678
ILE 679
ALA 682
LEU 686
LEU 708
H-bonds
hydrophobic
Pi-Pi stacking
water bridges
Ionic
cation-Pi

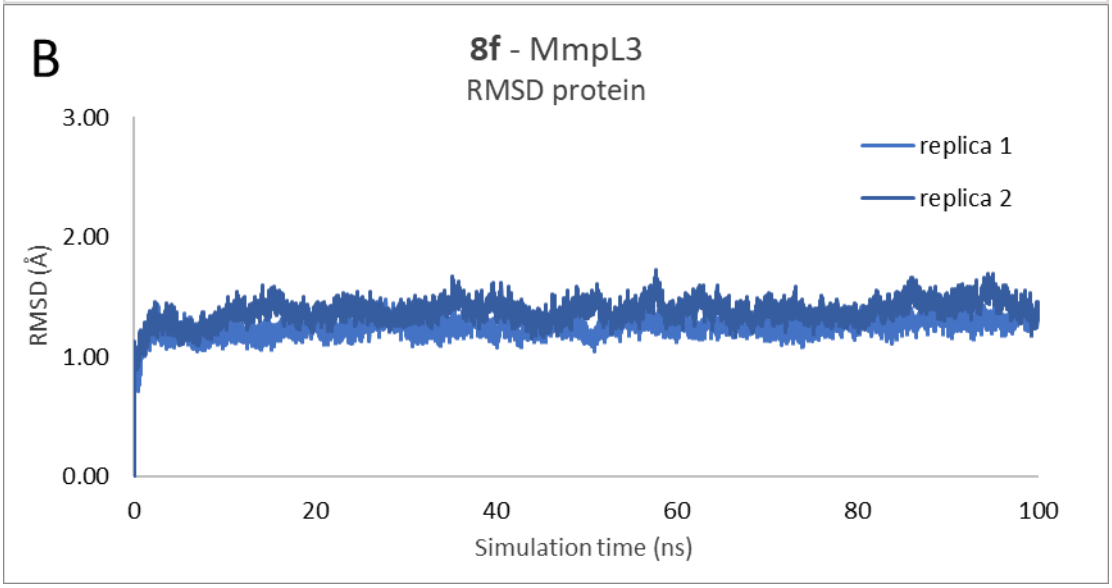
B
8f - MmpL3
RMSD protein
3.00
2.00
1.00
0.00
RMSD (Å)
replica 1
replica 2
0
20
40
60
80
100
Simulation time (ns)

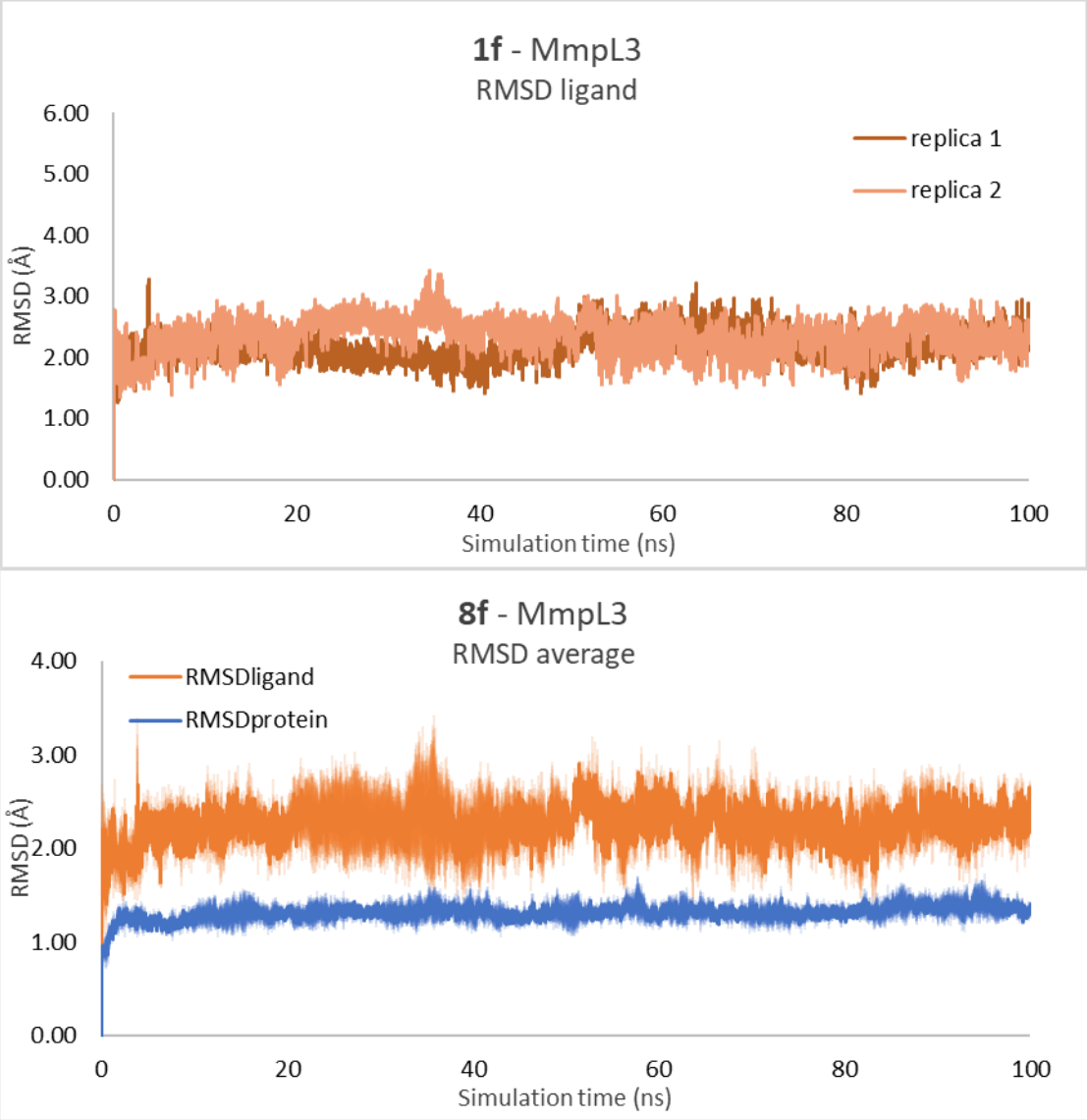

Figure S3 (contd.). MD simulation results of two replicas for MmpL3 with **8f**.

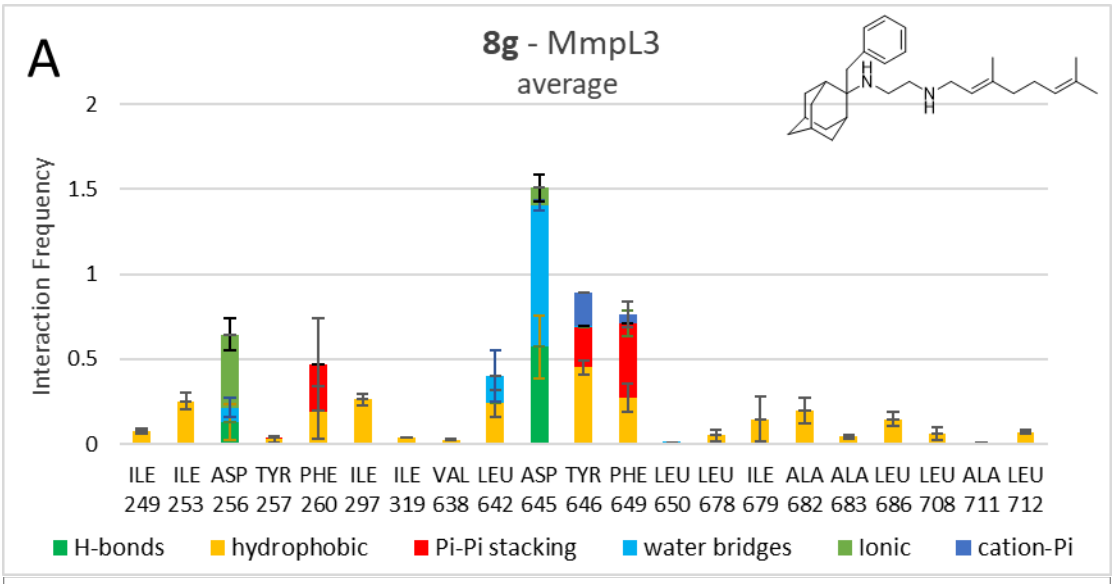
A
8g - MmpL3
average
Interaction Frequency
2
1.5
1
0.5
0
ILE 249
ILE 253
ASP 256
TYR 257
PHE 260
ILE 297
ILE 319
VAL 638
LEU 642
ASP 645
TYR 646
PHE 649
LEU 650
LEU 678
ILE 679
ALA 682
ALA 683
LEU 686
LEU 708
ALA 711
LEU 712
H-bonds
hydrophobic
Pi-Pi stacking
water bridges
Ionic
cation-Pi

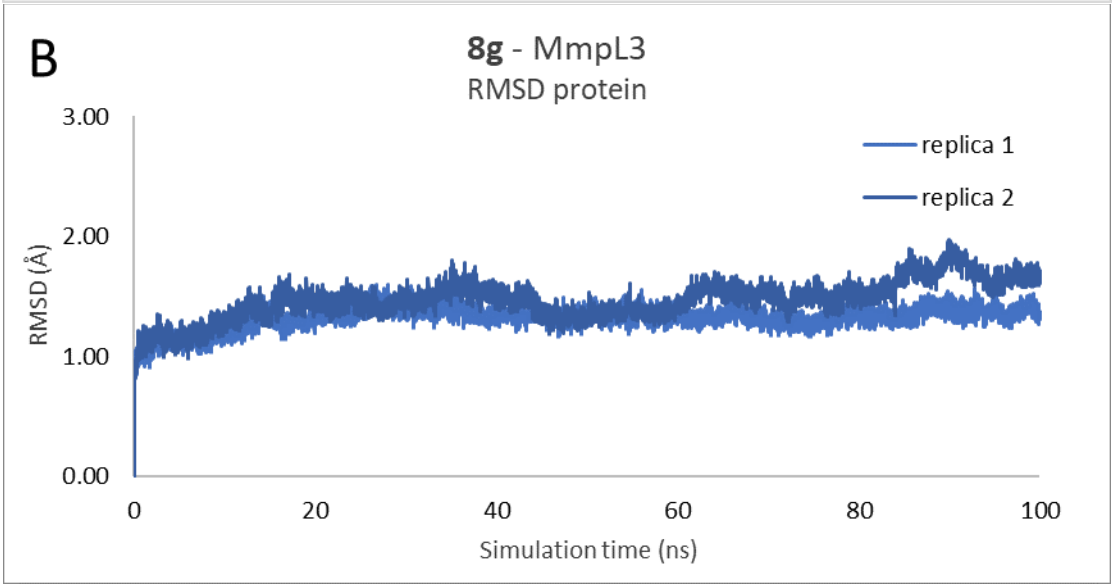
B
8g - MmpL3
RMSD protein
RMSD (Å)
3.00
2.00
1.00
0.00
0
20
40
60
80
100
Simulation time (ns)
replica 1
replica 2

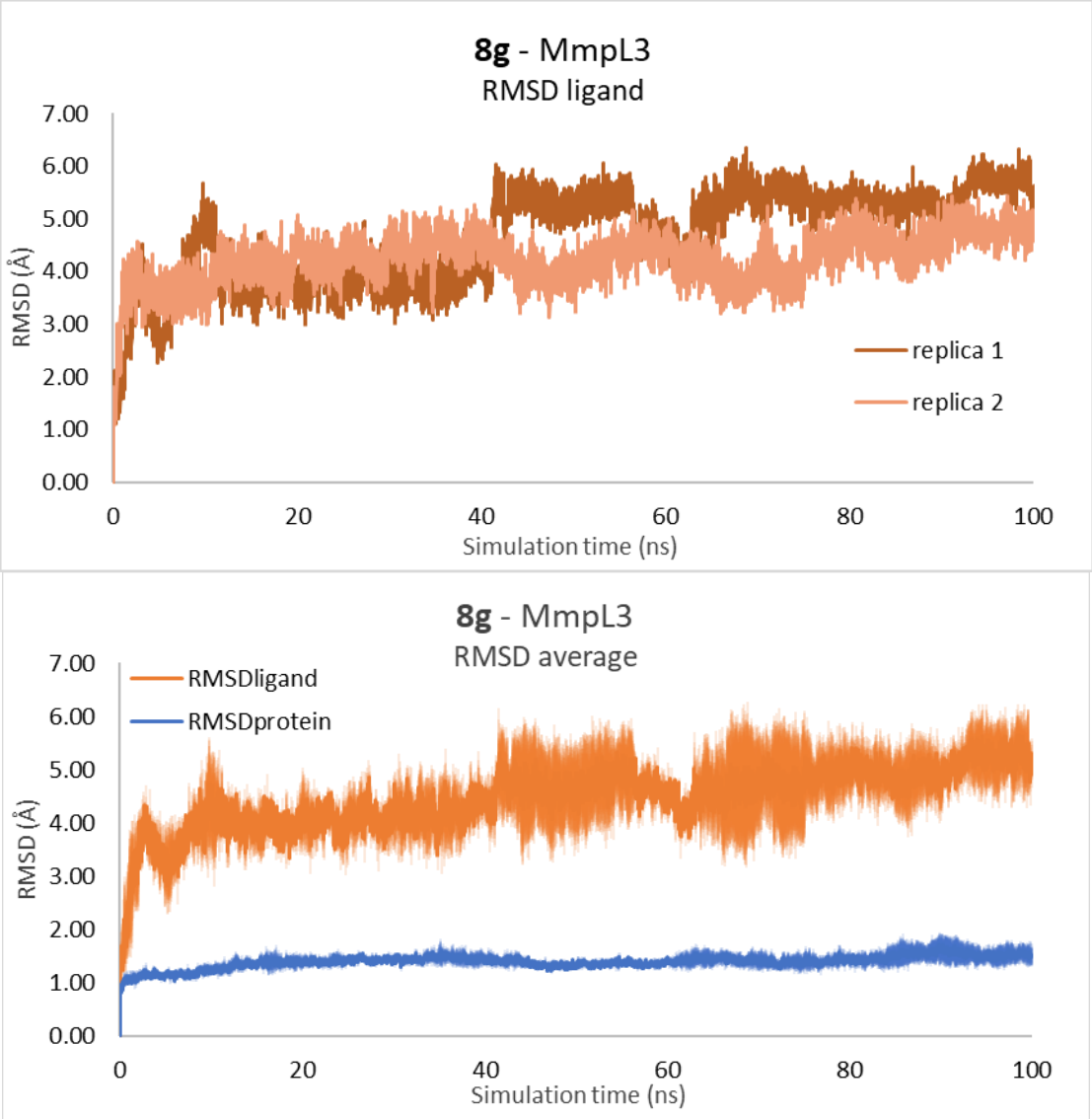

Figure S3 (contd.). MD simulation results of two replicas for MmpL3 with **8g**.

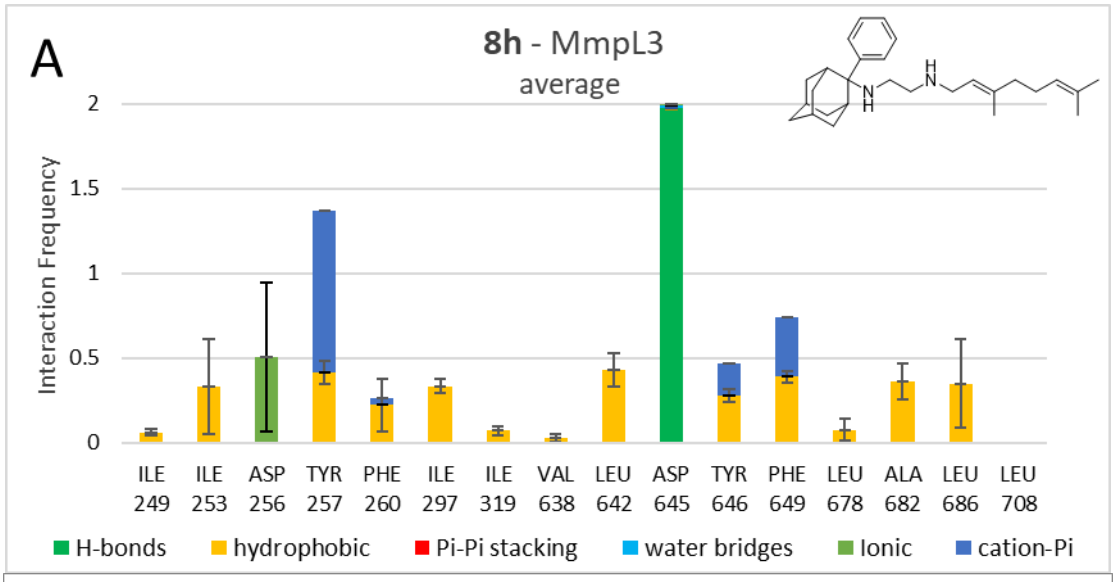
A
8h - MmpL3
average
Interaction Frequency
2
1.5
1
0.5
0
ILE 249
ILE 253
ASP 256
TYR 257
PHE 260
ILE 297
ILE 319
VAL 638
LEU 642
ASP 645
TYR 646
PHE 649
LEU 678
ALA 682
LEU 686
LEU 708
H-bonds
hydrophobic
Pi-Pi stacking
water bridges
Ionic
cation-Pi

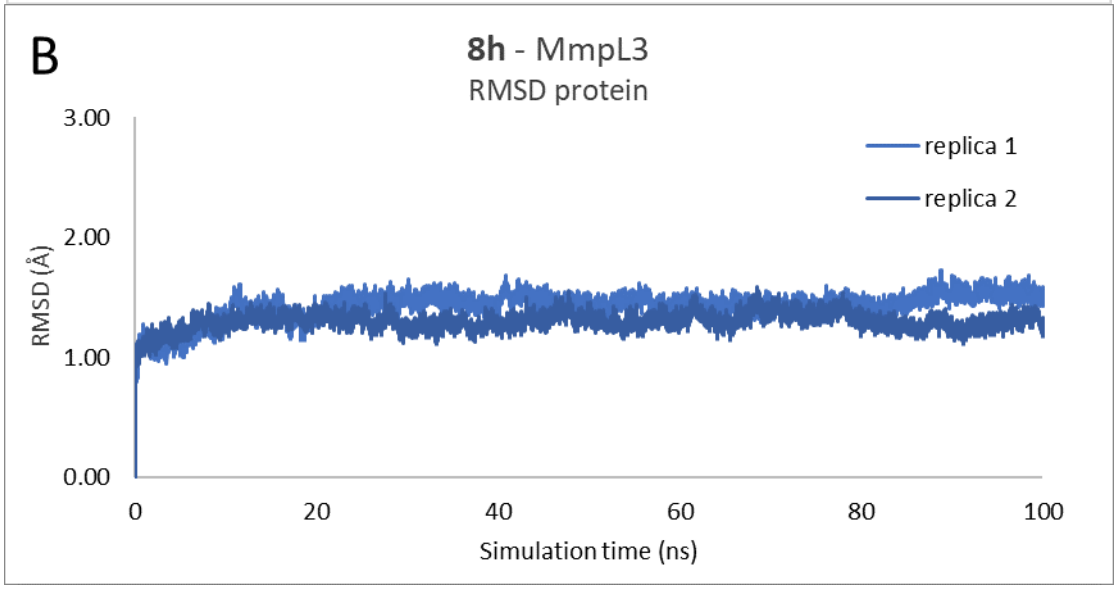
B
8h - MmpL3
RMSD protein
RMSD (Å)
3.00
2.00
1.00
0.00
0
20
40
60
80
100
Simulation time (ns)
replica 1
replica 2

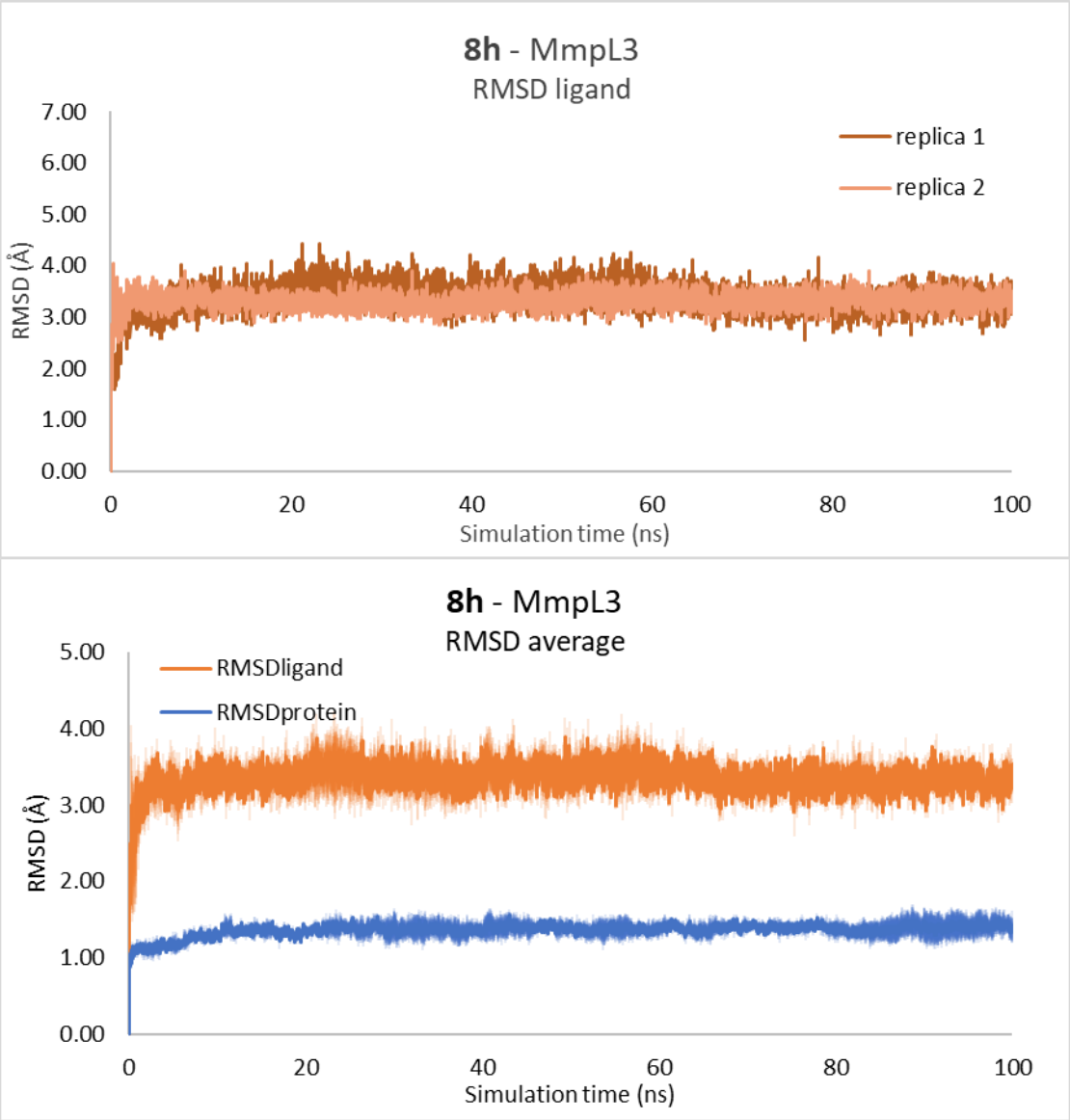

Figure S3 (contd.). MD simulation results of two replicas for MmpL3 with **8h**.

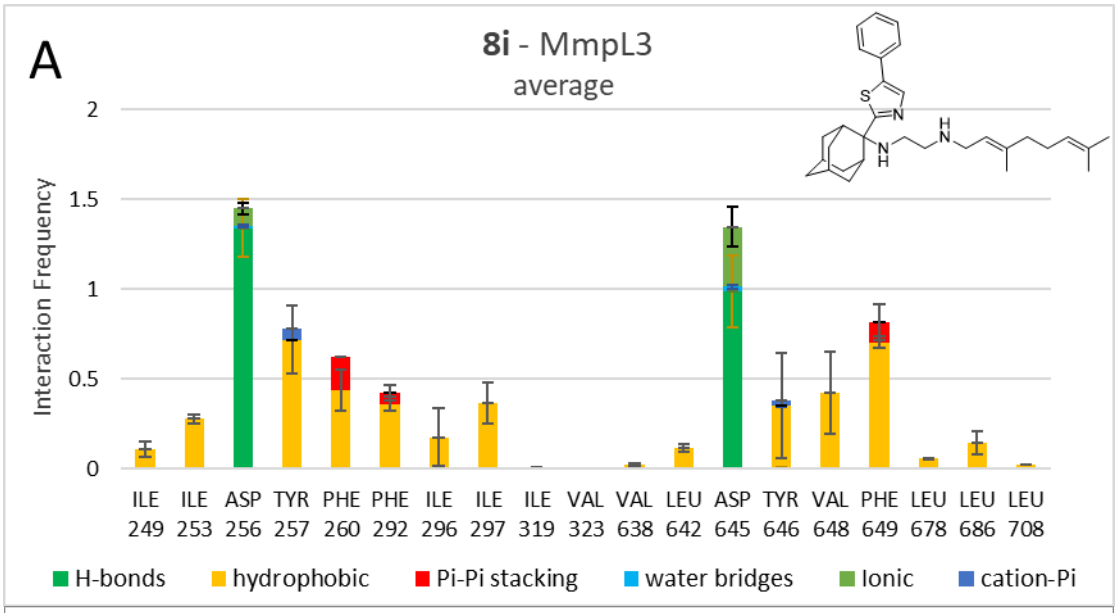
A
8i - MmpL3
average
Interaction Frequency
2
1.5
1
0.5
0
ILE 249
ILE 253
ASP 256
TYR 257
PHE 260
PHE 292
ILE 296
ILE 297
ILE 319
VAL 323
VAL 638
LEU 642
ASP 645
TYR 646
VAL 648
PHE 649
LEU 678
LEU 686
LEU 708
H-bonds
hydrophobic
Pi-Pi stacking
water bridges
Ionic
cation-Pi

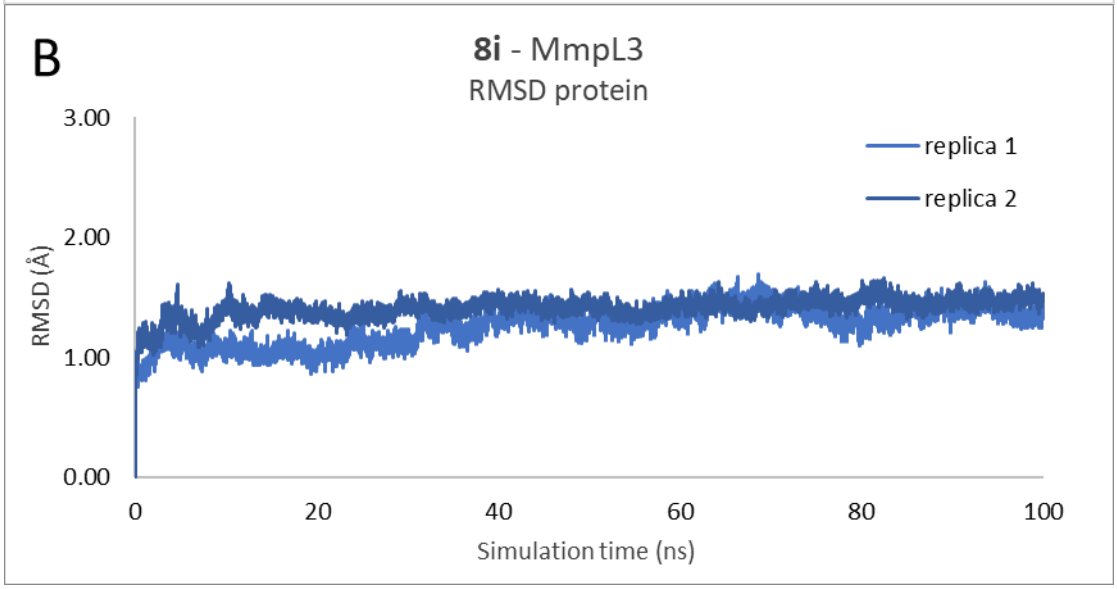
B
8i - MmpL3
RMSD protein
RMSD (Å)
3.00
2.00
1.00
0.00
0
20
40
60
80
100
Simulation time (ns)
replica 1
replica 2

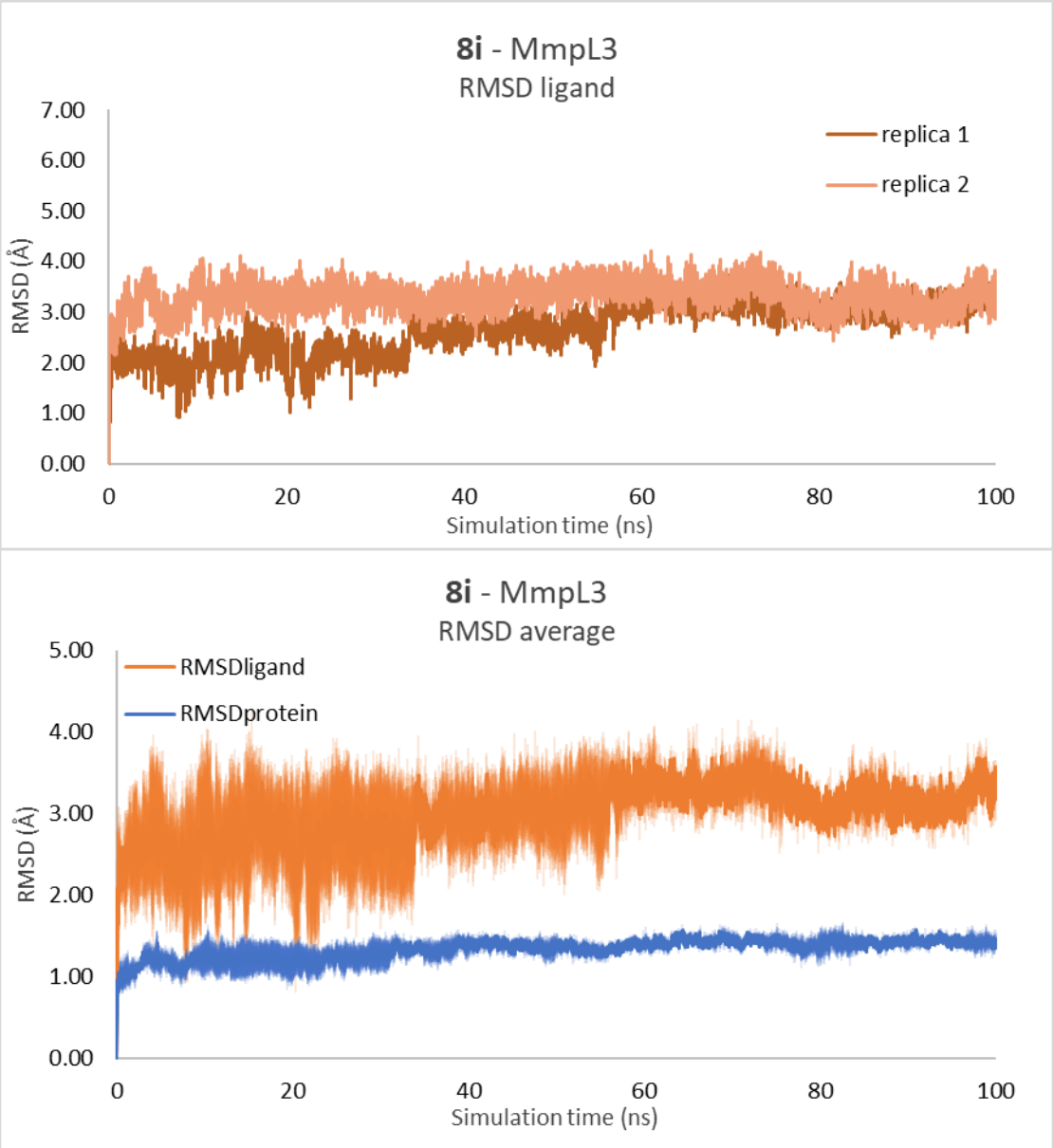

Figure S3 (contd.). MD simulation results of two replicas for MmpL3 with **8i**.

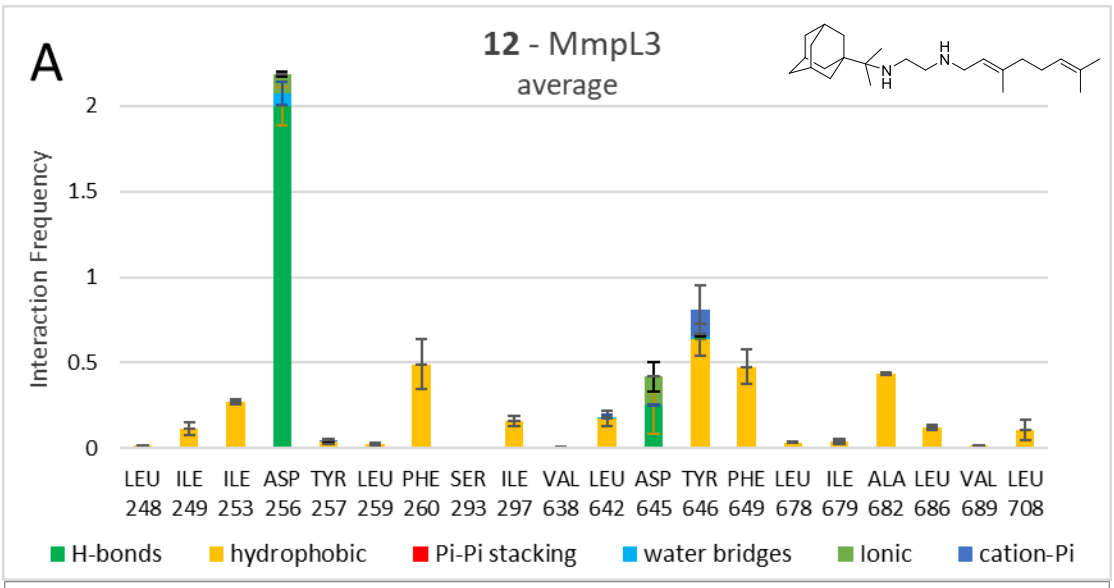
A
12 - MmpL3
average
Interaction Frequency
2
1.5
1
0.5
0
LEU 248
ILE 249
ILE 253
ASP 256
TYR 257
LEU 259
PHE 260
SER 293
ILE 297
VAL 638
LEU 642
ASP 645
TYR 646
PHE 649
LEU 678
ILE 679
ALA 682
LEU 686
VAL 689
LEU 708
H-bonds
hydrophobic
Pi-Pi stacking
water bridges
Ionic
cation-Pi

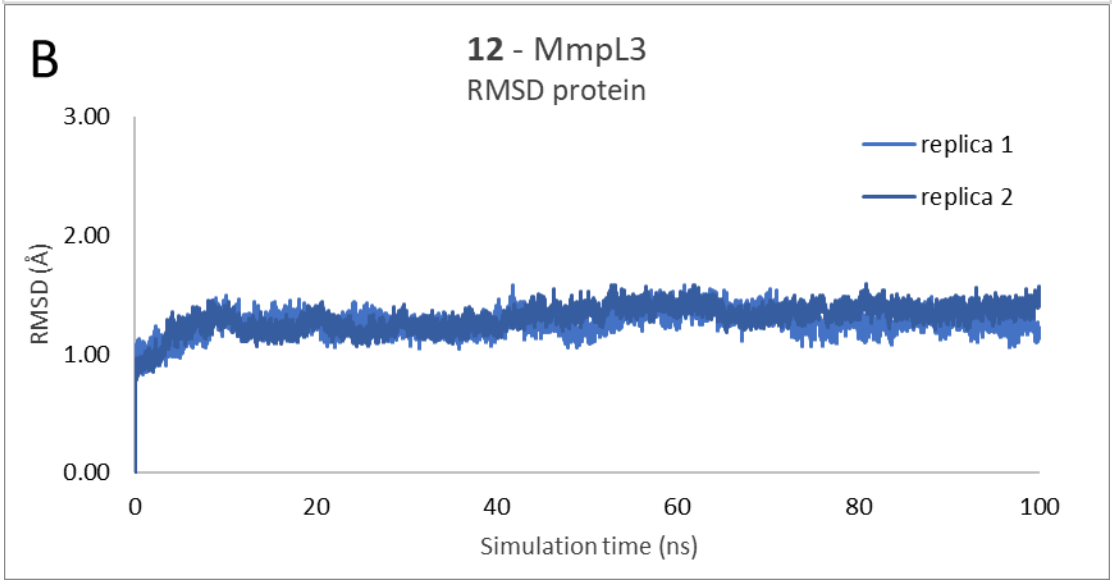
B
12 - MmpL3
RMSD protein
3.00
2.00
1.00
0.00
RMSD (Å)
replica 1
replica 2
0
20
40
60
80
100
Simulation time (ns)

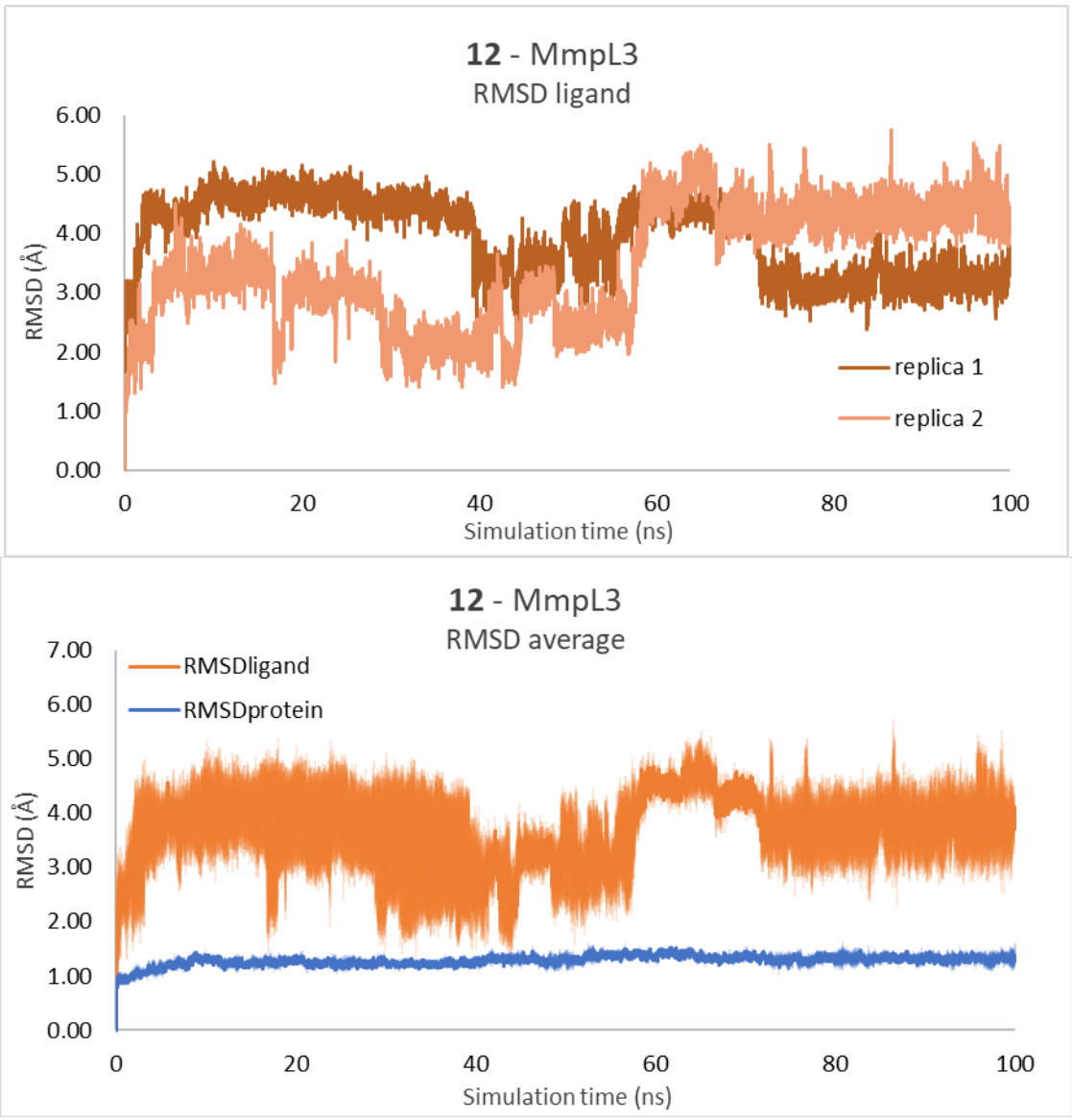

Figure S3 (contd.). MD simulation results of two replicas for MmpL3 with **12**.

500ns MD simulations plots of the monoprotonated ethylenediamine forms of SQ109 analogs in complex with MmpL3

Figure S4. In panels (A) for **8a**, **f**, **g**, **i** are shown the chemical structures of the ligands and the receptor-ligand interaction frequency histograms recorded from the 500 ns MD simulation trajectories of SQ109 analogues (monoprotonated ethylenediamine form) in complex with MmpL3. Hydrogen bonding interaction bar are depicted in green, Van der Waals in yellow, cation-pi in blue, pi-pi stacking in red, water bridges in light blue and ionic in light green. (B) The RMSD plots for the Ca carbons (blue) of transmembrane helices and the ligand heavy atoms (orange). For the protein, the experimental structure

of SQ109 in complex with MmpL3 (PDB ID 6AJG) was used as the starting structure for the MD simulations after excluding C-terminus, consisting of M1-E749 residues. The transmembrane region included the following helices and their residues: TM1 (14-33), TM2 (174-199), TM3 (208-224), TM4 (238-264), TM5 (271-301), TM6 (306-338), TM7 (396-415), TM8 (552-576), TM9 (583-601), TM10 (625-648), TM11 (660-690), TM12 (697-728).

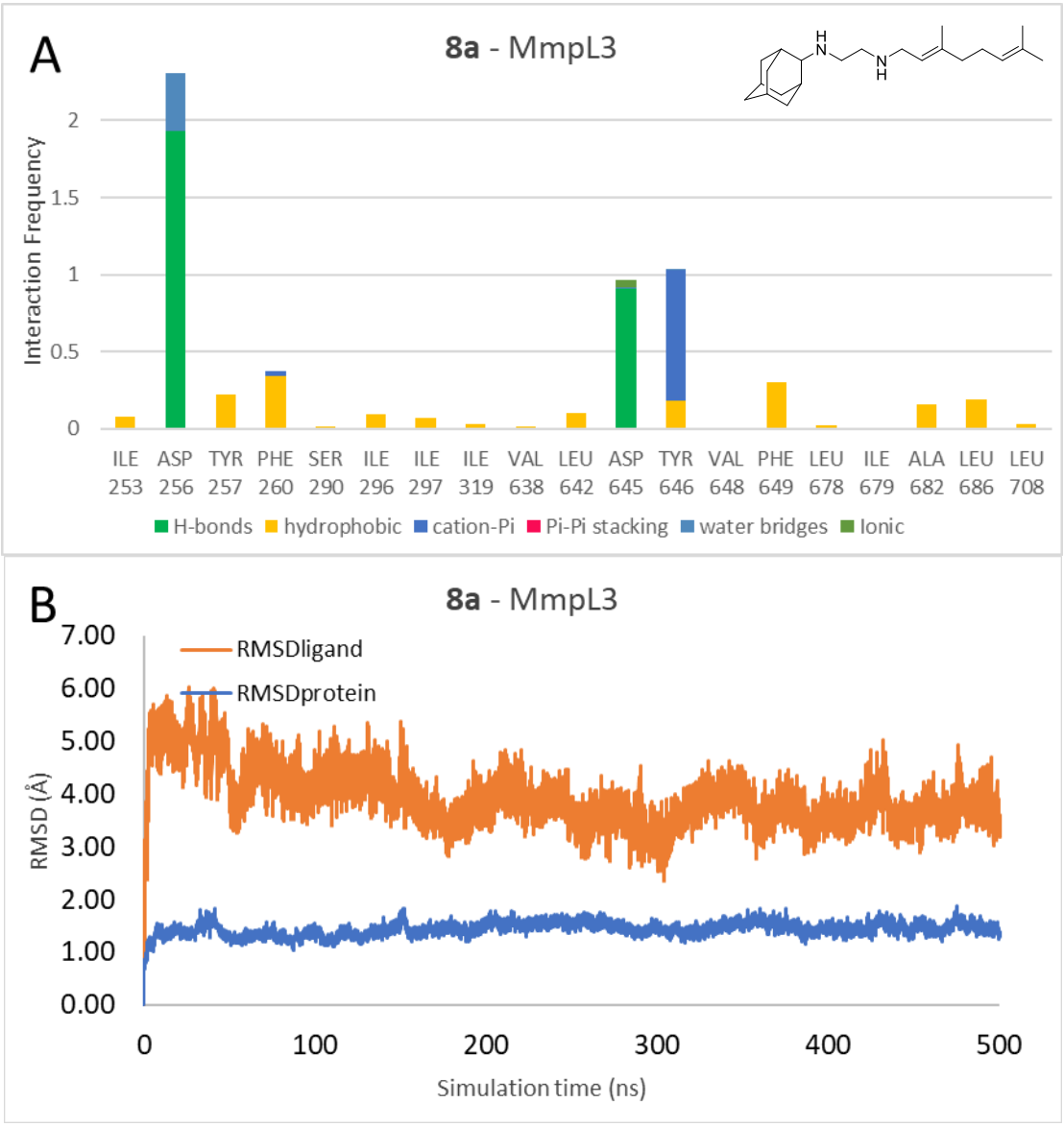

Figure S4 MD simulation results for MmpL3 with **8a**.

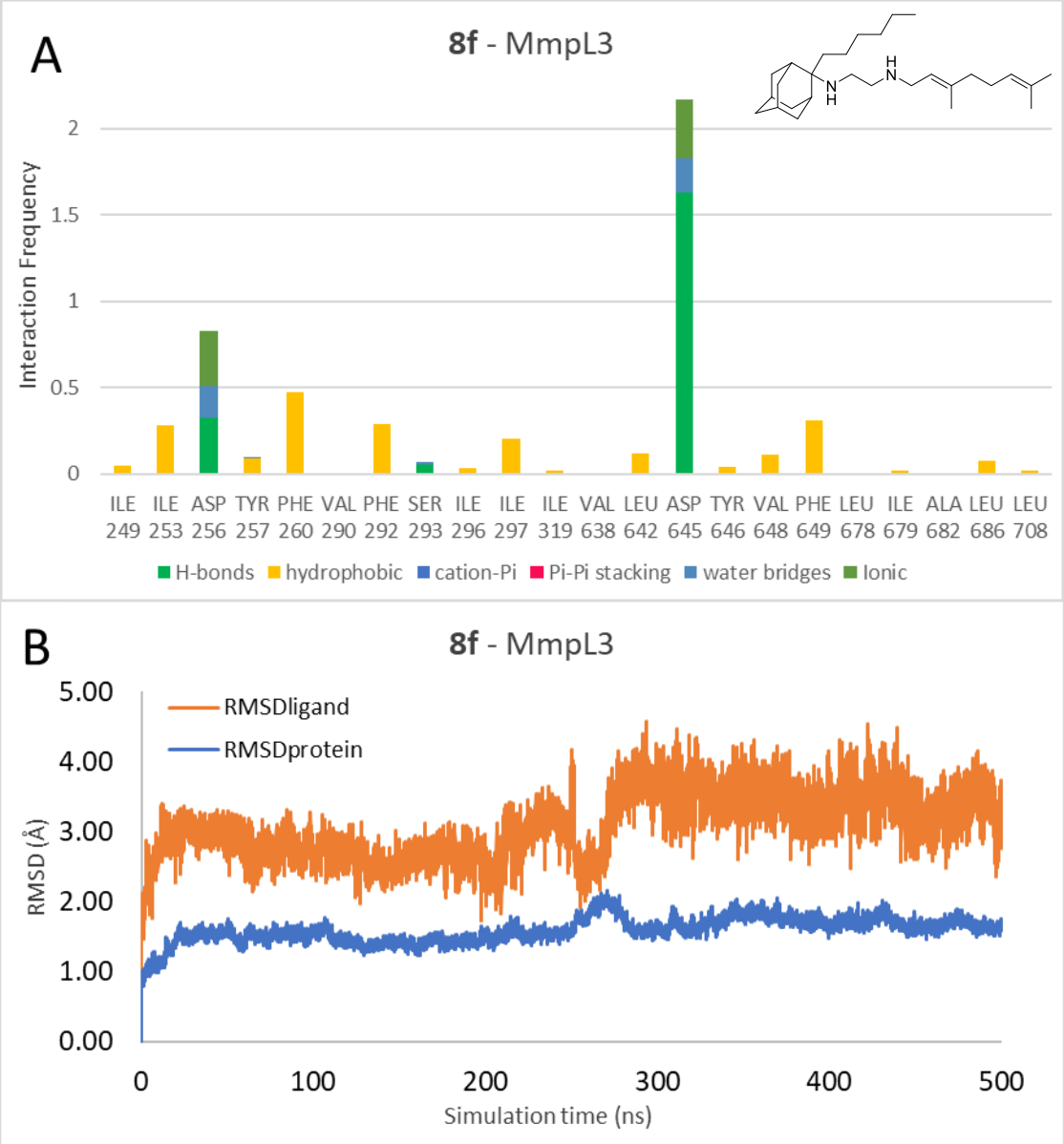

Figure S4 (contd.). MD simulation results for MmpL3 with **8f**.

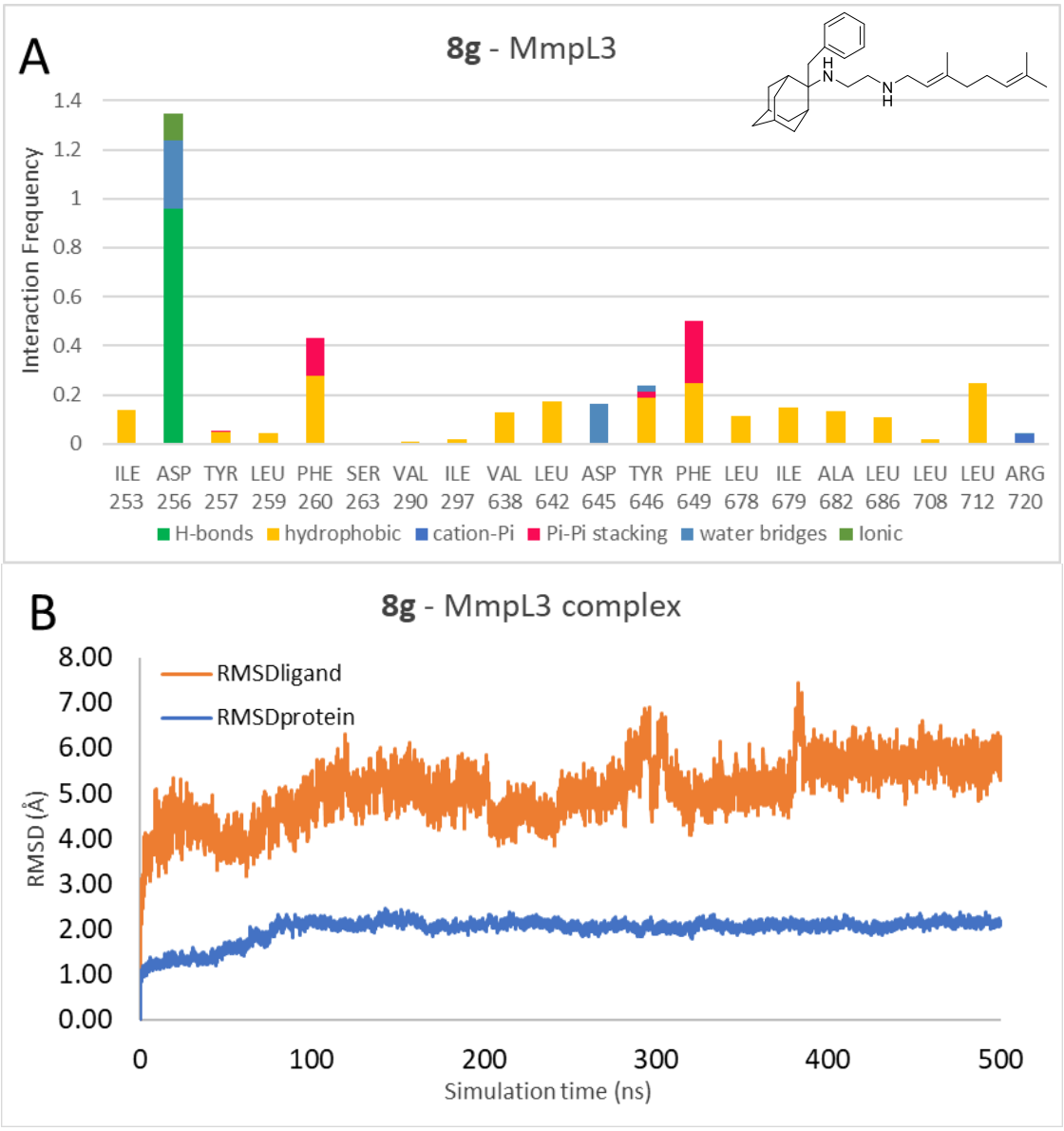

Figure S4 (contd.). MD simulation results for MmpL3 with **8g**.

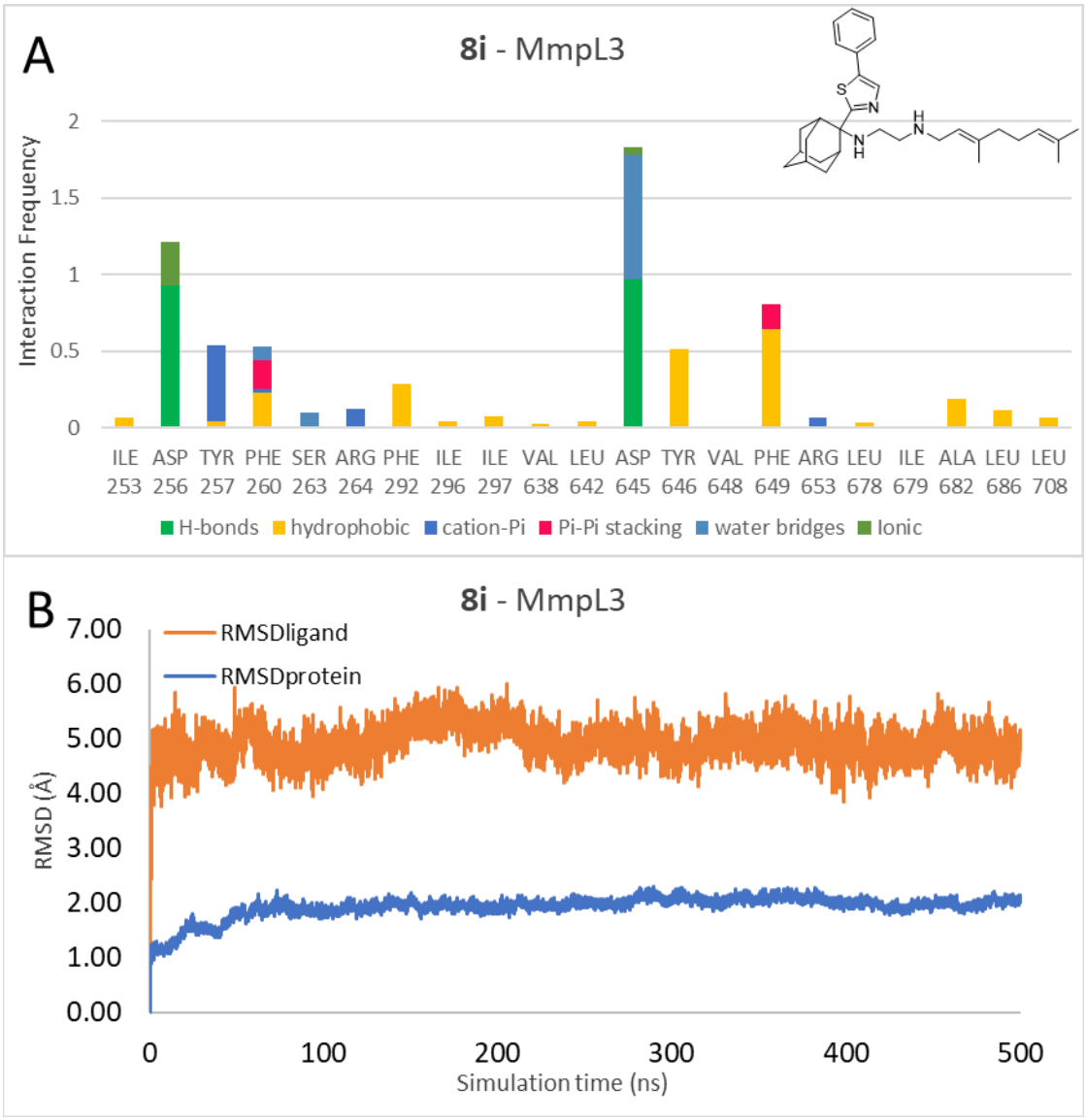

Figure S4 (contd.). MD simulation results for MmpL3 with **8i**.

500ns MD simulations plots of residues that interact with ligand amine groups

Figure S5. The RMSD plots for the sum of Ca carbons of residues Asp256, Asp645, Tyr257, Tyr646, Phe260, Phe649. For the protein, the experimental structure of SQ109 in complex with MmpL3 (PDB ID 6AJG) was used as the starting structure for the MD simulations after excluding C-terminus, consisting of M1-E749 residues.

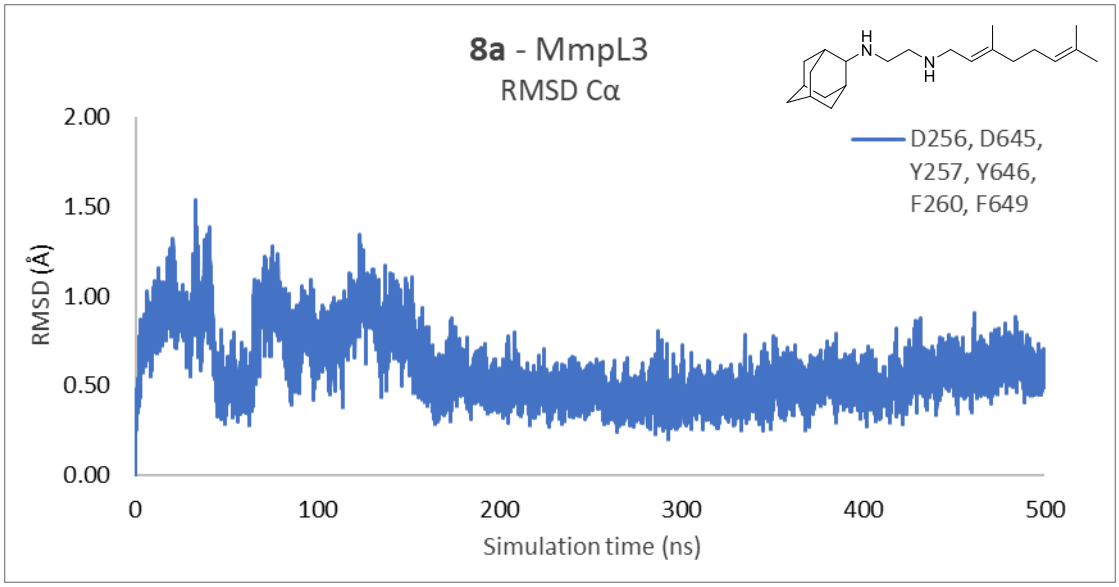

Figure S5 MD simulation results for MmpL3 with **8a**.

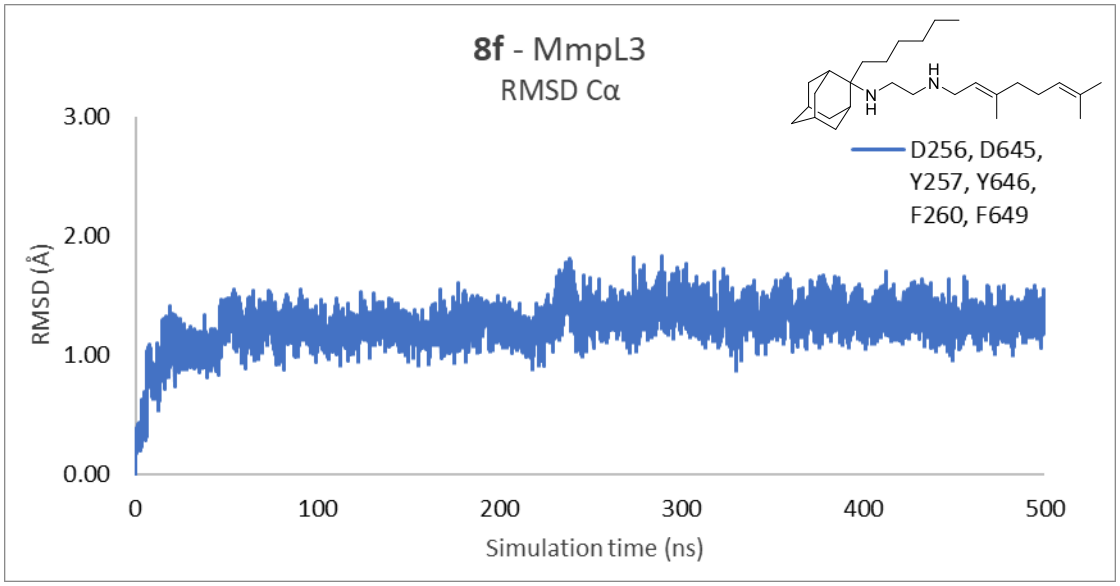

Figure S5 (contd.). MD simulation results for MmpL3 with **8f**.

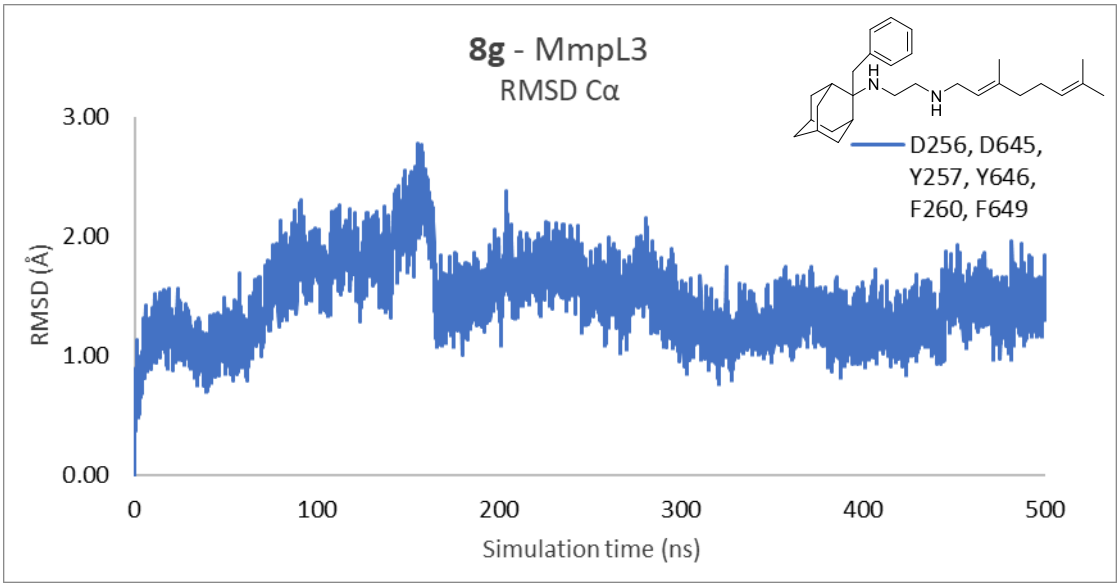

Figure S5 (contd.). MD simulation results for MmpL3 with **8g**.

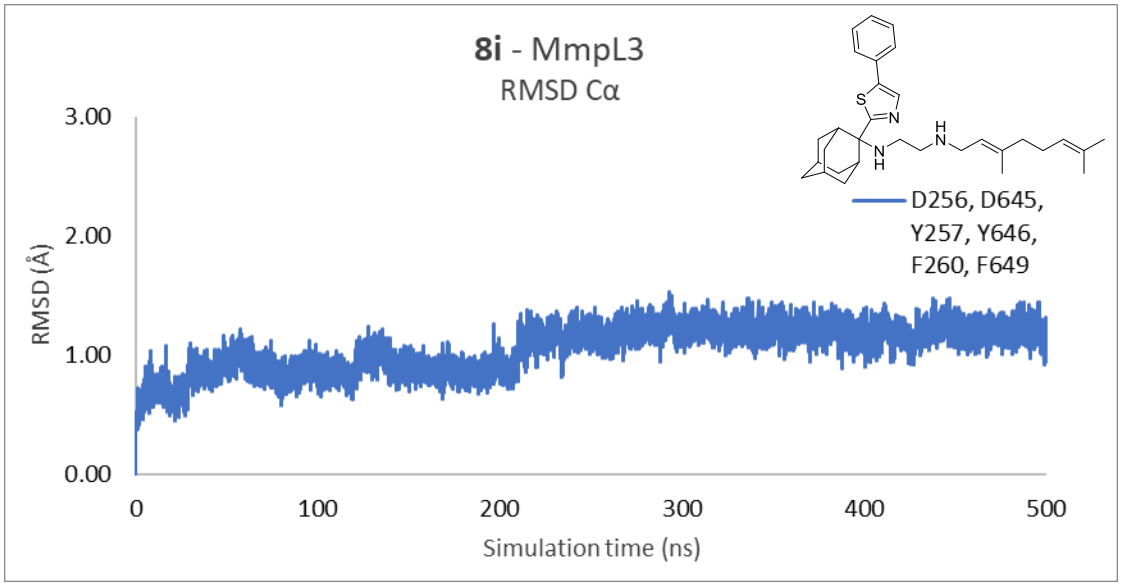

Figure S5 (contd.). MD simulation results for MmpL3 with **8i**.

Dose-response curves of SQ109 and analogs against protozoan parasites

T. cruzi

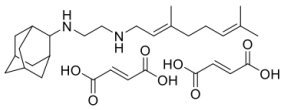

8a

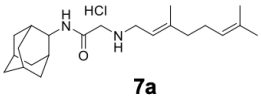

7a

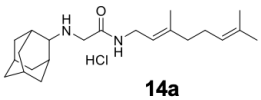

14a

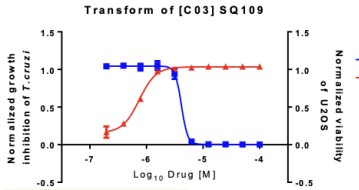

CC_{50}(U2OS) = 4.14 µM
EC_{50}(PAR) = 0.744 µM

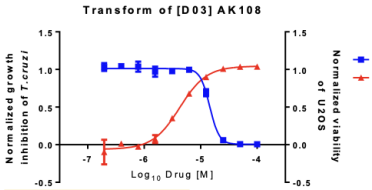

CC_{50}(U2OS) = 14.4 µM
EC_{50}(PAR) = 4.24 µM

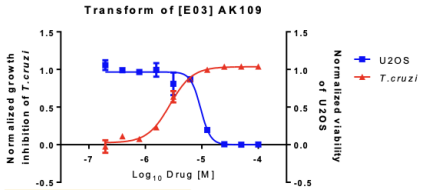

CC_{50}(U2OS) = 9.51 µM
EC_{50}(PAR) = 2.72 µM

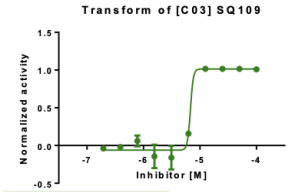

EC_{50}(EPI) = 6.77 µM

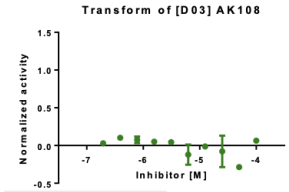

EC_{50}(EPI) > 100 µM

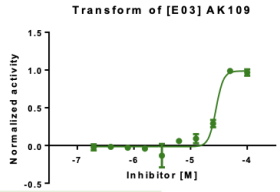

EC_{50}(EPI) = 28.2 µM

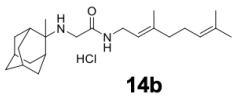

14b

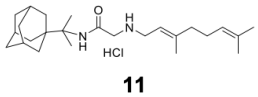

11

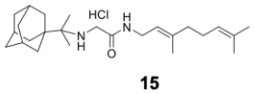

15

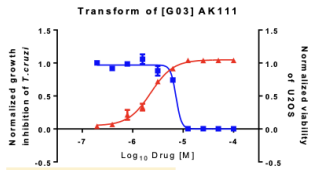

CC_{50}(U2OS) = 7.22 µM
EC_{50}(PAR) = 2.27 µM

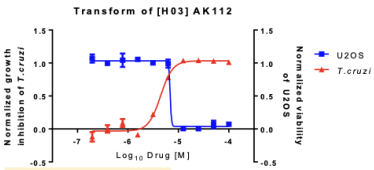

CC_{50}(U2OS) = 6.86 µM
EC_{50}(PAR) = 4.43 µM

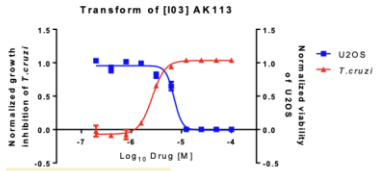

CC_{50}(U2OS) = 7.12 µM
EC_{50}(PAR) = 2.59 µM

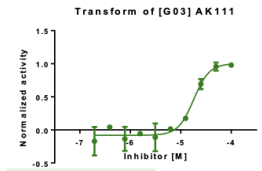

EC_{50}(EPI) = 18.0 µM

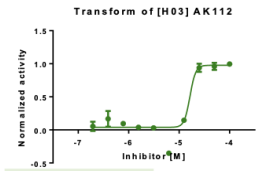

EC_{50}(EPI) = 16.4 µM

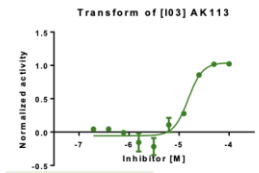

EC_{50}(EPI) = 15.2 µM

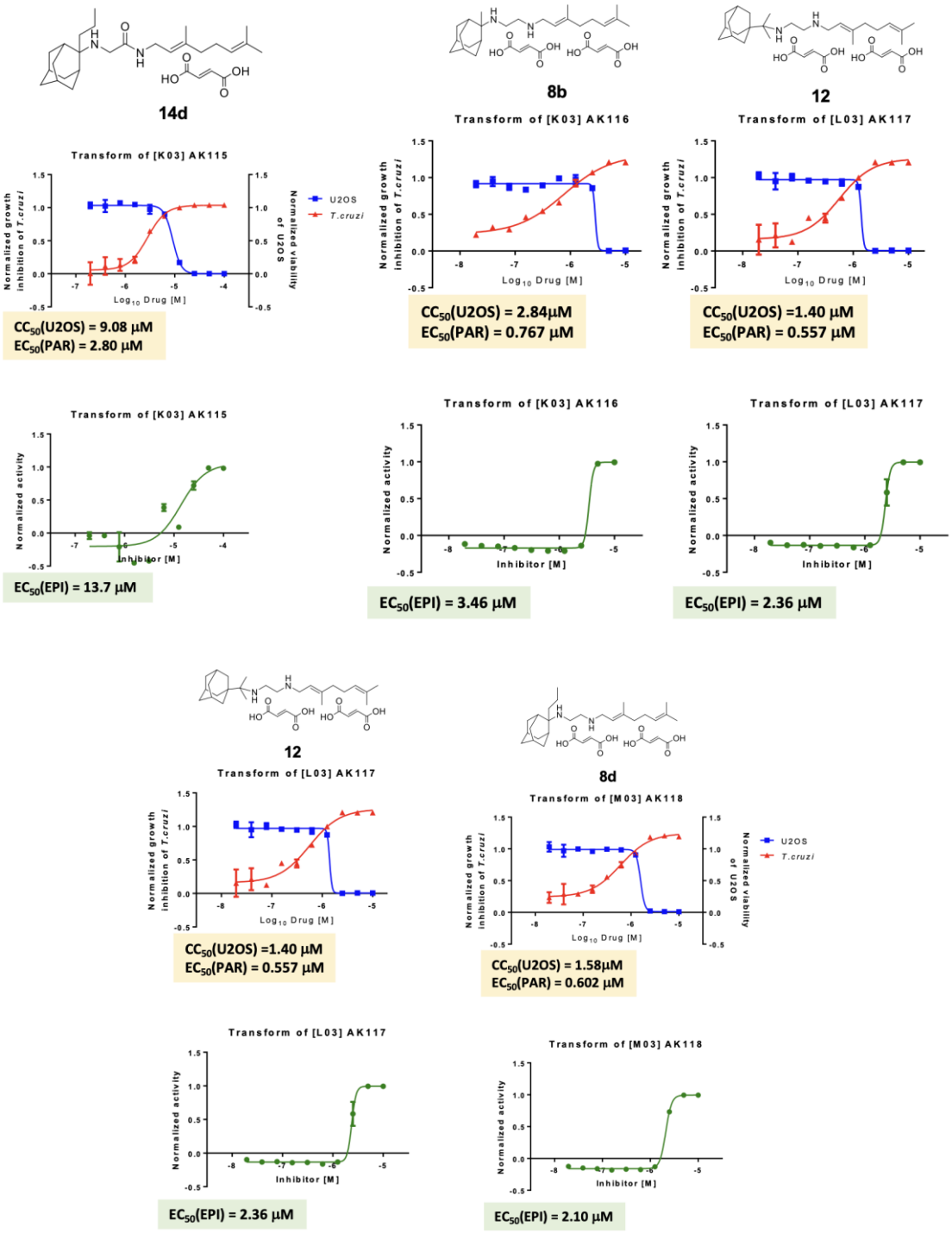

Figure S6 Representative dose-response curves of SQ109 analogs against protozoan parasites.

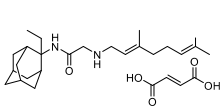

7c

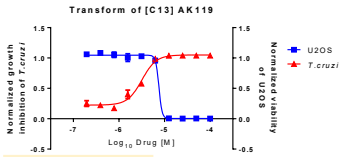

CC_{50}(U2OS) = 7.53 ɷM
EC_{50}(PAR) = 3.18 ɷM

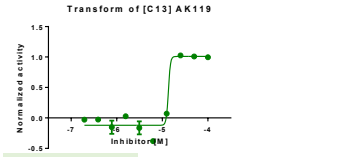

EC_{50}(EPI) = 13.5 ɷM

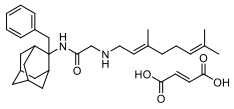

7g

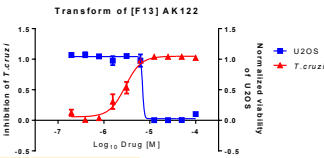

CC_{50}(U2OS) = 6.97 ɷM
EC_{50}(PAR) = 2.91 ɷM

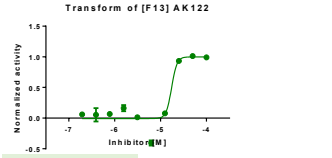

EC_{50}(EPI) = 17.4 ɷM

7e

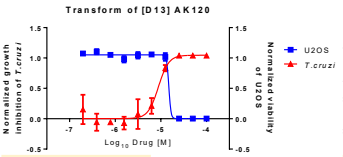

CC_{50}(U2OS) = 14.9 ɷM
EC_{50}(PAR) = 8.82 ɷM

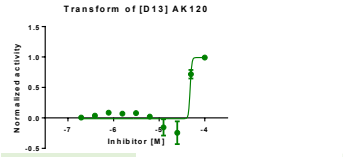

EC_{50}(EPI) = 48.0 ɷM

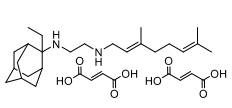

8c

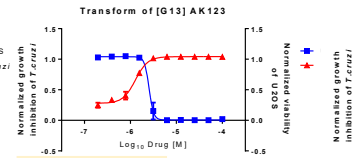

CC_{50}(U2OS) = 2.54 ɷM
EC_{50}(PAR) = 1.28 ɷM

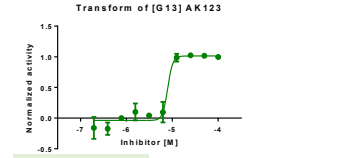

EC_{50}(EPI) = 7.95 ɷM

7h

CC_{50}(U2OS) = 7.04 ɷM
EC_{50}(PAR) = 3.37 ɷM

EC_{50}(EPI) = 18.0 ɷM

8e

CC_{50}(U2OS) = 1.70 ɷM
EC_{50}(PAR) = 0.838 ɷM

EC_{50}(EPI) = 2.45 ɷM

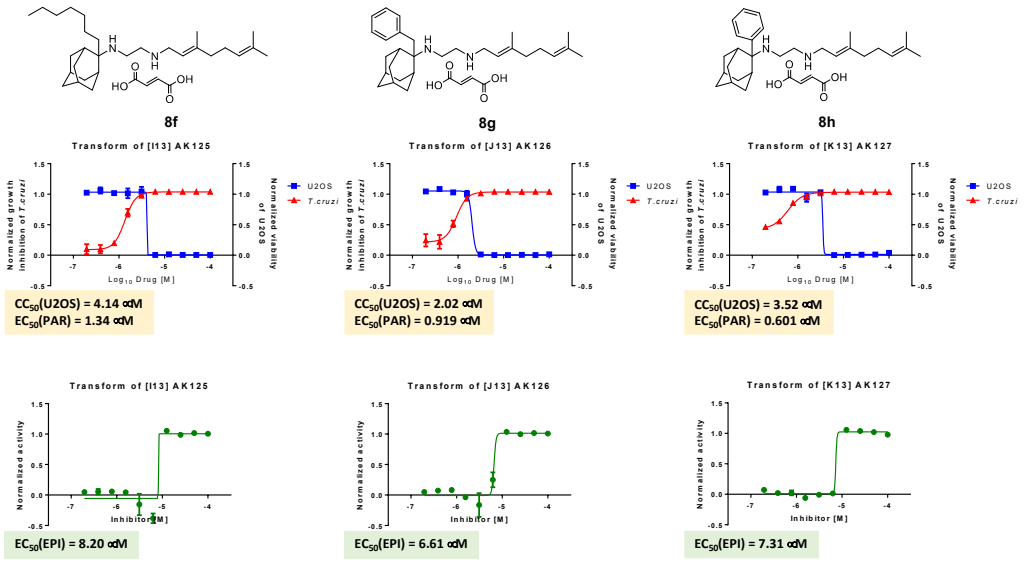

Figure S6 (contd.). Representative dose-response curves of SQ109 analogs against protozoan parasites.

L. donovani

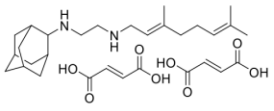

8a

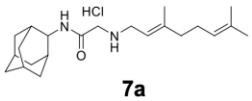

7a

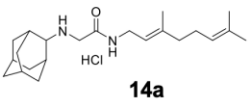

14a

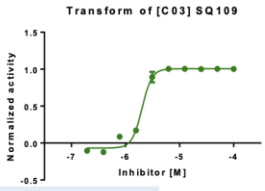

EC_{50}(PRO) = 2.01 µM

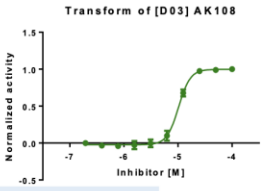

EC_{50}(PRO) = 10.2 µM

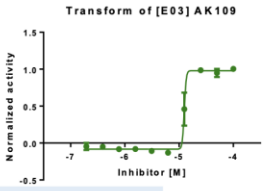

EC_{50}(PRO) = 12.4 µM

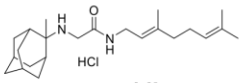

14b

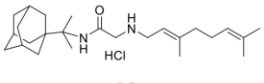

11

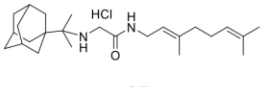

15

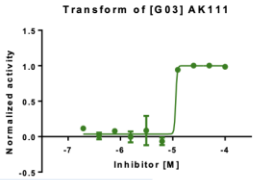

EC_{50}(PRO) = 11.4 µM

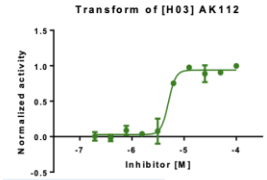

EC_{50}(PRO) = 5.00 µM

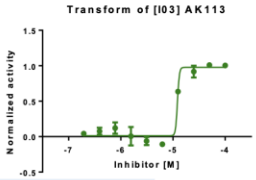

EC_{50}(PRO) = 12.2 µM

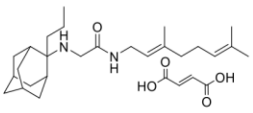

14d

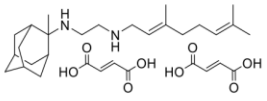

8b

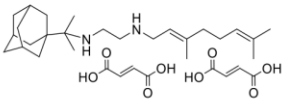

12

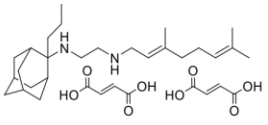

8d

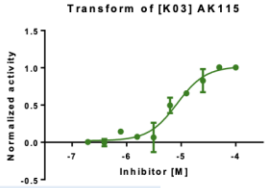

EC_{50}(PRO) = 8.42 µM

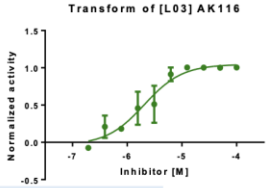

EC_{50}(PRO) = 2.04 µM

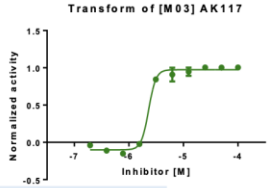

EC_{50}(PRO) = 2.30 µM

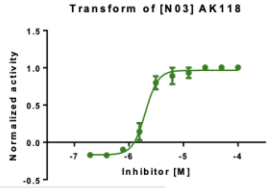

EC_{50}(PRO) = 2.00 µM

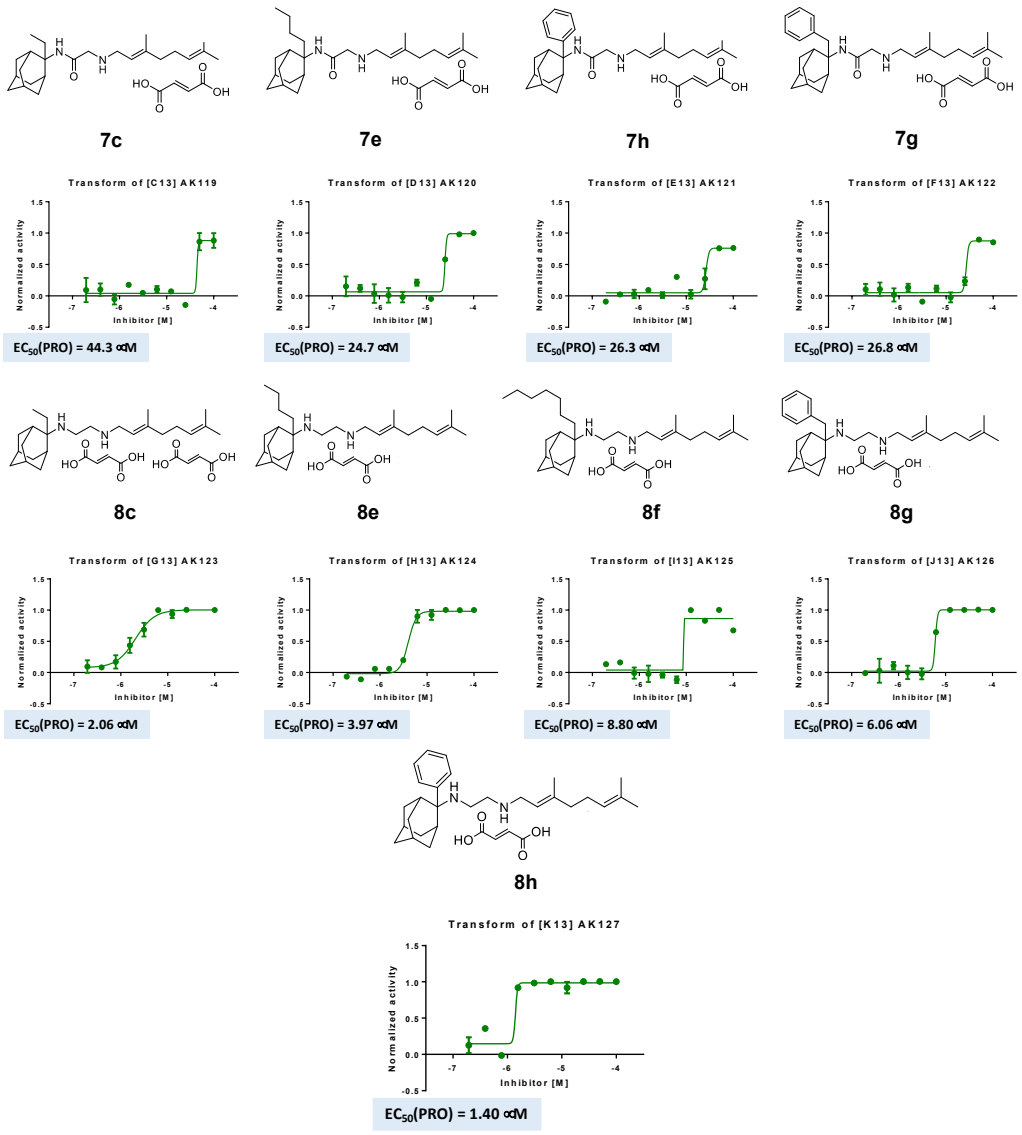

Figure S6 (contd.). Representative dose-response curves of SQ109 analogs against protozoan parasites.

T. brucei

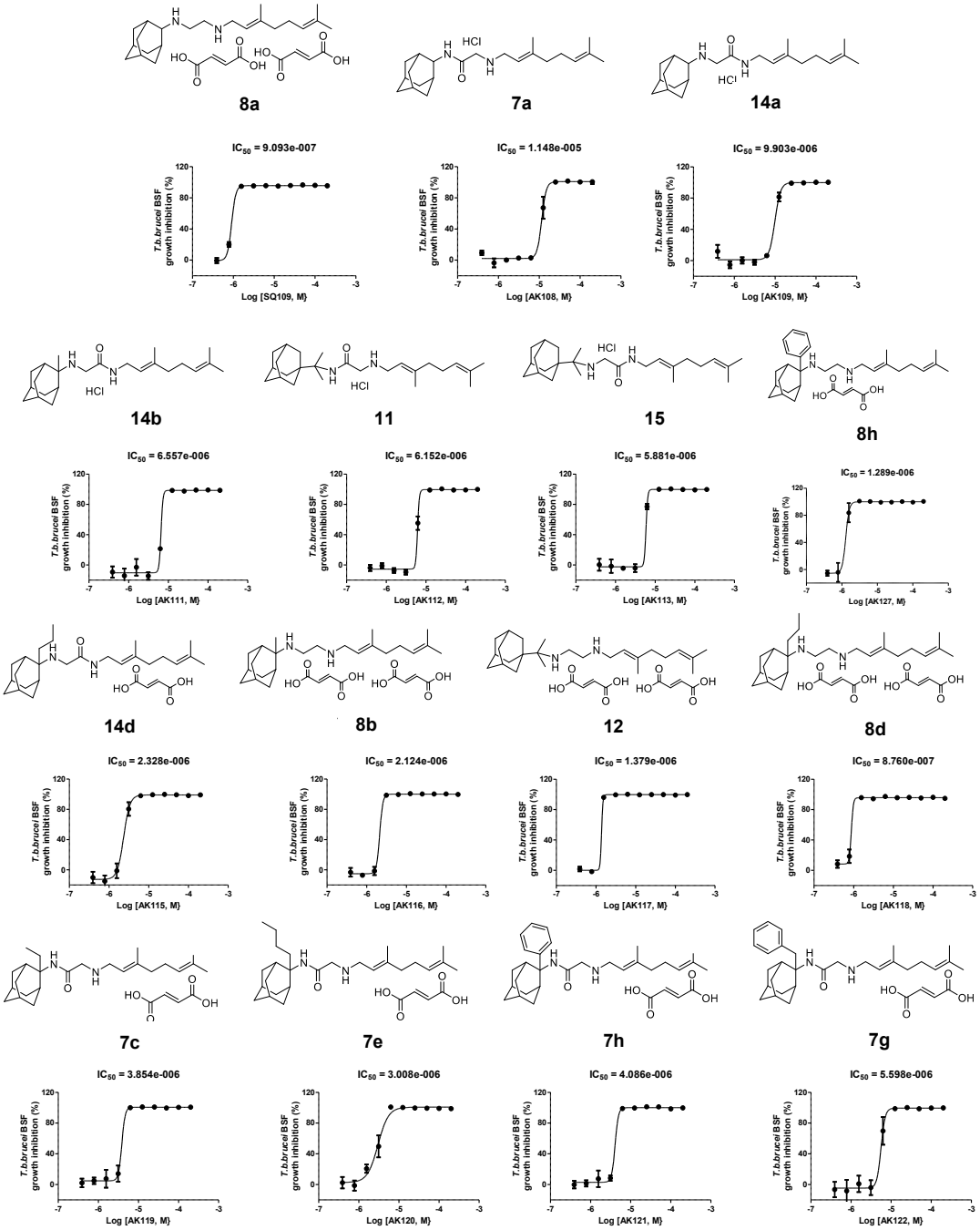
8a
7a
14a
IC50 = 9.093e-007
IC50 = 1.148e-005
IC50 = 9.903e-006
T.b.brucei BSF growth inhibition (%)
Log [SQ109, M}
Log [AK108, M}
Log [AK109, M}
14b
11
15
8h
IC50 = 6.557e-006
IC50 = 6.152e-006
IC50 = 5.881e-006
IC50 = 1.289e-006
Log [AK111, M}
Log [AK112, M}
Log [AK113, M}
Log [AK127, M}
14d
8b
12
8d
IC50 = 2.328e-006
IC50 = 2.124e-006
IC50 = 1.379e-006
IC50 = 8.760e-007
Log [AK115, M}
Log [AK116, M}
Log [AK117, M}
Log [AK118, M}
7c
7e
7h
7g
IC50 = 3.854e-006
IC50 = 3.008e-006
IC50 = 4.086e-006
IC50 = 5.598e-006
Log [AK119, M}
Log [AK120, M}
Log [AK121, M}
Log [AK122, M}

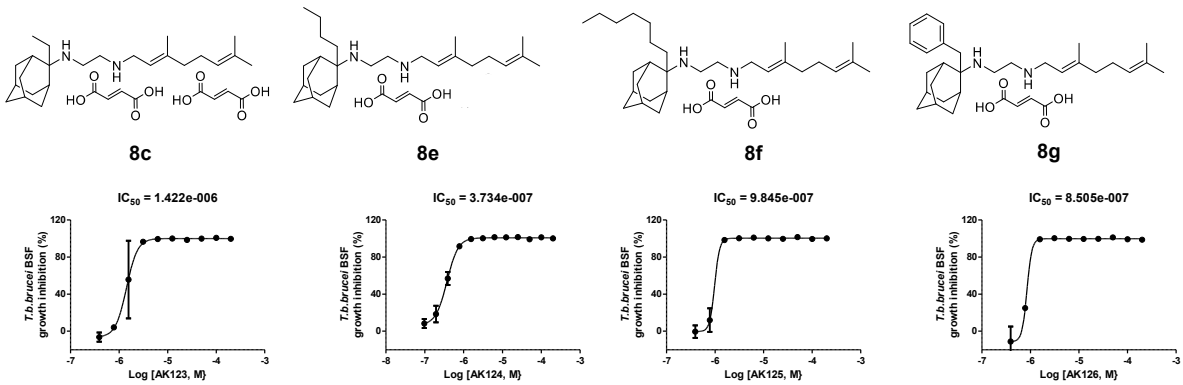

Figure S6 (contd.). Representative dose-response curves of SQ109 analogs against protozoan parasites.

SPR curves for SQ109 analogs (two-state model).

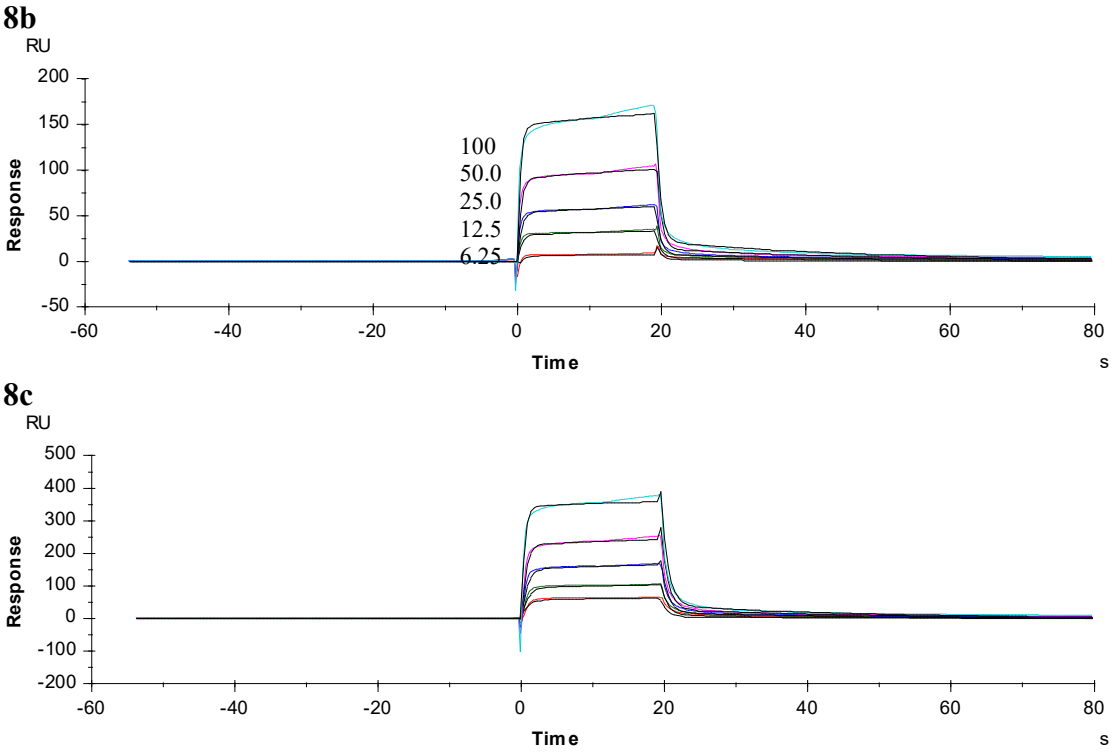

8d

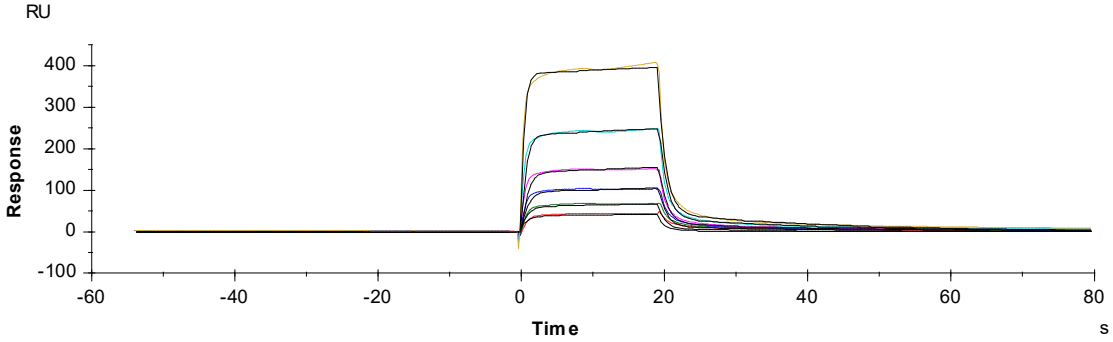
RU
400
300
200
100
0
-100
Response
-60
-40
-20
0
20
40
60
80
Time
s

8e

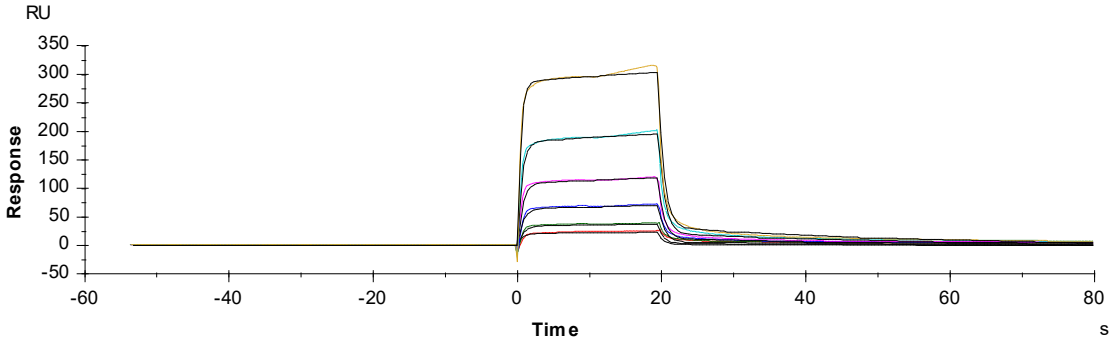
RU
350
300
250
200
150
100
50
0
-50
Response
-60
-40
-20
0
20
40
60
80
Time
s

8f

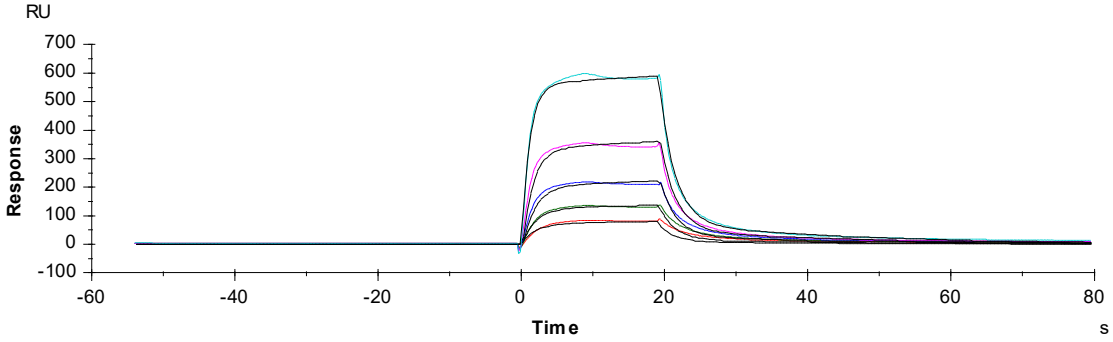
RU
700
600
500
400
300
200
100
0
-100
Response
-60
-40
-20
0
20
40
60
80
Time
s

8g

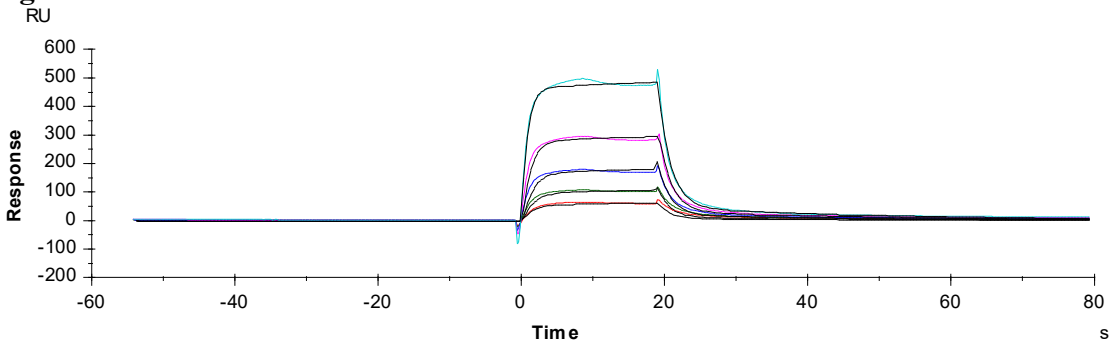
RU
600
500
400
300
200
100
0
-100
-200
Response
-60
-40
-20
0
20
40
60
80
Time
s

8h

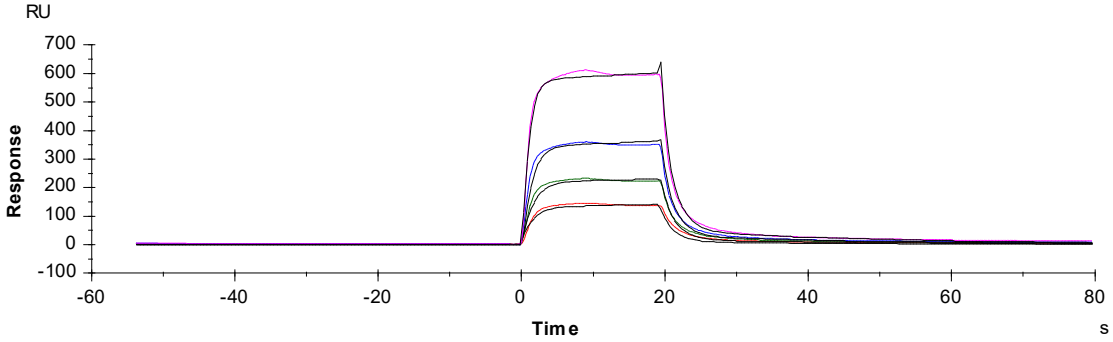
RU
700
600
500
400
300
200
100
0
-100
Response
-60
-40
-20
0
20
40
60
80
Time
s

12

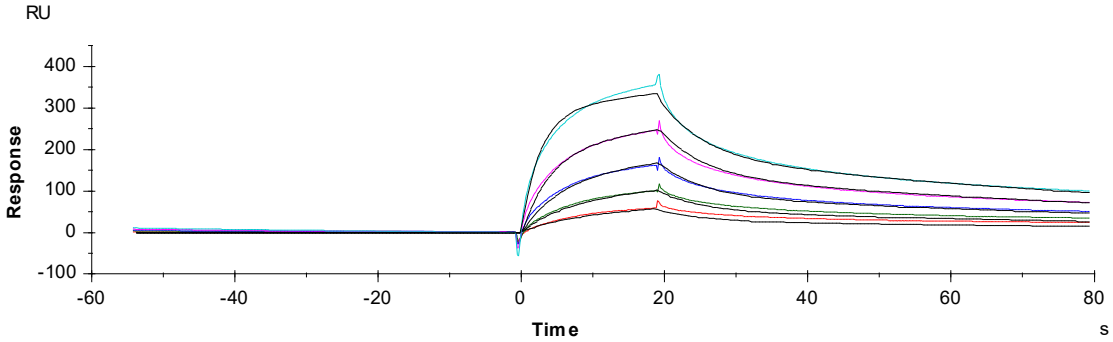
RU
400
300
200
100
0
-100
Response
-60
-40
-20
0
20
40
60
80
Time
s

8i

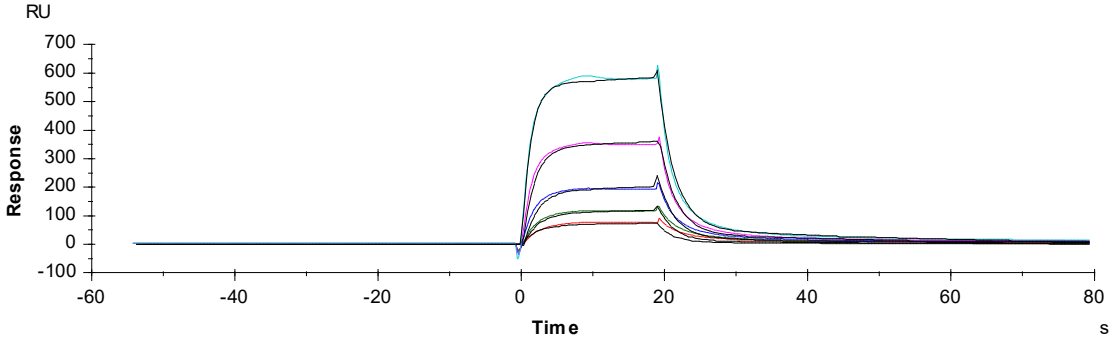
RU
700
600
500
400
300
200
100
0
-100
Response
-60
-40
-20
0
20
40
60
80
Time
s

7a

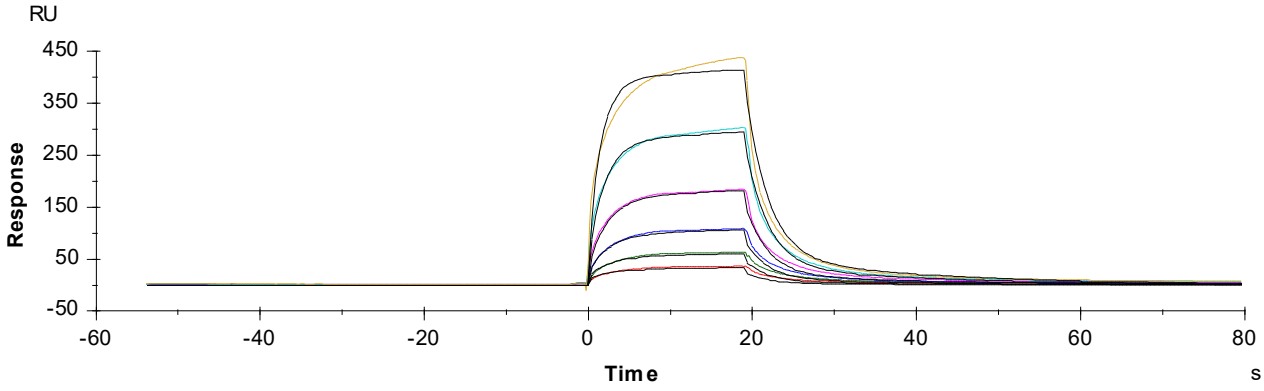
RU
450
350
250
150
50
-50
Response
-60
-40
-20
0
20
40
60
80
Time
s

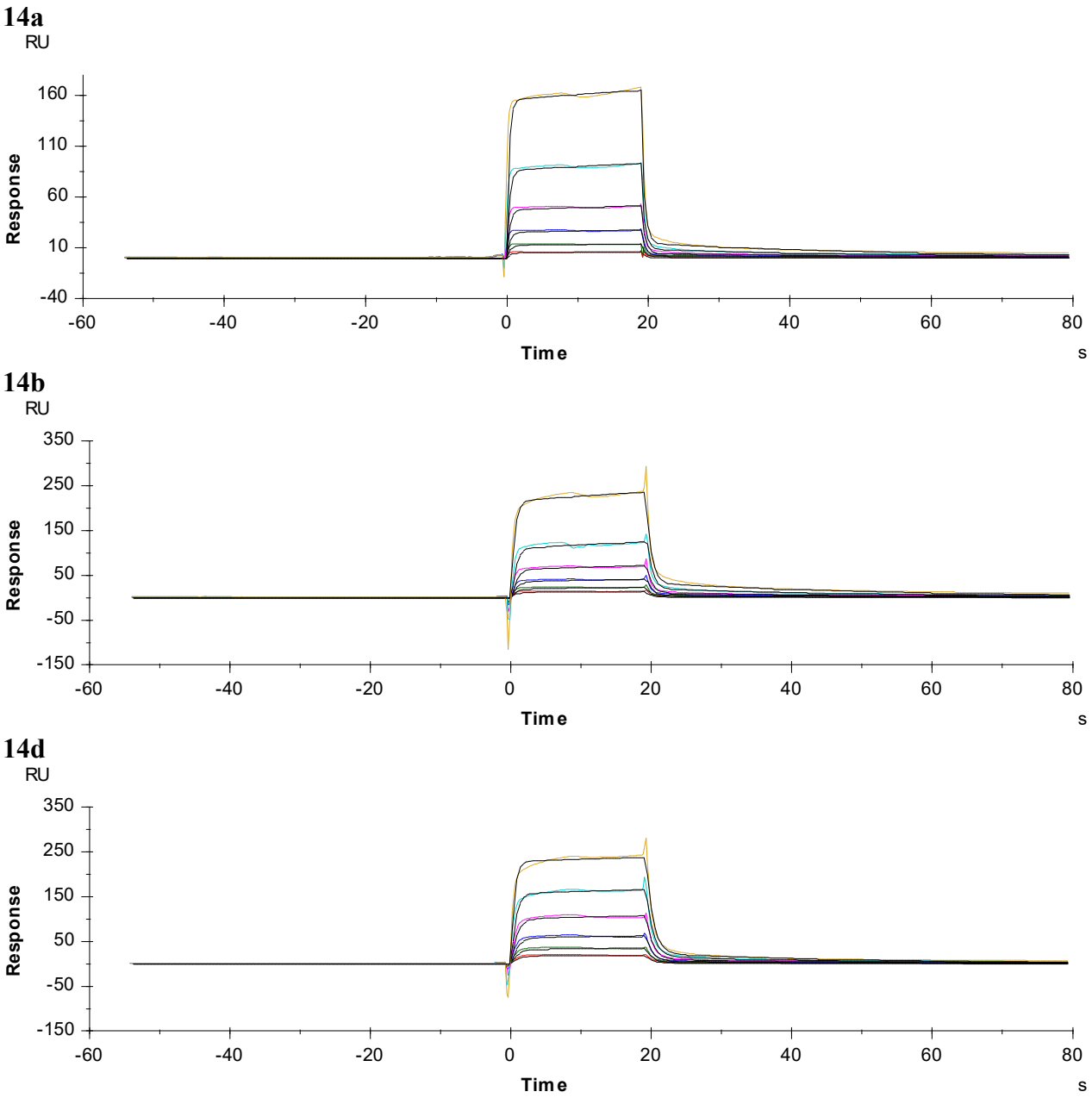

Figure S7 SPR sensorgrams for SQ109 analogs. Sensorgrams of up to six doubling concentrations (6.25 mM, 12.5 mM, 25.0 mM, 50.0 mM, 100.0 mM, 200.0 mM) of the indicated compounds are shown in different colors, with the lowest injected concentration 6.25 mM shown in red. The sensorgrams were fitted into several kinetic models. The best fits (black lines) were obtained with the Two-State Binding model, wherein conformational change occurs on the same time scale as ligand binding.

DSC cooling scans for DMPC/inhibitors.

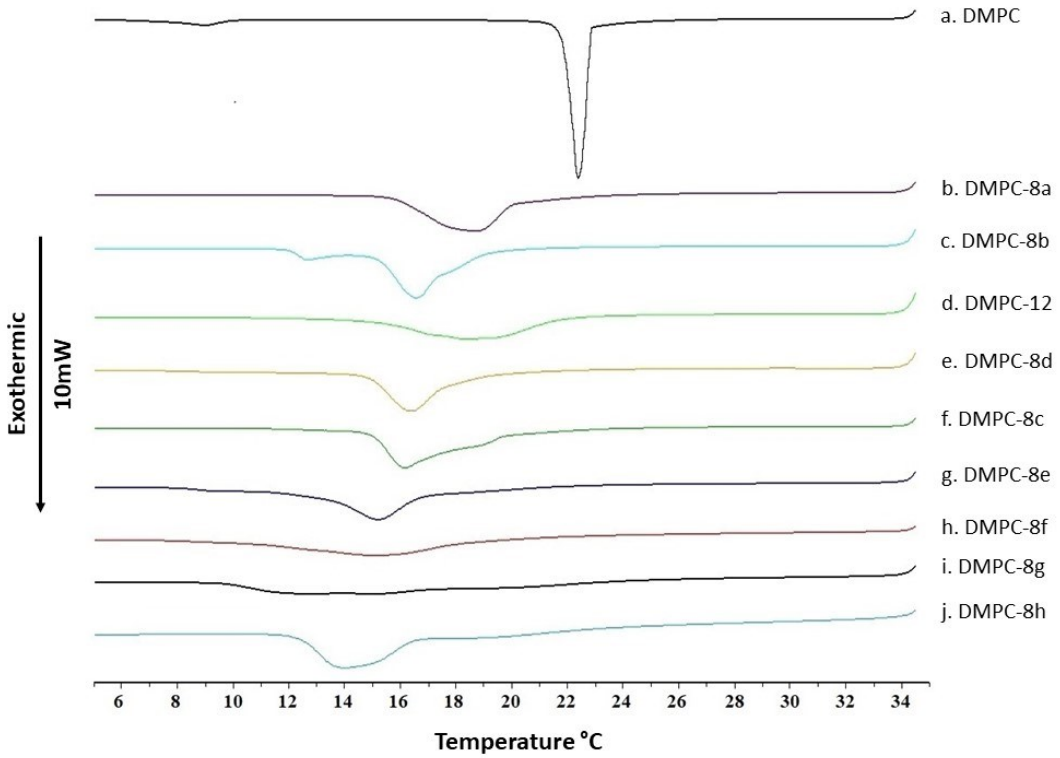

Figure S8 DSC cooling scans of (a) DMPC, (b) with SQ109 (**8a**), (c) with **8b**, (d) with **12**, (e) with **8d**, (f) with **8c**, (g) with **8e**, (h) with **8f**, (i) with **8g**, (j) with **8h**. All samples were hydrated with PBS (pH=7.4).

DSC cooling scans for DSPG/inhibitors.

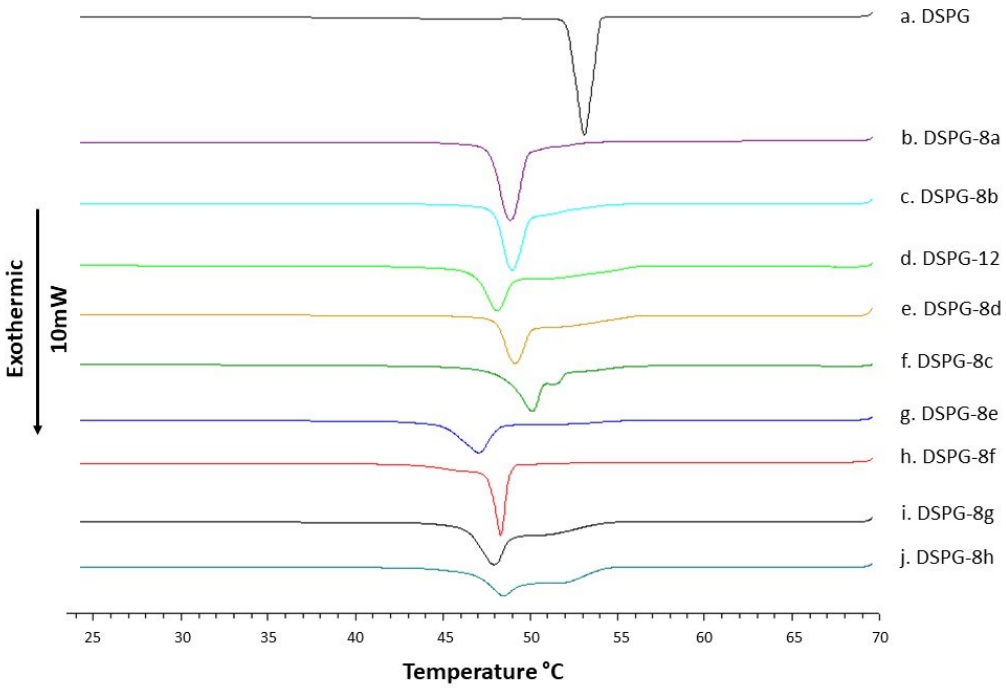

Figure S9 DSC cooling scans of (a) DSPG, (b) with SQ109 (**8a**), (c) with 8b, (d) with **12**, (e) with **8d**, (f) with **8c**, (g) with **8e**, (h) with **8f**, (i) with **8g**, (j) with **8h**. All samples were hydrated with PBS (pH=7.4).

Table S3 Calorimetric profiles (cooling) of DMPC or DSPG:SQ109 analogue mixtures, fully hydrated in PBS (pH=7.4).

Sample	T_m	$\Delta T_{1/2}$	ΔH	Sample	T_m	$\Delta T_{1/2,m}$	ΔH_m
DMPC	22.5	0.59	31.7	DSPG	52.2	1.1	48.5
DMPC:**8a** (H)	18.7	2.8	23.3	DSPG:**8a** (H)	47.6	1.4	55.4
DMPC:**8b** (Me)	16.6	1.9	26.5	DSPG:**8b** (Me)	47.7	1.4	52.9
DMPC:**12**	18.4	4.4	21.1	DSPG:**12**	46.8	1.5	57.2
DMPC:**8d** (Pr)	16.4	1.8	18.9	DSPG:**8d** (Pr)	47.9	1.4	48.0
DMPC:**8c** (Et)	16.2	2.8	25.6	DSPG:**8c** (Et)	48.9	1.6	49.0
DMPC:**8e** (Bu)	15.2	2.5	26.7	DSPG:**8e** (Bu)	45.7	2.0	36.9

DMPC:**8f** (Hex)	15.3	5.5	21.3	DSPG:**8f** (Hex)	47.1	0.8	36.1
DMPC:**8g** (Bn)	15.0	9.8	22.2	DSPG:**8g** (Bn)	46.6	1.8	55.6
DMPC: **8h** (Ph)	14.0	2.9	28.3	DSPG: **8h** (Ph)	47.2	5.2	52.0

T_m (°C), temperature at which heat capacity (ΔC_P) at constant pressure is maximum; $\Delta T_{1/2}$ (°C), half width at half peak height of the transition; ΔH (kJ mol^{-1}), transition enthalpy normalized per g of lipid. Results were the same after two repeats. ?H was determined over the 5-35 °C range.

Predicted sites of P450 oxidations of Compound 8h.

a

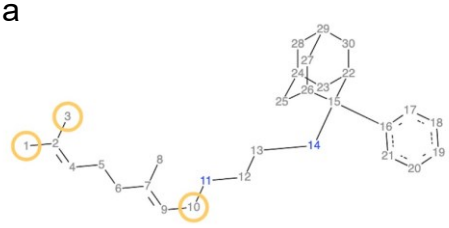

Atom	Probability
C.3	**0.57579**
C.1	**0.57579**
C.10	**0.492**
C.4	0.36067
C.5	0.278
C.2	0.27794
C.19	0.266
C.28	0.262
C.15	0.228
C.7	0.19694

b

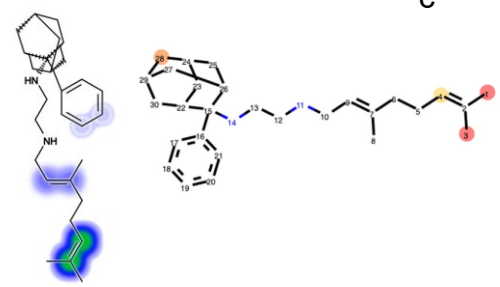

c

2D6 Ranking	Atom	2D6 Score
1	C.1	64.1
2	C.28	74.7
3	C.4	78.1
4	C.19	84.9
5	C.5	85.5
6	C.24	88.8

Figure S10 **P**redicted sites of P450 oxidations of Compound **8h**. (a) GloryFame2 results. (b) Xenosite results. (c) SmartCyp results (for CYP2D6). In addition to major oxygenations of the adamantyl (C28), terminal methyl (C1/C3) and allyic (C10) sites, additional oxygenation, of the phenyl ring, is predited using all three programs**.**

Table S4 Stability of SQ109 (8a), 8b and 8h in human, mice and rat liver microsomes.

Compd.	Human			Mice			Rat		
	% remanent (after 60 min)[a]	**$t_{1/2}$** (min) [b]	**CL_{int}** (mL/min* mg prot)[c]	**% remanent** (after 60 min)	**$t_{1/2}$** (min)	**CL_{int}** (mL/min* mg prot)	**% remanent** (after 60 min)	**$t_{1/2}$** (min)	CL_{int} (mL/min* mg prot)
SQ109 (**8a**)	1.5	9.71	53.87	0.8	7.33	105.76	1.2	4.57	120.84
8b	3.8	5.50	95.15	3.4	9.24	83.91	2.3	2.28	242.41
8h	0.3	5.25	99.73	0.7	8.69	89.16	0.0	2.08	265.68
Testosterone	6.02	14.97	34.95	0.09	4.62	167.77	0.13	1.20	458.77

[a] % is the percentage of the remaining compound after 1 h of incubation with microsomes at 37 °C; [b] $t_{1/2}$ is the half-life in min; [c] CL_{int}t is the intrinsic clearance in mL/min*mg prot.

^{1}H and ^{13}C NMR spectral data.

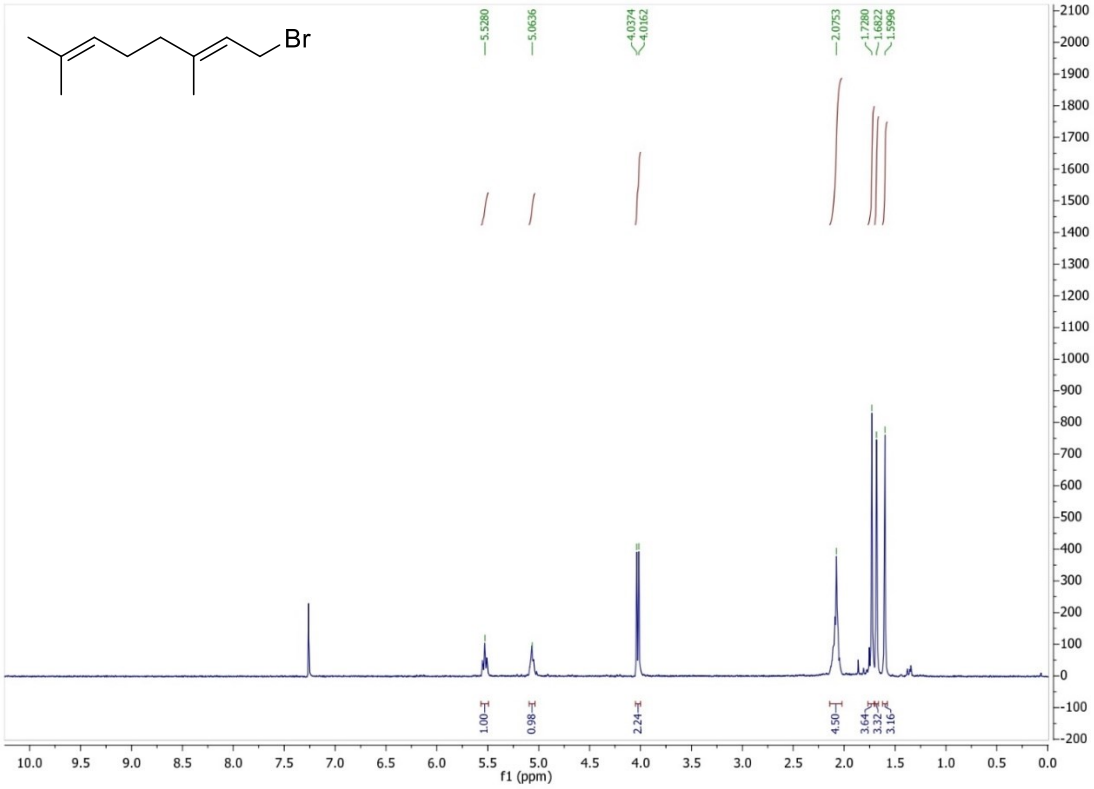

Figure S11 NMR spectra of compounds; ^{1}H NMR of geranylbromide.

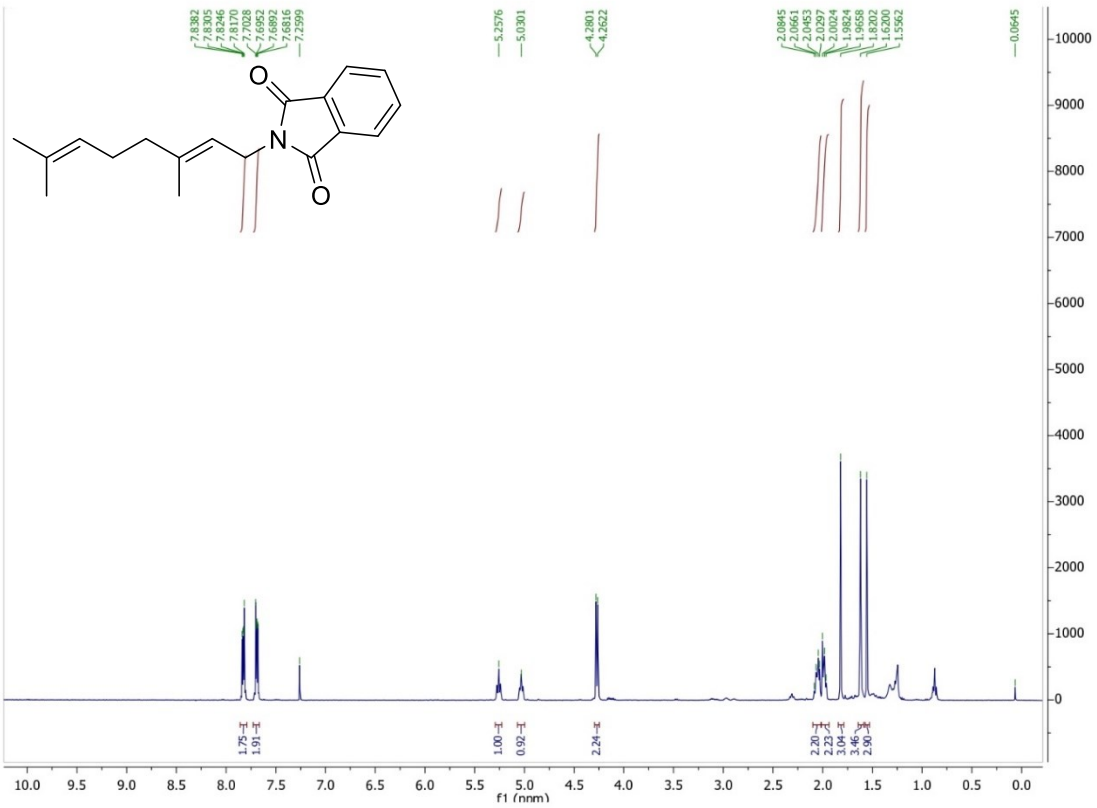

Figure S11 (contd.). NMR spectra of compounds; ^{1}H NMR of geranylphthalimide.

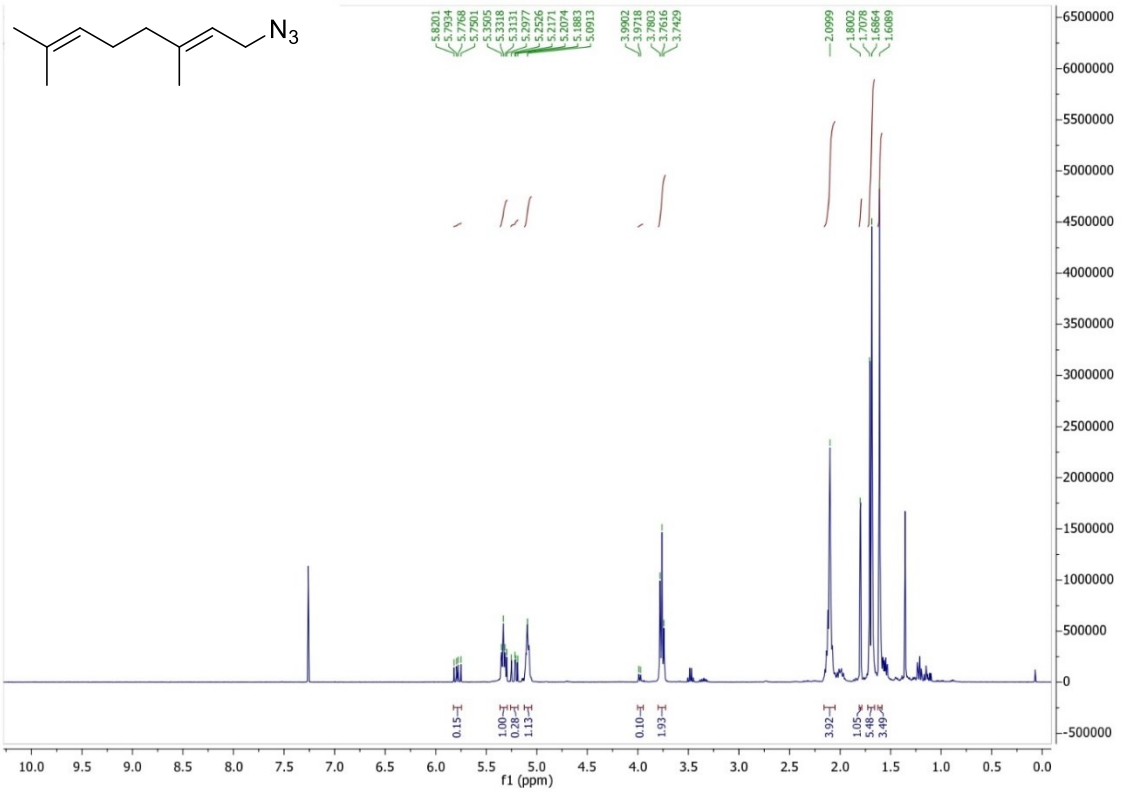

Figure S11 (contd.). NMR spectra of compounds; ^{1}H NMR of geranylazide.

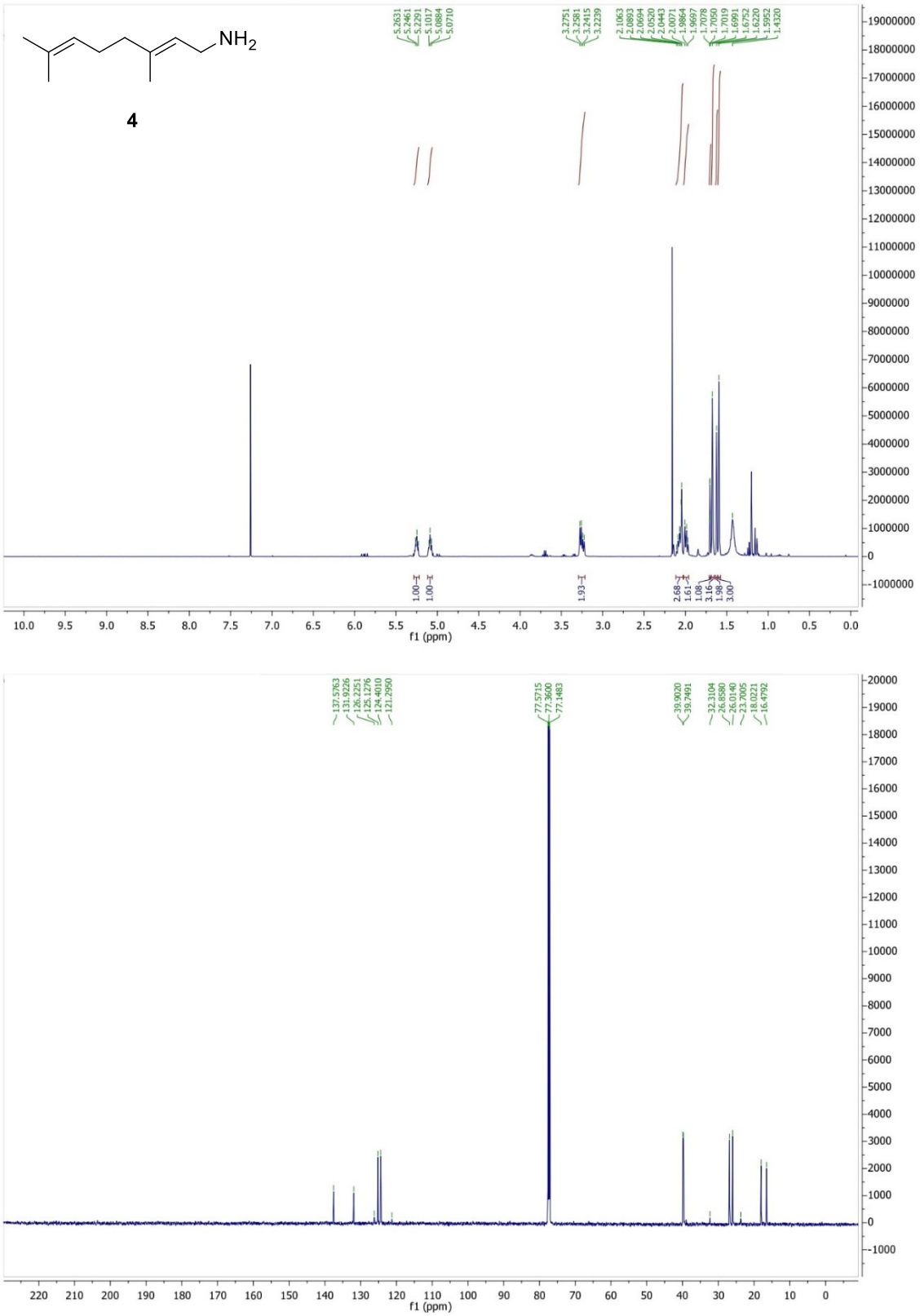

Figure S11 (contd.). NMR spectra of compounds; ^{1}H and ^{13}C NMR of compound **4**.

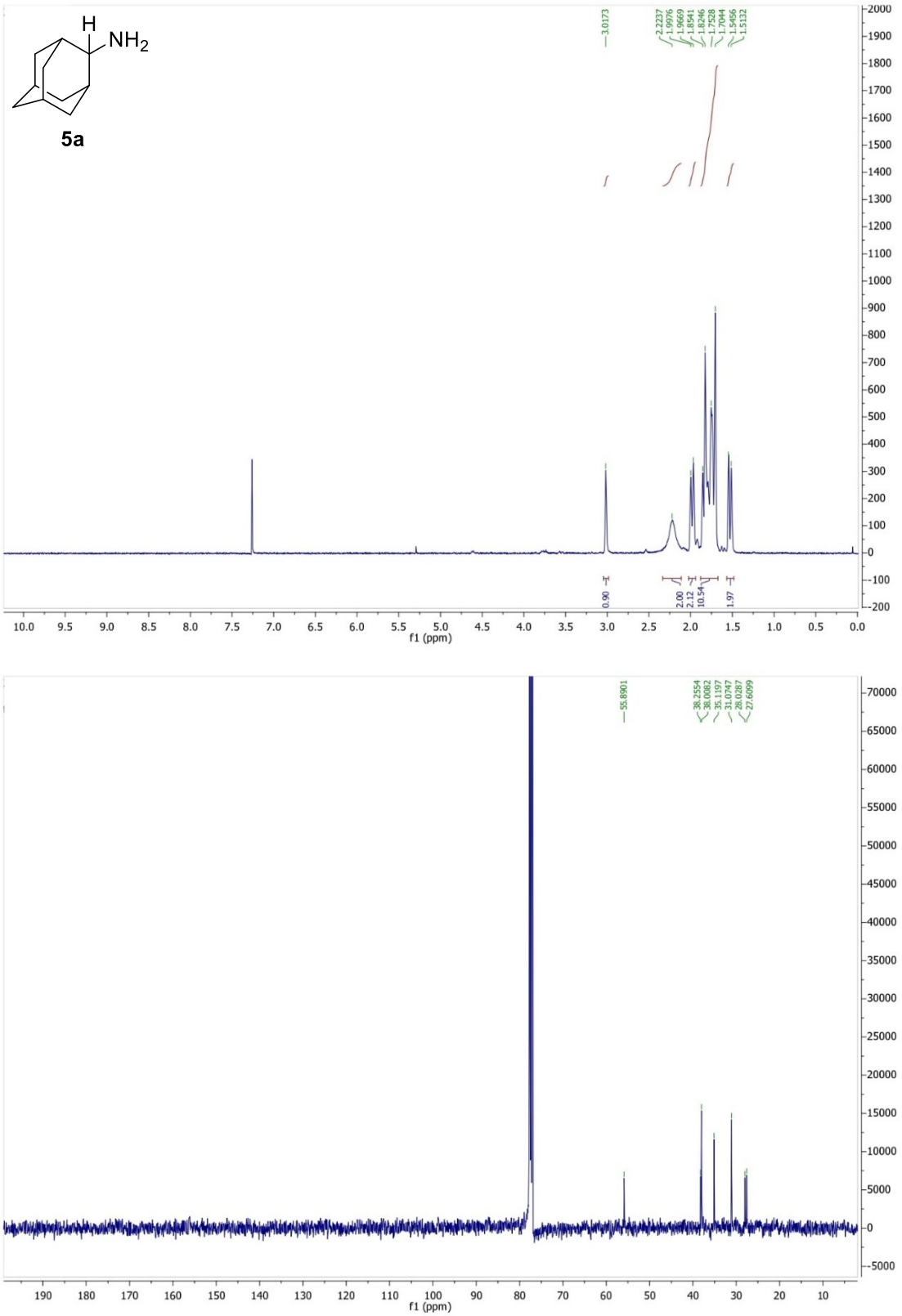

Figure S11 (contd.). NMR spectra of compounds; ^{1}H and ^{13}C NMR of compound **5a**.

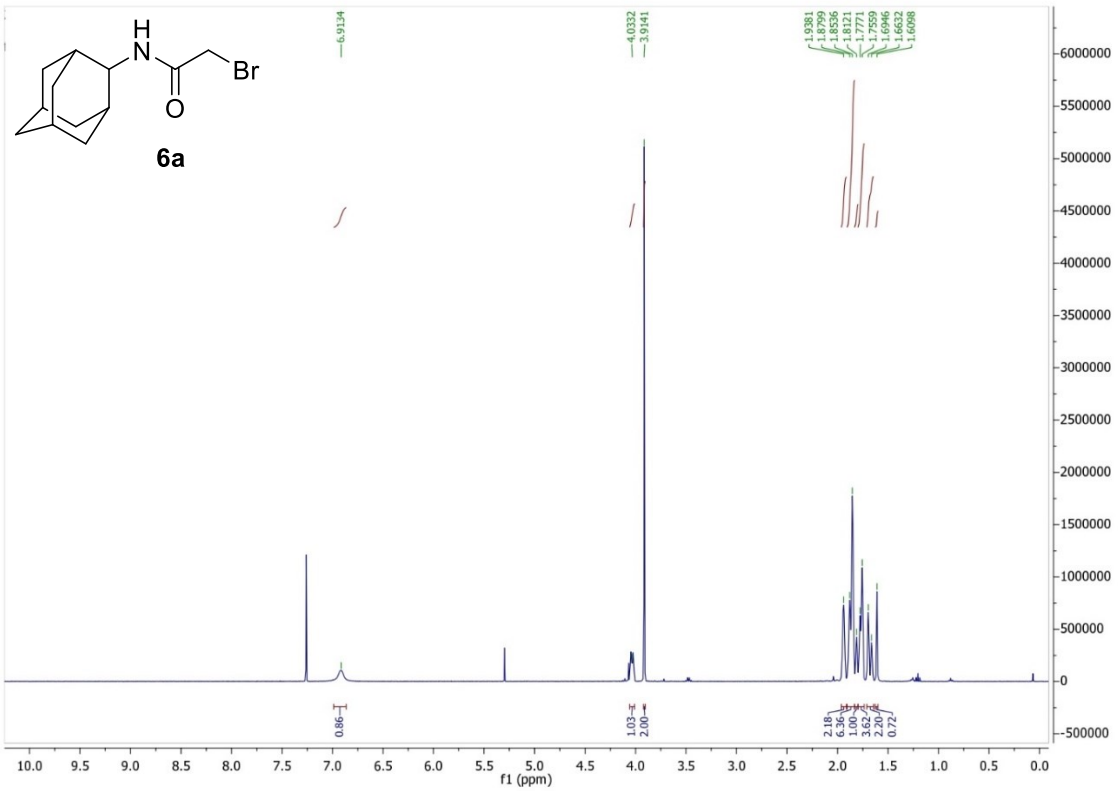

Figure S11 (contd.). NMR spectra of compounds; ^{1}H NMR of **6a**.

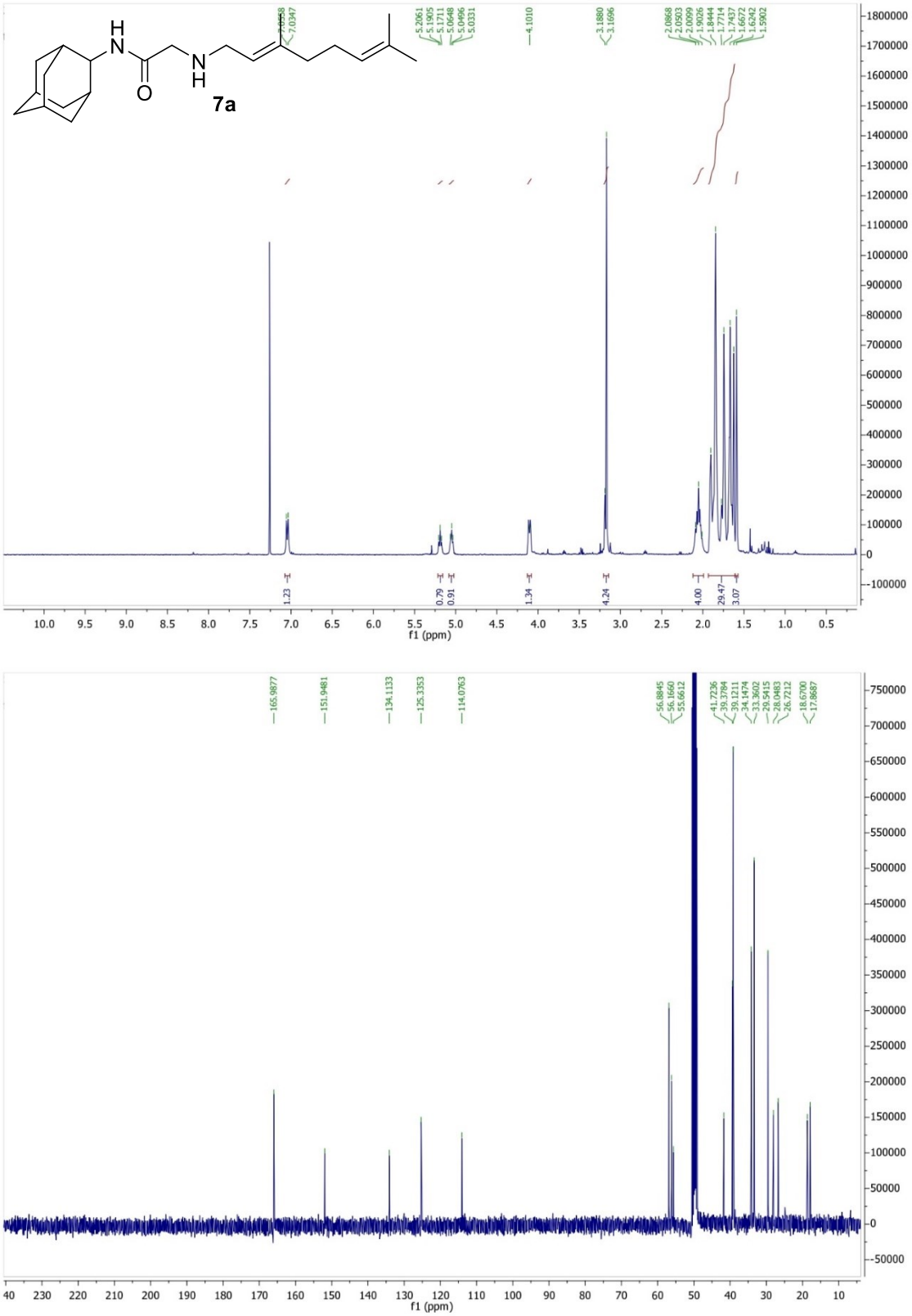

Figure S11 (contd.). NMR spectra of compounds; ^{1}H and ^{13}C NMR of **compound 7a**.

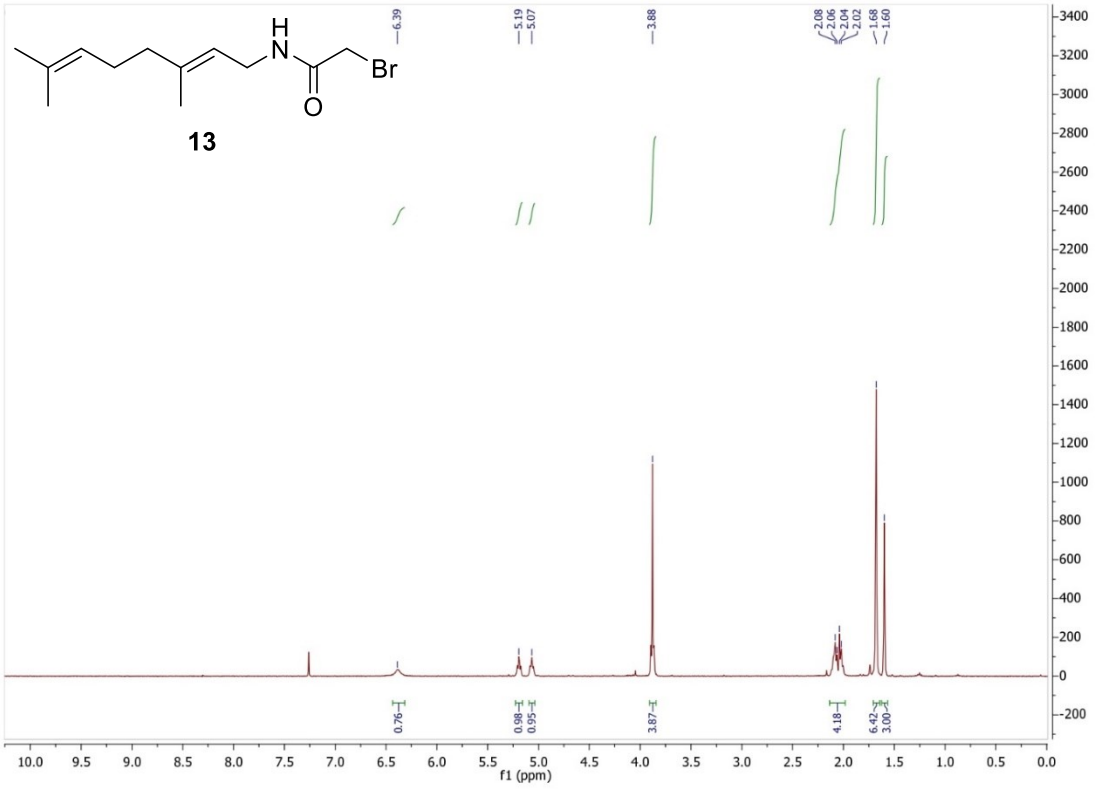

Figure S11 (contd.). NMR spectra of compounds; ^{1}H NMR of compound **13**.

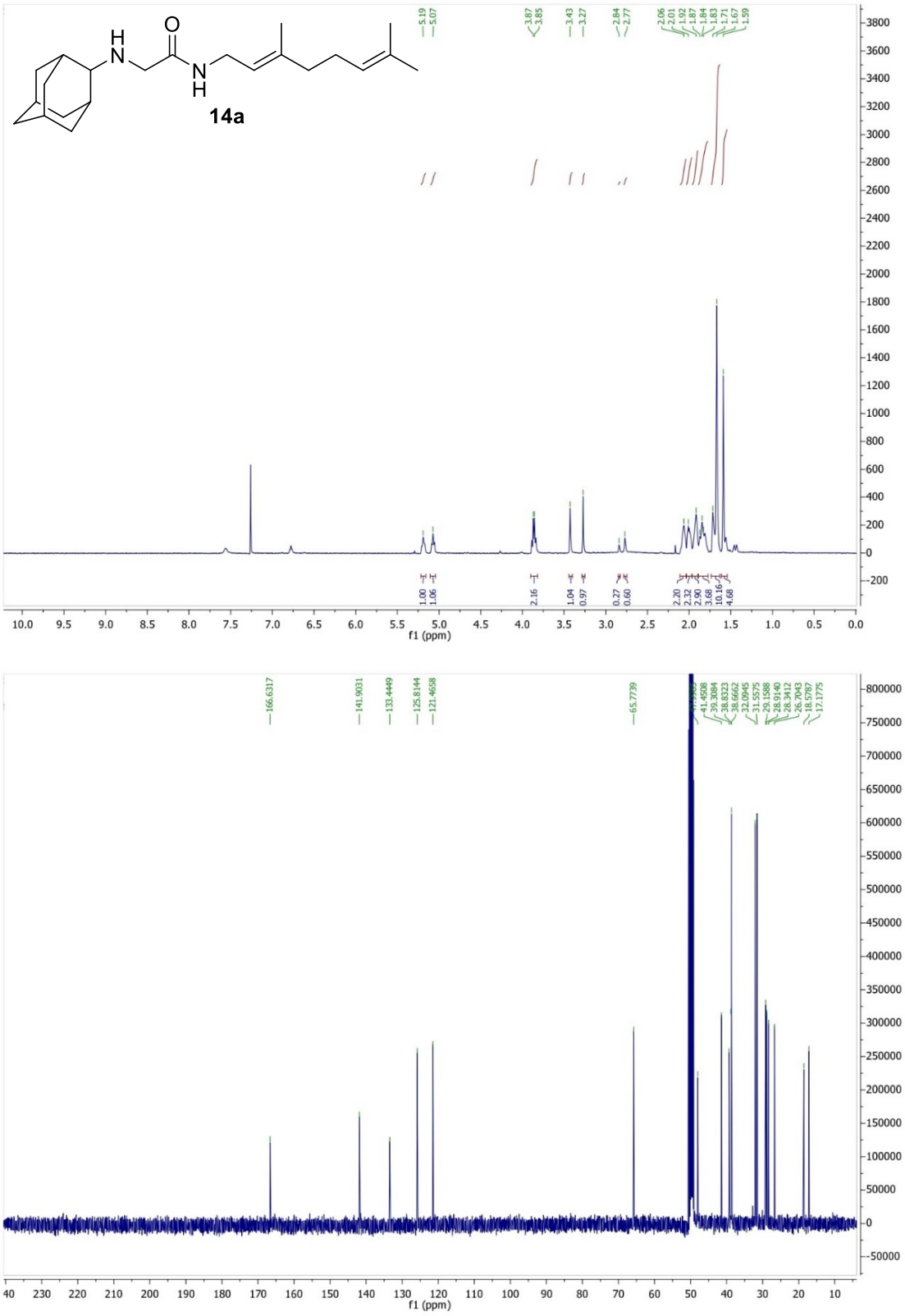

Figure S11 (contd.). NMR spectra of compounds; ^{1}H and ^{13}C NMR of compound **14a**.

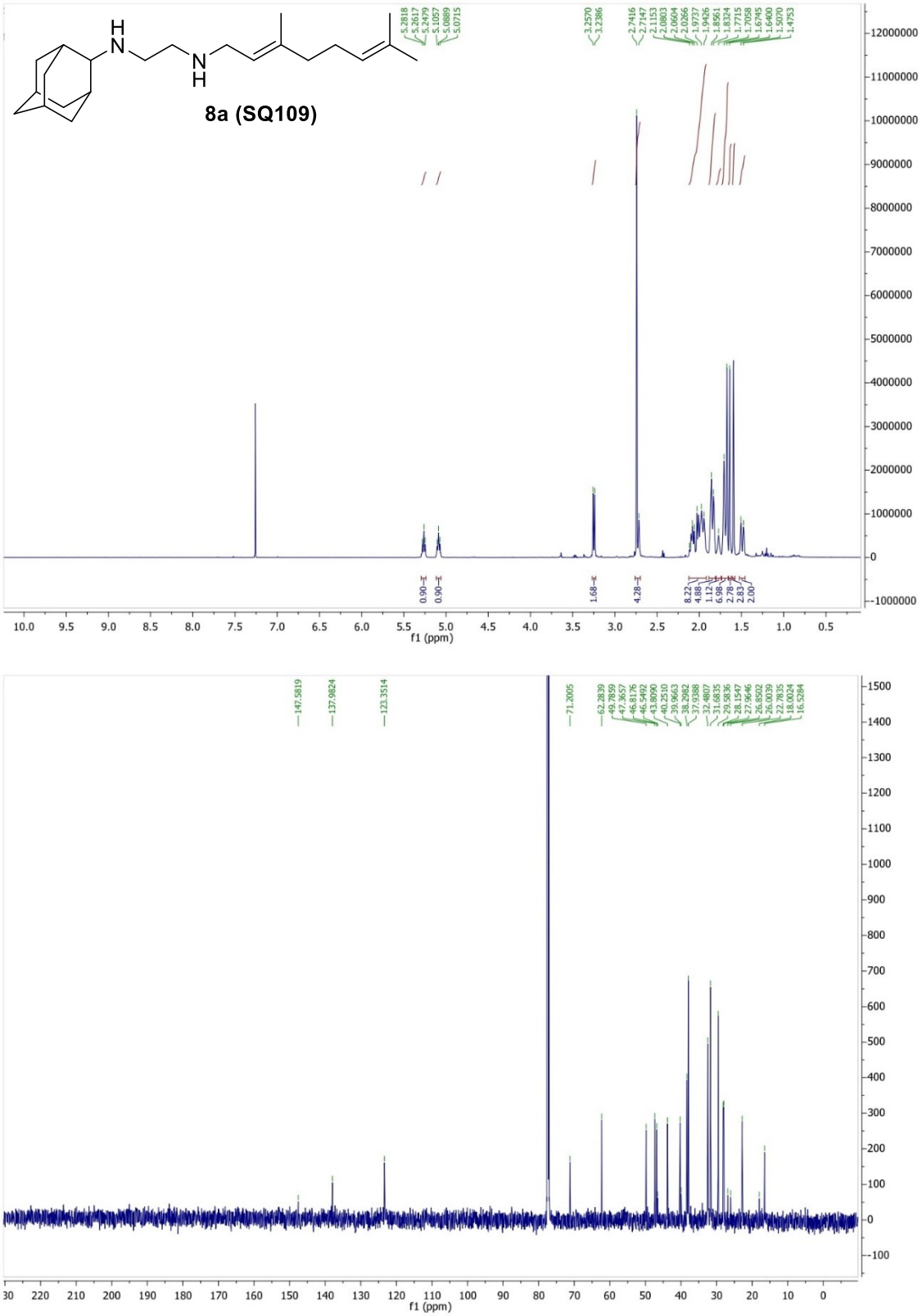

Figure S11 (contd.). NMR spectra of compounds; ^{1}H and ^{13}C NMR of compound **8a** (SQ109).

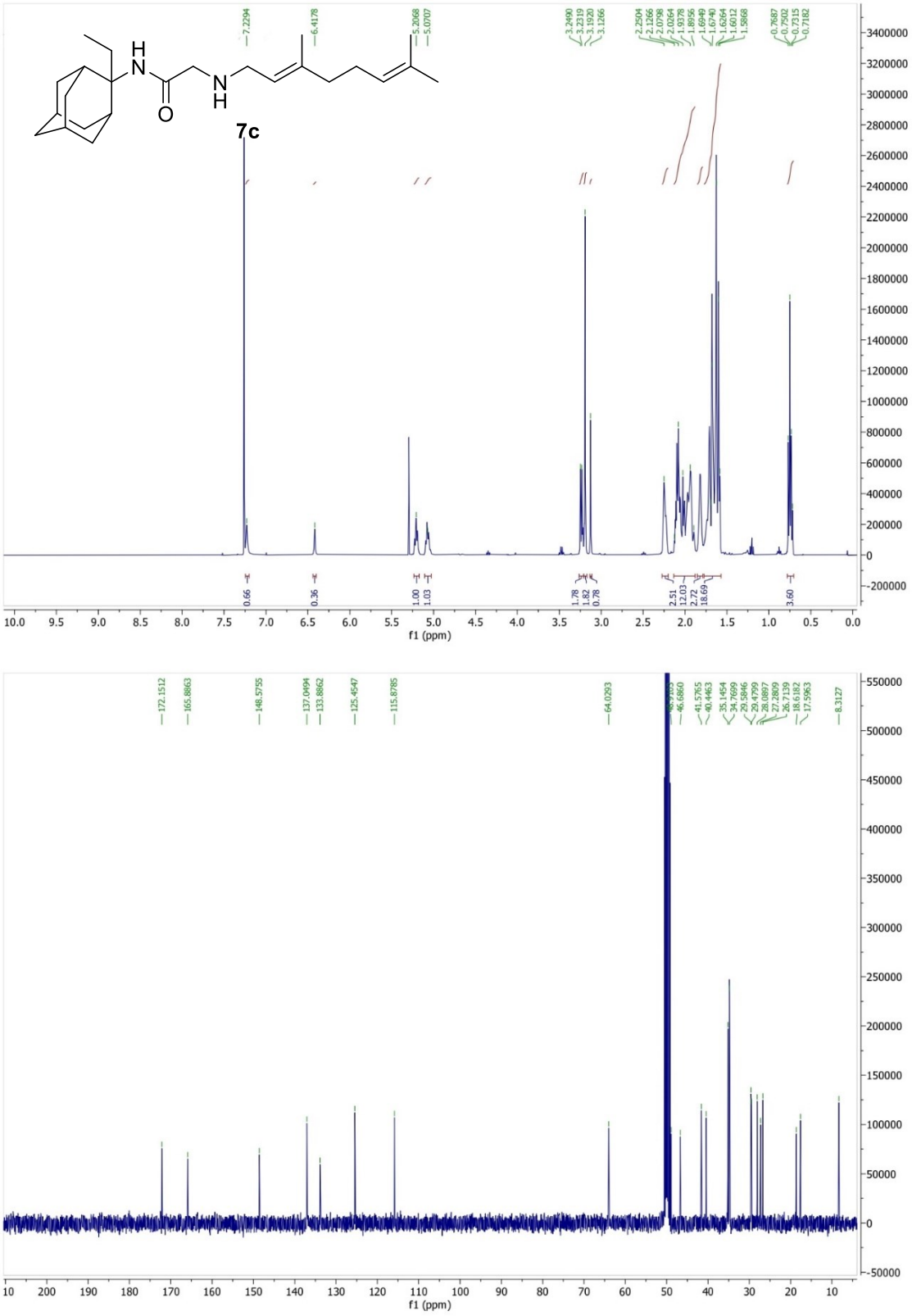

Figure S11 (contd.). NMR spectra of compounds; ^{1}H and ^{13}C NMR of compound **7c**.

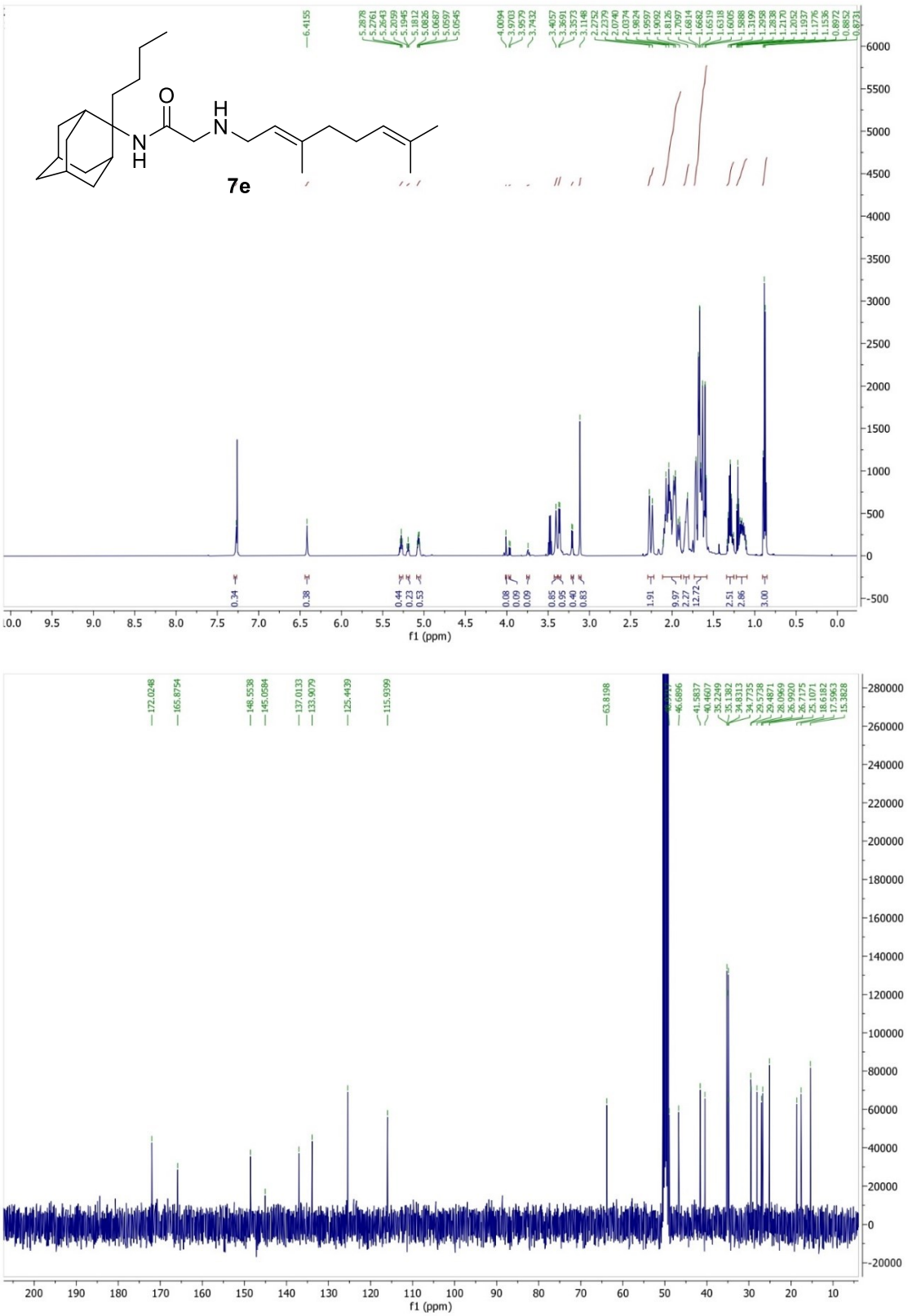

Figure S11 (contd.). NMR spectra of compounds; ^{1}H and ^{13}C NMR of compound **7e**.

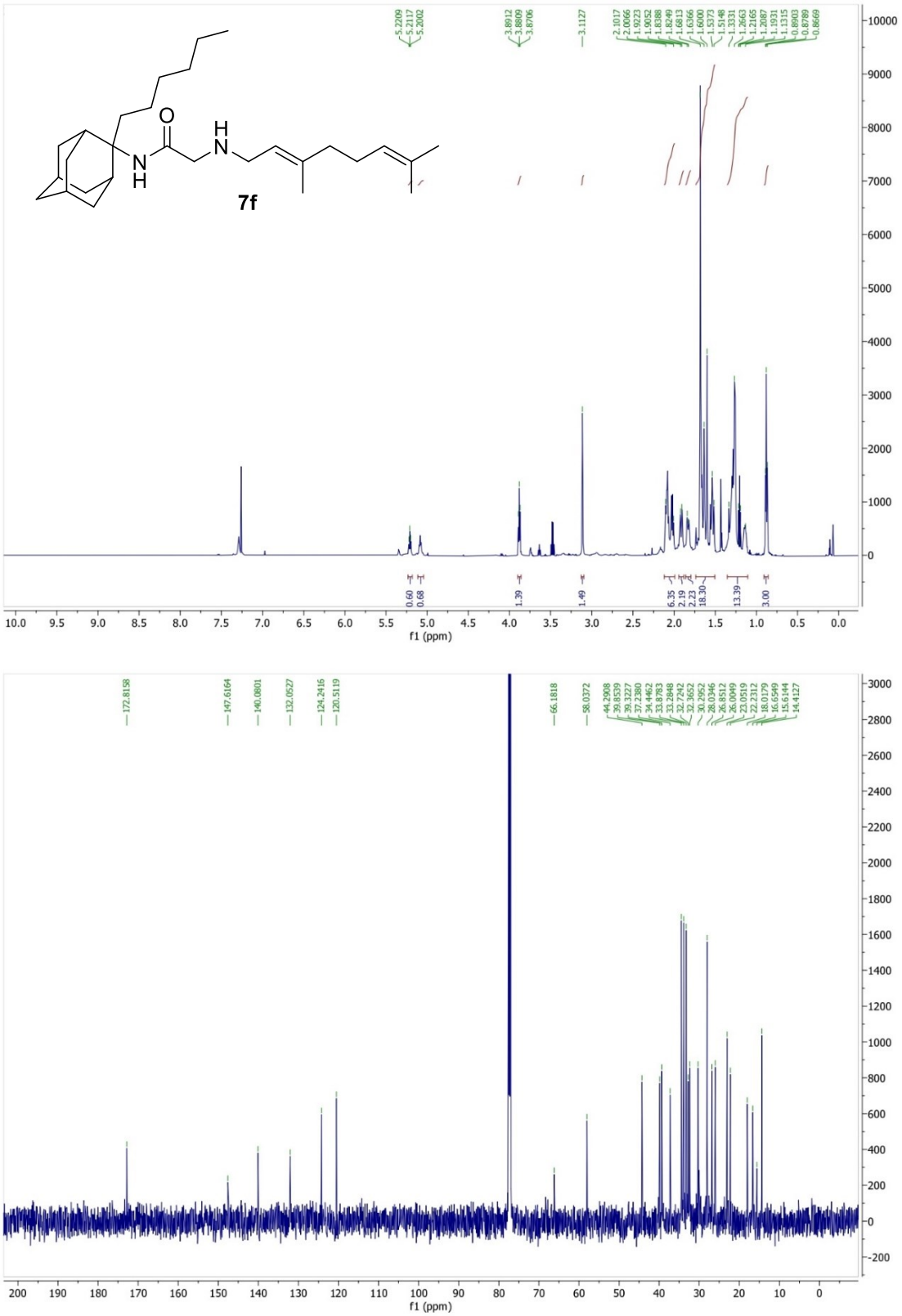

Figure S11 (contd.). NMR spectra of compounds; ^{1}H and ^{13}C NMR of compound **7f**.

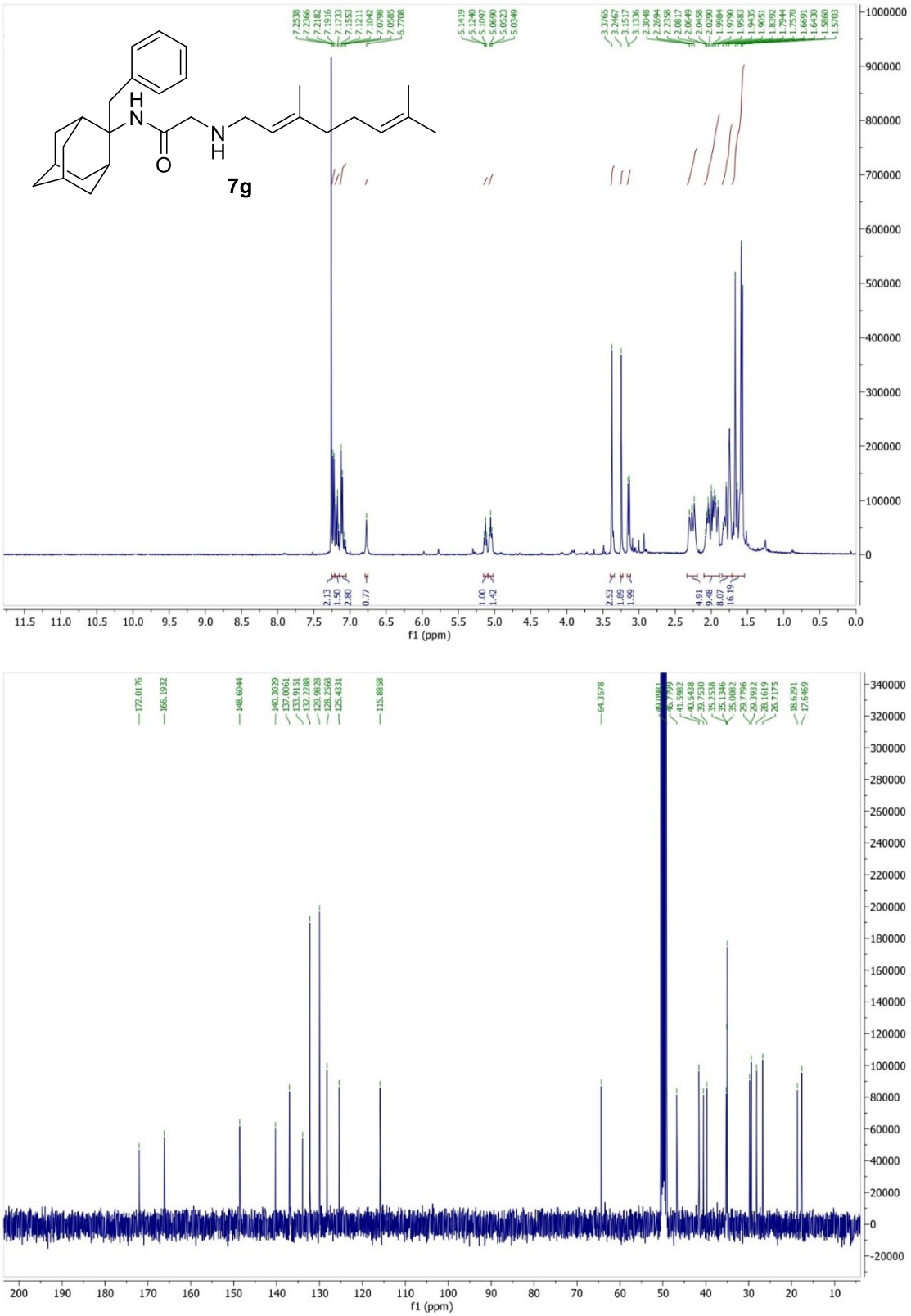

Figure S11 (contd.). NMR spectra of compounds; ^{1}H and ^{13}C NMR of compound **7g**.

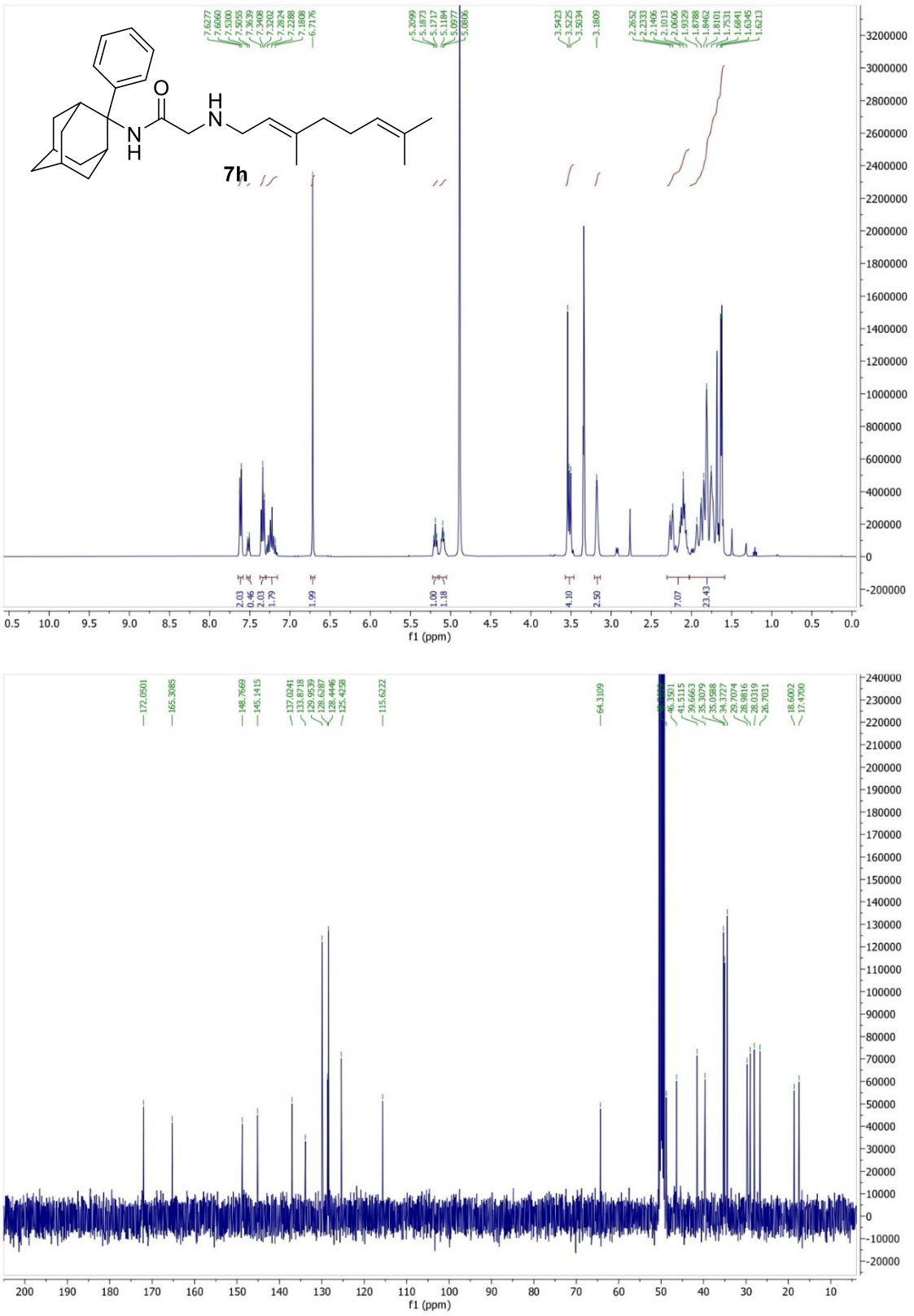

Figure S11 (contd.). NMR spectra of compounds; ^{1}H and ^{13}C NMR of compound **7h**.

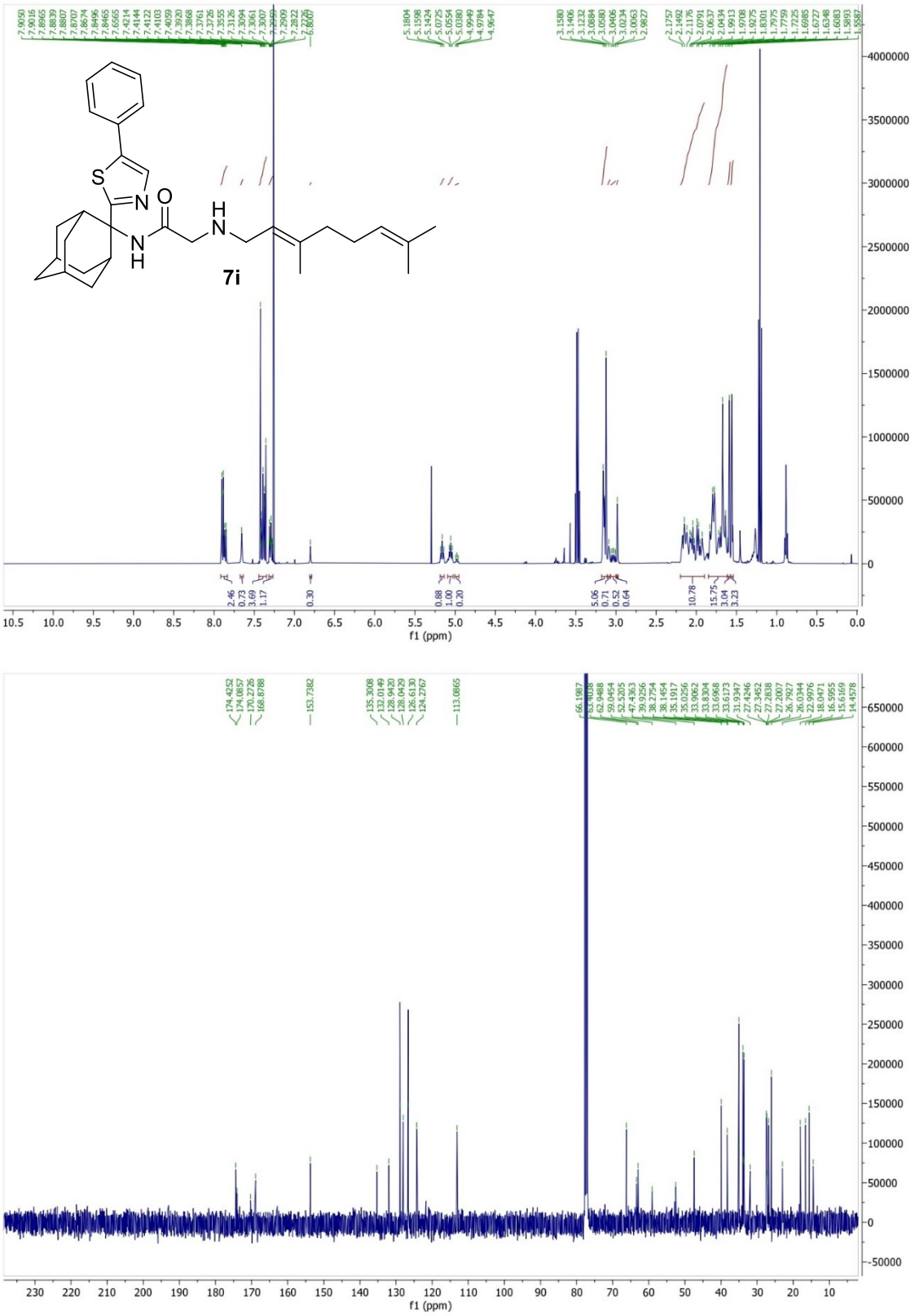

Figure S11 (contd.). NMR spectra of compounds; ^{1}H and ^{13}C NMR of compound **7i**.

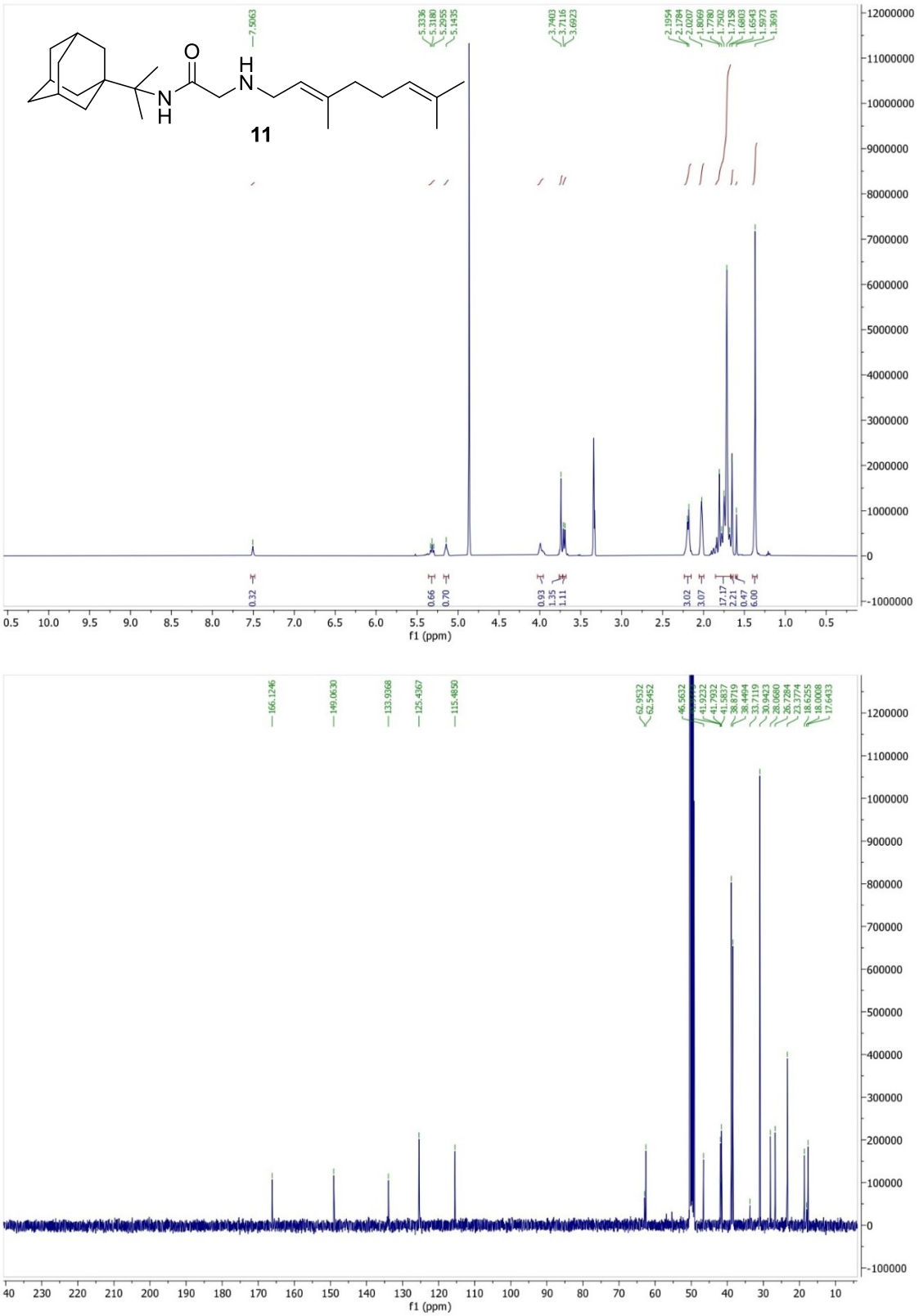

Figure S11 (contd.). NMR spectra of compounds; ^{1}H and ^{13}C NMR of compound **11**.

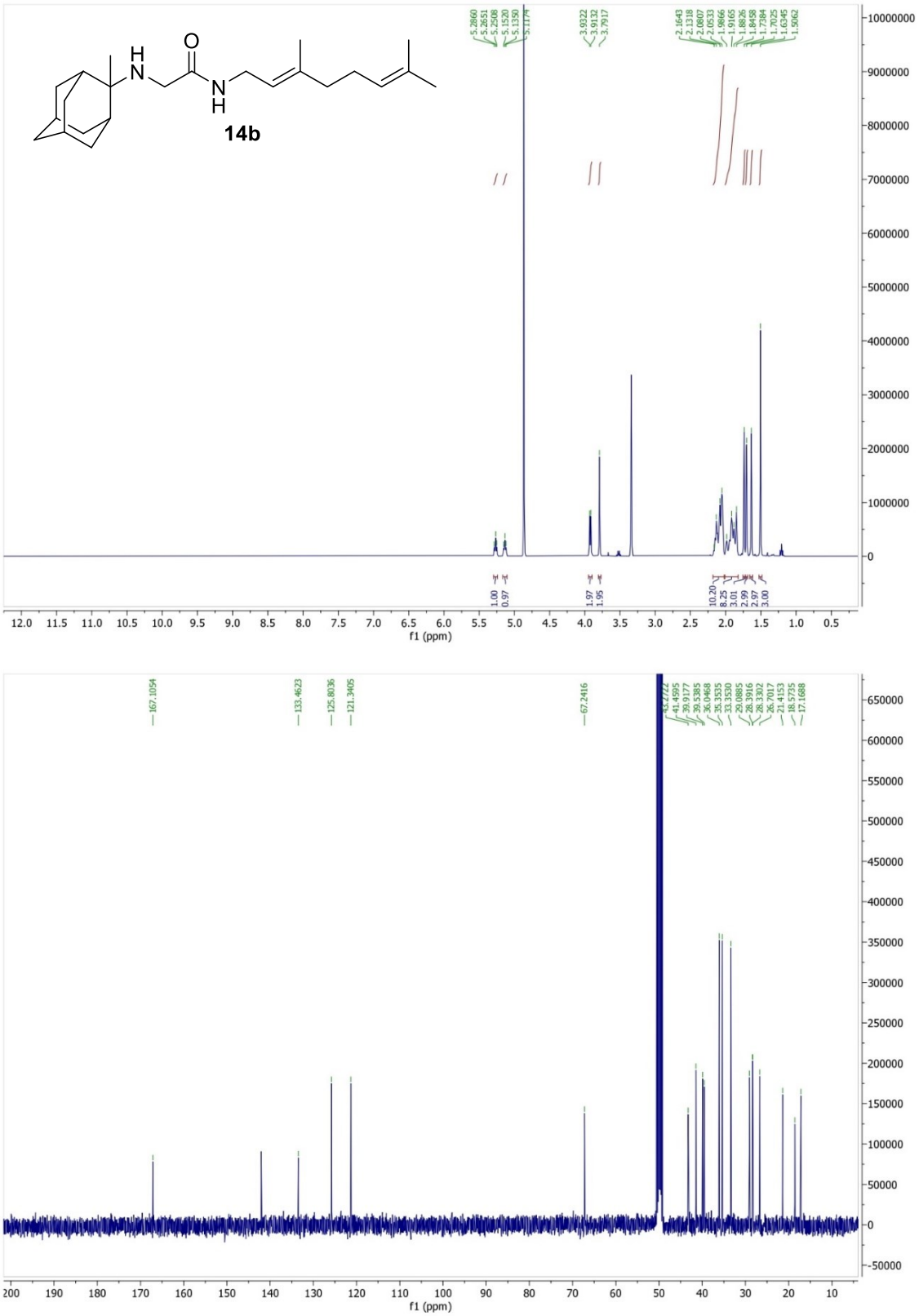

Figure S11 (contd.). NMR spectra of compounds; ^{1}H and ^{13}C NMR of compound **14b**.

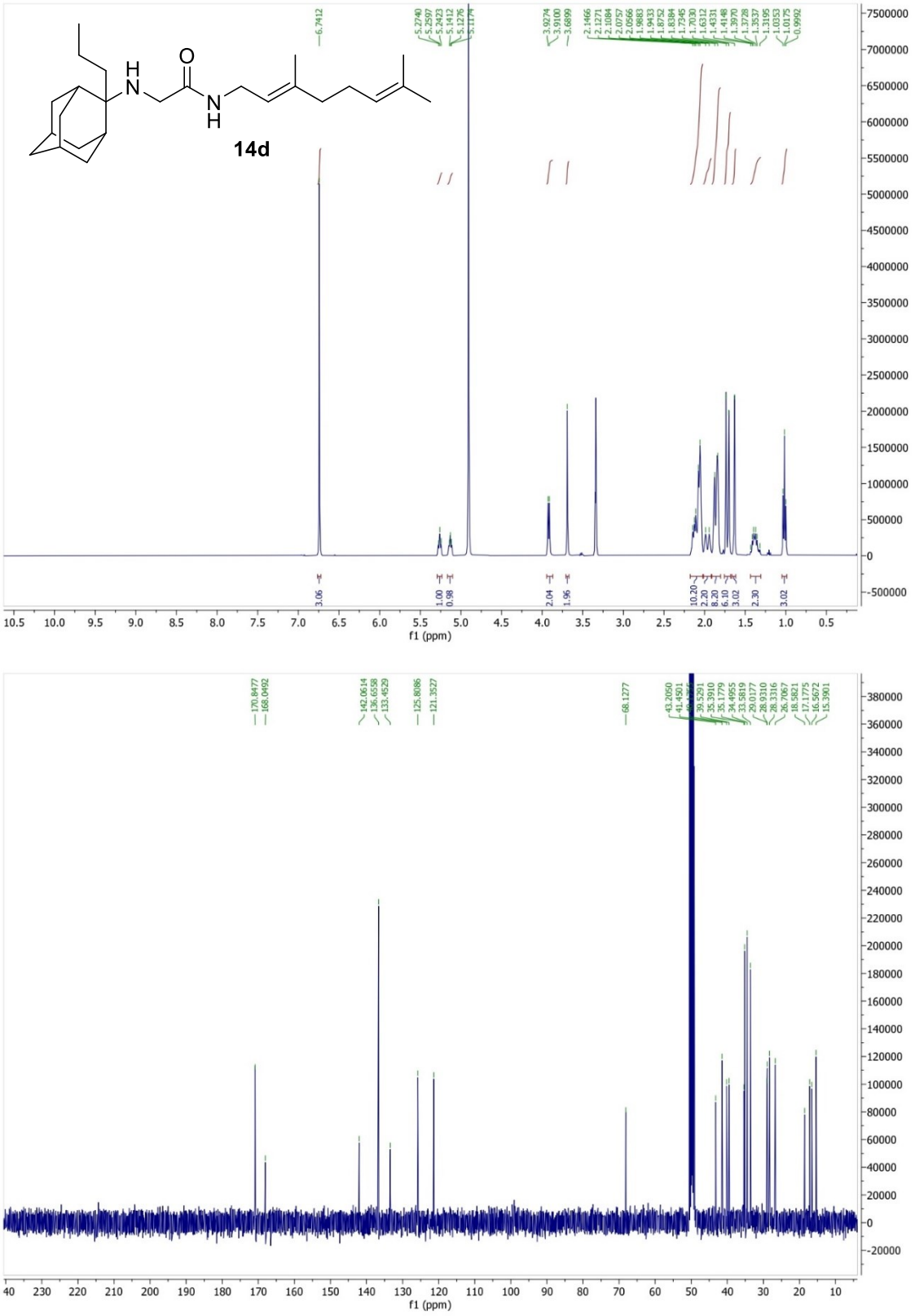

Figure S11 (contd.). NMR spectra of compounds; ^{1}H and ^{13}C NMR of compound **14d**.

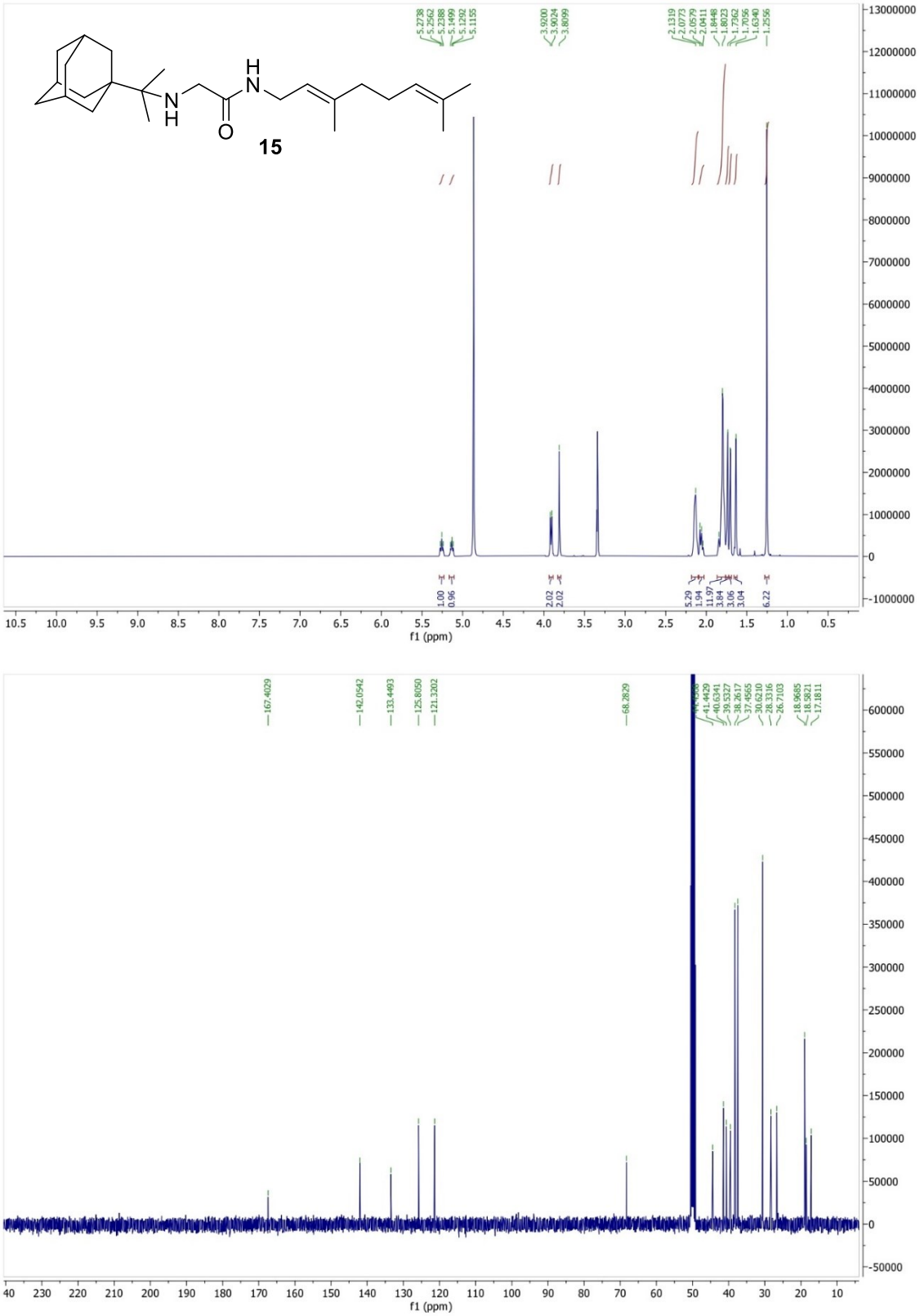

Figure S11 (contd.). NMR spectra of compounds; ^{1}H and ^{13}C NMR of compound **15**.

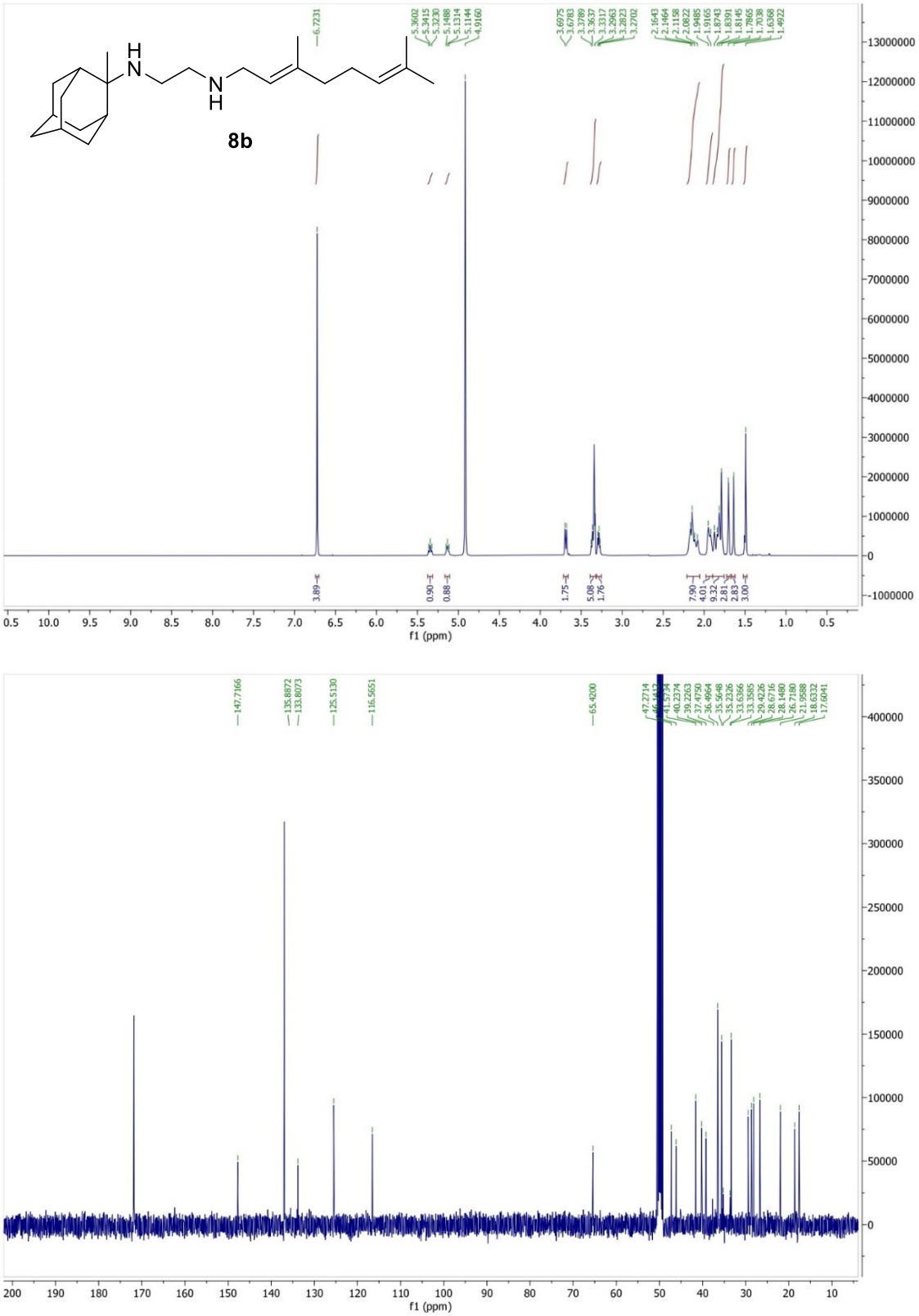

Figure S11 (contd.). NMR spectra of compounds; ^{1}H and ^{13}C NMR of compound **8b**.

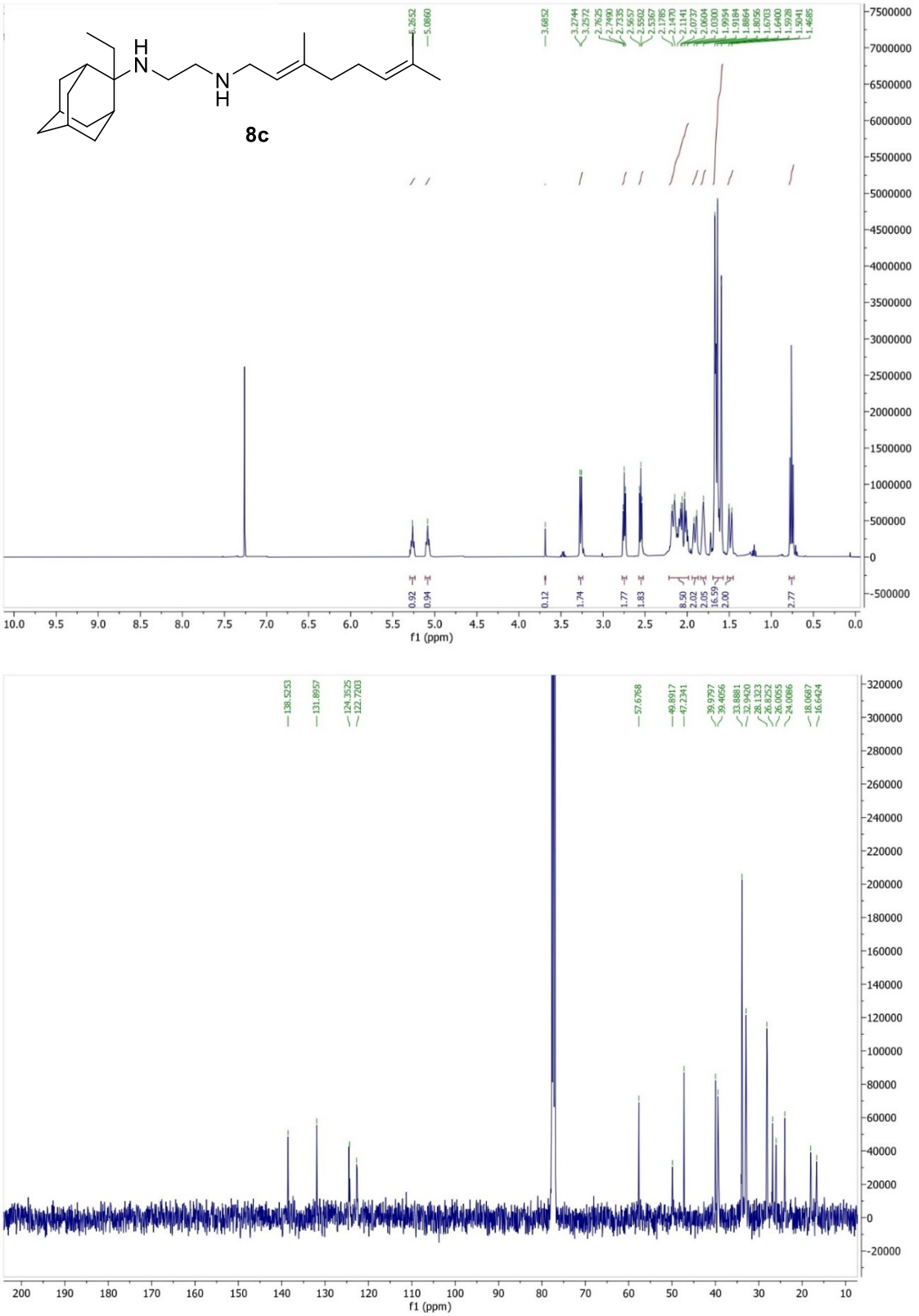

Figure S11 (contd.). NMR spectra of compounds; ^{1}H and ^{13}C NMR of compound **8c**.

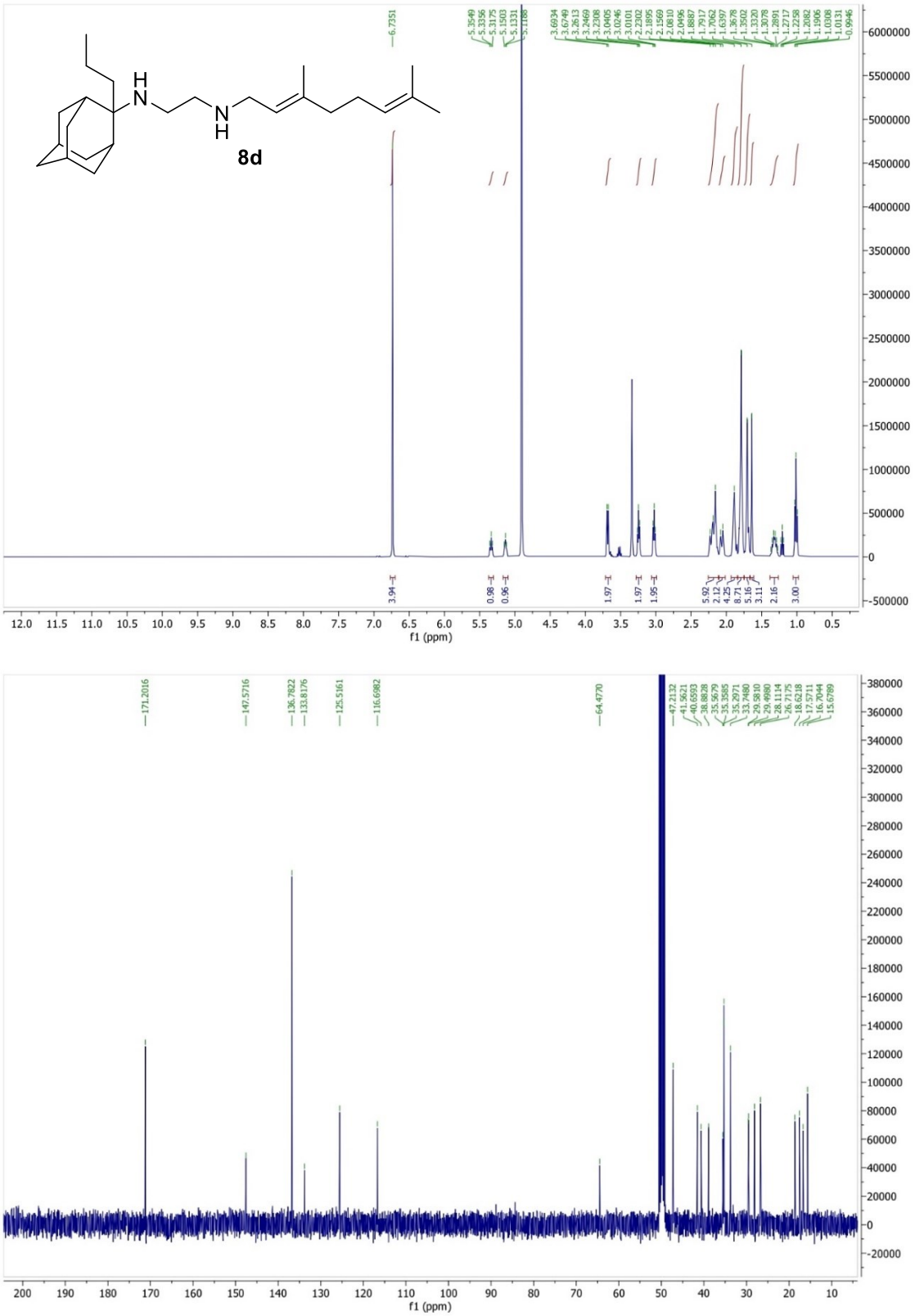

Figure S11 (contd.). NMR spectra of compounds; ^{1}H and ^{13}C NMR of compound **8d**.

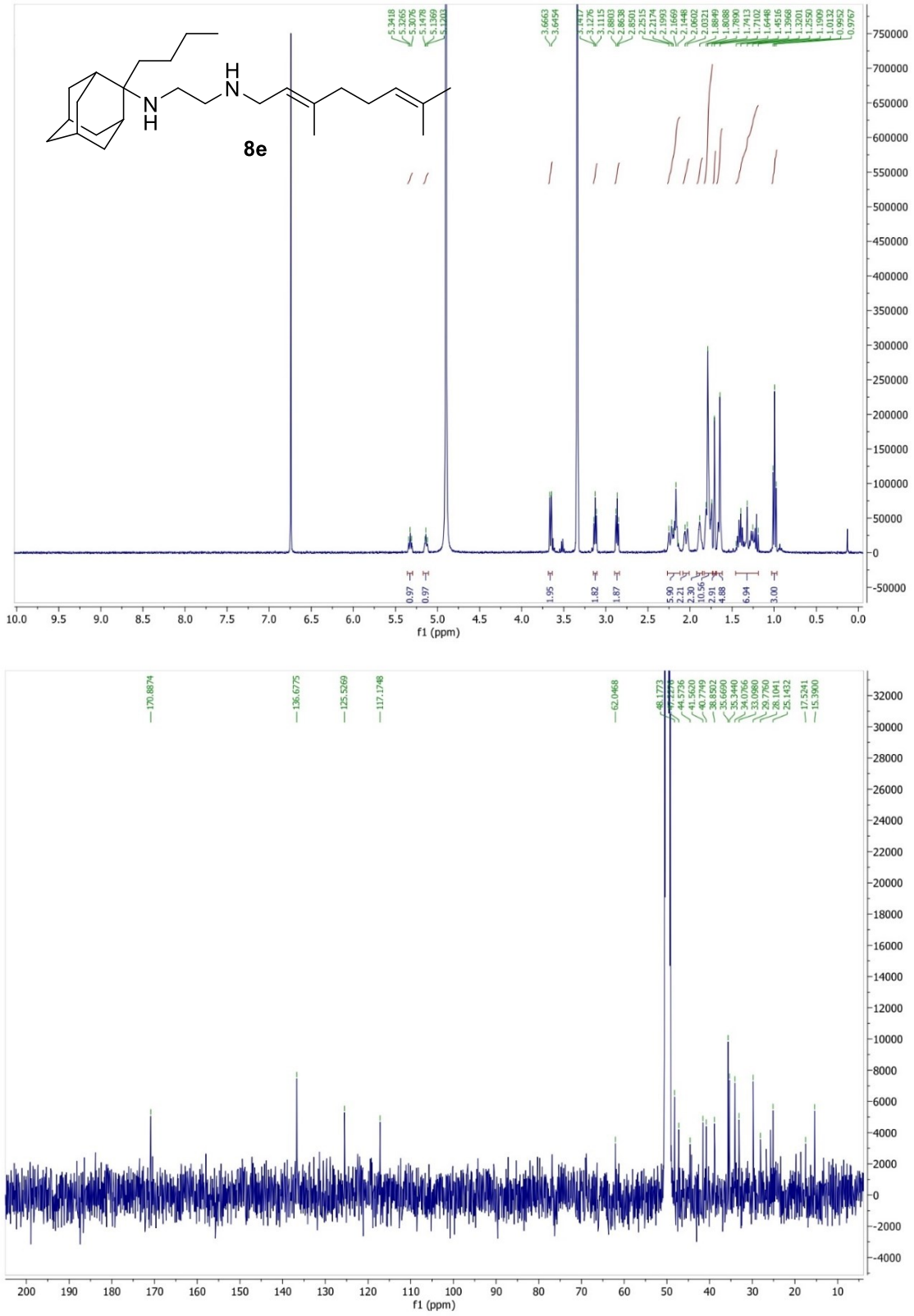

Figure S11 (contd.). NMR spectra of compounds; ^{1}H and ^{13}C NMR of compound **8e**.

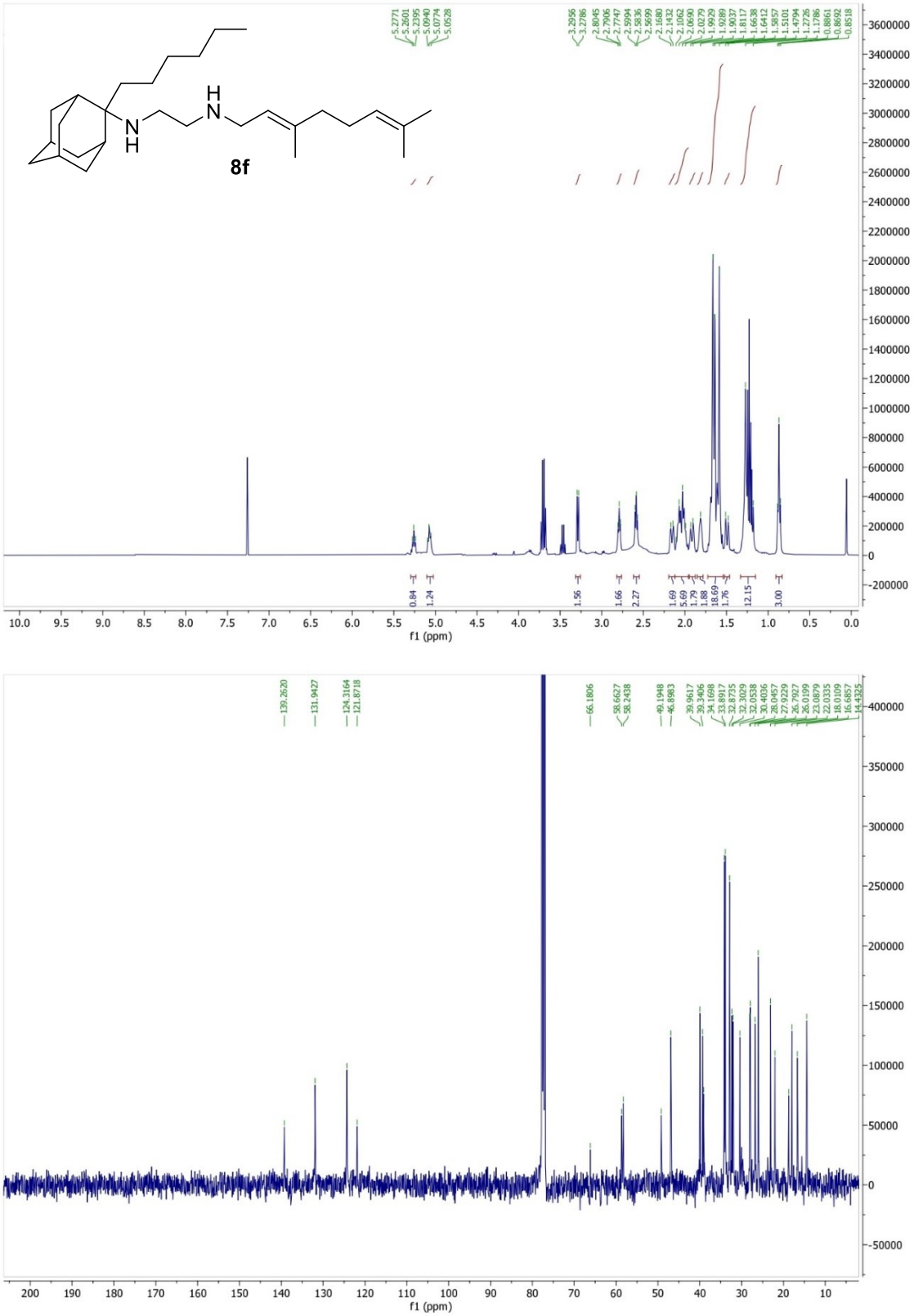

Figure S11 (contd.). NMR spectra of compounds; ^{1}H and ^{13}C NMR of compound **8f**.

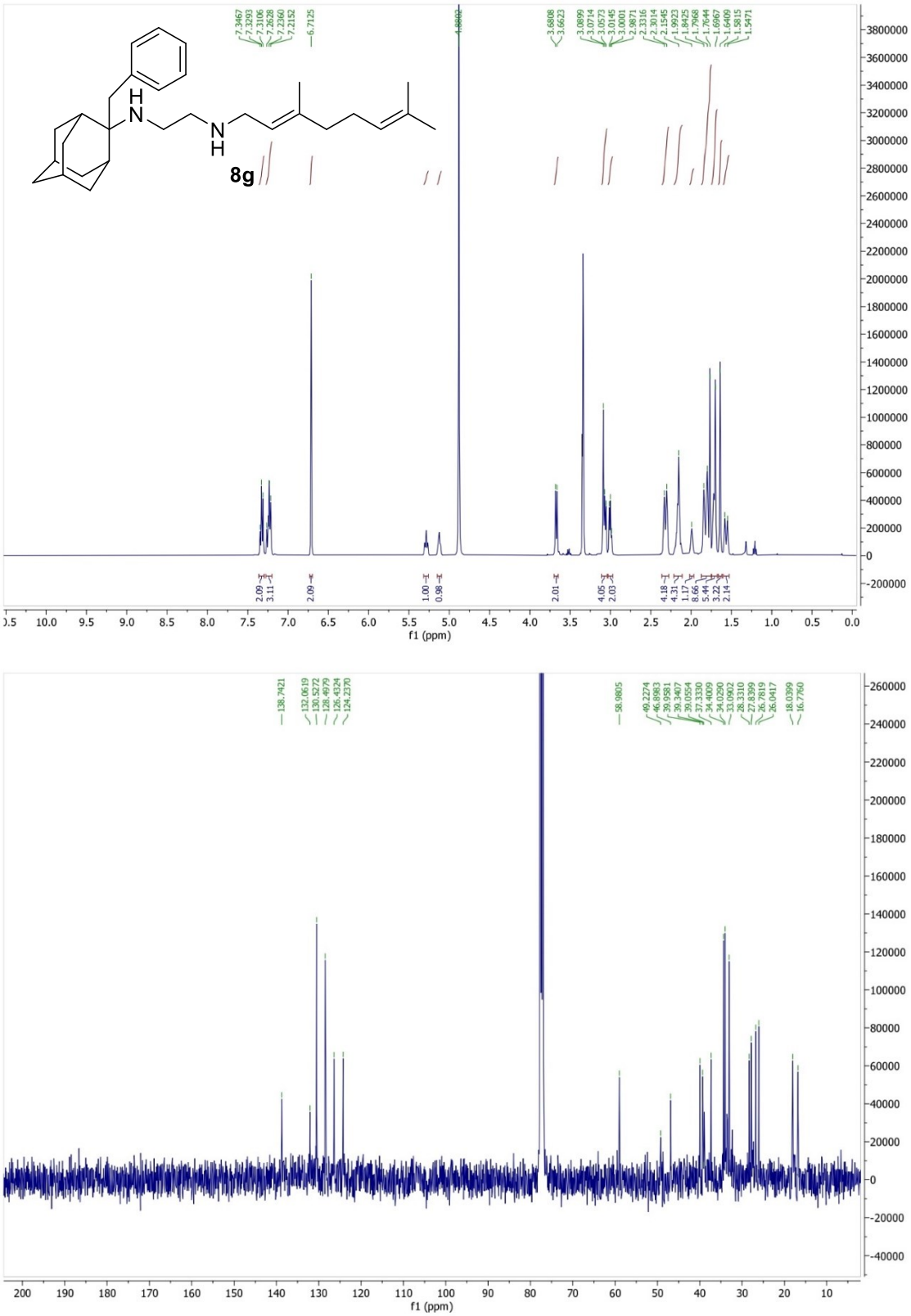

Figure S11 (contd.). NMR spectra of compounds; ^{1}H and ^{13}C NMR of compound **8g**.

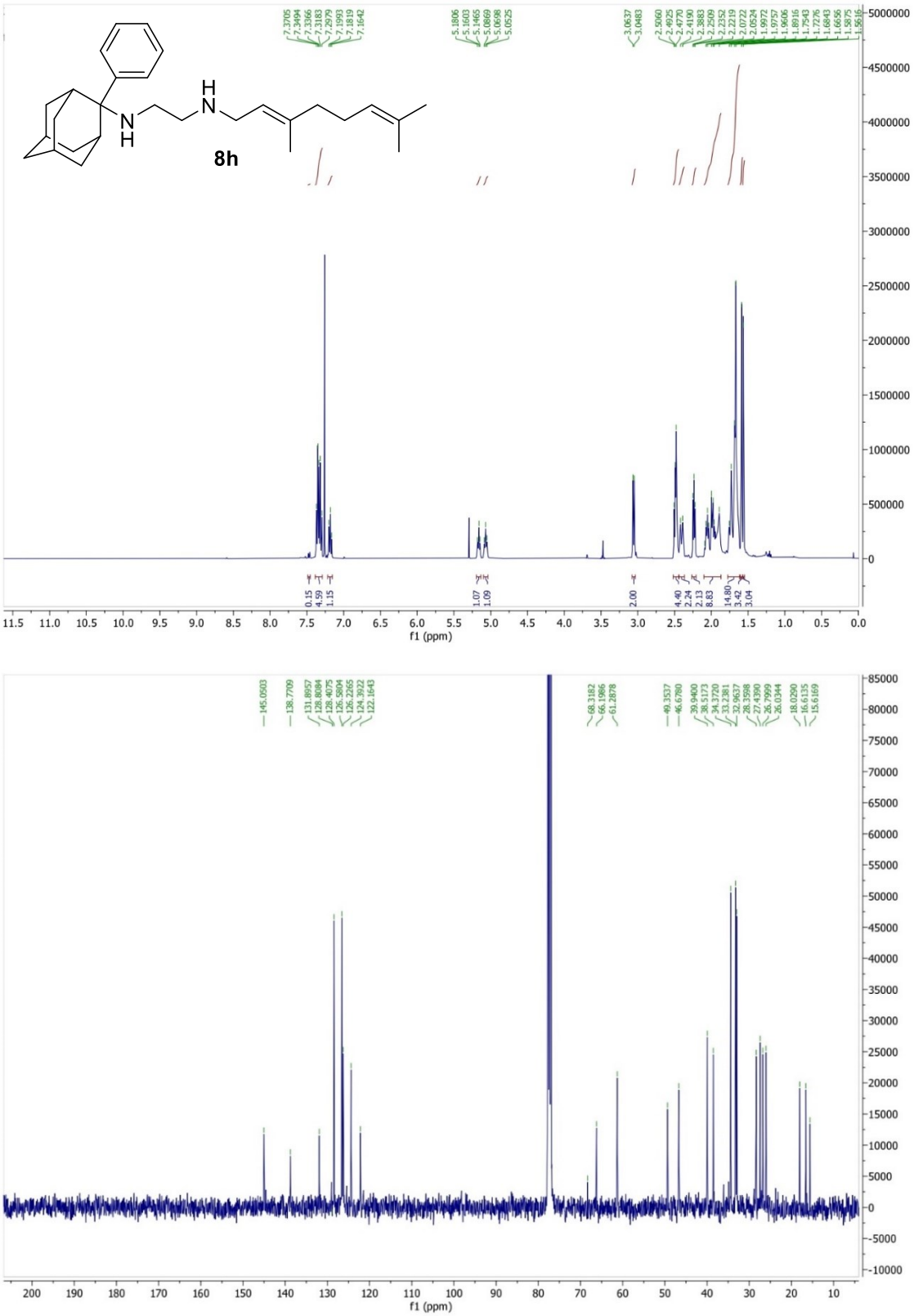

Figure S11 (contd.). NMR spectra of compounds; ^{1}H and ^{13}C NMR of compound **8h**.

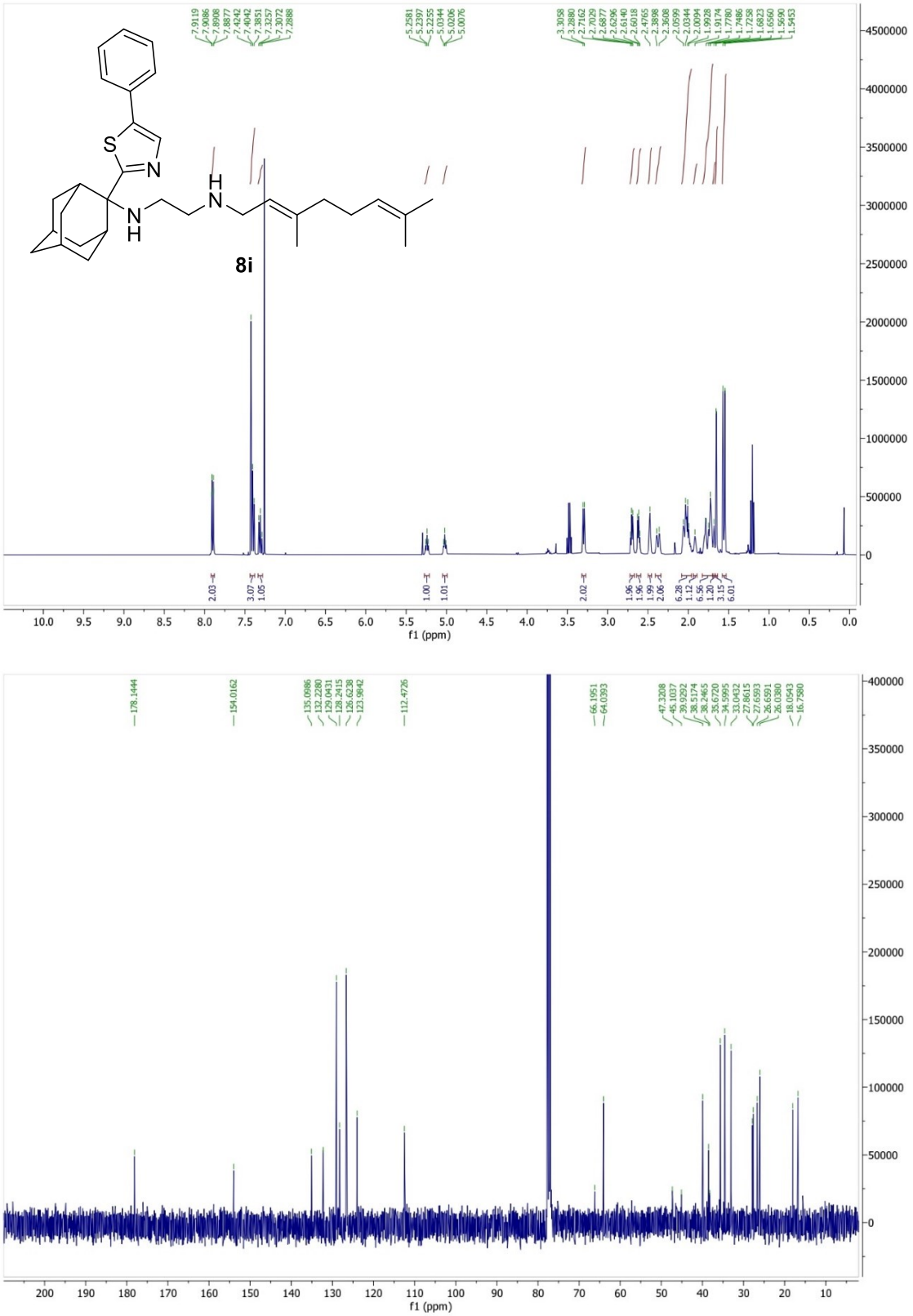

Figure S11 (contd.). NMR spectra of compounds; ^{1}H and ^{13}C NMR of compound **8i**.

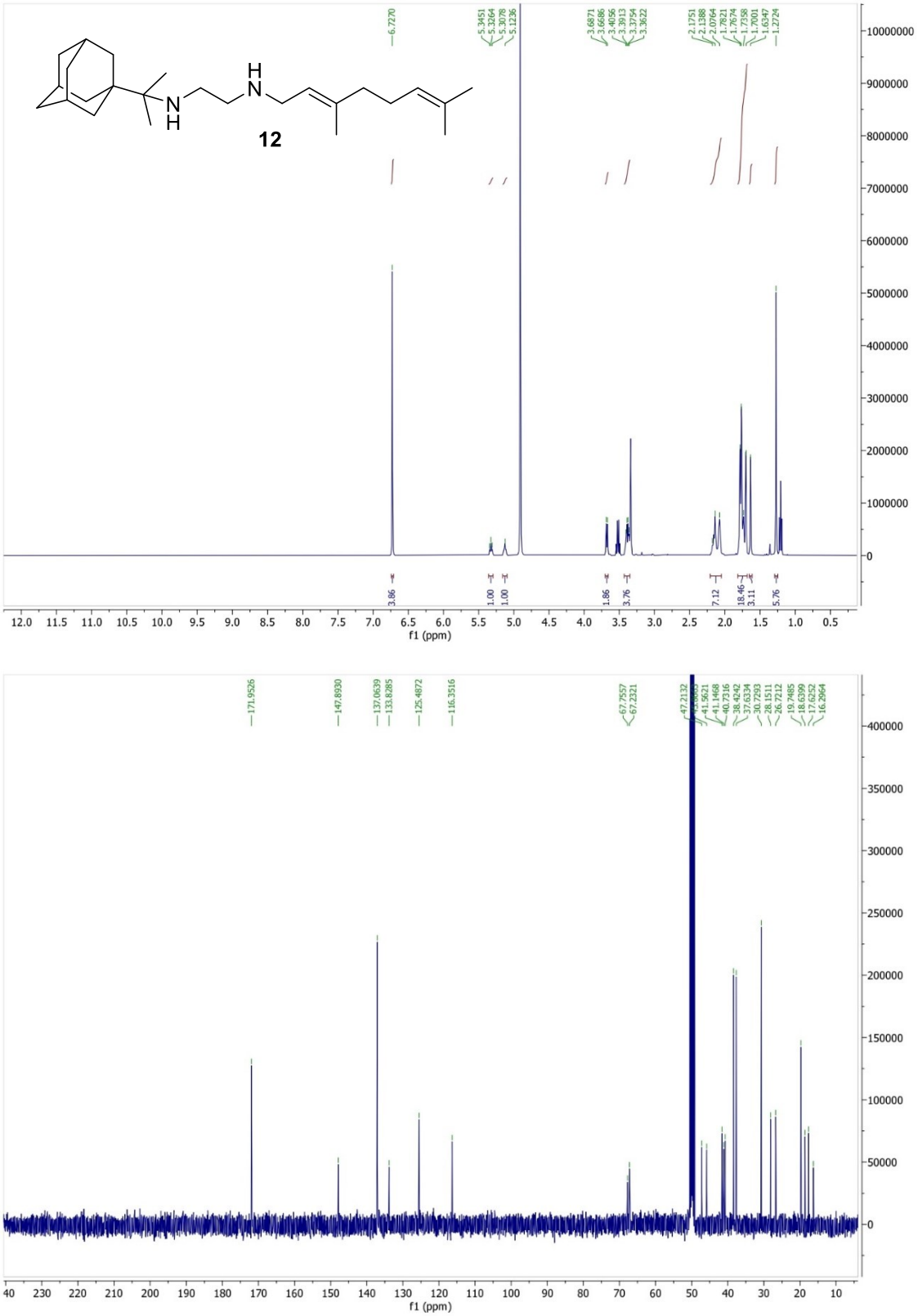

Figure S11 (contd.). NMR spectra of compounds; ^{1}H and ^{13}C NMR of compound **12**.

HPLC chromatograms

HPLC/UV chromatograms were determined with a HPLC Agilent 1260 Infinity II LC/MSD coupled to a photodiode array and mass spectrometer. 20 µL of sample 0.5 mg/mL in methanol or phase A : acetonitrile (1:1) were injected, using an Agilent Poroshell 120 EC-C18, 2.7 µm, 50 mm x 4.6 mm column at 40 °C. The mobile phase was a mixture of A = water with 0.05% formic acid and B = acetonitrile with 0.05% formic acid, with the method described as follows: flow 0.6 mL/min, 5% B-95% A 3 min, 100% B 4 min, 95% B-5% A 1 min. Purity is given as % of absorbance at 210 nm.

A. Blank sample at 210 nm

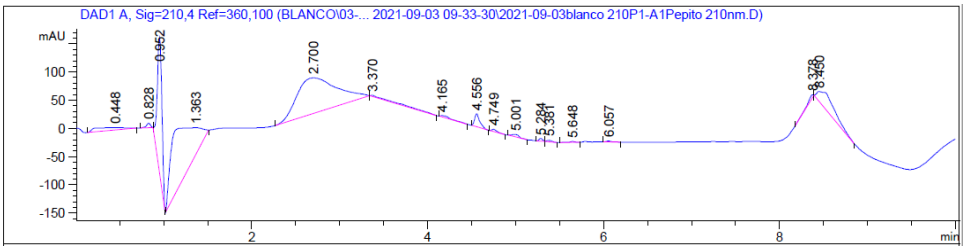

Signal 1: DAD1 A, Sig=210,4 Ref=360,100

Peak #	RetTime [min]	Type	Width [min]	Area [mAU*s]	Height [mAU]	Area %
1	0.448	BB	0.4297	127.28344	4.19874	2.3476
2	0.828	BB	0.0493	24.64111	7.70978	0.4545
3	0.952	BB	0.0585	865.54956	237.77800	15.9639
4	1.363	BB	0.4784	1811.65039	47.56133	33.4134
5	2.700	BB	0.4722	1966.11499	62.97413	36.2623
6	3.370	BB	0.3160	55.75306	2.13999	1.0283
7	4.165	BB	0.1121	20.58946	2.35285	0.3797
8	4.556	BB	0.0596	94.15643	23.09575	1.7366
9	4.749	BB	0.0616	14.14388	3.62047	0.2609
10	5.001	BB	0.0989	24.55610	4.15771	0.4529
11	5.284	BB	0.0438	12.51457	4.59502	0.2308
12	5.381	BB	0.0580	7.96658	2.21369	0.1469
13	5.648	BB	0.0752	8.13329	1.54998	0.1500
14	6.057	BB	0.0565	5.51645	1.51561	0.1017
15	8.378	BB	0.0955	30.69059	4.39144	0.5660
16	8.450	BB	0.2544	352.66684	16.97633	6.5045
Totals :				5421.92674	426.83083	

B. Compound 7a

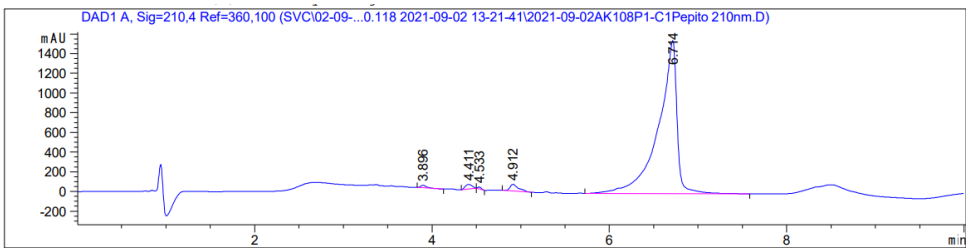

Signal 1: DAD1 A, Sig=210,4 Ref=360,100

Peak #	RetTime [min]	Type	Width [min]	Area [mAU*s]	Height [mAU]	Area %
1	3.896	BB	0.0669	121.06531	26.68560	0.5154
2	4.411	BB	0.0913	245.48805	45.23679	1.0450
3	4.533	BB	0.0443	50.22343	18.14256	0.2138
4	4.912	BB	0.1008	470.75082	67.94579	2.0039
5	6.714	BB	0.1936	2.26040e4	1554.90149	96.2219
Totals :				2.34915e4	1712.91223	

Figure S12 HPLC chromatograms.

B. Compound 7c

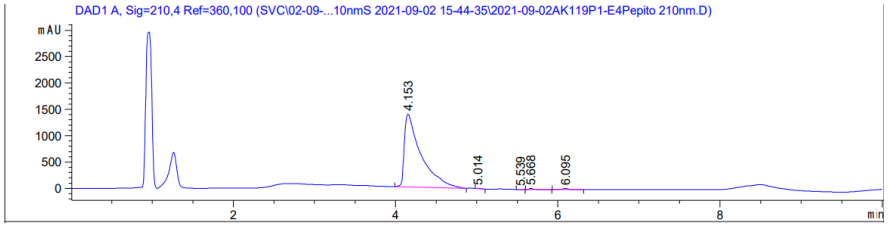

Signal 1: DAD1 A, Sig=210,4 Ref=360,100

Peak #	RetTime [min]	Type	Width [min]	Area [mAU*s]	Height [mAU]	Area %
1	3.403	BB	0.1199	8484.93750	990.64020	96.2801
2	4.537	BB	0.0515	90.53327	26.73654	1.0273
3	5.022	BB	0.0594	57.77774	14.21699	0.6556
4	5.286	BB	0.0501	49.97822	16.14174	0.5671
5	5.669	BB	0.0682	65.18999	14.03667	0.7397
6	6.096	BB	0.0632	64.34666	15.89738	0.7302
Totals :				8812.76339	1077.66951	

C. Compound 7e

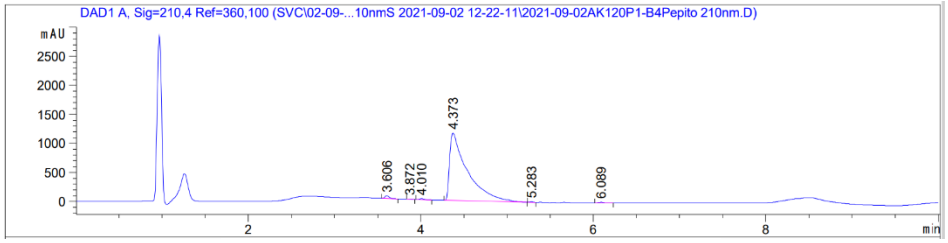

Signal 1: DAD1 A, Sig=210,4 Ref=360,100

Peak #	RetTime [min]	Type	Width [min]	Area [mAU*s]	Height [mAU]	Area %
1	3.606	BB	0.0555	165.07355	46.39963	0.9812
2	3.872	BB	0.0461	9.65483	3.30364	0.0574
3	4.010	BB	0.0583	64.20889	16.91945	0.3817
4	4.373	BB	0.1900	1.65204e4	1160.88782	98.1988
5	5.283	BB	0.0463	24.39436	8.79821	0.1450
6	6.089	BB	0.0613	39.69629	10.21384	0.2360
Totals :				1.68235e4	1246.52258	

D. Compound 7g

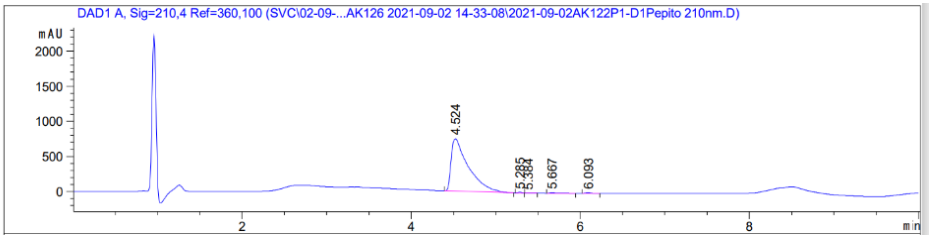

Signal 1: DAD1 A, Sig=210,4 Ref=360,100

Peak #	RetTime [min]	Type	Width [min]	Area [mAU*s]	Height [mAU]	Area %
1	4.524	BB	0.1951	1.05328e4	744.22437	98.8177
2	5.285	BB	0.0479	26.09593	8.97035	0.2448
3	5.384	BB	0.0777	10.15943	1.98393	0.0953
4	5.667	BB	0.0688	47.44333	10.10683	0.4451
5	6.093	BB	0.0589	42.31751	10.98515	0.3970
Totals :				1.06588e4	776.27063	

Figure S12 (contd.). HPLC chromatograms.

E. Compound 7h

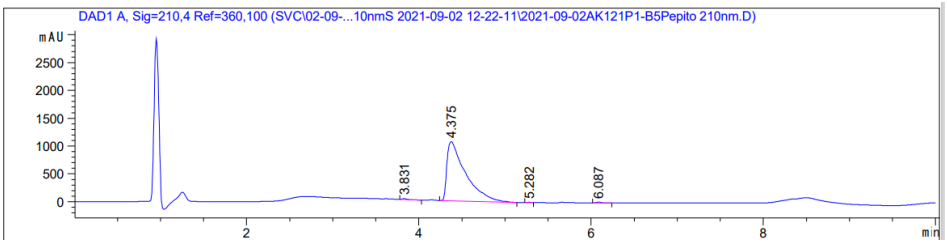

Signal 1: DAD1 A, Sig=210,4 Ref=360,100

Peak #	RetTime [min]	Type	Width [min]	Area [mAU*s]	Height [mAU]	Area %
1	3.831	BB	0.0570	61.50452	16.67539	0.3836
2	4.375	BB	0.2088	1.58970e4	1061.30896	99.1381
3	5.282	BB	0.0454	20.19656	7.05869	0.1260
4	6.087	BB	0.0602	56.50368	14.26974	0.3524
Totals :				1.60352e4	1099.31278	

F. Compound 8a

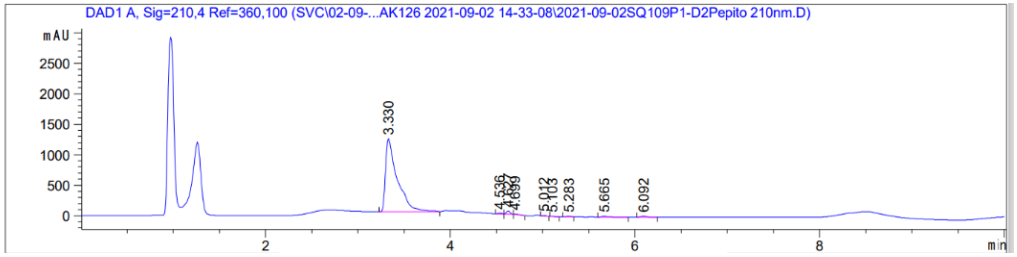

Signal 1: DAD1 A, Sig=210,4 Ref=360,100

Peak #	RetTime [min]	Type	Width [min]	Area [mAU*s]	Height [mAU]	Area %
1	3.330	BB	0.1231	1.05890e4	1197.71765	96.3327
2	4.536	BB	0.0433	50.68190	18.91561	0.4611
3	4.627	BB	0.0464	136.75783	49.17621	1.2441
4	4.699	BB	0.1264	21.93763	2.54842	0.1996
5	5.012	BB	0.0420	30.73908	11.96974	0.2796
6	5.103	BB	0.0461	6.81613	2.33107	0.0620
7	5.283	BB	0.0465	34.65716	11.72212	0.3153
8	5.665	BB	0.0641	60.12783	13.46442	0.5470
9	6.092	BB	0.0604	61.39497	15.43137	0.5585
Totals :				1.09921e4	1323.27662	

G. Compound 8b

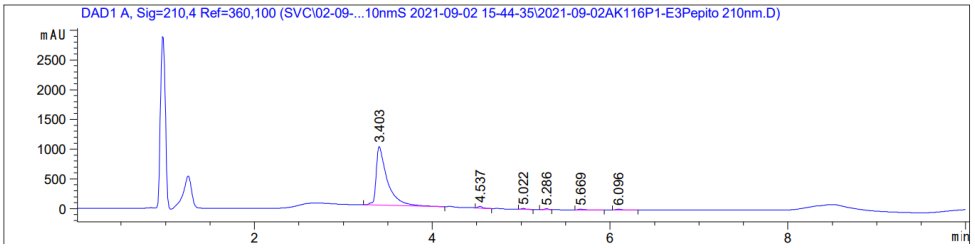

Signal 1: DAD1 A, Sig=210,4 Ref=360,100

Peak #	RetTime [min]	Type	Width [min]	Area [mAU*s]	Height [mAU]	Area %
1	3.403	BB	0.1199	8484.93750	990.64020	96.2801
2	4.537	BB	0.0515	90.53327	26.73654	1.0273
3	5.022	BB	0.0594	57.77774	14.21699	0.6556
4	5.286	BB	0.0501	49.97822	16.14174	0.5671
5	5.669	BB	0.0682	65.18999	14.03667	0.7397
6	6.096	BB	0.0632	64.34666	15.89738	0.7302
Totals :				8812.76339	1077.66951	

Figure S12 (contd.). HPLC chromatograms.

H. Compound 8c

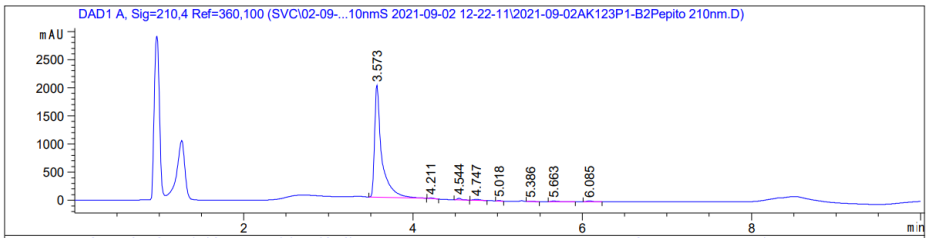

Signal 1: DAD1 A, Sig=210,4 Ref=360,100

Peak #	RetTime [min]	Type	Width [min]	Area [mAU*s]	Height [mAU]	Area %
1	3.573	BB	0.0848	1.16783e4	1981.63147	96.6711
2	4.211	BB	0.0622	37.88519	9.55903	0.3136
3	4.544	BB	0.0528	93.37370	26.71039	0.7729
4	4.747	BB	0.0830	97.25304	18.02235	0.8050
5	5.018	BB	0.0440	20.04850	7.31532	0.1660
6	5.386	BB	0.0664	22.01489	5.30594	0.1822
7	5.663	BB	0.0658	65.72585	14.80733	0.5441
8	6.085	BB	0.0596	65.84187	16.85728	0.5450
Totals :				1.20805e4	2080.20911	

J. Compound 8d

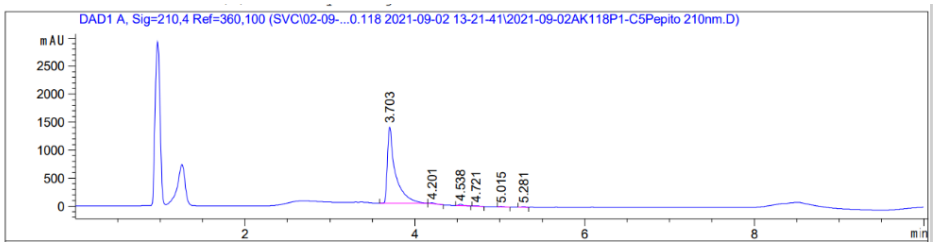

Signal 1: DAD1 A, Sig=210,4 Ref=360,100

Peak #	RetTime [min]	Type	Width [min]	Area [mAU*s]	Height [mAU]	Area %
1	3.703	BB	0.0906	8977.25879	1366.55078	97.6260
2	4.201	BB	0.0604	60.24472	15.15147	0.6551
3	4.538	BB	0.0531	83.69759	23.75171	0.9102
4	4.721	BB	0.0766	19.78190	4.22359	0.2151
5	5.015	BB	0.0451	20.27545	7.14769	0.2205
6	5.281	BB	0.0497	34.30367	11.21361	0.3730
Totals :				9195.56212	1428.03885	

K. Compound 8e

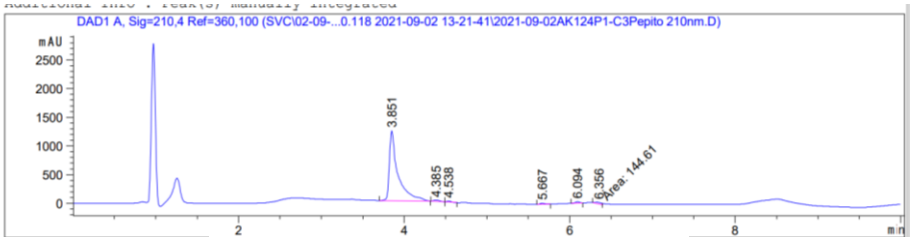

Signal 1: DAD1 A, Sig=210,4 Ref=360,100

Peak #	RetTime [min]	Type	Width [min]	Area [mAU*s]	Height [mAU]	Area %
1	3.851	BB	0.0978	8723.39746	1213.82544	95.0176
2	4.385	BB	0.0859	109.89513	21.39068	1.1970
3	4.538	BB	0.0475	65.32355	21.46842	0.7115
4	5.667	BB	0.0546	64.23743	17.59332	0.6997
5	6.094	BB	0.0579	73.35616	20.42494	0.7990
6	6.356	MM	0.0904	144.61026	26.65186	1.5751
Totals :				9180.81998	1321.35464	

Figure S12 (contd.). HPLC chromatograms.

L. Compound 8f

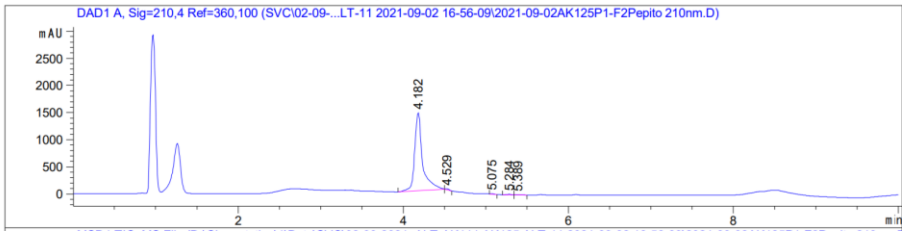

Signal 1: DAD1 A, Sig=210,4 Ref=360,100

Peak #	RetTime [min]	Type	Width [min]	Area [mAU*s]	Height [mAU]	Area %
1	4.182	BB	0.0995	9536.81543	1435.96277	98.8548
2	4.529	BB	0.0484	45.53699	15.44158	0.4720
3	5.075	BB	0.0430	19.52779	7.33892	0.2024
4	5.284	BB	0.0500	33.73574	10.35155	0.3497
5	5.389	BB	0.0794	11.67959	2.29222	0.1211
Totals :				9647.29553	1471.38703	

M. Compound 8g

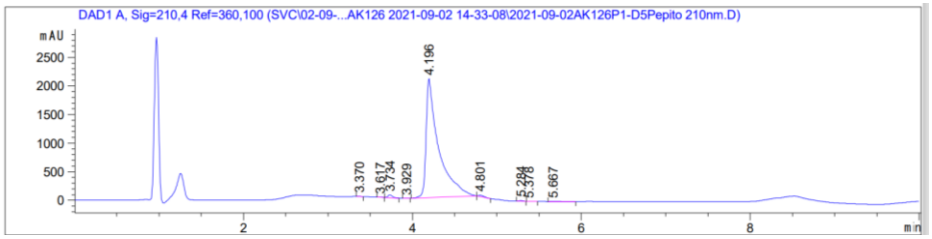

Signal 1: DAD1 A, Sig=210,4 Ref=360,100

Peak #	RetTime [min]	Type	Width [min]	Area [mAU*s]	Height [mAU]	Area %
1	3.370	BB	0.0406	16.20746	6.61533	0.0744
2	3.617	BB	0.0432	12.75164	4.76341	0.0586
3	3.734	BB	0.0560	166.15623	46.18147	0.7630
4	3.929	BB	0.0416	5.95397	2.34856	0.0273
5	4.196	BB	0.1363	2.13951e4	2074.75391	98.2466
6	4.801	BB	0.0823	112.63768	21.78938	0.5172
7	5.284	BB	0.0464	30.24860	10.26820	0.1389
8	5.378	BB	0.0689	5.19854	1.19197	0.0239
9	5.667	BB	0.0646	32.67900	7.25034	0.1501
Totals :				2.17770e4	2175.16256	

N. Compound 8h

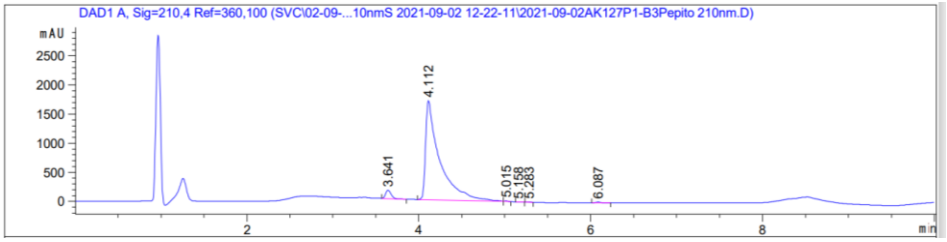

Signal 1: DAD1 A, Sig=210,4 Ref=360,100

Peak #	RetTime [min]	Type	Width [min]	Area [mAU*s]	Height [mAU]	Area %
1	3.641	BB	0.0683	628.64966	145.76141	3.1452
2	4.112	BB	0.1501	1.92728e4	1702.50195	96.4222
3	5.015	BB	0.0433	17.14541	6.38211	0.0858
4	5.158	BB	0.0690	8.55738	2.12580	0.0428
5	5.283	BB	0.0458	21.15603	7.76428	0.1058
6	6.087	BB	0.0607	39.61553	10.35098	0.1982
Totals :				1.99879e4	1874.88654	

Figure S12 (contd.). HPLC chromatograms.

O. Compound 11

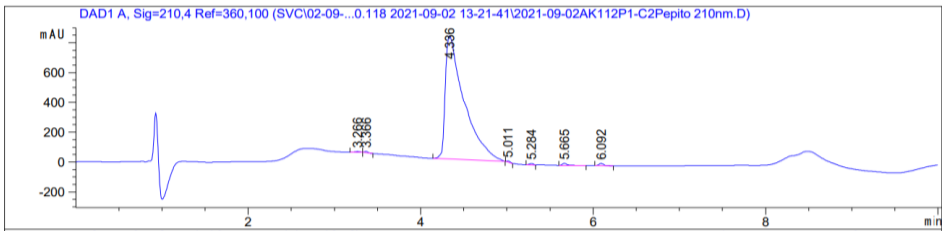

Peak #	RetTime [min]	Type	Width [min]	Area [mAU*s]	Height [mAU]	Area %
1	3.266	BB	0.0595	15.72553	4.21370	0.1236
2	3.366	BB	0.0454	21.01299	7.33597	0.1652
3	4.336	BB	0.2087	1.25137e4	826.24103	98.3776
4	5.011	BB	0.0433	18.21647	6.79378	0.1432
5	5.284	BB	0.0459	28.08868	9.66175	0.2208
6	5.665	BB	0.0659	65.16006	14.09522	0.5123
7	6.092	BB	0.0610	58.16316	15.09430	0.4573
Totals :				1.27200e4	883.43575	

P. Compound 12

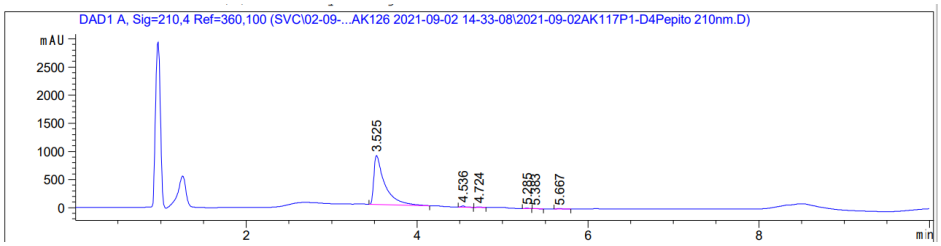

Signal 1: DAD1 A, Sig=210,4 Ref=360,100

Peak #	RetTime [min]	Type	Width [min]	Area [mAU*s]	Height [mAU]	Area %
1	3.525	BB	0.1236	7740.68848	871.79108	98.0780
2	4.536	BB	0.0515	68.55576	21.31982	0.8686
3	4.724	BB	0.0597	25.49978	6.81231	0.3231
4	5.285	BB	0.0479	23.79825	8.18991	0.3015
5	5.383	BB	0.0678	6.55111	1.47496	0.0830
6	5.667	BB	0.0594	27.28810	7.01464	0.3458
Totals :				7892.38148	916.60271	

Q. Compound 14a

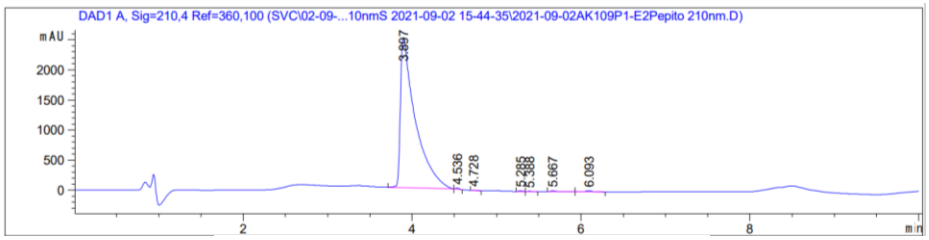

Signal 1: DAD1 A, Sig=210,4 Ref=360,100

Peak #	RetTime [min]	Type	Width [min]	Area [mAU*s]	Height [mAU]	Area %
1	3.897	BB	0.1666	3.03963e4	2486.41821	99.1896
2	4.536	BB	0.0469	55.32215	19.58862	0.1805
3	4.728	BB	0.0642	13.61010	3.43967	0.0444
4	5.285	BB	0.0476	30.65729	10.65267	0.1000
5	5.388	BB	0.0822	13.55960	2.46486	0.0442
6	5.667	BB	0.0641	56.92480	13.26489	0.1858
7	6.093	BB	0.0680	78.26924	16.90775	0.2554
Totals :				3.06447e4	2552.73666	

Figure S12 (contd.). HPLC chromatograms.

R. Compound 14b

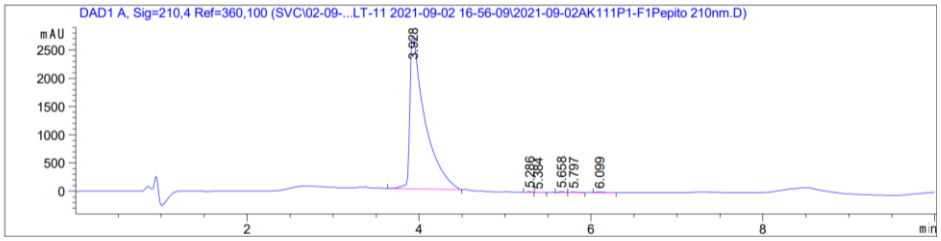

Signal 1: DAD1 A, Sig=210,4 Ref=360,100

Peak #	RetTime [min]	Type	Width [min]	Area [mAU*s]	Height [mAU]	Area %
1	3.928	BB	0.1616	3.29641e4	2716.26489	99.3815
2	5.286	BB	0.0495	36.25854	11.91480	0.1093
3	5.384	BB	0.0694	10.12397	2.39223	0.0305
4	5.658	BB	0.0628	59.08564	15.39407	0.1781
5	5.797	BB	0.0736	39.00004	7.89615	0.1176
6	6.099	BB	0.0626	60.66771	14.55526	0.1829
Totals :				3.31693e4	2768.41740	

S. Compound 14d

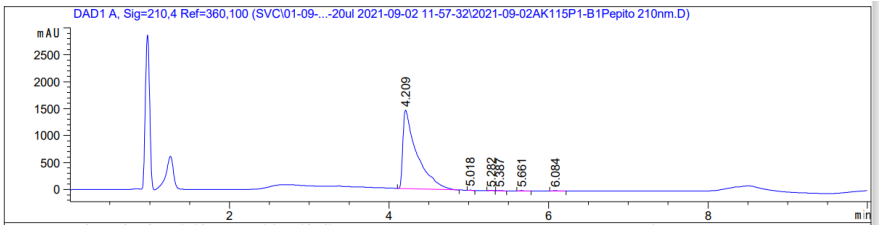

Signal 1: DAD1 A, Sig=210,4 Ref=360,100

Peak #	RetTime [min]	Type	Width [min]	Area [mAU*s]	Height [mAU]	Area %
1	4.209	BB	0.1630	1.78211e4	1454.30542	99.3865
2	5.018	BB	0.0461	16.17000	5.88454	0.0902
3	5.282	BB	0.0479	31.47665	10.82835	0.1755
4	5.387	BB	0.0628	14.78489	3.85447	0.0825
5	5.661	BB	0.0574	21.23606	5.70486	0.1184
6	6.084	BB	0.0600	26.34857	6.98244	0.1469
Totals :				1.79311e4	1487.56007	

O. Compound 15

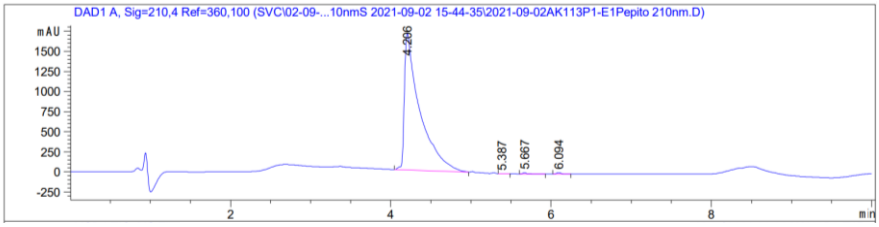

Signal 1: DAD1 A, Sig=210,4 Ref=360,100

Peak #	RetTime [min]	Type	Width [min]	Area [mAU*s]	Height [mAU]	Area %
1	4.206	BB	0.1758	2.27180e4	1701.49316	99.4753
2	5.387	BB	0.0697	9.49146	2.14295	0.0416
3	5.667	BB	0.0647	51.35463	11.82303	0.2249
4	6.094	BB	0.0613	58.97343	15.19532	0.2582
Totals :				2.28379e4	1730.65446	

Figure S12 (contd.). HPLC chromatograms.

Bioassays' procedures

***B. subtilis* growth inhibition assay.** An overnight starter culture (in LB both) of *B. subtilis* was diluted 1000-fold (in fresh LB media) and grown to an OD_{600} of ~0.3 (approximately 3.5 h at 37 °C). This log-phase culture was then diluted 500-fold into fresh LB broth to generate the working solution. This working solution (180 µL) was then transferred into every well in a flat-bottom 96-well plate except for the first column. Inhibitors were added at specific starting concentrations (100 µM−1 mM) with a total volume of 360 µL (diluted with working solution) into the first column. The inhibitors were then sequentially diluted 2-fold across 12 wells. Plates were incubated at 37 °C and shaken at 200 rpm for 12 h. The OD_{600} values were then measured to determine IC_{50} values using GraphPad Prism software (version 7.04). Experiments were carried out in duplicate or triplicate. IC_{50} values were determined using a four-parameter variable-slope function in the Prism program.

$$Y = \text{Bottom} + \frac{(\text{Top}-\text{Bottom})}{1+10^{((\text{Log}\,IC_{50}-X)\times \text{Hill slope})}}$$

***M. smegmatis* growth inhibition assay.** *M. smegmatis* (grown for 36−48 h) was diluted 1000-fold in fresh Middlebrook 7H9 (plus 10% ADC supplement, Sigma: M0553-1VL; 0.5% glycerol; 0.05% Tween 80) media to generate a working solution. This working solution (180 µL) was then transferred into every well in a flat-bottomed 96-well plate except for the second column and peripheral wells. Inhibitors were added at specific starting concentrations (100 µM−1 mM) with a total volume of 300 µL (diluted with working solution) to the second column. The inhibitors were then sequentially diluted 3-fold across 10 wells; 200 µL of water was added to each peripheral well to prevent water evaporation from the plate. Plates were incubated at 37 °C, with shaking at 200 rpm for 48 h. The OD_{600} values were then measured to determine bacterial growth inhibition, as described above.

***E. coli* growth-inhibition assay.** An overnight starter culture of *E. coli* (K12) was diluted 1000-fold and grown to an OD_{600} value of ~0.3. These log-phase cultures were then diluted 500-fold into fresh LB broth to generate a working solution. Working solution (200 µL) was transferred into each well of a 96-well culture plate. Inhibitors were then added at 1 mM and sequentially diluted 3-fold to 46 nM, keeping the volume and culture broth composition constant. Plates were incubated for 12 h at 37 °C with shaking at 200 rpm. The OD_{600} values were then measured to determine bacterial growth inhibition, as described above.

***M. tuberculosis* HN878 growth inhibition assay.** Compounds were dissolved in DMSO at 10 mM. For each compound, a ten-point two-fold dilution series was dispensed onto 96-well plates using a Tecan D300e Digital Dispenser to achieve the final incubation concentration range of 0.04883 to 25 µM. *M. tuberculosis* HN878 was grown in Middlebrook 7H9 medium (10% ADC, 0.2% glycerol, 0.05% Tween 80) to a mid-log optical density (OD_{600}) of 0.4 and diluted to OD_{600}=0.03. 200µL of adjusted culture were added per well. SQ109 (compound 1) was used as a positive control. Untreated control wells containing 1% DMSO were included on each plate. Two biological replicates were performed for each compound. Plates were incubated at 37°C with shaking (110 rpm) for 5 days. On day 5, wells were then resuspended manually and the OD_{600} was read with a Tecan Infinite M200 plate reader. Data is expressed as percent growth inhibition and curves were fit by using GraphPad Prism software using nonlinear regression (variable slope, four parameters). IC_{50} results and errors are shown in the text.

***M. tuberculosis* H37Rv Growth Inhibition Assay.** The compounds were assayed for inhibition of M. tuberculosis H37Rv cell growth as described previously. [278] In brief, cell growth MIC values were estimated visually by using series 2-fold inhibitor dilutions, in duplicate.

***M. tuberculosis* Erdman Growth Inhibition Assay.** The compounds were assayed for inhibition of *M. tuberculosis* Erdman cell growth as described previously. [279] In brief, cell growth inhibition MIC values were estimated visually by using series 2-fold inhibitor dilutions, in duplicate.

***M. abscessus* growth and Inhibition Assay**. *M. abscessus* CIP104536T was routinely grown and maintained at 37°C in Middlebrook 7H9 broth (BD Difco) supplemented with 0.025% Tyloxapol (Sigma-Aldrich) and 10% oleic acid, albumin, dextrose, catalase (OADC enrichment) (7H9T/OADC). Strain PIPD1R1 carrying a mutated mmpL3 allele (A309P) was reported earlier. [189] For drug susceptibility testing, bacteria were grown in Cation-Adjusted Mueller-Hinton Broth (CaMHB; Sigma-Aldrich) at 30°C. The minimal inhibitory concentrations (MIC) were determined according to the CLSI guidelines. [280] The broth micro-dilution method was used in CaMHB with an inoculum of $5x10^6$ CFU/mL in exponential growth phase. The bacterial suspension was seeded in 100 µL volumes in all of the wells of a 96-well plate, except for the first column, to which 198 µL of the bacterial suspension was added. In the first column, 2 µL of drug at 10 mg/ml was added to the first well containing 198 µL of bacterial suspension. Two-fold serial dilutions were then carried out and the plates were incubated for 4 days at 30 °C. MICs were recorded by visual

inspection. Rifabutin (RFB) was included as a control drug. Assays were completed in duplicate in three independent experiments. The results were the same so errors are not given.

***In vitro* activity assay for *T. cruzi* epimastigotes.** *T. cruzi* epimastigotes were cultured in liver infusion tryptose medium (BD Difco™) with 10% FBS at 28°C. The exponential growth phase of epimastigotes were treated with different concentrations of drugs or 0.1% DMSO as negative control and incubated for 3 days at 28°C. The viability of parasites was quantified with resazurin. 200 μM of resazurin sodium salt (Sigma) was added, and the samples were incubated for 5 h. After incubation, the parasites were fixed using 4% paraformaldehyde, and the plates were analyzed using a Spectramax plate reader at 590 nm (emission) and 530 nm (excitation).[281] Results were obtained from two independent biological repeats performed in technical duplicates and data were fit using a four-parameter variable-slope function in Prism.

***In vitro* activity assay for *T. cruzi* amastigotes**. U2OS human osteosarcoma cells were maintained in DMEM supplemented with high glucose, 10% FBS, and 1% P/S at 37°C with 5% CO_2 in air. U2OS cells were infected with TCTs at a multiplicity of infection (MOI) of 1:4 and treated with drugs simultaneously in 384-well plates. After 3 days of drug treatment, cells were then fixed with 4% paraformaldehyde (PFA), washed with 1× PBS, and stained with a fluorescent probe (Draq-5, Thermo Fisher). Cell images were acquired by an automated image analyzer (Operetta, Perkin Elmer Technology); analysis included at least 1000 cells in five fields per well. For the imaging of infected cells and parasites, Draq-5 was observed under a 20× air objective. An image analysis algorithm (Columbus, Perkin Elmer Technology) was used to detect the Draq-5 signal in the nuclei of cells and parasites. The number of parasites was defined by the value of the number of parasites in infected cells of the acquired image. Results were obtained from two independent biological repeats performed in technical duplicates and data were fit using a four-parameter variable-slope function in Prism.

***In vitro* activity assay for *L. donovani*.** *L. donovani* strain Ld1S (MHOM/SD/62/1S-CL2D) parasites were maintained at 28°C in modified M199 culture medium (Sigma) with 20 mM HEPES (Gibco), 0.1 mM adenine (Sigma), 0.0005% hemin (Sigma), 0.0001% biotin (Sigma), 0.0002% biopterin (Santa Cruz), and 4.62 mM $NaHCO_3$ (Sigma), supplemented with 10% FBS and 1% P/S. The cultures were diluted every 7~10 days and underwent no more than five passages to avoid generation of genetic variability. Promastigotes were treated with different concentrations of drugs or 0.1% DMSO as negative control and incubated for 3 days at 28°C. The viability of parasites was quantified with resazurin as described above. Results were

obtained from two independent biological repeats performed in technical duplicates and data were fit using a four-parameter variable-slope function in Prism.

In vitro* activity assay for *T. brucei. The bloodstream form (BSF) of *T. b. brucei* Lister strain 427 was cultivated in HMI-9 medium supplemented with 10% heat-inactivated fetal bovine serum (FBS, Gibco), 100 µg/mL penicillin, and 100 µg/mL streptomycin (1% P/S, Gibco) at 37°C and a 5% CO_2 atmosphere. Parasites were sub-cultured every 3 or 4 days and maintained for 10 passages. Growth inhibition of T. b. brucei was assayed by measuring the conversion of resazurin to resorufin. The assays were performed in 384-well plates that were seeded with T. brucei 427 BSF (5 × 104 cells per well). After seeding, the parasites were exposed to the compounds for 3 days. Then, 200 µM of resazurin sodium salt (Sigma) was added, and the samples were incubated for 5 h. After incubation, the parasites were fixed using 4% paraformaldehyde, and the plates were analyzed using a Spectramax plate reader at 590 nm (emission) and 530 nm (excitation). Results were obtained from two independent biological repeats performed in technical duplicates and data were fit using a four-parameter variable-slope function in Prism.

In vitro* activity against asexual blood stages of *P. falciparum. All *in vitro* experiments involving human blood donors and human malaria parasites holds ethics approval from the University of Pretoria Research Health Sciences Ethics Committee (506/2018) and Natural and Agricultural Sciences Ethics Committee (NAS 180000094). This work abides by the Declaration of Helsinki principles.

Antiproliferative activity was determined using a DNA-binding, SYBR Green I-based fluorescence assay as previously described. [231,232] Synchronized ring-stage parasites (1% parasitemia, 1% hematocrit) were exposed to drug pressure over a 96 h period under stationary, hypoxic conditions (90% N_2, 5% O_2, 5% CO_2) at 37 °C. Changes in parasite proliferation was determined by combining equal volumes (100 µL) of parasite suspension and SYBR Green I lysis buffer (0.2% µL/mL of 10 000X SYBR Green I, 20 mM Tris-HCl at pH 7.5, 5 mM EDTA, 0.008% (w/v) saponin and 0.08% (v/v) Triton-X 100) for 1 h in the dark. Fluorescence was read with a Fluoroskan Ascent FL plate reader at 485/538 nm. Nonlinear regression curves were generated from which the 50% inhibitory concentrations (IC_{50}) were determined. Data were obtained from three independent biological repeats performed in technical triplicates.

***In vitro* activity against HepG2 cells.** Human hepatocellular liver carcinoma cells (HepG2) were cultivated *in vitro* in Dulbecco's Modified Eagle's Medium (DMEM) supplemented with 10% (v/v) heat inactivated fetal bovine serum and 1% (v/v) penicillin/streptomycin. [232] Cells were detached with Trypsin treatment

(0.25%) at 80% confluency and 100 000 cells were seeded in 96-well plates to adhere for 24 h at 37°C under 5% CO_2, humid (95%) conditions. Cells were subsequently exposed to drug pressure for 48 h and cytotoxicity was then determined using the lactate dehydrogenase (LDH) release assay (Cytoselect Inc) through the colorimetric detection at 450 nm. Data obtained from at least two independent biological repeats performed in technical duplicates.

Microsomal stability. The human, rat and mice pooled microsomes, with a protein content of 20 mg mL^{-1}, were purchased from Tebu-Xenotech. The compounds were incubated in a 96-well microplate at 37 °C with the microsomes in 50 mM phosphate buffer (pH = 7.4) containing as cofactors 30 mM $MgCl_2$, 10 mM NADP, 100 mM glucose-6-phosphate and 40 U mL^{-1} glucose-6-phosphate dehydrogenase, using the following volumes: 300 mL PBS, 163 mL cofactors, 5 mL test compounds (at 5 mM) and 30 mL microsomes. Samples (75 µL) were taken from each well at 0, 10, 20, 40 and 60 min and transferred to a microplate. Acetonitrile (75 µL) and internal standard (rolipram) were then added for inactivating the microsomes, and water with 0.5% formic acid (30 µL) was subsequently added for improving the chromatographic conditions, keeping the mixtures at 4 °C. The plate was centrifuged at 46,000 g for 30 min at 15 °C and supernatants were taken and analyzed in a UPLC-MS/MS system (UPLC QSM Waters Acquity) using reverse phase Acquity UPLC® HSST3 1.7 µm (2.1 mm × 50 mm, Waters) as the stationary phase, 0.1% formic acid in water (A) / 0.1% formic acid in acetonitrile (B) as the mobile phase, a flow of 0.8 mL min^{-1}. The gradient was 95% A and 5% B at 0, 0.1 min; 100% B at 1, 2.5 mins and 95% A 5% B at 2.6, 3 mins. The metabolic stability of the compounds was calculated from the logarithm of the remaining compound at each of the time points studied.

7 APPENTIX B

Computational biochemistry methods

Protein Structure Preparation

Structures of the Rim, AK59, RL208, M2WJ352, and UBALT09 were sketched with the Maestro program and model-built with the Schrödinger 2021-2 platform (Schrödinger Release 2021-2: Maestro, Schrödinger, LLC, New York, NY, 2021; Maestro-Desmond Interoperability Tools, Schrödinger, New York, NY, 2021). The models were minimized using the conjugate gradient method, MMFF94 force field [197] and distance-dependent dielectric constant 4.0 until a convergence threshold of 2.4×10^{-5} kcal mol^{-1} $Å^{-1}$ was reached. The R–Rim, S–Rim, AK59, RL208, M2WJ352, and UBALT09 have a charged ammonium group at pH 7. The WT M2TM was modeled using the PDB ID 2KQT [73] structure in which Amt is complexed. The WT M2CD was modeled using the PDB ID 2L0J structure of WT M2CD apoprotein. [63] Previous PMF calculations [52] using the W41 χ2 dihedral as the reaction coordinate showed that the energetically favored conformation for Trp41 in AH M2 is t-90 instead of t-105 observed in the PDB ID 2L0J structure. [63] Accordingly, we set the W41 χ2 dihedrals to 90°. To form the M2CD–Amt complex, the heavy atoms of the TM helices between M2CD (PDB ID 2L0J) [63] and M2TM–Amt complex (PDB ID 2KQT) [73] were superimposed (root-mean-square deviation (RMSD) < 0.1 Å), and the M2TM was deleted. The protein preparation module in Schrödinger's 2021-2 Maestro (Schrödinger Release 2021-2: Maestro, Schrödinger, LLC, New York, NY, 2021-2; Maestro- Desmond Interoperability Tools, Schrödinger, New York, NY, 2021) was used to add missing hydrogen atoms. N- and C-termini of the M2 model systems were capped by acetyl and methylamino groups, respectively. The histidine residues (His37 and His57) were protonated at the Nε site according to experimental data. [65,91,111,282]All hydrogens of the protein complex were minimized using the OPLS2005 force field [200,275,283]and distance-dependent dielectric constant 4.0, with the conjugate gradient method until the RMSD of potential energy reached 2.4×10^{-5} kcal mol^{-1} $Å^{-1}$ by means of Maestro/Macromodel. [202] Geometries of the complexes were energy-minimized in the gas phase with OPLS2005 using the conjugate gradient method and a distance-dependent dielectric constant of 4 Å until a convergence value of 0.01 kcal mol^{-1} $Å^{-1}$ was reached.

MD simulations trajectories analysis

The analysis of the trajectories was performed with Desmond software, (Schrödinger Release 2021-1: Desmond Molecular Dynamics System, D. E. Shaw Research, New York, NY, 2021. Maestro-Desmond Interoperability Tools, Schrödinger, New York, NY, 2021). The Desmond trajectories (.cms) were viewed and analyzed within the Maestro interface. The RMSDs of Cα carbons and heavy atoms of ligand were calculated with modules using Schrödinger's python3 interpreter. A representative structure of the whole MD simulation was generated for each system using the average structure panel in Maestro and the RMSD plots were generated using python3.10 (matplotlib module). For the calculation of specific distances within MD simulation, a python3 script (monitor_asl.py) was used to monitor each residue. The measurements were performed using the center of mass (COM) of the residues Val27, Ala30, and Gly34 and the center of mass of the ligand's cage and of His COM and ligands charged amine group. Also using the Simulation Event Analysis panel from Maestro, the number of Hydrogen bonds between each ligand and the water molecules and Ala30 was monitored.

Table S5 Percent block of full-length A/Udorn/72 M2 WT or S31N current.

Compound	M2 WT	M2 S31N
Rmt [72, b]	96 ± 1[a]	1 ± 0.2
AK59 [72, b]	90 ± 0.2	21 ± 2
RL208 [101, b]	84.2 ± 0.5	2.0 ± 1.0
M2WJ352 [89, b]	20	91
UBALT09	7.1 ± 1.8	78.6 ± 1.8

[a]Mean ± SEM calculated at 2 min of drug (100 µM) perfusion (N=3); [b]values taken from the indicated references.

Table S6 Effects of compounds Rmt, AK59, RL208, M2WJ352, and UBALT09 on two influenza A M2CD variants in two conditions using 300 µM concentration.

Compound	CSPs in ^{15}N of G34 and side chain His37 / His37-His37 hydrogen bond			
	Drug binding at elevated temperature		Drug binding at low pH	
	WT	S31N	WT	S31N
Apo	- / yes	- / yes	- / yes	- / yes
Rmt [112]	LS, LS[a] / no	NB / yes	LS, LS / no	NB / yes
RL208	NB / yes	NB / yes	NB / yes	NB / yes
AK59	MS, MS / (20% left)	NB / yes	LS, LS / no	NB / yes
M2WJ352	NT	NT	NB / yes	NB / yes
UBALT09	NT	NT	LS, LS / partial[b]	NB / yes

[a] MS = medium shifts, LS = large shifts, NB = no binding, NT = not tested; [b] concentration at 6 mM

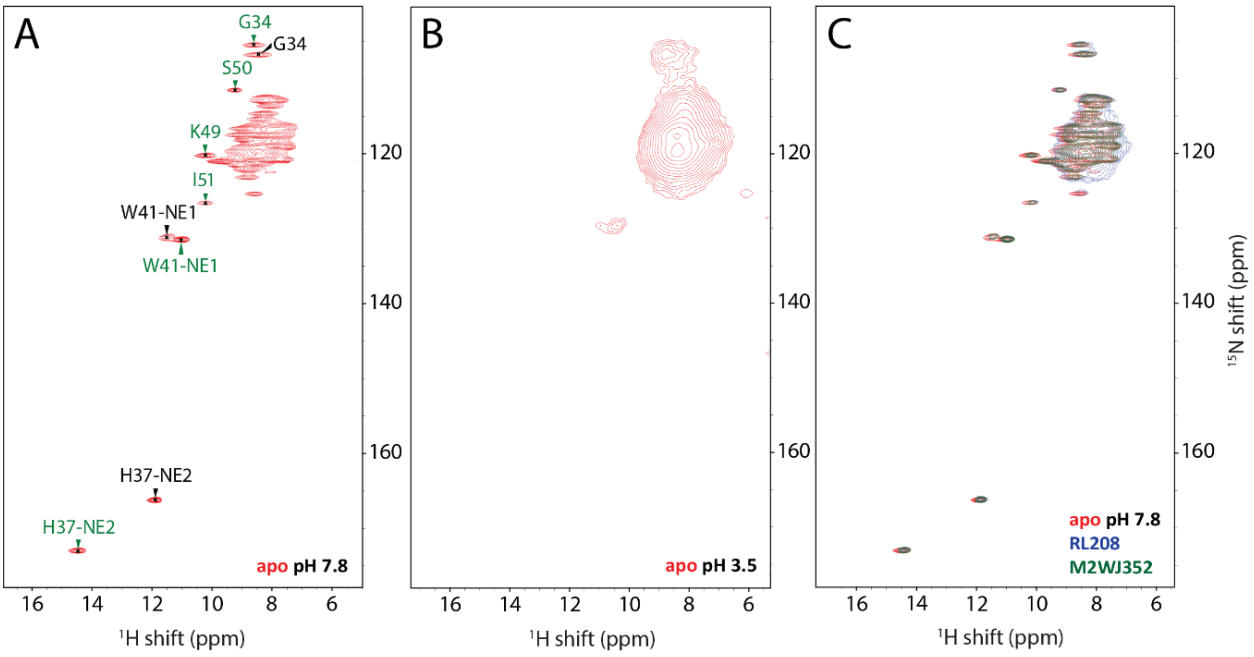

Figure S13 (H)NH spectra of WT M2CD (A) at pH 7.8, (B) at pH 3.5, (C) without (red) and in the presence of 300 µM of RL208 (blue) or M2WJ352 (green). The samples were reconstituted in DPhPC bilayers at pH 7.8 using a lipid:tetramer molar ratio of 25:1. Spectra with drug were recorded at pH 7.8 after relaxing the system at acidic pH 3.5 in the presence of the drug and switching back to alkaline pH.

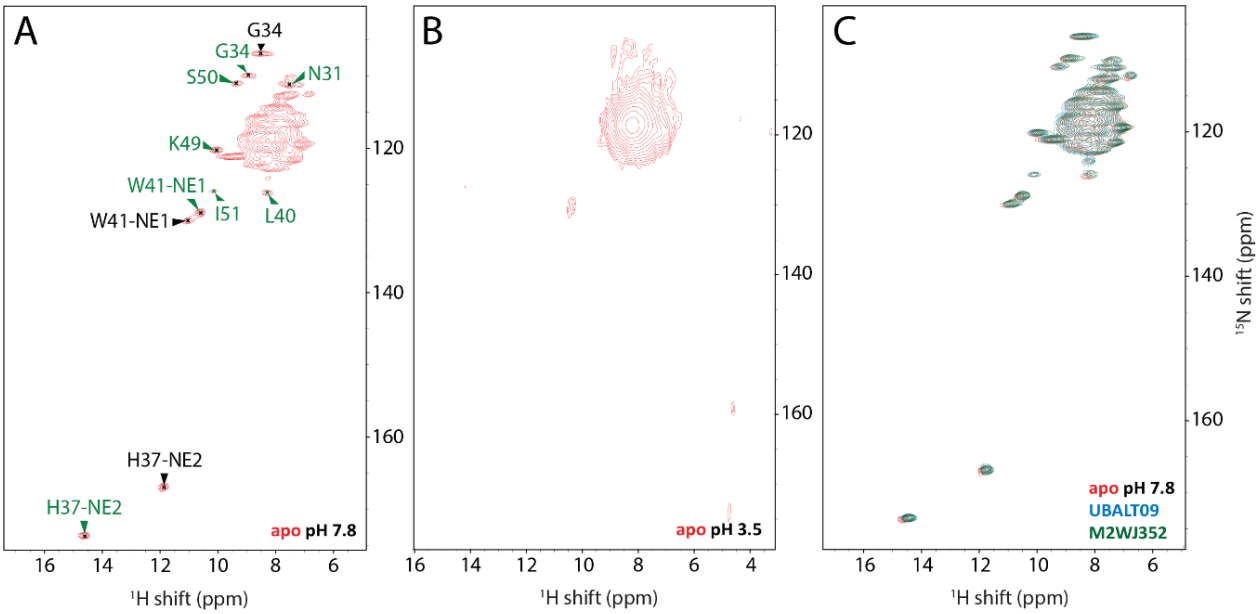

Figure S14 (H)NH spectra of S31N M2CD, (A) at pH 7.8, (B) at pH 3.5, (C) without (red) and in the presence of 300 µM of UBALT09 (blue) or M2WJ352 (green). The samples were reconstituted in DPhPC bilayers at pH 7.8 using a lipid:tetramer molar ratio of 25:1. Spectra with drug were recorded at pH 7.8 after relaxing the system at acidic pH 3.5 in the presence of the drug and switching back to alkaline pH.

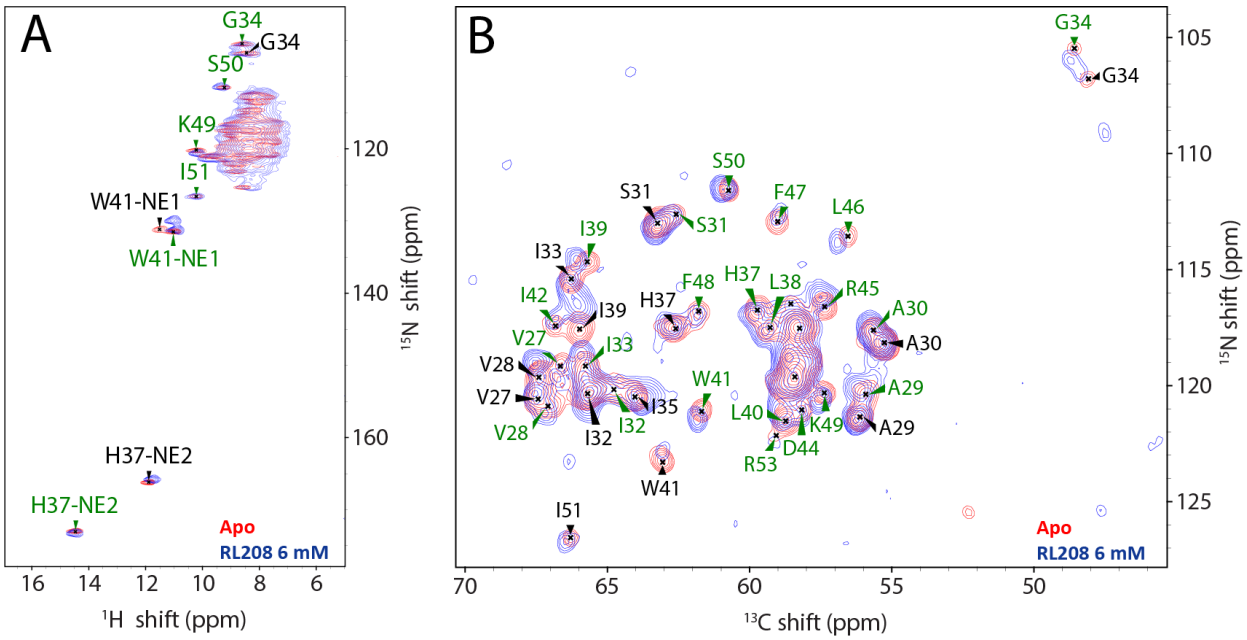

Figure S15 Monitoring the ^{1}H, ^{15}N, and ^{13}C chemical shift perturbation in WT M2CD resonances in the presence of 6 mM of RL208. (A) (H)NH spectrum of WT M2 with (blue) and without RL208 (red). (B) ^{15}N-$^{13}C\alpha$ projection of the (H)CANH spectrum of WT M2 with (blue) and without RL208 (red). The samples were reconstituted in DPhPC bilayers at pH 7.8 using a lipid:tetramer molar ratio of 25:1. Both spectra were recorded at pH 7.8 after relaxing the system at acidic pH 3.5 in the presence of the drug and switching back to alkaline pH.

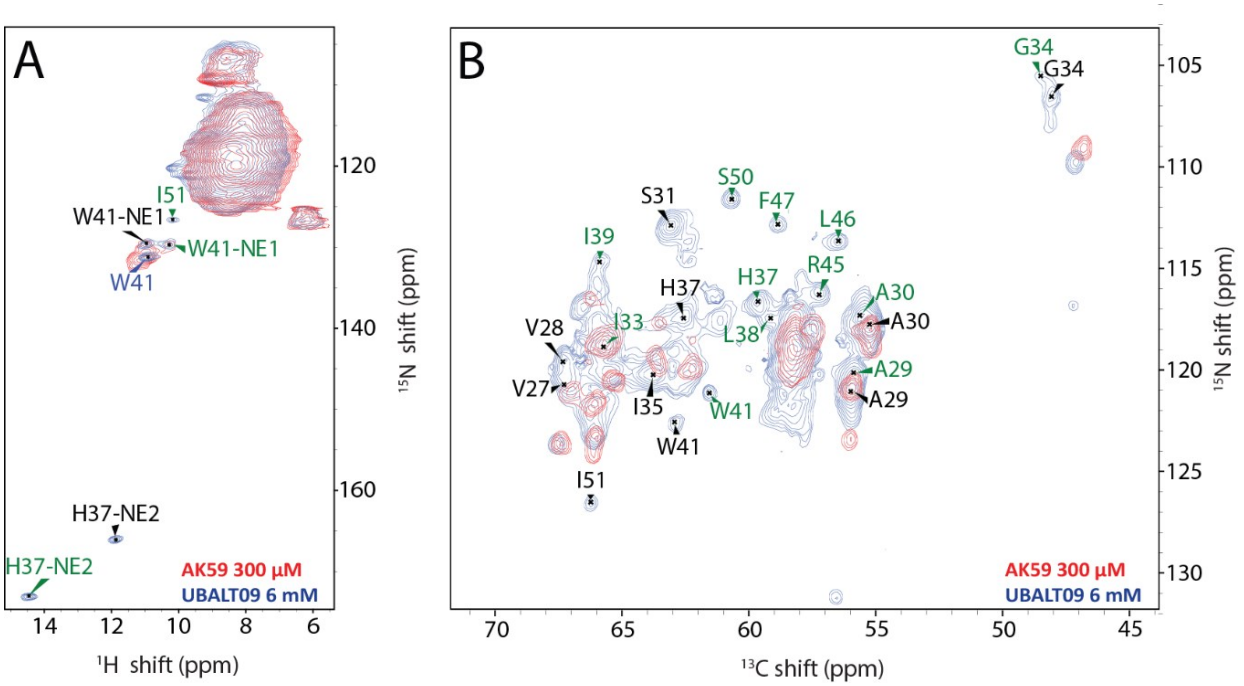

Figure S16 Monitoring the ^{1}H and ^{15}N chemical shift perturbation in WT M2CD resonances in the presence of 300 µM of AK59 and 6 mM of UBALT09. (A) (H)NH spectrum of WT M2 with AK59 (red) and UBALT09 (blue). (B) ^{15}N-$^{13}C\alpha$ projection of the (H)CANH spectrum of WT M2 with AK59 (red) and UBALT09 (blue). The samples were reconstituted in DPhPC bilayers at pH 7.8 using a lipid:tetramer molar ratio of 25:1. Both spectra were recorded at pH 7.8 after relaxing the system at acidic pH 3.5 in the presence of the drug and switching back to alkaline pH.

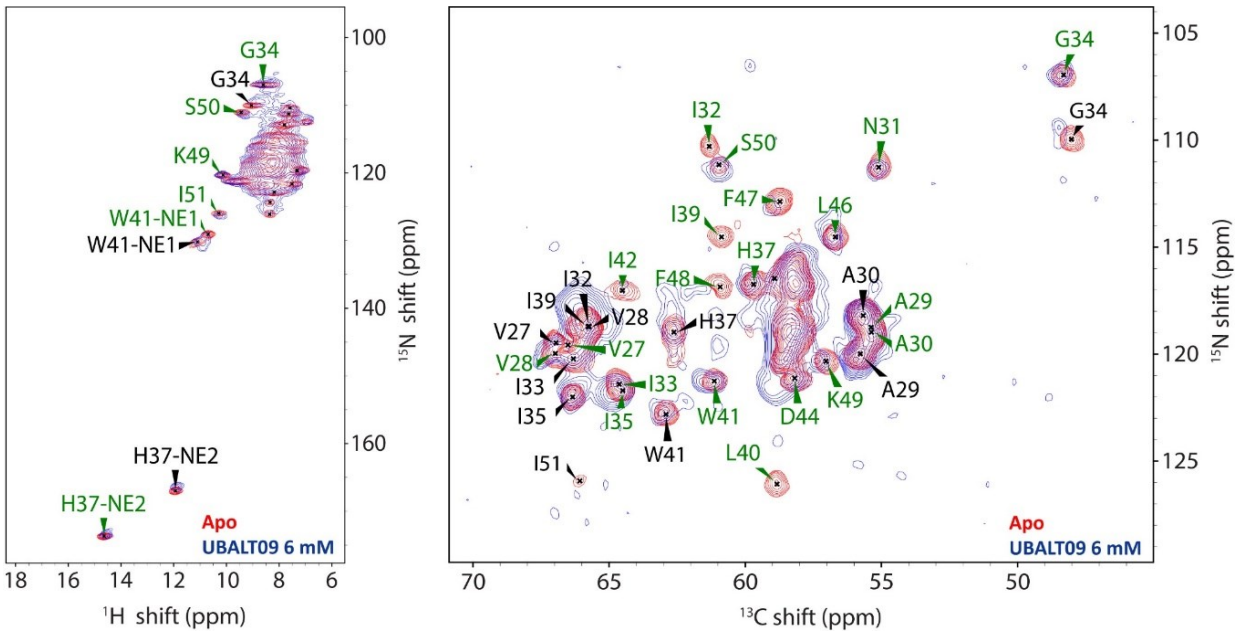

Figure S17 Monitoring the ^{1}H, ^{15}N, and ^{13}C chemical shift perturbation in S31N M2CD resonances in the presence of 6 mM of UBALT09. (A) (H)NH spectrum of S31N M2 with (blue) and without UBALT09 (red). (B) ^{15}N-$^{13}C\alpha$ projection of the (H)CANH spectrum of S31N M2 with (blue) and UBALT09 Rmt (red). The samples were reconstituted in DPhPC bilayers at pH 7.8 using a lipid:tetramer molar ratio of 25:1. Both spectra were recorded at pH 7.8 after relaxing the system at acidic pH 3.5 in the presence of the drug and switching back to alkaline pH.

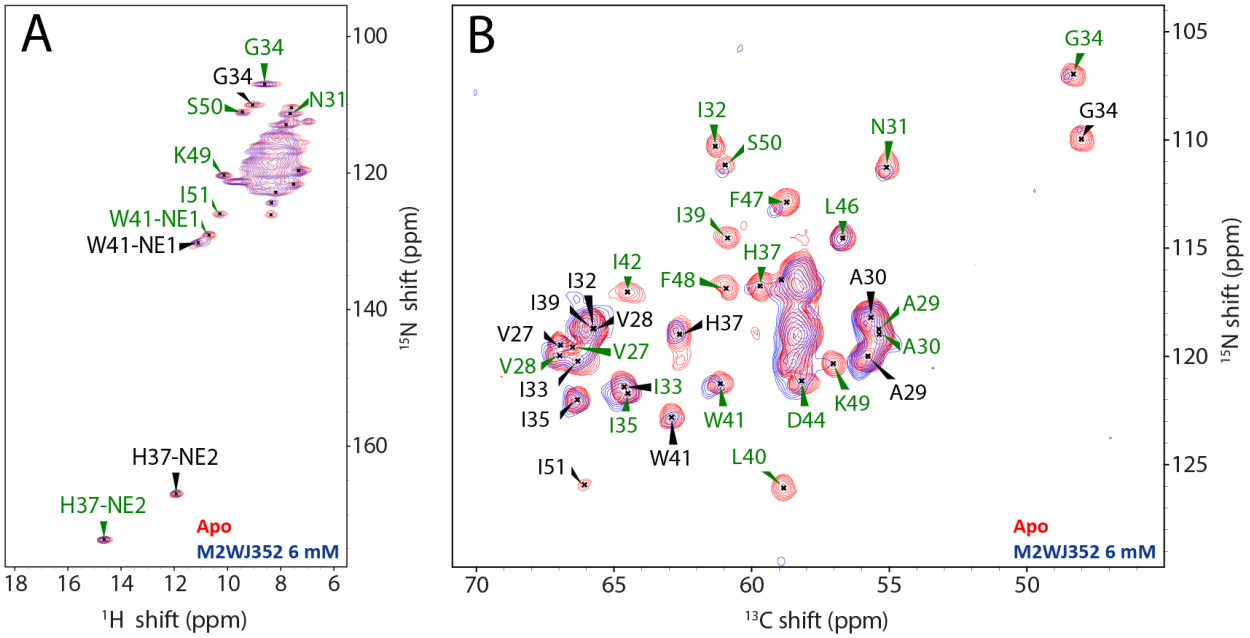

Figure S18 Monitoring the ^{1}H, ^{15}N, and ^{13}C chemical shift perturbation in S31N M2CD resonances in the presence of 6 mM of M2WJ352. (A) (H)NH spectrum of S31N M2 with (blue) and without M2WJ352 (red). (B) ^{15}N-$^{13}C\alpha$ projection of the (H)CANH spectrum of WT M2 with (blue) and M2WJ352 Rmt (red). The samples were reconstituted in DPhPC bilayers at pH 7.8 using a lipid:tetramer molar ratio of 25:1. Both spectra were recorded at pH 7.8 after relaxing the system at acidic pH 3.5 in the presence of the drug and switching back to alkaline pH.

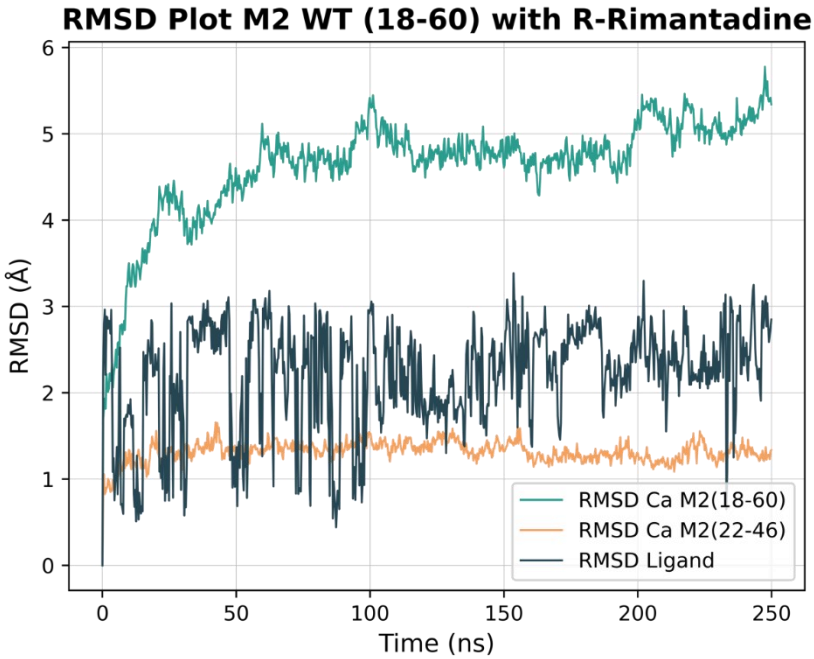

Figure S19 RMSD(Ca) and RMSD(ligand) in the MD simulations of the WT apo-protein and in complex with R-rimantadine during the 250ns-MD simulations with CHARMM36m force field.

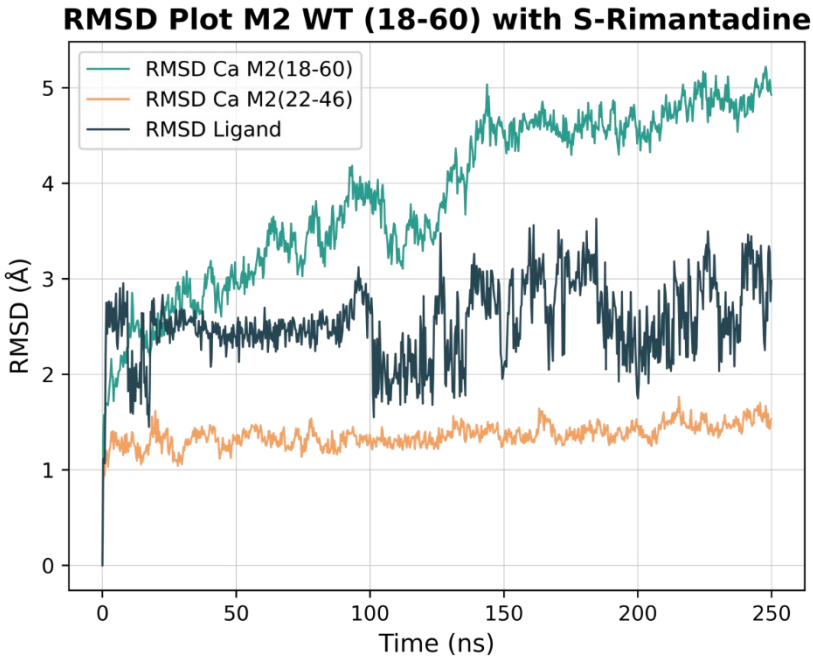

Figure S19 (contd.). RMSD(Ca) and RMSD(ligand) in the MD simulations of the WT apo-protein and in complex with S-rimantadine during the 250ns-MD simulations with CHARMM36m force field.

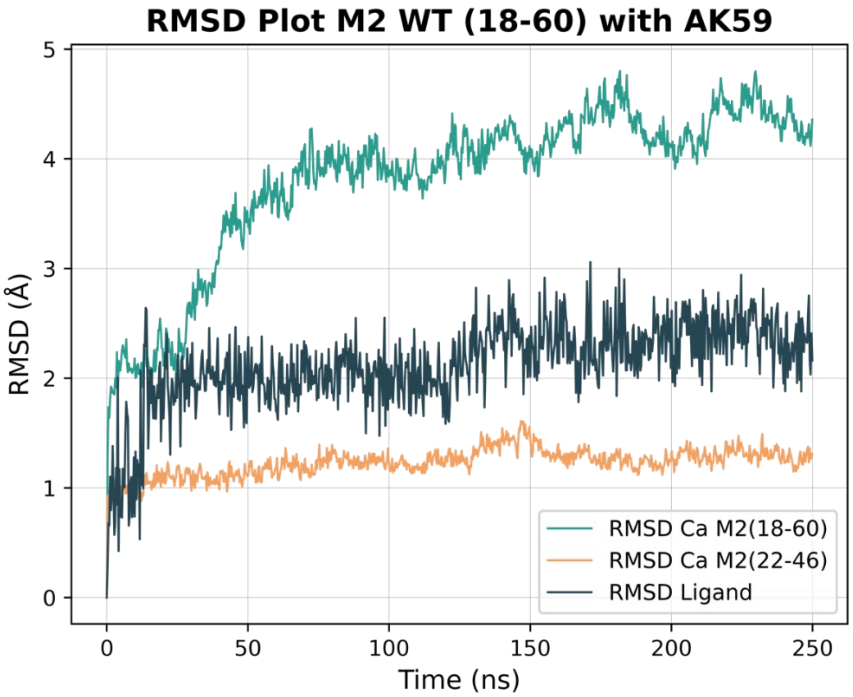

Figure S19 (contd.). RMSD(Ca) and RMSD(ligand) in the MD simulations of the WT apo-protein and in complex with AK59 during the 250ns-MD simulations with CHARMM36m force field.

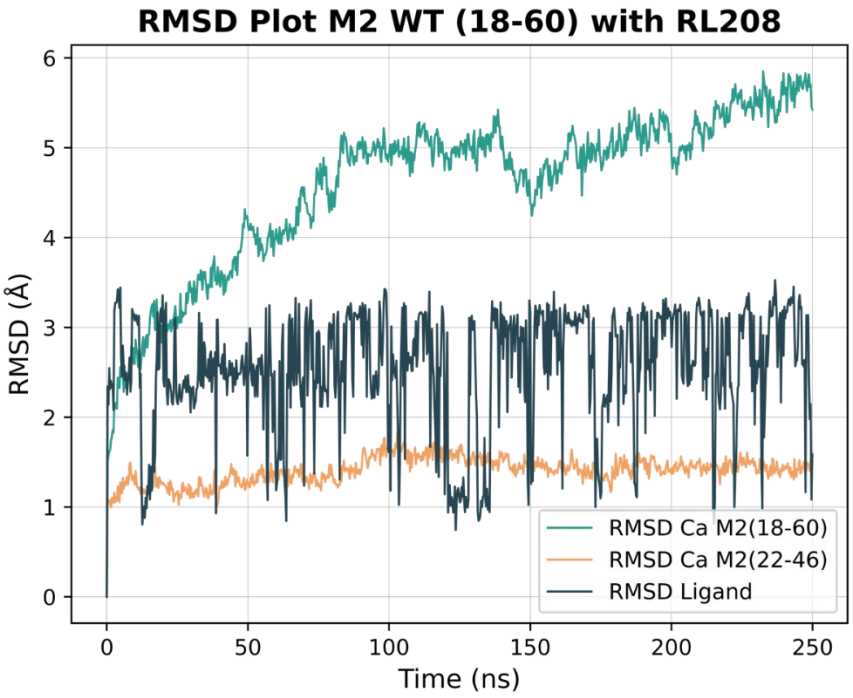

Figure S19 (contd.). RMSD(Ca) and RMSD(ligand) in the MD simulations of the WT apo-protein and in complex with RL208 during the 250ns-MD simulations with CHARMM36m force field.

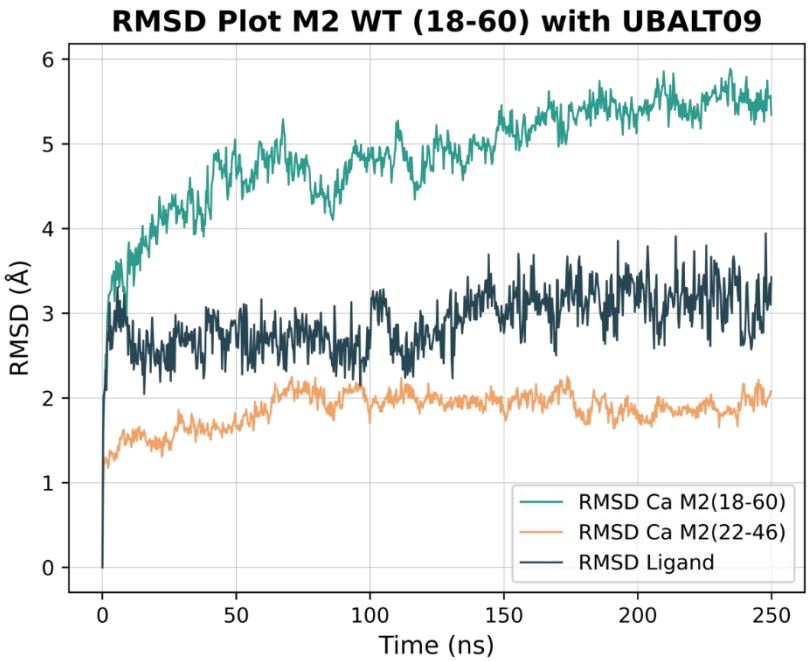

Figure S19 (contd.). RMSD(Ca) and RMSD(ligand) in the MD simulations of the WT apo-protein and in complex with UBALT09 during the 250ns-MD simulations with CHARMM36m force field.

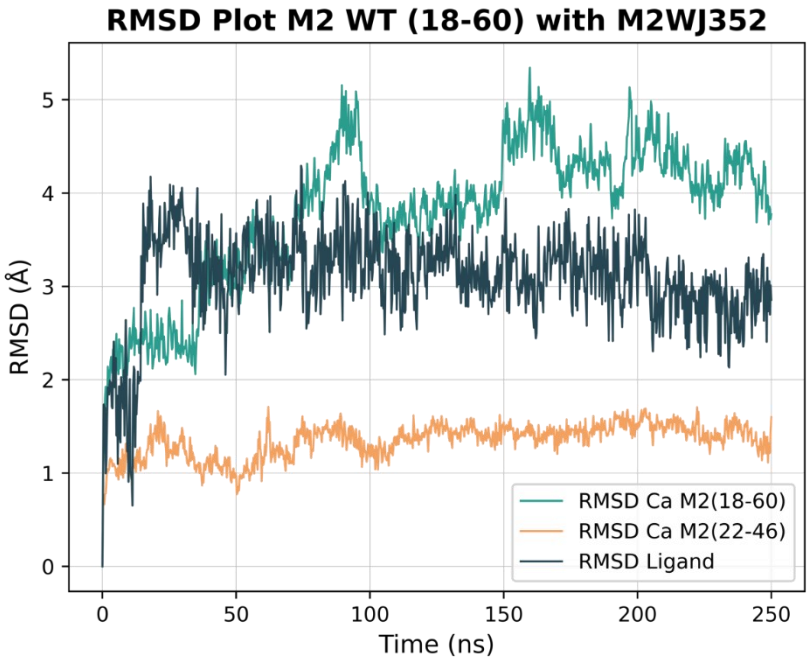

Figure S19 (contd.). RMSD(Ca) and RMSD(ligand) in the MD simulations of the WT apo-protein and in complex with M2WJ352 during the 250ns-MD simulations with CHARMM36m force field.

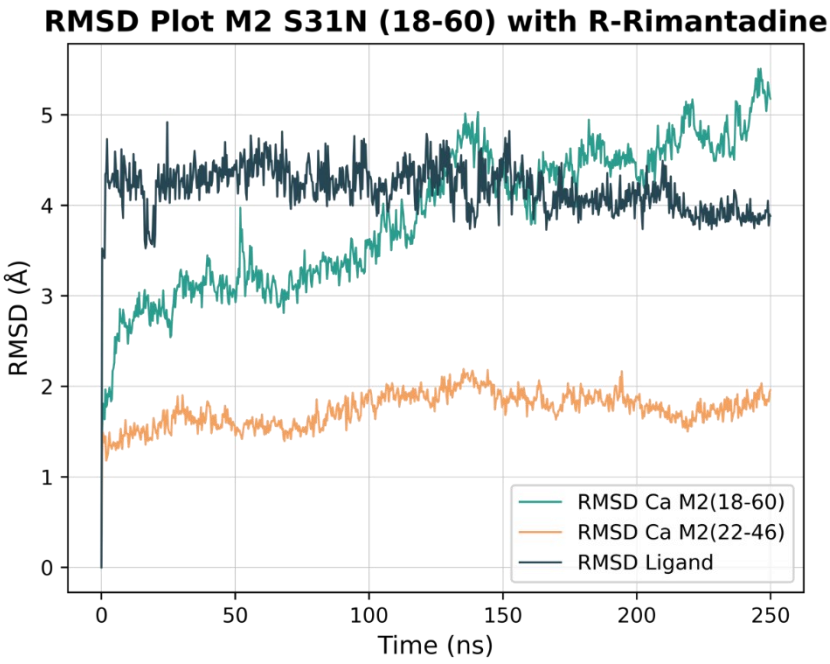

Figure S19 (contd.). RMSD(Ca) and RMSD(ligand) in the MD simulations of the S31N apo-protein and in complex with R-rimantadine during the 250ns-MD simulations with CHARMM36m force field.

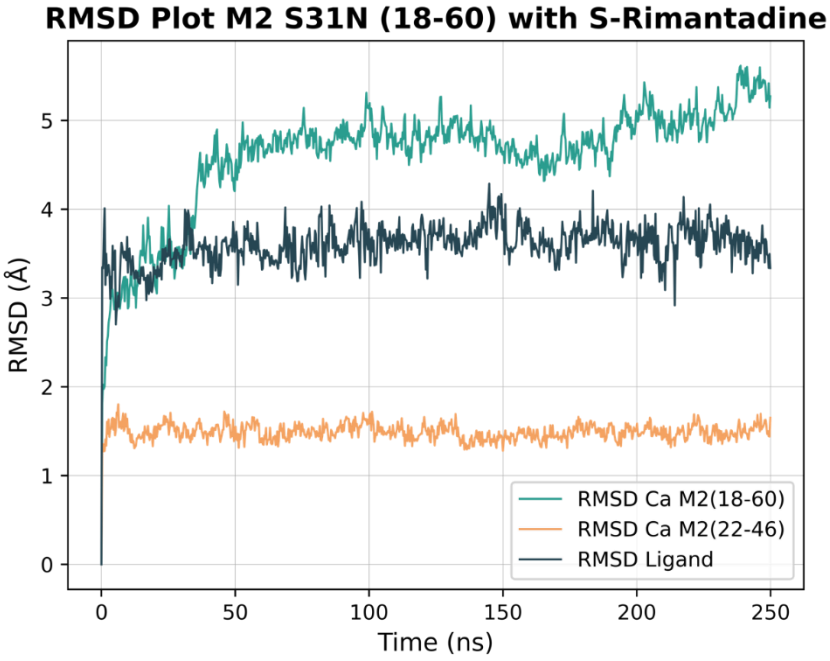

Figure S19 (contd.). RMSD(Ca) and RMSD(ligand) in the MD simulations of the S31N apo-protein and in complex with S-rimantadine during the 250ns-MD simulations with CHARMM36m force field.

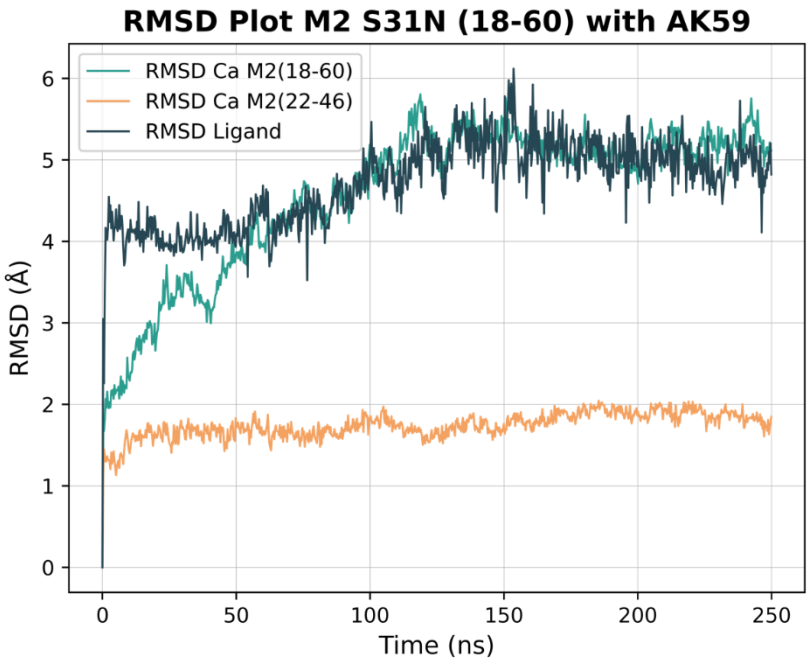

Figure S19 (contd.). RMSD(Ca) and RMSD(ligand) in the MD simulations of the S31N apo-protein and in complex with AK59 during the 250ns-MD simulations with CHARMM36m force field.

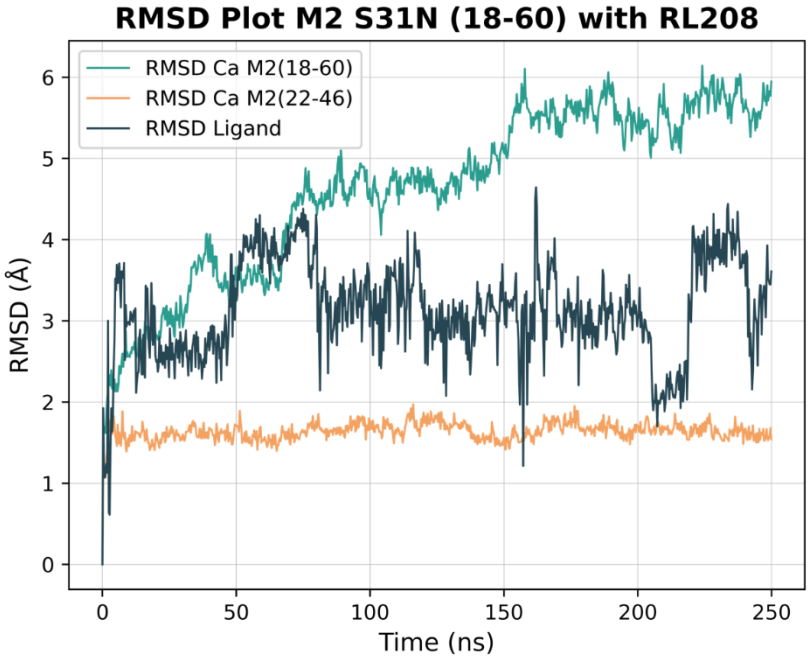

Figure S19 (contd.). RMSD(Ca) and RMSD(ligand) in the MD simulations of the S31N apo-protein and in complex with RL208 during the 250ns-MD simulations with CHARMM36m force field.

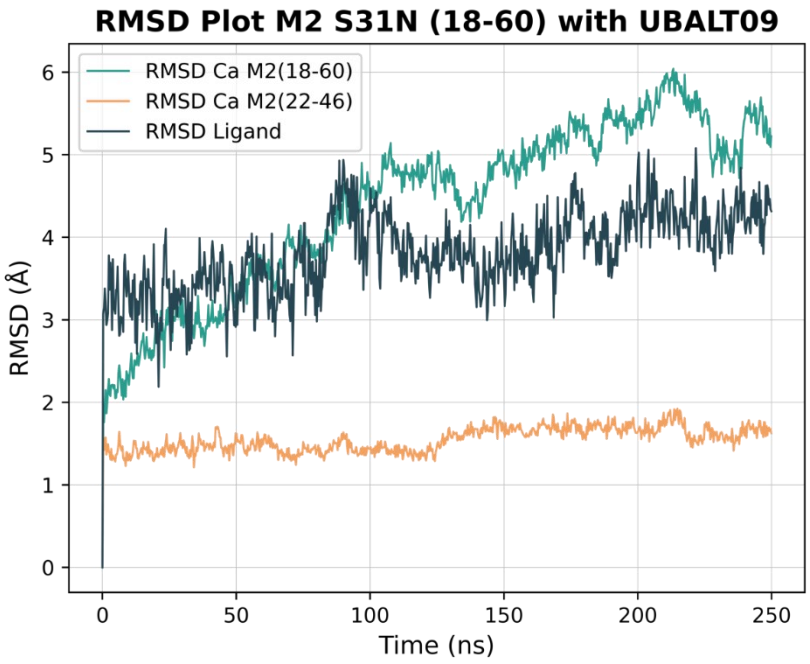

Figure S19 (contd.). RMSD(Ca) and RMSD(ligand) in the MD simulations of the S31N apo-protein and in complex with UBALT09 during the 250ns-MD simulations with CHARMM36m force field.

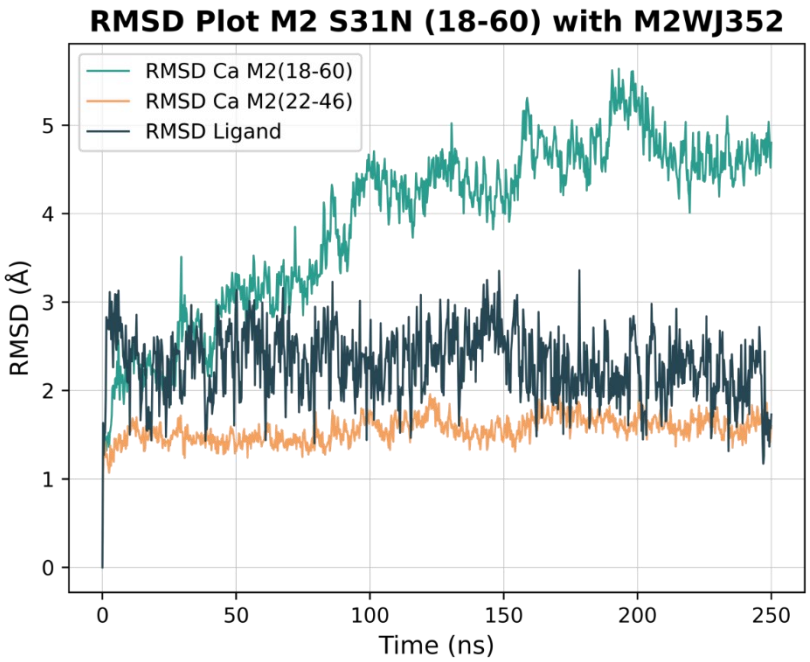

Figure S19 (contd.). RMSD(Ca) and RMSD(ligand) in the MD simulations of the S31N apo-protein and in complex with M2WJ352 during the 250ns-MD simulations with CHARMM36m force field.

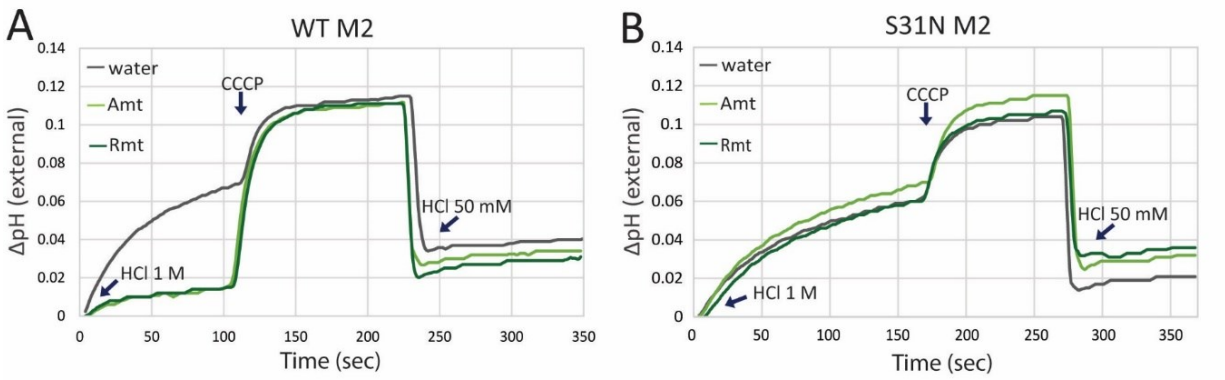

Figure S20 Liposomal proton flux assay applied to WT and S31N M2CD in the presence of Amt, Rmt. The 5-point moving average method was used to smoothen the data points of the curves. Time zero corresponds to the pH equilibration of the external solution at pH ~ 6.3 after the addition of 1 M HCl. M2CD activation and proton translocation into the liposome interior is shown as an increase of pH. Addition of proton uncoupler CCCP terminates the experiment. The buffering capacity of the system is evaluated by adding 50 mM HCl. (A), (B) Proton conduction of WT M2CD is strongly inhibited by 50 µM of Amt, Rmt. (C), (D) Proton conduction of S31N M2CD is not inhibited by any of the drugs tested. The time interval for measuring the proton conduction is extended in this case by 1 min.

8 References

1. Roth, G. A. *et al.* Global, regional, and national age-sex-specific mortality for 282 causes of death in 195 countries and territories, 1980–2017: a systematic analysis for the Global Burden of Disease Study 2017. *The Lancet* **392**, 1736–1788 (2018).
2. Marston, H. D., Folkers, G. K., Morens, D. M. & Fauci, A. S. Emerging Viral Diseases: Confronting Threats with New Technologies. *Sci Transl Med* **6**, (2014).
3. Morens, D. M. & Fauci, A. S. Emerging Infectious Diseases: Threats to Human Health and Global Stability. *PLoS Pathog* **9**, e1003467 (2013).
4. Baker, R. E. *et al.* Infectious disease in an era of global change. *Nature Reviews Microbiology 2021 20:4* **20**, 193–205 (2021).
5. Baker, R. E., Yang, W., Vecchi, G. A., Metcalf, C. J. E. & Grenfell, B. T. Assessing the influence of climate on wintertime SARS-CoV-2 outbreaks. *Nature Communications 2021 12:1* **12**, 1–7 (2021).
6. Mahmud, A. S., Martinez, P. P., He, J. & Baker, R. E. The Impact of Climate Change on Vaccine-Preventable Diseases: Insights From Current Research and New Directions. *Curr Environ Health Rep* **7**, 384–391 (2020).
7. Witek, T. J. How the Global COVID-19 Pandemic Brought Drug and Vaccine Development into the Public Mainstream. *Pharmaceut Med* **35**, 287 (2021).
8. Gully, P. R. Pandemics, regional outbreaks, and sudden-onset disasters. **33**, 164–169 (2020).
9. Walker, T. M. *et al.* The 2021 WHO catalogue of Mycobacterium tuberculosis complex mutations associated with drug resistance: a genotypic analysis. *Lancet Microbe* **3**, e265–e273 (2022).
10. Fogel, N. Tuberculosis: A disease without boundaries. *Tuberculosis* (2015).
11. Furin, J., Cox, H. & Pai, M. Tuberculosis. *The Lancet* **393**, 1642–1656 (2019).
12. Almeida Da Silva, P. E. & Palomino, J. C. Molecular basis and mechanisms of drug resistance in Mycobacterium tuberculosis: classical and new drugs. *Journal of Antimicrobial Chemotherapy* **66**, 1417–1430 (2011).
13. Mahesh S. Vasava, Sneha G. Nair, Sanjay K. Rathwa & Dhaval B. Patel. Development of new drug-regimens against multidrug-resistant tuberculosis. *Indian Journal of Tuberculosis* **66**, 12–19 (2019).
14. Aldridge, B. B. *et al.* The Tuberculosis Drug Accelerator at year 10: what have we learned? *Nature Medicine 2021 27:8* **27**, 1333–1337 (2021).
15. Dartois, V. A. & Rubin, E. J. Anti-tuberculosis treatment strategies and drug development: challenges and priorities. *Nature Reviews Microbiology 2022 20:11* **20**, 685–701 (2022).
16. Mdluli, K., Kaneko, T. & Upton, A. The Tuberculosis Drug Discovery and Development Pipeline and Emerging Drug Targets. *Cold Spring Harb Perspect Med* **5**, a021154--a021154 (2015).
17. Jackson, M. The mycobacterial cell envelope-lipids. *Cold Spring Harb Perspect Med* **4**, (2014).
18. Bansal-Mutalik, R. & Nikaido, H. Mycobacterial outer membrane is a lipid bilayer and the inner membrane is unusually rich in diacyl phosphatidylinositol dimannosides. *Proc Natl Acad Sci U S A* **111**, 4958–4963 (2014).

19. Lee, R. E. *et al.* Combinatorial Lead Optimization of [1,2]-DiaminesBased on Ethambutol as Potential Antituberculosis Preclinical Candidates. *J Comb Chem* **5**, 172–187 (2003).
20. Tahlan, K. *et al.* SQ109 Targets MmpL3, a Membrane Transporter of Trehalose Monomycolate Involved in Mycolic Acid Donation to the Cell Wall Core of Mycobacterium tuberculosis. *Antimicrob Agents Chemother* **56**, 1797–1809 (2012).
21. Grzegorzewicz, A. E. *et al.* Inhibition of mycolic acid transport across the Mycobacterium tuberculosis plasma membrane. *Nat Chem Biol* **8**, 334–341 (2012).
22. Zhang, B. *et al.* Crystal Structures of Membrane Transporter MmpL3, an Anti-TB Drug Target. *Cell* (2019).
23. Varela, C. *et al.* MmpL Genes Are Associated with Mycolic Acid Metabolism in Mycobacteria and Corynebacteria. *Chem Biol* **19**, 498–506 (2012).
24. Li, W. *et al.* Direct Inhibition of MmpL3 by Novel Antitubercular Compounds. *ACS Infect Dis* **5**, 1001–1012 (2019).
25. Belardinelli, J. M. *et al.* Structure–Function Profile of MmpL3, the Essential Mycolic Acid Transporter from Mycobacterium tuberculosis. *ACS Infect Dis* **2**, 702–713 (2016).
26. Su, C.-C. *et al.* MmpL3 is a lipid transporter that binds trehalose monomycolate and phosphatidylethanolamine. *Proc Natl Acad Sci USA* **116**, 11241–11246 (2019).
27. Bernut, A. *et al.* Insights into the smooth-to-rough transitioning in Mycobacterium bolletii unravels a functional Tyr residue conserved in all mycobacterial MmpL family members. *Mol Microbiol* **99**, 866–883 (2016).
28. Domenech, P., Reed, M. B. & Barry, C. E. Contribution of the Mycobacterium tuberculosis MmpL protein family to virulence and drug resistance. *Infect Immun* **73**, 3492–3501 (2005).
29. Adams, O. *et al.* Cryo-EM structure and resistance landscape of M. tuberculosis MmpL3: An emergent therapeutic target. *Structure* **29**, 1182-1191.e4 (2021).
30. Su, C. C. *et al.* Structures of the mycobacterial membrane protein MmpL3 reveal its mechanism of lipid transport. *PLoS Biol* **19**, e3001370 (2021).
31. Yang, X. *et al.* Structural Basis for the Inhibition of Mycobacterial MmpL3 by NITD-349 and SPIRO. *J Mol Biol* **432**, 4426–4434 (2020).
32. Carbone, J. *et al.* Inhibition Mechanism of Anti-TB Drug SQ109: Allosteric Inhibition of TMM Translocation of Mycobacterium Tuberculosis MmpL3 Transporter. *J Chem Inf Model* **63**, 5356–5374 (2023).
33. Li, W. *et al.* Novel insights into the mechanism of inhibition of MmpL3, a target of multiple pharmacophores in Mycobacterium tuberculosis. *Antimicrob Agents Chemother* **58**, 6413–6423 (2014).
34. Li, K. *et al.* Multitarget drug discovery for tuberculosis and other infectious diseases. *J Med Chem* **57**, 3126–3129 (2014).
35. Yang, T. *et al.* Amphiphilic Indole Derivatives as Antimycobacterial Agents: Structure-Activity Relationships and Membrane Targeting Properties. *J Med Chem* **60**, 2745–2763 (2017).
36. Feng, X. *et al.* Antiinfectives targeting enzymes and the proton motive force. *Proc Natl Acad Sci U S A* **112**, E7073–E7082 (2015).
37. Makobongo, M. O., Einck, L., Peek, R. M. & Merrell, D. S. In Vitro Characterization of the Anti-Bacterial Activity of SQ109 against Helicobacter pylori. *PLoS One* **8**, e68917 (2013).

38. Onajole, O. K. *et al.* SQ109 analogues as potential antimicrobial candidates. *Medicinal Chemistry Research* **20**, 1394–1401 (2011).
39. Reader, J. *et al.* Multistage and transmission-blocking targeted antimalarials discovered from the open-source MMV Pandemic Response Box. *Nat Commun* **12**, 269 (2021).
40. Veiga-Santos, P. *et al.* SQ109, a New Drug Lead for Chagas Disease. *Antimicrob Agents Chemother* **59**, 1950–1961 (2015).
41. Kirkwood, J. G. Statistical mechanics of fluid mixtures. *J Chem Phys* (1935).
42. Genheden, S., Nilsson, I. & Ryde, U. Binding Affinities of Factor Xa Inhibitors Estimated by Thermodynamic Integration and MM/GBSA. *J Chem Inf Model* **51**, 947–958 (2011).
43. He, X. *et al.* Fast, Accurate, and Reliable Protocols for Routine Calculations of Protein–Ligand Binding Affinities in Drug Design Projects Using AMBER GPU-TI with ff14SB/GAFF. *ACS Omega* **5**, 4611–4619 (2020).
44. Song, L. F., Lee, T.-S., Zhu, C., York, D. M. & Merz, K. M. Using AMBER18 for Relative Free Energy Calculations. *J Chem Inf Model* **59**, 3128–3135 (2019).
45. Prenner, E. & Chiu, M. Differential scanning calorimetry: An invaluable tool for a detailed thermodynamic characterization of macromolecules and their interactions. *J Pharm Bioall Sci* **3**, 39 (2011).
46. Pan, J. *et al.* Molecular structures of fluid phase phosphatidylglycerol bilayers as determined by small angle neutron and X-ray scattering. *Biochim Biophys Acta Biomembr* (2012).
47. Piret, J. & Boivin, G. Pandemics Throughout History. *Front Microbiol* **11**, (2021).
48. Park, E. K., Castrucci, M. R., Portner, A. & Kawaoka, Y. The M2 Ectodomain Is Important for Its Incorporation into Influenza A Virions. *J Virol* (1998).
49. Lamb, R. A., Zebedee, S. L. & Richardson, C. D. Influenza virus M2 protein is an integral membrane protein expressed on the infected-cell surface. *Cell* (1985).
50. Pinto, L. H., Holsinger, L. J. & Lamb, R. A. Influenza virus M2 protein has ion channel activity. *Cell* **69**, 517–528 (1992).
51. Chizhmakov, I. V. *et al.* Selective proton permeability and pH regulation of the influenza virus M2 channel expressed in mouse erythroleukaemia cells. *Journal of Physiology* **494**, 329–336 (1996).
52. Liang, R. *et al.* Acid activation mechanism of the influenza A M2 proton channel. *Proc Natl Acad Sci U S A* **113**, E6955–E6964 (2016).
53. Helenius, A. Unpacking the incoming influenza virus. *Cell* **69**, 577–578 (1992).
54. Lamb, R. A. & Choppin, P. W. The gene structure and replication of influenza virus. *Annu Rev Biochem* **52**, 467–506 (1983).
55. Sugrue, R. J. *et al.* Specific structural alteration of the influenza haemagglutinin by amantadine. *EMBO Journal* (1990).
56. Rossman, J. S., Jing, X., Leser, G. P. & Lamb, R. A. Influenza virus M2 protein mediates ESCRT-independent membrane scission. *Cell* **142**, 902–913 (2010).
57. Herneisen, A. L. *et al.* A Budding-Defective M2 Mutant Exhibits Reduced Membrane Interaction, Insensitivity to Cholesterol, and Perturbed Interdomain Coupling. *Biochemistry* **56**, (2017).
58. Rossman, J. S. & Lamb, R. A. Influenza virus assembly and budding. *Virology* **411**, 229–236 (2011).
59. Schnell, J. R. & Chou, J. J. Structure and mechanism of the M2 proton channel of influenza A virus. *Nature* **451**, 591–5 (2008).

60. Ma, C. *et al.* Identification of the functional core of the influenza A virus A/M2 proton-selective ion channel. *Proc Natl Acad Sci U S A* **106**, 12283–12288 (2009).
61. Hu, J. *et al.* Histidines, heart of the hydrogen ion channel from influenza A virus: Toward an understanding of conductance and proton selectivity. *Proc Natl Acad Sci U S A* (2006).
62. Pielak, R. M. & Chou, J. J. Influenza M2 proton channels. *Biochim Biophys Acta* **1808**, 522–529 (2011).
63. Sharma, M. *et al.* Insight into the mechanism of the influenza A proton channel from a structure in a lipid bilayer. *Science (1979)* **330**, 509–512 (2010).
64. Pinto, L. H. & Lamb, R. A. The M2 proton channels of influenza A and B viruses. *Journal of Biological Chemistry* vol. 281 8997–9000 (2006).
65. Wang, C., Lamb, R. A. & Pinto, L. H. Activation of the M2 ion channel of influenza virus: a role for the transmembrane domain histidine residue. *Biophys J* **69**, 1363–71 (1995).
66. Tang, Y., Zaitseva, F., Lamb, R. A. & Pinto, L. H. The gate of the influenza virus M2 proton channel is formed by a single tryptophan residue. *Journal of Biological Chemistry* **277**, 39880–39886 (2002).
67. Acharya, R. *et al.* Structure and mechanism of proton transport through the transmembrane tetrameric M2 protein bundle of the influenza A virus. *Proc Natl Acad Sci U S A* **107**, 15075–80 (2010).
68. Thomaston, J. L. *et al.* High-resolution structures of the M2 channel from influenza A virus reveal dynamic pathways for proton stabilization and transduction. *Proc Natl Acad Sci U S A* **112**, 14260–14265 (2015).
69. Williams, J. K., Zhang, Y., Schmidt-Rohr, K. & Hong, M. PH-dependent conformation, dynamics, and aromatic interaction of the gating tryptophan residue of the influenza M2 proton channel from solid-state NMR. *Biophys J* (2013).
70. Wang, C., Takeuchi, K., Pinto, L. H. & Lamb, R. A. Ion channel activity of influenza A virus M2 protein: characterization of the amantadine block. *J Virol* **67**, 5585–5594 (1993).
71. Jing, X. *et al.* Functional studies indicate amantadine binds to the pore of the influenza A virus M2 proton-selective ion channel. *Proc Natl Acad Sci U S A* **105**, 10967–10972 (2008).
72. Drakopoulos, A. *et al.* Affinity of Rimantadine Enantiomers against Influenza A/M2 Protein Revisited. *ACS Med Chem Lett* **8**, 145–150 (2017).
73. Cady, S. D. *et al.* Structure of the amantadine binding site of influenza M2 proton channels in lipid bilayers. *Nature 2010 463:7281* **463**, 689–692 (2010).
74. Stouffer, A. L. *et al.* Structural basis for the function and inhibition of an influenza virus proton channel. *Nature 2008 451:7178* **451**, 596–599 (2008).
75. Kolocouris, N. *et al.* Synthesis and antiviral activity evaluation of some aminoadamantane derivatives. *J Med Chem* **37**, 2896–2902 (1994).
76. Rey-Carrizo, M. *et al.* Easily accessible polycyclic amines that inhibit the wild-type and amantadine-resistant mutants of the M2 channel of influenza A virus. *J Med Chem* **57**, 5738–5747 (2014).
77. Wang, J. *et al.* Exploring the requirements for the hydrophobic scaffold and polar amine in inhibitors of M2 from influenza A virus. *ACS Med Chem Lett* **2**, 307–312 (2011).
78. Kolocouris, A. *et al.* Aminoadamantanes with persistent in vitro efficacy against H1N1 (2009) influenza A. *J Med Chem* **57**, 4629–4639 (2014).

79. Wang, J. *et al.* Molecular Dynamics (MD) Simulation Directed Rational Design of Inhibitors Targeting Drug-Resistant Mutants of Influenza A Virus M2. *J Am Chem Soc* 12834–12841 (2011).
80. Tzitzoglaki, C. *et al.* Binding and Proton Blockage by Amantadine Variants of the Influenza M2WT and M2S31N Explained. *J Med Chem* **60**, 1716–1733 (2017).
81. Garcia, V. & Aris-Brosou, S. Comparative dynamics and distribution of influenza drug resistance acquisition to protein M2 and neuraminidase inhibitors. *Mol Biol Evol* **31**, 355–363 (2014).
82. Schmidtke, M. *et al.* Amantadine resistance among porcine H1N1, H1N2, and H3N2 influenza a viruses isolated in Germany between 1981 and 2001. *Intervirology* **49**, 286–293 (2006).
83. Krumbholz, A. *et al.* High prevalence of amantadine resistance among circulating European porcine in fluenza A viruses. *Journal of General Virology* **90**, 900–908 (2009).
84. Principi, N. *et al.* Drugs for Influenza Treatment: Is There Significant News? *Front Med (Lausanne)* **6**, (2019).
85. Wang, J. *et al.* Discovery of Novel Dual Inhibitors of the Wild-Type and the Most Prevalent Drug-Resistant Mutant, S31N, of the M2 Proton Channel from Influenza A Virus. *J Med Chem* **56**, 2804–2812 (2013).
86. Wu, Y. *et al.* Flipping in the pore: Discovery of dual inhibitors that bind in different orientations to the wild-type versus the amantadine-resistant s31n mutant of the influenza a virus m2 proton channel. *J Am Chem Soc* **136**, 17987–17995 (2014).
87. Hu, Y. *et al.* Structure-Property Relationship Studies of Influenza A Virus AM2-S31N Proton Channel Blockers. *ACS Med Chem Lett* **9**, 1111–1116 (2018).
88. Wang, Y. *et al.* In Vitro Pharmacokinetic Optimizations of AM2-S31N Channel Blockers Led to the Discovery of Slow-Binding Inhibitors with Potent Antiviral Activity against Drug-Resistant Influenza A Viruses. *J Med Chem* **61**, 1074–1085 (2018).
89. Wang, J. *et al.* Structure and inhibition of the drug-resistant S31N mutant of the M2 ion channel of influenza A virus. *Proc Natl Acad Sci U S A* **110**, 1315–1320 (2013).
90. Andreas, L. B., Eddy, M. T., Pielak, R. M., Chou, J. & Griffin, R. G. Magic Angle Spinning NMR Investigation of Influenza A M218−60 : Support for an Allosteric Mechanism of Inhibition. *J Am Chem Soc* **132**, 10958–10960 (2010).
91. Colvin, M. T., Andreas, L. B., Chou, J. J. & Griffin, R. G. Proton Association Constants of His 37 in the Influenza-A M2 18–60 Dimer-of-Dimers. *Biochemistry* **53**, 5987–5994 (2014).
92. Hu, J. *et al.* Backbone structure of the amantadine-blocked trans-membrane domain M2 proton channel from influenza A virus. *Biophys J* **92**, 4335–4343 (2007).
93. Wang, J., Kim, S., Kovacs, F. & Cross, T. A. Structure of the transmembrane region of the M2 protein H+ channel. *Protein Sci* **10**, 2241 (2001).
94. Wright, A. K., Paulino, J. & Cross, T. A. Emulating Membrane Protein Environments-How Much Lipid Is Required for a Native Structure: Influenza S31N M2. *J Am Chem Soc* **144**, 2137–2148 (2022).
95. Cady, S., Wang, T. & Hong, M. Membrane-dependent effects of a cytoplasmic helix on the structure and drug binding of the influenza virus M2 protein. *J Am Chem Soc* **133**, 11572–11579 (2011).
96. Pielak, R. M., Oxenoid, K. & Chou, J. J. Structural investigation of rimantadine inhibition of the AM2-BM2 chimera channel of influenza viruses. *Structure* **19**, 1655–1663 (2011).

97. Thomaston, J. L. *et al.* Inhibitors of the M2 proton channel engage and disrupt transmembrane networks of hydrogen-bonded waters. *J Am Chem Soc* 15219–15226 (2018).
98. Movellan, K. T., Dervişoğlu, R., Becker, S. & Andreas, L. B. Pore-Bound Water at the Key Residue Histidine 37 in Influenza A M2. *Angewandte Chemie - International Edition* (2021).
99. Andreas, L. B., Eddy, M. T., Chou, J. J. & Griffin, R. G. Magic-Angle-Spinning NMR of the Drug Resistant S31N M2 Proton Transporter from Influenza A. *J Am Chem Soc* **134**, 7215–7218 (2012).
100. Colvin, M. T., Andreas, L. B., Chou, J. J. & Griffin, R. G. Proton association constants of his 37 in the influenza-A M218-60dimer-of-dimers. *Biochemistry* **53**, 5987–5994 (2014).
101. Stampolaki, M. *et al.* A Study of the Activity of Adamantyl Amines against Mutant Influenza A M2 Channels Identified a Polycyclic Cage Amine Triple Blocker, Explored by Molecular Dynamics Simulations and Solid-State NMR**. *ChemMedChem* (2023).
102. Movellan, K. T. *et al.* Imidazole-Imidazole Hydrogen Bonding in the pH-Sensing Histidine Side Chains of Influenza A M2. *J Am Chem Soc* **142**, 2704–2708 (2020).
103. Andreas, L. B. *et al.* Dynamic Nuclear Polarization Study of Inhibitor Binding to the M2 18–60 Proton Transporter from Influenza A. *Biochemistry* **52**, 2774–2782 (2013).
104. Thomaston, J. L. *et al.* Rimantadine Binds to and Inhibits the Influenza A M2 Proton Channel without Enantiomeric Specificity. *Biochemistry* **60**, 2471–2482 (2021).
105. Thomaston, J. L. *et al.* X-ray Crystal Structures of the Influenza M2 Proton Channel Drug-Resistant V27A Mutant Bound to a Spiro-Adamantyl Amine Inhibitor Reveal the Mechanism of Adamantane Resistance. *Biochemistry* **59**, 627–634 (2020).
106. Ioannidis, H. *et al.* Alchemical Free Energy Calculations and Isothermal Titration Calorimetry Measurements of Aminoadamantanes Bound to the Closed State of Influenza A/M2TM. *J Chem Inf Model* **56**, (2016).
107. Kolokouris, D., Kalenderoglou, I. E. & Kolocouris, A. Inside and out of the Pore: Comparing Interactions and Molecular Dynamics of Influenza A M2 Viroporin Complexes in Standard Lipid Bilayers. *J Chem Inf Model* **61**, 5550–5568 (2021).
108. Tzitzoglaki, C. *et al.* Chemical Probes for Blocking of Influenza A M2 Wild-type and S31N Channels. *ACS Chem Biol* **15**, 2331–2337 (2020).
109. Drakopoulos, A. *et al.* Unraveling the Binding, Proton Blockage, and Inhibition of Influenza M2 WT and S31N by Rimantadine Variants. *ACS Med Chem Lett* **9**, 198–203 (2018).
110. Miao, Y., Fu, R., Zhou, H. X. & Cross, T. A. Dynamic Short Hydrogen Bonds in Histidine Tetrad of Full-Length M2 Proton Channel Reveal Tetrameric Structural Heterogeneity and Functional Mechanism. *Structure* **23**, 2300–2308 (2015).
111. Fu, R., Miao, Y., Qin, H. & Cross, T. A. Observation of the Imidazole-Imidazolium Hydrogen Bonds Responsible for Selective Proton Conductance in the Influenza A M2 Channel. *J Am Chem Soc* **142**, 2115–2119 (2020).
112. Tekwani Movellan, K. *et al.* Real-time tracking of drug binding to influenza A M2 reveals a high energy barrier. *J Struct Biol X* **8**, (2023).
113. Andreas, L. B. *et al.* Structure and Mechanism of the Influenza A M218-60 Dimer of Dimers. *J Am Chem Soc* **137**, 14877–14886 (2015).
114. Cady, S. D., Wang, J., Wu, Y., Degrado, W. F. & Hong, M. Specific binding of adamantane drugs and direction of their polar amines in the pore of the influenza M2

transmembrane domain in lipid bilayers and dodecylphosphocholine micelles determined by NMR spectroscopy. *J Am Chem Soc* **133**, 4274–4284 (2011).
115. Williams, J. K. *et al.* Drug-induced conformational and dynamical changes of the S31N mutant of the influenza M2 proton channel investigated by solid-state NMR. *J Am Chem Soc* **135**, 9885–9897 (2013).
116. Watkins, L. C., Degrado, W. F. & Voth, G. A. Influenza A M2 Inhibitor Binding Understood through Mechanisms of Excess Proton Stabilization and Channel Dynamics. *J Am Chem Soc* **142**, 17425–17433 (2020).
117. Hu, J., Fu, R. & Cross, T. A. The Chemical and Dynamical Influence of the Anti-Viral Drug Amantadine on the M2 Proton Channel Transmembrane Domain. *Biophys J* **93**, 276–283 (2007).
118. Wright, A. K. *et al.* Differential Binding of Rimantadine Enantiomers to Influenza A M2 Proton Channel. *J Am Chem Soc* **138**, 1506–1509 (2016).
119. Leiva, R. *et al.* Pharmacological and Electrophysiological Characterization of Novel NMDA Receptor Antagonists. *ACS Chem Neurosci* (2018).
120. Stampolaki, M. *et al.* A Study of the Activity of Adamantyl Amines against Mutant Influenza A M2 Channels Identified a Polycyclic Cage Amine Triple Blocker, Explored by Molecular Dynamics Simulations and Solid-State NMR. *ChemMedChem* e202300182 (2023).
121. Meng, Q., Luo, H., Chen, Y., Wang, T. & Yao, Q. Synthesis of novel [1,2]-diamines with antituberculosis activity. *Bioorg Med Chem Lett* **19**, 5372–5375 (2009).
122. Onajole, O. K. *et al.* Synthesis and evaluation of SQ109 analogues as potential anti-tuberculosis candidates. *Eur J Med Chem* **45**, 2075–2079 (2010).
123. Li, K. *et al.* Oxa, Thia, Heterocycle, and Carborane Analogues of SQ109: Bacterial and Protozoal Cell Growth Inhibitors. *ACS Infect Dis* **1**, 215–221 (2015).
124. Stampolaki, M. & Kolocouris, A. Improved Synthesis of the Antitubercular Agent SQ109. *SynOpen* **5**, 321–326 (2021).
125. Galaka, T. *et al.* Antiparasitic activity of sulfur- and fluorine-containing bisphosphonates against trypanosomatids and apicomplexan parasites. *Molecules* **22**, 1–22 (2017).
126. Shallu, Sharma, M. L. & Singh, J. First total synthesis of a guanidine alkaloid Nitensidine D using immobilized ionic liquid, microwaves and formamidinesulfinic acid. *Journal of Chemical Sciences* **126**, 1869–1874 (2014).
127. Dogra, S., Sharma, M. L. & Singh, J. Comparative study of chemically immobilized and conventional homogeneous ionic liquids as phase-transfer catalysts for the N-alkylation of heterocyclic compounds. *Comptes Rendus Chimie* **18**, 945–953 (2015).
128. Buxton, C. A., Hachey, D. L. & Leresche, J. P. Deamination of Nerylamine and Geranylamine. *Journal of Organic Chemistry* **37**, 4036–4039 (1972).
129. Corky, E. J., Nicolaoi, K. C., Balanson, R. D. & Machida, Y. A useful method for the conversion of azides to amines. *Synthesis (Germany)* **1975**, 590–591 (1975).
130. Gololobov, Y. G., Zhmurova, I. N. & Kasukhin, L. F. Sixty years of staudinger reaction. *Tetrahedron* **37**, 437–472 (1981).
131. Bednarek, C., Wehl, I., Jung, N., Schepers, U. & Bräse, S. The Staudinger Ligation. *Chem Rev* **120**, 4301–4354 (2020).
132. Murahashi, S. I., Taniguchi, Y., Imada, Y. & Tanigawa, Y. Palladium(0)-Catalyzed Azidation of Allyl Esters. Selective Synthesis of Allyl Azides, Primary Allylamines, and Related Compounds. *Journal of Organic Chemistry* **54**, 3292–3303 (1989).

133. Ravinder, B., Rajeswar Reddy, S., Panasa Reddy, A. & Bandichhor, R. Amide activation by TMSCl: reduction of amides to amines by LiAlH4 under mild conditions. *Tetrahedron Lett* **54**, 4908–4913 (2013).
134. Becke, A. D. Density-functional thermochemistry. III. The role of exact exchange. *J Chem Phys* **98**, 5648–5652 (1993).
135. Lee, C., Yang, W. & Parr, R. G. Development of the Colle-Salvetti correlation-energy formula into a functional of the electron density. *Phys Rev B* (1988).
136. Francl, M. M. *et al.* Self-consistent molecular orbital methods. XXIII. A polarization-type basis set for second-row elements. *J Chem Phys* (1982).
137. Grimme, S., Ehrlich, S. & Goerigk, L. Effect of the damping function in dispersion corrected density functional theory. *J Comput Chem* **32**, 1456–1465 (2011).
138. Tomasi, J., Mennucci, B. & Cammi, R. Quantum Mechanical Continuum Solvation Models. *Chem Rev* (2005).
139. York, D. M. & Karplus, M. A smooth solvation potential based on the conductor-like screening model. *Journal of Physical Chemistry A* (1999).
140. Weast, R. C. Handbook of chemistry and physics. *Am J Med Sci* **49**, (1969).
141. Peach, M. L., Cachau, R. E. & Nicklaus, M. C. Conformational energy range of ligands in protein crystal structures: The difficult quest for accurate understanding. *Journal of Molecular Recognition* **30**, e2618 (2017).
142. Robertson, M. J., Meyerowitz, J. G., Panova, O., Borrelli, K. & Skiniotis, G. Plasticity in ligand recognition at somatostatin receptors. *Nature Structural & Molecular Biology 2022 29:3* **29**, 210–217 (2022).
143. Fusani, L., Palmer, D. S., Somers, D. O. & Wall, I. D. Exploring Ligand Stability in Protein Crystal Structures Using Binding Pose Metadynamics. *J Chem Inf Model* **60**, 1528–1539 (2020).
144. Malde, A. K. & Mark, A. E. Challenges in the determination of the binding modes of non-standard ligands in X-ray crystal complexes. *J Comput Aided Mol Des* **25**, 1–12 (2011).
145. van Zundert, G. C. P., Moriarty, N. W., Sobolev, O. V., Adams, P. D. & Borrelli, K. W. Macromolecular refinement of X-ray and cryoelectron microscopy structures with Phenix/OPLS3e for improved structure and ligand quality. *Structure* **29**, 913-921.e4 (2021).
146. Eldridge, M. D., Murray, C. W., Auton, T. R., Paolini, G. V. & Mee, R. P. Empirical scoring functions: I. The development of a fast empirical scoring function to estimate the binding affinity of ligands in receptor complexes. *J Comput Aided Mol Des* **11**, 425–445 (1997).
147. Maier, J. A. *et al.* ff14SB: Improving the Accuracy of Protein Side Chain and Backbone Parameters from ff99SB. *J Chem Theory Comput* **11**, 3696–3713 (2015).
148. Massova, I. & Kollman, P. A. Combined molecular mechanical and continuum solvent approach (MM- PBSA/GBSA) to predict ligand binding. *Perspectives in Drug Discovery and Design* vol. 18 113–135 (2000).
149. Weng, G. *et al.* Assessing the performance of MM/PBSA and MM/GBSA methods. 9. Prediction reliability of binding affinities and binding poses for protein-peptide complexes. *Physical Chemistry Chemical Physics* **21**, 10135–10145 (2019).
150. Wang, E. *et al.* End-Point Binding Free Energy Calculation with MM/PBSA and MM/GBSA: Strategies and Applications in Drug Design. *Chem Rev* **119**, 9478–9508 (2019).

151. Rizzo, R. C. & Jorgensen, W. L. OPLS all-atom model for amines: Resolution of the amine hydration problem. *J Am Chem Soc* **121**, 4827–4836 (1999).
152. Greene, D., Qi, R., Nguyen, R., Qiu, T. & Luo, R. Heterogeneous Dielectric Implicit Membrane Model for the Calculation of MMPBSA Binding Free Energies. *J Chem Inf Model* **59**, 3041–3056 (2019).
153. Botello-Smith, W. M. *et al.* Numerical Poisson-Boltzmann model for continuum membrane systems. *Chem Phys Lett* (2013).
154. Botello-Smith, W. M. & Luo, R. Applications of MMPBSA to Membrane Proteins I: Efficient Numerical Solutions of Periodic Poisson-Boltzmann Equation. *J Chem Inf Model* **55**, 2187–2199 (2015).
155. Xiao, L., Diao, J., Greene, D., Wang, J. & Luo, R. A Continuum Poisson-Boltzmann Model for Membrane Channel Proteins. *J Chem Theory Comput* (2017).
156. Aldeghi, M., Bodkin, M. J., Knapp, S. & Biggin, P. C. Statistical Analysis on the Performance of Molecular Mechanics Poisson-Boltzmann Surface Area versus Absolute Binding Free Energy Calculations: Bromodomains as a Case Study. *J Chem Inf Model* **57**, 2203–2221 (2017).
157. Genheden, S. & Ryde, U. The MM/PBSA and MM/GBSA methods to estimate ligand-binding affinities. *Expert Opin Drug Discov* **10**, 449–461 (2015).
158. Stampolaki, M. *et al.* Synthesis and Testing of Analogs of the Tuberculosis Drug Candidate SQ109 against Bacteria and Protozoa: Identification of Lead Compounds against Mycobacterium abscessus and Malaria Parasites. *ACS Infect Dis* (2023).
159. Pohorille, A., Jarzynski, C. & Chipot, C. Good Practices in Free-Energy Calculations. *J Phys Chem B* **114**, 10235–10253 (2010).
160. Lee, T. S. *et al.* Alchemical binding free energy calculations in AMBER20: Advances and best practices for drug discovery. *J Chem Inf Model* (2020).
161. Cournia, Z., Allen, B. & Sherman, W. Relative Binding Free Energy Calculations in Drug Discovery: Recent Advances and Practical Considerations. *J Chem Inf Model* **57**, 2911–2937 (2017).
162. Lenselink, E. B. *et al.* Predicting Binding Affinities for GPCR Ligands Using Free-Energy Perturbation. *ACS Omega* **1**, 293–304 (2016).
163. Deflorian, F. *et al.* Accurate prediction of GPCR ligand binding affinity with free energy perturbation. *J Chem Inf Model* **60**, 5563–5579 (2020).
164. Matricon, P. *et al.* Fragment optimization for GPCRs by molecular dynamics free energy calculations: Probing druggable subpockets of the A 2A adenosine receptor binding site. *Scientific Reports 2017 7:1* **7**, 1–12 (2017).
165. Wan, S. *et al.* Hit-to-lead and lead optimization binding free energy calculations for G protein-coupled receptors. *Interface Focus* **10**, (2020).
166. Keränen, H., Åqvist, J. & Gutiérrez-De-Terán, H. Free energy calculations of A2A adenosine receptor mutation effects on agonist binding. *Chemical Communications* **51**, 3522–3525 (2015).
167. Stampelou, M. *et al.* Dual A1/A3 Adenosine Receptor Antagonists: Binding Kinetics and Structure-Activity Relationship Studies Using Mutagenesis and Alchemical Binding Free Energy Calculations. *J Med Chem* **65**, 13305–13327 (2022).
168. Procacci, P. Multiple Bennett acceptance ratio made easy for replica exchange simulations. *J Chem Phys* **139**, 124105 (2013).

169. Tzitzoglaki, C. *et al.* Approaches to primary tert-alkyl amines as building blocks. *Tetrahedron* **75**, 130408 (2019).
170. Xie, J. *et al.* Allosteric Inhibitors of SHP2 with Therapeutic Potential for Cancer Treatment. *J Med Chem* **60**, 10205–10219 (2017).
171. Raynaud, C. *et al.* Active Benzimidazole Derivatives Targeting the MmpL3 Transporter in Mycobacterium abscessus. *ACS Infect Dis* **6**, 324–337 (2020).
172. Malwal, S. R. *et al.* Structure, in Vivo Detection, and Antibacterial Activity of Metabolites of SQ109, an Anti-Infective Drug Candidate. *ACS Infect Dis* **7**, 2492–2507 (2021).
173. Johansen, M. D., Herrmann, J. L. & Kremer, L. Non-tuberculous mycobacteria and the rise of Mycobacterium abscessus. *Nature Reviews Microbiology 2020 18:7* **18**, 392–407 (2020).
174. Sacksteder, K. A., Protopopova, M., Barry, C. E., Andries, K. & Nacy, C. A. Discovery and development of SQ109: a new antitubercular drug with a novel mechanism of action. *Future Microbiol* **7**, 823–837 (2012).
175. García-García, V., Oldfield, E. & Benaim, G. Inhibition of Leishmania mexicana growth by the tuberculosis drug SQ109. *Antimicrob Agents Chemother* **60**, 6386–6389 (2016).
176. Gil, Z. *et al.* SQ109 inhibits proliferation of Leishmania donovani by disruption of intracellular Ca2+ homeostasis, collapsing the mitochondrial electrochemical potential (ΔΨm) and affecting acidocalcisomes. *Parasitol Res* **119**, 649–657 (2020).
177. Jia, L. *et al.* Pharmacodynamics and pharmacokinetics of SQ109, a new diamine-based antitubercular drug. *Br J Pharmacol* **144**, 80 (2005).
178. Jia, L. *et al.* Interspecies pharmacokinetics and in vitro metabolism of SQ109. *Br J Pharmacol* **147**, 476–485 (2006).
179. Baek, K.-H. *et al.* In Vivo Efficacy of SQ109 against Leishmania donovani, Trypanosoma spp. and Toxoplasma gondii and In Vitro Activity of SQ109 Metabolites. *Biomedicines* **10**, 670 (2022).
180. de Bruyn Kops, C. *et al.* GLORY: Generator of the structures of likely cytochrome P450 metabolites based on predicted sites of metabolism. *Front Chem* **7**, 462655 (2019).
181. Stork, C. *et al.* NERDD: a web portal providing access to in silico tools for drug discovery. *Bioinformatics* **36**, 1291–1292 (2020).
182. Zaretzki, J., Matlock, M. & Swamidass, S. J. XenoSite: Accurately predicting cyp-mediated sites of metabolism with neural networks. *J Chem Inf Model* **53**, 3373–3383 (2013).
183. Rydberg, P., Gloriam, D. E., Zaretzki, J., Breneman, C. & Olsen, L. SMARTCyp: A 2D method for prediction of cytochrome P450-mediated drug metabolism. *ACS Med Chem Lett* **1**, 96–100 (2010).
184. Heinrich, N. *et al.* Early phase evaluation of SQ109 alone and in combination with rifampicin in pulmonary TB patients. *Journal of Antimicrobial Chemotherapy* **70**, 1558–1566 (2015).
185. Shetty, A. *et al.* Novel Acetamide Indirectly Targets Mycobacterial Transporter MmpL3 by Proton Motive Force Disruption. *Front Microbiol* **9**, 2960 (2018).
186. Xu, Z., Meshcheryakov, V. A., Poce, G. & Chng, S.-S. MmpL3 is the flippase for mycolic acids in mycobacteria. *Proceedings of the National Academy of Sciences* **114**, 7993–7998 (2017).

187. Viljoen, A. *et al.* The diverse family of MmpL transporters in mycobacteria: from regulation to antimicrobial developments. *Mol Microbiol* **104**, 889–904 (2017).
188. Grimme, S., Antony, J., Ehrlich, S. & Krieg, H. A consistent and accurate ab initio parametrization of density functional dispersion correction (DFT-D) for the 94 elements H-Pu. *J Chem Phys* **132**, 154104 (2010).
189. Dupont, C. *et al.* A new piperidinol derivative targeting mycolic acid transport in Mycobacterium abscessus. *Mol Microbiol* **101**, 515–529 (2016).
190. Delcour, A. H. Outer membrane permeability and antibiotic resistance. *Biochim Biophys Acta* **1794**, 808–816 (2009).
191. Clifton, L. A. *et al.* Asymmetric phospholipid: lipopolysaccharide bilayers; a Gram-negative bacterial outer membrane mimic. *J R Soc Interface* **10**, (2013).
192. McMullen, T. P. W., Lewis, R. N. A. H. & McElhaney, R. N. Calorimetric and spectroscopic studies of the effects of cholesterol on the thermotropic phase behavior and organization of a homologous series of linear saturated phosphatidylglycerol bilayer membranes. *Biochimica et Biophysica Acta (BBA) - Biomembranes* **1788**, 345–357 (2009).
193. Cong, W., Liu, Q., Liang, Q., Wang, Y. & Luo, G. Investigation on the interactions between pirarubicin and phospholipids. *Biophys Chem* **143**, 154–160 (2009).
194. Rowat, A. C., Keller, D. & Ipsen, J. H. Effects of farnesol on the physical properties of DMPC membranes. *Biochimica et Biophysica Acta (BBA) - Biomembranes* **1713**, 29–39 (2005).
195. Chapman, D. & Urbina, J. Biomembrane Phase Transitions STUDIES OF LIPID-WATER SYSTEMS USING DIFFERENTIAL SCANNING CALORIMETRY. *J Biol Chem* **249**, 2512–2521 (1974).
196. Frisch, M., Trucks, G., Schlegel, H. & Scuseria, G. Gaussian 03, revision C. 02; Gaussian, Inc.: Wallingford, CT, 2004. (2013).
197. Halgren, T. T. A. Merck molecular force field. I. Basis, form, scope, parameterization, and performance of MMFF94. *J Comput Chem* **17**, 490–519 (1996).
198. Shelley, J. C. *et al.* Epik: a software program for pK a prediction and protonation state generation for drug-like molecules. *Journal of Computer-Aided Molecular Design* vol. 21 681–691 Preprint at (2007).
199. Sastry, G. M., Adzhigirey, M., Day, T., Annabhimoju, R. & Sherman, W. Protein and ligand preparation: parameters, protocols, and influence on virtual screening enrichments. *J. Comput. Aided Mol. Des.* **27**, 221–234 (2013).
200. Jorgensen, W. L., Maxwell, D. S. & Tirado-Rives, J. Development and Testing of the OPLS All-Atom Force Field on Conformational Energetics and Properties of Organic Liquids. *J Am Chem Soc* **118**, 11225–11236 (1996).
201. Kaminski, G. A., Friesner, R. A., Tirado-Rives, J. & Jorgensen, W. L. Comparison with Accurate Quantum Chemical Calculations on Peptides. *Quantum* (2001).
202. Mohamadi, F. *et al.* Macromodel?an integrated software system for modeling organic and bioorganic molecules using molecular mechanics. *J Comput Chem* **11**, 440–467 (1990).
203. Jones, G., Willett, P., Glen, R. C., Leach, a R. & Taylor, R. Development and validation of a genetic algorithm for flexible docking. *J Mol Biol* **267**, 727–748 (1997).
204. Pettersen, E. F. *et al.* UCSF Chimera - A visualization system for exploratory research and analysis. *J Comput Chem* **25**, 1605–1612 (2004).

205. Lomize, M. A., Pogozheva, I. D., Joo, H., Mosberg, H. I. & Lomize, A. L. OPM database and PPM web server: resources for positioning of proteins in membranes. *Nucleic Acids Res* **40**, D370–D376 (2012).
206. Jorgensen, W. L., Chandrasekhar, J., Madura, J. D., Impey, R. W. & Klein, M. L. Comparison of simple potential functions for simulating liquid water. *J Chem Phys* **79**, 926–935 (1983).
207. Wang, J., Wolf, R. M., Caldwell, J. W., Kollman, P. A. & Case, D. A. Development and testing of a general Amber force field. *J Comput Chem* **25**, 1157–1174 (2004).
208. Bayly, C. I., Cieplak, P., Cornell, W. D. & Kollman, P. A. A well-behaved electrostatic potential based method using charge restraints for deriving atomic charges: The RESP model. *Journal of Physical Chemistry* **97**, 10269–10280 (1993).
209. D.A. Case *et al. AMBER 2018, University of California*. *University of California, San Francisco* (2018).
210. Koynova, R. & Caffrey, M. Phases and phase transitions of the phosphatidylcholines. *Biochimica et Biophysica Acta (BBA) - Reviews on Biomembranes* **1376**, 91–145 (1998).
211. Darden, T., York, D. & Pedersen, L. Particle mesh Ewald: An Nlog(N) method for Ewald sums in large systems. *J Chem Phys* **98**, 10089–10092 (1993).
212. Essmann, U. *et al.* A smooth particle mesh Ewald method. *J Chem Phys* **103**, 8577–8593 (1995).
213. Ryckaert, J. P., Ciccotti, G. & Berendsen, H. J. C. Numerical integration of the cartesian equations of motion of a system with constraints: molecular dynamics of n-alkanes. *J Comput Phys* **23**, 327–341 (1977).
214. Martyna, G. J., Klein, M. L. & Tuckerman, M. Nosé–Hoover chains: The canonical ensemble via continuous dynamics. *J Chem Phys* **97**, 2635–2643 (1992).
215. Martyna, G. J., Tobias, D. J. & Klein, M. L. Constant pressure molecular dynamics algorithms. *J Chem Phys* **101**, 4177–4189 (1994).
216. Humphreys, D. D., Friesner, R. A. & Berne, B. J. A Multiple-Time-Step Molecular Dynamics Algorithm for Macromolecules. *J Phys Chem* **98**, 6885–6892 (1994).
217. Maffucci, I. & Contini, A. Explicit ligand hydration shells improve the correlation between MM-PB/GBSA binding energies and experimental activities. *J Chem Theory Comput* **9**, 2706–2717 (2013).
218. Michaud-Agrawal, N., Denning, E. J., Woolf, T. B. & Beckstein, O. MDAnalysis: A toolkit for the analysis of molecular dynamics simulations. *J Comput Chem* **32**, 2319–2327 (2011).
219. Banks, J. L. *et al.* Integrated Modeling Program, Applied Chemical Theory (IMPACT). *J Comput Chem* **26**, 1752–1780 (2005).
220. Qiu, D., Shenkin, P. S., Hollinger, F. P. & Still, W. C. The GB/SA Continuum Model for Solvation. A Fast Analytical Method for the Calculation of Approximate Born Radii. *J Phys Chem A* **101**, 3005–3014 (1997).
221. Gohlke, H., Case, D. A., Biology, M., Scripps, T. & Rd, N. T. P. Converging Free Energy Estimates : MM-PB (GB) SA Studies on the Protein – Protein Complex Ras – Raf. 238–250 (2003).
222. Steinbrecher, T., Joung, I. & Case, D. A. Soft-core potentials in thermodynamic integration: Comparing one- and two-step transformations. *J Comput Chem* **32**, 3253–3263 (2011).

223. Shirts, M. R. & Pande, V. S. Comparison of efficiency and bias of free energies computed by exponential averaging, the Bennett acceptance ratio, and thermodynamic integration. *Journal of Chemical Physics* **122**, 144107 (2005).
224. Paliwal, H. & Shirts, M. R. A benchmark test set for alchemical free energy transformations and its use to quantify error in common free energy methods. *J Chem Theory Comput* (2011).
225. Tan, Z., Gallicchio, E., Lapelosa, M. & Levy, R. M. Theory of binless multi-state free energy estimation with applications to protein-ligand binding. *Journal of Chemical Physics* (2012).
226. Lee, T.-S., Hu, Y., Sherborne, B., Guo, Z. & York, D. M. Toward Fast and Accurate Binding Affinity Prediction with pmemdGTI: An Efficient Implementation of GPU-Accelerated Thermodynamic Integration. *J Chem Theory Comput* **13**, 3077–3084 (2017).
227. Lzaguirre, J. A., Catarello, D. P., Wozniak, J. M. & Skeel, R. D. Langevin stabilization of molecular dynamics. *Journal of Chemical Physics* **114**, 2090–2098 (2001).
228. Feller, S. E., Zhang, Y., Pastor, R. W. & Brooks, B. R. Constant pressure molecular dynamics simulation: The Langevin piston method. *J Chem Phys* **103**, 4613 (1995).
229. Berendsen, H. J. C., Postma, J. P. M., Van Gunsteren, W. F., Dinola, A. & Haak, J. R. Molecular dynamics with coupling to an external bath. *J Chem Phys* **81**, 3684–3690 (1984).
230. Su, P.-C. & Johnson, M. E. Evaluating thermodynamic integration performance of the new amber molecular dynamics package and assess potential halogen bonds of enoyl-ACP reductase (FabI) benzimidazole inhibitors. *J Comput Chem* **37**, 836–847 (2016).
231. Leshabane, M. *et al.* Benzimidazole Derivatives Are Potent against Multiple Life Cycle Stages of Plasmodium falciparum Malaria Parasites. *ACS Infect Dis* **7**, 1945–1955 (2021).
232. Verlinden, B. K. *et al.* Discovery of novel alkylated (bis)urea and (bis)thiourea polyamine analogues with potent antimalarial activities. *J Med Chem* **54**, 6624–6633 (2011).
233. Grzegorzewicz, A. E. *et al.* Assembling of the Mycobacterium tuberculosis cell wall core. *Journal of Biological Chemistry* **291**, 18867–18879 (2016).
234. Tikhonova, E. B., Dastidar, V., Rybenkov, V. V. & Zgurskaya, H. I. Kinetic control of TolC recruitment by multidrug efflux complexes. *Proc Natl Acad Sci U S A* **106**, 16416–16421 (2009).
235. Guros, N. B., Balijepalli, A. & Klauda, J. B. The Role of Lipid Interactions in Simulations of the α-Hemolysin Ion-Channel-Forming Toxin. *Biophys J* **115**, 1720–1730 (2018).
236. Cristian, L., Lear, J. D. & DeGrado, W. F. Use of thiol-disulfide equilibria to measure the energetics of assembly of transmembrane helices in phospholipid bilayers. *Proceedings of the National Academy of Sciences* **100**, 14772–14777 (2003).
237. Salom, D., Hill, B. R., Lear, J. D. & DeGrado, W. F. pH-dependent tetramerization and amantadine binding of the transmembrane helix of M2 from the influenza A virus. *Biochemistry* **39**, 14160–14170 (2000).
238. K. Wright, A., Paulino, J. & A. Cross, T. Emulating Membrane Protein Environments─How Much Lipid Is Required for a Native Structure: Influenza S31N M2. *J Am Chem Soc* **144**, 2137–2148 (2022).
239. Liao, S. Y., Lee, M. & Hong, M. Interplay between membrane curvature and protein conformational equilibrium investigated by solid-state NMR. *J Struct Biol* (2019).

240. Hu, F., Schmidt-Rohr, K. & Hong, M. NMR detection of pH-dependent histidine-water proton exchange reveals the conduction mechanism of a transmembrane proton channel. *J Am Chem Soc* **134**, 3703–3713 (2012).
241. Paschke, R., Mohr Swantje, Lange Sascha & Kozuch Jacek. *In-situ spectroscopic detection of large-scale reorientations of transmembrane α-helices during viroporin channel opening*. (2023).
242. Kolocouris, A., Hansen, R. K. & Broadhurst, R. W. Interaction between an amantadine analogue and the transmembrane portion of the influenza A M2 protein in liposomes probed by 1H NMR spectroscopy of the ligand. *J Med Chem* **47**, (2004).
243. Friesner, R. A. *et al.* Extra precision glide: Docking and scoring incorporating a model of hydrophobic enclosure for protein-ligand complexes. *J Med Chem* **49**, 6177–6196 (2006).
244. Best, R. B. *et al.* Optimization of the additive CHARMM all-atom protein force field targeting improved sampling of the backbone φ, ψ and side-chain χ1 and χ2 Dihedral Angles. *J Chem Theory Comput* **8**, 3257–3273 (2012).
245. Sherman, W., Day, T., Jacobson, M. P., Friesner, R. A. & Farid, R. Novel procedure for modeling ligand/receptor induced fit effects. *J Med Chem* **49**, 534–553 (2006).
246. Huang, J. & Mackerell, A. D. CHARMM36 all-atom additive protein force field: Validation based on comparison to NMR data. *J Comput Chem* **34**, 2135–2145 (2013).
247. Gleed, M. L. & Busath, D. D. Why bound amantadine fails to inhibit proton conductance according to simulations of the drug-resistant influenza A M2 (S31N). *Journal of Physical Chemistry B* **119**, 1225–1231 (2015).
248. Gleed, M. L., Ioannidis, H., Kolocouris, A. & Busath, D. D. Resistance-Mutation (N31) Effects on Drug Orientation and Channel Hydration in Amantadine-Bound Influenza A M2. *Journal of Physical Chemistry B* **119**, 11548–11559 (2015).
249. Pielak, R. M., Schnell, J. R. & Chou, J. J. Mechanism of drug inhibition and drug resistance of influenza A M2 channel. *Proc Natl Acad Sci U S A* **106**, 7379–7384 (2009).
250. Hong, M., Fritzsching, K. J. & Williams, J. K. Hydrogen-bonding partner of the proton-conducting histidine in the influenza M2 proton channel revealed from 1H chemical shifts. *J Am Chem Soc* **134**, 14753–14755 (2012).
251. Torres, E. *et al.* Synthesis and anti-influenza a virus activity of 2,2-dialkylamantadines and related compounds. *ACS Med Chem Lett* **3**, 1065–1069 (2012).
252. Barniol-Xicota, M. *et al.* Slow but Steady Wins the Race: Dissimilarities among New Dual Inhibitors of the Wild-Type and the V27A Mutant M2 Channels of Influenza A Virus. *J Med Chem* **60**, 3727–3738 (2017).
253. Torres, E. *et al.* Azapropellanes with anti-influenza a virus activity. *ACS Med Chem Lett* (2014).
254. Rey-Carrizo, M. *et al.* New polycyclic dual inhibitors of the wild type and the V27A mutant M2 channel of the influenza A virus with unexpected binding mode. *Eur J Med Chem* **96**, 318–329 (2015).
255. Rey-carrizo, M. *et al.* 3-azatetracyclo[5.2.1.15,8.01,5]undecane Derivatives: From wild-type inhibitors of the M2 ion channel of influenza A virus to derivatives with potent activity against the V27A mutant. *J Med Chem* **56**, 9265–9274 (2013).
256. Tzitzoglaki, C. *et al.* Amantadine variant – aryl conjugates that inhibit multiple M2 mutant – amantadine resistant influenza a viruses. *European Journal of Medicinal Chemistry Reports* **6**, 100083 (2022).

257. Schmidt, N. W., Mishra, A., Wang, J., Degrado, W. F. & Wong, G. C. L. Influenza virus A M2 protein generates negative gaussian membrane curvature necessary for budding and scission. *J Am Chem Soc* **135**, 13710–13719 (2013).
258. Thomaston, J. L. & DeGrado, W. F. Crystal structure of the drug-resistant S31N influenza M2 proton channel. *Protein Sci* **25**, 1551–4 (2016).
259. Thomaston, J. L. *et al.* X-ray Crystal Structure of the Influenza A M2 Proton Channel S31N Mutant in Two Conformational States: An Open and Shut Case. *J Am Chem Soc* **141**, 11481–11488 (2019).
260. Wang, J., Schnell, J. R. & Chou, J. J. Amantadine partition and localization in phospholipid membrane: a solution NMR study. *Biochem Biophys Res Commun* **324**, 212–217 (2004).
261. B. Andreas, L. *et al.* Structure and Mechanism of the Influenza A M218–60 Dimer of Dimers. *J Am Chem Soc* **137**, 14877–14886 (2015).
262. Vinod Chandran, C., Madhu, P. K., Kurur, N. D. & Bräuniger, T. Swept-frequency two-pulse phase modulation (SWf-TPPM) sequences with linear sweep profile for heteronuclear decoupling in solid-state NMR. *Magnetic Resonance in Chemistry* **46**, 943–947 (2008).
263. Shaka, A. J., Keeler, J. & Freeman, R. Evaluation of a new broadband decoupling sequence: WALTZ-16. *Journal of Magnetic Resonance (1969)* **53**, 313–340 (1983).
264. Zhou, D. H. & Rienstra, C. M. High-performance solvent suppression for proton detected solid-state NMR. *J Magn Reson* **192**, 167–172 (2008).
265. T. D. Goddard & D. G. Kneller. SPARKY 3, University of California, San Francisco.
266. Verdonk, M. L. *et al.* Modeling water molecules in protein-ligand docking using GOLD. *J Med Chem* **48**, 6504–6515 (2005).
267. Pettersen, E. F. *et al.* UCSF Chimera—A visualization system for exploratory research and analysis. *J Comput Chem* **25**, 1605–1612 (2004).
268. Pastor, R. W. & MacKerell, A. D. Development of the CHARMM force field for lipids. *Journal of Physical Chemistry Letters* **2**, 1526–1532 (2011).
269. Klauda, J. B. *et al.* Update of the CHARMM All-Atom Additive Force Field for Lipids: Validation on Six Lipid Types. *Journal of Physical Chemistry B* **114**, 7830–7843 (2010).
270. Zoete, V., Cuendet, M. A., Grosdidier, A. & Michielin, O. SwissParam: A fast force field generation tool for small organic molecules. *J Comput Chem* **32**, 2359–2368 (2011).
271. MacKerell, A. D., Feig, M. & Brooks, C. L. Improved Treatment of the Protein Backbone in Empirical Force Fields. *J Am Chem Soc* **126**, 698–699 (2004).
272. Bowers, K. J. *et al.* Scalable Algorithms for Molecular Dynamics Simulations on Commodity Clusters. 43–43 (2007).
273. Darden, T., York, D. & Pedersen, L. Particle mesh Ewald: An N·log(N) method for Ewald sums in large systems. *J Chem Phys* **98**, 10089–10092 (1993).
274. Kollman, P. A. *et al.* Calculating structures and free energies of complex molecules: Combining molecular mechanics and continuum models. *Acc Chem Res* **33**, 889–897 (2000).
275. And, G. A. K., Friesner*, R. A., And, J. T.-R. & Jorgensen, W. L. Evaluation and Reparametrization of the OPLS-AA Force Field for Proteins via Comparison with Accurate Quantum Chemical Calculations on Peptides†. (2001).

276. Wang, J., Cieplak, P. & Kollman, P. A. How Well Does a Restrained Electrostatic Potential (RESP) Model Perform in Calculating Conformational Energies of Organic and Biological Molecules? *J Comput Chem* **21**, 1049–1074 (2000).
277. Hornak, V. *et al.* Comparison of multiple amber force fields and development of improved protein backbone parameters. *Proteins: Structure, Function and Genetics* vol. 65 712–725 (2006).
278. Gruppo, V. *et al.* Rapid Microbiologic and Pharmacologic Evaluation of Experimental Compounds against Mycobacterium tuberculosis. *Antimicrob Agents Chemother* **50**, 1245 (2006).
279. Hoffman, A. E. *et al.* Co(II) and Cu(II) pyrophosphate complexes have selectivity and potency against Mycobacteria including Mycobacterium tuberculosis. *Eur J Med Chem* **70**, 589–593 (2013).
280. Woods, G. L. *et al.* Susceptibility Testing of Mycobacteria, Nocardiae, and Other Aerobic Actinomycetes. *Susceptibility Testing of Mycobacteria, Nocardiae, and Other Aerobic Actinomycetes* (2011).
281. Bowling, T., Mercer, L., Don, R., Jacobs, R. & Nare, B. Application of a resazurin-based high-throughput screening assay for the identification and progression of new treatments for human African trypanosomiasis. *Int J Parasitol Drugs Drug Resist* **2**, 262–270 (2012).
282. Hu, F., Luo, W. & Hong, M. Mechanisms of proton conduction and gating in influenza M2 proton channels from solid-state NMR. *Science (1979)* **330**, 505–508 (2010).
283. Shivakumar, D. *et al.* Prediction of Absolute Solvation Free Energies using Molecular Dynamics Free Energy Perturbation and the OPLS Force Field. *J Chem Theory Comput* **6**, 1509–1519 (2010).